The Whisper and the Bang: Cosmic fireworks in the lives of compact binaries

Thesis by
Kishalay De

In Partial Fulfillment of the Requirements for the
Degree of
Doctor of Philosophy

CALIFORNIA INSTITUTE OF TECHNOLOGY
Pasadena, California

2021
Defended April 23, 2021

Kishalay De
ORCID: 0000-0002-8989-0542

For Bapi, Mummy, Bublu and Tabbu

ACKNOWLEDGEMENTS

This thesis is a culmination of generous help, support and advice from some of the most wonderful people in my life, who I would like to thank:

I must begin by expressing my gratitude to my advisor, Mansi Kasliwal, who introduced me to the enigmatic world of astrophysical transients and guided me to become the scientist I am today. I recall the day when I discussed possible research topics with Mansi during my first year of graduate school, and she offered me a multitude of projects. With each project being as exciting as everything else – it was a problem of choice! I'm honored to have had the opportunity to be closely involved with many of those topics in my pursuit of understanding the transient universe. Your excitement for astrophysical discoveries have been a constant source of inspiration in this journey.

I am grateful to Shrinivas Kulkarni, who was extremely patient with my style of working in graduate school, and providing me constant wisdom to look at the bigger landscape in astronomy outside of individual projects. I sincerely appreciate Shri's advice and encouragement for expanding into X-ray astronomy, for organizing bi-weekly (virtual) coffee sessions during the pandemic, and for organizing a set of excellent lectures in X-ray astronomy.

The members of my thesis committee, Jim Fuller for enlightening discussions on theoretical aspects of transient phenomena, Gregg Hallinan for his insights into radio transients and synergies with radio surveys, and Chuck Steidel for stimulating discussions on infrared detectors and image processing. I would like to thank Lynne Hillenbrand for offering constant support during graduate school as well as a fun outlook on the plethora of Galactic transients and variables found by Palomar Gattini-IR (PGIR).

To the amazing PGIR team, who made possible the challenging engineering aspects of a remarkably fast infrared telescope – Matt Hankins, for sharing the difficult task of creating a completely robotic survey from telescope operations to data pipeline; Michael Ashley, for incredible help with setting up the survey and fascinating discussions on infrared detectors and robotic telescopes; Eran Ofek, for crucial insights into the mathematics of astronomical image processing; Anna Moore, Tony Travouillon and Jamie Soon for their incredible role in designing and setting up the hardware for the survey; Aliya Babul, Jeno Sokoloski, Ryan Lau and Roberto Soria

for enlightening discussions on the transient infrared universe.

To the PGIR engineering team at the Caltech Optical Observatories: Roger Smith, Dan McKenna, Timothee Greffe, David Hale, Alexandre Delacroix, Richard Dekany, Jill Burnham for their crucial role in designing the hardware for PGIR, and for their constant enthusiasm in helping me learn about the system.

To the members of the ZTF Theory Network – Lars Bildsten, Abigail Polin, Sterl Phinney, Eliot Quataert, Dan Kasen, and Peter Nugent, who offered insightful advice and guidance on transients from ZTF and PGIR. This thesis would not have been possible without the generous contributions and insights from all the senior members of the larger Caltech time domain group – Christoffer Fremling, Igor Andreoni, Scott Adams, Dmitry Duev, Michael Coughlin, Danny Goldstein, Lin Yan, Ashish Mahabal, Matthew Graham, Tom Prince. Thank you for teaching me the ropes of time domain astronomy in the initial years of graduate school and for your mentorship throughout this period.

To members of the amazing iPTF and ZTF collaborations for helping me learn the physics of supernova explosions, and offering excellent advice to support my scientific interests. I would like to thank Avishay Gal-Yam, Ragnhild Lunnan and Jesper Sollerman for teaching me fundamentals of supernova classification, pre-supernova mass loss and thermonuclear supernovae; to Adam Miller, Ofer Yaron, Steve Schulze and Daniel Perley for your support of my projects. I extend my warm thanks to the entire astrophysics group at Weizmann for hosting me multiple times during my thesis as I learned the physics of supernovae and the nuts and bolts of image processing. And to the larger group of the GROWTH collaboration who have helped me grow as a researcher with numerous stimulating discussions and talks.

The delightful cohort of graduate students made Caltech a really special experience. Thank you to Jacob Jencson, Anna Ho, Kaew Tinyanont, Yuhan Yao, Shreya Anand, Viraj Karambelkar and Yashvi Sharma for their friendship, and making the time domain group such an exciting and welcoming environment. I was fortunate to have joined with a remarkable class of students – Chris Bochenek, Lee Rosenthal, Dillon Dong, Nikita Kamraj, Jason Sun and Michael Zhang, who made solving homework so much fun during the first year and offered a friendly hand throughout graduate school. Thank you to my office mates over the years – Kevin Burdge, Marin Anderson, Mia de los Reyes, Ryan Rubenzahl, Ivanna Escala for making work at Cahill such a fun experience and teaching me about coffee. And to the larger group of graduate students at Caltech who've been wonderful companions in this journey.

Finally, I have been lucky to work with some extremely talented undergraduate researchers Andy Tzanidakis, Gokul Srinivasaragavan, Manasi Sharma, Thomas Waters, Sharne Sun and Aishwarya Dahiwale who have helped me learn astronomy with their amazing insights. And thank you to my roommates during my stay – Jash Banker, Michael Curi and Ali Palla, for bearing with awkward working hours during observing runs and for making Pasadena a friendly home.

This work would not have been possible without the excellent technical work of many people. I am thankful to Patrick Shopbell, Anu Mahabal and Carl Smay for their efforts in maintaining the Cahill IT systems, and for enthusiastically helping with numerous aspects of the PGIR data system. Palomar Observatory lies at the heart of my thesis, and I'm grateful to the staff at Palomar for their hard work in keeping Palomar running (even during the pandemic) – John Baker, Carolyn Heffner, Kajsa Peffer and Kevin Rykoski. Finally, I have been fortunate to spend a large amount of time observing on the mighty Keck telescopes in Hawaii, and owe thanks to several Support Astronomers for hosting me and helping me learn about the instruments – Percy Gomez, Luca Rizzi, Josh Walawander and Randy Campbell.

I end by thanking the people whose mentorship earlier in my career enabled me to reach here – Yashwant Gupta, Prateek Sharma, Gabriele Ponti, Indranil Chattopadhyay and Jeewan Pandey. And to the companionship of some of my oldest friends from college and high school – Debaditya, Sayak, Sandip, Amlan, Tamoghna, Mayukh, Subhendu, Sabareesh, Kaivalya, Atif, Akash, with whom I've shared some of the most fun memories over the last few years, and whose support helped me persevere through difficult times.

It goes without saying that my family is the reason I am here today. My grandfather was an inspiration to me for the fruits of hard work and dedication, and for his enthusiastic support of my childhood interests in the stars. I do not have words to express my gratitude to my brother and sister for their never-ending support, to my mother for her unconditional love and sacrifices to get me here today. And to my father, who was the reason why I got interested in staring at the skies and the physics of the universe – starting from his curiosity about the most basic TV antennas! I hope this thesis makes you proud.

ABSTRACT

Compact binaries, comprising of a white dwarf, neutron star or black hole in a tight orbit around another star are produced from binary evolution through a complex range of astrophysical processes – ranging from eruptive mass loss episodes ('the whisper') to spectacular explosions ('the bang') that have shaped the universe as we see it today. In pursuit of a complete road-map of the explosive lives of high mass and low mass stars in compact binaries, I undertook two major experiments.

In the first two parts of this thesis, I describe the largest volume-limited supernova classification experiment undertaken till date, using the Zwicky Transient Facility optical time domain survey. I present the identification of a new class of 'ultra-stripped' supernovae that form neutron stars in compact binary systems, that are likely direct progenitors of merging neutron stars detectable in LIGO/Virgo. Using the systematic sample of supernovae, I identify a class of helium shell explosions on low mass white dwarfs that likely represent the final fates of helium accreting white dwarfs. In the third part of this thesis, I present the development of Palomar Gattini-IR (PGIR), the first wide-field infrared survey capable of studying the dynamic infrared sky from timescales of seconds to years. I present a systematic search for nova eruptions in the Milky Way using PGIR, and show that optical surveys have systematically missed a large fraction of dust obscured novae to derive the first quantitative estimate of the Galactic nova rate. I present the first infrared constraints on the second-timescale emission from a Galactic Fast Radio Burst identified with a dust obscured Galactic magnetar.

This thesis helps set the stage for a systematic exploration of the local stellar graveyard using i) the Vera Rubin Observatory to probe the lowest luminosity stellar deaths in the local universe and ii) the upcoming assemblage of infrared surveys to study variability in Galactic compact objects in conjunction with the rich landscape of X-ray and radio sky surveys. By mapping out the demographics of explosive phenomena, it helps us interpret the astrophysical populations detectable with current and future gravitational wave observatories.

PUBLISHED CONTENT AND CONTRIBUTIONS

De, K. et al. (2021a). "A Population of Heavily Reddened, Optically Missed Novae from Palomar Gattini-IR: Constraints on the Galactic Nova Rate". In: *ApJ* 912.19, 20, p. 20. DOI: 10.3847/1538-4357/abeb75. arXiv: 2101.04045 [astro-ph.HE].
KDE led the pipeline and filter development that enabled the discovery of the transients, carried out observing programs for their characterization, contributed to data acquisition and analysis, and wrote the manuscript.

De, K. et al. (2021b). "The Peculiar Ca-rich SN2019ehk: Evidence for a Type IIb Core-collapse Supernova from a Low-mass Stripped Progenitor". In: *ApJL* 907.1, L18, p. L18. DOI: 10.3847/2041-8213/abd627. arXiv: 2009.02347 [astro-ph.HE].
KDE contributed to the program that led to the identification of the transient, contributed to data acquisition and analysis, and wrote the manuscript.

De, K. et al. (2020a). "Constraining the X-Ray-Infrared Spectral Index of Second-timescale Flares from SGR 1935+2154 with Palomar Gattini-IR". In: *ApJL* 901.1, L7, p. L7. DOI: 10.3847/2041-8213/abb3c5. arXiv: 2007.02978 [astro-ph.HE].
KDE wrote the pipeline for processing data from the specific mode, analyzed the data, and wrote the manuscript.

De, K. et al. (2020b). "Palomar Gattini-IR: Survey Overview, Data Processing System, On-sky Performance and First Results". In: *PASP* 132.1008, 025001, p. 025001. DOI: 10.1088/1538-3873/ab6069. arXiv: 1910.13319 [astro-ph.IM].
KDE led the development of the data pipeline of the survey, contributed to survey commissioning, robotic operations, and characterization of the survey performance, and wrote the manuscript.

De, K. et al. (2020c). "The Zwicky Transient Facility Census of the Local Universe. I. Systematic Search for Calcium-rich Gap Transients Reveals Three Related Spectroscopic Subclasses". In: *ApJ* 905.1, 58, p. 58. DOI: 10.3847/1538-4357/abb45c.
KDE contributed to the filter that led to the identification of the transients, carried out observing programs for their characterization, contributed to data acquisition, reduction, and analysis, and wrote the manuscript.

De, K. et al. (2019). "ZTF 18aaqeasu (SN2018byg): A Massive Helium-shell Double Detonation on a Sub-Chandrasekhar-mass White Dwarf". In: *ApJL* 873.2, L18, p. L18. DOI: 10.3847/2041-8213/ab0aec. arXiv: 1901.00874 [astro-ph.HE].
KDE contributed to the filter that led to the identification of the transient, carried out the observing program for its characterization, contributed to data acquisition, reduction, and analysis, and wrote the manuscript.

De, K. et al. (2018a). "iPTF 16hgs: A Double-peaked Ca-rich Gap Transient in a Metal-poor, Star-forming Dwarf Galaxy". In: *ApJ* 866.1, 72, p. 72. DOI: 10.3847/1538-4357/aadf8e. arXiv: 1806.10623 [astro-ph.HE].
KDE carried out multi-wavelength observing programs for the characterization of the transient, contributed to data reduction and analysis, and wrote the manuscript.

De, K. et al. (2018b). "A Hot and Fast Ultra-stripped Supernova that Likely Formed a Compact Neutron Star Binary". In: *Science* 362.6411, pp. 201–206. DOI: 10.1126/science.aas8693. arXiv: 1810.05181 [astro-ph.HE].
KDE contributed to data acquisition, reduction, and analysis, and wrote the manuscript.

TABLE OF CONTENTS

LIST OF ILLUSTRATIONS

LIST OF TABLES

Chapter 1

INTRODUCTION

1.1 Stellar binarity and fireworks

For stars born in isolation, the initial mass of the star (M_i) and its composition (characterized by its metallicity Z) decides its final fate when it runs out of fuel in its core. In the canonical picture of stellar evolution, low mass stars ($M_i \lesssim 8\,\mathrm{M}_\odot$) evolve into compact white dwarfs (WDs) supported by electron degeneracy pressure, with more massive stars evolving into carbon-oxygen (CO) WDs while the lowest mass stars evolve into helium (He) WDs. On the other hand, the most massive stars ($M_i \gtrsim 10\,\mathrm{M}_\odot$) are believed to leave behind[1] neutron stars (NSs) or black holes (BHs) with or without a magnificent supernova (SN) explosion at the end of their lives (Heger et al., 2003). The role of initial stellar composition is the most striking for the most massive stars, where wind mass loss (driven by metal opacity) plays a critical role in determining the amount of mass left over at the time of the SN, and thus the nature of the compact object (Woosley et al., 2002).

Fortunately, the universe is much more creative with regards to the fates of stars. Multiplicity is a fundamental property of the star formation process, and the binary fraction is estimated to be $\approx 40-60\%$ for solar mass stars (Raghavan et al., 2010), while it goes up to $> 100\%$ for high mass ($> 10\,\mathrm{M}_\odot$) stars (Sana et al., 2012). Mass transfer in close binary systems can directly alter the evolution pathway of the star, and lead to a plethora of phenomena that have shaped the universe as we see it today: the reionization of gas around the galaxies, the formation of WDs, NSs, and BHs, and the synthesis of all elements heavier than helium. Together, the fate of stars in binary systems is a result of a close interplay between mass loss, nuclear physics, angular momentum conservation, magnetic fields, and gravitational wave radiation (e.g. Postnov et al., 2014; Tauris et al., 2006).

The final products of close binary evolution are of particular interest for the current era of gravitational wave astronomy. Binary NSs and BHs formed from the progenitor massive star binaries[2] are already being regularly detected in the current Laser Interferometer Gravitational wave Observatory (LIGO) and Virgo observing

[1] Massive stars in a specific mass range may leave behind no remnants at all (Woosley, 2017).

[2] They may also be formed from dynamical capture in dense stellar systems (Grindlay et al., 2006).

runs (The LIGO Scientific Collaboration et al., 2020). On the other hand, WDs in binary systems that descend from lower mass binaries are going to be the loudest gravitational wave sources for the upcoming mHz gravitational wave observatory Laser Interferometer Space Antenna (LISA; Amaro-Seoane et al., 2012). Despite decades of theoretical and observational work into understanding these astrophysical populations, there remain fundamental unanswered questions regarding these systems – particularly those involving explosive transient phenomena. As a large fraction of the mass in the binary can be lost over timescales of a few weeks, these sudden mass loss episodes can cause drastic changes to the evolutionary pathway of the binary (Tauris et al., 2006), while also enriching the universe with heavy elements (Gehrz et al., 1998; Nomoto et al., 2013).

This PhD thesis focuses on large systematic experiments to study the transient optical and near-infrared sky in pursuit of constructing a coherent picture of explosive phenomena in the lives of compact binary systems. We begin by discussing the physics of explosions in compact binaries, and highlight key open issues regarding the role of explosive phenomena in the formation and long term evolution of these unique systems.

1.2 High mass stars in binaries and the kHz gravitational wave universe

Core-collapse supernovae (SNe) are observed in multiple flavors, depending on their photometric and spectroscopic properties (see Filippenko, 1997; Gal-Yam, 2017 for reviews). Type II SNe exhibit strong lines of hydrogen and are believed to arise from the deaths of massive stars that have retained their outer hydrogen envelopes. On the other hand, stripped envelope SNe do not exhibit signatures of hydrogen, and thus assumed to arise from massive stars that have lost their outer hydrogen envelopes. Depending on whether they have a residual helium envelope, they can be classified as Type Ib (with He) or Type Ic (without He) events (Figure 1.1). The high binary fraction of massive stars suggests that most undergo mass transfer during their lifetimes (Sana et al., 2012), and thus envelope stripping via binary interactions likely play a crucial role in producing the diversity of stripped envelope SNe (Smith et al., 2011).

The extent of stripping of the massive star is sensitively dependent on the nature and separation of the binary companion (Yoon et al., 2010; Zapartas et al., 2017b). Compact companions in close orbits are capable of removing nearly the entire outer envelope of the star, and possibly even preventing the collapse of the massive core

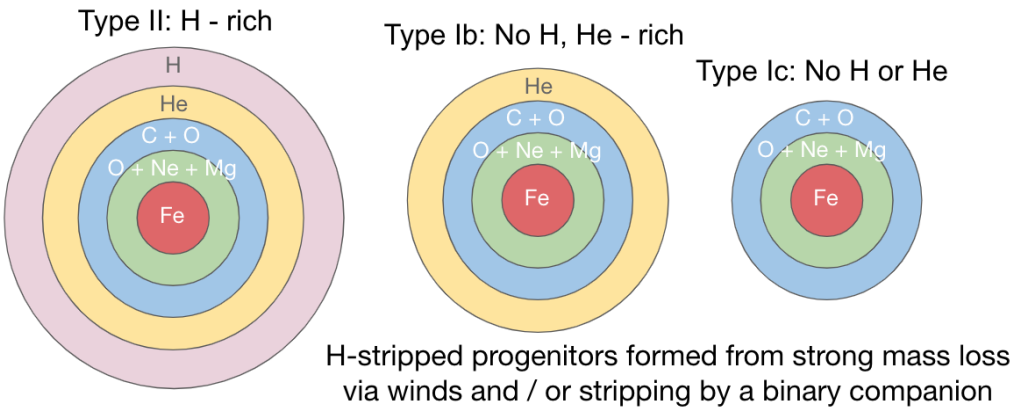

Figure 1.1: **A schematic depicting the pre-explosion internal structure of massive stars**. Different amounts of residual envelopes remaining at the time of explosion is believed to produce the diversity of spectra and light curves of core-collapse SNe.

(Tauris et al., 2015; Zapartas et al., 2017a). Since normal core-collapse SNe likely produce a NS, these highly stripped SNe have been suggested to leave behind NSs in very compact orbits around the surviving companion. These binaries can then evolve under the influence of gravitational wave radiation to subsequently merge, producing gravitational waves detectable by LIGO/Virgo (Tauris et al., 2017). Although this basic picture has been long suggested as a promising pathway to forming NSs in binary systems that merge within a Hubble time (in the field), critical uncertainties remain – How does the binary survive the two SN explosions? Why doesn't the NS birth kick unbind the system (Piran et al., 2005)? Does the final SN result from an iron core-collapse or a weak electron-capture SN (van den Heuvel, 2004)?

Some general considerations have long suggested that the final SN that gives birth to a neutron star in a compact binary system should have distinctive properties. First, the presence of the very close companion should have siphoned off most of the progenitor mass, such that the star retains only a thin He (and possibly H) layer at the time of explosion (Dewi et al., 2002; Ivanova et al., 2003; Tauris et al., 2015). The resulting SN would then eject a small amount of mass ($M \lesssim 1\,\mathrm{M}_{\odot}$), and thus exhibit a faint and fleeting light curve (Arnett, 1982). In fact, the low eccentricity and space velocities of known double NSs in Galaxy have long suggested that the final SN likely ejected a small amount of mass, and imparted only a small kick to the nascent NS (Beniamini et al., 2016; Piran et al., 2005; van den Heuvel, 2004).

Such 'ultra-stripped SNe' (Moriya et al., 2017; Tauris et al., 2013, 2015) were indeed

suggested to be associated with previously observed rapidly evolving transients (Drout et al., 2013; Kasliwal et al., 2010). However, it has been non-trivial to conclusively establish their massive star progenitors due to the lack of early time data that contains diagnostics of the pre-explosion progenitor star. In fact, it is easy to imagine a continuum of very low ejecta mass core-collapse SNe arising from massive stars in a range of binary orbital periods. Yet, the nature and even existence of these elusive explosions has remained unclear, leaving a gaping hole in our understanding of the formation of these gravitational wave sources.

1.3 Low mass stars in binaries and the mHz gravitational wave universe

When the primary star in a low mass binary system runs out of fuel in its core, an expansion phase ensues as the binary is likely engulfed in a common envelope (CE) phase where the two components are expected to spiral in due to the frictional force of the envelope (Ivanova et al., 2013). Depending on the outcome of this process, which is highly dependent on the poorly constrained physics of the common envelope phase, a variety of close binary systems can result as the primary star leaves behind a CO WD. Due to their relatively longer orbital periods, these WD binaries will be prime targets for upcoming mHz gravitational wave observatories like LISA (Lamberts et al., 2019).

Short period WDs with hydrogen-rich companions

CO WDs with short period ($\sim$ few hours), low mass, hydrogen-rich companions have been widely studied due to their dynamic temporal characteristics, grouped together in the class of Cataclysmic variables (CVs). These binaries lose angular momentum due to magnetic braking from the companion wind as well as gravitational wave radiation, as the main sequence star evolves to shorter periods while being consumed by accretion (Knigge et al., 2011; Townsley et al., 2003, 2009). While the dynamic temporal behavior in CVs can commonly arise from accretion disk outbursts (dwarf novae; Warner, 1995), the rarer nova eruptions produced by unstable thermonuclear ignition on the WD (Starrfield et al., 2016) are capable of ejecting nuclear processed material into the surrounding medium. Although the amount of material ejected in novae ($\sim 10^{-4}\,M_\odot$) is minuscule compared to SNe, their much higher rates (by $\sim 10^4$) implies that they play an important role in enriching the interstellar medium (Gehrz et al., 1998; José et al., 2006). Mass ejections in novae further play critical roles in the long term period evolution of the binary, as well as the underlying mass growth of the WD, providing a promising route to the possible Chandrasekhar mass

progenitors of Type Ia SNe (Soraisam et al., 2015; Starrfield et al., 2020a).

Despite the importance of the demographics of nova eruptions, our understanding of their rates even in our very Galactic backyard has remained elusive. Several previous studies have attempted to use rates of novae in external galaxies (e.g. Darnley et al., 2006) as well as the statistics of very bright and nearby optically discovered novae (e.g. Shafter, 2017) – where the completeness remains poorly characterized (Schaefer, 2014). However, these estimates are plagued by uncertainties regarding i) differences in the stellar populations between the Milky Way and external galaxies and ii) the distribution of mass and dust in the Galaxy since previous optical searches of novae are heavily limited by dust extinction.

Short period WDs with helium-rich companions

CO WDs with short period ($\lesssim$ 1 hour), low mass, hydrogen-poor (He-rich) companions have been observed as a special class of CVs, termed as the AM Canum Venaticorum (AM CVn) variables (Nelemans, 2005; Nelemans et al., 2004). These sources are believed to arise from a second common envelope when the secondary evolves off the main sequence, followed by evolution towards shorter periods due to gravitational wave radiation. As the He-rich companion (a He WD or a He-burning sdB star) accretes on to the CO WD, the gradually thickening He layer on the CO WD can undergo a series of rapid burning episodes (Bildsten et al., 2007). Depending on the relative timescales of the He burning (which depends on the pressure and temperature at the base of the layer) and local dynamical timescale, an explosive detonation can occur in the shell. The resulting explosion would be a '.Ia' SN (Shen et al., 2010), that ejects only a tenth of the mass in a Type Ia SN ($\sim 0.1\,M_{\odot}$).

Furthermore, if the shock wave from the shell detonation is strong enough to propagate into and detonate the CO core, a more powerful thermonuclear explosion can result that destroys the entire WD (e.g. Nomoto, 1982a,b; Woosley et al., 1986). Such double detonations were long proposed as explosion mechanisms of Type Ia SNe, but it has been difficult to reconcile the properties of SNe Ia with the expected signatures of these events. The explosive shell burning is expected to leave distinct imprints of the Fe group ash in terms of the red colors and strong line blanketing features (see Figure 1.2) in the SN (Kromer et al., 2010; Nugent et al., 1997; Polin et al., 2019), which is generally inconsistent with the majority of SNe Ia. Thus, a number of questions remain: What happens to the He accreted on to the surface of CO WDs? If the He detonates, what type of mass ejection takes place and how does

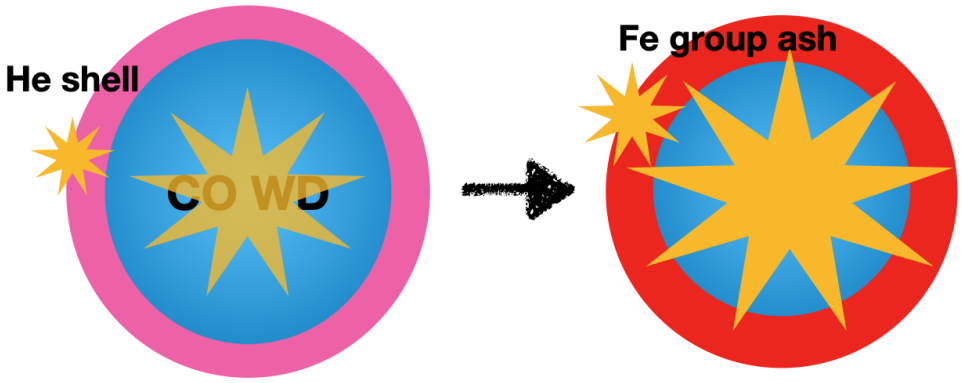

Figure 1.2: **Schematic of the detonation of a He shell accreted on a CO WD**. The shell detonation may trigger a detonation in the underlying CO core, in which case, the entire star explodes with a thick layer of Fe group ash produced by He burning in the outer ejecta.

it affect the binary system? What is the final fate of the AM CVn binaries?

1.4 Thesis outline and Discovery engines

The landscape of explosive transients from compact binaries discussed thus far have a general characteristic in common – they are characterized by faint and fast evolving light curves compared to normal supernovae. As a result, studies of these events are limited to the local universe within a radius of ≈ 200 Mpc for current time domain surveys that reach a depth of ≈ 20 mag. Furthermore, their likely rarity compared to ordinary SNe invokes the need for studying large statistical samples of nearby SNe to sift these events from normal SNe. On the other hand, the need of the hour for constraining the demographics of novae in our own Galaxy are wide-field infrared time domain searches in the Galactic plane to pierce through the intervening clouds of dust. Motivated thus by the fundamental questions, I undertook two major transient surveys during this thesis.

The largest volume-limited supernova experiment

I undertook the largest volume-limited supernova classification experiment till date using the Zwicky Transient Facility (ZTF; Bellm et al., 2019b; Graham et al., 2019; Masci et al., 2019) optical time domain survey. ZTF is a wide-field (47 deg^2) optical time domain survey that covered the entire visible sky from Palomar Observatory to a median depth of ≈ 20.5 mag, with a cadence of 3 days (between 2018 - 2020; ZTF Phase I). By systematically classifying all transients coincident with a known

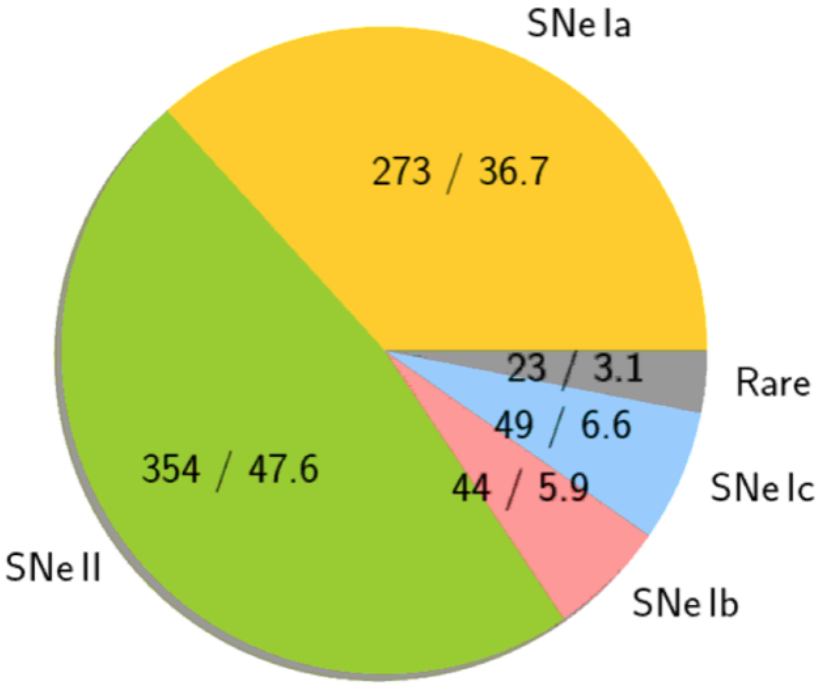

Figure 1.3: **Distribution of the classification types of transients in the ZTF volume-limited CLU experiment in the first 16 months of operations**. For each type, we show the statistics as X/Y where X is the number of events in the sample and Y is the percentage of events of that type in the total sample. Rare events include events like Tidal Disruption Events, Gap transients, and Luminous Blue Variable Outbursts.

nearby galaxy (see sample selection criteria in Chapter 6), the ZTF volume-limited Census of the Local Universe (CLU) experiment classified 754 supernovae in the first 16 months of operations[3]. Figure 1.3 shows the distribution of the classification types of SNe in the CLU experiment – the majority of events are core-collapse SNe, due to their intrinsically higher volumetric rates (Li et al., 2011).

In Part I of this thesis (Chapters 2 and 3), I present the identification of a new class of core-collapse supernovae that are consistent with the deaths of 'ultra-stripped' massive stars. The identification of this class was uniquely enabled by rapid and systematic follow-up of nearby supernovae, initially in the intermediate Palomar Transient Factory (Law et al., 2009; Rau et al., 2009) and subsequently in the ZTF CLU experiment to provide the first constraints on their rates (Yao et al., 2020b). Chapter 4 in Part II of this thesis discusses the identification of a new class of SNe Ia that are consistent with He shell explosions on low mass white dwarfs. In Chapters

[3]The total yield was $\approx$ 1300 SNe by the end of ZTF Phase I, and larger than the previous largest volume-limited effort by the decade-long Lick Observatory Supernova Search (Li et al., 2011).

5 and 6, I present observational evidence that these peculiar SNe Ia together with the previously mysterious class of Ca-rich transients (Kasliwal et al., 2012; Perets et al., 2010) likely arise from a continuum of He shell explosions involving a range of WD core and He shell masses.

The first wide-field census of the dynamic infrared sky

While wide-field optical time domain surveys have undergone a revolution in the last two decades, the high cost of infrared detectors as well as the challenging background limited imaging in the near infrared (NIR) bands has kept the dynamic infrared sky pristine and unexplored. I contributed to the commissioning and led the software development of the first wide-field 3π time domain survey of the NIR sky, Palomar Gattini-IR (PGIR; Moore et al., 2019), which I describe in Part III of this thesis. PGIR is a J-band ($\approx 1.2\mu$m) infrared time domain survey with a field of view of 25 deg^2 that covers the entire visible sky from Palomar Observatory every 2 nights to a median depth of ≈ 15.7 AB mag (De et al., 2020b). Chapter 7 provides an overview of the system performance and survey characteristics. Figure 1.4 shows the sky distribution of the depth of reference images created using the survey data until November 2019 (updated from De et al., 2020b). The stacked images surpass the depth of the historical 2MASS (Skrutskie et al., 2006) survey ($J \approx 17$ AB mag) over $\approx 60\%$ of the sky, while the deepest images reach depths of ≈ 18 AB mag.

In Chapter 8, I use the unique NIR wide-field capabilities of PGIR to provide the strongest constraints till date on the rate of novae in Milky Way. The thesis committee strongly encouraged pursuing potential once-in-a-lifetime transient science opportunities, particularly with the new phase space exploration capabilities of PGIR. To this end, I discuss in Part III on this thesis, a related exciting opportunity that emerged with the identification of the first Fast Radio Burst source associated with a Galactic magnetar SGR 1935+2154 (Bochenek et al., 2020; The CHIME/FRB Collaboration et al., 2020). Using a novel readout mode for the Palomar Gattini-IR system that allows sub-second timing resolution, I present in Chapter 9, NIR constraints on the second timescale emission from the heavily dust obscured source.

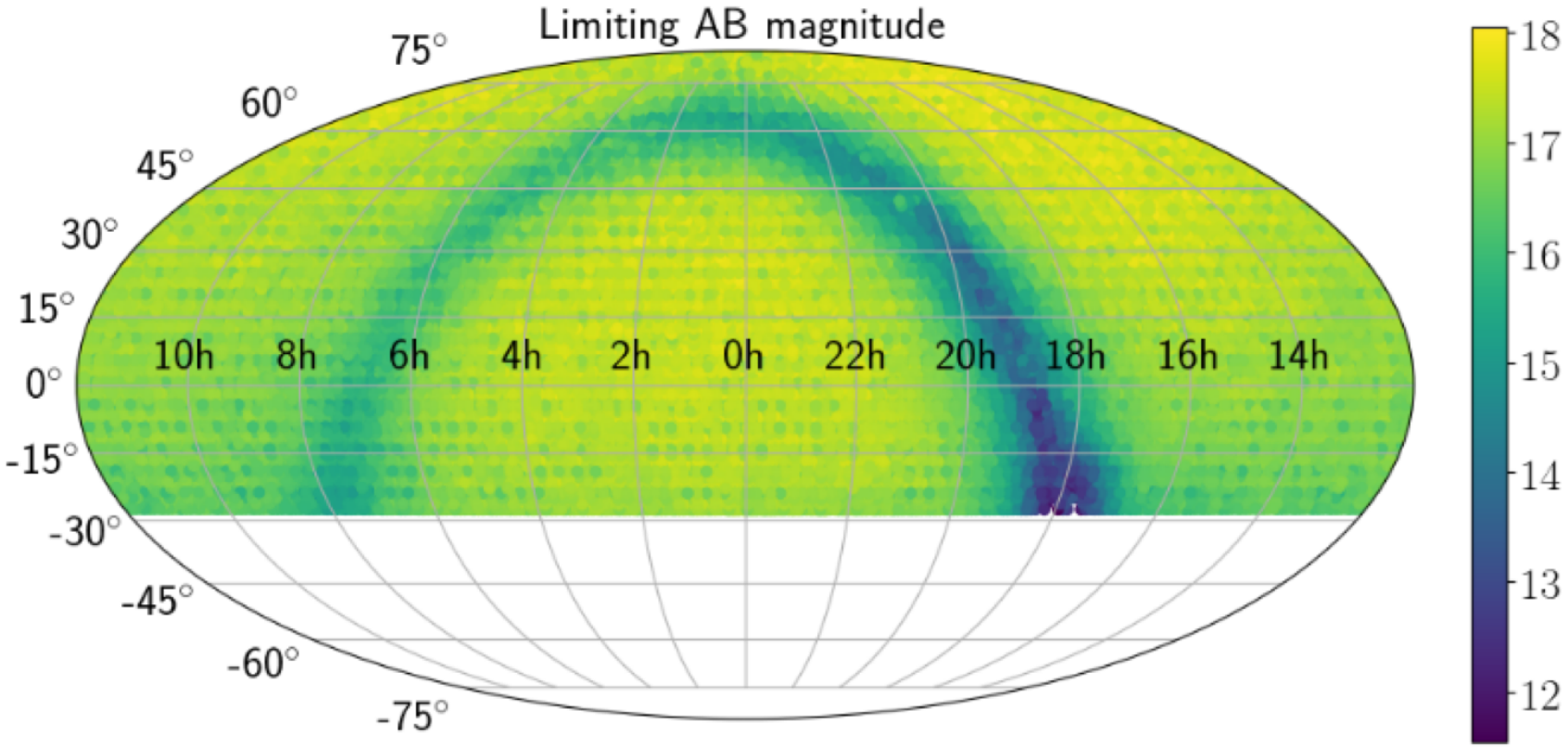

Figure 1.4: **Sky distribution of the 5σ limiting magnitude of PGIR reference images**. The stacked images are shallower near the Galactic plane due to confusion noise and the 8.7″pixel scale of the detector.

Part I: The formation of neutron stars in compact binary systems

Chapter 2

A HOT AND FAST ULTRA-STRIPPED SUPERNOVA THAT LIKELY FORMED A COMPACT NEUTRON STAR BINARY

De, K. et al. (2018). "A Hot and Fast Ultra-stripped Supernova that Likely Formed a Compact Neutron Star Binary". In: *Science* 362.6411, pp. 201–206. DOI: 10.1126/science.aas8693. arXiv: 1810.05181 [astro-ph.HE].

Kishalay De[1], Mansi M. Kasliwal[1], Eran O. Ofek[2], Takashi J. Moriya[3], Jamison Burke[4,5], Yi Cao[6], S. Bradley Cenko[7,8], Gary B. Doran[9], Gina E. Duggan[1], Robert P. Fender[10], Claes Fransson[11], Avishay Gal-Yam[2], Assaf Horesh[12], S. R. Kulkarni[1], Russ R. Laher[13], Ragnhild Lunnan[11], Ilan Manulis[2], Frank Masci[13], Paolo A. Mazzali[14,15], Peter E. Nugent[16,17], Daniel A. Perley[14], Tanja Petrushevska[18,19], Anthony L. Piro[20], Clare Rumsey[21], Jesper Sollerman[11], Mark Sullivan[22], and Francesco Taddia[11]

[1]Cahill Center for Astrophysics, California Institute of Technology, 1200 E. California Blvd., Pasadena, CA 91125, USA

[2]Department of Particle Physics and Astrophysics, Faculty of Physics, The Weizmann Institute of Science, Rehovot 76100, Israel

[3]Division of Theoretical Astronomy, National Astronomical Observatory of Japan, National Institutes of Natural Sciences, 2-21-1 Osawa, Mitaka, Tokyo 181-8588, Japan

[4]Las Cumbres Observatory, 6740 Cortona Drive, Suite 102, Goleta, CA 93117-5575, USA

[5]Department of Physics, University of California, Santa Barbara, CA 93106-9530, USA

[6]Department of Astronomy, University of Washington, Box 351580, Seattle, WA 98195-1580, USA

[7]Astrophysics Science Division, NASA Goddard Space Flight Center, Mail Code 661, Greenbelt, MD 20771, USA

[8]Joint Space-Science Institute, University of Maryland, College Park, MD 20742, USA

[9]Jet Propulsion Laboratory, California Institute of Technology, Pasadena, CA 91109, USA

[10]Department of Physics, Astrophysics, University of Oxford, Denys Wilkinson Building, Oxford OX1 3RH, UK

[11]Oskar Klein Centre, Department of Astronomy, Stockholm University, 106 91 Stockholm, Sweden

[12]Racah Institute of Physics, The Hebrew University of Jerusalem, Jerusalem, 91904, Israel

[13]Infrared Processing and Analysis Center, California Institute of Technology, MS 100-22, Pasadena, CA 91125, USA

[14]Astrophysics Research Institute, Liverpool John Moores University, Liverpool L3 5RF, UK

[15]Max-Planck-Institut für Astrophysik, Karl-Schwarzschild-Str. 1, D-85748 Garching bei München, Germany

[16]Lawrence Berkeley National Laboratory, Berkeley, California 94720, USA

[17]Department of Astronomy, University of California, Berkeley, CA, 94720-3411, USA

[18]Oskar Klein Centre, Department of Physics, Stockholm University, 106 91 Stockholm, Sweden

[19]Centre for Astrophysics and Cosmology, University of Nova Gorica, Vipavska 11c, 5270 Ajdovščina, Slovenia

[20]The Observatories of the Carnegie Institution for Science, 813 Santa Barbara Street, Pasadena, CA 91101, USA
[21]Astrophysics Group, Cavendish Laboratory, 19 J J Thomson Avenue, Cambridge CB3 0HE, UK
[22]Department of Physics and Astronomy, University of Southampton, Southampton, SO17 1BJ, UK

Abstract

Compact neutron star binary systems are produced from binary massive stars through stellar evolution involving up to two supernova explosions. The final stages in the formation of these systems have not been directly observed. We report the discovery of iPTF 14gqr (SN 2014ft), a Type Ic supernova with a fast evolving light curve indicating an extremely low ejecta mass (≈ 0.2 solar masses) and low kinetic energy ($\approx 2 \times 10^{50}$ ergs). Early photometry and spectroscopy reveal evidence of shock cooling of an extended He-rich envelope, likely ejected in an intense pre-explosion mass loss episode of the progenitor. Taken together, we interpret iPTF 14gqr as evidence for ultra-stripped supernovae that form neutron stars in compact binary systems.

2.1 Introduction

Core-collapse supernovae (SNe) are the violent deaths of massive stars when they run out of nuclear fuel in their cores and collapse, forming a neutron star (NS) or black hole (BH) (Woosley et al., 2002). For massive stars that have lost some or all of their outer hydrogen (H) and helium (He) envelope, the resulting collapse produces a stripped envelope SN (Smartt, 2009). The amount of material stripped from the star is a sensitive function of the initial mass of the star and its environment; if the star was born in a binary system, it also depends on the orbital properties of the system and the nature of the companion (Langer, 2012; Smartt, 2009).

Because most massive stars are born in close binary systems (Sana et al., 2012), stripping via binary interactions likely plays a large role in producing the observed diversity of stripped envelope SNe (Smith et al., 2011; Yoon et al., 2010). For the most compact companions in close orbits, the stripping of massive stars may be large enough to completely remove their outer layers, leaving behind a naked metal core close to the minimum mass required for the core to collapse (the Chandrasekhar mass). If massive enough, the highly stripped core eventually collapses to produce a faint and fast evolving SN explosion which ejects a small amount of material (Tauris et al., 2013, 2015). Although it has been difficult to securely identify these explosions, such ‘ultra-stripped’ SNe have been suggested to lead to the formation

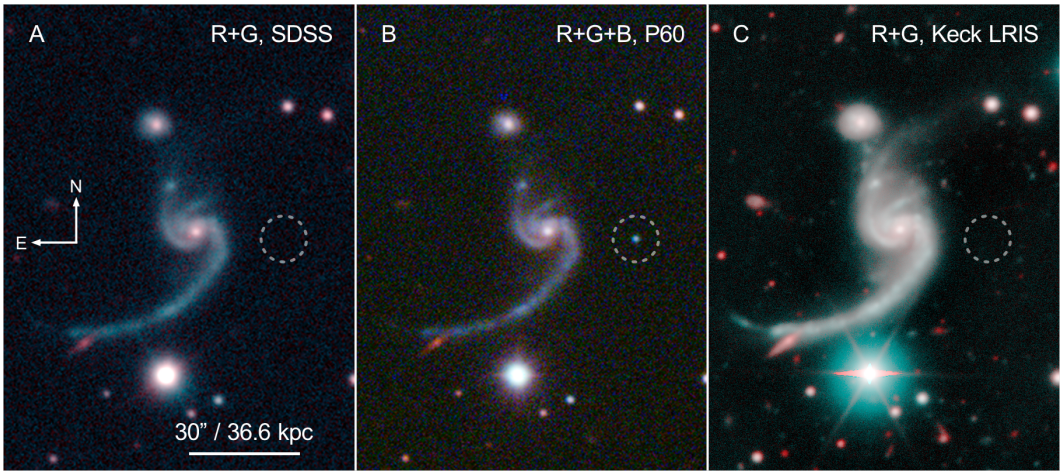

Figure 2.1: **Discovery field and host galaxy of iPTF 14gqr**. A. An optical image of the field from the Sloan Digital Sky Survey (SDSS); r and g filter images have been used for red and cyan colors respectively). B. Composite RGB image (r, g and B filter images have been used for red, green and blue colors respectively) of the iPTF 14gqr field from images taken near the second peak (19 October 2014) with the Palomar 60-inch telescope (P60), showing a blue transient inside the white dashed circle at the discovery location. C. Late-time composite R+G image (R and G filter images have been used for red and cyan colors respectively) of the host galaxy taken with the Low Resolution Imaging Spectrograph on the Keck-I telescope.

of a variety of compact NS binary systems (i.e. a NS in orbit around another NS, WD, or BH) (Tauris et al., 2013, 2017).

2.2 Discovery and follow-up of iPTF14gqr

iPTF 14gqr was discovered by the intermediate Palomar Transient Factory (iPTF; Cao et al., 2016; Masci et al., 2017) on 2014 October 14.18 UT (Coordinated Universal Time) at a g-band optical magnitude of $\approx$ 20.2 mag. The source was not detected in the previous observation on 2014 October 13.32 (0.86 days before discovery), with a limiting magnitude of $g \geq 21.5$ mag. The transient was found in the outskirts (at a projected offset of $\approx$ 29 kpc from the center) of a tidally interacting spiral galaxy (IV Zw 155) at a redshift $z = 0.063$ and luminosity distance $D = 284.5$ Megaparsecs (Figure 2.1). We obtained rapid ultraviolet (UV), optical, and near-infrared (NIR) follow-up observations of the source, including a sequence of four spectra within 24 hours from the first detection (Section 2.5).

We also obtained multi-epoch X-ray and radio observations and found that the

source remained undetected at these wavelengths (Section 2.5). These upper limits rule out luminous non-thermal emission, such as typically seen in relativistic and gamma-ray burst (GRB) associated SNe, but are not stringent enough to constrain the environment of the progenitor (Figure 2.17, Figure 2.18).

Our photometric follow-up indicated that the source rapidly faded within a day of detection, followed by re-brightening to a second peak on a longer timescale (rising over $\approx$ 7 days; see Materials and Methods) (Figure 2.2). The early decline was detected in all optical and UV photometric bands, and characterized by a blackbody spectrum which cooled rapidly from a temperature $T > 32000$ K near first detection to $T \sim 10000$ K at one day after discovery (Figure 2.3; Figure 2.4). Our early spectra also exhibit blackbody continua with temperatures consistent with those inferred from the photometry, superimposed with intermediate width emission lines of He II, C III, and C IV. Such high ionization lines, which are typically associated with elevated pre-explosion mass loss episodes in massive stars, have not been seen in early spectra of previously observed hydrogen-poor SNe. Although similar features are present in the early spectra of some hydrogen-rich core-collapse SNe (Gal-Yam et al., 2014; Khazov et al., 2016; Yaron et al., 2017) (Figure 2.12), the relatively large widths of the lines [Full Width at Half Maximum (FWHM) $\sim$ 2000 - 4000 km s^{-1}] as well as the rapid evolution of the 4686 Å emission feature (Figure 2.3) are not.

Spectra obtained near the second peak are dominated by emission from the expanding photosphere and exhibit relatively blue continua, with broad absorption features reminiscent of normal stripped envelope SNe of Type Ic, that do not exhibit absorption lines of H or He in the spectra (Gal-Yam, 2017) (Figure 2.13). We find associated absorption velocities of $\sim$ 10,000 km s^{-1} (Section 2.5). The photometric properties of the second peak are broadly consistent with a number of previously observed fast Type Ic events (Figure 2.9, Figure 2.10), but the rapidly declining first peak and the fast rise time to the second peak are unlike previously observed events. The source quickly faded after the second peak, declining at a rate of 0.21 mag day^{-1} in the g band (Section 2.5). Our final spectrum taken at $\approx$ 34 days after explosion shows that the source exhibited an early transition to the nebular phase, and on a timescale faster than previously observed core-collapse SNe. The nebular phase spectrum exhibits prominent [Ca II] emission similar to several other Type Ic SNe (Figure 2.14).

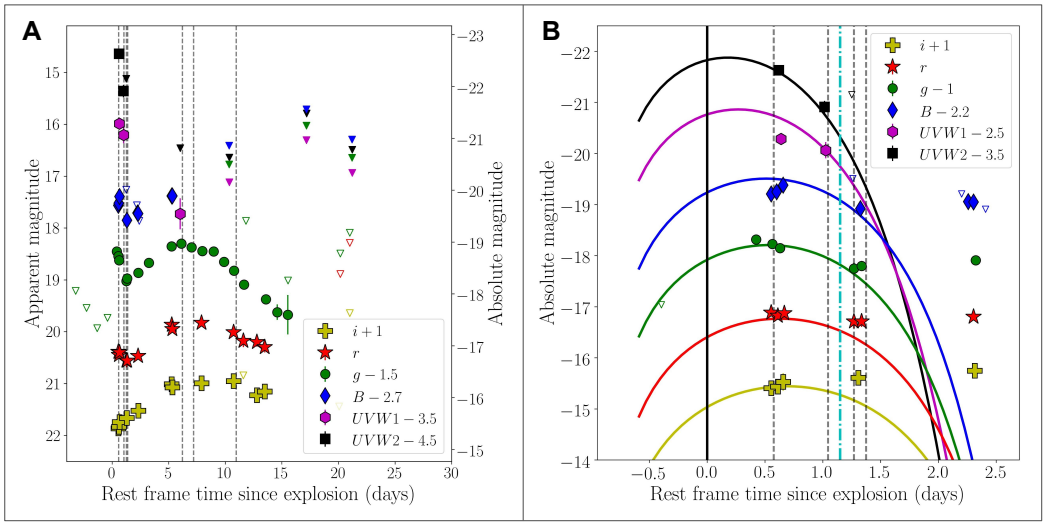

Figure 2.2: **Multi-color photometric observations of iPTF 14gqr**. A. Multi-color light curves of iPTF 14gqr from our photometric follow-up observations (magnitudes are corrected for galactic extinction, and offset vertically as indicated in the legend). Inverted triangles denote 5σ upper limits while other symbols denote detections. Hollow inverted triangles are upper limits from P48/P60 imaging and the filled inverted triangles are upper limits from Swift observations (filled green triangles are V band limits from Swift). Epochs when spectra were obtained are marked in both panels by vertical black dashed lines. B. Zoom-in of the early evolution of the light curve. The black solid line shows the assumed explosion epoch. The colored solid lines show the best-fitting shock cooling model for extended progenitors (Piro, 2015). Only photometric data before the cyan dot-dashed vertical line were used in the fitting (Section 2.5).

Multi-color photometry at multiple epochs allow us to trace the evolution of the optical / UV Spectral Energy Distribution (SED), which we use to construct bolometric light curves that contain flux integrated over all wavelengths (Figure 2.3; Figure 2.4; see Section 2.5). We fit the pseudo-bolometric light curve of iPTF 14gqr with a simple Arnett model (Arnett, 1982) to estimate the explosion parameters. Allowing the explosion time to vary as a free parameter, we estimate an ejecta mass $M_{\rm ej} \approx 0.15 - 0.30$ solar masses ($M_\odot$), an explosion kinetic energy $E_K \approx (1.0 - 1.9) \times 10^{50}$ ergs, and synthesized Ni mass $M_{\rm Ni} \approx 0.05$ $M_\odot$ (Figure 2.4, Figure 2.15; see Section 2.5). The inferred ejecta mass is lower than known core-collapse Type Ic SNe (Drout et al., 2011; Lyman et al., 2016a; Taddia et al., 2018), which have ejecta masses in the higher range of $\sim 0.7 - 15$ $M_\odot$, and with a mean of $2 - 3$ $M_\odot$ over a sample of ≈ 20 SNe. However, the parameters of iPTF 14gqr are similar to

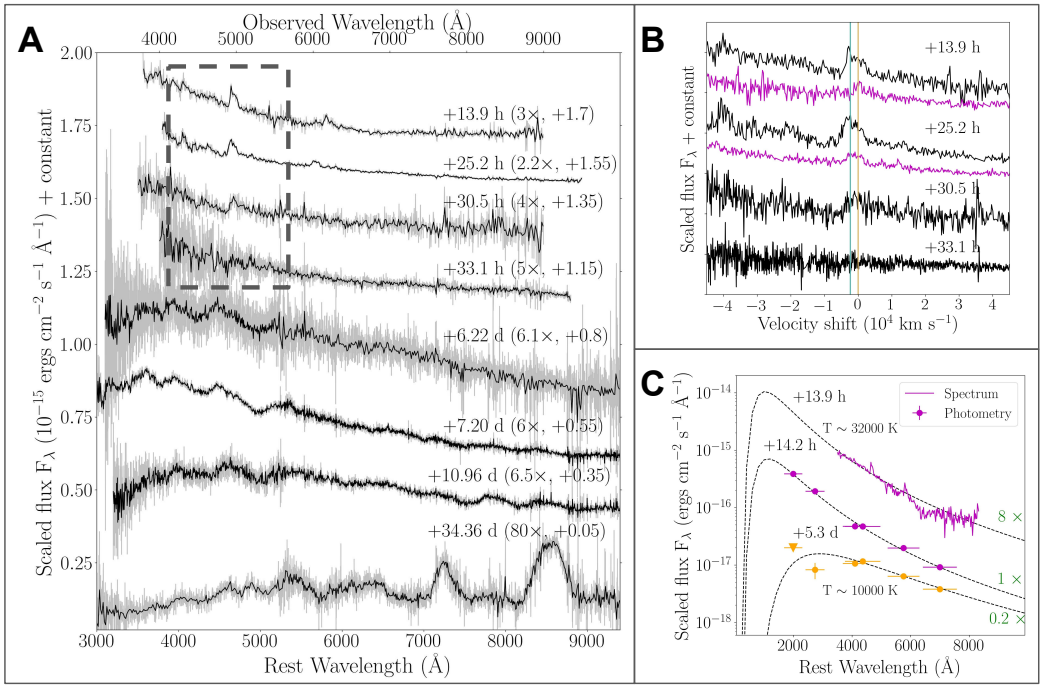

Figure 2.3: **Spectroscopic evolution of iPTF 14gqr.** A. Observed spectra before (gray) and after (black) binning. The epochs of the spectra along with the scaling and vertical shifts used are indicated next to each spectrum. B. Zoom-in of the early spectra, indicated by the black dashed box in (A), showing rapid evolution of the λ4686 feature within 24 hours of discovery. The x-axis indicates the velocity shift from the He II λ4686 line. The orange and cyan lines mark the locations of the λ4686 line and the C III λ4650 line, respectively. For the +13.9 h and +25.2 h spectra, additional magenta lines show the profiles of the C IV λ5801 and the C III λ5696 features, respectively, at the same epochs. C. Scaled optical / UV SEDs of the photometry and spectra obtained within the first light curve peak (see Figure 2) in magenta, along with photometry near the second peak in orange. The circles indicate observed photometric fluxes, while the triangle is a 5σ upper limit. The dashed black lines indicate the best fitting blackbody SEDs including all optical / UV data points for the first peak and including only the optical data points for the second peak (Section 2.5).

those inferred for the rapidly evolving Type I SNe SN 2005ek (Drout et al., 2013) and 2010X (Kasliwal et al., 2010), whose physical origins remain a matter of debate.

The rapid decline of the first peak observed in iPTF 14gqr is reminiscent of shock cooling emission from the outer layers of a progenitor after the core-collapse SN shock breaks out (Nakar et al., 2014; Sapir et al., 2017) (Figure 2.11). We consider alternative explanations (Section 2.5) and find them to be inconsistent with the data.

In particular, the observed double-peaked light curve in the redder optical bands requires the presence of an extended low mass envelope around the progenitor (Piro, 2015; Sapir et al., 2017). To constrain the properties of such an envelope, we use models (Piro, 2015) to construct multi-color light curves for a range of masses and radii of the envelope (M_e and R_e, respectively). We find a best-fitting model of $M_e \sim 8\times10^{-3}$ $M_\odot$ and $R_e \sim 3\times10^{13}$ cm ($\sim$ 450 solar radii ($R_\odot$)) (Figure 2 & Figure 2.16; see Section 2.5). Even though the model considered here is simplified (e.g. it ignores the density structure of the envelope), we expect the estimated parameters to be accurate within an order of magnitude (Piro et al., 2017), leading us to conclude that the progenitor was surrounded by an extended envelope with a mass of ~ 0.01 $M_\odot$ at a radius of ~ 500 $R_\odot$.

We constrain the composition of the outer envelope using the early spectra. The emission lines observed in the early spectra of iPTF 14gqr can be understood as arising from recombination in the outer regions of the extended circumstellar material (CSM), which was ionized by the high energy radiation produced in the shock breakout (e.g. Gal-Yam et al., 2014; Yaron et al., 2017; Figure 2.12). We estimate the location and mass of the emitting He II from the luminosity of the early 4686 Å line, and assuming a CSM density profile that varies with radius r as $\propto r^{-2}$ (Yaron et al., 2017). We find the emitting region to be located at $r \sim 6\times10^{14}\tau^{-2}$ cm, and contain a helium mass $M_{\rm He} \sim 0.01\tau^{-3}$ $M_\odot$, where τ is the optical depth of the region (Section 2.5). The absence of prominent Lorentzian scattering profiles in the lines suggest that the optical depth is small and assuming $\tau \approx 1$, we find $r \sim 6\times10^{14}$ cm (8.5×10^3 $R_\odot$) and $M_{\rm He} \sim 0.01$ $M_\odot$. Because our calculations are based on fitting a simple two-component Gaussian profile to the 4686 Å emission line (to estimate the unknown contamination of C III at 4650 Å), these estimates are uncertain by a factor of a few.

Using the C IV 5801 Å lines and similar methods as above, we estimate a CSM carbon mass of $\sim 4\times10^{-3}$ $M_\odot$, while the hydrogen mass is constrained to be $< 10^{-3}$ $M_\odot$. Additional constraints based on light travel time arguments also suggest that the envelope was located at $r \leq 6\times10^{15}$ cm from the progenitor (Section 2.5). The flash-ionized emission lines exhibit complex asymmetric profiles (Figure 2.3) that we attribute to light travel time effects, given the large size of the envelope and the high inferred wind velocities (Gräfener et al., 2016).

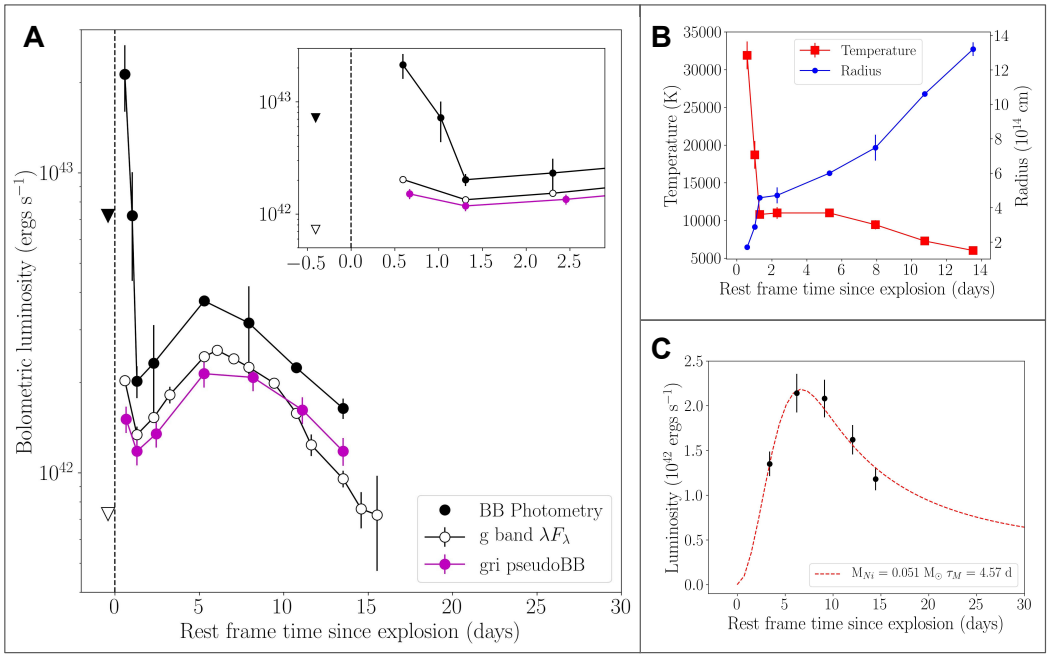

Figure 2.4: **Bolometric light curve and Arnett modeling of iPTF 14gqr.** A. Bolometric light curve of iPTF 14gqr. Filled black points indicate blackbody luminosities obtained from fitting multi-color photometry while the magenta points correspond to pseudo-bolometric luminosities (Section 2.5). The empty black circles indicate g-band luminosities obtained by multiplying the g-band flux F_λ with the wavelength λ of the filter. The inverted triangles denote estimated pre-detection 5σ upper limits on the respective luminosities (Section 2.5). The inset shows the bolometric light curves zoomed into the region of the first peak. B. The radius and temperature evolution of the fitted blackbody functions. C. Best-fitting Arnett model of the pseduo-bolometric light curve of the main (second) peak of iPTF 14gqr. The ^{56}Ni mass $M_{\rm Ni}$ and diffusion timescale τ_M corresponding to the model are indicated in the legend (Section 2.5).

2.3 An ultra-stripped progenitor

The low ejecta mass and explosion energy, as well as the presence of an extended He-rich envelope, indicate an unusual progenitor channel for iPTF 14gqr. The detection of the early shock cooling emission indicates a core-collapse origin of the explosion, while the bright radioactivity powered emission suggests that this explosion is associated with the class of iron core-collapse explosions. The low ejecta mass together with the small remaining amount of He in the progenitor rule out models of single star evolution as well as a non-degenerate massive star companion for the progenitor of iPTF 14gqr (Section 2.5), leaving only the most compact com-

panions (such as a NS, WD, or BH) as possible explanations of the highly stripped (or 'ultra-stripped') progenitor.

Ultra-stripped explosions have been modeled in the case of He star – NS binaries, where stripping of the He star by a NS in a close orbit leads to the subsequent collapse of an ultra-stripped He star (Moriya et al., 2017; Tauris et al., 2013, 2015). Hence, we compare theoretical bolometric light curves for ultra-stripped explosions (Moriya et al., 2017) to those of iPTF 14gqr in Figure 2.5, for a model with $M_{\rm ej} = 0.2$ $M_\odot$, $M_{\rm Ni} = 0.05$ $M_\odot$, and $E_K = 2 \times 10^{50}$ ergs. To account for the early declining emission, we also add a component corresponding to shock cooling of an extended envelope, for $M_e = 0.01$ $M_\odot$ and $R_e = 6 \times 10^{13}$ cm. The two component light curve matches the light curve data. We also compare the spectroscopic properties of iPTF 14gqr to those of ultra-stripped SN models in Figure 2.5. The models (Moriya et al., 2017) assumed fully mixed ejecta that led to the production of strong line blanketing features below 4000 Å, unlike this source. Thus, we re-calculated the models for ejecta with no mixing (as with the light curve calculations), and were able to match to the spectra of iPTF 14gqr near the second peak (Figure 2.5, Figure 2.19).

Our observations indicate the presence of an extended He-rich envelope around the progenitor at the time of collapse, thus providing insight into the terminal evolution of the progenitors of ultra-stripped SNe, and more broadly, the lowest mass progenitors of core-collapse SNe. Using the line widths in our early spectra, we estimate that the emitting envelope was expanding with a velocity of $\sim 1000 - 2000$ km s^{-1} at the time of collapse, consistent with the escape velocity from a compact He star (Section 2.5). When considered with the inferred size of the envelope (at least $\sim$ 500 $R_\odot$), the velocities suggest that the envelope was ejected $\sim 8 - 20$ days prior to the explosion.

The temporal coincidence of the ejection with the final SN suggests that the envelope was likely associated with an intense pre-SN mass loss episode of the progenitor (Section 2.5). Despite the close stripping, ultra-stripped progenitors are expected to retain a small amount of He (~ 0.01 $M_\odot$) in their outer layers. The prominent He and C lines in the early spectra are consistent with eruptive mass loss when considering the expected surface compositions of ultra-stripped progenitors (Tauris et al., 2015). The timescale of the ejection is similar to that expected for silicon flashes ($\sim$ 2

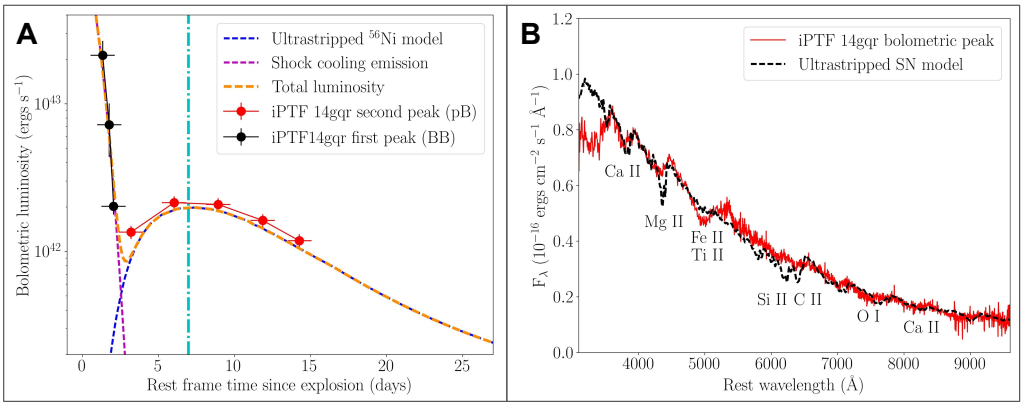

Figure 2.5: **Comparison of iPTF 14gqr to theoretical models of ultra-stripped SNe.** A. The bolometric light curve of iPTF 14gqr shown with a composite light curve consisting of ultra-stripped Type Ic SN models (Moriya et al., 2017) and early shock cooling emission (Piro, 2015). The blue dashed line corresponds to the ^{56}Ni powered peak in the ultra-stripped SN models for $M_{\rm ej}$ = 0.2 M$_\odot$, $M_{\rm Ni}$ = 0.05 M$_\odot$ and $E_K = 2 \times 10^{50}$ ergs, the magenta line corresponds to the early shock cooling emission, and the orange line is the total luminosity from summing the two components. We use the blackbody (BB) luminosities to represent the early emission, while we use the pseudo-bolometric (pB) luminosities for the second peak (Section 2.5). B. Comparison of the peak photospheric spectra of iPTF 14gqr (the epoch is indicated by the cyan dashed line in (A)) to that of the model in (A). The overall continuum shape, as well as absorption features of O I, Ca II, Fe II and Mg II, are reproduced (Section 2.5).

weeks before explosion) in the terminal evolution of low mass metal cores (Woosley et al., 2015), that have been suggested to lead to elevated mass loss episodes prior to the explosion. Such mass loss episodes are relevant to ultra-stripped progenitors as well (Moriya et al., 2017; Müller et al., 2018; Woosley et al., 2015).

iPTF 14gqr exhibits a projected offset of $\sim$ 15 kpc from the nearest spiral arms of its star forming host galaxy (Section 2.5), which is puzzling when compared to the expected locations of ultra-stripped SNe (Tauris et al., 2015). While we do not find evidence of an underlying stellar association or of galaxy emission features in late-time imaging and spectroscopy, the limits are not sensitive enough to rule out the presence of a dwarf galaxy or a star forming H-II region (characterized by its Hα emission) at or near the transient location (Section 2.5). Nonetheless, the tidally interacting environment of the host galaxy suggests that outlying star formation in collisional debris is likely in this system (Boquien et al., 2009), which could harbor young stellar systems (with ages of $\sim$ 5 - 100 Myrs) in the faint tidal tails (Figure

2.20). Hence, the discovery of a core-collapse SN in these outskirts is consistent with our interpretation.

While a number of previously observed fast Type Ic SNe (e.g. SN 2005ek (Drout et al., 2013) and SN 2010X (Kasliwal et al., 2010)) were suggested to be members of the ultra-stripped SN class, it has been difficult to confirm a core-collapse origin for these explosions because these events were discovered only near the maximum of the radioactively powered peak. Specifically, without early photometry and spectroscopy that can reveal the presence of a shock cooling component, these fast transients are also consistent with variants of models involving thermonuclear detonations on white dwarfs (e.g. (Darbha et al., 2010; Metzger, 2012; Shen et al., 2010)). The early discovery and prompt follow-up of iPTF 14gqr establish the presence of a shock cooling emission component that requires an extended progenitor consistent with a core-collapse explosion. In the probable scenario that iPTF 14gqr formed a NS in the explosion (we find a BH remnant to be unlikely given the observed properties of the SN (Section 2.5)), the low ejecta mass in the system suggests that the SN results in the formation of a bound and compact NS binary system (Section 2.5).

2.4 Implications for formation of compact NS binaries

Our interpretation of iPTF 14gqr as an ultra-stripped SN has implications in the wider context of stellar evolution. Compact NS binary systems evolve from binary massive stars that undergo several phases of mass transfer over their lifetime (Figure 2.6). The initial phases of such evolution, in which two massive stars evolve into interacting binaries consisting of a compact object in orbit around a massive star (X-ray binaries) have been observed in several systems in the local Universe (Benvenuto et al., 2017; Walter et al., 2015). However, the subsequent phases that lead to the formation of compact NS binary systems, have not been observed. This is due to the low occurrence rates of such systems, the short lifetimes ($\sim 10^6$ years) of the final stages, and observational selection effects disfavoring their detection (Götberg et al., 2017; Tauris et al., 2015; Zapartas et al., 2017a).

Binary evolution models suggest that the subsequent evolution proceeds via a common envelope phase, during which the loss of angular momentum via dynamical

friction leads to the formation of a close He star – compact object binary (Bhattacharya et al., 1991; Tauris et al., 2006, 2017). An additional phase of close gravitational stripping by the compact companion then leads to the formation of an ultra-stripped SN progenitor (Tauris et al., 2017), with properties which can be inferred from our observations of iPTF 14gqr. The measured orbital properties of known double NS systems suggest that the second NSs were created in weak and low ejecta mass explosions that impart a small natal kick to the newborn NS (Beniamini et al., 2016; Ferdman et al., 2013).

The presence of the extended He-rich envelope in iPTF 14gqr along with the lack of He in the low mass of ejecta suggest that the progenitor was highly stripped by a compact companion, such that only a thin He layer was retained on its surface. This He layer was then ejected in an intense pre-SN mass loss episode, as shown by the high velocity of the envelope. Taken together, these observations provide evidence of the terminal evolution of a post common envelope He star – compact object binary leading to the formation of a compact NS binary system (Figure 2.6).

While wide binaries containing a NS and another compact object may be formed in non-interacting systems of binary massive stars, ultra-stripped SNe have been suggested to precede the formation of almost all compact NS binary systems (Tauris et al., 2015). Thus, these explosions likely represent the only channel to forming NS – NS and NS – BH systems that are compact enough to merge within the age of the universe and produce observable merger signals for joint gravitational wave (e.g. (Abbott et al., 2017a)) and electromagnetic (e.g. (Abbott et al., 2017b; Kasen et al., 2017; Pian et al., 2017)) observations (Grindlay et al., 2006; Tauris et al., 2015; Voss et al., 2003). Given that only a fraction of the systems produced by these explosions will merge within that time, the rates of ultra-stripped explosions must be higher than the rates of their mergers.

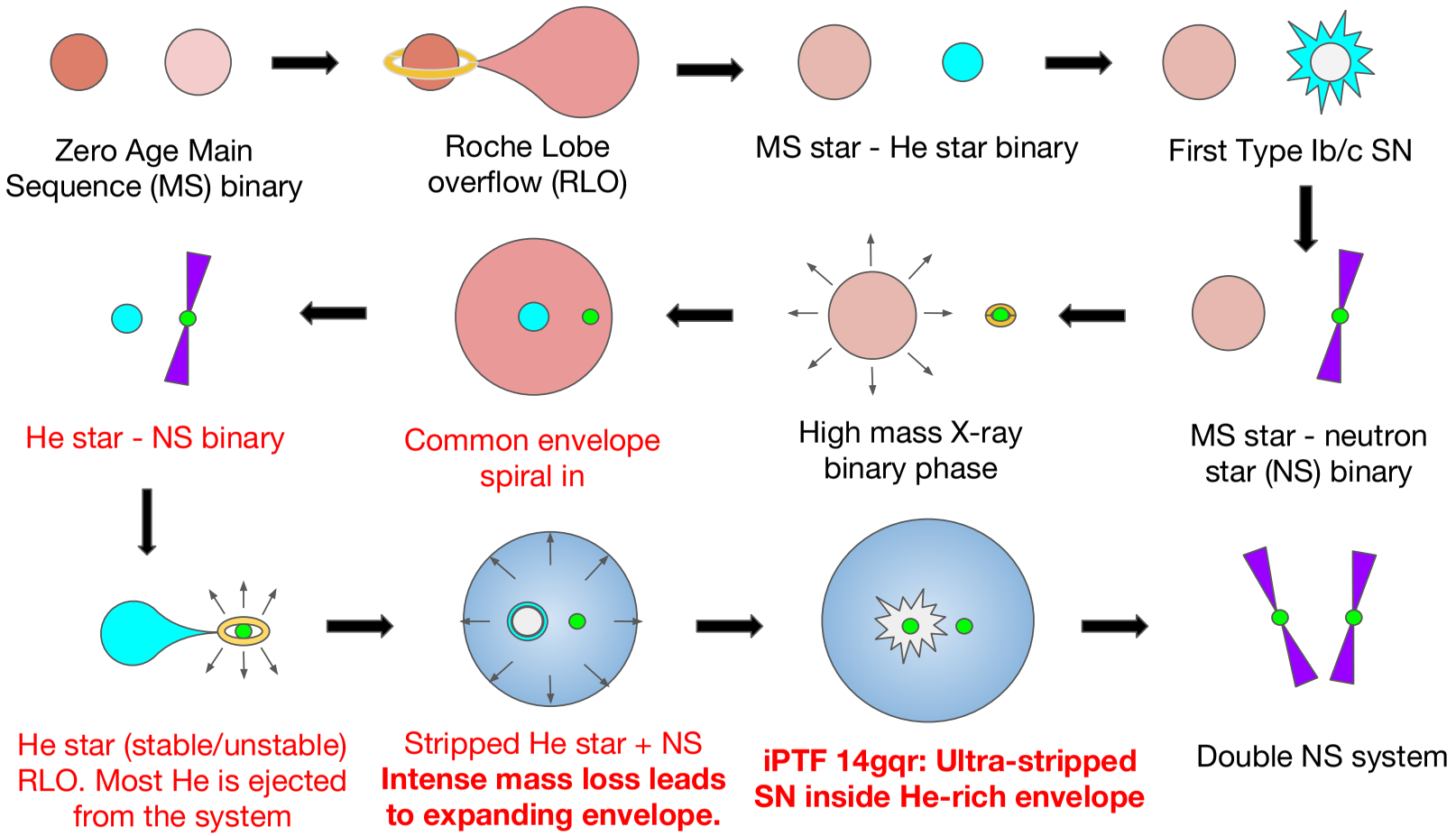

Figure 2.6: **Stellar evolutionary sequence leading from a binary system of massive stars (starting from the top left) to a NS – NS system, adapted from (Tauris et al., 2017)**. NS – BH systems are expected to arise from binaries where the first formed compact object is a BH. NS – WD systems follow a similar evolutionary sequence starting from the HMXB stage (where the NS is replaced by the WD), but require additional mass transfer in the earlier stages (Tauris et al., 2000). The material composition of the stars is indicated by their colors – red indicates H-rich material, cyan/blue indicate He-rich material, grey indicates CO-rich material, and green indicates degenerate matter (in NS). The specific phase of the evolution is indicated by the text next to the systems, with black text indicating phases that have been observed previously, while red text indicates phases that have not been previously observed, and bold red text phases we observed in this work.

2.5 Materials and methods

Observations

iPTF Discovery

iPTF 14gqr (SN 2014ft) was discovered by the intermediate Palomar Transient Factory (iPTF; (Law et al., 2009; Masci et al., 2017)) in data taken with the CFH12K 96-Megapixel camera (Law et al., 2010; Rahmer et al., 2008) mounted on the 48 inch Samuel Oschin Telescope at Palomar Observatory (P48), on 2014 October 14.18 [Modified Julian Date (MJD) 56944.18]. The source was discovered at coordinates right ascension (α) = $23^{\rm h}33^{\rm m}27.95^{\rm s}$, declination ($\delta$) = $33°38'46.1''$ (J2000 equinox), while it was not detected on 2014 October 13.32 (MJD 56943.32; 0.86 days before discovery) up to a limiting magnitude of $g \geq 21.5$. We nominally adopt the average MJD 56943.75 ± 0.43 as the explosion date, and calculate all phases with reference to this epoch. However, the actual explosion could have taken place before the last non-detection depending on the (unknown) behavior of the early emission. Hence, we allow the explosion time to vary as a free parameter in our modeling, and discuss the last non-detection individually in the context of the physical models.

Optical light curves

We obtained g band photometry of iPTF 14gqr with the P48 CFH12K camera, along with additional follow-up photometry in the $Bgri$ bands with the automated 60-inch telescope at Palomar Observatory (P60; Cenko et al., 2006). Point spread function (PSF) photometry was performed on the P48 images using the Palomar Transient Factory Image Differencing and Extraction (PTFIDE) pipeline (Masci et al., 2017), while the P60 images were reduced using an automated pipeline (Fremling et al., 2016). The photometric evolution of the source is shown in Figure 2 and the data are presented in Table 2.1. The data have been corrected for Galactic extinction (Schlafly et al., 2011) for $E(B-V) = 0.082$ mag and $A_{\rm V} = 0.255$ mag. We do not expect any additional host extinction owing to the remote location of the transient, which is consistent with the absence of Na I D absorption lines in all our spectra.

Additional follow-up photometry in $BVgri$ bands was obtained with the Las Cumbres Observatory (LCO) 1-meter telescope located at the McDonald Observatory (Brown et al., 2013). These data were processed using the tools available in the `lcogtsnpipe` package followed by PSF photometry (Valenti et al., 2016). Owing to the faint peak magnitude of the source (close to the sensitivity limit of LCO),

the photometry obtained from these observations are relatively noisy due to their low signal-to-noise ratio. Since P60 obtained contemporaneous observations with LCO with much higher signal-to-noise ratio, we chose not to include the LCO data in our analysis. Nonetheless, the contemporaneous photometry from LCO and P60 are completely consistent with each other, and we present the LCO photometry in Table 2.1 for completeness.

Swift UV / X-ray observations

We triggered the *Swift* follow-up of the source in the V, B, $UVW1$, and $UVW2$ bands with the *Swift* Ultra-Violet/Optical Telescope (UVOT; Roming et al., 2005) and X-ray follow-up with the *Swift* X-ray telescope (XRT; Burrows et al., 2005). We processed the data with the `HEAsoft` package and detected the transient in the $UVW1$ and $UVW2$ bands in the first three and two epochs of observation, respectively, while only non-detections were obtained at subsequent epochs. The UV photometric evolution is shown in Figure 2 along with the optical light curves, and the data are presented in Table 2.1, where we used empirical fits (Cardelli et al., 1989) to compute extinction coefficients for the $UVW1$ and $UVW2$ bands. Only upper limits were obtained in all epochs of *Swift* XRT observations. The corresponding flux limits are summarized in Table 2.2.

We also stacked all of the cleaned event files obtained over a period of 21.9 days, amounting to a total exposure time of 12.2 ks. We obtain a 5σ flux upper limit of 1.24×10^{-3} counts s^{-1} corresponding to a 0.3 - 10 keV unabsorbed flux limit of 3.5×10^{-14} ergs cm^{-2} s^{-1} (assuming a photon index $\Gamma = 2$). The Galactic neutral hydrogen column density along this line of sight is 5.7×10^{20} cm^{-2} (Winkel et al., 2016), yielding a corresponding X-ray luminosity limit of 3.4×10^{41} ergs s^{-1} for the source at a distance of $D = 284.5$ Mpc.

Optical spectroscopy

We obtained a sequence of spectroscopic observations of the source starting from 4.3 hours after first detection to +59 days after r band peak using the Dual Imaging Spectrograph (DIS) mounted on the 3.5 m Astrophysical Research Consortium telescope at Apache Point Observatory (APO), the auxiliary port camera (ACAM; Benn et al., 2008) on the 4.2 m William Herschel Telescope (WHT), Andalusia Faint Object Spectrograph and Camera (ALFOSC) on the Nordic Optical Telescope (NOT), the Gemini Multi-Object Spectrograph (GMOS; Hook et al., 2004) on the Gemini

North (N) telescope, the Low Resolution Imaging Spectrograph (LRIS; Oke et al., 1995) on the Keck I telescope, and the DEep Imaging Multi-Object Spectrograph (DEIMOS; Faber et al., 2003) on the Keck II telescope. All spectra were reduced using standard tasks in IRAF and IDL, including wavelength calibration using arc lamps and flux calibration using standard stars.

The sequence of spectra obtained are shown in Figure 2.3, and the times of the spectra are shown as dashed vertical lines in Figure 2. The spectroscopic observations are summarized in Table 2.3. We were unable to obtain a high signal-to-noise ratio (SNR) spectrum of the transient at epochs beyond $\approx$ 30 days from the light curve peak. We also obtained a spectrum of the apparent host galaxy nucleus with APO DIS on 2014 October 14 (shown in Figure 2.7) which was found to exhibit narrow emission lines of Hα, Hβ, [SII], [NII], [OII], and [OIII]. Additionally, we obtained one spectrum of the transient location $\sim$ 800 days after the explosion as a part of a spectroscopic mask observation and did not detect any nebular emission features at the source location. All spectra are available via the WISeREP repository (Yaron et al., 2012).

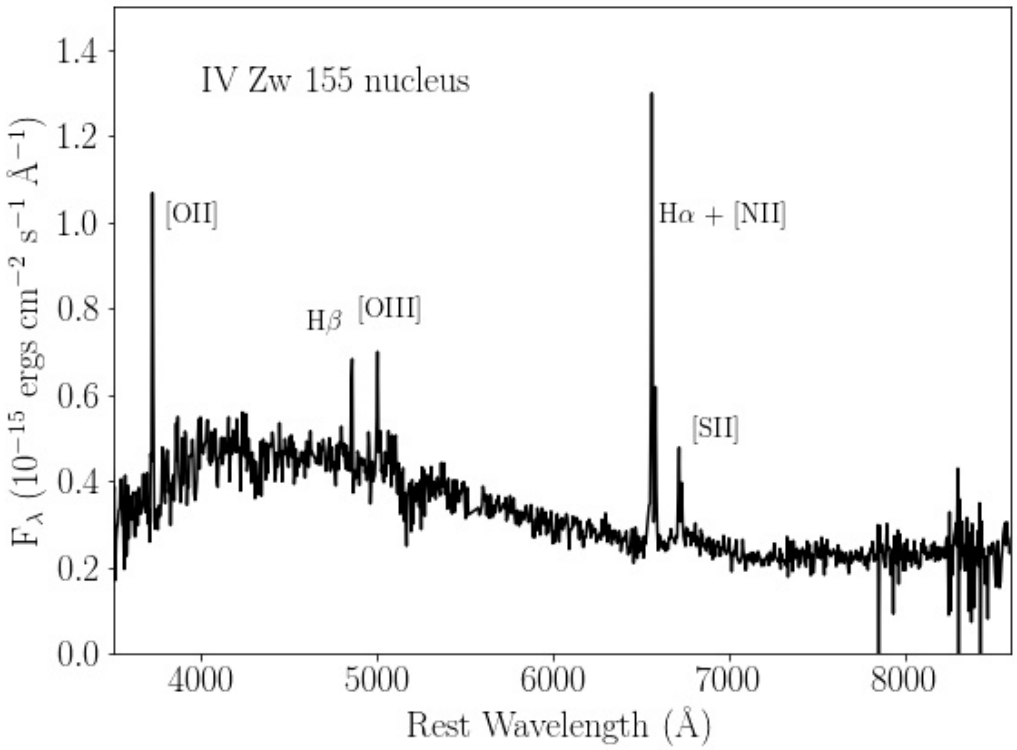

Figure 2.7: **Spectrum of the nucleus of the apparent host galaxy of iPTF 14gqr.** Prominent emission lines from the galaxy are marked in the spectrum.

NIR imaging

We observed the field of iPTF 14gqr using the Wide Field Infrared Camera (WIRC; Wilson et al. 2003) on the Palomar 200-inch telescope on the night of 2014 Oct 19 (UT). We obtained 21 images (1×60 s each) using the J filter, 25 images (2× 20 s each) using the K_s filter, and 24 images (2×20 s each) using the H filter, for a total integration time of 21, 16.7, and 16 minutes, respectively, in each band.

The data were processed using a custom reduction pipeline including flat-fielding and sky subtraction as well as special filtering steps to remove artifacts associated with the replacement detector in use at the time. The source is well-detected in all three filters in the final stacks. We performed aperture photometry within IDL and obtained magnitudes of $J = 19.76 \pm 0.08$, $H = 19.58 \pm 0.12$, and $K_s = 19.05 \pm 0.15$.

Radio observations

We observed iPTF 14gqr with the Very Large Array (VLA) radio telescope on both 2014 October 15.4 and 2014 October 25.0. Each observation was performed using C-band (centered at 6.1 GHz) and K-band (centered at 22 GHz) in the C configuration. The Wideband Interferometric Digital Architecture (WIDAR) correlator was used in continuum mode with a 2 GHz bandwidth in C-band and a 8 GHz bandwidth in K-band. We analyzed the data with standard AIPS routines, using 3C 48 as the flux calibrator and NVSS J234029+264157 as the phase calibrator. Our observations resulted in null detections in both bands at each epoch. The observational limits are 11.6 microJanskys (μJy) and 11.7 μJy at C-band and K-band [measured as the $1\,\sigma$ root-mean-squared (RMS) noise of the reduced image], respectively, on 2014 October 15. On 2014 October 25, the observational limits are 13.0 μJy and 15.0 μJy, respectively. An additional limit was obtained using the Arcminute Microkelvin Imager (AMI; Zwart et al., 2008) Large Array telescope. The AMI observation was undertaken on 2014 October 14.7 at a central frequency of 15 GHz. The reduction of the AMI observation was conducted using the fully-automated calibration and imaging pipeline AMIsurvey (Staley et al., 2015) and resulted in null detection with a $1\,\sigma$ RMS of 58 μJy.

Host imaging and spectroscopy

Late-time imaging

We undertook deep imaging of the source region in the g-band and R-band filters with LRIS on 2015 June 13 (MJD 57186.5) for a total exposure time of 960 s and 840

s, respectively. The data were reduced and processed with standard image reduction procedures in `lpipe` (Perley, 2019). No source was detected at the transient location down to a 3σ AB magnitude of $R > 26.1$ mag and $g > 26.5$ mag (without extinction correction). This constrains the presence of any stellar association at the location of the transient to $M_R > -11.4$ mag and $M_g > -11.1$ mag. Late-time images of the host galaxy region are shown in Figure 2.20.

Host environment spectroscopy

iPTF 14gqr was discovered in the outskirts of an extended spiral galaxy showing clear signs of tidal interactions with nearby companions. Since none of the apparent extended sources near the transient region had measured redshifts in the NASA/IPAC Extragalactic Database (NED), we undertook one spectroscopic mask observation on 2016 November 28 (≈ 800 days after discovery) of the region with LRIS on Keck I in order to confirm the interaction scenario. Additionally, this would allow us to ascertain whether any of the other nearby fainter galaxies could have potentially hosted the transient (i.e. was at a similar redshift) and if the spiral host galaxy itself was a part of a galaxy group or cluster.

We selected a total of 32 extended sources classified as galaxies (including the apparent spiral host) in the Sloan Digital Sky Survey (SDSS) within $5.4'$ of the transient location (out of a total of 254 objects) to place the slits on the spectroscopic mask, along with one slit at the location of the transient. The selection of sources for the slit mask was prioritized based on the projected distance of the galaxy from the transient. The spectra were reduced with standard routines in IRAF. Details of the spectroscopic mask observation are given in Table 2.3, while Table 2.4 lists the redshifts of the galaxies identified from the mask observation. The positions of the galaxies whose redshifts could be determined are shown in Figure 2.8 as circles, while all other cataloged SDSS galaxies are marked by crosses.

The faintest source placed in the mask had a SDSS magnitude of $r \approx 22.51$ mag, while the faintest mask source within 100 kpc ($\approx 81''$) of the transient had $r \approx 21.89$ mag. Amongst the galaxies whose redshifts could be determined, the faintest source had SDSS magnitude of $r \approx 22.11$ mag, while the same for galaxies within 100 kpc of the transient was $r \approx 21.60$ mag. Our redshift identification was complete for all sources brighter than $r \approx 20.29$ mag within 100 kpc of the transient, corresponding to an absolute magnitude of $M_r \approx -17.0$ at the source redshift.

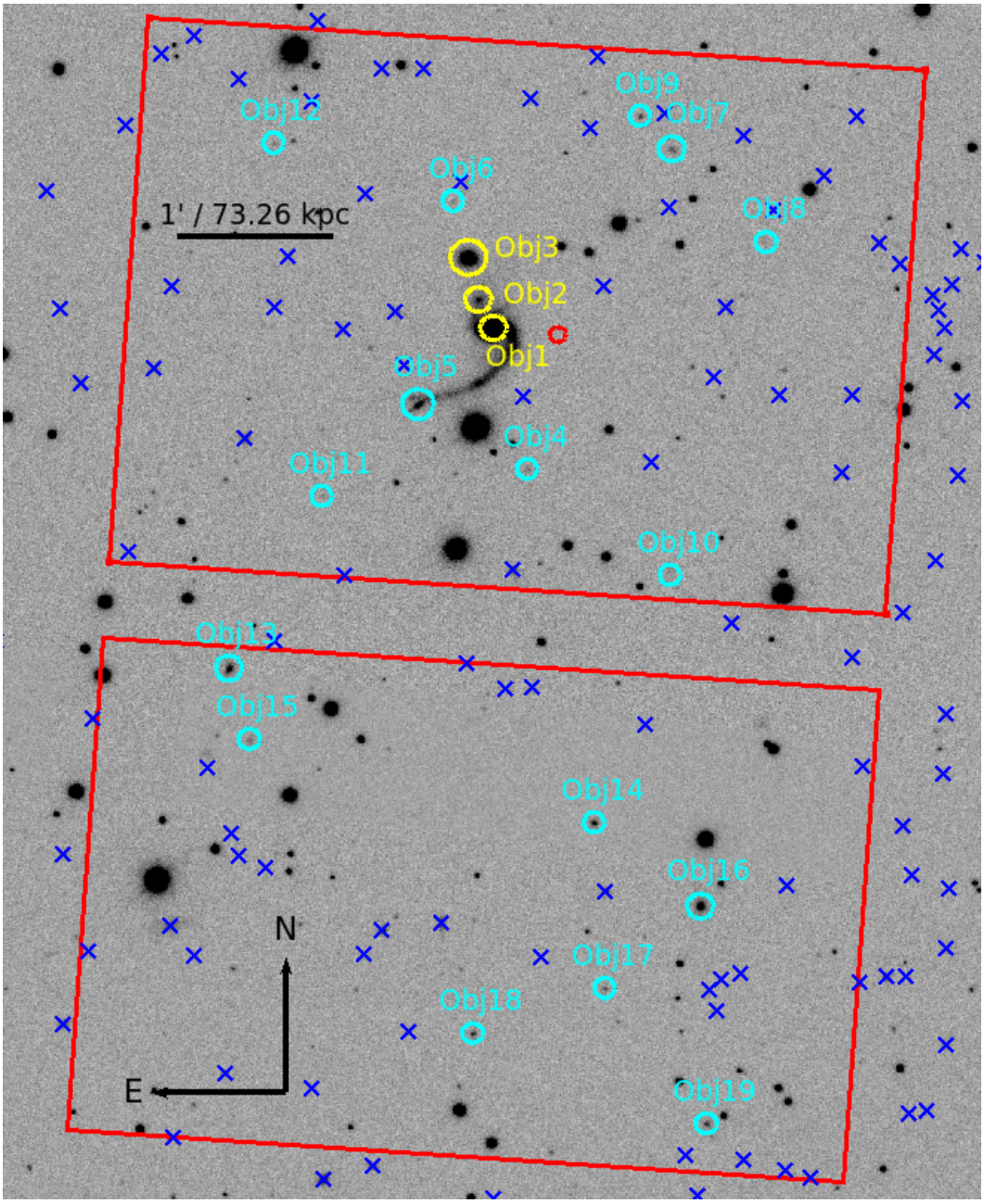

Figure 2.8: **SDSS *r* band image of the host environment of iPTF 14gqr.** The red circle marks the location of the transient, while the yellow circles mark the positions of the galaxies confirmed to be at the same redshift as that of the transient. The cyan circles mark the locations of galaxies identified as background galaxies in the mask. Blue crosses mark the locations of all other objects classified as galaxies in SDSS. The red boxes indicate the field of view of Keck LRIS during the mask observation. Redshifts could not be securely determined for other objects in the mask due to low SNR of the spectra.

Photometric evolution

Basic properties

We summarize the basic photometric properties of the light curve in the g, r, and i bands (where we had sufficient coverage) in Table 2.5. We find the peak magnitudes, time of maximum, and corresponding rise time (between assumed explosion time and peak of light curve) in each filter by fitting a low order polynomial to the photometry near peak. We characterize the post-peak light curve in terms of the light curve decline rate (magnitudes per day). The absence of photometric data points beyond ~ 10 days after peak does not allow us to estimate the more commonly used quantity Δm_{15}, the drop in magnitude in 15 days after light curve peak. The uncertainties on these parameters were estimated by Monte Carlo sampling of 1000 realizations of the photometric data points using their associated uncertainties.

The observed peak absolute magnitudes are on the low end of the distribution of SN Ic peak magnitudes reported in Drout et al., 2011, where SNe Ic were found to have peak $\langle M_R \rangle = -18.3 \pm 0.6$ (uncertainties are 1σ), while they are within the typical peak magnitudes found in the sample of Taddia et al., 2018 (who find $\langle M_r \rangle = -17.66 \pm 0.21$ and $\langle M_g \rangle = -17.28 \pm 0.24$). The rise times of the light curves are shorter in the bluer bands as typically observed in Type Ib/c SNe (Taddia et al., 2015). When compared to other Type Ic SNe, the r band light curve rise time for iPTF 14gqr falls on the extreme low end of the distribution observed in Type Ic and Ic-BL SNe. For example, Taddia et al., 2015 find $\langle t_{rise} \rangle$ of 11.5 ± 0.5 days and 14.7 ± 0.2 days for Type Ic and Ic-BL SNe, respectively, based on light curve from the SDSS-II supernova survey. If the decline rates are converted to an equivalent Δm_{15}, we find the estimated Δm_{15} (≈ 2.5 mag in g band and ≈ 1.3 mag in r band) to be much higher than that observed for all normal Type Ib/c SNe (Drout et al., 2011; Taddia et al., 2018), but similar to those observed in the fast Type I events SNe 2002bj (Poznanski et al., 2010), 2010X (Kasliwal et al., 2010), and 2005ek (Drout et al., 2013).

Comparison with other sources

We compare the multi-color light curves of iPTF 14gqr to other relatively faint and fast evolving Type I SNe from the literature in Figure 2.9. These include the core-collapse Type Ic SN 1994I (Richmond et al., 1996), the Ca-rich transient PTF 10iuv (Kasliwal et al., 2012), and the rapidly evolving transients SNe 2002bj (Poznanski et al., 2010), 2010X (Kasliwal et al., 2010), and 2005ek (Drout et al., 2013). We

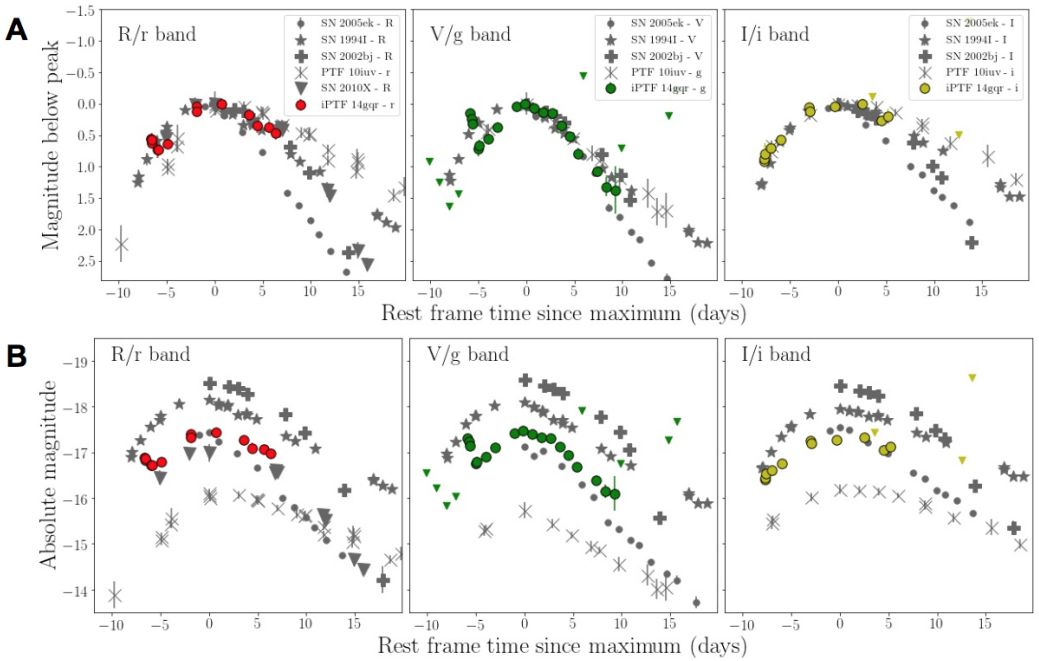

Figure 2.9: **Comparison of the photometric evolution of iPTF 14gqr to other fast evolving SNe**. These include SN 1994I (Richmond et al., 1996), SN 2002bj (Poznanski et al., 2010), SN 2005ek (Drout et al., 2013), SN 2010X (Kasliwal et al., 2010), and PTF 10iuv (Kasliwal et al., 2012). Panel A shows the photometric evolution normalized to peak magnitude, while the panel B shows the same on an absolute magnitude scale.

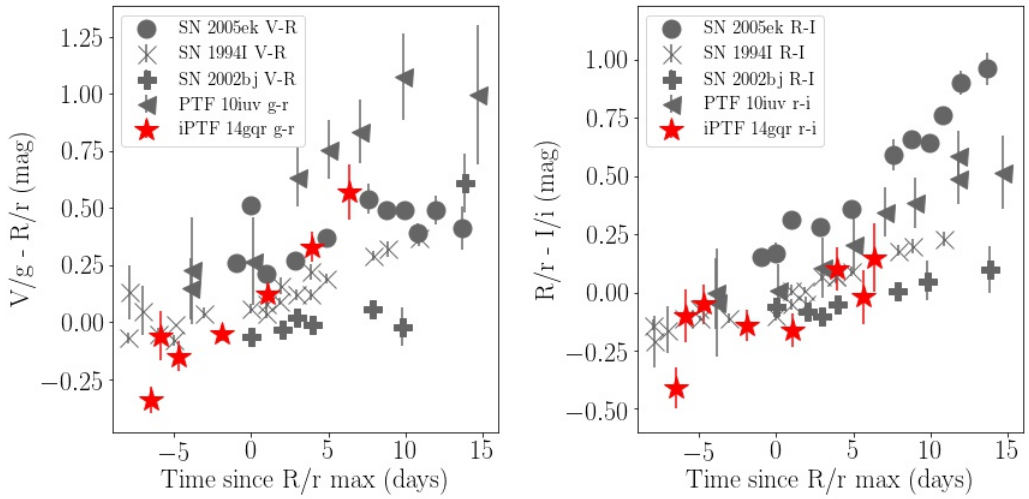

Figure 2.10: **Comparison of the color evolution of iPTF 14gqr with the other fast SNe shown in Figure 2.9**. Due to the absence of photometry in identical filters, we compare colors in corresponding filter pairs of V/g, R/r, and I/i as indicated in the legend.

plot the photometric evolution normalized to peak magnitude in the upper panel and on an absolute scale in the lower panel. Owing to the lack of observations in identical filters, we are constrained to compare the light curve evolution of these transients in corresponding pairs of R/r, V/g, and I/i bands (which in general we refer to as r, g, and i bands, respectively). We first focus on a comparison of the second peak of the light curve of iPTF 14gqr to that of these events.

Figure 2.9 shows that the light curve shape and timescales (for the second peak) of iPTF 14gqr are broadly similar to several of the events in this sample. In general, the light curves are faster than those of PTF 10iuv, but slower than the very fast decay exhibited by SN 2005ek. Overall, SN 1994I exhibits light curves most similar to that of iPTF 14gqr near peak light, although the rise time to peak for iPTF 14gqr is shorter than that of SN 1994I. For SN 2005ek, the best upper limit for the rise time was at ≈ 9 days before R band maximum while the same for SN 2002bj was 7 days. On the other hand, iPTF 14gqr attained a peak absolute magnitude (see Table 2.5) fainter than that of SN 2002bj and SN 1994I, but similar to that of SN 2005ek and SN 2010X.

We compare the color curves of these transients to that of iPTF 14gqr in Figure 2.10, in corresponding pairs of $V/g - R/r$ and $R/r - I/i$ colors. The sharp color jump after the first data point arises from the rapid blue first peak. Subsequently, iPTF 14gqr has one of the fastest color $g - r$ color evolution among this set of transients, displaying a progression from a very blue transient ($g - r \approx -0.4$ mag) at early times to a relatively red transient ($g - r \approx 0.5$) within 10 days of explosion. This fast reddening is indicative of rapid cooling of the ejecta since the spectra at these phases are broadly consistent with featureless continua with weak broad features. We conclude that the multi-color light curves of the main peak of iPTF 14gqr exhibit several similarities (light curve shape and timescales) as well as unique differences (short rise time) in this sample of transients.

The rapid first peak of the light curve is perhaps the most distinguishing feature of iPTF 14gqr when compared to this sample of transients, and hence we compare this first peak to that of other known SNe exhibiting double peaked light curves in Figure 2.11. These include the Type Ic iPTF 15dtg (Taddia et al., 2016), the GRB associated broad-lined Type Ic SN 2006aj (Brown et al., 2009), the Type Ib SN 2008D (Bianco et al., 2014), and the Type IIb SN 2011dh (Arcavi et al., 2011). We show the iPTF 14gqr light curve in g band since it has the best coverage. As shown, iPTF 14gqr has one of the fastest rise times (≤ 0.5 days, as constrained)

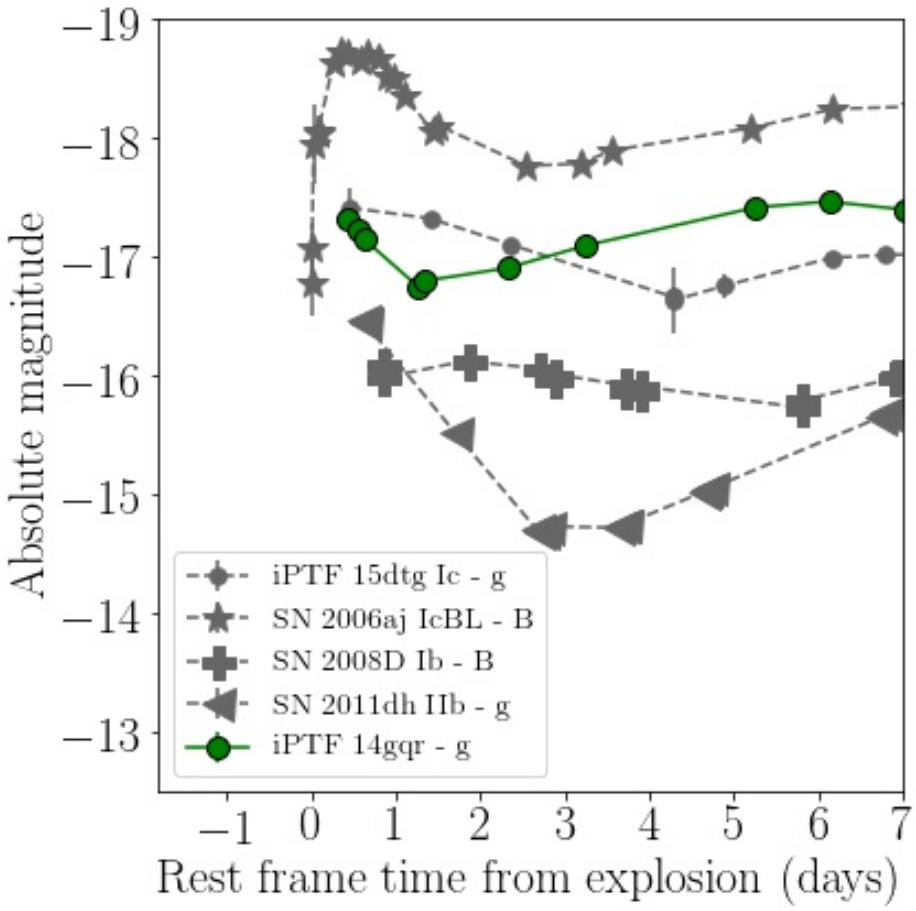

Figure 2.11: **Comparison of the first peak of the light curve of iPTF 14gqr with other known SNe exhibiting double peaked light curves.** The comparison sample includes the Type Ic SN iPTF 15dtg (Taddia et al., 2016), the Type Ic-BL SN 2006aj (Brown et al., 2009), the Type Ib SN 2008D (Bianco et al., 2014), and the Type IIb SN 2011dh (Arcavi et al., 2011).

and decay rates of the first peak in this sample. The width of the first peak of iPTF 14gqr is most similar to that of the Type Ic-BL SN 2006aj, while the peak absolute magnitude is similar to that of iPTF 15dtg.

Optical / UV SEDs

We performed blackbody fitting of the multi-color photometry at all epochs for which we had photometric detections in 3 or more filters. In particular, we have two epochs with photometric data from all optical / UV bands, and the resulting blackbody SEDs are shown in Figure 2.3. The first epoch was within the first peak of the light curve (at $\approx$ 14 hours after explosion), where the UV / optical photometry

is consistent with a blackbody of temperature > 30,000 K. For comparison, we plot a blackbody fit of a spectrum obtained within an hour before this epoch of photometry. This spectrum is also well described by a blackbody consistent with the photometric fit within the uncertainties. We also plot a blackbody fit to the second epoch where we had complete multi-color coverage, which was near the main peak of the light curve (at $\approx$ 5.3 d after explosion). In this case, the black dashed line represents a blackbody fit to the optical photometry only ($\lambda_{\rm eff} > 4000$ Å). The UV photometric points are found to be significantly fainter than the optical blackbody fit at this epoch (with T $\sim$ 10000 K), which is indicative of significant line blanketing at UV wavelengths (as expected from Fe group elements in the ejecta). The NIR photometric magnitudes obtained near this epoch ($\approx$ 1 day earlier) are also consistent with the optical blackbody fit.

Bolometric light curve

We construct a bolometric light curve of iPTF 14gqr using three methods. We first fit a Planck blackbody function to the observed photometry at all epochs where we have detections in 3 or more filters to obtain a best-fitting blackbody and corresponding temperature, radius, and luminosity. The relatively featureless optical continua of the source allows us to obtain good blackbody fits at all epochs where multi-color photometry is available. We constrain the blackbody luminosity before the first detection by calculating the fraction of total flux within g band at first detection ($\approx$ 2.6%), and use it to estimate the luminosity upper limit with the latest pre-discovery limit in g band. The resulting bolometric luminosity curve is shown in Figure 2.4 as black filled circles. The corresponding radius and temperature evolution is also shown in Figure 2.4. Although the blackbody approximation is valid within the first peak (as indicated by the best fitting SEDs), the fit overestimates the luminosity during the second peak of the light curve due to line blanketing in the UV.

We therefore compute a pseduo-bolometric light curve of the source by performing trapezoidal integration of the gri photometric fluxes (from the lower wavelength edge of the g band to the higher wavelength edge of the i band) at all available epochs. Our peak photospheric spectra indicate the presence of additional flux at wavelengths $\lambda \leq 4000$ Å (the lower edge of the g band) as well as at $\lambda \geq 8000$ Å (the upper edge of the i band), which are not accounted for by a simple trapezoidal integration. Hence, we estimate the contribution of these fluxes by integrating the optical spectra from 4000 Å to 8000 Å and comparing them to the integrated value

over 3000 Å to 10000 Å (the full range of our optical spectra). Performing this procedure on multiple spectra around peak light, we find that the simple trapezoidal integration underestimates the total optical flux by a factor ranging from 1.42 to 1.56 over multiple epochs. Since we do not have simultaneous spectroscopy with all epochs of multi-band photometry, we choose to scale the fluxes obtained from a trapezoidal integration by an average factor of 1.48, while conservatively adding an uncertainty of 10% to account for the possible errors on this fraction.

The pseudo-bolometric light curve is shown in Figure 2.4, which is found to be consistently smaller than the blackbody luminosity as expected. The true bolometric luminosity for the second peak lies in between these two estimates, and is likely to be very close to the pseudo-bolometric luminosity we estimate. Hence, we use the pseudo-bolometric luminosities for modeling the properties of the second light curve peak. We also compute a g band luminosity λF_λ for comparison, and show it as black empty circles in Figure 2.4.

Since our observations did not capture the rise to the first peak, we can only constrain the peak luminosity of this phase to be greater than $\sim 2 \times 10^{43}$ ergs s^{-1} (i.e. the luminosity near first detection), while the corresponding temperature at the first peak to be higher than $\sim 32,000$ K. The second peak reaches a peak (pseudo-bolometric) luminosity of $\sim 2.2 \times 10^{42}$ ergs s^{-1} with a peak temperature of $\sim$ 10,000 K. The total integrated energy emitted within the second peak (starting from ≈ 2 days to $\approx$ 14 days after explosion) of the pseudo-bolometric light curve is $\sim 1.8 \times 10^{48}$ ergs. The blackbody temperatures exhibit rapid cooling from $> 32,000$ K to $\sim 10,000$ K at initial phases (< 2 days after explosion), followed by a slower cooling phase at later epochs. Similarly, the blackbody radius exhibits an initial fast increase with time, followed by a slower increase at later phases. A linear fit to the photospheric radius evolution after peak light (between 8 and 15 days after explosion) produces an expansion velocity of $\sim 11,400$ km s^{-1}, while the same for the early light curve (< 2 days from explosion) gives an expansion velocity of $\sim 33,500$ km s^{-1}.

Spectroscopic evolution

First peak

The spectroscopic sequence for iPTF 14gqr is shown in Figure 2.3. The earliest spectra were obtained within a day from explosion, and exhibit intermediate width emission lines of He II, C III, and C IV which evolve rapidly with time. In particular, the earliest +13.9 h spectrum exhibits emission lines of He II (λ4686) and C IV

(λ5801, 5812) with FWHMs of $\sim 5000\,\mathrm{km\,s^{-1}}$ and ~ 2000 km s^{-1}, respectively, although the He II line may be contaminated with emission from a nearby C III λ4650 line. The presence of C III is confirmed from the spectrum taken at +25.2 hours where the C III λ5696 line becomes prominent.

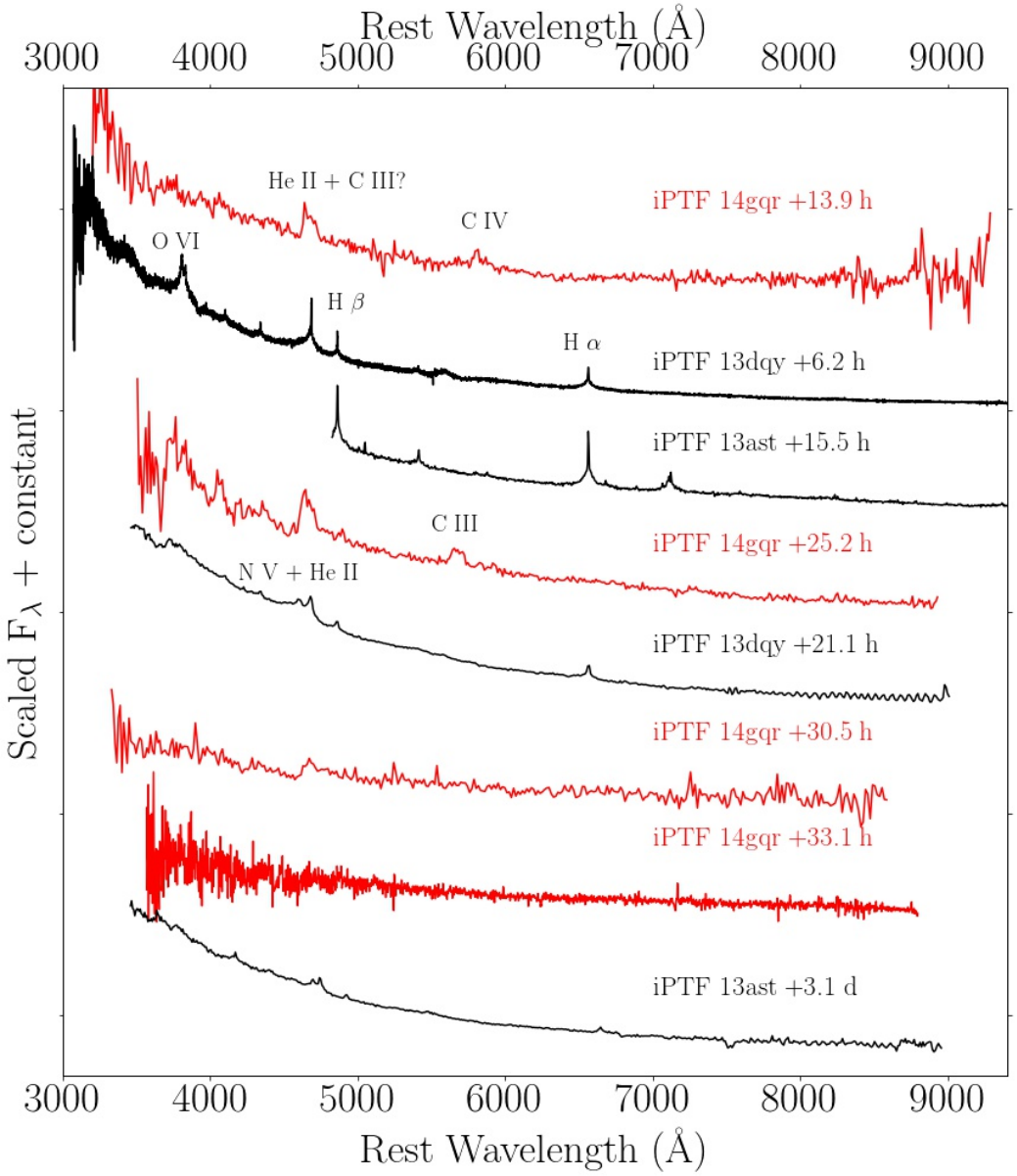

Figure 2.12: **Comparison of early (flash) spectra of iPTF 14gqr (red) to those of iPTF 13ast and iPTF 13dqy (black)**. These SNe also showed rapid temporal evolution in their early spectra. Prominent emission lines are marked along with phases (with respect to explosion time) of the spectra.

The intermediate width He II line weakens in the +30.5 h spectrum while exhibiting signatures of an extended red wing, before disappearing in a spectrum taken about

3 hours later. We highlight the rapid evolution of the He II line in Figure 2.3, where we plot F_λ as function of velocity shift from the He II line for all spectra taken within the first day of detection. In Figure 2.12, we compare our early spectra to those of the SNe iPTF 13ast (Gal-Yam et al., 2014) and iPTF 13dqy (Yaron et al., 2017), where early spectroscopy had also revealed significant temporal evolution of the flash ionized spectra. Both these events were of Type II and hence exhibit prominent H emission lines which are absent in iPTF 14gqr. The He II λ4686 line is a common prominent feature of the flash ionized spectra of these events, and the C III λ4650 and C IV λ5801 lines were also observed in iPTF 13ast. Note that the flash ionized spectra of these events exhibit significantly narrower emission lines (with central FWHM of $\sim$ 100 km s^{-1} superimposed on broad Lorentzian wings) compared to those of iPTF 14gqr.

The spectral evolution of the C high ionization lines in the early spectra is very similar to that seen in the WC sub-type evolution of galactic Wolf-Rayet stars (Crowther, 2007; Sander et al., 2012). In particular, the C III λ5696 / C IV λ5801 ratio increases in the later and cooler sub-types (WC7 - WC9) of this class, consistent with the increasing ratio observed in this source with decreasing photospheric temperature. On the other hand, the C III λ4650 line decreases in strength with decreasing temperature in the later WC stars as the C III λ5696 line becomes stronger (Sander et al., 2012). We can confirm the presence of He II in the spectra by noting that the λ4686 emission feature is continuously present from +13.9 h to +30.5 h, even after the C III λ5696 disappears in the +30.5 h spectrum (this C III feature is expected to become stronger than the λ4650 feature at lower temperatures (Crowther, 2007; Sander et al., 2012)), suggesting that this emission feature has a dominant contribution from a species different from C III (i.e. He II). Nonetheless, the λ4686 feature in the earlier spectra (at and before 25 h) may have a contribution from C III λ4650, as is observed in the earlier sub-types of WC stars (Sander et al., 2012).

Photospheric phase

Spectra taken about a week after explosion show characteristic absorption features of Type Ic SNe, including lines of Fe II, Ca II, O I, and Ti II. We compare the photospheric phase spectra of iPTF 14gqr to those of other fast and normal Type Ic SNe in Figure 2.13. The comparison candidates include the fast Type Ic events SN 2010X (Kasliwal et al., 2010) and SN 2005ek (Drout et al., 2013), as well as the spectroscopically normal events SN 1994I (Filippenko et al., 1995) and SN 2004aw

(Taubenberger et al., 2006). The phases of the spectra indicated in this section are relative to the r/R-band peak because the explosion times for the literature events are not well constrained. The comparison clearly shows that the photospheric spectra of iPTF 14gqr remain relatively blue and featureless compared to those of the normal Type Ic SNe (SN 1994I and SN 2004aw) at similar phases.

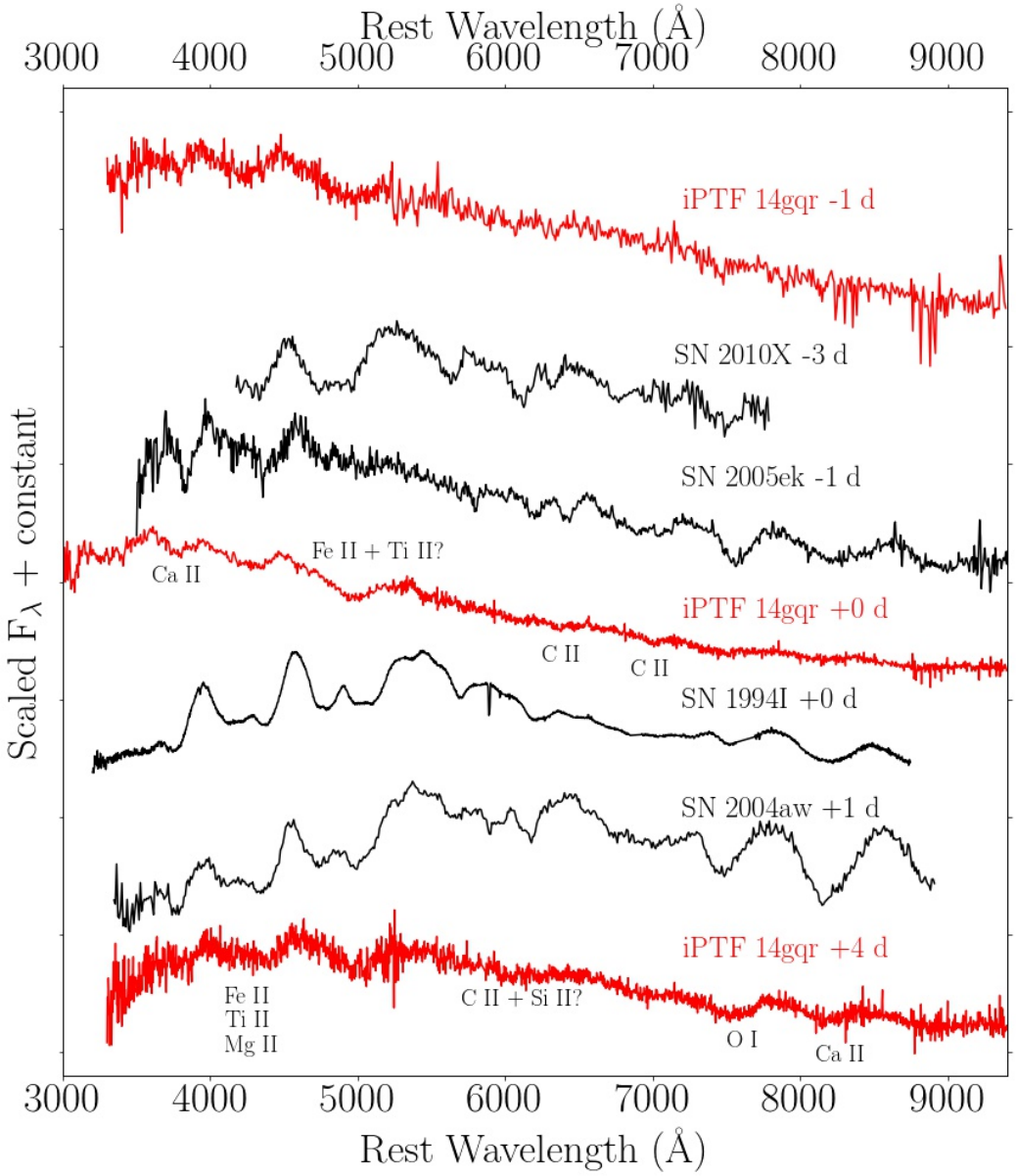

Figure 2.13: **Comparison of the peak photospheric spectrum of iPTF 14gqr (red) to some other known Type Ic SNe (black).** Indicated phases are with respect to R/r band maximum since the explosion times are not well constrained for the events from the literature. Prominent absorption features are marked in the spectra.

The only prominent features in the −1 d and +0 d spectra are those of Fe II and Ca II,

which are also seen in the spectra of the other events. Also apparent are weaker features of C II at 6300 Å and 6900 Å. The spectrum obtained at +4 days shows a progressively cooling continuum as P-Cygni absorption features of O I and Ca II become prominent in the red part of the spectrum. A possible weak absorption feature of Si II also appears near 6200 Å. The continuum shape as well as several spectral features (Fe II and Ca II on the blue side in particular) at this phase are best matched to that of SN 2005ek near peak light. However, SN 2005ek also displays prominent absorption features of Si II and C II near 6500 Å, which are relatively weaker in iPTF 14gqr.

We measure the photospheric velocities from the spectra obtained at +0 d and +4 d from *r* band maximum. We are restricted to measuring only the Fe II λ5169 velocity since we do not see a prominent Si II λ 6355 line in any of our photospheric spectra. We measure the velocity of the Fe II line by fitting a parabola to the absorption minimum. The resulting fits give a velocity of $\approx 10,500$ km s^{-1} and $9,600$ km s^{-1} for the +0 d and +4 d spectra, respectively. A similar fitting procedure performed on the O I λ7773 P-Cygni profile in our +4 d spectrum gives a velocity of $\approx 9,100$ km s^{-1}.

Type Ic SNe generally also exhibit the nearby Fe II lines of λ5018 and λ4924, which are blended into a single blue-shifted feature with respect to the λ5169 line (see for example, the spectra of SN 1994I and SN 2004aw in Figure 2.13). The three features are blended into a single broad absorption component in the case of the high velocity Type Ic-BL SNe, and can potentially cause errors in a velocity measurement if this effect is not taken into account (Modjaz et al., 2016). Although we do not separately detect these features in our spectra, we do see a broad Fe II absorption feature, so we followed the methods given in (Modjaz et al., 2016) to ascertain if the absence of these features could be explained by velocity broadening. The best fitting models produce absorption features that have markedly different shapes, in particular, that are symmetric with respect to the minimum, unlike the shape observed here, and hence, a high velocity broadening is unlikely to be present. Thus, we conclude that the λ5018 and λ4924 features are present (owing to the presence of an asymmetric Fe feature), but not prominent enough to create a separate absorption feature in these spectra.

Early nebular phase

Our final spectrum (with good SNR) was obtained ≈ 34 days after explosion, and show that the source was transitioning very early into the nebular phase. Prominent features in this spectrum include the Ca II IR triplet, [Ca II] $\lambda\lambda$7291, 7324, and a weak feature of [O I] $\lambda\lambda$ 6300, 6364. In particular, the early appearance of [Ca II] $\lambda\lambda$7291, 7324 and the apparent high ratio of [Ca II]/[O I] is similar to that seen in the class of Ca-rich gap transients (Kasliwal et al., 2012; Lunnan et al., 2017). We compare the only nebular spectrum of iPTF 14gqr to the nebular spectra of other Type I SNe which exhibited an early nebular transition at similar phases in Figure 2.14. This sample includes the Type Ic SNe SN 1987M (Filippenko et al., 1990) and SN 1994I (Filippenko et al., 1995), the Ca-rich transients PTF 10iuv (Kasliwal et al., 2012) and SN 2012hn (Valenti et al., 2014), SN 2010X (Kasliwal et al., 2010), and SN 2005ek (Drout et al., 2013).

Amongst the normal Type Ic SNe, the nebular spectrum of iPTF 14gqr is perhaps closest to that of SN 1987M in terms of the prominent nebular lines ([Ca II] $\lambda\lambda$7291, 7324 and the Ca II near-IR triplet), albeit at a later phase (≈ +60 d). SN 1994I exhibits a stronger [O I] feature compared to iPTF 14gqr. Both SN 2010X and SN 2005ek also show a strong Ca II near-IR feature, but still show prominent P-Cygni profiles of O I near 7700 Å. The best spectral match to iPTF 14gqr in this sample are to that of the Ca-rich gap transients PTF 10iuv and SN 2012hn. Both these transients subsequently evolved to exhibit a strong [Ca II] 7300 Å feature at later phases (with a high [Ca II]/[O I] ratio) characteristic of Ca-rich transients. We could not obtain a good SNR spectrum of iPTF 14gqr at later epochs to trace the evolution of the Ca features, although the association of iPTF 14gqr to the class of Ca-rich transients is unlikely (see supplementary text).

Modeling

Arnett Model for the main peak

Type I SNe which do not show signs of interaction (such as iPTF 14gqr) are predominantly powered by energy released in the radioactive decay chain of ^{56}Ni to ^{56}Co to ^{56}Fe. Since the peak photospheric spectra of iPTF 14gqr display a number of similarities to those of fast and normal SNe Ic, we prefer the scenario where this peak is powered by ^{56}Ni decay as in normal SNe Ic, and we derive explosion parameters using a simple Arnett model (Arnett, 1982). We use the analytic light curve expressions for a ^{56}Ni powered photospheric phase light curve given in Lyman

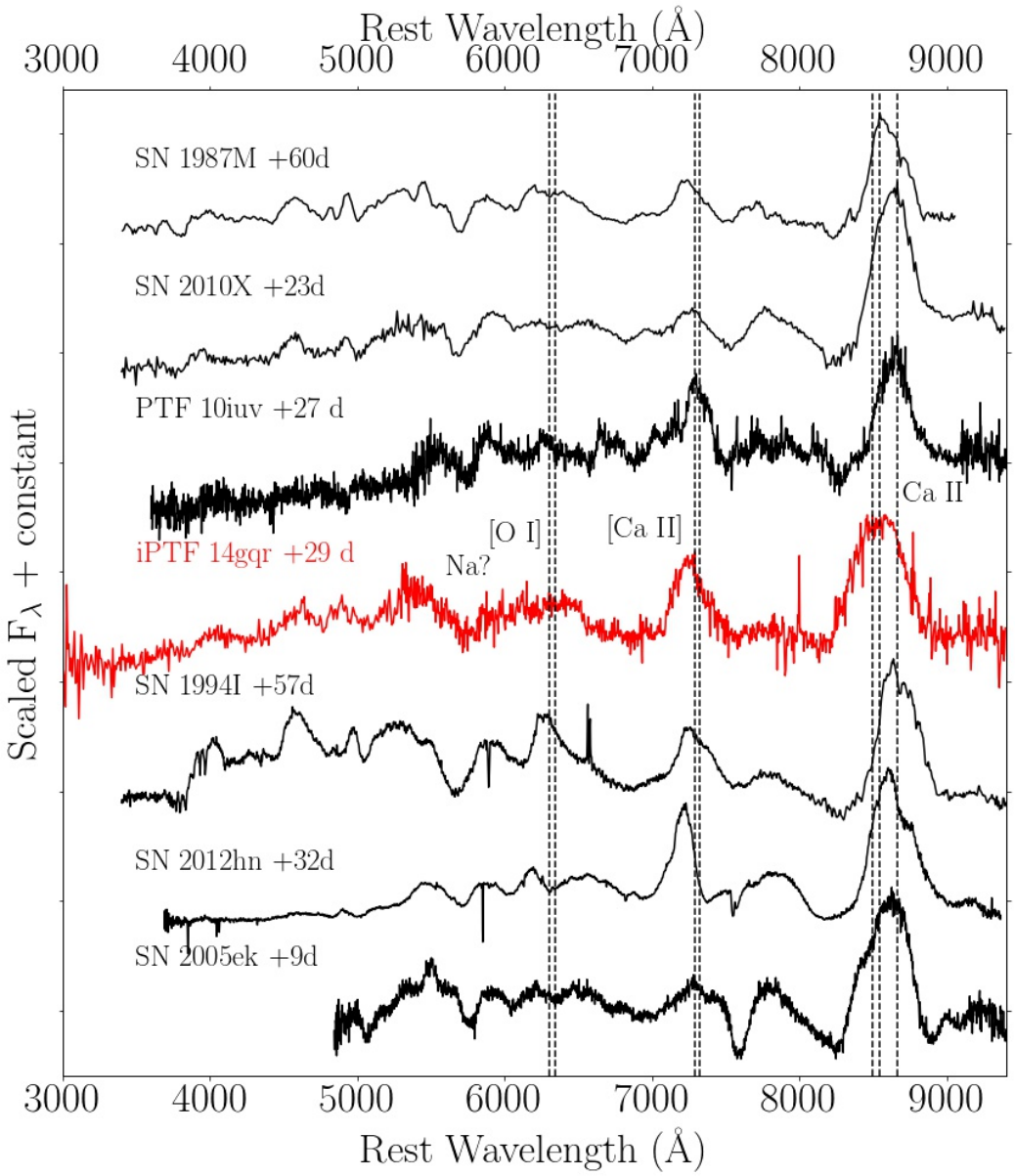

Figure 2.14: **Comparison of the early nebular spectrum of iPTF 14gqr (red) to other Type I SNe (black) which exhibited a fast nebular transition.** The phases of the spectra are with respect to r/R band peak. Prominent nebular lines and absorption features are marked. The dashed vertical lines mark the wavelengths of the [O I] $\lambda\lambda$ 6300, 6364 doublet, the [Ca II] $\lambda\lambda$7291, 7324 doublet, and the Ca II IR triplet. The feature near 5700 Å may be from Na, as was suggested in SN 1987M (Filippenko et al., 1990), or due to Co III.

et al., 2016a and Valenti et al., 2008b to fit the pseudo-bolometric light curve of iPTF 14gqr. We exclude the data points within the first peak (< 2 days from assumed explosion) for this modeling.

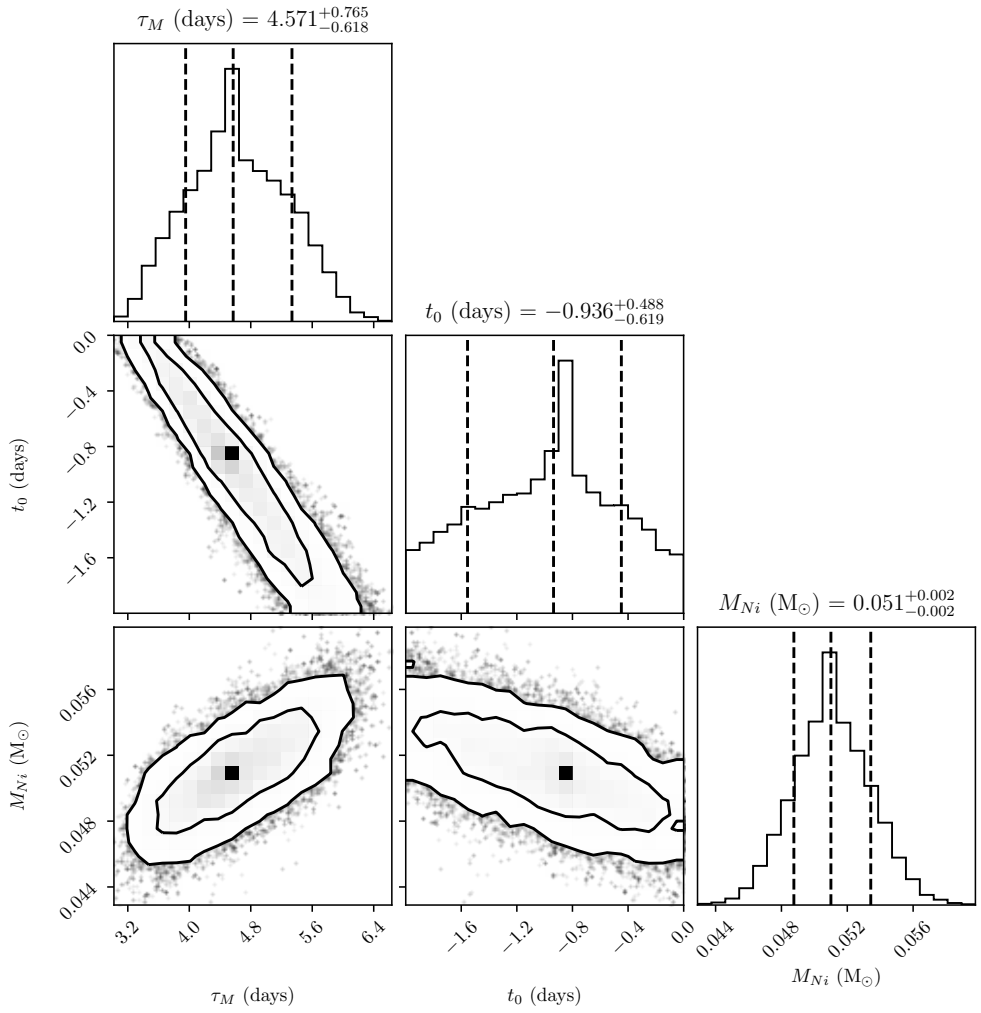

Figure 2.15: **Confidence intervals of the parameters of the Arnett model that is used to fit the bolometric light curve of iPTF 14gqr.** The plot has been derived from the MCMC simulations performed with the `emcee` package. The vertical lines in the histograms indicate the median (best-fitting) value along with the 68% confidence intervals on the parameters. The contours in the two dimensional scatter plots represent 68% and 95% confidence intervals in the respective phase space. The best-fitting values along with their uncertainty intervals are also indicated above the individual histograms.

The only parameters of this model are the nickel mass $M_{\rm Ni}$ and the photon diffusion timescale τ_M. The photon diffusion timescale is related to the ejecta mass M_{ej} and explosion kinetic energy E_k by equation (3) in Lyman et al., 2016a, or equivalently to the peak photospheric velocity v_{ph} and M_{ej} by their equation (1). We fit the observed bolometric light curve to this model using the Markov Chain Monte Carlo (MCMC) method in the Python `emcee` package (Foreman-Mackey et al., 2013).

Keeping the explosion time t_0 as an additional free parameter, we obtain a best-fit model (shown in Figure 2.4) with $M_{Ni} = 0.051^{+0.002}_{-0.002}$ M$_\odot$, $\tau_M = 4.57^{+0.77}_{-0.62}$ days and $t_0 = -0.94^{+0.49}_{-0.62}$ days (i.e. the explosion occurred 0.94 days before the assumed explosion time). The uncertainties indicate 68% confidence intervals estimated from the MCMC simulations although these are likely more conservative because we adopted conservative uncertainties when calculating the bolometric light curve. We caution that the Arnett model has several simplistic assumptions (see below) which likely affect the estimation of the uncertainty intervals.

The best-fitting explosion time is earlier than our last non-detection (0.43 days before assumed explosion), although the predicted flux from the Arnett model would be below our detection threshold. However, this explosion time could still be inconsistent with the pre-discovery limits depending on the exact evolution of the first peak. We show the degeneracies between the various model parameters in Figure 2.15, where the degeneracy between t_0 and τ_M is particularly prominent, since τ_M controls the width of the light curve. For a photospheric velocity of 10^4 km s^{-1} and optical opacity of $\kappa_{opt} = 0.07$ cm^2 g^{-1} relevant for stripped envelope SNe (Cano, 2013; Lyman et al., 2016a; Taddia et al., 2018), we derive $M_{ej} = 0.23^{+0.08}_{-0.06}$ M$_\odot$ and explosion kinetic energy of $E_K = 1.38^{+0.51}_{-0.35} \times 10^{50}$ ergs, where the uncertainty intervals (given at 68% confidence) may again be affected by the assumptions of the model. The lack of late-time photometric coverage does not allow us to put any constraints on this model at later epochs.

The several assumptions of the Arnett model may also affect our estimates. These include assumptions of homologous expansion, spherical symmetry, completely centralized location of ^{56}Ni, and of optically thick ejecta (as in the photospheric phase). The rise and early decay of the bolometric light curve depends sensitively on the extent of mixing of ^{56}Ni in the outer layers of the ejecta. A comparison of parameters derived from the Arnett model to hydrodynamic simulations by Dessart et al., 2016 suggest that the Arnett model can over-estimate the ^{56}Ni mass by about 50%. Additionally, they find the assumption of constant opacity to be a major limitation of this model since the derived parameters depend sensitively on the assumed opacity. For instance, if we adopt $\kappa_{opt} = 0.1$ cm^2 g^{-1} (relevant for material with one electron per four nucleons, e.g., singly ionized He), our ejecta mass estimate would change to 0.16 M$_\odot$.

Nonetheless, we find our estimate of the extremely low ejecta mass (lower than previously known core-collapse SNe) and low explosion energy to be fairly robust.

One potential caveat in the estimation of the ejecta mass is if the ejecta contain He that is effectively transparent. Piro et al., 2014b discuss the possibility that some stripped envelope SNe may have transparent He in their outer layers that does not contribute to the ejecta opacity, since He is effectively transparent in the continuum at low temperatures. They show that some stripped envelope SNe indeed show low photospheric temperatures ($< 10^4$ K) simultaneously with low photospheric velocities (< 8000 km s^{-1}), suggesting that some of the outer (and faster) He layers may be transparent. However, the photospheric temperatures in iPTF 14gqr are higher than 10^4 K up to peak bolometric light (near the epochs of the peak photospheric spectra) while the velocities are also high ($\sim 10,000$ km s^{-1}). Thus, the properties of this source are different from the events where He could have been hidden, suggesting that this effect is not prominent in this source.

Shock cooling model for the first light curve peak

The collapse of the core in a SN explosion produces a radiation mediated shock that travels outward through the stellar envelope, accelerating and heating material along the way. When the optical depth to the shock becomes low enough, the shock breaks out while the shock-heated envelope subsequently cools, producing early optical / UV emission. Nakar et al., 2014 show that the shock cooling emission arising in normal progenitors (i.e. progenitors with no extended envelopes) can create double peaked light curves in the blue and UV bands, but not in the redder R and I bands. The presence of a double peaked structure in the redder bands requires the presence of a low mass extended envelope, where the low mass allows for a short photon diffusion time (and hence a rapid peak and decline) while the extended structure prevents large adiabatic losses at initial times. This corresponds to a case where the shock breaks out from the surrounding circumstellar material (also known as a 'CSM breakout'; e.g. Ofek et al., 2013; Waxman et al., 2016).

In the case of iPTF 14gqr, we observe a double-peaked structure in r band as well, hence we refer to the extended progenitor models of Nakar et al., 2014. The envelope mass can be derived using the velocity of the external envelope v_{ext}, the rise time to peak t_p, and the assumed opacity κ. While early spectroscopy near the first peak should allow a measurement of photospheric velocity at this phase, the relatively featureless continuum of our spectra do not allow us to measure this velocity. Instead, we use equation (13) in Nakar et al., 2014 to estimate the radius of the external envelope R_{ext} from our first temperature measurement in the bolometric

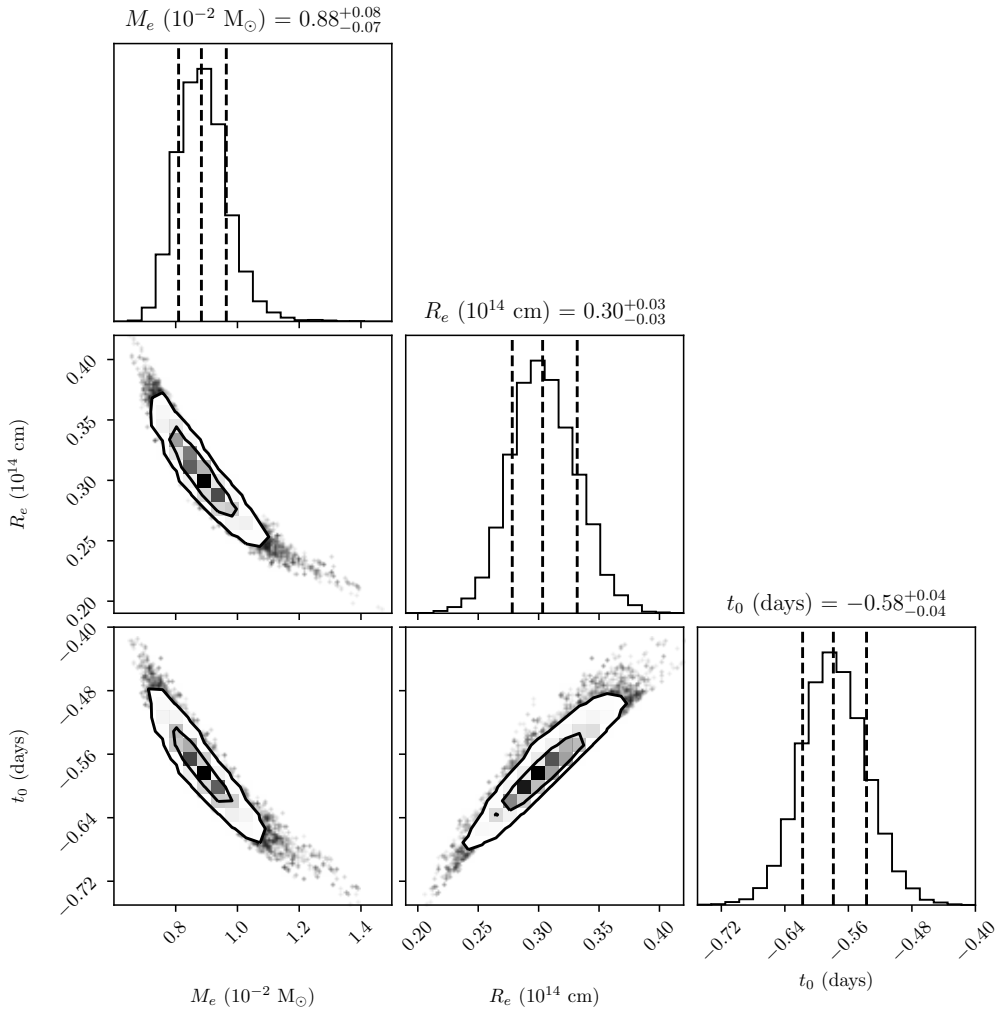

Figure 2.16: **Confidence intervals of the parameters used to fit the early peak using the shock cooling models for extended progenitors, as presented in Piro, 2015.** The figure shows confidence intervals as in Figure S9, but for the parameters of the Piro, 2015 model.

light curve (which is lower than the temperature at bolometric peak $T_{obs,peak}$). For $\kappa \approx 0.2$ cm^2 g^{-1} (relevant for electron scattering dominated opacity in a hydrogen free atmosphere), $t_p \leq 0.5$ days, and $T_{obs,peak} \geq 30000$ K, we get $R_{ext} \geq 1.5 \times 10^{12}$ cm.

Piro, 2015 developed analytic light curves for the shock cooling emission from such an extended envelope, and we use them to compare to the early multi-color light curves of iPTF 14gqr. The model uses a simple one-zone treatment of the extended envelope, where all of the mass M_e is assumed to be concentrated around a radius R_e. The only other parameters are the velocity of the extended material v_e and

the mass of the core M_c, where we set $M_c = 0.23$ M$_\odot$ the explosion energy to $E = 1.38 \times 10^{50}$ ergs to derive v_e. We also let the explosion time t_0 vary such that the model is consistent with the last non-detection. Comparisons between the model and the data are done by performing synthetic photometry on the blackbody spectra predicted by the model.

We fitted the model parameters with the observed data using the Markov Chain Monte Carlo method in the Python `emcee` package (Foreman-Mackey et al., 2013). We only use photometric detections obtained within 1.1 days from the assumed explosion date since we find later times to be affected by the rising portion of the ^{56}Ni light curve. We find a best-fitting model with $M_e = 8.8^{+0.8}_{-0.7} \times 10^{-3}$ M$_\odot$, $R_e = 3.0^{+0.3}_{-0.3} \times 10^{13}$ cm (430^{+43}_{-43} R$_\odot$), and $t_0 = -0.58^{+0.04}_{-0.04}$ days (i.e. the explosion occurred 0.58 days before the assumed explosion time). The resulting light curves for this set of parameters is shown in Figure 2. The error bars indicate the 68% confidence interval for the derived parameters, as estimated from the MCMC simulations.

The shock cooling models for an extended progenitor envelope reproduce the optical light curves (Figure 2), although there are discrepancies in the UV light curve. Such discrepancies were also noted by Piro et al., 2017 who suggest that the acceleration of the shock near the lower density edge of the envelope can cause a stronger temperature evolution than predicted by the one zone model, leading to a poorer match at shorter wavelengths. The optical light curves (particularly in the redder bands) start rising around 1.5 days after explosion, suggesting that the underlying ^{56}Ni light curve becomes important at this phase. As in the case of the Arnett model, we expect the simple assumptions of this model to produce values which are only approximately correct. We thus conclude that the early shock cooling emission was produced by an extended envelope with a mass of ~ 0.01 M$_\odot$ and located at a radius of ~ 500 R$_\odot$.

We show the degeneracies between the model parameters in Figure 2.16. Although there are degeneracies between the parameters, the range of values occupy a relatively small phase space around the best-fitting value. We also consider how the assumed ejecta mass and explosion energy affect the derived parameters by considering the range derived from the Arnett modeling. Adopting the lower end of ejecta mass and explosion energy, we find a best-fitting model with $M_e = 8.2^{+0.8}_{-0.6} \times 10^{-3}$ M$_\odot$, $R_e = 3.6^{+0.3}_{-0.3} \times 10^{13}$ cm, and $t_0 = -0.53^{+0.04}_{-0.05}$ days. On the other hand, adopting the higher end of the ejecta mass and explosion energy distribution, we find

$M_e = 10^{+1}_{-0.9} \times 10^{-3}$ M$_\odot$, $R_e = 2.4^{+0.2}_{-0.2} \times 10^{13}$ cm, and $t_0 = -0.64^{+0.04}_{-0.04}$ days. Thus, our estimates of the envelope properties appear to be fairly insensitive to the adopted ejecta mass and explosion energy.

Interaction with a companion

An alternative explanation of the early excess emission in iPTF 14gqr might be the interaction of the SN ejecta with a non-degenerate companion. Such interaction signatures have been previously observed in some Type Ia SNe (Cao et al., 2015a; Hosseinzadeh et al., 2017; Marion et al., 2016; see Gal-Yam, 2017 for a review of SN classification) where comparison of the data to theoretical models (Kasen, 2010) allows the inference of the orbital separation of the binary system. The models show that the presence of a companion can produce a void in the expanding ejecta, producing a reverse shock that powers excess luminosity at early times when viewed close to the direction of the void. In such a scenario, we might expect high ionization emission lines in the spectra arising from recombination of the companion wind, although the relatively large widths of the lines would suggest unusually high wind velocities for the companion. However, despite the high signal-to-noise ratio of our early spectra, we see no evidence for the presence of broad lines, as expected from the reverse shock produced in the ejecta-companion interaction.

We consider the photometric properties of the first peak in a companion interaction scenario. As shown in Kasen, 2010, the early luminosity evolution depends on the viewing angle of the observer, where the excess flux is most prominent along the direction of the companion and relatively weak along directions perpendicular to or oriented away from the companion. In the case of iPTF 14gqr, we observe a very rapid decline of the bolometric luminosity at early times ($\sim$ a factor of 10 in <1 day), ruling out viewing angles away from the companion (Kasen, 2010, their figure 2). For viewing angles along the companion direction, the bolometric luminosity is well approximated by the analytic equations presented in Kasen, 2010.

We attempted to fit the early multi-color photometry with the models presented in Kasen, 2010, but were unable to obtain a good fit to the data. This is primarily because the luminosity from the interaction is relatively long-lived (a few days) when the peak luminosity is large (at least $\sim 2 \times 10^{43}$ ergs s^{-1}), while the predicted color evolution is very different. This is readily apparent when comparing the luminosity and temperature evolution of the model with the observations – the analytical model predicts a luminosity evolution scaling with time as $t^{-1/2}$, which is almost the same

as the color temperature evolution, which scales as $t^{-37/72}$. Our early observations clearly show that the luminosity drops by a factor of 10, while the temperature drops by only a factor of 3. Thus, we find the companion interaction scenario to be inconsistent with the properties of the early peak.

Analysis of early spectra

The early spectra of iPTF 14gqr exhibit prominent emission features of highly ionized He and C that are broader (FWHM $\sim$ 3000 km s^{-1}) than that typically observed in the flash ionized spectra of other core-collapse events. We consider two possible scenarios for the origin of these features – one where they arise from recombination of material surrounding the progenitor after ionization during the SN shock breakout, and one where they are powered by interaction of the SN ejecta with a dense CSM. While the intermediate width features seen in the early spectra are somewhat similar in width to those seen in interacting SNe at and before peak light (Smith, 2016), the observed recombination of highly ionized species is better explained by shock cooling of extended material. In particular, we observe clear evidence of recombination of C IV in our earliest spectra followed by C III in later spectra, that is more consistent with shock cooling emission rather than continued energy supply from interaction. We thus favor shock cooling emission as the origin of the early excess emission as well as the intermediate width emission lines.

We analyze the properties of the flash ionized spectra of iPTF 14gqr to estimate properties of the emitting material surrounding the progenitor, where the optically thin flash ionized lines originate. Following the methods outlined in Ofek et al., 2013 and Yaron et al., 2017, where they estimate the mass loss rate from the luminosity of the Hα line at 6563 Å, we can relate the mass of the doubly ionized helium region generating the He II λ4686 line to the line luminosity using,

$$L_{\mathrm{He\ II},\lambda 4686} \sim \frac{A}{m_{He}} \int_{r_1}^{r} n_e 4\pi r^2 \rho(r) dr \tag{2.1}$$

where $L_{\mathrm{He\ II},\lambda 4686}$ is the luminosity of the λ4686 line, $A = \frac{4\pi j_{\lambda 4686}}{n_e\, n_{He^{++}}}$, $j_{\lambda 4686}$ is the emission coefficient for the λ4686 transition, m_{He} is the mass of a He nucleus, $n_{He^{++}}$ is the number density of the doubly ionized He, and n_e is the number density of electrons. The order of magnitude approximation holds because there may be unknown collisional excitation and de-excitation processes operating, in addition to the recombination processes considered here.

We use $A \approx 1.3 \times 10^{-24}$ ergs cm^3 s^{-1} (Storey et al., 1995) for a temperature of 10^4 K, electron density of $\sim 10^{10}$ cm^{-3} (the value of A is fairly insensitive to the assumed electron density), and Case B recombination. We consider a density profile with the density ρ varying as $\rho = Kr^{-2}$, where K is the mass loading parameter. The total mass in a region between r_1 and r is given by Ofek et al., 2013,

$$M_{He} = \int_{r_1}^{r} 4\pi r^2 \rho(r) dr = 4\pi K \beta r \tag{2.2}$$

where $\beta = (r - r_1)/r$ is assumed to be of the order unity and M_{He} is the total mass of the emitting material. Assuming $n_e \approx 2n_{He^{++}}$, and using the density profile, we write the λ4686 luminosity as,

$$L_{\text{He II},\lambda 4686} \sim \frac{8\pi A \beta}{m_{He}^2} K^2 r^{-1}. \tag{2.3}$$

We first attempted to measure the luminosity of the λ4686 line by subtracting the best-fitting blackbody continuum from the spectrum and fitting a Gaussian profile to the λ4686 line in the +13.9 h spectrum. With the absence of simultaneous photometry for the +25.2 h spectrum, we are unable to accurately measure the luminosity of the line in this spectrum. We thus only use the +13.9 h line luminosity for our calculations. Since the λ4686 feature likely has a non-negligible contamination from C III λ4650 feature at this epoch, we find that the simple Gaussian fit has a blue-shifted peak (with respect to λ4686) and a red shoulder excess (consistent with λ4686).

Using the +25.2 h spectrum which has a higher signal-to-noise ratio to only better estimate the relative contributions, we are able to get a better fit using a simple two component Gaussian profile, which suggests that the He II line has a FWHM of $\sim$ 4500 km s^{-1} and contributes 60% of the flux in the line, while the C III feature has a FWHM of $\sim$ 2000 km s^{-1} and contributes the remaining 40% of the flux. The width of the C III feature is similar to that measured for the C IV λ5801 feature in the first spectrum. We are unable to better constrain the contributions of He II λ4686 and C III λ4650 in the +13.9 h spectrum than adopting the above measured ratio of 3:2 for the contribution of the He II and C III lines. This suggests that the He II line has a luminosity of $\sim 1.1 \times 10^{40}$ ergs.

The location of the emitting region can be constrained by requiring that the Thompson optical depth in the region must be small for the lines to escape. The Thompson

optical depth produced by this ionized material can be written as,

$$\tau = \frac{2\sigma_T}{m_{He}} K \beta r^{-1} \tag{2.4}$$

where τ must be small for the lines to escape. This gives a lower limit on the location of the line forming region at,

$$r \sim L_{\text{He II},\lambda 4686} \frac{\sigma_T^2 \beta}{2\pi A \tau^2}. \tag{2.5}$$

Taking the +13.9 h luminosity measured for the λ4686 line, we get $r \sim 6 \times 10^{14} \beta \tau^{-2}$ cm, $K \sim 2.9 \times 10^{15} \tau^{-1}$ g cm^{-1}, and $M_{He} \sim 0.01 \beta^2 \tau^{-3}$ M$_\odot$ where we take $\beta \sim 1$. These estimates can be affected if the CSM was not characterized by a wind-like r^{-2} profile, if the emitting region was confined to a thin shell ($\beta \ll 1$), if the emitting region was not spherically symmetric (e.g. if it was clumped), or if our estimate of the C III λ4650 contamination in the λ4686 emission feature was incorrect by a factor of a few. Given these caveats, we take the calculated values to be accurate to an order of an magnitude only. The inferred radius of the optically thin material is larger than the envelope producing the early shock cooling emission as seen in the light curve, and suggests that the highly ionized lines likely arise from a lower density extension of the same envelope.

An additional consistency check for the location of the emitting material can be found by noting that the line emission produced due to a short ionizing burst of radiation would be visible for at least the light crossing time between the part of the shell pointing towards the Earth and the part perpendicular to this line of sight (i.e. $t_{cross} = r/c$). This is because the inferred recombination times at these high densities ($n_e = 2Kr^{-2}/m_{He} \sim 10^9 - 10^{10}$ cm^{-3}) are short ($\sim$ 10 minutes), and hence the emitting material recombines promptly after shock breakout. While there is some uncertainty in the time of explosion, the light curve models for the first peak, as well as the Arnett model, favor earlier explosion times than the one assumed. We thus constrain the first spectrum to have been taken between $\approx$ +14 h (for the assumed explosion time) and $\approx$ +36 h after explosion (for an explosion at 0.92 days before the assumed time). Similar constraints for the last featureless spectrum within the first day of detection suggest that it was taken between $\approx$ +33 h and $\approx$ +55 h after explosion. This constrains the emitting region to $r \leq 6 \times 10^{15}$ cm, noting that this estimate is relatively insensitive (within a factor of $\approx$ 2) to the exact time (between +33 h and +55 h after explosion) when the lines disappear.

Given the large inferred size of the emitting envelope ($\sim 6\times10^{14}$ cm, corresponding to a light travel time of ~ 5 hours), we now consider potential effects of light travel time (LTT) on the observed spectrum. A study of the flash-ionized spectrum of SN 2013cu by Gräfener et al., 2016 suggest that including LTT effects decreases the expected luminosity of the spectral lines and affects the observed line profiles depending on the location of the line forming region in the envelope. The lower luminosity has the equivalent effect of increasing the inferred mass of the envelope, as was inferred in the modeling of SN 2013cu (Gräfener et al., 2016). While the emitting mass in iPTF 14gqr may also be higher than our estimates, the rapid rise time of the early peak constrains the mass to be ~ 0.01 $M_\odot$.

Gräfener et al., 2016 also show that lines formed in the outer region of the envelope are substantially blue shifted for high wind velocities, while lines formed in the central regions are less affected. Comparing to our observations, we note that the blue-shifted peak of the λ4686 feature and C III λ5696 lines in the +13.9 h and +25.2 h spectra can potentially be explained by LTT effects. The blue-shifted profile of the λ4686 feature may not require contamination by C III λ4650 in such a case. The observed blue-shift corresponds to a velocity of ~ 2200 km s^{-1}, similar to the velocity inferred from the widths of the emission lines.

Assuming that the electron density in the envelope is dominated by He ionization ($n_e \sim 10^{10}$ cm^{-3}), we try to estimate the amount of C in the envelope. Using the C IV line in the +13.9 spectrum, we measure a C IV λ5801, 5812 luminosity of $\sim 6.1\times10^{39}$ ergs. Using a C IV λ5801, 5812 recombination coefficient of $A = 1.4 \times 10^{-24}$ ergs cm^3 s^{-1} (Kingsburgh et al., 1995), we determine a C mass of $\sim 4\times10^{-3}$ $M_\odot$. We can use our early spectra to place constraints on the amount of hydrogen in the envelope using the non-detection of the Hα emission. We use the +13.9 h spectrum to place a 3σ upper limit on the Hα luminosity of 4.5×10^{39} ergs s^{-1}. Taking an electron density of $n_e \sim 10^{10}$ cm^{-3} in the emitting region and recombination coefficient of $A = 2.6 \times 10^{-25}$ ergs cm^3 s^{-1}, we constrain the hydrogen mass of the envelope to a 3σ upper limit of $\sim 10^{-3}$ $M_\odot$.

Radio analysis

Radio emission in SNe arises from synchrotron radiation produced by shock accelerated electrons in the circumstellar medium. As the forward shock propagates outwards, it accelerates electrons producing a power law electron energy distribution, which then gyrate in the post-shock magnetic field producing synchrotron

radiation that peaks in the radio bands (Chevalier, 1982, 1998). Thus, radio emission can be used as a tracer of the environment of the explosion, and place constraints on the mass-loss history of the progenitor.

Radio emission from SNe has been previously observed in a number of events, and are often conspicuously associated with relativistic Type Ic-BL SNe (see Gal-Yam, 2017 for a description of this subtype), with or without an associated gamma ray burst (GRB) (see for example, Kulkarni et al., 1998; Soderberg et al., 2006). Normal Type Ib/c SNe can also exhibit bright radio emission depending on the environment of the progenitor. We show a comparison of the observed radio light curves of other Type Ib/c SNe to the radio limits on iPTF 14gqr in Figure 2.17. Our early radio observations rule out radio emission similar to most relativistic SNe, as well as the bright afterglows associated with GRBs (which are typically brighter than the Ic-BL SNe; see for example, Corsi et al., 2016; Perley et al., 2014). However, we are not sensitive to the radio emission phase space occupied by the majority of the normal Type Ib/c population, primarily due to the large distance of iPTF 14gqr and the resulting weak luminosity constraints.

In order to place the radio observations of iPTF 14gqr in physical context, we use the synchrotron self-absorption (SSA) model of Chevalier, 1998 to generate analytic radio light curves for various kinds of circumstellar environments. We generate these light curves for two types of environments – one characterized by a constant pre-explosion mass loss ($\rho = Kr^{-2}$, where $K = \frac{\dot{M}}{4\pi v_w}$ with $\dot{M}$ as the mass loss rate and v_w as the wind velocity) and one for a constant density interstellar medium (ISM; ρ = constant). Since our observations were obtained at relatively early times after the explosion (within $\sim$ 10 days of explosion), we assume that the shock velocity is constant, instead of assuming a density structure for the outer envelope and a corresponding velocity evolution. We consider a range of shock velocities for a filling factor of 0.5 (see Chevalier, 1998). We also assume that the electrons and magnetic field in the post-shock region share constant fractions (= 0.1) of the post-shock energy density, as denoted by ϵ_e and ϵ_B, respectively, and an electron energy power law index of $p = 3$.

We show model light curves and the radio upper limits in Figure 2.18. The 22 GHz radio upper limits barely intersect the optically thick locus of the models, while the 6 GHz upper limits are well above the optically thick locus. Hence, these upper limits do not constrain the circumstellar environment. The models shown in Figure 2.18 are for the closest set of parameters to the radio upper limits, and correspond

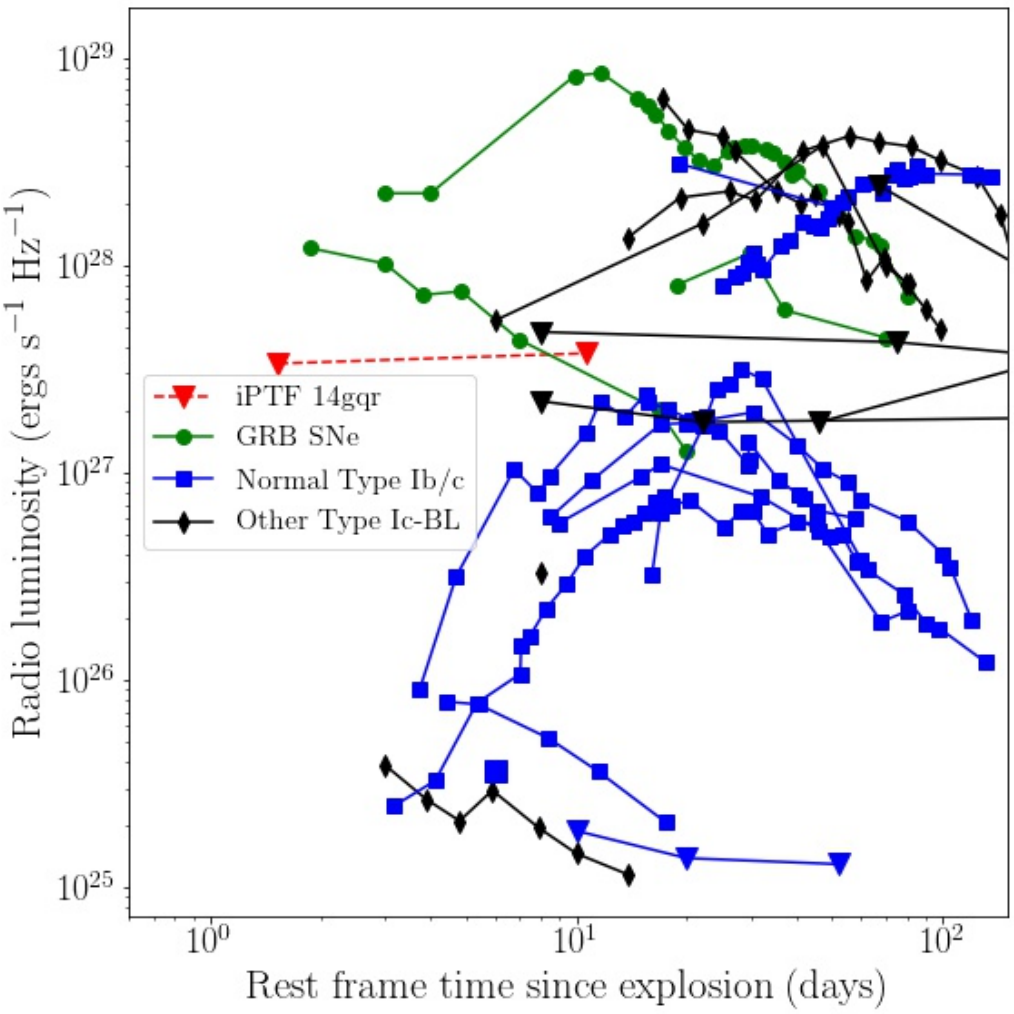

Figure 2.17: **Comparison of the VLA radio constraints on iPTF 14gqr (3σ limits at 6 GHz) to the observed radio light curves of other Type Ib/c SNe and relativistic SNe at 8.5 GHz.** Events have been color coded into categories of GRB associated Type Ic-BL SNe (green circles), other Type Ic-BL SNe (black diamonds), normal Type Ib/c SNe (blue squares) along with iPTF 14gqr (red). Inverted triangles denote upper limits. The sources in the GRB SNe sample (and their original published data) are SN 1998bw (Kulkarni et al., 1998), SN 2006aj (Soderberg et al., 2006), and SN 2010bh (Margutti et al., 2013), while the other Type Ic-BL SNe are SN 2009bb (Soderberg et al., 2010a), SN 2007bg (Salas et al., 2013), SN 2002ap (Berger et al., 2002), PTF 12as, PTF 13u, PTF 13ebw, PTF 14gaq, PTF 14dby (Corsi et al., 2016), and PTF 12gzk (Horesh et al., 2013). The normal Type Ib/c events include SN 2013ge (Drout et al., 2016), SN 2007gr (Soderberg et al., 2010b), SN 2003L (Soderberg et al., 2005), SN 2004cc, SN 2004dk, SN 2004gq (Wellons et al., 2012), SN 1994I (Weiler et al., 2011), SN 2008D (Soderberg et al., 2008; van der Horst et al., 2011), and iPTF 13bvn (Cao et al., 2013).

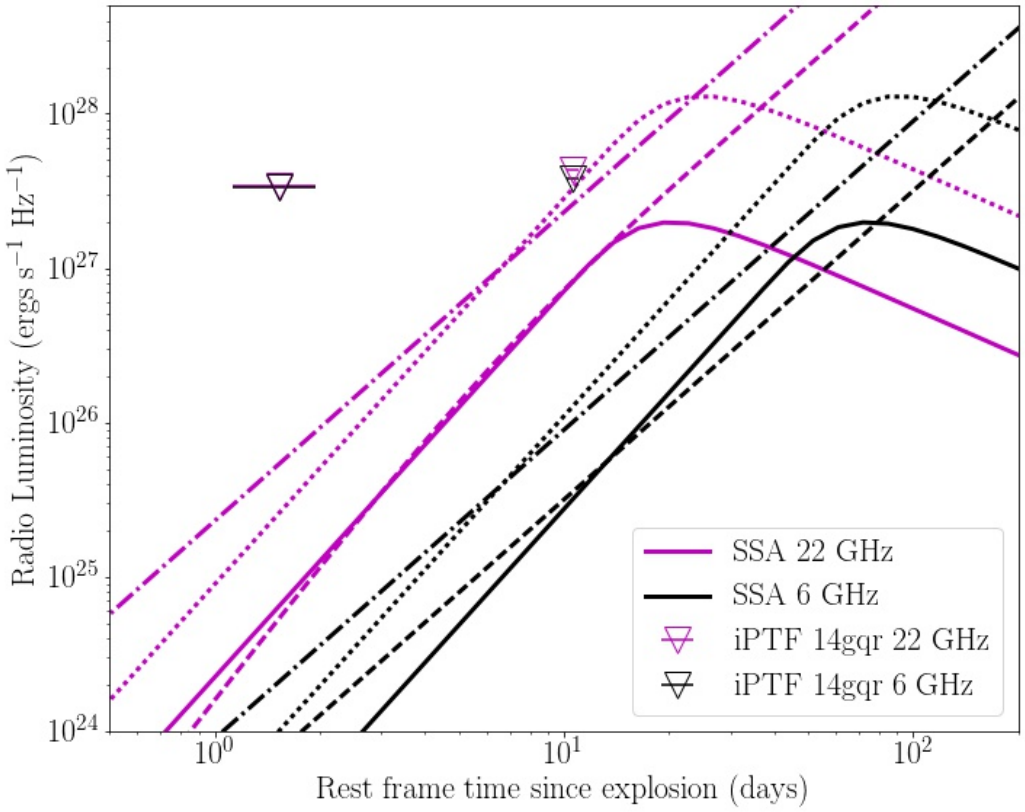

Figure 2.18: **Radio light curves for the synchrotron self absorption model of Chevalier, 1998 plotted along with the radio upper limits of iPTF 14gqr.** The magenta and black curves correspond to observation frequencies of 22 GHz and 6 GHz, respectively, while the upper limits on iPTF 14gqr are also denoted by identical colors. We assume a constant magnetic field and electron energy fraction with respect to the post-shock energy density of $\epsilon_B = \epsilon_e = 0.1$. Although the radio upper limits lie above the optically thick locus of the model light curves, we show these light curves for the closest set of parameters, corresponding to $K \sim 6 \times 10^{12}$ g cm^{-1} in the wind CSM case, and to $n = 3 \times 10^5$ cm^{-3} in the constant ρ case. The solid and the dotted lines correspond to the wind CSM models (for shock velocities of 2×10^4 km s^{-1} and 4×10^4 km s^{-1}, respectively), while the dashed and dot-dashed lines indicate the constant density models (for shock velocities of 2×10^4 km s^{-1} and 4×10^4 km s^{-1}, respectively).

to $K \sim 6 \times 10^{12}$ g cm^{-1} in the wind CSM case, and to $n = 3 \times 10^5$ cm^{-3} in the constant ρ case. The value of K corresponds to a $\dot{M} \approx 10^{-4} \frac{v_w}{1000\,\mathrm{km\ s^{-1}}}$ M$_\odot$ yr^{-1}. For each circumstellar density model and observing frequency, we show light curves for shock velocities of 2×10^4 km s^{-1} and 4×10^4 km s^{-1}. We conclude that while CSM parameters similar to those indicated here would have been detected at the 3σ level in our 22 GHz observations, they do not constrain the environment any further.

Ultra-stripped SN modeling

We compare the bolometric light curve and peak photospheric spectra of iPTF 14gqr to models of ultra-stripped SNe (as described in Moriya et al., 2017; Tauris et al., 2013) in Figure 2.5. As discussed earlier, the optical / UV SED of the first peak of iPTF 14gqr is consistent with blackbody emission through the optical / UV wavelengths, while the second peak SEDs show evidence of line blanketing in the UV. Hence, we compare these models to the bolometric luminosity for the first peak, and to the pseudo-bolometric luminosity for the second peak.

While the shape of the ^{56}Ni powered peak of iPTF 14gqr was found to be well matched to a model with 0.2 $M_\odot$ of ejecta and 2×10^{50} ergs of kinetic energy (similar to the explosion parameters estimated in our Arnett modeling), the observed light curve was found to be marginally brighter than that predicted in the model. This is because current models of ultra-stripped SNe synthesize $\approx 0.03 - 0.04$ $M_\odot$ of ^{56}Ni, compared to the higher value ($\approx 0.04 - 0.05$ $M_\odot$) required to explain the luminosity of iPTF 14gqr. Such discrepancies in the ^{56}Ni mass may originate from small differences in the progenitor structure, core masses and / or explosion energy (note that 2D models synthesize higher ^{56}Ni masses compared to the 1D models we use here (Suwa et al., 2015)). Recent calculations of nucleosynthesis in ultra-stripped SNe (Yoshida et al., 2017) suggest that there are likely to be additional power sources for these light curves (increasing the luminosity by up to a factor of ~ 2), including those from additional iron-peak isotopes (mainly ^{57}Ni and ^{66}Cu) as well as light trans-iron elements. Hence, the observed luminosity difference is not significant, and we explicitly set the ^{56}Ni mass to 0.05 $M_\odot$ in our 1D models to account for the higher observed luminosity.

Since the early luminous peak arising from the He-rich extended envelope was not predicted in these models, there were large discrepancies in the bolometric light curve at early times. Hence, we added a shock cooling emission component based on the models of Piro, 2015 for $M_e = 0.01$ $M_\odot$ and $R_e = 6 \times 10^{13}$ cm (as found earlier), and found the best explosion time by minimizing the residuals between the total model luminosity and the observed luminosity. Taken together, we were able to find an excellent match between the observed bolometric light curve and this two-component light curve for an explosion occurring ≈ 0.75 days before the nominally assumed date (Figure 2.5).

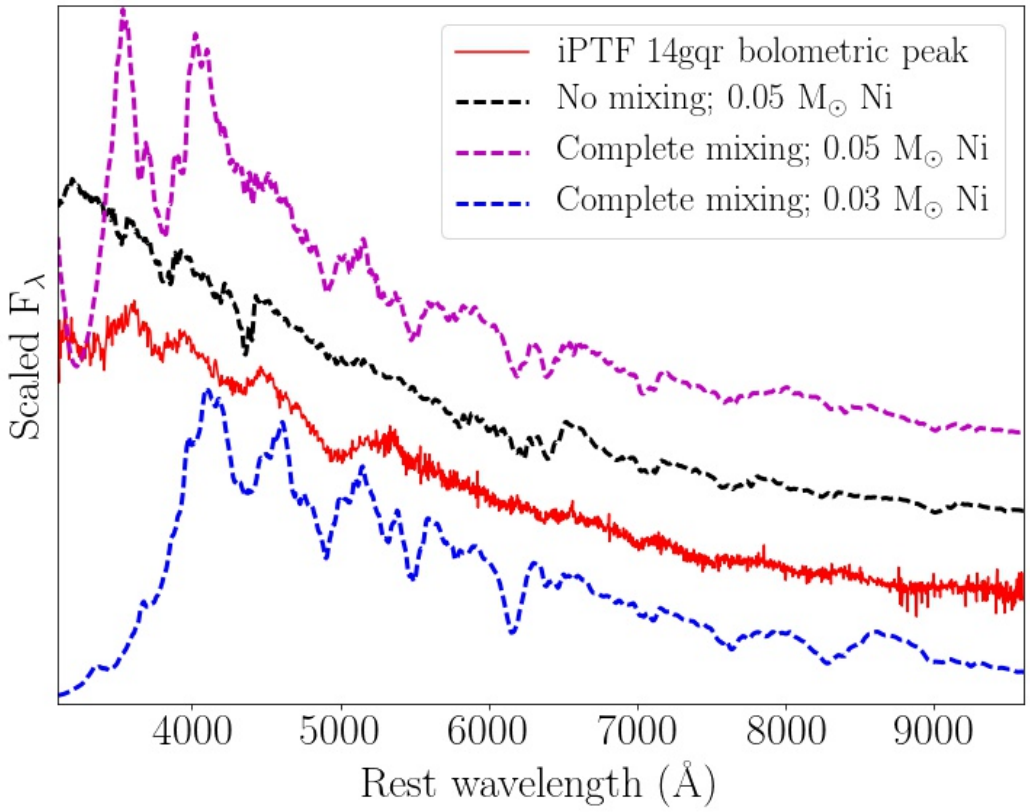

Figure 2.19: **Comparison of synthetic spectra for ultra-stripped SNe to that of iPTF 14gqr.** We show the original spectra presented in Moriya et al., 2017 (for $M_{ej} = 0.2$ M$_\odot$, $E = 2.5 \times 10^{50}$ ergs and $M_{Ni} = 0.03$ M$_\odot$) as the blue dashed line, which exhibits significant line blanketing below 4000 Å due to the assumption of completely mixed ejecta. The magenta line is for a model with complete ejecta mixing and higher Ni mass of 0.05 M$_\odot$, and exhibits bluer spectra still affected by deep absorption features at bluer wavelengths. The black line shows a spectrum from a model with the same parameters as the magenta line, but with no mixing in the ejecta. This model reproduces both the continuum shape and prominent absorption features.

The light curve models presented in Moriya et al., 2017 did not assume any ^{56}Ni mixing in the ejecta, whereas the original synthetic spectra in Moriya et al., 2017 assumed complete mixing of the ejecta. This assumption leads to strong line blanketing below 4000 Å, due to the relatively high fraction of Fe group elements in the outer layers of the ejecta (blue curve in Figure 2.19). Hence, we recalculated these synthetic spectra in the same way as in Moriya et al., 2017 with the one-zone Monte Carlo spectral synthesis code developed by Mazzali et al., 1993. Since we use the one-zone spectral synthesis code, we do not directly put the stratified chemical structure obtained by the explosive nucleosynthesis modeling into the code. We use

the chemical composition just above the photosphere as input. This assumption is valid because most of the lines are formed just above the photosphere. Additionally, we generate these spectra for models with synthesized Ni mass of 0.05 $M_\odot$ to account for the higher luminosity.

The higher Ni mass in these models broadly lead to bluer spectra at peak bolometric light, as compared to the original models with 0.03 $M_\odot$ of Ni (blue curve in Figure 2.19). Nonetheless, models with complete mixing of the ejecta predict deep absorption features (magenta curve in Figure 2.19) and line blanketing at blue wavelengths (below $\sim$ 4500 Å) unlike what we observe. We find a much better match to the observed peak spectra for ejecta with no mixing and 0.05 $M_\odot$ of Ni (black curve in Figure 2.19). As shown, the overall continuum shape, as well as all prominent absorption features (of O I, Ca II, Mg II, and Fe II) are very well reproduced in this model. We also observe weak absorption features of Si II and C II near 6300 Å as predicted in the model. Although there are some minor discrepancies in the strengths of the Mg II, Si II, and C II features, we overall conclude that the spectral properties of iPTF 14gqr are in very good agreement with the ultra-stripped SN models.

We show the chemical abundances of the photosphere found in this model in Table 2.7. The specific model used here was directly taken from the binary evolution simulations of Tauris et al., 2015, and also contains 0.03 $M_\odot$ of He. However, Moriya et al., 2017 show that He optical lines are not expected in this model even when including non-thermal excitations due to the low He mass, which is below the 0.06 $M_\odot$ limit suggested by Hachinger et al., 2012. As shown earlier, the low γ-ray opacity of the ejecta also suggest that the lack of He excitation lines is likely due to a genuine low abundance of He in the ejecta, even in the limit of very low ^{56}Ni mixing. Modeling of the light curve and spectral properties of the fast Type Ic SN 1994I, which was also suggested to arise from a highly stripped progenitor (Nomoto et al., 1994), also require a strongly centralized distribution of ^{56}Ni (Hachinger et al., 2012).

Absence of He in the peak photospheric spectra

The classification of iPTF 14gqr as a Type Ic SN arises from the absence of H, He, and prominent Si lines in the observed peak photospheric spectra. However, the absence of He lines in optical spectra can be either due to the genuine lack of He in the ejecta or due to lack of non-thermal He excitation in the He-rich regions of

the ejecta (Dessart et al., 2011, 2012, 2015b). In particular, it has been suggested that the absence of He lines in Type Ic SNe can also be explained only by the lack of ^{56}Ni mixing into the outer He-rich layers, that prevents non-thermal excitation of He by fast electrons arising from Compton scattering of γ-rays produced in ^{56}Ni decay. It is thus necessary to consider the effect of mixing in hiding He lines in our peak photospheric spectra.

Modeling a continuum of progenitor structures leading from Type Ib to Type Ic SNe (including a certain amount of mixing), Hachinger et al., 2012 show that a He mass of at least 0.06 $M_\odot$ is required to produce He lines in the optical spectra. Our modeling of the peak photospheric spectra and light curve of iPTF 14gqr in the context of ultra-stripped SNe suggest that the ^{56}Ni needs to be centrally located in order to explain the lack of line blanketing at < 4000 Å near peak optical light. While this could potentially contribute to hiding He lines in this source, we show below that such a scenario is unlikely due to the low ejecta mass of the system, and the resulting low γ-ray optical depth of the ejecta.

We first estimate the γ-ray escape fraction from ^{56}Ni decay for a centralized ^{56}Ni distribution (as inferred from the modeling) using the methods in Valenti et al., 2008a. The γ-ray escape fraction is given by $e^{-(F/t)^2}$, where $F \approx 32 M_{ej,\odot} / \sqrt{E_{51}}$ days, $M_{ej,\odot}$ is the ejecta mass in units of solar masses, and E_{51} is the explosion energy in units of 10^{51} ergs. For the parameters inferred for iPTF 14gqr, we get F $\approx$ 14.3 days, and hence find the escape fraction at 11 days (the epoch of the last photospheric phase spectrum) to be $\approx 20\%$. This is in stark contrast to normal Type Ib/c SNe, where the larger ejecta masses lead to negligible γ-ray escape up to ~ 2 months after the explosion (Dessart et al., 2011). Hence, Ni mixing into the outer He layers has been suggested to be a necessary criterion for producing He optical lines in normal Type Ib/c SNe. In particular, Dessart et al., 2012 show that a Ni mass fraction of at least 0.01 in the outer layers is enough to produce prominent He optical lines in mixed ejecta, for He mass fractions as low as 0.2 - 0.3 in the outer layers. If we consider the outer 0.05 - 0.1 $M_\odot$ ejecta of iPTF 14gqr, this corresponds to a Ni mass of (0.5 - 1) $\times 10^{-3}$ $M_\odot$ in the outer layers.

Since the role of ^{56}Ni in the outer ejecta layers is to non-thermally excite He by γ-ray energy deposition, we can compare the γ-ray flux required for the production of He optical lines to the actual rate estimated from the escape fraction. Considering the γ-ray escape fraction from the entire ejecta of 20%, we find that the γ ray flux from the centrally located 0.05 $M_\odot$ of ^{56}Ni is at least an order of magnitude larger than

what would be produced from (0.5 - 1) $\times 10^{-3}$ $M_\odot$ of ^{56}Ni in the outer layers. Taken together, the lack of He excitation lines in the presence of a significant γ-ray flux suggests that the mass fraction of He in the outer layers is indeed low ($X_{He} < 0.2$, as suggested by Dessart et al., 2012). Although the above estimate is very simplified compared to the detailed radiative transfer involved in the production of He lines, it nevertheless demonstrates that the ejecta of iPTF 14gqr is deficient in He.

Host galaxy and environment

Host identification

iPTF 14gqr was discovered at a large projected offset of $\approx 24''$ from the nearest apparent host galaxy, a two-tailed spiral galaxy showing signs of tidal interaction with at least three companion galaxies. The association of the transient with the host galaxy was confirmed from the early spectroscopy of the transient, which exhibited flash ionized He II lines at the same redshift $z = 0.063$ as that of the galaxy. The offset corresponds to a projected distance of ≈ 29 kpc at the redshift of the galaxy. We nominally adopt this galaxy as the host of iPTF 14gqr, but also discuss several other possible scenarios below.

Although no stellar association was visible in the SDSS and PTF reference images at the location of the transient, it was not possible to rule out the presence of a faint dwarf galaxy or globular cluster underneath the transient. We thus undertook deep late-time imaging of the host region and did not find any stellar association down to absolute magnitude limits of $M_r > -11.4$ mag and $M_g > -11.1$ mag. Although these limits rule out a certain luminosity space for a potential host, they are not stringent enough to rule out the entire population of dwarf galaxies and stellar clusters given the observed luminosity function of these systems in the local group (Harris, 1996; Lyman et al., 2014; McConnachie, 2012). We also do not detect any galaxy emission lines at the location of the transient in our late-time spectra.

Host properties

The host galaxy IV Zw 155 is a spiral of morphology Sa, and has been previously cataloged in the SDSS (Abolfathi et al., 2017) and the Two Micron All Sky Survey (2MASS) (Skrutskie et al., 2006) as the source SDSS J233329.84+333848.2 and 2MASX J23332981+3338484, respectively. The galaxy was also detected as a UV source in the Galaxy Evolution Explorer (GALEX) source catalogs (Bianchi et al., 2014) as the source GALEXASC J233330.19+333840.3. The broadband

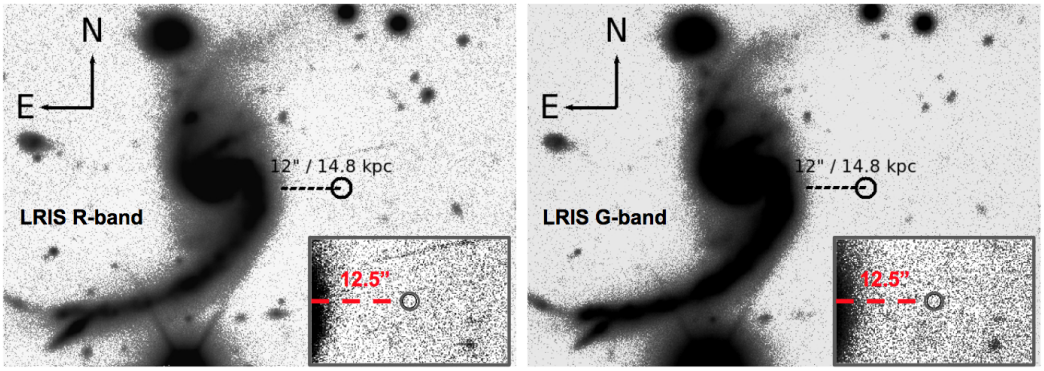

Figure 2.20: **Late-time *R*-band and *G*-band image of the host galaxy of iPTF 14gqr.** There are extended tidal tails of the host galaxy arising from tidal interactions of the host with its companions, and an extended halo around the spiral arms. The insets show a zoomed-in portion of the image centered on the location of the transient. Although we are not sensitive to low surface brightness features (spiral arms and tidal tails) at the distance of the galaxy, the brighter tidal tails of the host galaxy extend to much larger distances than the observed offset of iPTF 14gqr.

photometric magnitudes of the galaxy are summarized in Table 2.6. We use the spectrum of the core of the galaxy to measure the emission line fluxes of Hα, Hβ, [O II], [O III], [N II], and [S II] by fitting Gaussian profiles to the individual lines. The fluxes obtained are given in Table 2.6.

We estimate the metallicity of the host galaxy using the `pyMCZ` code (Bianco et al., 2016) to calculate the host oxygen metallicity (12 + log(O/H)). The code is based on Kewley et al., 2002 with updates from Kewley et al., 2008, and calculates a number of metallicity calibrators based on strong emission lines along with uncertainty estimates derived from Monte-Carlo sampling. The oxygen abundance estimates we derive are $8.58^{+0.07}_{-0.08}$ on the O3N2 scale of Pettini et al., 2004 and $8.78^{+0.13}_{-0.22}$ on the scale of McGaugh, 1991. Similarly, using the multi-color integrated magnitudes of the galaxy in SDSS, we find 12 + log(O/H) = 8.77 on the 03N2 scale of Pettini et al., 2004 using the luminosity – color – metallicity relation of Sanders et al., 2013 with a typical scatter of 0.07. Overall, the estimates are roughly consistent with a solar metallicity host galaxy (where $[12 + \log(\mathrm{O/H})]_{\mathrm{solar}} = 8.69 \pm 0.05$; Asplund et al., 2009).

We fit the broadband photometry measurements of the galaxy to estimate parameters for the host stellar population. We use the `FAST` code (Kriek et al., 2009) to fit a galaxy model to the observed photometry using a Maraston, 2005 stellar population synthesis model, a Salpeter IMF, a delayed star formation history, and a Milky-way

(MW) like extinction law. Additionally, we constrain the metallicity to be $Z = Z_{\odot}$ based on our spectroscopic measurements. Using these inputs, we find a best-fitting stellar mass of $3.02^{+0.36}_{-0.33} \times 10^{10}$ $M_{\odot}$ and a stellar population age of $7.08^{+0.17}_{-3.69} \times 10^{8}$ yrs. The GALEX UV photometry measurements allow us to constrain the best-fitting star formation rate to 2.3 - 7.6 $M_{\odot}$ yr^{-1}. Overall, the host of iPTF 14gqr is found to be a solar metallicity, star forming, spiral galaxy.

Type Ib/c SNe generally show a preference for high metallicity environments (Leloudas et al., 2011; Sanders et al., 2012; Smartt, 2009), which is consistent with the requirement of substantial line driven mass loss in the progenitors. Additionally, Arcavi et al., 2010 show that Type Ic SNe also show a preference for giant host galaxies as compared to Type Ib or Type II events. Thus, taken at face value, the host galaxy of iPTF 14gqr is indeed similar to the typical host galaxies of Type Ic SNe. All of the fast Type I transients in our light curve comparison sample were also found in star forming galaxies, with the exception of PTF 10iuv, which was found near an old elliptical galaxy.

Explosion site properties

The 29 kpc central offset of the location of iPTF 14gqr corresponds to a host normalized offset of ≈ 4.8 $R_{\rm eff}$ (where $R_{\rm eff}$ is the half-light radius of the galaxy), placing this source at the extreme high end of the distribution of host offsets found for all SNe (Prieto et al., 2008; Kasliwal et al., 2012). For example, iPTF 14gqr has the second largest host offset in terms of physical distance when compared to the PTF sample of core-collapse SNe, with SN 2010jp (PTF 10aaxi; Smith et al., 2012) as the only other core-collapse event with a larger offset ($\approx$ 33 kpc). When considered in terms of host-normalized offset of PTF SNe, iPTF 14gqr occupies a position on the higher end of the distribution of even SN Ia as well as of short GRBs (Fong et al., 2013; Lunnan et al., 2017).

We can attempt to place limits on the presence of an underlying H II region based on the non-detection of nebular Hα emission in in our late-time spectra. Using our LRIS spectrum obtained at $\approx$ 61 days after explosion, we place a 5σ upper limit of the Hα flux to be be $\sim 10^{-17}$ ergs cm^{-2} s^{-1}, corresponding to Hα luminosity of 9.6×10^{37} ergs s^{-1}. We thus derive a corresponding upper limit of 7.6×10^{-4} $M_{\odot}$ yr^{-1} on the star formation rate (SFR) (Kennicutt, 1998) within the 1" slit ($\sim$ 1.2 kpc at the galaxy redshift) used for the spectrum. The Hα luminosity upper limit is much lower than the average luminosity observed for H II regions associated

with core-collapse SNe (Crowther, 2013), although it does not rule out the complete range of Hα luminosities associated with Type Ib/c SNe. Nonetheless, the absence of a H II region would potentially suggest that the progenitor was not formed in situ at the location, or was older than the $\sim$ 10 Myr lifetimes of giant H II regions (Osterbrock et al., 2006). This would be in contrast to the general trend where Type Ib/c SNe are found to be more likely to be associated with H II regions than Type II events, in accordance with the shorter lifetimes of their more massive progenitors (Anderson et al., 2012; Crowther, 2013).

Tidally interacting environment

Since the host galaxy appeared to be part of a tidally interacting galaxy group, we undertook a spectroscopic mask observation of the host region to determine if the spiral host was a part of a galaxy group or a larger cluster in the region. As shown in Figure 2.8, the galaxies marked *Obj2* and *Obj3* were found to be at a redshift consistent with that of the nominal host *Obj1*. While we did find an unrelated background galaxy cluster at a redshift of $\approx$ 0.19 with at least 8 members within $\pm$ 3000 km s^{-1} of z = 0.19, we did not find evidence of a cluster environment for the host galaxy of the transient.

We conclude that the host of iPTF 14gqr is part of a galaxy group of at least three tidally interacting members, as evident from the stretched tidal tails of the host (see Figure 2.20). All of the three galaxies at the host redshift show prominent signs of star formation via their emission features of Hα, Hβ, and Hγ. However, given that the other two members of this group are at much larger projected offsets from the transient location (Table 2.4), it seems relatively unlikely that they could have hosted the progenitor.

The remote location in the context of ultra-stripped SN models

The remote location of iPTF 14gqr with respect to its host galaxy remains to be understood in the context of the ultra-stripped SN models discussed earlier. Tauris et al., 2015 suggest that the locations of ultra-stripped SN within their host galaxies should be primarily near star forming regions (within 1 kpc) as indicated by the relatively short lifetimes of the collapsing star ($\sim$ 7 – 40 Myr) and the small average systemic velocities ($\sim$ 10 km s^{-1}) corresponding to average NS kicks of $\sim$ 50 km s^{-1} predicted in their calculations. The small systemic velocities arise in particular due to the requirement of wide binary systems that can survive the common envelope

(CE) ejection after the High Mass X-ray Binary (HMXB) phase (see Tauris et al., 2006 for a review).

Instead, iPTF 14gqr displays a $\sim$ 29 kpc projected offset from the center of its host galaxy. If we consider the minimum projected offset of the location from the edge of the visible galaxy, the distance still remains at $\sim$ 15 kpc. For the 40 Myr estimated lifetime of the progenitors, the required systemic velocity for the binary system would be $\sim$ 350 km s^{-1} (note that the system moves out of its host's gravitational potential, and hence the velocity is unlikely to be constant), which is much larger than the predicted systemic velocities after the first SN.

There are several possible explanations of this discrepancy. The lifetimes of giant H II regions ($\sim$ 10 Myr) are shorter than the expected lifetime of the ultra-stripped progenitors. While we did obtain an upper limit of $\sim 10^{38}$ ergs s^{-1} on the Hα luminosity at the location of the transient, lower Hα luminosities have been previously observed in H II regions associated with Type Ic SNe (Crowther, 2013). Outlying H II regions around galaxies are also not unforeseen, and have been observed out to projected distances larger than the $\sim$ 30 kpc offset observed in iPTF 14gqr (Werk et al., 2010). Thus, we cannot rule out the presence of either a low luminosity H II region at the transient location or an H II region that has faded away within the progenitor lifetime.

The presence of a tidally interacting galaxy group associated with the host galaxy of iPTF 14gqr provides another possible clue to its remote location. Tidal tails formed during galaxy mergers are known to host star forming clusters within them (Knierman et al., 2003; Mullan et al., 2011; Tran et al., 2003), arising from tidally induced periodic density waves similar to those seen in the spiral arms of galaxies (Renaud et al., 2009). Ages inferred from modeling of the broadband photometry as well as spectroscopy of some of these star clusters indicate that they are typically younger than their parent tidal tails, which is strongly suggestive of in-situ formation (Knierman et al., 2003; Trancho et al., 2007). Studies of star formation in collisional debris of interacting galaxies in the nearby universe indicate that the instantaneous star formation rate (SFR) in such outlying debris can be as high as 80% of the total SFR of the entire system, with a median value of 20% (Boquien et al., 2009).

Our late-time images of the host galaxy clearly show that the tidal tails of the host galaxy extend to larger projected distances compared to the offset of iPTF 14gqr, and hence a faint tidal tail at the location of iPTF 14gqr is not unexpected. However, the large distance to the source and the low surface brightness of tidal tails would

not allow us to detect such a feature even if it were present underneath the location of iPTF 14gqr (note the faint tidal tails in Figure 2.20), while our photometric limits are not deep enough to constrain the population of star clusters found in such tidal tails (with typical $M_V \approx -8.5$). There are also known examples of tidal dwarf galaxies forming in tidal tails that can host star formation several 100 Myrs after the formation of the parent tail (Knierman et al., 2003; Saviane et al., 2004).

One potential channel in this context is the delayed core-collapse SNe suggested by (Zapartas et al., 2017a), arising from interacting binaries consisting of a massive star and an intermediate mass star, where mass transfer pushes the intermediate mass star above the mass threshold for core-collapse, which can produce a core-collapse SN as late as 200 Myr after the initial star formation episode. In that case, the companion to the progenitor would be a WD while the required systemic velocity would be ~ 70 km s^{-1}, if the binary was formed in the spiral arms.

We briefly consider the potential biases against finding faint transients like iPTF 14gqr on bright galaxy backgrounds, referring to recovery efficiencies of PTF presented in Frohmaier et al., 2017. From our late time-time imaging, we estimate that the surface brightness of the host galaxy varies between < 23 mag arcsec^{-2} in the spiral arms to < 21 mag arcsec^{-2} near the nucleus. Taking the peak magnitude of iPTF 14gqr and assuming a typical seeing of 1.5 $''$, the recovery efficiency can vary between 80% in the spiral arms to <20% in the nucleus. On the other hand, the recovery efficiency at the actual location of the transient would be $\approx 95\%$ given the negligible background. While this potentially suggests that faint events like iPTF 14gqr may be missed by PTF on bright galaxy backgrounds, we caution against drawing conclusions about the population of ultra-stripped SNe based on one event, which can only be resolved with larger samples of these fast transients from wide-field transient surveys (Bellm et al., 2017; Tonry et al., 2018).

2.6 Supplementary text

The nature of the companion star

Stripping of the outer H and He envelopes in stripped envelope SNe can arise either due to mass loss via strong winds or due to stripping by a binary companion (Smartt, 2009). We thus first consider the possibility of explaining the highly stripped progenitor of iPTF 14gqr from single star evolution. Several theoretical calculations for a wide range of stellar mass loss rates and metallicity show that the minimum progenitor mass from single star evolution of massive stars is > 5

$M_\odot$ (Eldridge et al., 2006; Georgy et al., 2009; Meynet et al., 2005), and hence we expect ejecta masses of > 3 $M_\odot$. Such large pre-explosion masses for single star progenitors are observationally consistent with masses inferred for single Wolf-Rayet (WR) stars in the galaxy. Nonetheless, these estimates are at least an order of magnitude larger than the ejecta mass inferred for iPTF 14gqr (≈ 0.2 $M_\odot$), and rules out a single star progenitor for iPTF 14gqr.

Next, we consider a scenario where the progenitor of iPTF 14gqr can be explained from close binary evolution of two non-degenerate massive stars, as calculated in Yoon et al., 2010. Although Yoon et al., 2010 show that main sequence companions of lower mass stripped-envelope SN progenitors can efficiently strip the progenitor to low core masses at the time of core-collapse, these progenitors end up retaining a significant amount of He in their outer layers in all such cases (~ 0.20 $M_\odot$, where $> 80\%$ of the mass in the ejecta would be He). Our estimates of the He mass in this event are ~ 0.01 $M_\odot$ (in the ejected envelope), with a negligible additional amount in the ejecta. This is again an order of magnitude lower than these predictions. We thus conclude that a binary system consisting of two massive stars cannot reproduce the extreme stripping observed in the progenitor of iPTF 14gqr.

We now consider the case for a lower mass main sequence (MS) companions to the progenitor of iPTF 14gqr. In order to explain the extreme stripping of the He star, one would need a system that is close enough such that the He star fills its Roche lobe during its late evolutionary expansion and begins mass transfer on to the companion. In this context, we refer to Zapartas et al., 2017b, who presented a binary population synthesis study of the progenitors for stripped envelope SNe for different initial parameters of the binary system. In particular, they find that systems with very small mass ratios initially ($q < 0.2$, as would be required for a compact main sequence companion for iPTF 14gqr) are very unlikely for progenitor final masses < 2 $M_\odot$ (Zapartas et al., 2017b, see their figure 5). Thus, based on the existing literature of stellar evolutionary models, we find that a low mass MS companion does not appear to be a likely channel to explain the extreme stripping.

Several studies in the literature have shown that highly stripped progenitors, as that inferred for iPTF 14gqr, are expected to arise in the case of compact binary companions such as a NS, WD, or BH (Tauris et al., 2013, 2015; Zapartas et al., 2017b), where close (and possibly dynamically stable) gravitational stripping by the compact companion is able to strip most of the outer layers of the initial He star, leaving behind only a thin layer of He before core-collapse. Even in the presence of

a NS companion, such extreme stripping appears to be only possible when the initial orbital period (at the start of the He main sequence of the progenitor) is less than 0.1 days (Tauris et al., 2015), and hence an orbital separation of less than ~ 1 $R_\odot$. This allows only the most compact companions to explain the stripping. Taken together, we conclude that the case for a NS, WD, or BH companion is most consistent with the inferred properties of the progenitor of iPTF 14gqr.

The remnant of the explosion

The mass of the remnant of iPTF 14gqr is likely to be dominated by the mass of the iron core at the time of core-collapse (i.e. the Chandrasekhar mass), as is applicable for massive stars with initial masses < 20 $M_\odot$ that can lead to ultra-stripped progenitors (Tauris et al., 2015; Woosley et al., 2002; Zapartas et al., 2017b). Taking the ejecta mass of ≈ 0.2 $M_\odot$ observed in iPTF 14gqr, and assuming negligible fallback of material during the SN explosion, we infer a progenitor mass of ≈ 1.5 $M_\odot$.

Although some amount of fallback is expected in all SNe, this will be prominent only for stars that were initially more massive than ~ 30 $M_\odot$ (Fryer, 1999; Fryer et al., 2001; MacFadyen et al., 2001; Woosley et al., 2002). The binding energy of the progenitor envelope is high in such cases, and leads to infall of the inner layers of the star on to the proto-neutron star, potentially leading to the formation of a black hole. Since most of the ^{56}Ni is synthesized in the inner layers of the explosion, the resulting SN would be faint with little or no radioactive ^{56}Ni ejected in the explosion (unless the ^{56}Ni was well-mixed prior to the fallback). In the context of iPTF 14gqr, we find that the explosion ejected a relatively large amount of ^{56}Ni (comprising $\approx 25\%$ of the ejecta by mass) that was located in the inner regions of the ejecta, further suggesting that fallback was negligible in this source. We thus conclude that iPTF 14gqr most likely formed a NS in the explosion.

Origin of the extended He-rich envelope

Our early spectra indicate that the SN explosion occurred inside a He-rich envelope with a mass of ~ 0.01 $M_\odot$, located at a radius of $\sim 500 - 10^4$ $R_\odot$. By fitting a two-component Gaussian profile to the λ4686 feature (to account for the He II and C III features) and a simple Gaussian profile to other C III and C IV lines, we estimate line FWHMs in the range of $\sim 2000 - 4000$ km s^{-1}, consistent with an expanding envelope at the time of explosion. Taking the widths of the Gaussian (the standard deviation, or σ) to be representative of the expansion velocity, we infer the

envelope velocity to be $\sim 1000 - 2000$ km s^{-1}. This suggests that the envelope was ejected $\sim 8 - 20$ days before the core-collapse when considering that the envelope is located at a radius of at least ~ 500 R$_\odot$. The high inferred mass loss rate (~ 0.05 M$_\odot$ yr^{-1}) also suggests that the envelope cannot be associated with a long term wind given the low mass of the progenitor.

The ejecta traveling at $\sim 10^4$ km s^{-1} would take $\sim 1 - 7$ days to sweep up the extended material lying between 500 and 10^4 R$_\odot$ and hence, the disappearance of the emission lines within 2 days after explosion favors a recombining envelope scenario. The measured velocity is very similar to the expected escape velocity of 1000 km s^{-1} for a compact He star (with $M \sim 1.5$ M$_\odot$ and $R \sim 0.5$ R$_\odot$).

When considering the required presence of a close compact companion to explain the low ejecta mass, a possible explanation of the expanding envelope could be due to a (partial) common envelope ejection preceding the terminal core-collapse. For example, multiple theoretical studies on the evolution of compact He star – NS and He star – WD binaries find evidence of unstable mass transfer between the He star and the compact object as the He star moves off the He burning main sequence (Dewi et al., 2003; Tauris et al., 2000; Zapartas et al., 2017a). The result of such unstable mass transfer is the formation of a common envelope that engulfs the binary. The common envelope phase triggers a rapid inspiral of the compact object, where the common envelope may be ejected on a few dynamical timescales ($\sim$ few days; Ivanova et al., 2013). However, the inspiral may also be slowed down before the envelope is ejected if the binary enters a self-regulated inspiral stage, which may last much longer ($\sim 10^3 - 10^4$ years; Podsiadlowski, 2001).

Depending on the exact time left until the SN explosion and the ejection of the envelope, the second SN may take place inside a common envelope, or after the compact object has spiraled in to a tight orbit and the common envelope has been ejected (Dewi et al., 2003). Numerical calculations of the evolution of isolated low mass He stars indeed suggest that they undergo rapid expansion at the onset of the He shell burning phase and as they approach core-collapse, reaching radii of the order of $10^2 - 10^3$ R$_\odot$ (Woosley et al., 1995). Hence, the formation of a common envelope arising out of such an expansion shortly before core-collapse is indeed plausible. Nonetheless, the exact temporal co-incidence between the ejection and the final core-collapse requires fine-tuning of either the formation of the common envelope (if ejected on a dynamical timescale) or its ejection (if ejected after a self-regulated phase).

Calculations of the evolution of such He stars in He star – NS binaries by Tauris et al., 2015 suggest that although the NS is able to strip off almost the entire He layer of the exploding star, a small amount of He (with a mass of ~ 0.01 $M_{\odot}$) remains unstripped in its outer layers at the time of explosion. Given the observed temporal coincidence between the expansion of the envelope and the final core-collapse, as well as the very similar estimated mass of the He envelope, we favor a scenario where the observed envelope is likely associated with the rapid expansion of the remaining He layer prior to core-collapse. Indeed, there are several known examples of massive stars that undergo vigorous outbursts just before the final explosion, leading to the ejection of large amounts of mass into the surrounding medium (Smith, 2014).

Such an eruption would be consistent, for instance, with unstable nuclear burning in the late stages of the progenitor's evolution (Quataert et al., 2012; Shiode et al., 2014), and potentially associated with Si flashes expected to occur only ~ 2 weeks before the SN explosion in lower mass cores (Woosley et al., 2015). In fact, the detection of prominent high ionization He and C lines in the early spectra is consistent with a scenario where the surface layers of the star are ejected, since ultra-stripped progenitors are expected to have a surface composition rich in He and C (Tauris et al., 2015). While similar detailed calculations for He star – BH and He star – WD binaries are not available, similar physics should also apply to these ultra-stripped SN progenitors due to the similar compact nature of the companion.

iPTF 14gqr and the class of Ca-rich gap transients

iPTF 14gqr exhibits a number of similarities to the class of Ca-rich gap transients (Kasliwal et al., 2012). Of the several proposed properties of this class, it exhibits faster photometric evolution than normal SNe, photospheric velocities comparable to normal SNe, rapid evolution to the nebular phase, and an (early) nebular spectrum dominated by Calcium emission (similar to the Ca-rich transients PTF 10iuv and SN 2012hn). While the remote location of the transients was not used as a defining property of this class, iPTF 14gqr was also found in the remote outskirts of its host galaxy, as were all confirmed Ca-rich gap transients (Kasliwal et al., 2012; Lunnan et al., 2017). The confirmed association of the apparent host to a small galaxy group further strengthens a possible relation to these gap transients, which are found to be preferentially located in dense group and cluster environments (Lunnan et al., 2017).

There are several reasons why the above association is unlikely to be physical. The

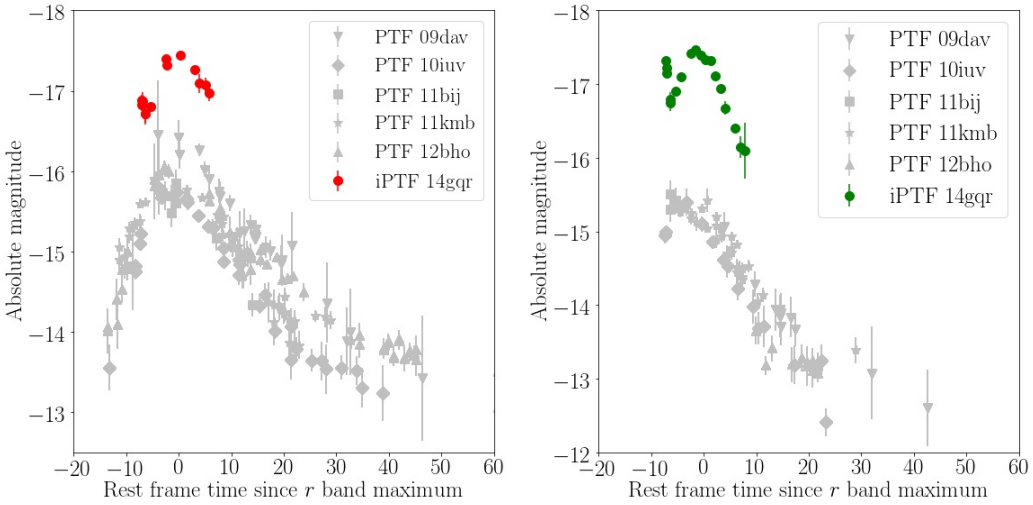

Figure 2.21: **Comparison of the r (left) and g (right) band light curves of iPTF 14gqr to those of some known Ca-rich gap transients.** These include PTF 09dav (Sullivan et al., 2011), PTF 10iuv and PTF 11bij (Kasliwal et al., 2012), and PTF 11kmb and PTF 12bho (Lunnan et al., 2017).

peak luminosity of iPTF 14gqr is much larger than those of the Ca-rich gap transients, which occupy the luminosity 'gap' between novae and SNe (peak absolute magnitude $-15.5 \geq M_{peak} \geq -16.5$). Instead, the peak absolute magnitude of iPTF 14gqr ($M_{peak} \approx -17.45$ in r and g band) is comparable to those of normal SNe Ib/c. The multi-color light curves of iPTF 14gqr are also very different in shape compared to those of the Ca-rich transients, which otherwise form a fairly homogeneous class. This is demonstrated in Figure 2.21, which compares the r and g band light curves of iPTF 14gqr to those of Ca-rich gap transients discovered by the Palomar Transient Factory (PTF). Additionally, none of these Ca-rich gap transients exhibited double-peaked light curves as in iPTF 14gqr, even though some of these sources had early enough photometric follow-up to be able to detect such a component if present.

Examining the final nebular spectrum of iPTF 14gqr, we find the [Ca II]/[O I] ratio to be ≈ 2.5 by fitting Gaussian profiles to the line regions, which is marginally higher than that observed in Type Ib/c SNe (e.g. Milisavljevic et al., 2017, their figure 11). In contrast, the [Ca II]/[O I] ratio in the Ca-rich gap transients are typically much higher (≥ 3, but typically as high as $6-10$; Milisavljevic et al., 2017), and hence iPTF 14gqr is likely to be more closely related to the Ib/c SN class (Milisavljevic et al., 2017 put the threshold for a Ca-rich classification at a ratio of 2). Overall, we conclude that while iPTF 14gqr may be considered to be marginally 'Ca-rich' as compared to other SNe, it is photometrically not a part of the class of Ca-rich

gap transients. There have also been reports of other Type I SNe (e.g. iPTF 15eqv; Milisavljevic et al., 2017) that have been found to be Ca-rich spectroscopically, but are not members of this class photometrically.

We thank the anonymous referees for a careful reading of the manuscript, that helped improve the quality of the paper. We thank C. Steidel, N. Stone, D. Stern, P. Hopkins, S. de Mink, Y. Suwa, A. Heger, and T. M. Tauris for valuable discussions. MMK thanks J. Fuller, E. S. Phinney, L. Bildsten, and E. Quataert for stimulating discussions at the Skyhouse during a PTF-TN meeting. We thank Tim Staley and Gemma Anderson for help with scheduling of the AMI observations. Additional facility acknowledgments are given in the Supplementary Material.

The Intermediate Palomar Transient Factory project is a scientific collaboration between the California Institute of Technology, Los Alamos National Laboratory, the University of Wisconsin, Milwaukee, the Oskar Klein Center, the Weizmann Institute of Science, the TANGO Program of the University System of Taiwan, and the Kavli Institute for the Physics and Mathematics of the Universe. This work was supported by the GROWTH (Global Relay of Observatories Watching Transients Happen) project funded by the National Science Foundation under PIRE Grant No 1545949. GROWTH is a collaborative project between California Institute of Technology (USA), University of Maryland College Park (USA), University of Wisconsin Milwaukee (USA), Texas Tech University (USA), San Diego State University (USA), Los Alamos National Laboratory (USA), Tokyo Institute of Technology (Japan), National Central University (Taiwan), Indian Institute of Astrophysics (India), Indian Institute of Technology Bombay (India), Weizmann Institute of Science (Israel), The Oskar Klein Centre at Stockholm University (Sweden), Humboldt University (Germany), Liverpool John Moores University (UK).

AH acknowledges support by the I-Core Program of the Planning and Budgeting Committee and the Israel Science Foundation. AG-Y is supported by the EU via ERC grant No. 725161, the Quantum Universe I-Core program, the ISF, the BSF Transformative program and by a Kimmel award. EOO. is grateful for support by grants from the Willner Family Leadership Institute Ilan Gluzman (Secaucus NJ), Israel Science Foundation, Minerva, BSF, BSF-transformative, and the I-Core program by the Israeli Committee for Planning and Budgeting and the Israel Science Foundation (ISF). FT and JS gratefully acknowledge the support from the Knut and Alice Wallenberg Foundation. The Oskar Klein Centre is funded by the Swedish Research Council. This research used resources of the National Energy Research

Scientific Computing Center, a DOE Office of Science User Facility supported by the Office of Science of the U.S. Department of Energy under Contract No. DE-AC02-05CH11231. MS acknowledges support from EU/FP7 ERC grant no. [615929]. PEN acknowledges support from the DOE through DE-FOA-0001088, Analytical Modeling for Extreme-Scale Computing Environments. TJM is supported by the Grants-in-Aid for Scientific Research of the Japan Society for the Promotion of Science (16H07413, 17H02864). Numerical computations were in part carried out on a PC cluster at the Center for Computational Astrophysics, National Astronomical Observatory of Japan. Part of this research was carried out at the Jet Propulsion Laboratory, California Institute of Technology, under a contract with the National Aeronautics and Space Administration.

Based on observations obtained with the Apache Point Observatory 3.5-meter telescope, which is owned and operated by the Astrophysical Research Consortium. Based on observations made with the Nordic Optical Telescope, operated by the Nordic Optical Telescope Scientific Association at the Observatorio del Roque de los Muchachos, La Palma, Spain, of the Instituto de Astrofisica de Canarias. The data presented here were obtained in part with ALFOSC, which is provided by the Instituto de Astrofisica de Andalucia (IAA) under a joint agreement with the University of Copenhagen and NOTSA. Based on observations obtained at the Gemini Observatory, which is operated by the Association of Universities for Research in Astronomy, Inc., under a cooperative agreement with the NSF on behalf of the Gemini partnership: the National Science Foundation (United States), the National Research Council (Canada), CONICYT (Chile), Ministerio de Ciencia, Tecnología e Innovación Productiva (Argentina), and Ministério da Ciência, Tecnologia e Inovação (Brazil). Some of the data presented herein were obtained at the W.M. Keck Observatory, which is operated as a scientific partnership among the California Institute of Technology, the University of California, and the National Aeronautics and Space Administration. The Observatory was made possible by the generous financial support of the W.M. Keck Foundation. The authors wish to recognize and acknowledge the very significant cultural role and reverence that the summit of Mauna Kea has always had within the indigenous Hawaiian community. We are most fortunate to have the opportunity to conduct observations from this mountain. The William Herschel Telescope is operated on the island of La Palma by the Isaac Newton Group of Telescopes in the Spanish Observatorio del Roque de los Muchachos of the Instituto de Astrofisica de Canarias. The National Radio Astronomy Observatory is a facility of the National Science Foundation operated

under cooperative agreement by Associated Universities, Inc. This research made use of Astropy, a community-developed core Python package for Astronomy The Astropy Collaboration et al., 2018. The data of GALEX presented in this paper were obtained from the Mikulski Archive for Space Telescopes (MAST). This publication makes use of data products from the Two Micron All Sky Survey, which is a joint project of the University of Massachusetts and the Infrared Processing and Analysis Center/California Institute of Technology, funded by the National Aeronautics and Space Administration and the National Science Foundation. This research has made use of the NASA/IPAC Extragalactic Database (NED) which is operated by the Jet Propulsion Laboratory, California Institute of Technology, under contract with the National Aeronautics and Space Administration. IRAF is distributed by the National Optical Astronomy Observatory, which is operated by the Association of Universities for Research in Astronomy (AURA) under a cooperative agreement with the National Science Foundation. Funding for the Sloan Digital Sky Survey (SDSS) IV has been provided by the Alfred P. Sloan Foundation, the U.S. Department of Energy Office of Science, and the Participating Institutions. SDSS acknowledges support and resources from the Center for High-Performance Computing at the University of Utah. The SDSS web site is www.sdss.org. This research has made use of NASA's Astrophysics Data System.

Table 2.1: **Photometric follow-up of iPTF 14gqr in the optical and UV bands.** The data have been corrected for Galactic extinctions of 0.158 mag (i-band), 0.212 mag (r-band), 0.307 mag (g-band), 0.337 mag (B-band), 0.553 mag ($UVW1$ band), and 0.748 mag ($UVW2$ band). Upper limits indicated are 5σ upper limits in the respective bands.

MJD	Rest frame phase (days from explosion)	Filter	Magnitude	Telescope
56944.41	0.62	$UVW2$	19.14 ± 0.07	UVOT
56944.83	1.02	$UVW2$	19.86 ± 0.12	UVOT
56945.08	1.25	$UVW2$	> 19.62	UVOT
56950.15	6.02	$UVW2$	> 20.96	UVOT
56954.77	10.37	$UVW2$	> 21.14	UVOT
56962.02	17.19	$UVW2$	> 20.29	UVOT
56966.30	21.21	$UVW2$	> 20.99	UVOT
56944.43	0.64	$UVW1$	19.49 ± 0.10	UVOT
56944.84	1.03	$UVW1$	19.71 ± 0.16	UVOT
56950.15	6.02	$UVW1$	21.23 ± 0.30	UVOT
56954.77	10.37	$UVW1$	> 20.62	UVOT
56962.01	17.18	$UVW1$	> 19.81	UVOT
56966.30	21.21	$UVW1$	> 20.44	UVOT
56944.34	0.56	B	20.26 ± 0.08	P60

56944.39	0.60	*B*	20.22 ± 0.08	P60
56944.45	0.66	*B*	20.09 ± 0.09	P60
56945.09	1.26	*B*	> 19.96	P60
56945.16	1.33	*B*	20.55 ± 0.08	P60
56946.09	2.20	*B*	> 20.26	P60
56946.15	2.26	*B*	20.41 ± 0.10	P60
56946.20	2.30	*B*	20.42 ± 0.10	P60
56946.31	2.41	*B*	> 20.56	P60
56949.36	5.28	*B*	20.08 ± 0.06	P60
56949.41	5.32	*B*	20.08 ± 0.05	P60
56954.75	10.35	*B*	> 19.11	UVOT
56962.01	17.18	*B*	> 18.41	UVOT
56966.28	21.19	*B*	> 18.99	UVOT
56940.34	-3.21	*g*	> 20.71	P48
56941.36	-2.25	*g*	> 21.04	P48
56942.36	-1.31	*g*	> 21.43	P48
56943.33	-0.40	*g*	> 21.23	P48
56944.20	0.42	*g*	19.95 ± 0.05	P48
56944.35	0.56	*g*	20.04 ± 0.04	P60
56944.42	0.63	*g*	20.12 ± 0.05	P60
56945.10	1.27	*g*	20.52 ± 0.11	P60
56945.17	1.34	*g*	20.47 ± 0.10	P60
56946.22	2.32	*g*	20.36 ± 0.04	P60
56947.21	3.25	*g*	20.17 ± 0.07	P48
56949.34	5.26	*g*	19.85 ± 0.02	P60
56950.26	6.12	*g*	19.80 ± 0.03	P48
56951.22	7.03	*g*	19.87 ± 0.03	P48
56952.23	7.98	*g*	19.94 ± 0.04	P60
56953.29	8.97	*g*	19.95 ± 0.05	P48
56954.27	9.90	*g*	20.15 ± 0.05	P48
56955.21	10.78	*g*	20.32 ± 0.04	P60
56956.14	11.66	*g*	20.59 ± 0.09	P60
56956.33	11.83	*g*	> 19.36	P48
56958.19	13.58	*g*	20.87 ± 0.07	P60
56959.26	14.59	*g*	21.12 ± 0.15	P48
56960.26	15.53	*g*	21.17 ± 0.38	P48
56960.28	15.55	*g*	> 20.51	P48
56965.19	20.17	*g*	> 19.99	P60
56966.08	21.01	*g*	> 19.59	P60
56954.75	10.35	*V*	> 18.53	UVOT
56962.01	17.18	*V*	> 17.78	UVOT
56966.28	21.19	*V*	> 18.40	UVOT
56944.34	0.56	*r*	20.39 ± 0.07	P60
56944.40	0.61	*r*	20.45 ± 0.07	P60
56944.46	0.67	*r*	20.40 ± 0.11	P60
56945.10	1.27	*r*	20.56 ± 0.13	P60
56945.17	1.34	*r*	20.56 ± 0.11	P60
56946.20	2.30	*r*	20.47 ± 0.06	P60
56949.36	5.28	*r*	19.87 ± 0.04	P60
56949.41	5.32	*r*	19.95 ± 0.05	P60
56952.15	7.90	*r*	19.83 ± 0.04	P60
56955.17	10.74	*r*	20.01 ± 0.06	P60

56956.09	11.61	*r*	20.18 ± 0.12	P60
56957.35	12.79	*r*	20.20 ± 0.09	P60
56958.09	13.49	*r*	20.30 ± 0.10	P60
56965.19	20.17	*r*	> 18.89	P60
56966.08	21.01	*r*	> 18.29	P60
56944.34	0.56	*i*	20.86 ± 0.10	P60
56944.40	0.61	*i*	20.83 ± 0.13	P60
56944.45	0.66	*i*	20.74 ± 0.17	P60
56945.14	1.31	*i*	20.66 ± 0.08	P60
56946.21	2.31	*i*	20.52 ± 0.06	P60
56949.35	5.27	*i*	20.01 ± 0.08	P60
56949.41	5.32	*i*	20.07 ± 0.09	P60
56952.15	7.90	*i*	19.99 ± 0.06	P60
56955.17	10.74	*i*	19.95 ± 0.08	P60
56956.08	11.60	*i*	> 19.84	P60
56957.35	12.79	*i*	20.22 ± 0.07	P60
56958.08	13.48	*i*	20.15 ± 0.11	P60
56965.08	20.07	*i*	> 20.44	P60
56966.08	21.01	*i*	> 18.64	P60
56945.32	1.48	*B*	20.68 ± 0.18	LCO
56947.10	3.15	*B*	20.17 ± 0.11	LCO
56949.08	5.02	*B*	19.99 ± 0.12	LCO
56954.31	9.94	*B*	20.15 ± 0.13	LCO
56956.26	11.77	*B*	20.63 ± 0.12	LCO
56959.22	14.55	*B*	21.27 ± 0.19	LCO
56945.33	1.49	*V*	20.36 ± 0.14	LCO
56947.11	3.16	*V*	20.01 ± 0.10	LCO
56949.09	5.02	*V*	19.85 ± 0.09	LCO
56954.32	9.94	*V*	19.86 ± 0.11	LCO
56956.27	11.78	*V*	20.25 ± 0.11	LCO
56959.23	14.56	*V*	20.56 ± 0.21	LCO
56945.34	1.50	*g*	20.33 ± 0.17	LCO
56947.12	3.17	*g*	20.14 ± 0.11	LCO
56949.10	5.03	*g*	19.81 ± 0.10	LCO
56954.33	9.95	*g*	20.16 ± 0.11	LCO
56956.28	11.79	*g*	20.38 ± 0.13	LCO
56959.24	14.57	*g*	21.03 ± 0.09	LCO
56945.35	1.50	*r*	20.54 ± 0.20	LCO
56947.13	3.18	*r*	20.20 ± 0.10	LCO
56949.11	5.04	*r*	19.87 ± 0.10	LCO
56954.34	9.96	*r*	19.98 ± 0.12	LCO
56956.29	11.79	*r*	19.87 ± 0.14	LCO
56945.36	1.51	*i*	20.49 ± 0.26	LCO
56947.13	3.18	*i*	20.18 ± 0.14	LCO
56949.12	5.05	*i*	20.15 ± 0.15	LCO
56954.35	9.97	*i*	20.06 ± 0.14	LCO
56956.29	11.80	*i*	20.11 ± 0.13	LCO
56959.25	14.59	*i*	20.34 ± 0.12	LCO

Table 2.2: **Swift XRT flux limits on iPTF 14gqr.** The upper limits indicated are 5σ. The count rates have been converted to flux upper limits for a photon index of $\Gamma = 2$ and zero galactic foreground absorption.

MJD	Rest frame phase (days since explosion)	Exposure time (s)	Count rate (10^{-3} counts s^{-1})	Flux (0.3 - 10 keV) 10^{-13} ergs cm^{-2} s^{-1}
56944.41	0.62	1800	< 8.43	< 2.39
56944.81	1.00	990	< 15.53	< 4.41
56945.08	1.25	162	< 96.66	< 27.44
56950.14	6.01	1564	< 9.79	< 2.78
56954.75	10.35	3524	< 4.28	< 1.22
56962.01	17.18	1221	< 12.36	< 3.51
56966.28	21.19	2966	< 5.07	< 1.44

Table 2.3: **Summary of spectroscopic observations of iPTF 14gqr.** † denotes epochs where we did not get a good signal to noise ratio spectrum. * Slit mask observation to measure the redshifts of potential host galaxies near the transient.

Observation Date	MJD	Rest frame phase (days from explosion)	Telescope + Instrument	Range (Observed Å)	Resolution (FWHM Å)
2014 Oct 14.36	56944.36	0.58	APO + DIS	3315 – 9880	6
2014 Oct 14.86	56944.86	1.05	WHT + ACAM	3400 – 9500	13
2014 Oct 15.10	56945.10	1.27	NOT + ALFOSC	3450 – 9140	17
2014 Oct 15.21	56945.21	1.38	Gemini N + GMOS	3790 – 9350	7
2014 Oct 20.36	56950.36	6.22	Keck I + LRIS	3100 – 10300	6
2014 Oct 21.41	56951.41	7.20	Keck I + LRIS	3100 – 10300	6
2014 Oct 25.40	56955.40	10.96	Keck I + LRIS	3200 – 10250	6
2014 Nov 19.27	56980.27	34.36	Keck I + LRIS	3060 – 10300	6
2014 Dec 17.25†	57008.25	60.67	Keck I + LRIS	3070 – 10290	6
2014 Dec 21.27†	57012.27	64.46	Keck II + DEIMOS	4490 – 9650	4
2016 Nov 28.27*	57720.27	–	Keck I + LRIS mask	–	6

Table 2.4: **Redshifts and locations of galaxies near iPTF 14gqr, as identified in the spectroscopic mask (Figure 2.8).** The last column indicates the offset of the galaxy from the location of the transient. † Apparent host galaxy of iPTF 14gqr.

Object name	α (J2000)	δ (J2000)	Redshift	Offset ($''$)
Obj1†	$23^h33^m29.85^s$	$33°38'48.22''$	0.063	23.8
Obj2	$23^h33^m30.39^s$	$33°39'0.21''$	0.063	33.5
Obj3	$23^h33^m30.70^s$	$33°39'16.87''$	0.063	46.1
Obj4	$23^h33^m28.89^s$	$33°37'52.44''$	0.743	55.0
Obj5	$23^h33^m32.24^s$	$33°38'18.32''$	0.222	60.4
Obj6	$23^h33^m31.18^s$	$33°39'39.55''$	0.292	66.9
Obj7	$23^h33^m24.46^s$	$33°40'0.42''$	0.190	86.2
Obj8	$23^h33^m21.57^s$	$33°39'23.25''$	0.190	87.9
Obj9	$23^h33^m25.44^s$	$33°40'13.58''$	0.258	92.9
Obj10	$23^h33^m24.52^s$	$33°37'10.07''$	0.480	105.2
Obj11	$23^h33^m35.20^s$	$33°37'41.58''$	0.250	111.1
Obj12	$23^h33^m36.68^s$	$33°40'2.76''$	0.185	133.2
Obj13	$23^h33^m38.04^s$	$33°36'32.74''$	0.183	183.5
Obj14	$23^h33^m26.85^s$	$33°35'31.12''$	0.197	195.5
Obj15	$23^h33^m37.42^s$	$33°36'4.38''$	0.295	200.3
Obj16	$23^h33^m23.59^s$	$33°34'57.65''$	0.197	234.9
Obj17	$23^h33^m26.52^s$	$33°34'24.85''$	0.197	261.9
Obj18	$23^h33^m30.57^s$	$33°34'6.88''$	0.288	281.2
Obj19	$23^h33^m23.41^s$	$33°33'30.78''$	0.182	320.4

Table 2.5: **Basic properties of the light curve of iPTF 14gqr in the g, r and i bands.** The apparent magnitudes have been corrected for galactic extinction, while the light curve decay rates are calculated in the rest frame of the transient. We estimate the decay rate in each filter by fitting the light curve of the transient between +10 and +16 days from explosion with a straight line. The i band decline is not well constrained owing to the lack of post-peak photometry in that filter.

Filter	MJD_{peak}	$m_{app,max}$ (mag)	$M_{abs,max}$ (mag)	τ_{rise} (days)	Decay rate (mag day^{-1})
g	56950.39 ± 0.15	19.82 ± 0.01	-17.45 ± 0.01	6.25 ± 0.46	0.21 ± 0.02
r	56951.36 ± 0.37	19.82 ± 0.03	-17.45 ± 0.03	7.16 ± 0.53	0.11 ± 0.04
i	56952.51 ± 0.78	19.92 ± 0.09	-17.35 ± 0.09	8.24 ± 0.89	–

Table 2.6: **Emission line fluxes of the nucleus of the host galaxy IV Zw 155, along with broadband integrated photometry measurements.** The photometry measurements were taken from the GALEX source catalogs (Bianchi et al., 2014), SDSS (Abolfathi et al., 2017), and 2MASS (Skrutskie et al., 2006). All fluxes and magnitude measurements have been corrected for galactic extinction using A_V=0.255 mag and a Cardelli et al., 1989 extinction law.

Spectral line / Photometric band	Wavelength (Å)	Flux (10^{-15} ergs s^{-1} cm^{-2})	AB magnitude mag
[O II]	3727	5.57 ± 0.79	–
Hβ	4861	1.95 ± 1.09	–
[O III]	5007	2.09 ± 0.58	–
Hα	6563	8.92 ± 0.53	–
[N II]	6583	2.97 ± 0.48	–
[S II]	6717	1.90 ± 0.13	–
[S II]	6731	1.63 ± 0.35	–
GALEX FUV	1540	–	17.60 ± 0.09
GALEX NUV	2314	–	17.20 ± 0.05
SDSS *u*	3562	–	16.740 ± 0.030
SDSS *g*	4719	–	15.292 ± 0.004
SDSS *r*	6185	–	14.762 ± 0.003
SDSS *i*	7500	–	14.451 ± 0.003
SDSS *z*	8961	–	14.314 ± 0.007
2MASS *J*	12376	–	14.44 ± 0.06
2MASS *H*	16476	–	14.31 ± 0.08
2MASS *K*	21621	–	14.41 ± 0.12

Table 2.7: **Elemental abundances at the photosphere for the ultra-stripped SN model found to be consistent with the observed data.**

Z	Element	Mass fraction (X)
6	C	0.082
8	O	0.464
10	Ne	0.382
11	Na	0.003
12	Mg	0.059
13	Al	0.003
14	Si	0.004
	Fe group	0.0017

Chapter 3

A FAST-EVOLVING, HYDROGEN-RICH CORE-COLLAPSE SUPERNOVA FROM A HIGHLY STRIPPED LOW MASS PROGENITOR

De, K. et al. (2021). "The Peculiar Ca-rich SN2019ehk: Evidence for a Type IIb Core-collapse Supernova from a Low-mass Stripped Progenitor". In: *ApJL* 907.1, L18, p. L18. DOI: 10.3847/2041-8213/abd627. arXiv: 2009.02347 [astro-ph.HE].

Kishalay De[1], U. Christoffer Fremling[1], Avishya Gal-Yam[2], Ofer Yaron[2], Mansi M. Kasliwal[1], and S. R. Kulkarni[1]

[1]Cahill Center for Astrophysics, California Institute of Technology, 1200 E. California Blvd., Pasadena, CA 91125, USA
[2]Benoziyo Center for Astrophysics, The Weizmann Institute of Science, Rehovot 76100, Israel

Abstract

The nature of the peculiar 'Ca-rich' SN 2019ehk in the nearby galaxy M100 remains unclear. Its origin has been debated as either a stripped core-collapse supernova or a thermonuclear helium detonation event. Here, we present very late-time photometry of the transient obtained with the Keck I telescope at ≈ 280 days from peak light. Using the photometry to perform accurate flux calibration of a contemporaneous nebular phase spectrum, we measure an [O I] luminosity of $(0.19-1.08)\times10^{38}$ erg s^{-1} and [Ca II] luminosity of $(2.7-15.6)\times10^{38}$ erg s^{-1} over the range of the uncertain extinction along the line of sight and distance to the host galaxy. We use these measurements to derive lower limits on the synthesized oxygen mass of $\approx 0.004-0.069\,M_\odot$. The oxygen mass is a sensitive tracer of the progenitor mass for core-collapse supernovae, and our estimate is consistent with explosions of very low mass CO cores of $1.45-1.5\,M_\odot$, corresponding to He core masses of $\approx 1.8-2.0\,M_\odot$. We present high quality peak light optical spectra of the transient and highlight features of hydrogen in both the early ('flash') and photospheric phase spectra, that suggest the presence of $\gtrsim 0.02\,M_\odot$ of hydrogen in the progenitor at the time of explosion. The presence of H, together with the large [Ca II]/[O I] ratio ($\approx 10-15$) in the nebular phase is consistent with SN 2019ehk being a Type IIb core-collapse supernova from a stripped low mass ($\approx 9-9.5\,M_\odot$) progenitor, sim-

ilar to the Ca-rich SN IIb iPTF 15eqv. These results provide evidence for a likely class of 'Ca-rich' core-collapse supernovae from stripped low mass progenitors in star forming environments, distinct from the thermonuclear Ca-rich gap transients in old environments.

3.1 Introduction

Ca-rich gap transients are an intriguing class of faint and fast evolving explosions characterized by their conspicuously strong [Ca II] $\lambda\lambda 7291, 7324$ emission (compared to [O I] $\lambda\lambda 6300, 6364$) in the nebular phase (De et al., 2020c; Filippenko et al., 2003; Gal-Yam, 2017; Kasliwal et al., 2012; Lunnan et al., 2017; Milisavljevic et al., 2017; Perets et al., 2010; Valenti et al., 2014). Tracking down the progenitors and explosion mechanisms of these unique transients is important for our understanding of the fates of close binary systems, the progenitors of Type Ia SNe, and the cosmic nucleosynthesis of Ca (De et al., 2020c; Frohmaier et al., 2019; Mulchaey et al., 2014).

The peculiar SN 2019ehk was discovered in the galaxy M100 (Grzegorzek, 2019), and subsequent follow-up showed that the source exhibited fast photometric and spectroscopic evolution to the nebular phase dominated by strong [Ca II] emission, consistent with several known properties of Ca-rich events (Jacobson-Galán et al., 2020b; Nakaoka et al., 2020). Jacobson-Galán et al., 2020b suggested that its early fast spectroscopic evolution and double peaked light curve is likely explained with an explosive thermonuclear detonation ignited during a white dwarf merger involving a low mass hybrid white dwarf. However, archival Hubble Space Telescope (HST) images could not rule out a core-collapse explosion from a $< 10\,M_{\odot}$ massive star. On the other hand, Nakaoka et al., 2020 favored a scenario involving a low-mass core-collapse supernova (SN) from an inflated and 'ultra-stripped' He star in a close binary system (Tauris et al., 2013, 2015) – a channel which has been suggested to lead to the formation of neutron stars in compact binary systems. As one of the nearest potential members of the class of Ca-rich events, constraining the nature of the progenitor of SN 2019ehk can reveal important clues to the broader population of events.

With the advent of large systematic experiments for supernova (SN) classification, it is now well established that Ca-rich gap transients are relatively common ($\approx 15\%$ of the SN Ia rate) and predominantly occur in old environments in the outskirts of early type galaxies, suggesting progenitor systems likely involving explosive He

shell burning on low mass white dwarfs (De et al., 2020c; Frohmaier et al., 2018; Kasliwal et al., 2012; Lunnan et al., 2017; Perets et al., 2010). The dominance of cooling via [Ca II] emission as opposed to Fe emission (seen in normal Type Ia SNe) has been recently shown to be a hallmark feature of explosions involving shell detonations (Dessart et al., 2015a; Waldman et al., 2011) with low total (core + shell) masses (Polin et al., 2021).

However, the discovery of Ca-rich SNe such as iPTF 15eqv (Milisavljevic et al., 2017) and iPTF 16hgs (De et al., 2018a) in actively star forming environments (as in the case of SN 2019ehk) have also led to suggestions involving core-collapse supernovae from low mass progenitors. Yet, the high [Ca II]/[O I] ratio seen in the population of Ca-rich transients (De et al., 2020c; Milisavljevic et al., 2017; Valenti et al., 2014) is strikingly different from that seen in normal stripped core-collapse SNe (Fang et al., 2019).

Oxygen in the ejecta of core-collapse SNe is formed primarily in the hydrostatic burning phase of the progenitor (increasing with zero age main sequence mass), while Ca is explosively synthesized by O burning (Fransson et al., 1989; Woosley et al., 2007). As a result, the O mass in the ejecta and Ca/O ratio is a powerful tracer of the progenitor mass for core-collapse SNe (Fransson et al., 1989; Jerkstrand et al., 2014, 2015). In the case of the Ca-rich SN 2005cz, Kawabata et al., 2010 thus first suggested that the high [Ca II]/[O I] ratio could be explained by an explosion of a low mass progenitor that was stripped by a binary companion.

In this paper, we attempt to constrain the progenitor of SN 2019ehk with new late-time photometry and high quality optical spectra obtained near peak light. Section 3.2 provides an overview of the observations and data analysis procedures. We use the observations to constrain the composition of the ejecta in both the early photospheric and late nebular phase in Section 3.3. We present a discussion on the likely progenitor for SN 2019ehk in Section 3.4 and conclude with a summary in Section 3.5. We adopt a nominal distance of 16.2 Mpc and redshift of $z = 0.005$ to M100 for the rest of this work (Folatelli et al., 2010). However, there is a span of $\approx 14.2 - 21.4$ Mpc in reported distances using Cepheid variables (e.g. Freedman et al., 2001; as in the NASA Extragalactic Database), which we use as the range of possible distances to the host galaxy in estimating uncertainty intervals.

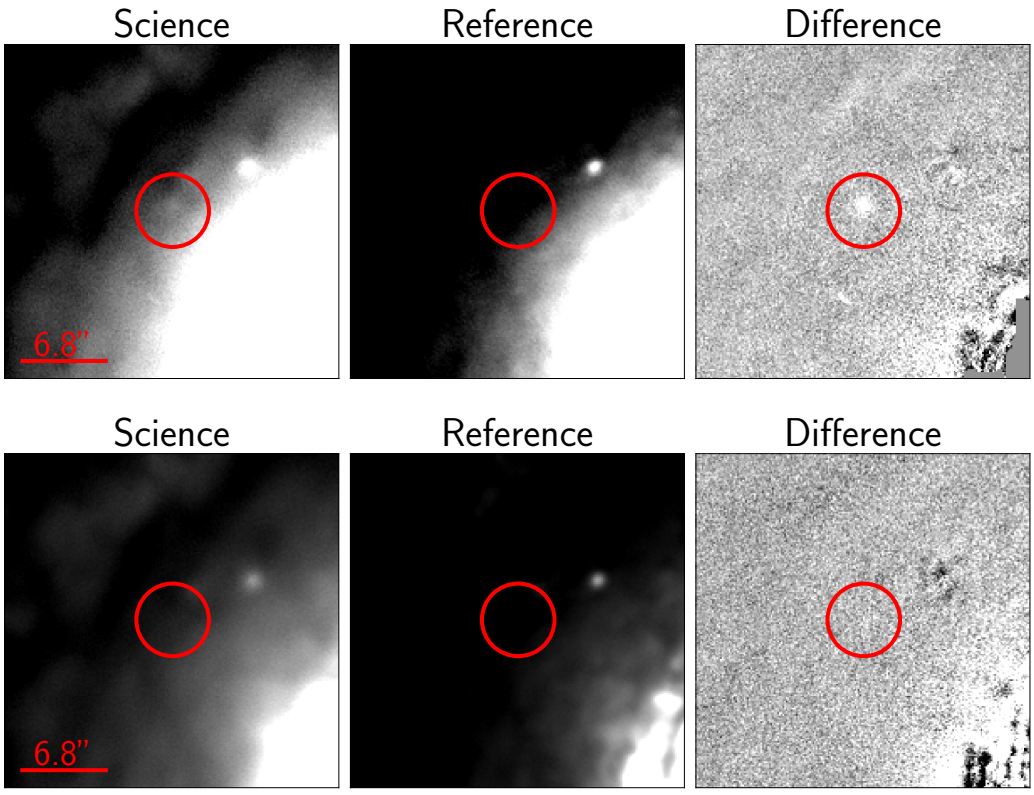

Figure 3.1: **Late-time images of SN 2019ehk obtained with the Keck-I telescope.** (Top panel) Late-time I-band detection of SN 2019ehk with the Keck-I telescope, with North up and East left. The left panel is the image taken at $\approx$ 280 days from peak light, the middle panel is the template image acquired at $\approx$ 400 days after peak light and the right panel is the difference image obtained after image subtraction. (Bottom panel) Same as top panel showing non-detection of SN 2019ehk at the same epoch in g band.

3.2 Observations and analysis

We obtained one epoch of late-time imaging of SN 2019ehk with the Low Resolution Imaging Spectrometer (LRIS; Oke et al., 1995) on the Keck-I telescope on UT 2020-02-18.62, at a phase of $\approx$ 280 days from r-band peak, for a total exposure time of 300 s and 390 s in g and I bands, respectively. We obtained a reference epoch for the source on UT 2020-06-23.32 to use as a template for image subtraction of the host galaxy light, for a total exposure time of 520 s and 440 s in g and I bands, respectively. The data were reduced using `lpipe` (Perley, 2019) and image subtraction was performed using `HOTPANTS` (Becker, 2015).

Photometric calibration was performed against SDSS catalog magnitudes of secondary standards in the field. The source is clearly detected in the I-band subtracted

image at a magnitude of $I = 22.10 \pm 0.15$ AB mag (Figure 3.1), while the source is not detected in g-band to a 3σ depth of 23.55 AB mag. Based on the observed decay rate of the late-time light curve ($\gtrsim 0.02$ mag day^{-1}; Jacobson-Galán et al., 2020b), we expect the flux of the source at the template image epoch (≈ 400 days) to be $\gtrsim 10\times$ smaller than the science epoch, and thus not contaminate our measurements significantly.

We use the observed late-time photometry to calibrate the published late-time spectrum at ≈ 260 days in Jacobson-Galán et al., 2020b, noting that the strong [Ca II] line falls completely within the observed I band. We perform spectrophotometric calibration by convolving the filter function with the observed spectrum, and then measure the resulting line fluxes by trapezoidal integration of the respective wavelength regions. Uncertainties in this method are estimated by Monte Carlo sampling of the estimated fluxes by adding noise (scaled to nearby regions with no line emission) to the line profile, and add it in quadrature to the uncertainty of the photometric measurement. We measure the resulting [Ca II] line flux to be $(4.0 \pm 0.6) \times 10^{-15}$ erg cm^{-2} s^{-1} and the corresponding observed [O I] line flux to be $(2.1 \pm 0.4) \times 10^{-16}$ erg cm^{-2} s^{-1}.

We also present optical spectroscopy of the transient obtained with the Double Beam Spectrograph (DBSP; Oke et al., 1982) on the Palomar 200-inch telescope (P200) on UT 2019-05-13, corresponding to a phase of $\approx +0$ days from r-band peak. The DBSP data were reduced using the `pyraf-dbsp` pipeline (Bellm et al., 2016). The data presented here will be publicly released on WISERep (Yaron et al., 2012).

3.3 Results

Constraints on host galaxy extinction

There is evidence for significant host galaxy extinction towards SN 2019ehk (Jacobson-Galán et al., 2020b; Nakaoka et al., 2020). A deep Na I D line is clearly detected in its peak light spectra, and suggests a large host extinction of $E(B-V) \gtrsim 1$ based on canonical relationships between $E(B-V)$ and the equivalent width (EW) of the Na D line (Poznanski et al., 2012). However, the very large equivalent width ($EW \approx 3$ Å) falls in a regime where published relationships become uncertain (Poznanski et al., 2012). The adopted extinction thus introduces an additional uncertainty in the determination of the absolute luminosity of the supernova and the nebular phase spectral lines.

However, the double-peaked light curve of SN 2019ehk shares several similarities

with previously reported fast evolving Type I SNe in the literature, including the SN Ic iPTF 14gqr (De et al., 2018b) as well as the SN Ib iPTF 16hgs (De et al., 2018a). Nakaoka et al., 2020 show that the photometric properties of SN 2019ehk can match either the low peak luminosity of iPTF 16hgs or the higher luminosity of iPTF 14gqr for assumed extinctions of $E(B-V) = 0.5$ mag and $E(B-V) = 1.0$ mag, respectively, with the true value being likely in between these two[1]. Taking these two values of extinction as limiting cases, we obtain extinction corrected [O I] flux of $(7.2 \pm 1.3) \times 10^{-16}$ erg cm^{-2} s^{-1} and $(2.5 \pm 0.4) \times 10^{-15}$ erg cm^{-2} s^{-1}, respectively, assuming $R_V = 3.1$ and a Cardelli et al., 1989 extinction law. The corresponding [Ca II] line fluxes are $(1.1 \pm 0.2) \times 10^{-14}$ erg cm^{-2} s^{-1} and $(2.9 \pm 0.4) \times 10^{-14}$ erg cm^{-2} s^{-1}.

Constraints on the oxygen mass

Uomoto, 1986 provides an analytical formula to calculate the minimum O mass required for a given [O I] luminosity, which depends on the temperature of the emitting region. The relationship holds in the high density limit ($N_e \gtrsim 10^6$ cm^{-3}) where the electron density is above the [O I] critical density ($\sim 7 \times 10^5$ cm^{-3}), and is estimated to hold in this case for the estimated ejecta mass of ≈ 0.5 M$_\odot$ (Jacobson-Galán et al., 2020b; Nakaoka et al., 2020). However, we caution that such O mass estimates assume that the radioactive power deposited in the O-rich shells of the ejecta is released via cooling in the [O I] lines. Dessart et al., 2020 show that even small amounts of Ca mixing (~ 0.01 by mass fraction) from the underlying Si-rich layers can drastically reduce the [O I] line fluxes since [Ca II] is a much more effective coolant than [O I]. In the case of SN 2019ehk, it is clear that the majority of the cooling is arising from the [Ca II] line, which may be due to either a very low O layer mass compared to the Si-rich layer, or due to enhanced mixing of Ca into O-rich layers. As such, these O mass estimates should be treated as lower limits on the O mass in the ejecta.

While the temperature can be constrained with the line ratio of the [O I] λ5577 Å line to the [O I] $\lambda\lambda$6300, 6364 doublet (Houck et al., 1996), the weak [O I] line in the SN 2019ehk spectrum at +260 days does not allow this measurement. Instead, we adopt a range of typical values estimated from the [O I] emission in other core-collapse SNe of $\approx 3400 - 4000$ K (Elmhamdi, 2011; Sollerman et al., 1998). We derive lower limits on the O mass in the range of $\approx 0.004 - 0.069$ M$_\odot$ over the range

[1]The value of $E(B-V) = 0.47$ adopted in Jacobson-Galán et al., 2020b is at the lower limit of the range of extinction assumed here.

of temperature, extinction, and distance estimates to the host galaxy. In particular, we note that the derived masses are typically one order of magnitude smaller than the inferred O masses in normal core-collapse SNe (Dessart et al., 2020; Elmhamdi, 2011; Jerkstrand et al., 2015).

We caution that elemental abundance estimates at late epochs is challenging with faint emission features. In particular, as the Uomoto, 1986 estimate does not capture time evolution, we compare this estimate to detailed models from Jerkstrand et al., 2015 in Figure 3.2. As shown, the analytical estimate for the assumed temperature range well constrains the [O I] luminosity evolution between $\approx$ 150 and $\approx$ 350 days (for the nucleosynthetic yields of the Jerkstrand et al., 2015 models), suggesting that the approximated mass range is a conservative estimate for the total O mass.

The mass estimates derived here are inconsistent with that reported in Jacobson-Galán et al., 2020b, who derive a much higher O mass of $\gtrsim 0.15\,M_{\odot}$. This is likely because i) they derived these estimates using a spectrum at an earlier phase ($\approx$ 60 days from peak) where the source was not completely nebular and ii) they assume that the Ca and O emitting regions are co-located in the ejecta so that the observed [Ca II]/[O I] ratio directly constraints the Ca/O mass fraction and O mass via the [Ca II] luminosity. However, we find this interpretation to be unlikely as detailed modeling of core-collapse SNe has shown that the [Ca II] line serves as the primary coolant of the energy deposited in the Si-rich layers, while the [O I] emission arises from the outer O-rich layers produced largely in the hydrostatic burning phase (Dessart et al., 2020; Jerkstrand et al., 2015). Similar arguments for ejecta stratification also have been demonstrated with detailed modeling of thermonuclear shell detonations (Dessart et al., 2015a).

Constraints on the progenitor mass

First, in order to directly compare the observed [O I] luminosity with detailed nebular phase models of stripped envelope SNe and constrain the progenitor mass, we show in Figure 3.2 tracks of the [O I] luminosity evolution for models of different initial ZAMS masses from Jerkstrand et al., 2015. As shown, the nebular models of relatively higher mass progenitors ($\approx 12 - 15\,M_{\odot}$) from Jerkstrand et al., 2015 significantly overestimate the [O I] luminosity, suggesting a much lower progenitor core mass for SN 2019ehk. Note that this conclusion is independent of the assumed extinction, since the [O I] luminosity and the ^{56}Ni luminosity scale similarly with varying extinction.

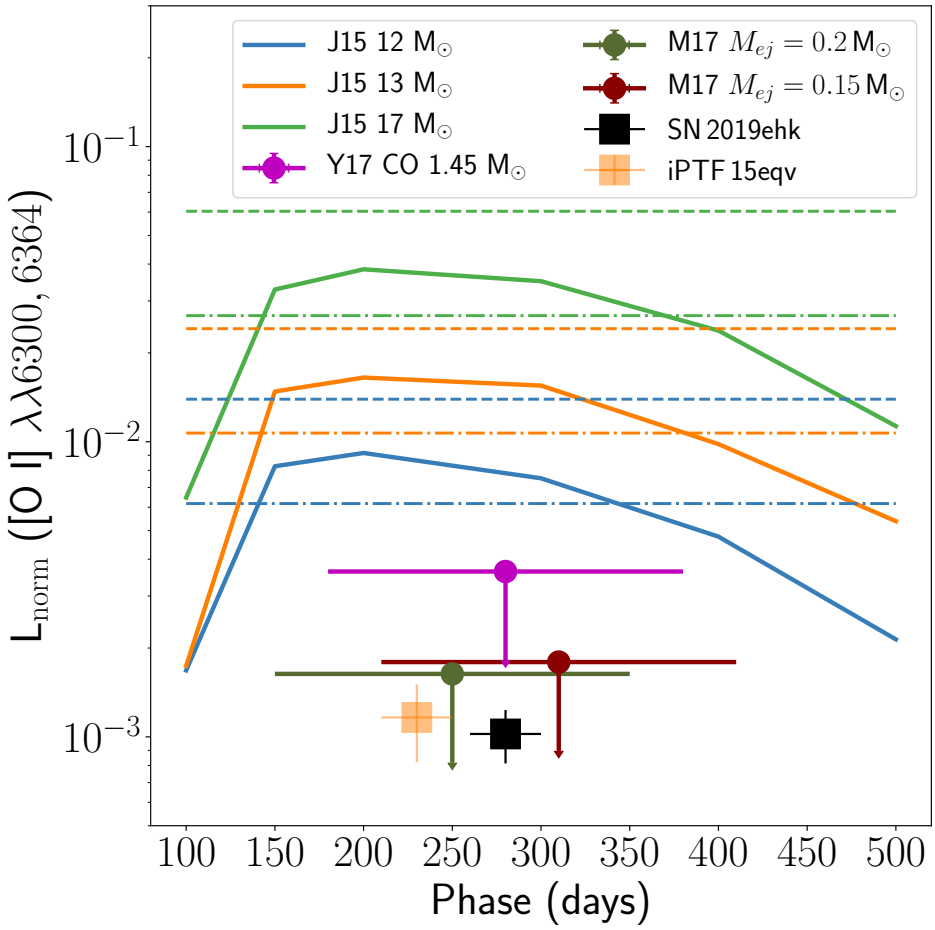

Figure 3.2: **Comparison of the [O I] luminosity of SN 2019ehk to models of stripped envelope core-collapse supernovae from Jerkstrand et al., 2015**. The [O I] luminosity on the y-axis (denoted as L_{norm}) is normalized to the radioactive energy deposition rate from ^{56}Co decay. We show estimated [O I] luminosities from the nucleosynthesis calculations of Moriya et al., 2017[M17 for different ejecta masses from a 1.5 $M_\odot$ CO core] and Yoshida et al., 2017[Y17], where we use the approximate relationship between [O I] luminosity and oxygen mass in Uomoto, 1986, assuming a temperature of 3500 K. The ultra-stripped model luminosity estimates have been arbitrarily shifted in phase for better visualization since the Uomoto, 1986 estimate does not capture time evolution. For comparison, we also show the Uomoto, 1986 estimate of the [O I] luminosity for the nucleosynthetic yields of Jerkstrand et al., 2015 and the range of assumed temperatures (between the dot-dashed and dashed horizontal lines of the same color), showing that the time-independent estimates well constrain the [O I] luminosity evolution between ≈ 150 and ≈ 350 days. For comparison, we also show the measured normalized [O I] luminosity of another Ca-rich SN IIb iPTF 15eqv.

Estimates of the O yields for such low progenitor (and CO core) masses are sparse in the literature, and have thus far been calculated for the case of the highly stripped

He cores of ultra-stripped SNe (Tauris et al., 2013). In these scenarios, relatively low mass He stars ($\lesssim 3.5\,M_\odot$) are stripped down to the CO core by a close binary companion, leaving behind low mass CO cores of $\approx 1.45 - 1.6\,M_\odot$ at the time of explosion (Tauris et al., 2015). Although the presence of strong He lines in the spectra of SN 2019ehk suggests that the stripping did not extend down to the CO core, the nucleosynthetic O yields in these models are applicable to constrain the CO core mass at the time of explosion. Specifically, we note that the CO core mass is relatively insensitive to the mass loss processes via binary interactions that occur in the very late stages of stellar evolution (Jerkstrand et al., 2015; Laplace et al., 2020; Podsiadlowski et al., 1992; Woosley et al., 2015), and hence a good tracer of the progenitor ZAMS mass (Fransson et al., 1989; Jerkstrand et al., 2014, 2015).

We use the nucleosynthetic yields from Moriya et al., 2017 and Yoshida et al., 2017 to estimate the [O I] (Uomoto, 1986) and ^{56}Ni luminosity in the nebular phase for low mass CO cores of $1.45 - 1.5\,M_\odot$, under different assumptions of the explosion energy and ejecta mass. The [O I] luminosity estimate assumes that all the synthesized O emits in [O I] and hence serve as upper limits to the observed luminosity. Figure 3.2 shows that the upper limits on the [O I] luminosity for the low mass CO core models are very similar to the low [O I] luminosity measured for SN 2019ehk.

Next, we also use the derived O mass limits to constrain the progenitor ZAMS mass for SN 2019ehk. In Figure 3.3, we plot model tracks showing the steep dependence of synthesized O mass on the progenitor ZAMS mass from Nomoto et al., 1997, Rauscher et al., 2002 and Limongi et al., 2003. For comparison, we show estimated O masses from a sample of core-collapse SNe of Type II and Type Ib/c from the compilation of Elmhamdi, 2011, demonstrating that the O yields in most normal core-collapse SNe are consistent with $\approx 12 - 20\,M_\odot$ progenitor ZAMS masses.

Specifically, Figure 3.3 demonstrates that the small O mass estimated for SN 2019ehk requires a much smaller progenitor ZAMS mass (and CO core mass) than the canonical models of core-collapse SNe that have been published for ZAMS masses of $\gtrsim 12\,M_\odot$ (corresponding to CO core mass $\gtrsim 2.0\,M_\odot$; Woosley et al., 2015). We thus compare the O mass estimate to smaller CO core masses that have been simulated in the context of ultra-stripped SNe (Moriya et al., 2017; Yoshida et al., 2017). As shown in Figure 3.3, the synthesized O mass estimates for these low mass CO cores are consistent with the range estimated for SN 2019ehk.

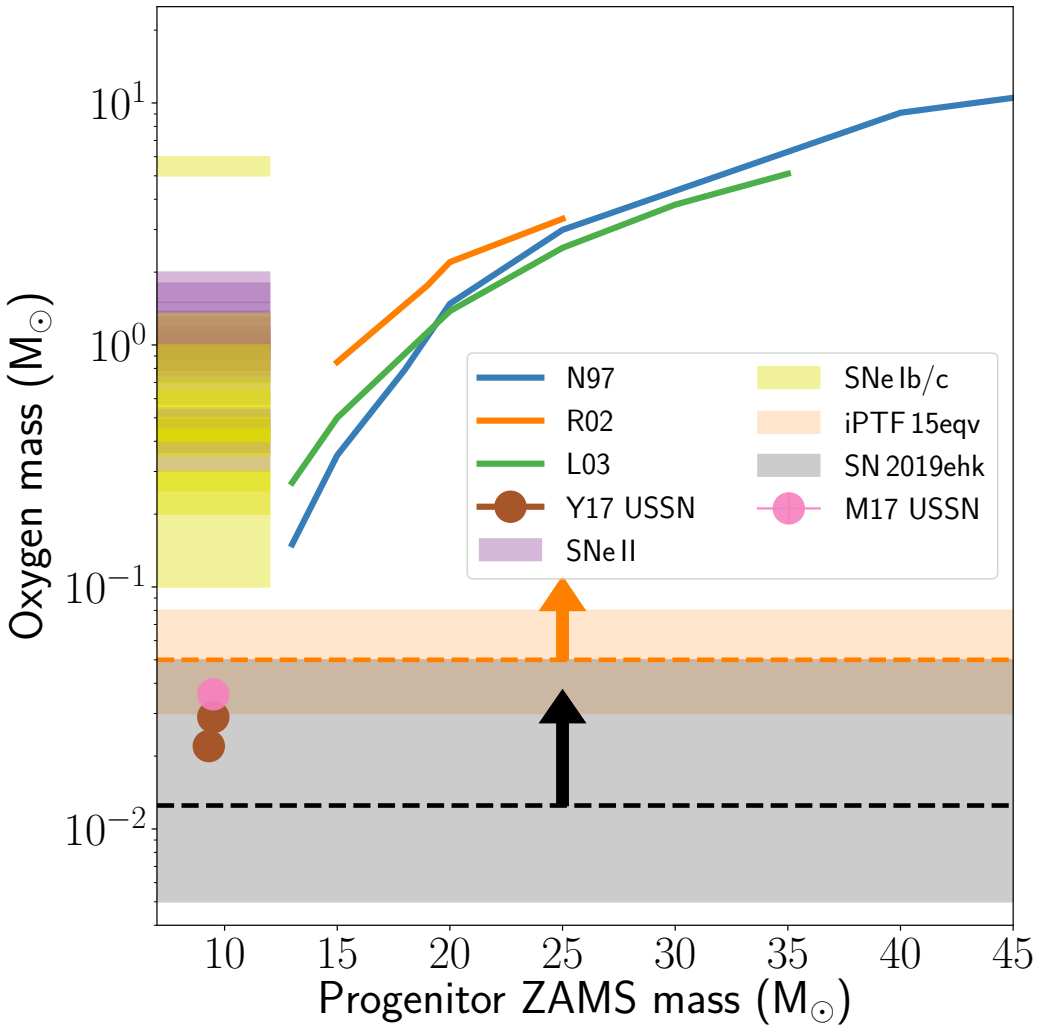

Figure 3.3: **Comparison of the O mass lower limit estimate for SN 2019ehk (in shaded grey region) to models of synthesized O mass in core-collapse SNe as a function of the progenitor ZAMS mass.** The blue, green and orange lines refer to nucleosynthesis models of Nomoto et al., 1997[N97], Rauscher et al., 2002[R02] and Limongi et al., 2003[L03]. We also plot O nucleosynthetic yields for models of low mass CO cores of ultra-stripped SNe (USSNe) from Moriya et al., 2017[M17] and Yoshida et al., 2017[Y17] scaled to the corresponding ZAMS mass expected from stellar evolution (Woosley et al., 2015). For comparison, we plot estimated O masses for normal core-collapse SNe II and Ib/c on the left y-axis. We also show our estimated O mass for a late-time spectrum of another Ca-rich SN IIb iPTF 15eqv.

On the presence of hydrogen in the ejecta

SN 2019ehk was classified as a hydrogen-poor SN Ib in Jacobson-Galán et al., 2020b and Nakaoka et al., 2020, while De et al., 2020c reported the classification of this object as a Type IIb SN. In Figure 3.4, we plot peak-light optical spectra of

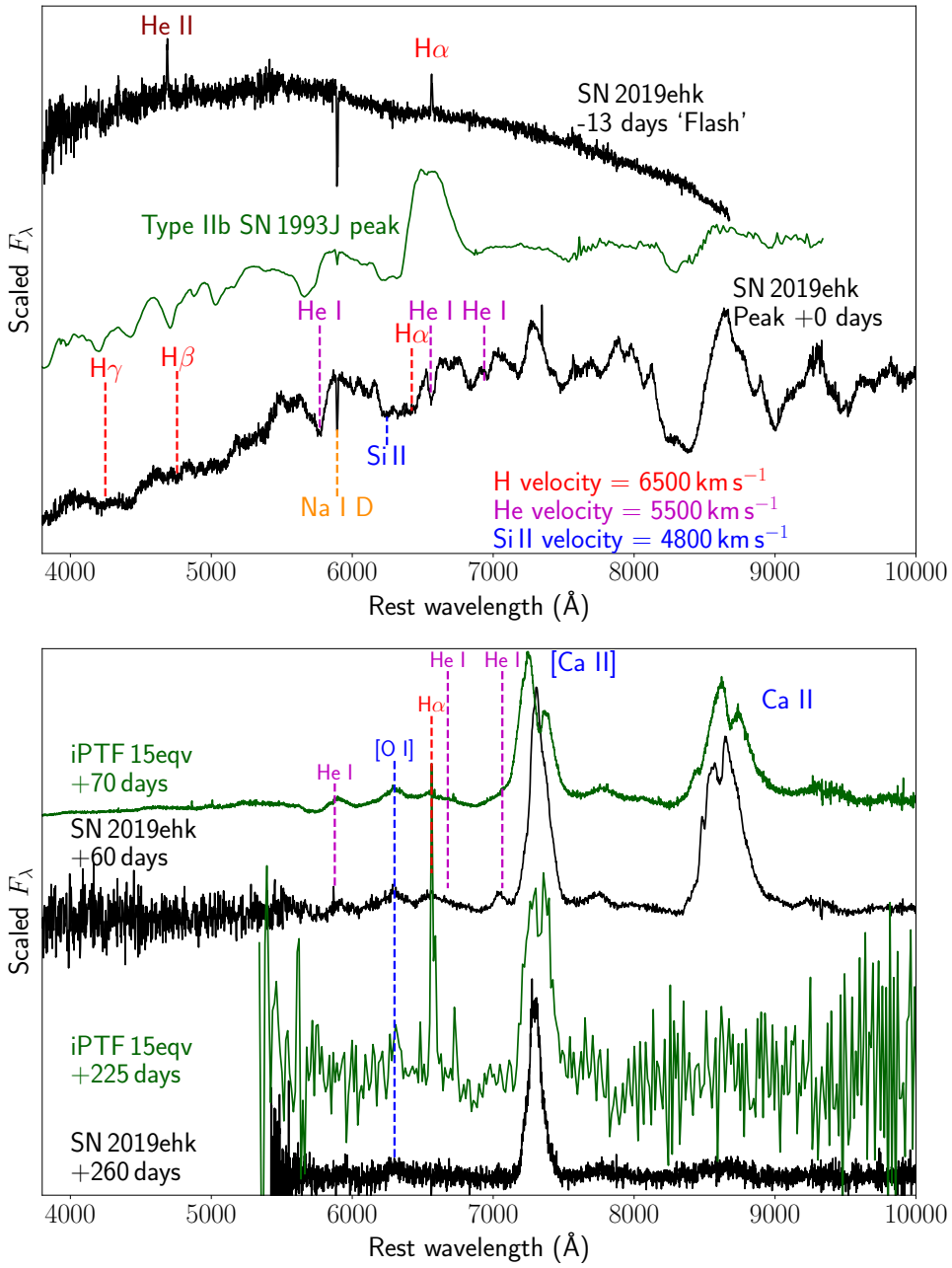

Figure 3.4: **Evidence for the presence of hydrogen in SN 2019ehk throughout its evolution.** (Top panel) Spectra of SN 2019ehk around peak light. The very early spectrum at −13 days shows clear narrow emission lines of Hα and He II, suggesting a 'flash-ionized' hydrogen-rich CSM. We show a comparison of our peak light spectrum of SN 2019ehk to that of the Type IIb SN 1993J, highlighting apparent absorption features of H at a velocity of 6500 km s^{-1} and He I at a velocity of 5500 km s^{-1}. The spectrum of SN 1993J has been artificially reddened with $E(B-V) = 0.75$ to match the continuum shape of SN 2019ehk for better visualization. Note the striking similarities between the two objects in the apparent Balmer and He I absorption features. (Bottom panel) Comparison of the early and late nebular phase spectra of SN 2019ehk and iPTF 15eqv (from Jacobson-Galán et al., 2020b and Milisavljevic et al., 2017), highlighting features of H, He I, [O I] and [Ca II].

SN 2019ehk together with a spectrum of the Type IIb SN 1993J (Matheson et al., 2000). We highlight the presence of absorption features in all the Balmer series transitions at velocities of 7500 km s^{-1}, and distinct He I transitions at 5000 km s^{-1}, consistent with compositionally stratified and homologous expanding ejecta for Type IIb SNe (Dessart et al., 2011). We emphasize the similarities between SN 1993J and SN 2019ehk in the presence of all the Balmer absorption features as well as the flat-bottomed Hα structure seen in other Type IIb SNe (Marion et al., 2014; Silverman et al., 2009).

To demonstrate the presence of hydrogen, we created a synthetic spectrum model for the source using `SYNOW` (Thomas et al., 2011). We use a combination of the most prominent ions in the observed spectrum at their respective velocities – He I, Si II, Ca II, Ti II, and Fe II. Using a photospheric temperature of 5000 K and reddening of $E(B-V) = 0.75$ mag, we create two spectral models – one containing H and one without H. As shown in Figure 3.5, the combination without H shows a single P-Cygni absorption near $\approx$ 6100 Å from Si II, but is unable to produce the flat-bottomed feature near 6400 Å. On the other hand, the addition of H explains the shape of that feature as well as the weaker Hβ transition seen around 4750 Å. We note that the `SYNAPPS` spectroscopic fit (without H) for SN 2019ehk in Jacobson-Galán et al., 2020b does not reproduce the striking combination of Hα and He I λ6678 emission/absorption features at $\approx$ 6400 – 6700 Å, while the Hγ absorption is not reproduced by their ions. Furthermore, the canonical population of Ca-rich events are not known to exhibit such prominent Hα P-Cygni peak and flat bottomed absorption (e.g., Figure 6 in De et al., 2020c), suggesting SN 2019ehk is distinctive.

The early time 'flash' spectra presented in Jacobson-Galán et al., 2020b also exhibit narrow but resolved emission lines of Hα and He II (Figure 3.4). Such features are commonly seen in early time spectra of hydrogen-rich core-collapse SNe (Gal-Yam et al., 2014; Yaron et al., 2017). In the early nebular phase, SN 2019ehk exhibits nearly identical spectroscopic features as that of iPTF 15eqv (Figure 3.4), which was reported as a peculiar hydrogen-rich SN IIb which exhibited a nebular phase spectrum dominated by [Ca II] emission (Milisavljevic et al., 2017). We specifically note the presence of a broad emission feature near the Hα transition, suggesting the presence of H in iPTF 15eqv. Since H features in Type IIb SNe become weaker with time (as He features get stronger; Gal-Yam, 2017), the detection of H several weeks after peak light led to the classification of this object as a hydrogen-rich SN IIb (Cao

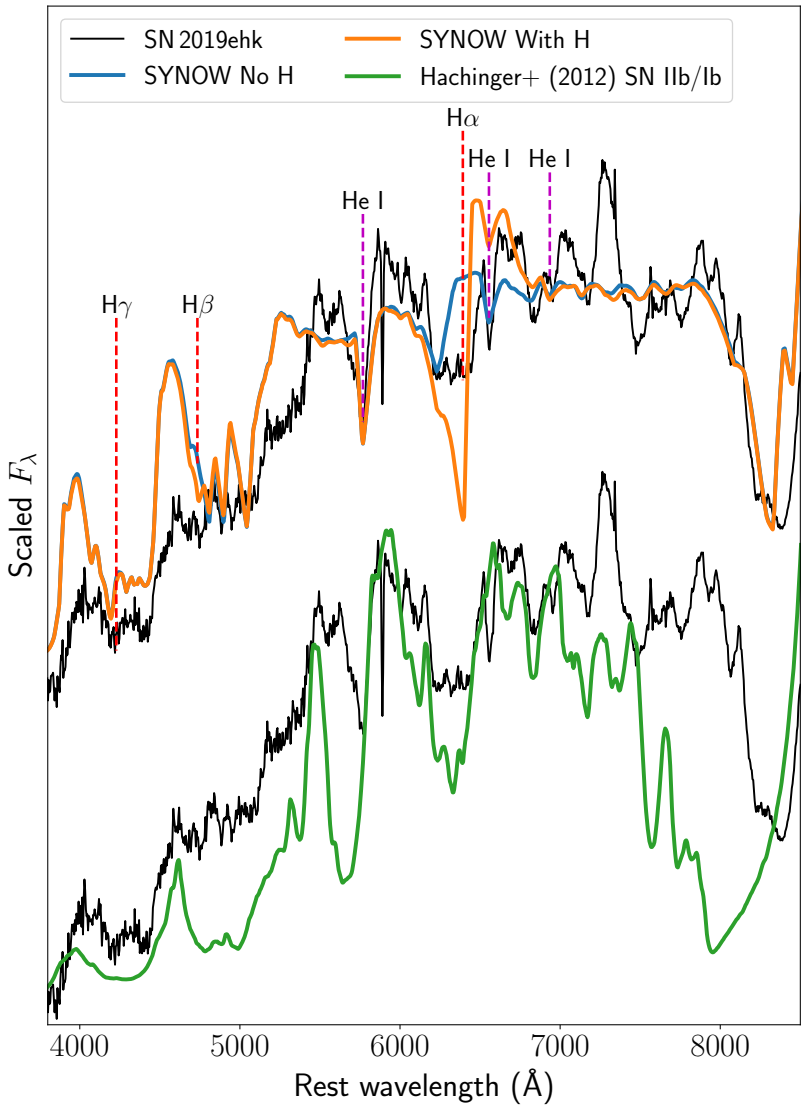

Figure 3.5: **Modeling of the peak spectrum of SN 2019ehk with SYNOW and comparison to radiative transfer models for Type Ib/IIb SNe.** Comparison of the peak spectrum of SN 2019ehk with a synthetic model created using SYNOW as well as more realistic models for transitional Type Ib/IIb SNe. In the top set of spectra, we overplot the observed spectrum with two SYNOW fits – one containing hydrogen (in orange) and one without hydrogen (in blue). As shown, the addition of the hydrogen explains the broad trough near $\approx$ 6500 Å as well as the distinctive Hβ feature near 4750 Å. In the lower set of spectra, we overplot SN 2019ehk (in black) with a transitional SN IIb / SN Ib model from Hachinger et al., 2012 in green. The model spectra are strikingly consistent with SN 2019ehk, in particular, explaining the flat-bottomed feature near $\approx$ 6500 Å as well as other Balmer features.

et al., 2015b; Milisavljevic et al., 2017). At very late phases (> 200 days after peak), the spectra both SN 2019ehk and iPTF 15eqv are dominated by only [Ca II]

emission, leading to their classification as 'Ca-rich' supernovae.

Hachinger et al., 2012 performed radiative transfer simulations for a range of stripped envelope SN progenitors with varying amounts of H and He left at the time of explosion (see their Figure 10). Although they discuss detailed modeling of SN 1993J and SN 1994I, they use their model grid to provide estimates of the amount of H and He required in the ejecta to detect the respective spectral features. Specifically, they show that the flat-bottomed feature near ≈ 6400 Å as well as the weaker higher order Balmer series absorption features are commonly seen in their transitional Type IIb/Ib models, formed by absorption from the nearby Hα and Si II λ6355 transition. In Figure 3.5, we also compare their transitional SN IIb/SN Ib model (after reddening) at a phase of 30 days after explosion[2] with the observed spectra. The model spectra are strikingly similar in terms of the observed features and explain the clear flat-bottomed feature at ≈ 6500 Å. In particular, although the line ratios are not perfectly reproduced in our SYNOW model, they are consistent with the realistic models presented in this work. These transitional Type IIb/Ib models are achieved with small amounts of residual hydrogen in the progenitor, and suggest a remaining H mass of at least $M_H \approx 0.02 - 0.03\,\mathrm{M}_\odot$ in SN 2019ehk. These estimates are similar to that suggested for other SNe Ib possibly showing trace amounts of high velocity hydrogen (e.g. Elmhamdi et al., 2006).

3.4 Discussion

In this work, we have demonstrated that i) the late-time [O I] luminosity in SN 2019ehk is consistent with very low O mass expected for low mass ($\approx 1.45-1.5\,\mathrm{M}_\odot$) CO cores of core-collapse SNe and ii) there is evidence for hydrogen in the early flash-ionized phase, photospheric phase, and nebular phase spectra of SN 2019ehk, suggesting the presence of at least $M_H \approx 0.03\,\mathrm{M}_\odot$ in and around the progenitor at the time of explosion. In particular, the presence of photospheric H with multiple transitions at consistent velocities argues for the classification of SN 2019ehk a SN IIb since the SN Ib classification has been suggested to be applicable for events that show no H at all (Gal-Yam, 2017).

In the case of the interpretation as a thermonuclear transient initiated by a He detonation during a white dwarf merger (Jacobson-Galán et al., 2020b), it was suggested that the early time narrow H features were consistent with H-rich CSM

[2] Given the low ejecta mass (by a factor of ≈ 10) of SN 2019ehk compared to normal SNe IIb/Ib/Ic, we expect the optical depth of the ejecta at peak (≈ 15 days after explosion) to be comparable with the models at about ≈ 30 days after explosion.

(with hydrogen mass of $M_H \sim 10^{-4}\,\mathrm{M}_\odot$) ejected at the time of the merger. However, the presence of photospheric hydrogen suggests $M_H \gtrsim 0.02 - 0.03\,\mathrm{M}_\odot$, which is difficult to reconcile with this scenario since the progenitor CO + He binary white dwarfs are expected to be very deficient in hydrogen ($M_H \lesssim 10^{-4}\,\mathrm{M}_\odot$; Lawlor et al., 2006; Podsiadlowski et al., 2003; Zenati et al., 2019a).

While detailed nucleosynthetic yields of the hybrid CO WD merger scenario proposed in Jacobson-Galán et al., 2020b have not been published, we note that the requirement of having $M_H \gtrsim 10^{-3}\,\mathrm{M}_\odot$ based on the early flash spectra was suggested to favor a low mass secondary CO WD of $\approx 0.5\,\mathrm{M}_\odot$, as more massive WDs have much smaller H layers. On the other hand, it has been shown in previous works that the O yield in sub-Chandrasekhar mass CO core detonations increases rapidly for smaller core masses (Polin et al., 2019; Shen et al., 2018; Sim et al., 2010; Townsley et al., 2016). For instance, detonations of $0.8\,\mathrm{M}_\odot$ cores in Shen et al., 2018 produce $\approx 0.2 - 0.3\,\mathrm{M}_\odot$ of O while $1.0\,\mathrm{M}_\odot$ cores produce $\approx 0.05 - 0.10\,\mathrm{M}_\odot$ of O. Similarly, detonation of the lowest mass $0.6\,\mathrm{M}_\odot$ cores in Polin et al., 2019 produce $\approx 0.48\,\mathrm{M}_\odot$ of mostly O. We thus find the requirement of substantial amounts of residual H together with the small O yield inferred from the data are inconsistent with the WD scenario.

While Nakaoka et al., 2020 suggested that SN 2019ehk originated in an ultra-stripped core-collapse SN, hydrogen in not expected in the ejecta of ultra-stripped SNe with compact objects as close binary companions (Tauris et al., 2015). However, low mass progenitors of stripped core-collapse SNe can retain a large range of H and He masses depending on the nature of the companion and the initial binary period (Laplace et al., 2020; Yoon et al., 2010; Zapartas et al., 2017a). The O mass estimate for SN 2019ehk suggests a ZAMS $\approx 9 - 9.5\,\mathrm{M}_\odot$ progenitor that forms a He core mass of $\approx 1.8 - 2.0\,\mathrm{M}_\odot$. Assuming a residual H mass of $\lesssim 0.1\,\mathrm{M}_\odot$, the inferred ejecta mass of SN 2019ehk of $\approx 0.5 - 0.6\,\mathrm{M}_\odot$ is consistent with a final CO core mass of $\approx 1.45 - 1.5\,\mathrm{M}_\odot$ that collapses to form a $\approx 1.3\,\mathrm{M}_\odot$ neutron star and ejects $\approx 0.5\,\mathrm{M}_\odot$ of material.

The evidence for dense nearby CSM as seen in the early time light curve and spectra (Jacobson-Galán et al., 2020b) would then be explained by elevated mass loss prior to explosion as expected for low mass He cores (Laplace et al., 2020; Woosley, 2019). Comparing our inferred parameters of SN 2019ehk to the single star models of Woosley et al., 2015 and binary models of Laplace et al., 2020, who present detailed calculations of the late phase evolution of low mass He cores, we find that

their solar metallicity models of progenitors between 9.0 and 9.5 $M_\odot$ are strikingly similar to the estimated CO core mass and large pre-explosion radius (see Table A.2 in Laplace et al., 2020). Finally, the low mass stripped core-collapse progenitor scenario is consistent with the $< 10\,M_\odot$ star pre-explosion imaging constraints discussed in Jacobson-Galán et al., 2020b.

Recently, Jacobson-Galán et al., 2020a presented additional late-time photometry of SN 2019ehk up to ≈ 390 days from peak, and presented two primary arguments against the massive star scenario. First, they estimate the O mass in the ejecta to be $\approx 0.2-0.35\,M_\odot$, much larger than our estimates. However, their estimate is derived assuming that the Ca abundance in the ejecta is very small based on the arguments in Jacobson-Galán et al., 2020b. As we argue in Section 3.3, their Ca mass ratio limits are derived assuming nearly complete mixing of the Ca and O regions, which has been demonstrated to be unlikely in both core-collapse and thermonuclear SNe. Thus, if the Ca contributes substantially more opacity in the ejecta, then the required O mass would be much smaller. Next, they compare their estimate of the ^{57}Co/^{56}Co mass ratio in the ejecta to different progenitor models. In particular, we note that their ^{57}Co/^{56}Co estimate is similar to that expected for the low mass CCSN models (green hexagons in their Figure 4) in Wanajo et al., 2018, except with a larger ejecta mass. Since the ejecta mass depends sensitively on the nature and separation of the companion in the final stages prior to core-collapse, while the nucleosynthetic yields are largely unaffected, we find that our favored model of a low mass CCSN remains consistent with their measurements.

The interpretation of the Ca-rich SN 2019ehk as a core-collapse SN adds another member to a growing class of core-collapse SNe that exhibit strong [Ca II] lines[3] – the others being the SN IIb iPTF 15eqv (Milisavljevic et al., 2017), SN Ic iPTF 14gqr (De et al., 2018b), and possibly the SN Ib iPTF 16hgs (De et al., 2018a), although iPTF 16hgs may also be consistent with a thermonuclear detonation. Kawabata et al., 2010 suggested that the SN Ib 2005cz could also have originated via this scenario, although its old environment argues against this interpretation (Perets et al., 2011). Some of the Ca-rich SNe reported in Filippenko et al., 2003 that were found in star forming galaxies may also be members of this class, although their poor photometric and spectroscopic coverage precludes a secure identification (Kasliwal et al., 2012).

iPTF 15eqv is perhaps the closest analog of SN 2019ehk, and was also shown to be a

[3] In the case of the fast evolving ultra-stripped SN 2019dge (Yao et al., 2020b), the late-time spectrum was dominated by CSM interaction with He-rich material, likely hiding the underlying nebular emission features from the ejecta.

Type IIb core-collapse SN in a star forming environment (Milisavljevic et al., 2017) with a large [Ca II]/[O I] $\gtrsim 10$. For comparison, as in SN 2019ehk, we calibrate the latest nebular spectrum of iPTF 15eqv at ≈ 225 days with reported late-time photometry to derive the [O I] luminosity with [Ca II]/[O I] = 10 (Milisavljevic et al., 2017). We derive a [O I] luminosity of $\approx 1.2 \times 10^{38}\,\mathrm{erg\,s^{-1}}$, corresponding to a O mass of $\approx 0.03 - 0.08\,\mathrm{M_\odot}$ (shown in Figure 3.3). Using the estimated range of ^{56}Ni masses for this object, we also plot the normalized [O I] luminosity for this object in Figure 3.2. Both the [O I] luminosity and the O mass estimate for this object is consistent with a very low mass progenitor similar to SN 2019ehk.

Taking the large nebular [Ca II]/[O I] ratio and low [O I] luminosity as a signature of the low progenitor mass, the primary difference between SN 2019ehk and iPTF 15eqv would then be the final mass at the time of explosion. This leads to the different ejecta masses of $\approx 0.5\,\mathrm{M_\odot}$ in SN 2019ehk and $\approx 2 - 4\,\mathrm{M_\odot}$ in iPTF 15eqv (Milisavljevic et al., 2017), where iPTF 15eqv has a slightly more massive O core (higher [O I] luminosity) and H envelope (larger ejecta mass). Since stars in this low mass range ($\approx 9 - 9.5\,\mathrm{M_\odot}$) are still left with massive H envelopes of $\approx 7\,\mathrm{M_\odot}$ at the time of the SN (Woosley et al., 2015) in single star evolution, the differences between the progenitors can be explained as differences in the binary stripping, which is a function of the nature and orbital period of the companion.

3.5 Summary

We have presented very late-time imaging of the peculiar Ca-rich SN 2019ehk with the Keck-I telescope, which we use to perform accurate flux calibration of a contemporaneous late-time spectrum, and derive fluxes for the two most prominent nebular phase lines of [O I] and [Ca II]. In addition, we presented a high signal-to-noise peak light optical spectrum of the source, which we use to constrain the ejecta composition. To summarize our findings,

- The low [O I] luminosity in the nebular spectrum of SN 2019ehk suggests a very low O mass of $\approx 0.004 - 0.069\,\mathrm{M_\odot}$ (over the range of extinction and temperature assumptions). The inferred value is at least one order of magnitude smaller than that inferred for typical SNe II and SNe Ib/c.

- Comparing the inferred O mass to models of core-collapse SNe, we find consistency with the O yields expected from low CO cores of $\approx 1.45 - 1.5\,\mathrm{M_\odot}$, corresponding to He core masses of $\approx 1.8 - 2.0\,\mathrm{M_\odot}$ and ZAMS masses in

the range of $\approx 9.0 - 9.5\,M_\odot$, as derived from models of massive stars in both single and binary systems.

- We highlight the presence of Balmer series features in the peak light and early nebular phase spectra of SN 2019ehk, as well as the striking similarity of the Hα profile shape to previous observations and radiative transfer models of SNe IIb. In addition, the H-rich CSM inferred from very early photometry and spectroscopy is similar to that observed in several young Type II core-collapse SNe. We thus suggest the classification of SN 2019ehk as a SN IIb.
- We find that the presence of photospheric hydrogen features (suggesting $M_H \gtrsim 0.02 - 0.03\,M_\odot$) is inconsistent with models involving the thermonuclear detonation of a He shell during a white dwarf merger, as they are expected to retain only $M_H \sim 10^{-4}\,M_\odot$.
- We thus favor the interpretation of SN 2019ehk as a core-collapse supernova from a low mass $\approx 9.5\,M_\odot$ progenitor, which has been stripped of most of its hydrogen envelope by a binary companion.

Our results provide evidence for a class of Ca-rich core-collapse SNe (including SN 2019ehk and iPTF 15eqv) from low mass CO cores that form a distinct population from the thermonuclear Ca-rich gap transients found in old environments. While it is currently not obvious what photometric and spectroscopic properties distinguish this class from the old thermonuclear Ca-rich transients (apart from their star forming host environments), the presence of hydrogen in the ejecta of some objects (as demonstrated by peak light spectra of iPTF 15eqv and SN 2019ehk) provides strong evidence for the massive star scenario where the progenitors can retain a substantial amount of hydrogen ($M_H \gtrsim 0.01\,M_\odot$) at the time of explosion. Detailed nebular phase modeling of the nucleosynthetic products generated from core-collapse explosions of low mass CO cores, which have not been presented in the literature till this date, hold the potential to reveal significant insights into this phenomenon.

We thank S. Hachinger for providing the model spectral sequences used in this work. We thank the anonymous referee for a careful reading of the manuscript that significantly improved the quality of the paper. We thank W. Jacobson-Galan for providing the spectral sequence of SN 2019ehk. We thank J. Sollerman and C. Fransson for constructive comments on this manuscript. We thank L. Bildsten and A. Polin for valuable discussions. We thank D. Perley for assistance with `lpipe`.

MMK acknowledges generous support from the David and Lucille Packard Foundation. This work was supported by the GROWTH (Global Relay of Observatories Watching Transients Happen) project funded by the National Science Foundation under PIRE Grant No 1545949. Some of the data presented herein were obtained at the W.M. Keck Observatory, which is operated as a scientific partnership between the California Institute of Technology, the University of California and the National Aeronautics and Space Administration. The Observatory was made possible by the generous financial support of the W.M. Keck Foundation. The authors wish to recognize and acknowledge the very significant cultural role and reverence that the summit of Mauna Kea has always had within the indigenous Hawaiian community. We are most fortunate to have the opportunity to conduct observations from this mountain. AGY's research is supported by the EU via ERC grant No. 725161, the ISF GW excellence center, an IMOS space infrastructure grant, and BSF/Transformative and GIF grants, as well as The Benoziyo Endowment Fund for the Advancement of Science, the Deloro Institute for Advanced Research in Space and Optics, The Veronika A. Rabl Physics Discretionary Fund, Paul and Tina Gardner, Yeda-Sela, and the WIS-CIT joint research grant; AGY is the recipient of the Helen and Martin Kimmel Award for Innovative Investigation.

Part II: The explosive fates of helium accreting white dwarfs

Chapter 4

A MASSIVE HELIUM-SHELL DOUBLE DETONATION ON A SUB-CHANDRASEKHAR MASS WHITE DWARF

De, K. et al. (2019). "ZTF 18aaqeasu (SN2018byg): A Massive Helium-shell Double Detonation on a Sub-Chandrasekhar-mass White Dwarf". In: *ApJL* 873.2, L18, p. L18. DOI: 10.3847/2041-8213/ab0aec. arXiv: 1901.00874 [astro-ph.HE].

Kishalay De[1], Mansi M. Kasliwal[1], Abigail Polin[2,3], Peter E. Nugent[2,3], Lars Bildsten[4,5], Scott M. Adams[1], Eric C. Bellm[6], Nadia Blagorodnova[1], Kevin B. Burdge[1], Christopher Cannella[1], S. Bradley Cenko[7,8], Richard G. Dekany[9], Michael Feeney[9], David Hale[9], U. Christoffer Fremling[1], Matthew J. Graham[1], Anna Y. Q. Ho[1], Jacob E. Jencson[1], S. R. Kulkarni[1], Russ R. Laher[10], Frank J. Masci[10], Adam A. Miller[11,12], Maria T. Patterson[6], Umaa Rebbapragada[13], Reed L. Riddle[9], David L. Shupe[10], and Roger M. Smith[9]

[1]Cahill Center for Astrophysics, California Institute of Technology, 1200 E. California Blvd., Pasadena, CA 91125, USA
[2]Department of Astronomy, University of California, Berkeley, CA, 94720-3411, USA
[3]Lawrence Berkeley National Laboratory, Berkeley, California 94720, USA
[4]Department of Physics, University of California, Santa Barbara, CA 93106, USA
[5]Kavli Institute for Theoretical Physics, University of California, Santa Barbara, CA 93106, USA
[6]DIRAC Institute, Department of Astronomy, University of Washington, 3910 15th Avenue NE, Seattle, WA 98195, USA
[7]Astrophysics Science Division, NASA Goddard Space Flight Center, Mail Code 661, Greenbelt, MD 20771, USA
[8]Joint Space-Science Institute, University of Maryland, College Park, MD 20742, USA
[9]Caltech Optical Observatories, California Institute of Technology, Pasadena, CA 91125, USA
[10]IPAC, California Institute of Technology, 1200 E. California Blvd, Pasadena, CA 91125, USA
[11]Center for Interdisciplinary Exploration and Research in Astrophysics (CIERA) and Department of Physics and Astronomy, Northwestern University, 2145 Sheridan Road, Evanston, IL 60208, USA
[12]The Adler Planetarium, Chicago, IL 60605, USA
[13]Jet Propulsion Laboratory, California Institute of Technology, Pasadena, CA 91109, USA

Abstract

The detonation of a helium shell on a white dwarf has been proposed as a possible explosion triggering mechanism for Type Ia supernovae. Here, we report ZTF 18aaqeasu (SN 2018byg/ATLAS 18pqq), a peculiar Type I supernova, consistent with being a helium-shell double-detonation. With a rise time of ≈ 18 days from explosion, the transient reached a peak absolute magnitude of $M_R \approx -18.2$ mag,

exhibiting a light curve akin to sub-luminous SN 1991bg-like Type Ia supernovae, albeit with an unusually steep increase in brightness within a week from explosion. Spectra taken near peak light exhibit prominent Si absorption features together with an unusually red color ($g - r \approx 2$ mag) arising from nearly complete line blanketing of flux blue-wards of 5000 Å. This behavior is unlike any previously observed thermonuclear transient. Nebular phase spectra taken at and after ≈ 30 days from peak light reveal evidence of a thermonuclear detonation event dominated by Fe-group nucleosynthesis. We show that the peculiar properties of ZTF 18aaqeasu are consistent with the detonation of a massive ($\approx 0.15\,M_\odot$) helium shell on a sub-Chandrasekhar mass ($\approx 0.75\,M_\odot$) white dwarf after including mixing of $\approx 0.2\,M_\odot$ of material in the outer ejecta. These observations provide evidence of a likely rare class of thermonuclear supernovae arising from detonations of massive helium shells.

4.1 Introduction

In the double-detonation model for Type Ia supernovae (SNe), the explosive detonation of a helium (He) shell on the surface of a sub-Chandrasekhar mass white dwarf (WD) triggers a detonation in the core of the WD, leading to an explosion of the entire star (Livne et al., 1995; Nomoto, 1980, 1982a,b; Woosley et al., 1986, 1994). Several key issues in this mechanism have been studied in recent years, including the conditions for the detonation of the He shell (that is accreted from a He-rich companion) and if the detonation in the shell can trigger a detonation in the underlying CO core (Bildsten et al., 2007; Fink et al., 2007, 2010; Shen et al., 2014a; Sim et al., 2010). These studies have generally concluded that detonations in the shell are triggered for He shell masses larger than $\sim 0.01\,M_\odot$, while at the same time inevitably leading to a detonation of the core (Bildsten et al., 2007; Fink et al., 2010; Shen et al., 2010, 2014b).

Consequently, several studies have also explored the observational signatures of these events and if they are consistent with observed diversity of Type Ia SNe (Kromer et al., 2010; Polin et al., 2019; Sim et al., 2010; Woosley et al., 2011). While simulations of the double detonation scenario in bare sub-Chandrasekhar mass CO WDs (i.e. without including the effects of the overlying He shell) have found that these explosions are capable of reproducing the observed diversity of Type Ia SNe (Shen et al., 2018; Sim et al., 2010), the results are quite different when including the ashes of the overlying He shell (rich in He burning products) in the radiative transfer calculations (Hoeflich et al., 1996; Kromer et al., 2010; Nugent

et al., 1997; Polin et al., 2019; Woosley et al., 2011).

In particular, these models find that He shell double detonation events exhibit spectra that are strongly influenced by Fe-group line blanketing features from the overlying burned material, thus producing unusually red colors near peak light. These features remain generally inconsistent with the observed variety of Type Ia SNe for the minimum He shell masses that have been previously suggested to detonate the core ($\sim 0.05\,M_\odot$; as found in the initial simulations of Bildsten et al., 2007 and Fink et al., 2010). Several solutions to these discrepancies have been proposed, including possible differences in the composition of the burnt He shell (e.g. due to pollution of the initial He shell by C; Kromer et al., 2010). Alternatively, it has been suggested that the observed variety of Type Ia SNe could be produced from detonations of thin He shells with even lower masses ($\lesssim 0.01\,M_\odot$) that may still detonate the core (Polin et al., 2019; Shen et al., 2014b, 2018).

In this paper, we present observations of ZTF 18aaqeasu, a peculiar Type I SN that exhibits remarkable similarities to expected signatures of a He-shell double detonation on a white dwarf. Section 4.2 presents the observations of the transient. Section 4.3 presents a comparison of this source to known Type Ia SNe. Section 4.4 presents a comparison of the data to models of He shell detonations presented in Kromer et al., 2010 and a larger grid presented in Polin et al., 2019. We end with a discussion of the observations in the broader context of Type Ia SNe in Section 4.5. Calculations in this paper assume a ΛCDM cosmology with $H_0 = 70\,\mathrm{km\,s^{-1}\,Mpc^{-1}}$, $\Omega_M = 0.27$ and $\Omega_\Lambda = 0.73$ (Komatsu et al., 2011).

4.2 Observations

Detection and classification

On 2018 May 04.27[1] (MJD 58242.268), ZTF 18aaqeasu was first detected by the Zwicky Transient Facility (ZTF; Bellm et al., 2019b; Graham et al., 2019) using the 48-inch Samuel Oschin Telescope (P48) at Palomar Observatory in a nightly cadence experiment. This detection was at an r-band magnitude of ≈ 20.57 mag and J2000 coordinates α = 12h23m21.57s, δ = +46°36′08.3″. The source was not detected on 2018 April 25.20 (MJD 58233.198; 9.07 days before first detection) up to a limiting magnitude of $r \geq 20.11$ mag.

[1] UT times are used throughout the paper.

On 2018 May 07, ZTF 18aaqeasu met machine-learning thresholds and was flagged by a science program filter on the GROWTH Marshal (Kasliwal et al., 2019) that is designed to look for transients in the vicinity of nearby galaxies. ZTF 18aaqeasu was detected in the outskirts of an elliptical galaxy at a redshift of $z = 0.066$ (Figure 4.1). On 2018 May 08.19, we obtained the first spectrum, which exhibited blue continua with broad absorption features below 5000 Å (Section 4.2). On 2018 May 14.34, a subsequent spectrum exhibited prominent Si II absorption features as well as a sharp cut-off in flux below 5000 Å. As such, due to the strong Si II features and absence of any H features, we tentatively classified the transient as a peculiar Type Ia SN (see Filippenko, 1997 for a review).

On 2018 May 22.42, the transient was independently detected at 18.9 mag by the ATLAS survey (Tonry et al., 2018) as ATLAS18pqq. On 2018 May 25, ATLAS reported this event to the Transient Name Server (TNS), and the event was given the IAU name AT 2018byg. On 2018 Nov 19, we reported the spectroscopic classification, and it was re-named as SN 2018byg. Hereafter, we refer to the source by the name ZTF 18aaqeasu.

Optical Photometry

We obtained r-band photometry of ZTF 18aaqeasu with the ZTF camera, along with gri-band photometry with the Spectral Energy Distribution Machine (SEDM; Blagorodnova et al., 2018) mounted on the automated 60-inch telescope (P60; Cenko et al., 2006) at Palomar Observatory. The P48 images were reduced with the Zwicky Transient Facility Image Differencing pipeline (Masci et al., 2019), which performs host subtracted point spread function (PSF) photometry, while the P60 images were reduced using the pipeline described in Fremling et al., 2016. We also obtained one epoch of g-band imaging with the Wafer Scale Imager for Prime (WASP) instrument mounted on the 200-inch Hale telescope at Palomar Observatory on 2018 June 09. These images were reduced with a custom-developed imaging pipeline based in `python`.

We correct all our photometry for galactic extinction for $A_V = 0.032$ mag from the maps of Schlafly et al., 2011. We do not correct for any additional host extinction

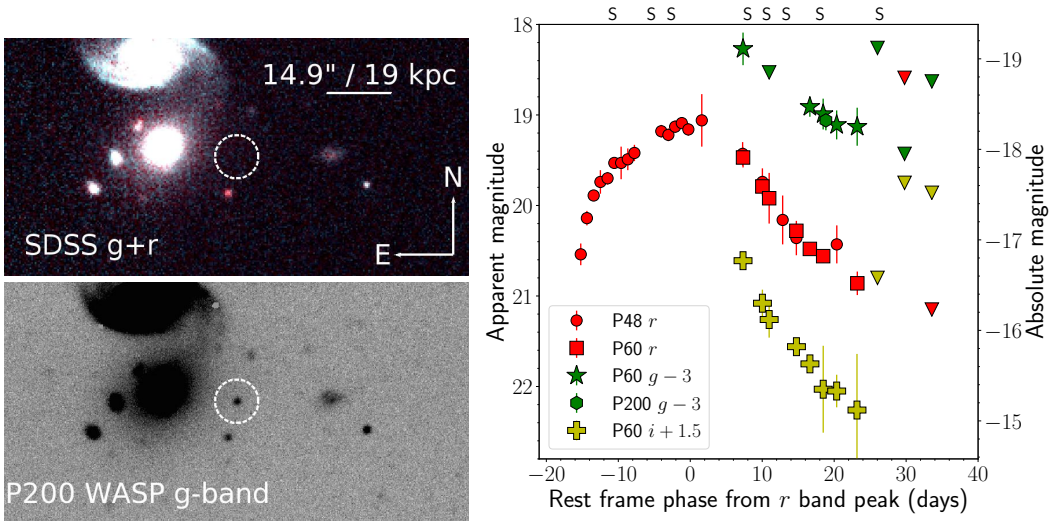

Figure 4.1: **Host galaxy, environment and photometric evolution of SN 2018byg**. (Left) Detection field and host galaxy of ZTF 18aaqeasu. The top panel is an archival SDSS image of the region while the lower panel shows an image taken with WASP on P200. The location of the transient is marked with the white circle – it is at a projected offset of $\approx$ 17.2″corresponding to a physical projected distance of 21.9 kpc at the host galaxy redshift. (Right) Multi-color light curves of ZTF 18aaqeasu. The inverted triangles are upper limits. The epochs of spectroscopy are marked with 'S' on the top axis.

due to the offset location of the transient, and the absence of any Na I D absorption at the host redshift in our spectra. We show the multi-color light curves (magnitudes are in the AB system) of ZTF 18aaqeasu in Figure 4.1. For all subsequent discussion of this object, phases are measured with respect to the maximum of the r-band light curve.

Optical spectroscopy

We obtained optical spectroscopic follow-up of the transient starting from ≈ -10 d to $\approx +53$ d after r-band peak using the Double Beam Spectrograph (DBSP) on the 200-inch Hale telescope (Oke et al., 1982), the Low Resolution Imaging Spectrograph (LRIS) on the Keck-I telescope (Oke et al., 1995), the SEDM, and the DeVeny spectrograph on the Discovery Channel Telescope (Bida et al., 2014). Details of the spectroscopic observations are given in Table 4.1, and the spectroscopic sequence is shown in Figure 4.2. All spectra will be made publicly available via the WISeREP repository (Yaron et al., 2012).

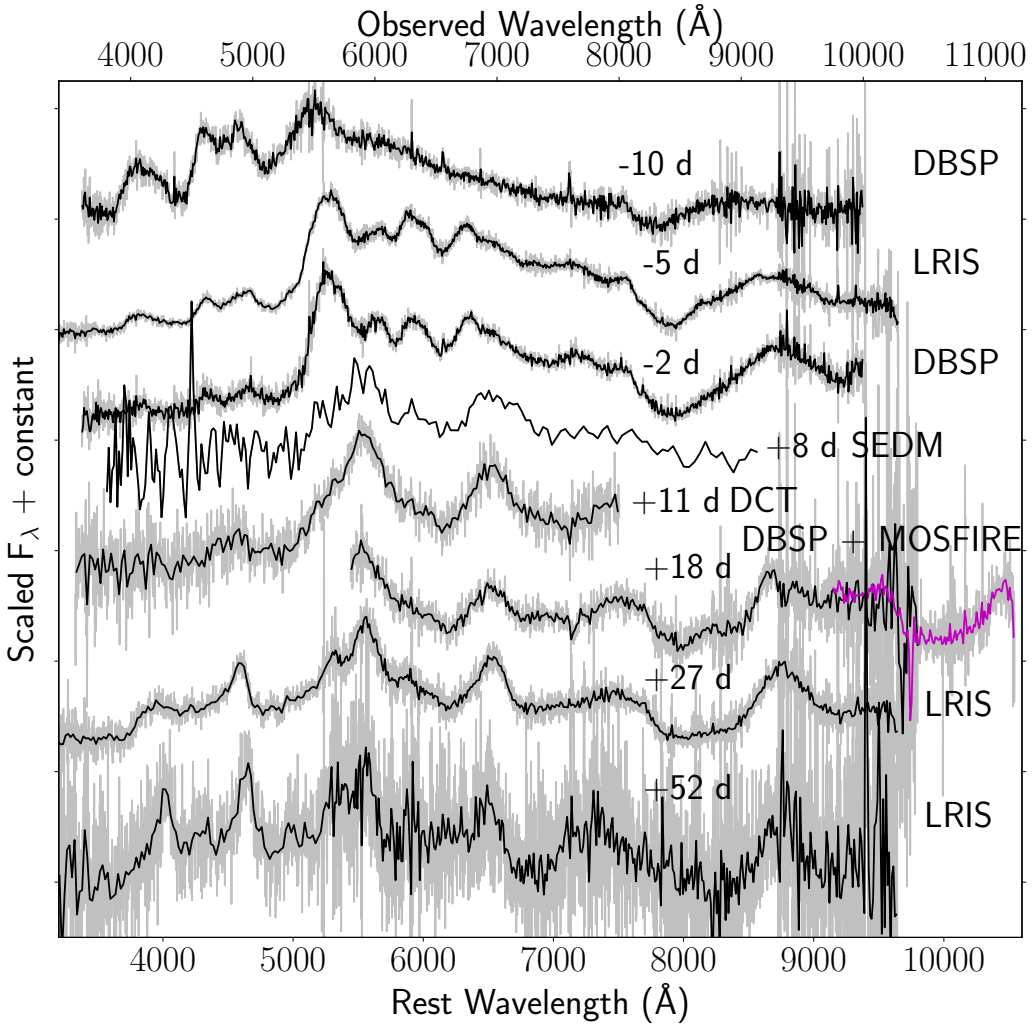

Figure 4.2: **Spectroscopic evolution of SN 2018byg**. Phases with respect to r-band peak and instruments used are indicated next to each spectrum. The black lines are binned from the raw spectra shown in gray lines. The magenta line at +18 days indicates the only NIR spectrum of the source in Y band from MOSFIRE.

NIR photometry and spectroscopy

We obtained Near Infrared (NIR) JHK band imaging of the transient using the Multi-Object Spectrometer for Infrared Exploration (MOSFIRE; McLean et al., 2012) on the Keck-I telescope on 2018 June 03 ($\approx$ 13 days after r-band peak). Dithered science exposures of the target field were obtained in each band for a total exposure time of 231 s, 192 s, and 128 s in J, H, and K_s bands, respectively. The images were reduced using a custom-built `python`-based imaging pipeline, and the transient was detected in all three filters. We measure Vega magnitudes of $J = 19.92 \pm 0.10$ mag, $H = 19.70 \pm 0.25$ mag, and $K_s = 19.29 \pm 0.22$ mag. We

also obtained a Y-band (9700–11100 Å) spectrum of the transient with MOSFIRE on 2018 June 03, for a total integration time of 720 s. The spectra were reduced with the MOSFIRE Data Reduction Pipeline, and are shown in Figure 4.2.

Swift XRT observations

We obtained X-ray follow-up of the transient with the Swift X-ray telescope (XRT; Burrows et al., 2005) on the Neil Gehrels Swift Observatory (Swift; Gehrels et al., 2004). The Swift Observatory observed the location of the transient on 2018 May 27 ($\approx$ 8 days after r-band peak) for a total exposure time of 3.8 ks. No source was detected at the location of the transient down to a 3σ limiting flux of 3.5×10^{-3} count s^{-1}, corresponding to a 0.3–10 keV flux of 1.2×10^{-13} ergs cm^{-2} s^{-1}. This corresponds to an X-ray luminosity of $\lesssim 1.3 \times 10^{42}$ ergs s^{-1} at the distance of the host galaxy for a photon index of $\Gamma = 2$. In the same observation, no source was detected with the Ultraviolet Optical telescope (UVOT; Roming et al., 2005) in the UVW2 filter, down to a 5σ limiting AB magnitude of 22.40.

4.3 Analysis

Photometric properties

The transient exhibited a light curve fainter than the normal Type Ia SNe, but similar to the subluminous 1991bg-like events. To this end, we compare the photometric evolution of ZTF 18aaqeasu to the light curves of the normal Type Ia SNe 2011fe (Nugent et al., 2011) as well as the sub-luminous (SN 1991bg-like) Type Ia SN 2005bl (Contreras et al., 2010) in Figure 4.3 (data taken from the Open Supernova Catalog; Guillochon et al., 2017). We also show a comparison to the light curves of the peculiar SNe Ia SN 2016jhr (Jiang et al., 2017), iPTF 14atg (Cao et al., 2015a), and SN 2006bt (Foley et al., 2010), that have been previously associated with He shell detonation scenarios (Jiang et al., 2017).

The source exhibited an initial fast rise (at < -10 days from peak) of ≈ 0.4 mag day^{-1} similar to the normal SN Ia SN 2011fe, but subsequently slowed in its rise transitioning to a sub-luminous SN Ia light curve. Both SN 2006bt and SN 2016jhr exhibit light curves similar to SN 2011fe before peak, and are more luminous (by ≈ 0.8 mag) than ZTF 18aaqeasu. The peak luminosity and timescales of the light curve of ZTF 18aaqeasu are similar to that of iPTF 14atg, which exhibited an early UV flash suggested to arise from companion-ejecta interaction.

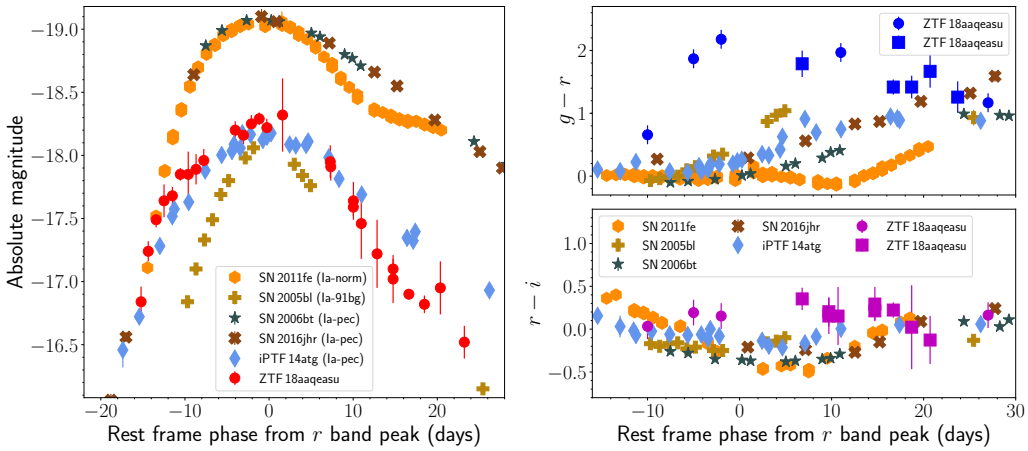

Figure 4.3: **Comaprison of the photometric evolution of SN 2018byg to other Type Ia supernovae.** (Left) Comparison of the r-band light curve of ZTF 18aaqeasu to other normal and sub-luminous Type Ia SNe. (Right) Comparison of the $g-r$ and $r-i$ color evolution of ZTF 18aaqeasu (circles are colors derived from spectra while squares denote colors from photometry) to the same sample of SNe as in the left panel.

By fitting the peak of the light curve with a low order polynomial, we find a best-fit peak time in r-band of MJD 58258.49, and a peak absolute magnitude of $M_r = -18.27 \pm 0.04$ mag. Integrating the total flux in the optical spectrum of the source near peak light (at ≈ -2 days; after performing an absolute calibration with respect to r-band photometry), we find a lower limit on the peak luminosity of $\approx 2.4 \times 10^{42}$ ergs s^{-1}. Using Arnett's law for the synthesized ^{56}Ni mass (Arnett et al., 1985), we use the peak luminosity to find ^{56}Ni mass $\gtrsim 0.11\,M_\odot$.

Although we do not have multi-color photometric coverage before the peak of the r-band light curve, we use our well sampled sequence of spectra to construct color curves for the transient before peak light. We constructed $g-r$ and $r-i$ color curves of the transient by performing synthetic photometry on the spectra, while adding a 10% uncertainty on the measurements to account for potential inaccuracies in flux calibration. The colors derived from spectroscopy are consistent with contemporaneous multi-color photometry at epochs after peak light. The color evolution is shown in Figure 4.3.

Comparing the color curves to the other Type Ia SNe, we find that while the $r-i$

color evolution is similar to the subluminous Type Ia SNe in the light curve comparison sample, the $g-r$ color of the transient ($g-r \approx 2.2$ at peak light) is ≈ 1.8 mag redder near peak light than all the Type Ia SNe in the comparison sample. In particular, the $g-r$ color of ZTF 18aaqeasu is ≈ 1.9 mag and ≈ 2.0 mag redder than SN 2016jhr and SN 2006bt at peak light, respectively. Both the $g-r$ and $r-i$ color evolution are also qualitatively different from the other events, although the colors eventually converge near ≈ 25 days after peak light. This argues against dust extinction as a cause of the unusual red colors.

Spectroscopic properties

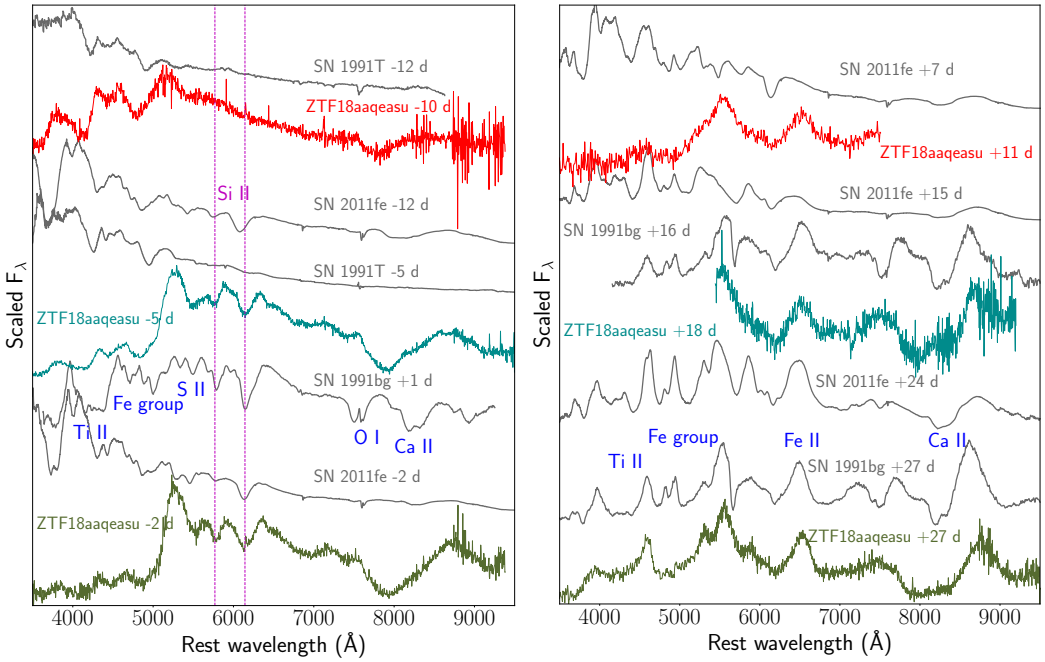

Figure 4.4: **Comaprison of the spectroscopic evolution of SN 2018byg to other Type Ia supernovae.** Comparison of the pre-maximum (left) and post-maximum (right) spectra of ZTF18aaqeasu to the normal Type Ia SN 2011fe (Maguire et al., 2014), the over-luminous SN 1991T (Filippenko et al., 1992a), and the sub-luminous SN 1991bg (Filippenko et al., 1992b). The magenta dashed lines in the left panel indicate Si II lines at a velocity of 10,000 km s^{-1}. Prominent emission / absorption features are marked in both panels. Spectroscopic data for the comparison SNe were obtained from the WISEReP repository (Yaron et al., 2012).

We show a comparison of the pre-maximum and post-maximum spectroscopic evolution of ZTF 18aaqeasu with other Type Ia SNe in Figure 4.4. The earliest spectrum of the source was obtained ≈ 10 days before r-band peak and exhibits blue continua

with broad absorption features at wavelengths shorter than ≈ 5500 Å , notably without any Si II features that are characteristic of normal and sub-luminous Type Ia SNe at similar phases (Figure 4.4). However, there are several similarities between this spectrum and SN 1991T at a similar phase, particularly in the absence of a Si II feature and the presence of broad absorption features of Ti II and Fe group elements near 4100 Å and 4700 Å, respectively. This spectrum also shows signatures of an absorption feature in the Ca II NIR triplet.

Subsequent spectra taken at ≈ 5 and ≈ 2 days before r-band peak exhibit the hallmark Si II absorption features found in Type Ia SNe near peak light. Using the minimum of the Si II P-Cygni profile, we measure a photospheric velocity of $\approx 10,500\,\mathrm{km\,s^{-1}}$, similar to SN 1991bg at the same phase (magenta dashed line in Figure 4.4). However, the bluer parts of the spectra exhibit unusually strong line blanketing features leading to nearly complete absorption of flux blue-wards of 5000 Å. Comparing with the subluminous Type Ia SN 1991bg at a similar phase, we attribute this absorption to complete line blanketing by Fe group elements and Ti II. To our knowledge, such strong line blanketing features (and consequent red $g - r$ colors) have never been previously seen in any variant of a Type Ia SN at peak light. The sharp cut-off in flux at ≈ 5000 Å also argues against dust extinction (which would cause a gradual suppression of the blue continuum) as a cause of the unusual red colors observed in the photometry. The Ca II triplet also develops into a deep, high velocity ($\approx 25,000\,\mathrm{km\,s^{-1}}$) absorption feature at 7500–8500 Å near peak.

Post-maximum spectra starting from ≈ 10 days after peak (Figure 4.4) begin to develop broad emission features suggesting a transition to the optically thin phase. The only NIR spectrum taken at +18 days exhibits a deep absorption feature at ≈ 9950 Å. If associated with He I at 1.083 μm, the corresponding absorption velocity would be $\approx 26,000\,\mathrm{km\,s^{-1}}$. Spectra obtained at ≈ 27 and ≈ 52 days after peak are similar to the Type Ia SN 1991bg at similar phases, and exhibit emission lines of Fe group elements, Ti II, and Ca II. The late-time similarities and Fe-group dominated nucleosynthesis suggest a thermonuclear origin of the explosion, consistent with ZTF 18aaqeasu representing an unusual variant of a Type Ia-like SN. However, the peculiar spectral features observed at peak light are unique to ZTF 18aaqeasu and warrant further inspection with respect to a possible explosion mechanism.

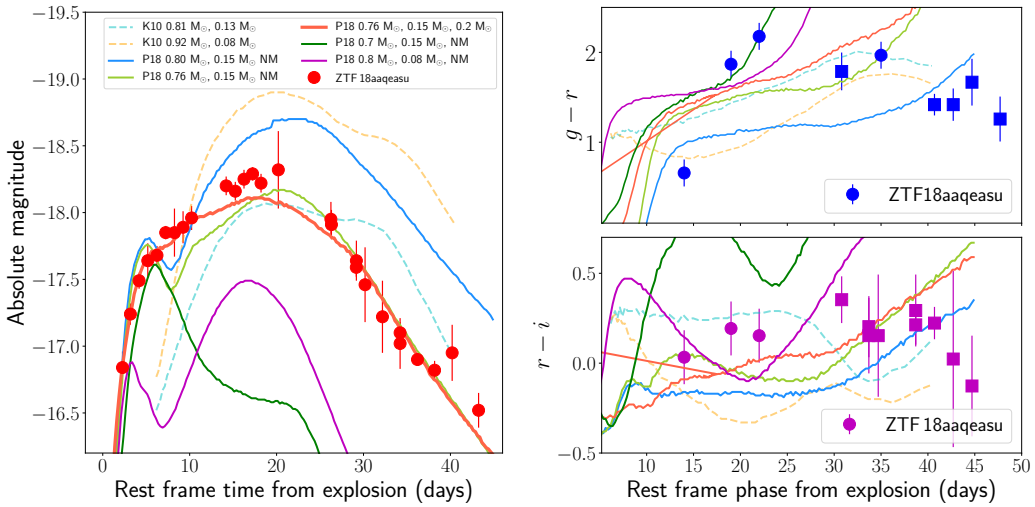

Figure 4.5: **Constraints on the white dwarf core and shell mass in SN 2018byg using comparisons of its light curve and color evolution to models of helium shell detonations.** Comparison of the photometric evolution of ZTF 18aaqeasu with that of the He shell double detonation models in Kromer et al., 2010 (K10; dashed lines) and Polin et al., 2019 (P18; solid lines). The model parameters are indicated in the legend as (WD mass, shell mass, mixing length), and NM stands for No Mixing. The left panel shows the r-band evolution while the right panels show the $g - r$ and $r - i$ color evolution with the same color schemes for the models. On the right panel, circles denote colors derived from the spectra while squares denote colors derived from photometry.

4.4 Model comparisons

We first consider the photometric properties of ZTF 18aaqeasu with regard to an explosion scenario. In particular, its fast rising light curve until $\approx$ 10 days before peak light (Section 4.3) can arise from several proposed scenarios for early 'flashes' in SNe Ia. These include interaction of the ejecta with a companion (Kasen, 2010), interaction with circumstellar material (Dessart et al., 2014; Levanon et al., 2015; Piro et al., 2016), or the presence of surface radioactive material due to the detonation of a He shell (Polin et al., 2019). Both the ejecta interaction scenarios predict blue colors ($g - r \approx 0$) at early times, while ZTF 18aaqeasu is consistently red before peak (Figure 4.3). For comparison, its $g - r$ color is ≈ 0.5 mag redder than iPTF 14atg (Cao et al., 2015a) at $\approx$ 10 days before peak, which is the best known example of a UV bright companion interaction event. In addition, while the ejecta interaction scenarios can qualitatively match the early fast rise, they cannot explain the strong line blanketing features observed near peak.

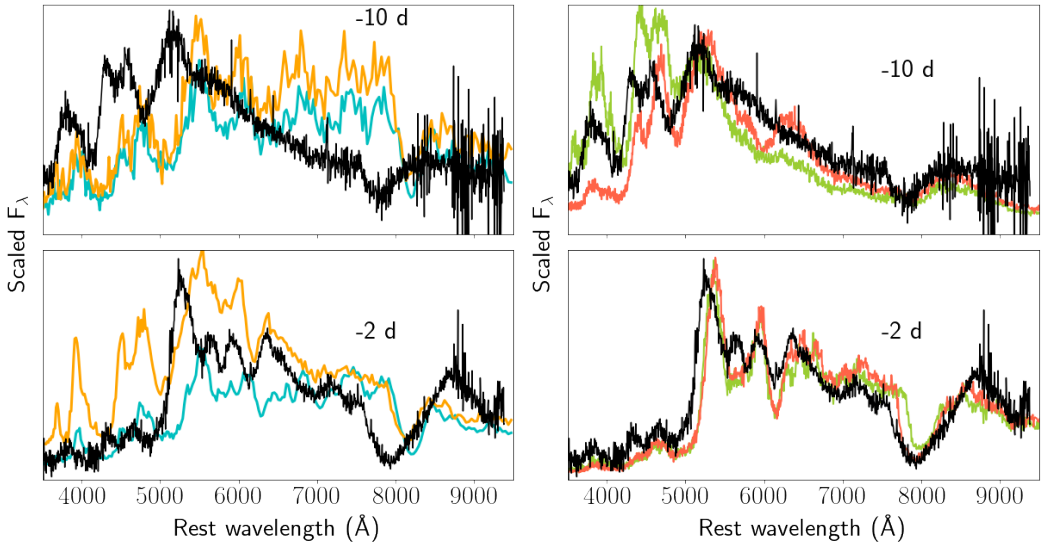

Figure 4.6: **Comparison of the spectroscopic evolution of SN 2018byg to models of helium shell detonations on low mass white dwarfs.** Comparison of the spectra of ZTF 18aaqeasu at and before peak light (shown as black lines) to models of He shell double detonations from Kromer et al., 2010 (left; for the two models shown in the light curve comparison) and Polin et al., 2019 (right; for two cases of ejecta mixing with the best fit WD and shell mass from the light curves). In both panels, the epochs of spectroscopic comparison are indicated according to the phase of the light curve (days from *r*-band peak), and the model spectra have the same color scheme as in Figure 4.5.

The strong line blanketing features of Fe group elements (and consequent red colors) observed in the peak spectra suggest that the outer layers of the ejecta are unusually rich in Fe group elements. The presence of such radioactive material in the outer ejecta would also be consistent with the fast rise observed in the early light curve (Piro et al., 2014a), and is a hallmark signature of the decay of radioactive elements in the outermost ejecta (^{48}Cr, ^{52}Fe, and ^{56}Ni with half-lives of 0.90 days, 0.35 days, and 6.07 days, respectively) for an explosion powered by a He shell detonation (e.g. Kromer et al., 2010; Nugent et al., 1997; Polin et al., 2019). This scenario would naturally explain the high velocity Ca II features observed near peak light, as a known He detonation product in the outer layers of the ejecta (Fink et al., 2010; Kromer et al., 2010; Moore et al., 2013).

We thus compare the properties of ZTF 18aaqeasu to simulations in the grid of models of He shell double detonations in Kromer et al., 2010, who modeled the observable signatures for the minimum shell masses found in Bildsten et al., 2007.

We show a comparison of the r-band light curve, as well as the $g-r$ and $r-i$ colors of ZTF 18aaqeasu to their angle averaged light curves in Figure 4.5 (dashed lines). As shown, their lowest core mass model (with a WD core mass of $0.81\,M_\odot$; their Model 1) shows similarities to the data both in terms of absolute luminosity and red colors near peak, although the light curve shapes are not well matched. The larger luminosity of models involving higher mass WDs (yellow dashed lines) disfavor WD masses $\gtrsim 0.8\,M_\odot$.

We also compare the light curves to the larger grid of shell and WD masses presented in the simulations of Polin et al., 2019, including additional simulations performed to match the data (shown as solid lines in Figure 5). We model the explosion of a 50% carbon + 50% oxygen WD with an isentropic helium shell. The hydrodynamics and nuclear processes are modeled from the helium ignition until the ejecta reaches homologous expansion using the compressible hydrodynamics code Castro (Almgren et al., 2010). Once the explosion reached homology, radiative transport calculations are performed using the Sedona code (Kasen et al., 2006) to produce light curves and spectra from the ejecta.

Since the early rise in the light curve is powered by the radioactive He shell detonation products (^{48}Cr, ^{52}Fe, and ^{56}Ni), we can constrain the mass of the shell. We note that a model involving a fixed WD mass of $0.8\,M_\odot$ and a shell of $0.15\,M_\odot$ shell reasonably reproduces the early rise, while the same WD with a smaller $0.08\,M_\odot$ shell under-predicts the r-band luminosity on the early rise. We then constrain the WD mass to be between 0.7 and $0.8\,M_\odot$ by noting that models involving a $0.8\,M_\odot$ WD and $0.7\,M_\odot$ WD (each with a $0.15\,M_\odot$ shell) have a higher and lower peak luminosity than ZTF 18aaqeasu, respectively. With these constraints, we find that a model with a $0.76\,M_\odot$ WD and a $0.15\,M_\odot$ shell reproduces the overall r-band evolution. The corresponding synthesized ^{56}Ni mass is $0.18\,M_\odot$.

The light curves in these models also exhibit an early peak and decline, arising from the decay of radioactive material in the outer ejecta and the assumption of no mixing. Although we do observe signatures of a fast rising early peak, we do not have evidence of a decline as in the models, suggesting a possible influence of mixing in the ejecta. Hence, we also show an additional model with the best-fit WD mass and shell mass, but with ejecta mixed across a zone of $0.18\,M_\odot$ that

is applied before performing the radiative transport. This model reproduces the early-time rise and the overall light curve. Although the red colors of the source near peak light are also well reproduced, the models become redder with time much faster than observed in the data. These discrepancies likely arise due to assumptions of local thermodynamic equilibrium (LTE) in Sedona, which break down as the source transitions to the optically thin nebular phase at ≈ 20 days after peak light.

We also compare the spectroscopic properties of ZTF 18aaqeasu to double detonation models in Figure 4.6. While there are several similarities between the model spectra of Kromer et al., 2010 and spectra near peak light ($\approx$ 2 days before peak light), including the strong line blanketing features below 5000 Å and deep Ca II absorption features, their limited grid of models does not correctly reproduce the line velocities and strengths of the prominent Si II and Ca II absorption features. Additionally, these models exhibit strong line blanketing features below 5000 Å and Si II absorption even at $\approx$ 10 days before peak, unlike the observed properties of this event where Si II lines appear only near peak light.

Comparing to the best-fit light curve model from Polin et al., 2019, we find a better match to the observed spectra both before and at peak light (Figure 4.6). In the case of the early spectra ($\approx$ 10 days before peak), the models exhibit blue continua in the unmixed case similar to the data, although the absorption features become more prominent in the case of mixed ejecta as expected. The peak light spectra ($\approx$ 2 days before peak) are well reproduced both in terms of line velocities and strengths, and are not appreciably affected by mixing in the ejecta. Taken together, we find that a model involving the detonation of a $\approx 0.15\,M_\odot$ He shell on a $\approx 0.75\,M_\odot$ WD reproduces the observed signatures of the event after including mixing of $\approx 0.2\,M_\odot$ in the outer ejecta.

4.5 Discussion and conclusion

In this paper, we have presented observations of the transient ZTF 18aaqeasu, and have shown it to be a unique supernova. While its photometric and nucleosynthetic properties share several similarities to subluminous Type Ia SNe, its peak photospheric spectra are marked by extremely strong line blanketing features and red colors, unlike any previously observed Type Ia SN. By comparing the data to a grid of models, we show that the observed properties can be well explained by

the detonation of a massive ($\approx 0.15\,M_\odot$) He shell on a sub-Chandrasekhar mass ($\approx 0.75\,M_\odot$) white dwarf. In particular, it is important to note that the He shell mass inferred is much larger than the thin He shells required to explain the properties of the broader population of Type Ia SNe ($\lesssim 0.01\,M_\odot$; Kromer et al., 2010; Polin et al., 2019; Shen et al., 2018; Sim et al., 2010).

The inferred shell and core masses are consistent with what is predicted in the well studied He burning star donor scenario of a $0.48\,M_\odot$ sdB star losing matter to a C/O WD (Nomoto, 1982b; Woosley et al., 1994, 2011). While much of the early work assumed a constant accretion rate, more recent calculations (Bauer et al., 2017; Brooks et al., 2015) have self-consistently calculated the evolution of the donor with mass loss and a self-consistent varying accretion rate. The properties inferred for ZTF 18aaqeasu are remarkably close to the recent calculation of Bauer et al., 2017 for the evolution of the known sdB + WD binary CD $-30°11223$ (Geier et al., 2013), with Bauer et al., 2017 finding a He shell mass of $0.16\,M_\odot$ on the initial WD of mass $0.76\,M_\odot$ at the time of detonation. As this is the forward evolution of a known system, it is possible to say that CD $-30°11223$ is indeed an example of the progenitor of ZTF 18aaqeasu-like events.

There is now emerging evidence for excess emission in the early light curves of a number of thermonuclear SNe, some of which may be associated with surface radioactivity from a He shell detonation. Jiang et al., 2017 presented evidence for an early red excess in SN 2016jhr, that was suggested to arise from a He shell detonation. They also found evidence for a class of spectroscopically similar objects that include SN 2006bt (Foley et al., 2010). On the other hand, early blue excesses have been reported in iPTF 14atg (Cao et al., 2015a), SN 2017cbv (Hosseinzadeh et al., 2017), and SN 2018oh (Dimitriadis et al., 2019; Shappee et al., 2019), which have been suggested to be consistent with interaction of the ejecta with circumstellar material or a non-degenerate companion.

The properties of ZTF 18aaqeasu are distinct from all these events, both in terms of photometric and spectroscopic evolution (Section 4.6). In particular, the consistent red colors of ZTF 18aaqeasu before peak are markedly different from the early blue colors reported for iPTF 14atg, SN 2017cbv, and SN 2018oh, arguing against a shell detonation scenario for these events. To date, tentative evidence for only one other

example of a relatively thin He shell detonation has been presented for SN 2016jhr (Jiang et al., 2017). Specifically, the early red excess in this event, together with its normal peak luminosity and deep Ti II absorption features near peak light was interpreted as evidence for a thin ($\lesssim 0.05\,M_\odot$) He shell detonation on a near Chandrasekhar mass WD (see also Polin et al., 2019). Although the explosion scenario for ZTF 18aaqeasu is similar, our modeling implies a much more massive shell (producing the stronger line blanketing features) on a lower mass WD compared to SN 2016jhr, and thus, a likely different progenitor system.

The relatively luminous and slow evolving light curve of ZTF 18aaqeasu (compared to e.g. SN 1991bg-like events) suggests that similar events should be easily detectable in a reasonably large volume of the local universe (out to $z \approx 0.1$ for a limiting magnitude of $r = 20.5$ mag). However, no such event has been reported in previous studies of large samples of thermonuclear SNe (e.g., Hicken et al., 2009; Krisciunas et al., 2017; Maguire et al., 2014; Scolnic et al., 2018). Thus, ZTF 18aaqeasu being the first of its kind suggests that massive He shell double detonations must be intrinsically rare in the population of thermonuclear SNe.

This work was supported by the GROWTH project funded by the National Science Foundation under PIRE Grant No 1545949. This research benefited from interactions at a ZTF Theory Network meeting, funded by the Gordon and Betty Moore Foundation through Grant GBMF5076. ZTF is supported by the National Science Foundation and a collaboration including Caltech, IPAC, the Weizmann Institute for Science, the Oskar Klein Center at Stockholm University, the University of Maryland, the University of Washington, Deutsches Elektronen-Synchrotron and Humboldt University, Los Alamos National Laboratories, the TANGO Consortium of Taiwan, the University of Wisconsin at Milwaukee, and Lawrence Berkeley National Laboratories. Operations are conducted by COO, IPAC, and UW. Alert distribution is provided by DIRAC@UW (Patterson et al., 2019).

We thank the anonymous referee for providing valuable comments which helped improve the content of the paper. We thank Markus Kromer and Stuart Sim for providing their model data for comparisons. We thank A. Goobar, A. Gal-Yam, E. O. Ofek, J. Fuller, T. Kupfer, and A. V. Filippenko for valuable discussions. Part of this research was carried out at the Jet Propulsion Laboratory, California

Observation Date	MJD	Rest frame phase (days from r peak)	Telescope + Instrument	Range (Observed Å)
2018 May 08.19	58246.192	−10	P200 + DBSP	3500 – 10000
2018 May 14.34	58252.338	−5	Keck-I + LRIS	3200 – 10000
2018 May 17.29	58255.290	−2	P200 + DBSP	3500 – 10000
2018 May 28.26	58266.262	+8	P60 + SEDM	3800 – 9100
2018 May 31.16	58269.159	+11	DCT + DeVeny	3600 – 8000
2018 June 03.31	58272.308	+15	Keck-I + MOSFIRE	9750 – 11240
2018 June 08.20	58277.201	+18	P200 + DBSP	5600 – 10000
2018 June 17.28	58286.268	+27	Keck-I + LRIS	3200 – 10000
2018 July 13.31	58312.307	+52	Keck-I + LRIS	3200 – 10000

Table 4.1: **Summary of spectroscopic observations of ZTF 18aaqeasu.** The DBSP and DCT spectra were obtained at parallactic angle on the sky while the LRIS data were obtained with an Atmospheric Dispersion Corrector.

Institute of Technology, under a contract with the National Aeronautics and Space Administration. Some of the data presented herein were obtained at the W.M. Keck Observatory, which is operated as a scientific partnership between the California Institute of Technology, the University of California, and the National Aeronautics and Space Administration. The Observatory was made possible by the generous financial support of the W.M. Keck Foundation. The authors wish to recognize and acknowledge the very significant cultural role and reverence that the summit of Mauna Kea has always had within the indigenous Hawaiian community. We are most fortunate to have the opportunity to conduct observations from this mountain. These results made use of the Discovery Channel Telescope at Lowell Observatory. Lowell is a private, non-profit institution dedicated to astrophysical research and public appreciation of astronomy, and operates the DCT in partnership with Boston University, the University of Maryland, the University of Toledo, Northern Arizona University, and Yale University. The upgrade of the DeVeny optical spectrograph has been funded by a generous grant from John and Ginger Giovale.

4.6 Appendix: Comparison to SNe Ia with early excess

In Figure 4.7, we compare the early r-band light curve of ZTF 18aaqeasu to the light curves of other SNe Ia where early excess emission has been observed. These include the normal brightness SNe Ia 2016jhr (Jiang et al., 2017), 2017cbv (Hosseinzadeh et al., 2017), and 2018oh (Shappee et al., 2019), as well as the subluminous iPTF 14atg (Cao et al., 2015a). For comparison, we also show the light curve of SN 2011fe, which did not exhibit an early excess in its light curve. While iPTF 14atg exhibited a strong early ultra-violet excess, its r-band light curve exhibits a smooth rise unlike the fast rise and subsequent slow-down seen in ZTF 18aaqeasu. Both SN 2017cbv and SN 2018oh exhibit a clear excess over the light curve of SN 2011fe at early

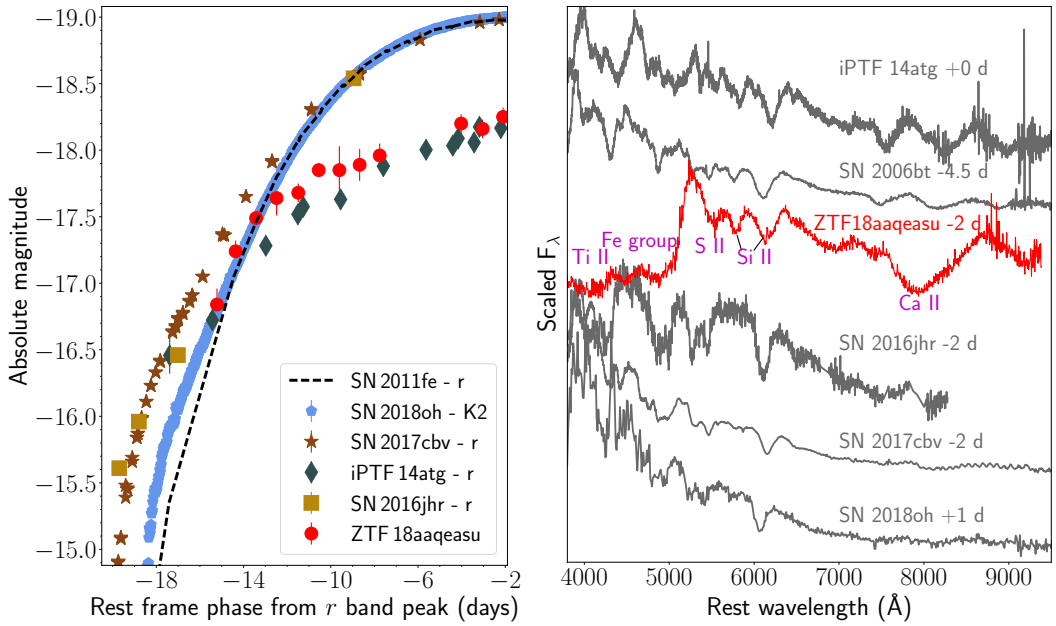

Figure 4.7: **Comparison the light curve of SN 2018byg to other Type Ia supernovae with early light curve excess**. (Left) Comparison of the early r-band light curve of ZTF 18aaqeasu to other SNe Ia reported with early excess emission. We show the K2 filter light curve for SN 2018oh. The light curves of the events with normal peak brightness have been normalized to the peak magnitude of SN 2011fe. We show the early light curve of SN 2011fe (which did not exhibit an early excess) as a black dashed line to highlight the early excess seen in the other objects. The photometric data for the comparison objects have been taken from Nugent et al., 2011, Cao et al., 2015a Hosseinzadeh et al., 2017, Jiang et al., 2017, and Shappee et al., 2019. (Right) Comparison of the peak light spectra of early excess SNe Ia to ZTF 18aaqeasu. The light curve phases are indicated next to each spectrum. As shown, none of the early excess events exhibit the extremely strong line blanketing seen in ZTF 18aaqeasu near peak light. Spectroscopic data for the comparison events have been taken from Cao et al., 2015a, Foley et al., 2010, Jiang et al., 2017, Hosseinzadeh et al., 2017, and Li et al., 2019.

times, but subsequently their light curve rise becomes similar to that of SN 2011fe near peak light. A similar behavior is also seen in the case of SN 2016jhr, although the early excess in this event was redder in color (Jiang et al., 2017). We also note that the early excess in SN 2016jhr was visible at a earlier phase compared to the fast rising portion of the early light curve of ZTF 18aaqeasu.

The light curve of ZTF 18aaqeasu is distinctly different from all these events, in that its early fast rise is similar to that of SN 2011fe, but it subsequently exhibits a prominent turn-over to a sub-luminous SN Ia light curve fainter by ≈ 0.8 mag at peak.

We also compare the peak light spectra of these events with ZTF 18aaqeasu in Figure 4.7. Although the light curve of iPTF 14atg is broadly similar to ZTF 18aaqeasu (Figure 4.3), it is spectroscopically different due to its lower velocity features and blue continuum near peak light. Both SN 2017cbv and SN 2018oh display spectroscopic characteristics of a normal SN Ia with a strong blue continuum and weak Ti II absorption near peak. On the other hand, ZTF 18aaqeasu exhibits nearly complete suppression of flux below 5000 Å and a deep, high velocity Ca absorption feature in the Ca II NIR triplet. While both SN 2006bt and SN 2016jhr exhibit strong Ti II absorption similar to sub-luminous SNe Ia, they exhibit blue continua near peak and lack the complete line blanketing of flux below 5000 Å as seen in ZTF 18aaqeasu.

Chapter 5

A DOUBLE-PEAKED CALCIUM-RICH GAP TRANSIENT IN A METAL POOR, STAR FORMING DWARF GALAXY

De, K. et al. (2018). "iPTF 16hgs: A Double-peaked Ca-rich Gap Transient in a Metal-poor, Star-forming Dwarf Galaxy". In: *ApJ* 866.1, 72, p. 72. DOI: 10.3847/1538-4357/aadf8e. arXiv: 1806.10623 [astro-ph.HE].

Kishalay De[1], Mansi M. Kasliwal[1], Therese Cantwell[2], Yi Cao[3], S. Bradley Cenko[4,5], Avishay Gal-Yam[6], Joel Johansson[7], Albert Kong[8], S. R. Kulkarni[1], Ragnhild Lunnan[9], Frank Masci[10], Matt Matuszewski[1], Kunal P. Mooley[1], James D. Neill[1], Peter E. Nugent[11,12], Eran O. Ofek[6], Yvette Perrott[13], Umaa D. Rebbapragada[14], Adam Rubin[6], Donal OŚullivan[1], and Ofer Yaron[6]

[1]Cahill Center for Astrophysics, California Institute of Technology, 1200 E. California Blvd., Pasadena, CA 91125, USA
[2]Jodrell Bank Centre for Astrophysics, Alan Turing Building, School of Physics and Astronomy, The University of Manchester, Oxford Road, Manchester M139PL, UK
[3]Department of Astronomy, University of Washington, Box 351580, Seattle, WA 98195-1580, USA
[4]Astrophysics Science Division, NASA Goddard Space Flight Center, Mail Code 661, Greenbelt, MD 20771, USA
[5]Joint Space-Science Institute, University of Maryland, College Park, MD 20742, USA
[6]Department of Particle Physics and Astrophysics, Faculty of Physics, The Weizmann Institute of Science, Rehovot 76100, Israel
[7]Department of Physics and Astronomy, Division of Astronomy and Space Physics, Uppsala University, Box 516, SE 751 20 Uppsala, Sweden
[8]Institute of Astronomy and Department of Physics, National Tsing Hua University, Hsinchu 30013, Taiwan
[9]Oskar Klein Centre, Department of Astronomy, Stockholm University, 106 91 Stockholm, Sweden
[10]Infrared Processing and Analysis Center, California Institute of Technology, MS 100-22, Pasadena, CA 91125, USA
[11]Lawrence Berkeley National Laboratory, Berkeley, California 94720, USA
[12]Department of Astronomy, University of California, Berkeley, CA, 94720-3411, USA
[13]Astrophysics Group, Cavendish Laboratory, 19 J. J. Thomson Avenue, Cambridge CB3 0HE, UK
[14]Jet Propulsion Laboratory, California Institute of Technology, Pasadena, CA 91109, USA

Abstract

Calcium-rich gap transients represent an intriguing new class of faint and fast evolving supernovae that exhibit strong [Ca II] emission in their nebular phase spectra. In this paper, we present the discovery and follow-up observations of a faint and fast evolving transient iPTF 16hgs, that exhibited a double-peaked light curve. Exhibiting a Type Ib spectrum in the photospheric phase and an early transition

to a [Ca II] dominated nebular phase, iPTF 16hgs shows properties consistent with the class of Ca-rich gap transients, with two important exceptions. First, while the second peak of the light curve is similar to other Ca-rich gap transients, the first blue and fast fading peak (declining over ≈ 2 days) is unique to this source. Second, we find that iPTF 16hgs occurred in the outskirts (projected offset of ≈ 6 kpc ≈ 1.9 $R_{\rm eff}$) of a low metallicity (≈ 0.4 $Z_{\odot}$), star forming, dwarf spiral galaxy. Deep limits from late-time radio observations suggest a low density environment for the source. If iPTF 16hgs shares explosion physics with the class of Ca-rich gap transients, the first peak can be explained by the presence of 0.01 $M_{\odot}$ of ^{56}Ni in the outer layers of the ejecta, reminiscent of some models of He-shell detonations on WDs. However, if iPTF 16hgs is physically unrelated to the class, the first peak is consistent with shock cooling emission (of an envelope with a mass of ≈ 0.08 $M_{\odot}$ and radius of ≈ 13 $R_{\odot}$) in a core-collapse explosion of a highly stripped massive star in a close binary system.

5.1 Introduction

The luminosity 'gap' between novae and supernovae (SNe) has been populated with a variety of new classes of transients with the advent of wide field and high cadence transient surveys in recent years (Kasliwal, 2012). In particular, Calcium-rich gap transients have emerged as an intriguing new class of faint explosions, proposed to be defined by their (1) intermediate luminosity ('gap' transients), (2) faster photometric evolution (rise and decline) than normal SNe, (3) photospheric velocities comparable to those of SNe, (4) rapid evolution to the nebular phase, and (5) a nebular spectrum dominated by calcium emission (Kasliwal et al., 2012). Although not used as a defining characteristic of this class, these transients have been almost exclusively found at very large projected offsets from their host galaxies, potentially suggesting their association with old progenitor populations that have traveled far away from their host galaxies (Lunnan et al., 2017; Lyman et al., 2014; Perets et al., 2010).

Following the discovery of the prototype event of this class SN2005E (Perets et al., 2010; who also reported 7 other Ca-rich SNe with limited photometric information), five additional events have been reported by the Palomar Transient Factory (PTF; Law et al., 2009): PTF 09dav (Kasliwal et al., 2012; Sullivan et al., 2011), PTF 10iuv, PTF 11bij (Kasliwal et al., 2012), PTF 11kmb and PTF 12bho (Foley, 2015; Lunnan et al., 2017); one event reported by PESSTO (SN 2012hn; Valenti et al.,

2014) as well as one source found in archival observations (SN 2007ke; Kasliwal et al., 2012; Perets et al., 2010). Additionally, Milisavljevic et al., 2017 reported follow-up observations of iPTF 15eqv, a Type IIb SN discovered in a star forming galaxy, and classified it as 'Ca-rich' based on its nebular spectrum, although photometrically it is not a member of this class owing to its high peak luminosity and slow light curve evolution (with an unconstrained rise time to peak).

While the properties of all confirmed Ca-rich gap transients are consistent with the aforementioned criteria, there remain several differences in other observed properties of these sources. For example, the photospheric spectra of these sources show significant diversity, although all but one of these events show He-rich spectra akin to Type Ib SNe at peak light (Filippenko, 1997; Gal-Yam, 2017). Such diversity is potentially indicative of heterogeneity in the progenitor channels, as previously suggested in several studies (Lunnan et al., 2017; Sell et al., 2015). Nevertheless, Lunnan et al., 2017 show that the light curves of these sources form a fairly uniform class, showing very similar rise and decay characteristics. However, the small number of known events leave considerable uncertainty on the spread of the intrinsic properties of this unique class of events.

The progenitor systems of Ca-rich gap transients remain largely uncertain, although it has been generally suggested that they are associated with very old progenitor systems. With a sample of 8 events (some of which had sparse photometric coverage) from the Lick Observatory Supernova Search (LOSS), Perets et al., 2010 showed that the only Type Ib/c SNe to be found in early type galaxies were 'Ca-rich' similar to SN 2005E. Additionally, the host galaxy type distribution of Ca-rich SNe were shown to be markedly skewed towards early type galaxies with old stellar populations (unlike other Type Ib/c SNe associated with star formation), suggesting that Ca-rich SNe represented a separate population of Type Ib/c SNe. Subsequently, more evidence has been gathered from their remote locations, as well as associated stringent limits on the presence of stellar associations and star formation at the locations of these transients (Kasliwal et al., 2012; Lunnan et al., 2017; Lyman et al., 2013, 2014, 2016b; Perets et al., 2010; Perets, 2014; Perets et al., 2011).

Consequently, the several proposed explosion channels for these events arise from old binary progenitor systems, such as tidal detonations of low mass He WDs by

neutron stars or black holes (MacLeod et al., 2016; Margalit et al., 2016; Metzger, 2012; Perets et al., 2010; Sell et al., 2015; Zenati et al., 2019b), and He shell detonations on the surface of C/O white dwarfs (WDs) (also known as .Ia detonations; Bildsten et al., 2007; Dessart et al., 2015a; Perets et al., 2010; Shen et al., 2010; Waldman et al., 2011), possibly induced by hardening of a WD-WD binary due to gravitational interactions with a central super-massive black hole in the host galaxy (Foley, 2015). Although their old environments argue against scenarios involving the collapse of a massive star, those found in star forming environments could be associated with highly stripped massive star progenitors that collapse to produce fast transients with ejecta masses of $\approx 0.2 - 0.4$ $M_\odot$ (Moriya et al., 2017; Tauris et al., 2015).

In this paper, we present the discovery and follow-up observations of a unique Ca-rich gap transient, iPTF 16hgs, which exhibited a double peaked light curve. The paper is organized as follows. We describe the discovery and follow-up observations of the transient in Section 5.2. We analyze the photometric and spectroscopic properties of the source in the context of Ca-rich gap transients in Section 5.3. We model the unique light curve of the transient in Section 5.4. Section 5.5 presents an analysis of the radio observations of the source in the context of models of a SN shock interacting with a CSM as well as a tidal detonation event. We discuss the host galaxy and local explosion environment of the transient in Section 5.6. We end with a broader discussion of the properties of Ca-rich gap transients in the context of this discovery in Section 5.7. Calculations in this paper assume a ΛCDM cosmology with $H_0 = 70$ km s^{-1} Mpc^{-1}, Ω_M=0.27 and Ω_Λ=0.73 (Komatsu et al., 2011).

5.2 Observations

Discovery and classification

iPTF 16hgs (= SN 2016hgs) was discovered by the intermediate Palomar Transient Factory (iPTF; Cao et al., 2016; Law et al., 2009; Masci et al., 2017; Rau et al., 2009) and was detected first in r band photometry taken with the CFH12K 96-Megapixel camera (Law et al., 2010; Rahmer et al., 2008) mounted on the 48 inch Samuel Oschin Telescope at Palomar Observatory (P48), on 2016 October 20.32 (MJD 57681.32)[1] at J2000 coordinates α = 00h50m51.39s. $\delta = +27°22'48.0''$. The source was discovered at an apparent magnitude of $r \approx 18.9$ mag, while it was not detected on 2016 October 08.01 (MJD 57669.01; 12.31 days before discovery) up

[1]UTC times are used throughout this paper.

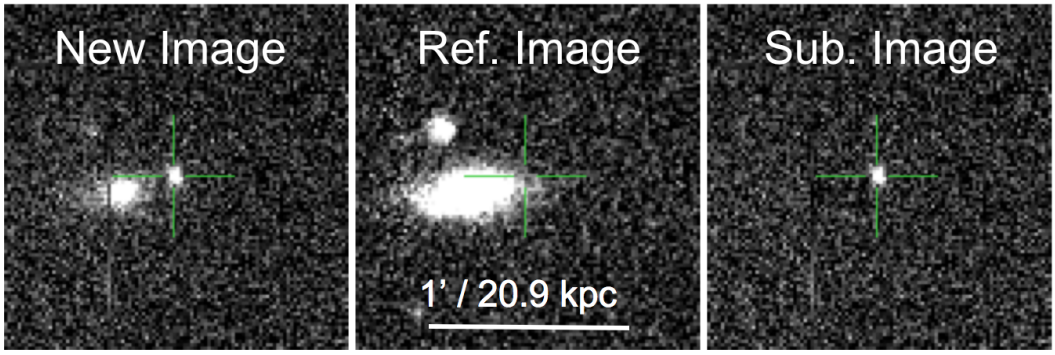

Figure 5.1: **Discovery field of iPTF 16hgs**. Shown here are the discovery (left), reference (middle), and subtracted transient image (right) of iPTF 16hgs from the Palomar 48-inch telescope in r band. North is upwards and East is due left in the images. The location of the transient is highlighted by the green cross.

to a limiting magnitude of $r \geq 20.8$.

The transient was found in the outskirts of a nearly edge-on spiral host galaxy with a photo-z of 0.017, and at a projected offset of $\approx 17''$ ($\approx 1.9\ \mathrm{R}_{eff}$) from the nucleus (Figure 5.1). We obtained a spectrum of the source on 2016 October 22 with the Discovery Channel Telescope (DCT), to find a Type Ib-like SN spectrum, similar to the pre-peak photospheric spectrum of the Ca-rich transient PTF 10iuv for the assumed photo-z of the host galaxy. A subsequent spectrum of the apparent host galaxy confirmed a redshift of z = 0.017, corresponding to a luminosity distance of D_L = 73.8 Mpc. Subsequent follow-up photometry and spectroscopy of the transient revealed that the source exhibited a faint peak absolute magnitude ($M_r \approx -15.5$) and early transition (at $\approx +30$ days) to a nebular phase dominated by [Ca II] emission, thus leading to its classification as a Ca-rich gap transient.

Photometry

We obtained r and g band photometry of iPTF 16hgs with the P48 CFH12K camera, along with gri band photometry with the automated 60-inch telescope at Palomar (P60; Cenko et al., 2006). PTF image reduction is presented in Laher et al., 2014 and its photometric calibration and magnitude system is described in Ofek et al., 2012. P48 images were reduced with the Palomar Transient Factory Image Differencing and Extraction (PTFIDE) pipeline (Masci et al., 2017), which performs host subtracted point spread function (PSF) photometry, while the P60 images were

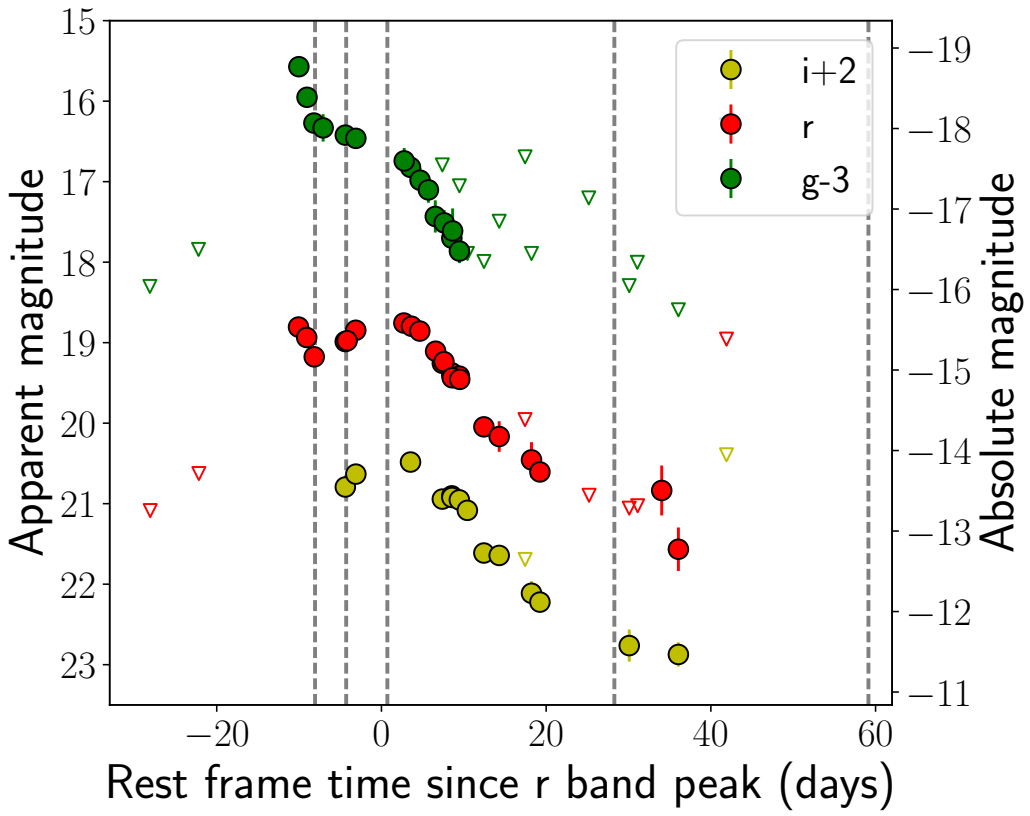

Figure 5.2: **Multicolor light curves of iPTF 16hgs.** The filled circles denote magnitudes where the source was detected while the open triangles indicate epochs where only upper limits where obtained. The dashed lines denote epochs of spectroscopy.

reduced using the pipeline described in Fremling et al., 2016. We correct all our photometry for galactic extinction for $E(B-V) = 0.056$ from the maps of Schlafly et al., 2011. We do not correct for any additional host extinction since we do not detect any Na D absorption at the host redshift in our spectra (Section 5.2).

We show the multi-color light curves for iPTF 16hgs in Figure 5.2, while the data are presented in Table 5.1. As shown, the source exhibited a double peaked light curve in all photometric bands where we had early time coverage. For all subsequent discussions, we refer to the second peak of the light curve as the main peak as well as specify all observation phases with respect to this peak.

Spectroscopy

We obtained spectroscopic follow-up of the transient starting from ≈ -8 d to $\approx +59$ d after r band peak using the DeVeny spectrograph on the Discovery Channel Telescope (Bida et al., 2014), the Double Beam Spectrograph (DBSP) on the 200-inch Hale telescope (Oke et al., 1982), and the Low Resolution Imaging Spectrograph (LRIS) on the Keck-I telescope (Oke et al., 1995). Our last spectrum of the source obtained at +59 days after r band peak was in the form of a spectroscopic mask observation aimed to characterize the host environment of the transient. We present our sequence of spectra in Figure 5.3 (the spectroscopy epochs are indicated as dashed lines in Figure 5.2), while the spectroscopic observations are summarized in Table 5.2. We discuss the spectroscopic evolution of the source in Section 5.3. We also obtained a spectrum of the nucleus of the host galaxy of iPTF 16hgs with LRIS, which was found to exhibit prominent emission lines of Hα, Hβ, [NII], [SII], [OII], and [OIII], as shown in Figure 5.4.

All spectra and photometry will be made available by the WISeREP repository (Yaron et al., 2012) [2].

Swift Observations

We obtained X-ray follow-up of the transient with the *Swift* X-ray telescope (XRT; Burrows et al., 2005). The source was observed on 2017 February 17 (MJD 57801; Phase $\sim$ +107 days) for a total exposure time of 5 ks, and the data was processed with the `HEAsoft` package[3]. No source was detected at the location of the transient to a 3σ upper limit of 2.2×10^{-3} counts s^{-1}, corresponding to an unabsorbed 0.3 - 10 keV flux upper limit of 7.5×10^{-14} ergs cm^{-2} s^{-1} for a photon index of $\Gamma = 2$[4]. This constrains the unabsorbed X-ray luminosity from the source to $< 4.9 \times 10^{40}$ ergs s^{-1}.

The Swift Ultraviolet / Optical telescope (UVOT; Roming et al., 2005) also simultaneously observed the field in the UVW2 band. No source was detected at the transient location up to a 5σ limiting AB magnitude of 23.05.

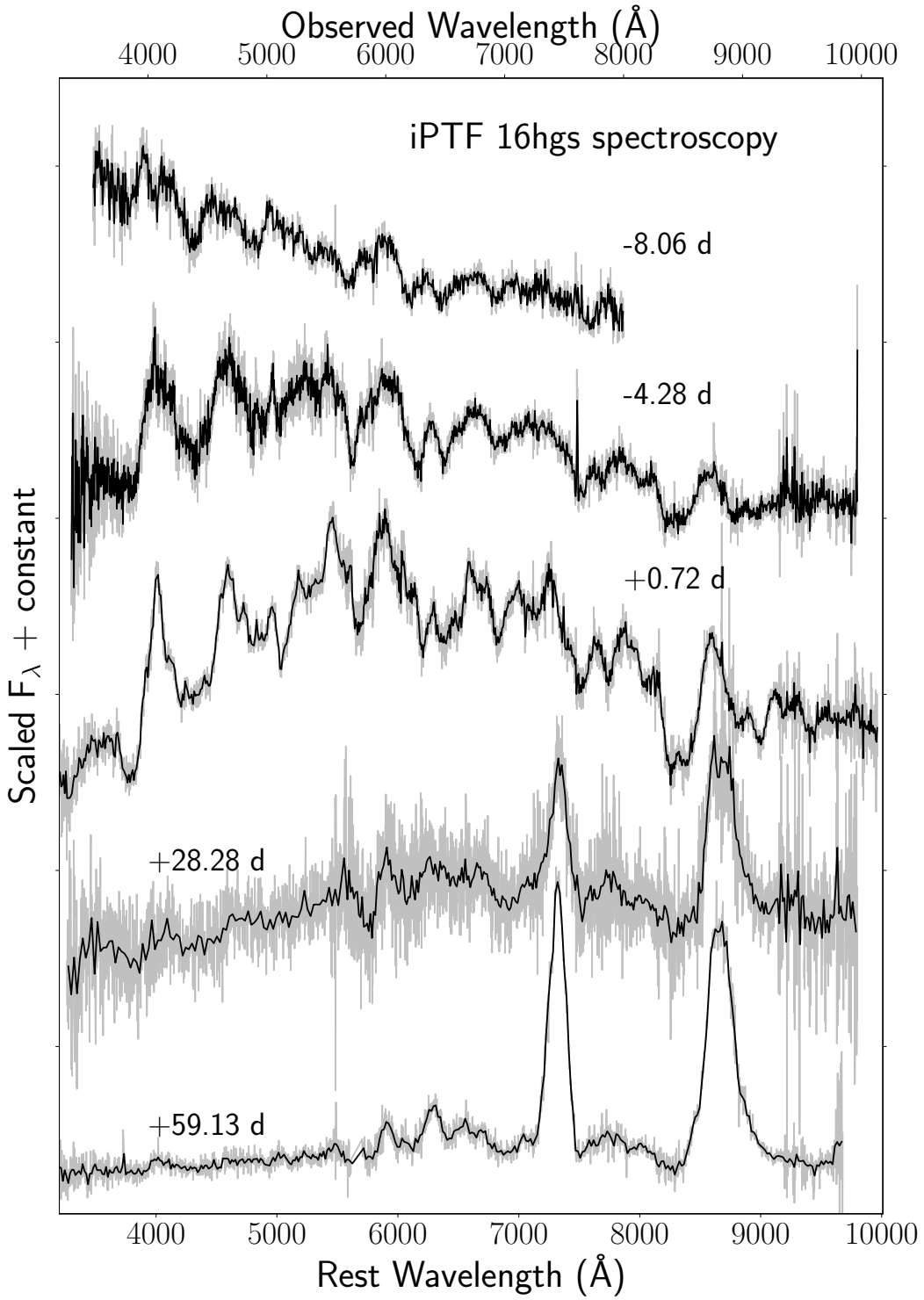

Figure 5.3: **Spectroscopic sequence for iPTF 16hgs.** The black lines indicate binned spectra while the gray lines show the unbinned spectra. The phase of the light curve at the time of the spectrum (with respect to *r* band peak) is indicated alongside each spectrum.

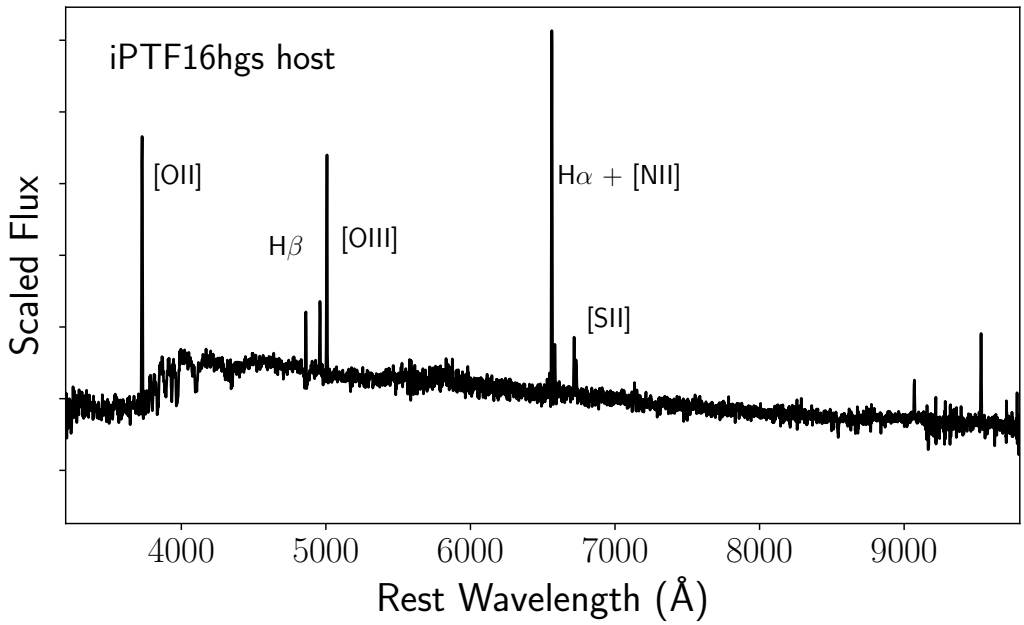

Figure 5.4: **Spectrum of the core of the host galaxy of iPTF 16hgs.** Prominent emission lines are marked.

Host observations

Host environment spectroscopy

Our last spectrum of the source (where the transient was detected) was obtained as a part of a spectroscopic mask observation with LRIS, where we placed additional slits on a number of extended sources classified as galaxies in Sloan Digital Sky Survey (SDSS) catalog. The aim of the mask observation was to measure redshifts of galaxies near the transient region, in order to ascertain if the host galaxy was a part of a galaxy group or cluster (as is typically found for Ca-rich gap transient host galaxies; Lunnan et al., 2017). These measurements were then combined with previously measured redshifts of galaxies in NED within a projected offset of 1 Mpc from the apparent host galaxy.

We selected a total of 37 sources classified as galaxies in SDSS within $\approx 6'$ of the transient location, with the source selection prioritized by the projected offset from the location of the transient. The data were reduced with standard routines in

[2] `https://wiserep.weizmann.ac.il`

[3] `http://heasarc.nasa.gov/lheasoft/`

[4] The WebPIMMS interface at `https://heasarc.gsfc.nasa.gov/cgi-bin/Tools/w3pimms/w3pimms.pl` was used for this calculation.

IRAF. Details of the spectroscopic mask observation are given in Table 5.2, while the measured redshifts of the galaxies are given in Table 5.4. Figure 5.14 shows the positions of the galaxies whose redshifts could be measured from the spectra. As shown, only one of all the sources placed in the spectroscopic mask was found to be at the same redshift as that of the apparent host galaxy. However, we caution that this galaxy was coincident with the diffuse outskirts of the brighter apparent host galaxy, and hence this source may be an H-II region in the outskirts of the host galaxy instead.

The faintest source placed in the spectroscopic mask had an r-band magnitude of 25.4, while the faintest source for which a redshift could be identified had an r-band magnitude of 24.1. The faintest source measured was also the nearest in terms of projected offset from the transient location ($\approx 4''$), and coincident with the position of the unidentified radio source mentioned in Section 5.2. Based on sources classified as galaxies in SDSS, we estimate that our redshift identification procedure was complete up to an apparent magnitude of $r \approx 22.08$ within a projected offset of 50 kpc ($\approx 143''$) of the transient, corresponding to an absolute magnitude of $M_r \approx -12.3$ at the redshift of the transient.

Late-time imaging and spectroscopy

We undertook deep imaging of the transient region in g and r bands with Keck LRIS on 2017 September 13 (MJD 58009.4) for a total exposure time of 1500s and 600s, respectively. The data were reduced with standard procedures in `lpipe`[5]. No source was detected at the transient location up to a 3σ limiting magnitude of 27.0 mag and 25.5 mag in the g and R bands, respectively. At the distance of the transient, these limits correspond to an extinction corrected absolute magnitude limit of $M_g = -7.6$ and $M_R = -9.0$.

We also obtained one late-time spectrum of the transient region with LRIS on 2017 September 13 for a total exposure time of 3600s. We did not detect any continuum or broad nebular emission features at the transient location, although narrow galaxy emission features from the host galaxy are clearly detected. These emission features were also detected on top of the SN continuum in deep spectroscopy taken ≈ 60 days after peak light when the transient had faded significantly.

[5]http://www.astro.caltech.edu/ dperley/programs/lpipe.html

Host IFU observations

iPTF 16hgs is unique in that it has the smallest host offset (both in terms of absolute distance and host normalized offset) of all known Ca-rich gap transients (Section 5.6). Hence, iPTF 16hgs provides a unique opportunity to study the local ISM environments of a Ca-rich gap transient in detail. We thus observed the host region of iPTF 16hgs with the Palomar Cosmic Web Imager (PCWI) on 2017 October 18 to measure spatially resolved metallicity, star formation rate, and ISM electron density for the host galaxy.

The PCWI is an integral field spectrograph mounted on the Cassegrain focus of the 200-inch Hale telescope at Palomar Observatory (Matuszewski et al., 2010). The instrument has a field of view of 40" x 60 " divided across 24 slices with dimensions of 40" x 2.5" each. The spectrograph uses an image slicer and volume phase holographic gratings. For our observations, we selected the red, R $\sim$ 5000 grating and red filter to achieve an instantaneous bandwidth of $\approx$ 550 Å. A complete description of the instrument, observing approach, and data analysis methodology can be found in Martin et al., 2014.

The PCWI field of view matches the projected dimensions of the apparent host galaxy on the sky ($\approx 1'$ along the major axis), and hence this observation was carried out to characterize spatially resolved properties of the environment of the transient, as well as the overall host galaxy (Section 5.6). The instrument was used with its red grating and filter, and configured to a central wavelength of 6630 Å, covering the wavelength range from approximately 6400 Å to 6900 Å . This specific wavelength range was chosen to include a number of redshifted emission lines from the host galaxy, including Hα, [N II] λ6584, and [S II] $\lambda\lambda$6716, 6731, that can be used as tracers of star formation, metallicity, and the local electron density of the medium.

We obtained a total of 12 dithered exposures of the host galaxy (centered around its nucleus), each with an exposure time of 1200 s. In order to obtain similar spatial sampling in two directions, half of these exposures were obtained with the IFU slices oriented in North-South direction, while the other half had slices oriented in the East-West direction. The host galaxy exposures were interleaved with exposures of a nearby empty sky region to subtract emission features from the sky. We also

obtained calibration images including arc lamp spectra, dome flats, and a standard star spectrum (GD 248). The two dimensional spectra were sliced, rectified, spatially aligned, and wavelength calibrated using the calibration images to produce data cubes for each sky exposure, sampled at (RA, Dec., λ) intervals of (2.6″, 0.6″, 0.22 Å).

The sky background cubes were then subtracted from the source cubes to remove the sky emission lines, followed by flux calibration using the standard star GD 248. The flux calibrated (and dithered) spectral cubes for each source exposure were then combined spatially to produce a final spectral cube covering a sky area of $\approx$ 70″$\times$ 70″, and with a spatial sampling of 0.6 ″ along both axes. The spatial resolution is thus completely seeing limited ($\approx$ 1.2″on the night of the observation), and corresponds to a projected resolution of $\approx$ 0.4 kpc at the redshift of the host galaxy.

Radio Observations

Owing to its apparent close location to its host galaxy and potential proximity to relatively dense ISM, we initiated deep radio follow-up of the transient to constrain the presence of a radio counterpart, as potentially expected in some proposed models for Ca-rich gap transients (e.g. tidal detonations of white dwarfs that produce a relativistic jet, or a core-collapse explosion of a massive star).

AMI observations

We observed iPTF 16hgs with the Arcminute MicroKelvin Imager Large Array (AMI-LA; Hickish et al., 2018; Zwart et al., 2008) radio telescope. The data have 4096 frequency channels across a 5 GHz bandwidth between 13–18 GHz. The observations were made on 2017 March 12 (MJD 57824.65) for a duration of three hours, with the phase calibrator J0057+3021 observed every 10 minutes for a duration of two minutes. The AMI-LA data were binned to 8$\times$0.625 GHz channels and processed (RFI excision and calibration) with a fully-automated pipeline, AMI-REDUCE (e.g. Davies et al., 2009). Daily measurements of 3C48 and 3C286 were used for the absolute flux calibration, which is good to about 10%. The calibrated and RFI-flagged data were then imported into CASA and imaged with the task *clean* to produce 512$\times$512 pix^2 (4″pix^{-1}). We do not detect iPTF 16hgs in the resulting image, and although the RFI was substantial, we can place a stringent upper limit

to the flux density at 15.5 GHz of 210 μJy (3σ). This constrains the 15 GHz radio luminosity of the source to $\lesssim 1.4 \times 10^{27}$ ergs s^{-1} Hz^{-1}.

JVLA observations

We obtained radio observations of the transient with the Very Large Array (VLA) under the Director's Discretionary Time (DDT) program (17A-427; PI: De). The VLA observed the source on 2017 June 24 (in C configuration; $\sim$ 250 days after r band peak) at X band (centered at 10 GHz) for a total on source time of $\approx$ 1.8 hours, with the Wideband Interferometric Digital Architecture (WIDAR) correlator configured in continuum mode with 4 GHz bandwidth. The data were flagged and calibrated with the VLA calibration pipeline, while deconvolution and imaging was performed with standard routines in CASA. 3C48 was used as the flux and bandpass calibrator while the source J0042+2320 was used as the phase calibrator. The final processed image has a noise RMS of $\approx 2.6\,\mu$Jy/beam.

Although we find a faint radio source very close to the transient location, its position is offset by 5" from the source and coincident with a background galaxy in the late-time LRIS image, and hence not associated with the transient. We also obtained a spectrum of the background galaxy in our spectroscopic mask observation (Section 5.2), and found it to be consistent with an Active Galactic Nucleus (AGN) at a redshift of 0.362, and clearly unrelated to the transient. No other source is detected at the transient location up to a 3σ limiting flux density of $\approx 7.8\,\mu$Jy (Figure 5.5). At the redshift of the host galaxy, the flux upper limit constrains the 10 GHz radio luminosity to $\lesssim 5.1 \times 10^{25}$ ergs s^{-1} Hz^{-1}.

uGMRT Observations

We obtained radio follow-up of the source with the upgraded Giant Metrewave Radio Telescope (uGMRT) under the DDT program (DDTB272; PI: De). The source was observed on 2017 July 19 ($\sim$ 275 days after r band peak) at L band (centered at 1.2 GHz) for a total on source time of $\approx$ 4.5 hours. We used the GMRT Wideband Backend (GWB; Reddy et al., 2017) configured in the continuum interferometric mode with 400 MHz bandwidth. 3C48 was used as the flux density and bandpass calibrator, while the source J0029+349 was used as the phase calibrator. The data were analyzed using the Astronomical Image Processing System (AIPS). After flagging the original data set for non-working antennas and Radio Frequency Inter-

ference (RFI), data from a single frequency channel of the flux and phase calibrators were used to construct time-based amplitude and phase calibrations, while bandpass calibration was done with the flux calibrator.

No source was detected at the location of the optical transient (Figure 5.5) up to a 3σ limiting flux of $\approx 50\mu$Jy, corresponding to a 1.2 GHz radio luminosity of 3.3×10^{26} ergs s^{-1} Hz^{-1}. We note that the faint radio source detected at a 5" offset in the VLA image is also well detected in the GMRT image at L band, coincident with a background galaxy in the late-time LRIS image.

5.3 Analysis

In this section, we analyze the photometric and spectroscopic properties of iPTF 16hgs and show that it is a member of the class of Ca-rich gap transients as defined by Kasliwal et al., 2012.

Light curve properties

We first analyze the properties of the light curve of iPTF 16hgs, which we show to be unique in comparison to other known Ca-rich gap transients. The multi-color light curves of iPTF 16hgs are shown in Figure 5.2. The light curve of iPTF 16hgs shows clear evidence for two distinct components – an early declining phase (which was caught at discovery), followed by re-brightening to a second (main) peak which was followed up to late times. The early declining phase was detected in both r and g bands, and was characterized by significantly bluer colors than the rest of the light curve, as evident from the rapid early decline in g band.

Figure 5.6 compares the multi-color light curves of iPTF 16hgs to that of other known Ca-rich gap transients from PTF (Kasliwal et al., 2012; Lunnan et al., 2017). As shown, the second light curve peak of iPTF 16hgs is well matched to that of the light curves of the other Ca-rich transients, although the rapid decline from the first peak distinguishes it from the entire sample. At the same time, the i-band light curve of iPTF 16hgs is fainter than all the other events starting from $\approx$ 10 days after r-band peak. Since some of the previously known transients have very well sampled early light curves, we can rule out the possibility that a first peak at similar timescales was missed in the case of PTF 10iuv, PTF 11kmb, and PTF 12bho. However, a similar feature cannot be ruled out in the case of PTF 09dav and PTF 11bij which had sparse

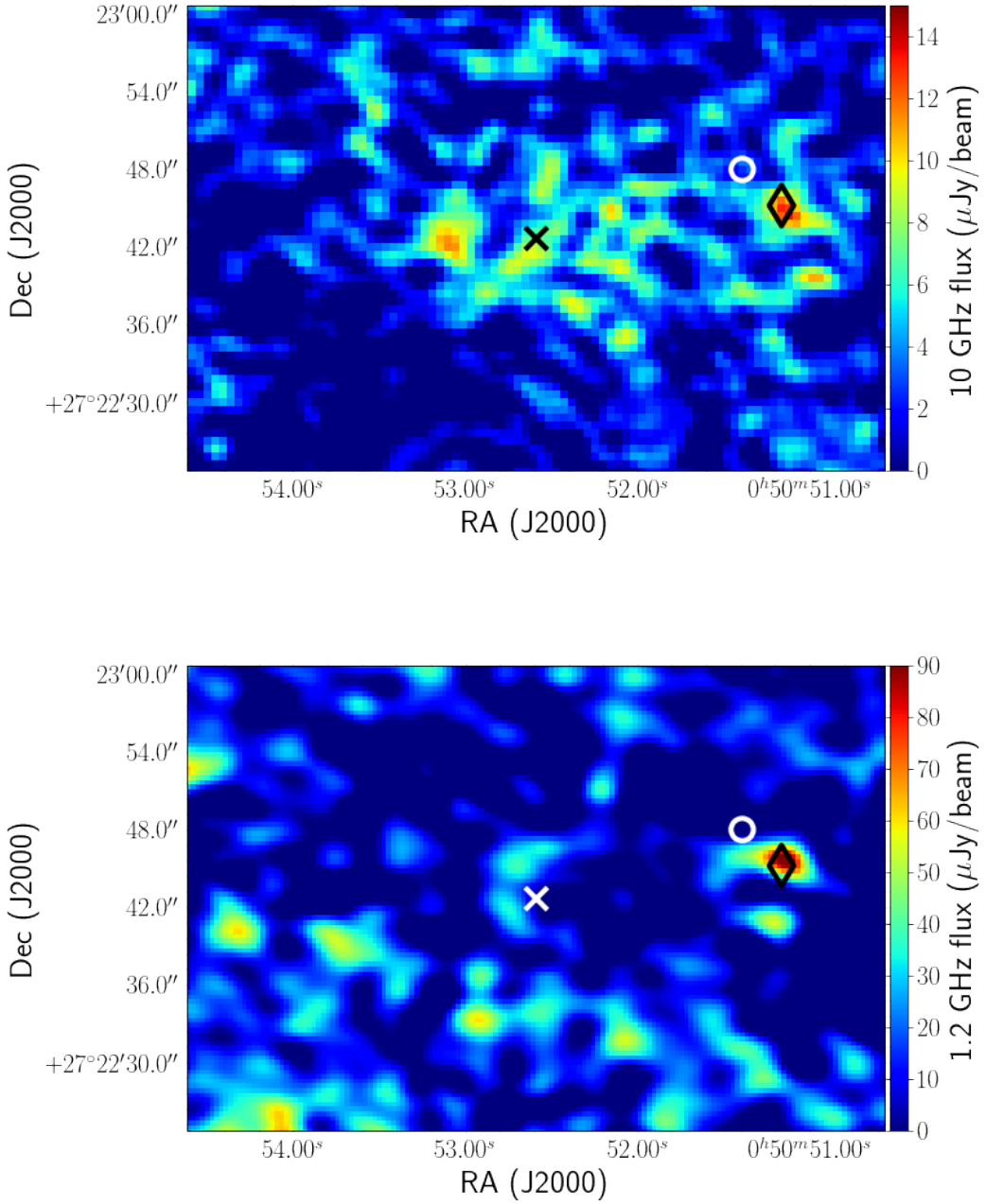

Figure 5.5: **Radio images of the host region of iPTF 16hgs from observations with the VLA (10 GHz; Left) and the uGMRT (1.2 GHz; Right).** The nucleus of the host is indicated by the cross, while the location of the transient is indicated by the white circle. While a radio source is detected very close to the transient in both these observations (indicated by the black diamond), its position is consistent with a background AGN identified in the spectroscopic mask observation, and hence unrelated to the transient. The Image RMS is $\approx 2.6\mu$Jy for the VLA X band image, and $\approx 17\mu$Jy for the GMRT L band image.

photometric coverage before peak light.

Figure 5.6 also shows the $g-r$ and $r-i$ color evolution of iPTF 16hgs compared to the Ca-rich transient PTF 10iuv (which had good multi-color photometric coverage). As shown, iPTF 16hgs exhibited very blue colors at the early times after discovery (with $g-r \approx -0.2$), while it subsequently exhibited rapid reddening over the next ≈ 20 days, evolving to $g-r \approx 1.5$ at ≈ 10 days after the r band peak. The $r-i$ color also exhibits reddening with time, although the evolution is much slower. For comparison, the color curves of PTF 10iuv also exhibited similar but less rapid reddening with time, although iPTF 16hgs remained redder at similar light curve phases.

We fit a third order polynomial to the main peak of the r band light curve (which is best sampled) to find a peak magnitude of $M_r = -15.65$ and a peak time of MJD 57691.59. All phases mentioned in this paper are with respect to this epoch. We note that the peak absolute magnitude is similar to that of several previously confirmed Ca-rich gap transients. Determining the explosion time for this transient is non-trivial due to the presence of the early declining emission, thus precluding a conventional t^2 fit to the early light curve. Additionally, the first rise is not sampled due to a gap in coverage of ≈ 12 days between the last non-detection and the first detection. Nonetheless, we try to estimate the rise time by fitting a parabolic function to the main peak of the light curve in flux space, and find a best fit rest frame rise time of ≈ 9.9 days. Based on the last non-detection, we can put an upper limit of ≈ 12.3 days on the rise time of the first peak.

Spectroscopic properties

Photospheric phase spectra taken near the second peak show typical features of Type Ib SNe, most notably prominent lines of He I, O I, Mg II, and Ca II. We compare the photospheric phase spectra of iPTF 16hgs to example spectra of other Ca-rich transients in Figure 5.7. The photospheric spectrum of iPTF 16hgs exhibits a number of good similarities to that of PTF 11kmb and PTF 10iuv, most notably in the strong He features. He features in photospheric spectra are indeed common in many Ca-rich transients (PTF 11kmb, PTF 10iuv, SN 2005E, and SN 2007ke), although it is not used to exclusively define this class. Indeed, as noted by Lunnan et al., 2017, the photospheric phase diversity may point to different progenitor channels of this

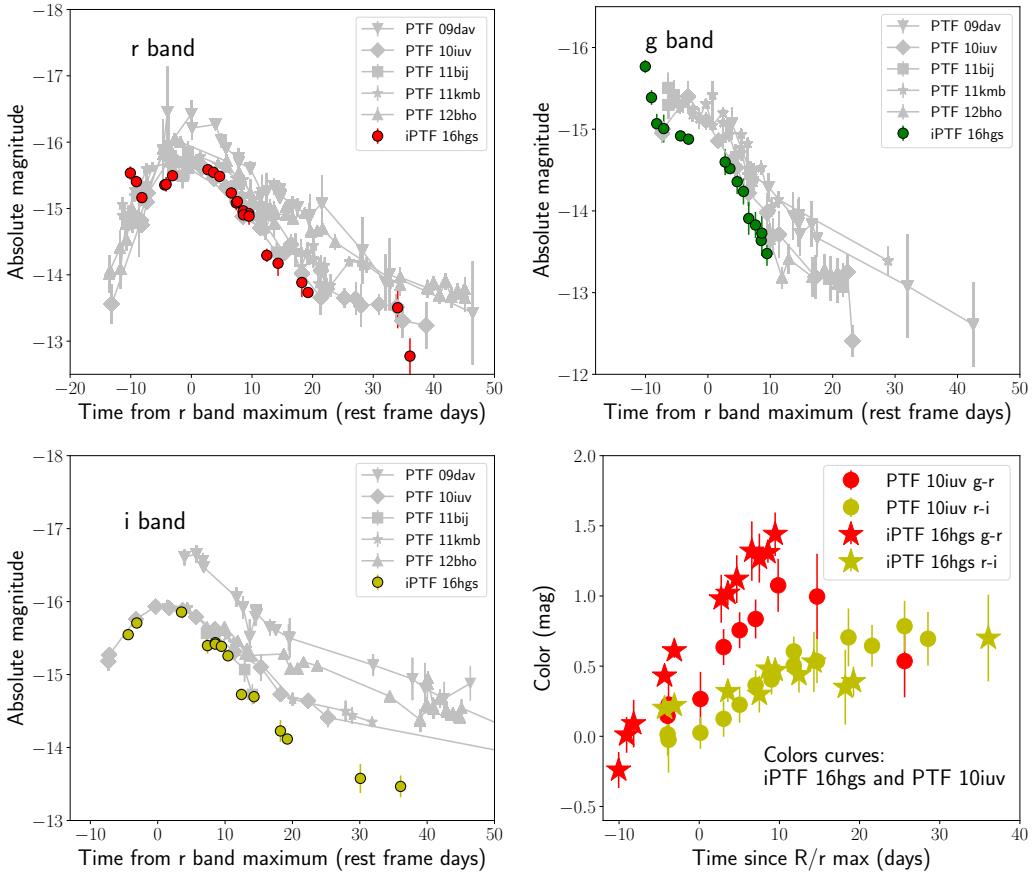

Figure 5.6: **Comparison of the multi-color light curves (in r, g, and i bands) of iPTF 16hgs to that of other Ca-rich gap transients discovered by PTF** – PTF 09dav, PTF 10iuv, PTF 11bij, PTF 11kmb, and PTF 12bho. The lower right panel shows a comparison of the $g-r$ and $r-i$ color evolution of iPTF 16hgs compared to that of PTF 10iuv.

observationally defined class. From the peak photospheric spectrum (taken at 0.72 days after r band peak in the source rest frame), we measure a photospheric velocity of $\approx 10,000$ km s^{-1} for this source.

We identify prominent features in the -4.28 d spectrum of iPTF 16hgs with SYNOW (Fisher, 2000) in Figure 5.8 (note that SYNOW may not be self-consistent and is only suggestive for line identification). We constrain the fit by matching the visible features along with the relative strengths of the features in order to constrain the composition of the ejecta as well as the photospheric velocities of the lines. The most prominent features include He I, Mg II, Si II, O I, and Ca II, along with weaker features of Fe II and Al II. The SYNOW model uses a continuum temper-

ature of 8000 K and velocities in the range of 8,000 – 12,000 km s^{-1}, with He I found to be at the highest velocity of $\approx 12,000$ km s^{-1}. The velocities of other prominent ions include O I at 10000 km s^{-1}, Mg II at 8000 km s^{-1}, Si II at 9000 km s^{-1}, Ca II at 8000 km s^{-1}, Al II at 10000 km s^{-1}, and Fe II at 8000 km s^{-1}. Overall, the SYNOW fit fairly reproduces all the absorption features in the spectrum.

Figure 5.7 also shows a comparison of a nebular spectrum of iPTF 16hgs to that of other Ca-rich gap transients. These spectra exhibit weak continua superimposed with strong forbidden and permitted lines of Ca and O. In particular, iPTF 16hgs exhibits the characteristic nebular features of this class, i.e., strong [Ca II]$\lambda\lambda$ 7291, 7324 emission combined with relatively weak [O I]$\lambda\lambda$ 6300, 6363 emission (with a [Ca II]/[O I] ratio of ≈ 7). For comparison, we also show the photospheric and nebular phase spectra of SN 2009jf (Valenti et al., 2011) which exhibits significantly stronger [O I] emission than [Ca II] in the nebular phase. The [Ca II]/[O I] ratio has been used as a defining feature of the class of 'Ca-rich transients', e.g. Milisavljevic et al., 2017 suggest that a [Ca II]/[O I] ratio of > 2 separates the class of Ca-rich transients from other Type Ib/c SNe. We analyze this issue further in Section 5.7.

In Figure 5.9, we show a comparison of the velocity profiles of the nebular [Ca II] and [O I] emission lines. Interestingly, this last nebular spectrum taken at $\approx +60$ days shows clear evidence of host galaxy emission features of Hα and [O II] $\lambda\lambda$3727, 3729 (on the blue side). These were also detected in a late-time Keck LRIS spectrum taken after the transient faded away. Hence, as opposed to other Ca-rich gap transients that are found in the far outskirts of their host galaxies (Kasliwal et al., 2012; Lunnan et al., 2017), iPTF 16hgs shows evidence of being located inside its host galaxy. However, we cannot rule out a scenario where the transient was located significantly behind the host galaxy, so that the galaxy emission features arise from the foreground. We note that the narrow Hα feature is found superimposed on a broader underlying component (Figure 5.9), that could be potentially associated with hydrogen in the ejecta. A similar H feature was also observed in the nebular spectrum of PTF 09dav (Kasliwal et al., 2012), and potentially in PTF 11kmb as well (Milisavljevic et al., 2017). However, Milisavljevic et al., 2017 suggest that the feature could also be associated with Ca I] λ6572.

Taken together, we have thus far demonstrated that iPTF 16hgs exhibited (1) a low

peak luminosity of $M_r \approx -15.6$, (2) rapid photometric evolution similar to other known Ca-rich gap transients, (3) normal photospheric velocities ($\sim 10,000$ km s^{-1}), (4) early transition to a nebular phase (at ≈ 30 days after r band peak), and (5) a nebular phase spectrum dominated by [Ca II] emission. Thus, despite its unique light curve, iPTF 16hgs falls squarely in the class of Ca-rich gap transients.

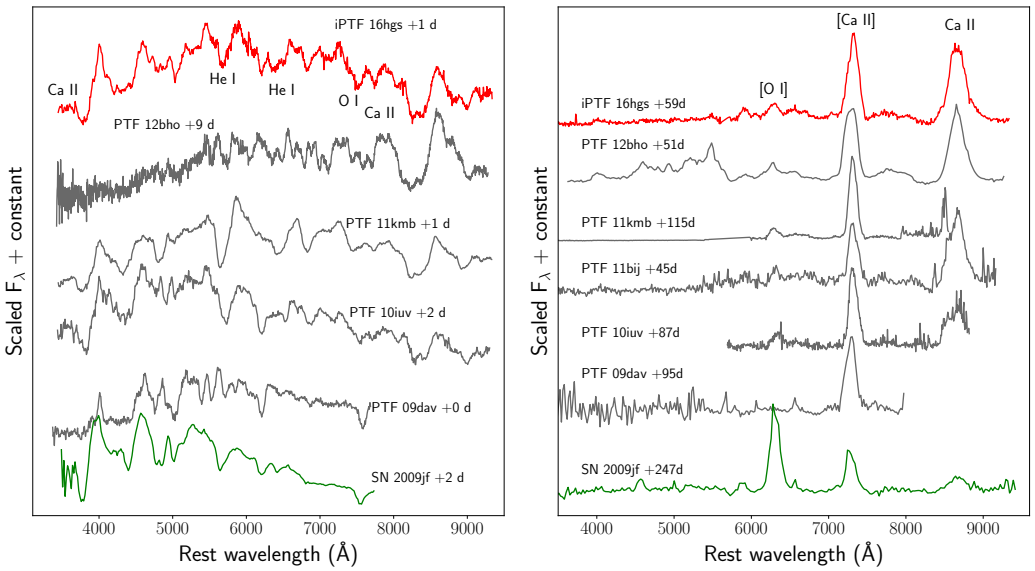

Figure 5.7: **Comparison of the spectra of iPTF 16hgs to that of other Ca-rich gap transients** – PTF 09dav, PTF 10iuv, PTF 11bij (Kasliwal et al., 2012), and PTF 11kmb and PTF 12bho (Lunnan et al., 2017). We also show photospheric and nebular phase spectra of the normal Type Ib SN 2009jf (in green; from Valenti et al., 2011) for comparison.

5.4 Modeling the double-peaked light curve

Bolometric light curve

We begin our modeling by constructing a bolometric light curve for the transient. For epochs where we have contemporaneous photometry in gri bands, we compute a pseudo-bolometric luminosity by performing a trapezoidal integration of the multi-color fluxes till the edges of the g and i band. In order to account for additional flux below 4000 Å and above 8000 Å, we use the peak photospheric spectrum (at +0.72 days) to determine the fraction of flux missed between 3000 Å and 10000 Å. We find that the gri trapezoidal integration misses 23% of the total flux, and hence we scale all the photospheric phase fluxes by a factor of 1.3. We also add a 5% uncertainty to the computed luminosities to account for potential uncertainties

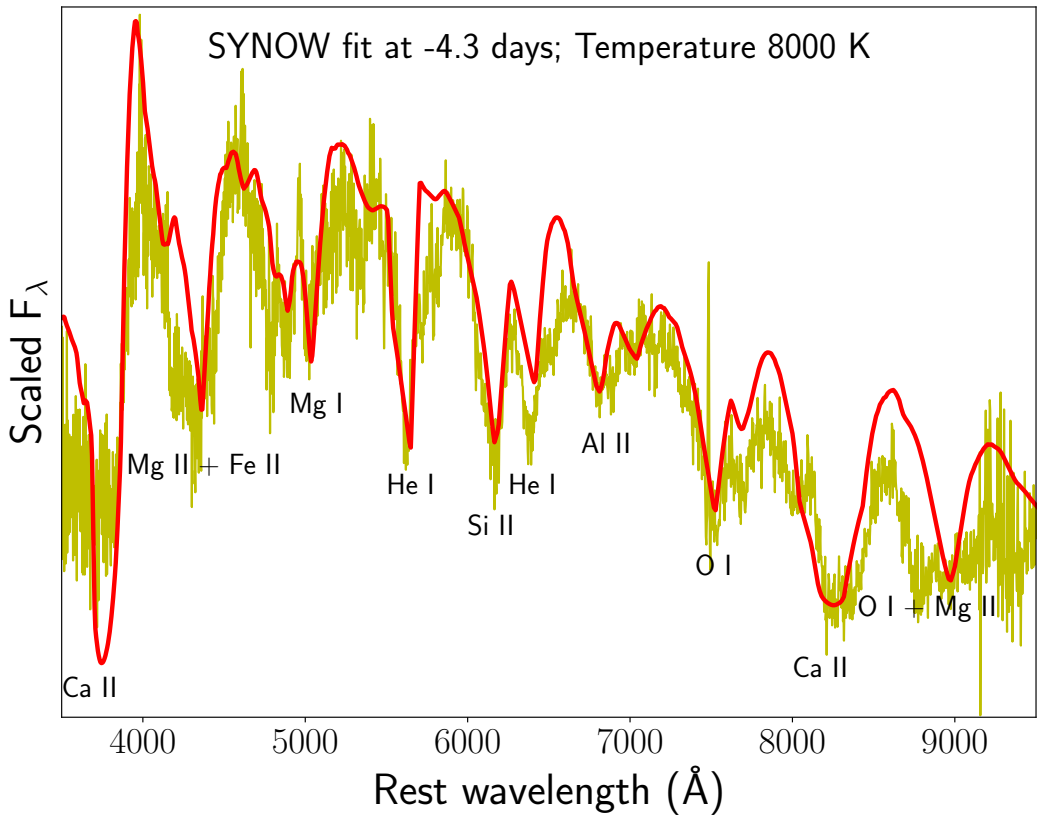

Figure 5.8: **Identification of spectral lines in the** −4.28 **days spectrum of iPTF 16hgs using SYNOW.** The yellow line indicates the observed spectrum while the red line indicates the SYNOW fit. The elements corresponding to the absorption features are marked.

in the fraction of flux missed.

Although the bolometric luminosity for the first peak is important to understand its origin, we do not have photometry in *i* band for the early peak. Hence, we use the only spectrum taken within the early decline (at −8.06 days) to find the fraction of flux missed between 3500 Å and 8000 Å in a *gr* trapezoidal flux estimate (≈ 33%), and scale all the *gr* trapezoidal fluxes within the first peak. Lastly, we have one epoch of contemporaneous *ri* detection at ≈ +35 days. For this epoch, we use the +28 d spectrum to similarly estimate the fraction of flux missed between 3000 Å and 10000 Å (≈ 50%), and scale the *ri* trapezoidal luminosity to account for it. Note that the pseudo-bolometric luminosity estimates above are strict lower limits on the total bolometric luminosity from the source.

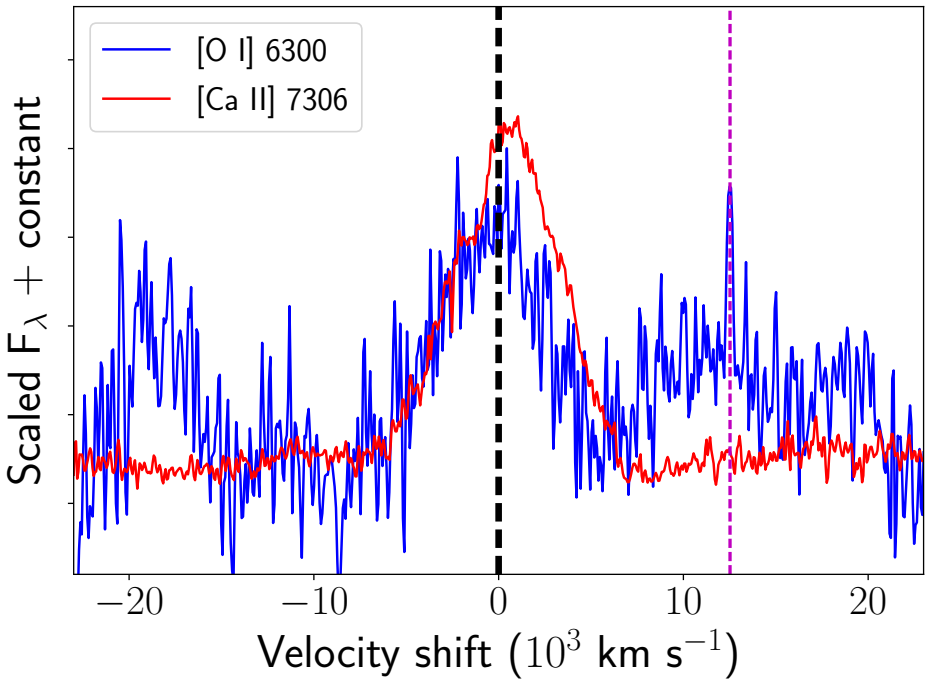

Figure 5.9: **Velocity profiles of the late-time nebular [Ca II]$\lambda\lambda$ 7291, 7324 (red) and [O I]$\lambda\lambda$ 6300, 6364 (blue) lines in iPTF 16hgs.** There is clear evidence of a narrow galaxy Hα feature red-wards of the [O I] feature (marked with the magenta dashed line), along with an underlying broader feature. The broad nebular feature blue-wards of the [O I] line is likely from He.

The bolometric light curve thus obtained is shown in Figure 5.10, clearly exhibiting a rapidly declining and relatively luminous early peak, followed by a rise to a second (main) peak and subsequent decline. The main peak reaches a peak bolometric luminosity of $\approx 3 \times 10^{41}$ ergs s^{-1}, while the peak luminosity for the first component was at least $\approx 4 \times 10^{41}$ ergs s^{-1}. The last photometric data point around 30 days after r-band peak indicates that the source faded to $\lesssim 4 \times 10^{40}$ ergs s^{-1} by this epoch.

Radioactively powered main peak

We first try to understand the power source for the main peak of the light curve. Since the main peak is very similar to that observed in other Ca-rich gap transients, we consider a radioactively powered light curve for the main peak. We fit a simple Arnett model to the bolometric light curve assuming that the decay of ^{56}Ni powers the main peak of the light curve. Note that the Arnett model has several simplifications, including that of homologous expansion, spherical symmetry, constant opacity, and centrally located ^{56}Ni in the ejecta. We do not include data points

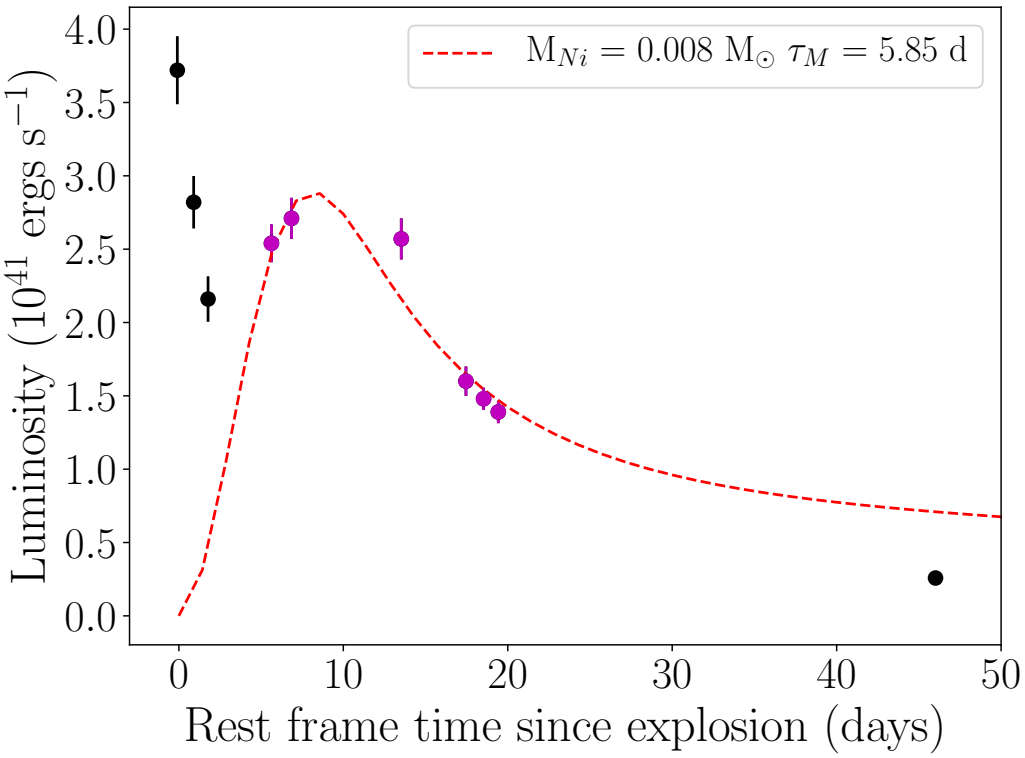

Figure 5.10: **Pseudo-bolometric light curve of iPTF 16hgs (as described in the text) along with a Arnett model fit to the main peak (red dashed line).** Only the magenta colored points were used in the Arnett model fitting. The best-fit ^{56}Ni mass and diffusion time τ_M are shown.

within the first peak (at < -5 days from r-band maximum), as well as the last data point since the Arnett model is only valid in the optically thick photospheric phase.

We use the analytic relations presented in Lyman et al., 2016a and Valenti et al., 2014 for this fitting, for which the only free parameters are the diffusion time through the ejecta τ_M and the Ni mass M_{Ni}. Keeping the explosion time as an additional free parameter, we get the best fit Arnett model as shown by the red dashed line in Figure 5.10. As shown, the model reasonably reproduces the bolometric evolution of the main peak, although there are clear discrepancies near peak light. This is not unexpected, as the Arnett model is very simplified, for instance, it ignores potential effects of ^{56}Ni mixing in the outer layers of the ejecta, that can significantly affect the rise of the light curve. The best-fit model indicates a ^{56}Ni Mass of 8×10^{-3} M$_\odot$ and diffusion time of ≈ 5.9 days. The best-fit explosion time is 9.96 days before r-band peak, which is very close to our initial estimate based on the t^2 law fitting to

the r band light curve.

We note that the last luminosity estimate from $\approx$ 45 days after the explosion is clearly much fainter than the predicted Arnett model luminosity. This is expected, as γ-ray trapping is likely to be inefficient at these late phases given the low ejecta mass, and hence the Arnett model is not applicable at late times (Valenti et al., 2014). Using an optical opacity of $\kappa = 0.07$ cm^2 g^{-1} (Cano, 2013; Taddia et al., 2018) and ejecta velocity of 10,000 km s^{-1} for the second peak, we derive an ejecta mass of 0.38 M$_\odot$ and explosion kinetic energy of $\approx 2.3 \times 10^{50}$ ergs. Note that these estimates do not include the (yet) unknown power source of the first peak, which is clearly not consistent with the Arnett model presented here. Given that such an early emission component has never been observed in Ca-rich gap transients, we discuss several potential power sources for the first peak in the following sections.

Radioactively powered first peak

Since the second peak of the light curve peak of iPTF 16hgs can be well understood by radioactive decay, we first consider a radioactively powered scenario for the first peak. In this case, the shape of the early emission with respect to the main peak puts strong constraints on the radial distribution of the radioactive material. Dessart et al., 2012 and Piro et al., 2016 show that a radial monotonically decreasing distribution of ^{56}Ni in the ejecta lead to smoothly rising light curves for radioactively powered Type Ib/c SNe. As the early decline in iPTF 16hgs is distinctly separated from the main peak, it is likely that the relevant radioactive isotope was strongly mixed into the surface of the progenitor, and separated from the radioactive material powering the second peak.

We can obtain approximate estimates for the amount of radioactive material, and the ejecta mass above it by analyzing the early bolometric light curve. Taking the peak luminosity of the first peak to be $> 4 \times 10^{41}$ ergs s^{-1}, we estimate that $\gtrsim 7 \times 10^{-3}$ M$_\odot$ of ^{56}Ni in the outer layers would be required if the early component was powered by ^{56}Ni decay. However, we do not have strong constraints on the rise time of the first peak since the transient was discovered on the early declining phase. Given that the Arnett model fitting of the main peak suggests that the explosion occured at $\approx$ 10 days before the r band peak (which is almost at the epoch when the transient

was first discovered), we consider the case where the observed width of the first component of ≈ 2 days corresponds to the diffusion time through the ejecta above this radioactive layer. In such a case, the mass above this layer would be $\gtrsim 0.05$ $M_\odot$ taking an opacity of $\kappa = 0.07$ cm^2 g^{-1} and ejecta velocity of 12,000 km s^{-1} (as measured from the first spectrum of the source).

We note that the derived ^{56}Ni estimates are similar to that of some other Type Ib/c SNe with early excess blue emission (Bersten et al., 2013; Drout et al., 2016), and where a radioactivity powered first peak was also suggested. Alternatively, it is possible that the first peak is powered by the decay of other radioactive species. For instance, modeling of He shell detonations in the context of faint and fast evolving SNe by Waldman et al., 2011 and Sim et al., 2012 show that radioactive isotopes like ^{48}Cr, ^{52}Fe, and ^{44}Ti can be important in powering the light curves of these events, particularly at early times for short-lived isotopes such as ^{52}Fe.

Interaction with a companion

A possible explanation for the early peak could be due to interaction of the SN ejecta with a non-degenerate companion (Kasen, 2010). Such interaction signatures depend sensitively on the binary separation of the companion as well as the viewing angle of the observer, with the most prominent signatures arising when the source is viewed along the direction of the companion. These signatures have been previously suggested in Type Ia SNe (e.g. Cao et al., 2015a; Hosseinzadeh et al., 2017), allowing one to estimate the separation of the companion and its radius (assuming Roche lobe overflow). For viewing angles oriented close to the direction of the companion, the analytic equations in Kasen, 2010 yield good estimates of the expected emission.

We attempted to fit the early g and r band light curves with the Kasen, 2010 models, but could not get a reasonable match to the data. This is particularly because the colors of iPTF 16hgs on the declining phase are markedly different than that predicted in the companion interaction models. For instance, we observe colors of $g - r \approx 0$ about one day after discovery when the bolometric luminosity is $\gtrsim 2.5 \times 10^{41}$ ergs. Taking equation (22) in Kasen, 2010 for $t_{day} = 1$, $v_9 = 1.2$, and $M_c = 0.3$, the bolometric luminosity requires the separation a to be $\gtrsim 2.5 \times 10^{11}$ cm. At the same time, the $g - r$ color suggests that the color temperature of the emission is ~ 5500

K assuming a blackbody spectrum, which gives $a \sim 2.4 \times 10^{10}$ cm using equation Kasen's equation (25). Note that this result is insensitive to the exact epoch of this observation since the model luminosity and temperature scale similarly ($\propto t^{-1/2}$) with time after explosion.

Hence, we find that a companion interaction scenario is unable to account for the early declining emission within the framework of the analytic equations presented in Kasen, 2010. However, we note that viewing angle dependencies may affect our conclusions. For example, Figure 2 in Kasen, 2010 shows that both the peak luminosity and morphology of the companion interaction light curve may be significantly affected along lines of sight away from the companion. In fact, the early drop of a factor of ≈ 1.7 in luminosity over the first 2 days in iPTF 16hgs is indeed reminiscent of the bolometric evolution predicted along directions $\sim 90^{\circ}$ to the companion, as shown in Kasen, 2010. As the simulations with varying viewing angles (in Kasen, 2010) were specifically for Type Ia SN ejecta, future modeling will be required to understand if these signatures would be similar in ejecta with different compositions as in iPTF 16hgs.

Interaction with circumstellar material

We now consider if interaction with dense external circumstellar material (CSM) can explain the early blue emission in iPTF 16hgs. Given the projected location of iPTF 16hgs inside its host galaxy (and hence its likely proximity to dense CSM), such a scenario can potentially explain the uniqueness of the light curve of iPTF 16hgs with respect to the other members of this class. We can obtain rough estimates of the characteristics of this CSM by using the early bolometric light curve and the methods presented in Smith, 2016. The interaction luminosity can be estimated using,

$$L = \frac{1}{2} 4\pi R^2 \rho V^3 \tag{5.1}$$

which depends on the velocity of the ejecta material V and the density of the medium ρ.

Assuming a constant density CSM, and using $L \gtrsim 3 \times 10^{41}$ ergs s^{-1}, $V \sim 12000$ km s^{-1} at $t \sim 1$ day after the explosion, we find $\rho \sim 3 \times 10^{-15}$ g cm^{-3}. This corresponds to a particle density of 5×10^{8} cm^{-3} if the CSM was dominated by He at a

distance of $\sim 10^{14}$ cm from the progenitor. Instead, if we assume a constant mass loss wind like CSM density profile, using the same values as above, we estimate a $\dot{M} \sim 7 \times 10^{-5} \frac{v_{CSM}}{100\,\mathrm{km/s}}$ $\mathrm{M}_\odot$ yr^{-1}. However, we note that there is no evidence for spectral signatures of circumstellar interaction (as seen in Type IIn and Type Ibn SNe) in iPTF 16hgs, which would argue against a CSM interaction scenario. Nevertheless, such signatures may be hidden in the case of asymmetric CSM configurations (e.g. in the form of a disk) where the interaction region is hidden by the expanding ejecta (Smith, 2016).

Shock cooling of an extended progenitor

The double peaked light curves of some stripped envelope core-collapse SNe have been explained using shock cooling emission of an extended envelope around the progenitor. Such extended envelopes have been shown to be particularly relevant for sources that exhibit an early peak in the redder r and i bands, since 'normal' progenitors (i.e. progenitors without an extended envelope) cannot reproduce such light curves (Nakar et al., 2014; Piro, 2015; Sapir et al., 2017). Since iPTF 16hgs was found in a star forming host galaxy (indicating a core-collapse supernova origin is a possibility given the presence of a young stellar population), we examine if the early declining emission (which was detected in g and r bands) can be explained by shock cooling emission of an extended progenitor.

We use the extended envelope models of Piro, 2015 to fit the first peak of iPTF 16hgs. Adopting the ejecta mass and explosion energy as derived in the Arnett model and an optical opacity of $\kappa = 0.2$ cm^2 g^{-1}, the only other free parameters in the model are the mass in the extended envelope M_e and the radius of the envelope R_e. Keeping the explosion time t_0 as an additional free parameter, we obtain the best-fit model as shown in Figure 5.11. As shown, an extended envelope model with $M_e = 0.08$ $\mathrm{M}_\odot$ and $R_e = 13.0$ $\mathrm{R}_\odot$ is able to well reproduce the early peak for an explosion time $t_0 = -12.7$ days before the main peak of the r band light curve. Although the model used here is very simplified in that it ignores the crucial density structure of the envelope, the numbers derived are expected to be correct to an order of magnitude (as shown in more realistic simulations including density profiles; Piro et al., 2017).

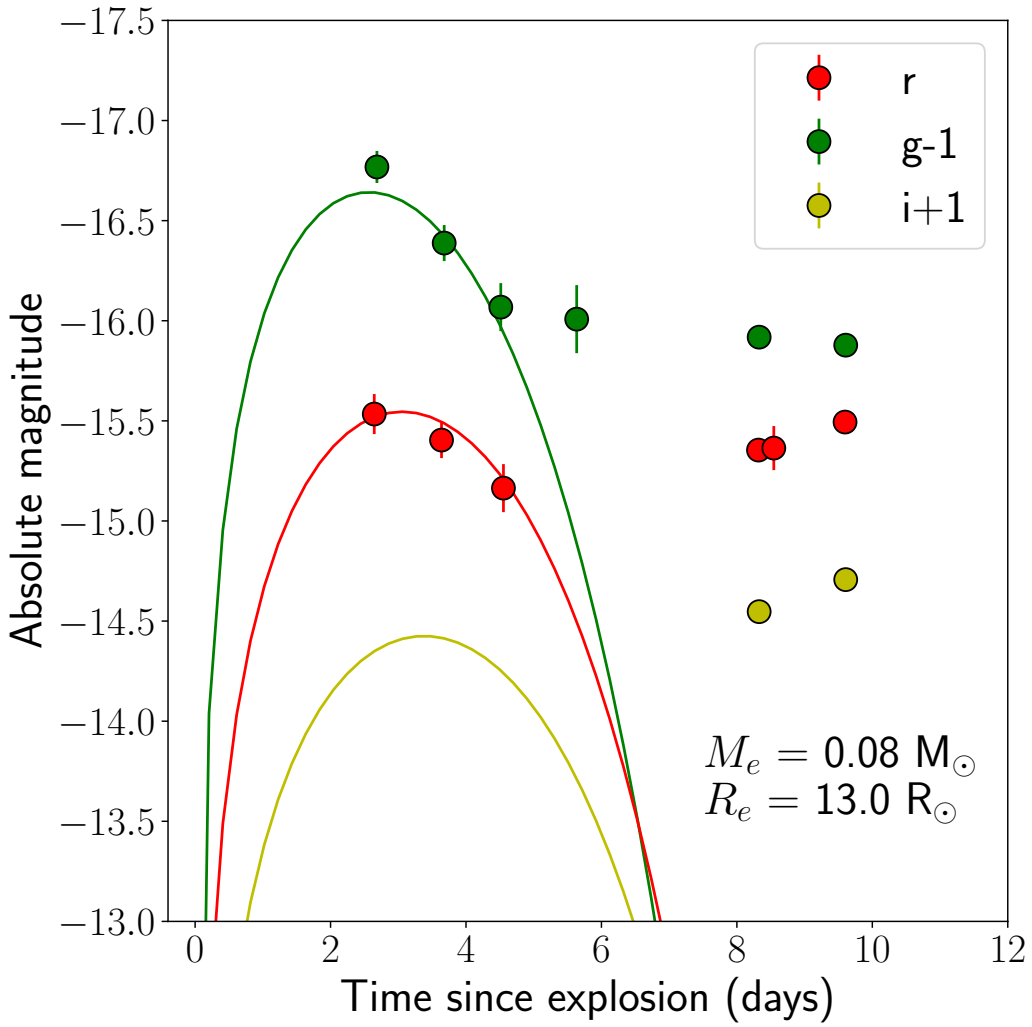

Figure 5.11: **The early light curve of iPTF 16hgs fit with a shock cooling model of an extended envelope**, as presented in Piro, 2015. The best-fit model indicates an extended mass of $M_e = 0.08\ \mathrm{M}_\odot$, $R_e = 13.0\ \mathrm{R}_\odot$, and explosion time of 12.7 days before the main peak of the r band light curve.

5.5 Constraints on radio emission

Although the progenitors for Ca-rich gap transients remain elusive, we expect a number of proposed progenitor channels to be associated with potentially bright radio counterparts if the explosion took place in a dense CSM. For example, radio emission from core-collapse and thermonuclear SNe can arise from synchrotron radiation produced by electrons accelerated in the forward shock of the SN explosion (Chevalier, 1998). On the other hand, if Ca-rich gap transients are associated with tidal disruptions of WDs, one would expect bright radio emission arising from the interaction of a relativistic collimated jet or a fast wind outflow with the surrounding CSM (MacLeod et al., 2016; Margalit et al., 2016; Metzger, 2012).

However, their preference for remote locations far away from their host galaxies suggest that they also explode in likely low CSM density environments where such radio emission would be easily suppressed. Given its location close to its host galaxy (and thus potentially in a dense ISM environment), iPTF 16hgs is thus useful to constrain models that predict significant radio emission from these transients. We thus use our radio limits to constrain models of radio emission associated with both spherical SN shocks as well as afterglows expected with collimated jet-like outflows in tidal disruption events.

Radio emission from a spherical shock

We use the synchrotron self-absorption model of Chevalier, 1998 to generate analytic radio light curves for a range of circumstellar environments. We follow the prescription given in Chomiuk et al., 2016, who present analytic equations for the expected radio light curves of Type Ia SNe based on Chevalier, 1998 (but are also applicable to other hydrogen-poor SNe). We generate these light curves for both a constant wind mass loss environment (where $\rho = Kr^{-2}$, with $K = \frac{\dot{M}}{4\pi v_w}$) and a constant density environment (ρ = constant), using an outer ejecta density profile of $\rho \propto r^{-10}$, as appropriate for compact progenitor stars (Matzner et al., 1999). By comparing the predicted radio light curves to those of our upper limits, we constrain the wind mass loss parameter K and the external circumstellar density n_0 by obtaining the limiting cases for a 3σ detection, as shown in Figure 5.12.

In the case of a wind mass loss environment, the strongest constraints arise from

the VLA (10 GHz) and uGMRT (1.2 GHz) observations, which we use to constrain the mass loss rate to $\dot{M} \lesssim 2 \times 10^{-6} \frac{v_w}{100\mathrm{km/s}}$ $\mathrm{M}_\odot$ yr^{-1} for $\epsilon_B = 0.1$. Adopting $\epsilon_B = 0.01$, the VLA and uGMRT observations constrain the mass loss rate to $\dot{M} \lesssim 8 \times 10^{-6} \frac{v_w}{100\mathrm{km/s}}$ $\mathrm{M}_\odot$ yr^{-1}. For the case of a constant density environment, the strongest constraints arise from the uGMRT observations, which limit the circumstellar density to $n_0 \lesssim 125$ cm^{-3} for $\epsilon_B = 0.1$, and to $n_0 \lesssim 800$ cm^{-3} for $\epsilon_B = 0.01$.

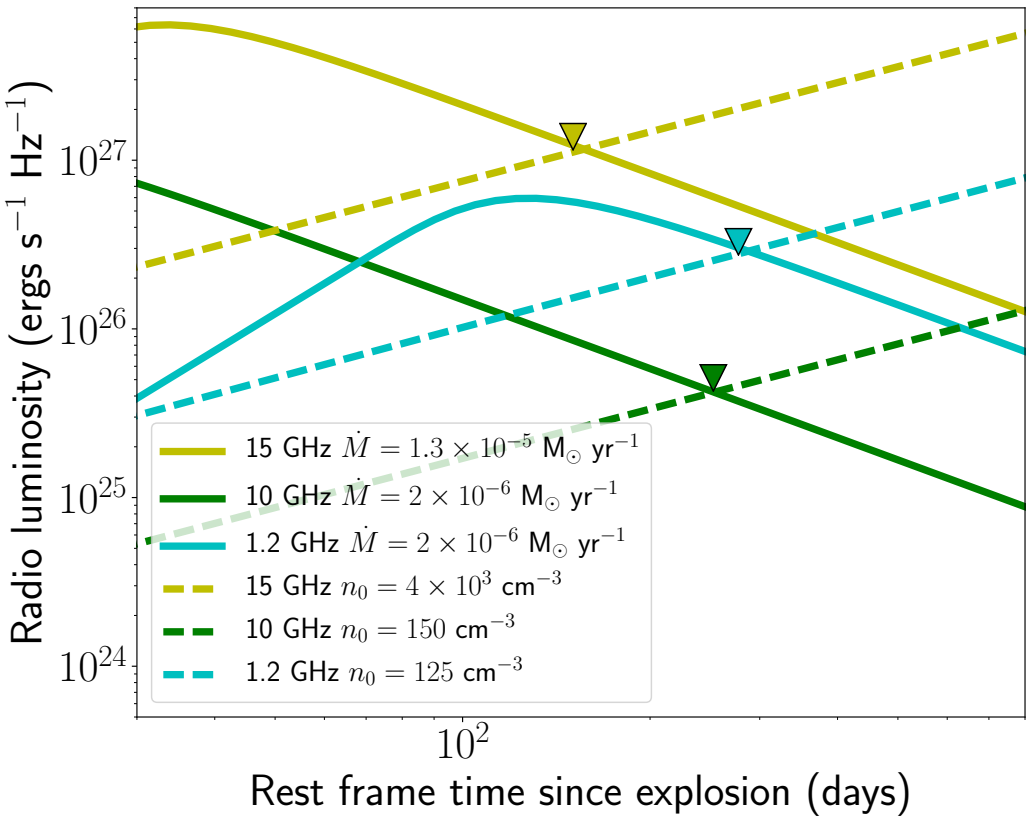

Figure 5.12: **Model radio light curves compared with radio limits on iPTF 16hgs.** The solid lines correspond to the limiting models consistent with the radio non-detections, for a wind-like CSM density profile ($\rho \propto r^{-2}$) at 15 GHz (yellow), 10 GHz (green), and 1.2 GHz (cyan), respectively. The corresponding limiting mass loss rates for $\epsilon_B = 0.1$ and $v_w = 100$ km s^{-1} are indicated in the legend. If we adopt $\epsilon_B = 0.01$ instead, the limiting mass loss rates are $5.5 \times 10^{-5} \frac{v_w}{100\mathrm{km/s}}$ $\mathrm{M}_\odot$ yr^{-1}, $8 \times 10^{-6} \frac{v_w}{100\mathrm{km/s}}$ $\mathrm{M}_\odot$ yr^{-1}, and $8 \times 10^{-6} \frac{v_w}{100\mathrm{km/s}}$ $\mathrm{M}_\odot$ yr^{-1} for the AMI, VLA, and uGMRT observations, respectively. The dashed lines (with the same color coding) indicate the light curve models for a constant density environment, with $\epsilon_B = 0.1$. The corresponding limiting densities for $\epsilon_B = 0.01$ are $n_0 \lesssim 2.5 \times 10^4$ cm^{-3}, $n_0 \lesssim 10^3$ cm^{-3}, and $n_0 \lesssim 8 \times 10^2$ cm^{-3} for the AMI, VLA, and uGMRT observations respectively.

Radio emission from a relativistic jet

Sell et al., 2015 proposed that Ca-rich gap transients could arise from tidal disruptions of low mass He WDs by intermediate mass black holes, based on the work of Rosswog et al., 2009 (see also Rosswog et al., 2008; MacLeod et al., 2014). In this scenario, when a low mass WD comes within the tidal radius of a massive compact object (with a mass of $\lesssim 10^5$ $M_\odot$), the WD is tidally crushed leading to a runaway thermonuclear detonation powering an optical transient. The accretion of the WD on to the compact object would then also power a super-Eddington X-ray flare, potentially leading to the launch of a relativistic jet (MacLeod et al., 2016; Sell et al., 2015). One direct prediction of such a model is that these transients should then also be associated with prominent X-ray and radio emission for suitably oriented observing angles.

MacLeod et al., 2016 presented simulations of disruptions of 0.6 $M_\odot$ WDs by an intermediate mass black hole, including predictions for expected light curves and spectra of the thermonuclear transient. They show that the disruption of the WD together with the explosive detonation leads to less than half of the WD mass being accreted on to the BH. They also predict several characteristics of the radio emission that would be expected if these events produced relativistic jets that eventually interact with the surrounding interstellar medium (ISM). We thus use our deep radio limits on iPTF 16hgs to constrain the phase space of jet energy and ISM density for different viewing angles of the observer.

The super-Eddington flare of accretion in such a disruption event can lead to the launching of a relativistic jet that carries away some fracion of the rest mass energy of the accreted WD (MacLeod et al., 2016). We thus consider a range of jet energies from 10^{47} ergs to 2×10^{51} ergs. If the disruption event in iPTF 16hgs involved a 0.4 $M_\odot$ He WD (as expected from the He-rich spectra), the range of jet energies corresponds to a fraction of $\sim 10^{-6} - 10^{-2}$ of the rest mass energy of the accreted half of the WD. We then use the `BOXFIT` code (van Eerten et al., 2010) to generate simulated multi-frequency radio light curves for different surrounding ISM densities (in the range between $10^{-6} - 1$ cm^{-3}). As suggested in MacLeod et al., 2016, we also assume that the jet has an initial starting Lorentz factor of $\Gamma \sim 10$ and an opening angle of 0.2 rad (i.e. a jet beaming factor of 0.02).

We show the contour plots (in the phase space of jet energy and circumstellar density) of the expected radio fluxes at the epochs of the VLA and GMRT observations for different viewing angles, together with our limits on the radio emission of this source in Figure 5.13. In each of the panels, the phase space ruled out by our observations are indicated by the hatched region. There are several interesting factors to note from the allowed phase space. First, for a nearly along the line of sight jet ($\approx 10^{\circ}$), the GMRT upper limits completely rule out jet energies higher than about 10^{49} ergs for ISM densities as low as 10^{-6} cm^{-3}. Note that the critical density of the universe is $\sim 10^{-6}$ cm^{-3} while the electron density inside the host galaxy should be at least an order of magnitude larger, ruling out the on-axis case completely. For a viewing angle of 45°, the GMRT and VLA upper limits together rule out ISM densities $\sim 10^{-4}$ cm^{-3} if the jet energy is larger than 10^{49} ergs. For lower jet energies, our radio limits do not constrain the ISM environment since the limits lie above the optically thick locus of the light curves. Lastly, for a 90° observing angle, the radio limits are least constraining, but nevertheless rule out ISM densities $\sim 10^{-2}$ cm^{-3} if the jet energy was larger than about 5×10^{48} ergs, but are not constraining if the jet energy was lower.

5.6 The host galaxy of iPTF 16hgs

The host environment and location of iPTF 16hgs is interesting in the context of Ca-rich gap transients for a number of reasons. First, it is only the second Ca-rich gap transient after PTF 09dav to be found in a star forming spiral galaxy, as indicated by our spectrum of the host galaxy (Section 5.2). Apart from their preference for old environments, Ca-rich gap transients have also been noted for their large offsets from their host galaxies (Kasliwal et al., 2012; Lunnan et al., 2017; Perets et al., 2010; Yuan et al., 2013). Perets, 2014 suggest that the remote locations can be understood as an outcome of their association with old stellar populations, which reside primarily in the bulges and halos of their early type galaxy hosts. While biases against finding transients on bright galaxy backgrounds of early type hosts could explain their almost exclusive preference for remote locations in the outer halos of galaxies, the offsets appear to be intrinsic even after accounting for the detection biases of the PTF survey (Frohmaier et al., 2018; Frohmaier et al., 2017). Thus, it is interesting to note that iPTF 16hgs exhibits the smallest projected host offset of ≈ 5.9 kpc (≈ 1.9 R_{eff}) of all known Ca-rich gap transients, both in terms of physical and host-normalized offset.

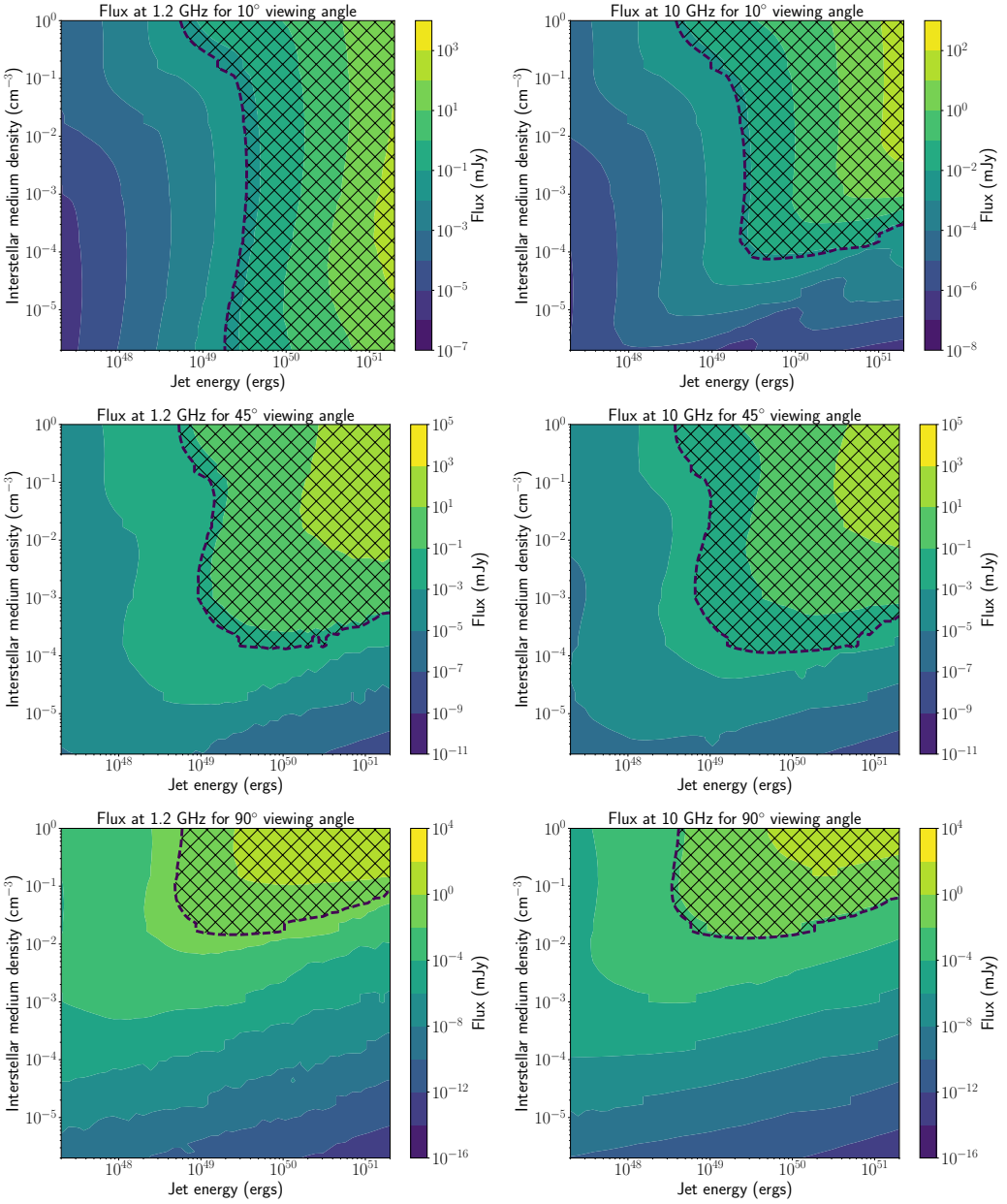

Figure 5.13: **Constrained parameter space for a collimated jet outflow in iPTF 16hgs (for different viewing angles), as suggested by the radio non-detection with the uGMRT and VLA at late times.** In each of the panels, we show a contour plot of the expected fluxes in the GMRT (1.2 GHz) and VLA (10 GHz) bands for a phase space of jet energy and ISM electron densities at a fixed observing angle (see text). The black dotted line in each panel shows the location of the 3σ radio upper limit on iPTF 16hgs. *Only the phase space with a lower flux than the dotted line in each panel is allowed by the observations.* The hatched region is ruled out by our observations under the assumptions of the jetted outflow model.

Lunnan et al., 2017 show that Ca-rich gap transients also show a preference for group and cluster environments, as 7 out the 8 transients reported thus far were found in galaxy clusters or groups. In order to test such a scenario for iPTF 16hgs, we searched NED for all galaxies within a projected offset of 1 Mpc from the host galaxy, and within a velocity of 3000 km s^{-1}, and found 9 such galaxies. 6 of these 9 galaxies had redshift within 500 km s^{-1} of the host galaxy of iPTF 16hgs, while an additional 3 galaxies were found to be clustered around a velocity offset of 2000 km s^{-1} from the transient host galaxy. The locations of these galaxies are shown in Figure 5.14, with yellow circles indicating the galaxies within 500 km s^{-1} of the transient host galaxy, while magenta circles indicate the group offset by 2000 km s^{-1}.

Since none of these galaxies were at close projected offsets (<10′) from the host galaxy of iPTF 16hgs, we undertook a spectroscopic mask observation of the region around the host galaxy with Keck LRIS to determine redshifts of nearby objects classified as galaxies in SDSS. The locations of the objects placed in the spectroscopic mask are shown in the lower panel of Figure 5.14, while the redshifts are reported in Table 5.4. As shown, only one of the objects ($Obj2$) selected was found to be at the same redshift as the host galaxy. Although $Obj2$ is classified as a galaxy in SDSS, it lies right on top of the disk of the host galaxy, and is more likely to be a star forming region in the host galaxy itself. We show the relative velocity distribution of the galaxy velocities of all objects found to be at the same redshift as iPTF 16hgs in the histogram in Figure 5.14. With a total of 6 – 10 objects (depending on whether the cluster at 2000 km s^{-1} is associated to the host galaxy group) at the same redshift, we conclude that iPTF 16hgs was located in a sparse galaxy group (Cox, 2000), consistent with other members of the class of Ca-rich gap transients.

Global properties of the host galaxy

We first estimate the gas phase metallicity of the host galaxy using the emission lines fluxes in the spectrum of its nucleus and the `pyMCZ` code (Bianco et al., 2016). The measured emission line fluxes are presented in Table 5.3. The code calculates the host oxygen metallicity, and is based on the original code of Kewley et al., 2002 with updates from Kewley et al., 2008. Typical metallicity estimates derived using this method indicate 12 + log(O/H) metallicity of $8.26^{+0.03}_{-0.03}$ on the O3N2 scale of Pettini

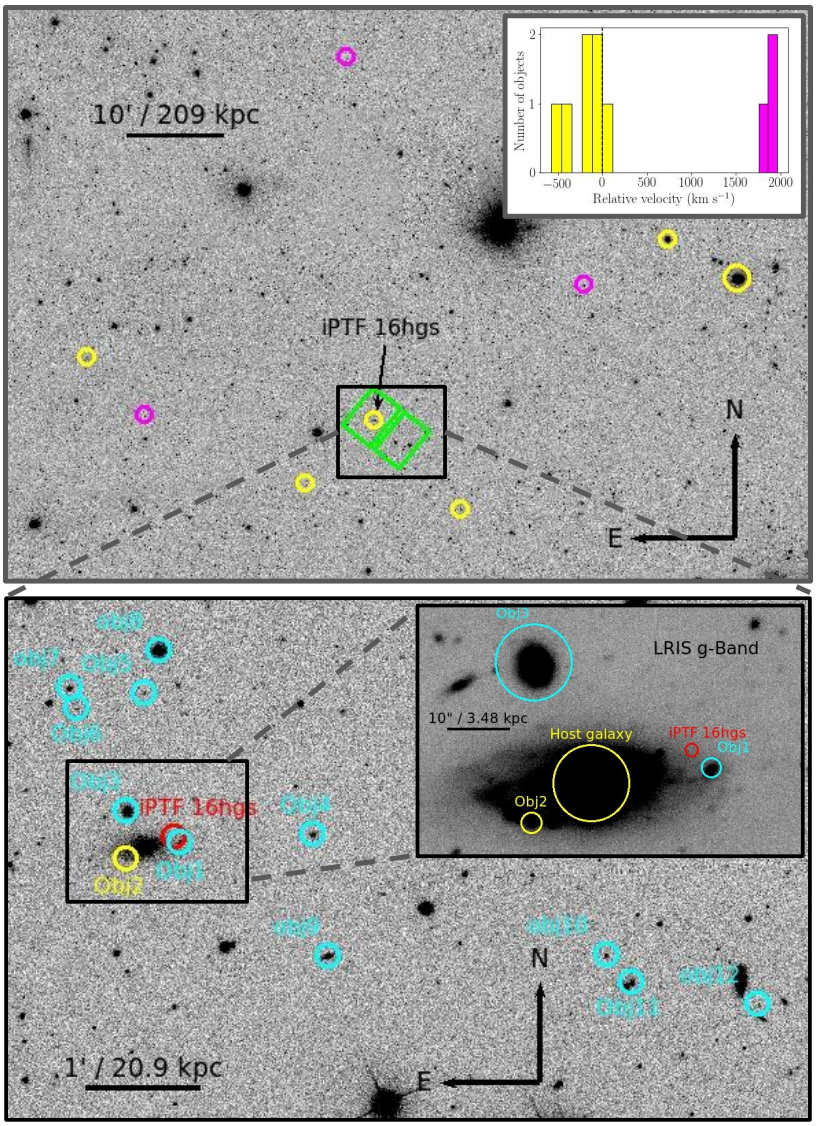

Figure 5.14: **Host environment of iPTF 16hgs.** (Top) SDSS r-band image of the host region, with yellow circles indicating galaxies confirmed to be at a redshift consistent with that of the transient, and within 1 Mpc from its host galaxy. The magenta circles show galaxies with marginally different redshifts but within $\sim$ 1800 km s^{-1} of the host galaxy. The green boxes indicate the field of the view of Keck LRIS during the spectroscopic mask observation. The inset shows the velocity histogram (with respect to the host galaxy) of the galaxies found at a similar redshift as that of the apparent host galaxy. (Bottom) Galaxies with redshifts identified in the spectroscopic mask observation (within the green boxes in the top panel). Only the host galaxy $Obj2$ was found to be at the same redshift as that of the transient in this region (marked in yellow), while all other galaxies were found to be background sources (marked in cyan). The red circle marks the location of the transient. The inset shows the Keck LRIS g band image of the host galaxy zoomed into the environment of the transient.

et al., 2004 and $8.21^{+0.02}_{-0.02}$ on the O3N2 scale of Marino et al., 2013. In general, we note that all the derived oxygen metallicity indicators suggest a significantly sub-solar metallicity (where $12 + \log(\mathrm{O/H})_\odot \approx 8.69$; Asplund et al., 2009) of ≈ 0.4 $Z_\odot$ ($Z \approx 0.008$) for the spectrum of the nucleus. The low metallicity estimate places the host galaxy in the lowest 10% of the distribution of host galaxy metallicities of Type Ib/c SNe, while it is on the lowest 30% of the range of the host galaxies of Type Ic-BL SNe (Sanders et al., 2012).

Next, we use the integrated fluxes of the host galaxy to estimate the global properties of the stellar population in the host galaxy of iPTF 16hgs. The photometric fluxes in the SDSS $ugriz$, 2MASS JHK, and GALEX FUV/NUV bands were fit using the `FAST` code (Kriek et al., 2009). The fitting was performed assuming a Maraston, 2005 stellar population, an exponentially declining star formation history, a Salpeter IMF, and a Milky Way like extinction law. We also constrain the models to be at a sub-solar metallicity (as indicated by the spectra of the host galaxy) of $Z = 0.01$ (0.5 $Z_\odot$), which is the model grid closest to the inferred metallicity.

Using this model, we obtain a best-fit stellar mass of $6.45^{+0.31}_{-0.29} \times 10^8$ $M_\odot$, mean stellar population age of $1.99^{+0.05}_{-0.17} \times 10^8$ years. The integrated star formation rate is poorly constrained from the photometry only, and hence we estimate it from the Hα maps in our IFU observations (see Section 5.6). Integrating the Hα flux over the entire map where Hα emission is detected, we find a total Hα flux of $\approx 10^{-13}$ ergs cm^{-2} s^{-1}. Converting this to an equivalent star formation rate using the redshift of the host galaxy (total Hα luminosity of $\approx 6.5 \times 10^{40}$ ergs s^{-1}) and the relations in Kennicutt, 1998, we get an integrated star formation rate of 0.5 $M_\odot$ yr^{-1}, placing this galaxy in the lower half of the distribution of star formation rates found in the hosts of stripped envelope SNe (Galbany et al., 2014).

We also use our Keck-LRIS spectrum of the nucleus of the host galaxy to estimate the stellar age and stellar phase metallicity of the older stellar populations in the galaxy. Similar to the analysis presented in Galbany et al., 2016, we fit the stellar continuum and absorption features in the host nucleus spectrum using the STARLIGHT code (Cid Fernandes et al., 2005). Using a Cardelli et al., 1989 dust extinction law and Bruzual et al., 2003 stellar population models at a range of metallicities (from Z = 0.001 to Z = 0.05), we find the best-fit spectrum as shown in Figure 5.15. The

insets in Figure 5.15 also show the best-fit stellar population mixture computed by STARLIGHT. As shown, the stellar continuum is well fit by a mixture of both old (age $\gtrsim$ 1 Gyr) and young (age $\lesssim$ 0.5 Gyr) stellar populations, where > 65 % of the stellar population in the STARLIGHT fit is in the former category.

In terms of metallicity, more than 70% of the stellar population in the best STARLIGHT fit is at a sub-solar metallicity ($Z < 0.02$), with $\approx$ 50 % of the population at $Z < 0.001$. Note that the stellar metallicity reflects the galaxy metallicity when the stars were formed (which is likely to be lower than the current metallicity), while the emission line based estimates reflect the current gas-phase metallicity in the galaxy. Weighting over the entire population mixture produced by the model, we find a mean stellar age of 7.2×10^8 yrs and a mean stellar metallicity of $Z = 0.012$. Thus, the mean stellar age estimated from the nuclear spectrum is older than that inferred for the whole galaxy from the broadband photometry, while the mean stellar metallicity is similar to the gas phase metallicity estimated from the emission line fluxes in the nuclear spectrum. Taken together, we conclude that the host galaxy of iPTF 16hgs is a metal-poor, star forming dwarf galaxy with a mixture of both young and old stellar populations.

Spatially resolved properties of the host galaxy

Due to its small offset from its host galaxy, we obtained IFU observations of the host galaxy with the PCWI to study the spatially resolved ISM of the host galaxy, and in particular, the local ISM environment of iPTF 16hgs. For each pixel in the reduced and stacked spectral cube from the PCWI, we modeled the continuum emission using a low degree polynomial, and subtracted it to measure the emission line fluxes of the most prominent lines from the host galaxy. The lines that were within the spectral cube include Hα, [N II] λ6584, [S II] λ6716, and λ6731. For the strongest Hα emission line, we also measure the velocity by fitting a Gaussian profile to the continuum subtracted Hα feature, its equivalent width, and full width at half maximum (FWHM). The resulting maps are shown in Figure 5.16. For comparison, we also show a continuum image of the host galaxy, as obtained from the late-time LRIS observation in Figure 5.16.

A few features are readily apparent from the maps in Figure 5.16. iPTF 16hgs occurred in a star forming spiral galaxy, as indicated by the morphology of the galaxy

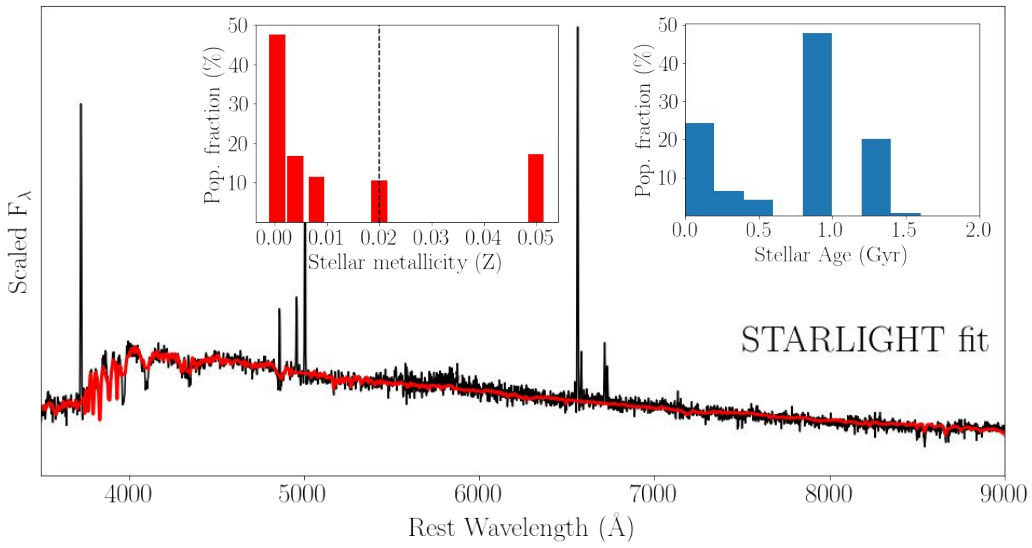

Figure 5.15: **The stellar continuum and absorption line spectrum of the nucleus of the host galaxy of iPTF 16hgs fit with the STARLIGHT code** (Cid Fernandes et al., 2005). The black line is the raw spectrum while the red line is the best-fit star light model. The histograms in the inset panels show the stellar population mixtures (in terms of age and metallicity) found in the best-fit model. As shown, the stellar continuum suggests a mixture of both old (age $\gtrsim$ 1 Gyr) and young (age $\lesssim$ 0.5 Gyr) stellar populations in the host galaxy. The majority of the stellar population is found to be at a sub-solar metallicity (solar metallicity is indicated by the dashed line in the metallicity panel), consistent with the low metallicity inferred from the emission line spectrum.

in the continuum image and the prominent Hα emission extending through out the image. The multiple blobs of Hα emission are likely to be individual H-II regions in the disk of the galaxy. The Hα velocity map clearly shows evidence of ordered rotation of the spiral arms of the galaxy (reaching a velocity of $\approx$ 100 km s^{-1} near the edges) such that the location of iPTF 16hgs is on the receding arm of the galaxy that is viewed close to the plane of the disk. In particular, we note that the object $Obj2$ in the spectroscopic mask (that was classified as a separate galaxy in SDSS) is consistent with being an individual H-II region in the host galaxy given that its velocity lies exactly on the rotation curve of the host.

The Hα equivalent width (EW) map also shows regions of very high EW ($\gtrsim$ 100 Å), suggestive of very young stellar populations in the host galaxy. The metal emission lines of S and N are significantly weaker than the bright Hα emission (as would be

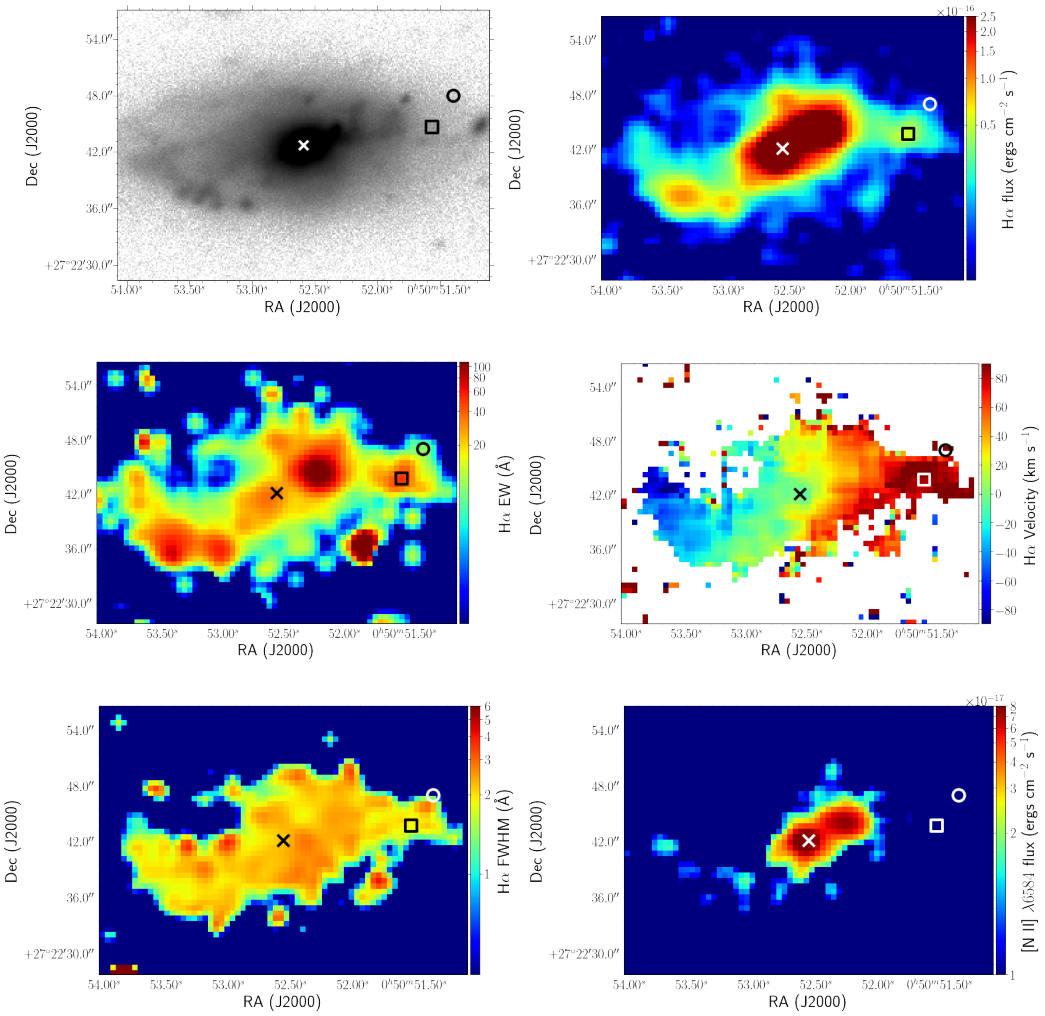

Figure 5.16: **Emission maps obtained from the late-time observations of the host galaxy of iPTF 16hgs.** (Top: left) Late time LRIS g-band image of the host galaxy of iPTF 16hgs. (Top: right) Hα flux map of the host galaxy. (Middle: left) Hα equivalent width (EW) map of the host galaxy. (Middle: right) Hα velocity map (with respect to the systemic velocity of the host galaxy). The rotation of the spiral galaxy is clearly visible. (Botttom: left) Map of the Full Width at Half Maximum (FWHM) of the Hα line over the galaxy. (Bottom: right) [N II] λ6584 flux map of the host galaxy. (see text). In each of the panels, the cross denotes the cataloged position of the center of the host galaxy, the circle denotes the location of the transient, and the square denotes the location of the nearest H-II region to the location of the transient.

expected from a metal-poor galaxy), and are thus detected only near the nucleus, and along the plane of the galaxy. In particular, we note that the metal emission line maps show evidence of bright emission regions co-located with the bright blobs of Hα emission near the nucleus of the host galaxy.

Star formation density

We use the Hα flux map from our observations to measure the equivalent star formation surface density using the relations in Kennicutt, 1998. Since the galaxy is viewed nearly edge on, we caution that the star formation density will be subject to a projection effect. Nevertheless, we show the spatially resolved star formation density in Figure 5.17. As shown, the host galaxy of iPTF 16hgs exhibits multiple prominent blobs of star formation, reaching surface densities $\gtrsim 0.1$ $M_\odot$ yr^{-1} kpc^{-2}. Interestingly, there is evidence for outlying H-II regions in the host galaxy, as evidenced by the bright Hα emission blob located to the south-west of the nucleus, which is very faint in the continuum image (and hence has a very high EW). Given that this blob lies on the rotation curve of the galaxy, it likely represents a very young star forming H-II region as opposed to a companion dwarf galaxy. Additionally, there is clear evidence of a large star forming region close to the location of iPTF 16hgs, at a projected offset of $\approx 3''$($\approx$ 1 kpc at the redshift of the galaxy; denoted by the black square) from the location of the transient.

Metallicity map

Next, we examine the spatially resolved gas phase metallicity of the host galaxy of iPTF 16hgs. The wavelength range of our observations include a number of important metallicity diagnostics, i. e., the [N II] λ6584 and the [S II] $\lambda\lambda$6716, 6731 lines. We thus compute the oxygen metallicity 12 + log(O/H) using two different estimators. We use the N2 index calibration as presented in Pettini et al., 2004, which uses the ratio of the [N II] λ6584 and the Hα line to estimate the metallicity. Additionally, we also use the calibration presented in the Dopita et al., 2016 (hereafter D16), which is based on photo-ionization models and is robust to changes in ionization parameter. The D16 index is based on the [N II] λ6584 and Hα lines, in addition to the [S II] $\lambda\lambda$6716, 6731 lines.

The metallicity maps of the host galaxy are shown in Figure 5.17 for both the N2 index and the D16 scale. Owing to the relatively weaker strengths of the metal emission lines, the metallicity could be reliably measured only near the nucleus of the galaxy. In particular, it is easy to see that both the metallicity calibrations

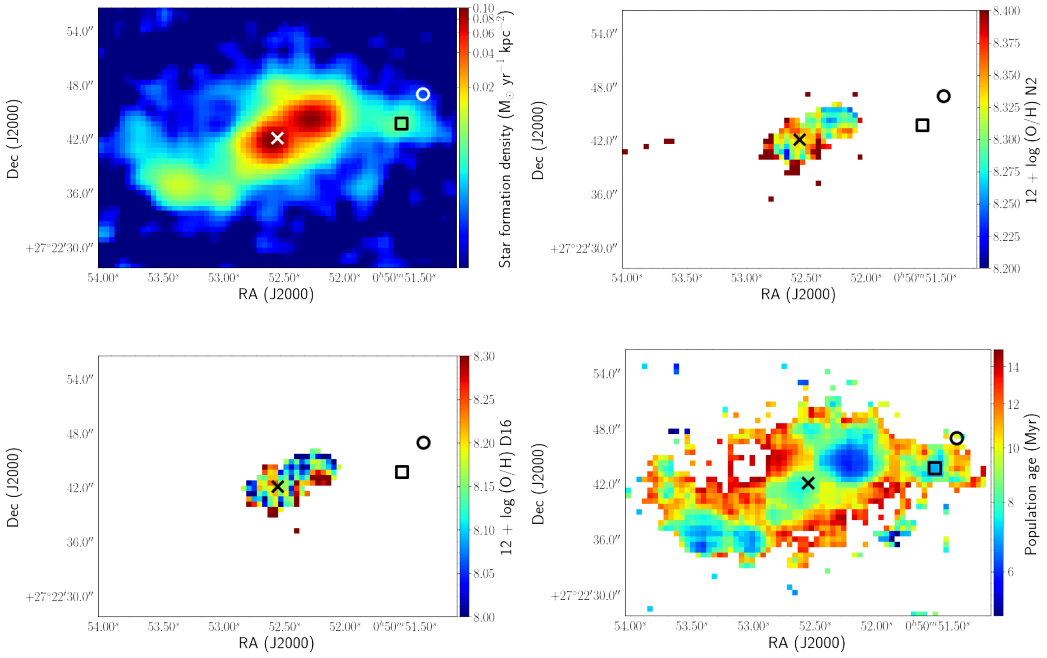

Figure 5.17: **Spatially resolved physical properties of the host, as derived from the IFU observations.** (Top left) Star formation density derived from the Hα flux map using the relations in Kennicutt, 1998. (Top right) Metallicity map of the host galaxy using the N2 index. (Bottom left) Metallicity map of the host galaxy using the D16 index (see text). (Bottom right) Population age inferred from the equivalent width of the Hα emission line. In each of the panels, the cross denotes the cataloged position of the center of the host galaxy, the circle denotes the location of the transient, and the square denotes the location of the nearest H-II region to the location of the transient.

suggest that the host galaxy of iPTF 16hgs is a low metallicity galaxy, consistent with our estimates from the spectrum of the host nucleus. There is an apparent offset between the D16 scale and the N2 index of ≈ 0.15 dex, similar to the offset noted by Krühler et al., 2017 between the D16 scale and electron temperature based values. The gas phase metallicity exactly at the location of the transient could not be reliably measured in these observations due to the low flux of the metal emission lines. Nevertheless, given the observed metallicity gradients in galaxies (Zaritsky et al., 1994), the metallicity at the location of iPTF 16hgs is likely to be lower than at the nucleus.

Stellar population age

Ages of the youngest stellar populations in a galaxy can be estimated using the equivalent widths of the Balmer emission lines. However, we note that these estimates can be heavily affected by various assumptions in the emission model (e.g. stellar multiplicity, metallicity). Regardless, such a comparison can provide estimates of the ages of the youngest stellar populations in the environment of the transient, which translates to an age estimate for the SN progenitor if the explosion was powered by the core-collapse of a massive star.

Following Kuncarayakti et al., 2016, 2017, we use the simple stellar population (SSP) models from Starburst99 (Leitherer et al., 1999) to translate our Hα equivalent width measurements into an equivalent youngest stellar population age. Based on our metallicity measurements of the host galaxy (12 + log(O/H) $\approx$ 8.2), we also fix the metallicity of the models to $Z = 0.008$ (the closest metallicity available in the model grid). The star formation is also assumed to occur in an instantaneous burst, with mass distributed according to a Salpeter IMF. The resulting maps of the stellar population age are shown in Figure 5.17.

Consistent with our expectations from the bright Hα emission extending throughout the galaxy, the stellar population age maps consistently suggest that the host galaxy contains multiple clumps of young stellar populations coincident with the bright H II regions. In particular, the bright clump of Hα emission located near the transient (offset by $\approx$ 1 kpc and marked by a square) exhibits ages of $\lesssim$ 8 Myr. The Hα EW inferred age right at the location of the transient, however, suggests that iPTF 16hgs exploded in an environment containing a stellar population with ages of $\gtrsim$ 11 Myr. If iPTF 16hgs originated in a core-collapse explosion of a massive star that was formed in its local explosion environment, the inferred population age puts a lower limit on the age of the progenitor of iPTF 16hgs.

Explosion site properties

In this section, we use both the IFU maps of the host galaxy as well as the deeper late-time LRIS spectrum at the location of the transient to measure the properties of the stellar population at the site of the explosion. First, the projected offset of the explosion site from the nucleus of the host galaxy (1.9 $R_{\rm eff} \approx$ 6 kpc) is typical of the

host nucleus offsets of core-collapse SNe found by PTF (Kasliwal et al., 2012; see also Galbany et al., 2014), while it is on the lower end of the distribution (cumulative fraction $\lesssim 50\%$) found in Type Ia SNe from PTF (Lunnan et al., 2017; L. Hangard et al., in prep.). The host normalized offset is also on the lower end (cumulative fraction $\lesssim 50\%$) of the distribution of both Type Ia SNe (Lunnan et al., 2017) and short GRBs (Fong et al., 2013).

Using the late-time LRIS spectrum which exhibits a number of galaxy emission lines, we measure a Hα flux of $\approx 2.5 \times 10^{-17}$ ergs cm^{-2} s^{-1}. This is consistent with the value estimated from the location of the transient in the IFU observations (Figure 5.16). At the redshift of the host galaxy, this corresponds to a Hα luminosity of $\approx 1.6 \times 10^{37}$ ergs s^{-1}. Translated to an equivalent star formation rate using the relations in Kennicutt, 1998, we infer a star formation rate of $\approx 1.3 \times 10^{-4}$ M$_\odot$ yr^{-1} within the 1″ slit used for the observations. The measured Hα luminosity is similar to the majority of H-II regions associated with Type Ib/c SNe (Crowther, 2013; Kuncarayakti et al., 2017).

As noted earlier, we find that the Hα map of the host galaxy indicate the presence of a large H-II region with a young stellar population at a projected offset of ≈ 1 kpc from the location of the transient (see square symbols in Figure 5.16). The integrated Hα luminosity over this H-II region is $\approx 1.1 \times 10^{39}$ ergs s^{-1}, corresponding to a star formation rate of ≈ 0.01 M$_\odot$ yr^{-1}. When compared to the typical Hα luminosities of H-II regions hosting core-collapse SNe, this association lies on the brightest end of the observed distribution of all types of core-collapse SNe (Kuncarayakti et al., 2017). Hence, if iPTF 16hgs was due to the core-collapse explosion of a massive star, it appears likely that the progenitor could have originated in this H-II region. Given the offset of ≈ 1 kpc from the explosion site, the required systemic velocity of the progenitor would be ~ 50 km s^{-1} assuming a progenitor lifetime of ~ 20 Myr. Additionally, the observed offset would also be consistent (although at the higher end) with the distribution of offsets of stripped envelope SNe from their likely parent H-II regions (Galbany et al., 2014).

5.7 Discussion

We have presented the discovery and follow-up observations of a double-peaked and fast evolving transient iPTF 16hgs. Based on its photometric and spectroscopic properties, we have also shown that iPTF 16hgs is unambiguously a member of the class of Ca-rich gap transients (as defined by Kasliwal et al., 2012), as indicated by its rapid evolution, low peak luminosity, early nebular transition, and [Ca II] emission dominated nebular phase. This makes the total number of such confirmed transients to nine. Nevertheless, there are some striking features of interest in this source that separate it from the other members of this class, in particular, its double-peaked light curve and its young star forming environment, and we discuss the implications of these below.

The double-peaked light curve and implications on the nature of the explosion

The overall light curve of iPTF 16hgs (i.e. its main peak and subsequent decline) is well consistent with the other members of this class. In particular, our modeling suggests that the main peak can be well modeled by a ^{56}Ni powered light curve with ≈ 0.4 M$_\odot$ of ejecta and $\approx 8 \times 10^{-3}$ M$_\odot$ of radioactive ^{56}Ni. This is similar to the explosion parameters estimated for other members of this class (Kasliwal et al., 2012; Lunnan et al., 2017; Perets et al., 2010; Valenti et al., 2014). Despite its overall similarity to the class of Ca-rich gap transients, the double-peaked light curve of iPTF 16hgs is unique amongst the members of this class. Hence, we now discuss the progenitor channels relevant for the various power sources that could power the first peak of the light curve.

A thermonuclear detonation?

We considered a radioactive powered scenario for the early peak in iPTF 16hgs, and found that ≈ 0.01 M$_\odot$ of ^{56}Ni in the outer 0.05 M$_\odot$ of the ejecta can explain the early bump in the light curve. Interestingly, such configurations have been suggested for some physical scenarios relevant for the potential progenitors of Ca-rich gap transients. For example, double detonation models for Type Ia SNe invoke explosive ignition of a He layer on the surface of a carbon-oxygen WD that leads to the formation of iron group radioactive isotopes near its surface and subsequently, an explosive detonation of the entire star (Fink et al., 2010; Kromer et al., 2010, 2016). The presence of such radioactive material close to the surface has been shown to produce bluer colors at early times (Dessart et al., 2012; Piro et al., 2016; Shen

et al., 2010), consistent with the observed early blue colors of iPTF 16hgs.

For the specific case of Ca-rich gap transients, a widely discussed progenitor channel involves the detonation of a He shell on the surface of a WD (Dessart et al., 2015a; Perets et al., 2010; Waldman et al., 2011). Such a configuration could arise from a close binary system with a CO WD that accretes He-rich matter from a He WD or a He-rich non-degenerate companion (Bildsten et al., 2007; Dessart et al., 2015a; Shen et al., 2010; Waldman et al., 2011). Numerical simulations for the expected optical signatures of these events were performed by Shen et al., 2010 and Sim et al., 2012, and we show a comparison of these models to iPTF 16hgs in Figure 5.18. Interestingly, as shown in Figure 5.18, Shen et al., 2010 did find double peaked light curves in their simulations of He shell detonations for some combinations of core and shell masses. In particular, their models suggest that the first peak arises out of radial stratification of short lived radioactive isotopes (^{52}Fe, ^{48}Cr, and ^{44}Ti) in the outer ejecta, whereas the second peak is powered by ^{56}Ni decay deeper in the ejecta.

Thus, qualitatively, the double peaked light curve of iPTF 16hgs does appear to be consistent with some predictions of this model, noting that this would suggest that the first peak is likely powered by a different radioactive isotope than ^{56}Ni. However, the .Ia detonation models presented in Shen et al., 2010 involved detonations of typically low mass shells ($\lesssim 0.3$ M$_\odot$) so that overall, their light curves evolve faster (rising over $\approx 7-10$ days) and are brighter ($M_{peak} < -17$) than the light curve of iPTF 16hgs. Even if the first peak is somewhat reproduced, the low shell masses lead to much faster evolving second peaks than iPTF 16hgs. On the other hand, Sim et al., 2012 did not find such double-peaked light curves in their 2D models. Although the timescales of the overall light curve of iPTF 16hgs are similar to the Sim et al., 2012 models, they are also brighter than that of iPTF 16hgs. We thus find that while some features of the light curve of iPTF 16hgs are reproduced in these models, they would require larger shell masses (than the Shen et al., 2010 models) and smaller amounts of synthesized radioactive isotopes to explain the lower luminosity.

There are also a number of spectroscopic differences between the predictions of the He shell detonation models (as in Shen et al., 2010 and Sim et al., 2012) and our

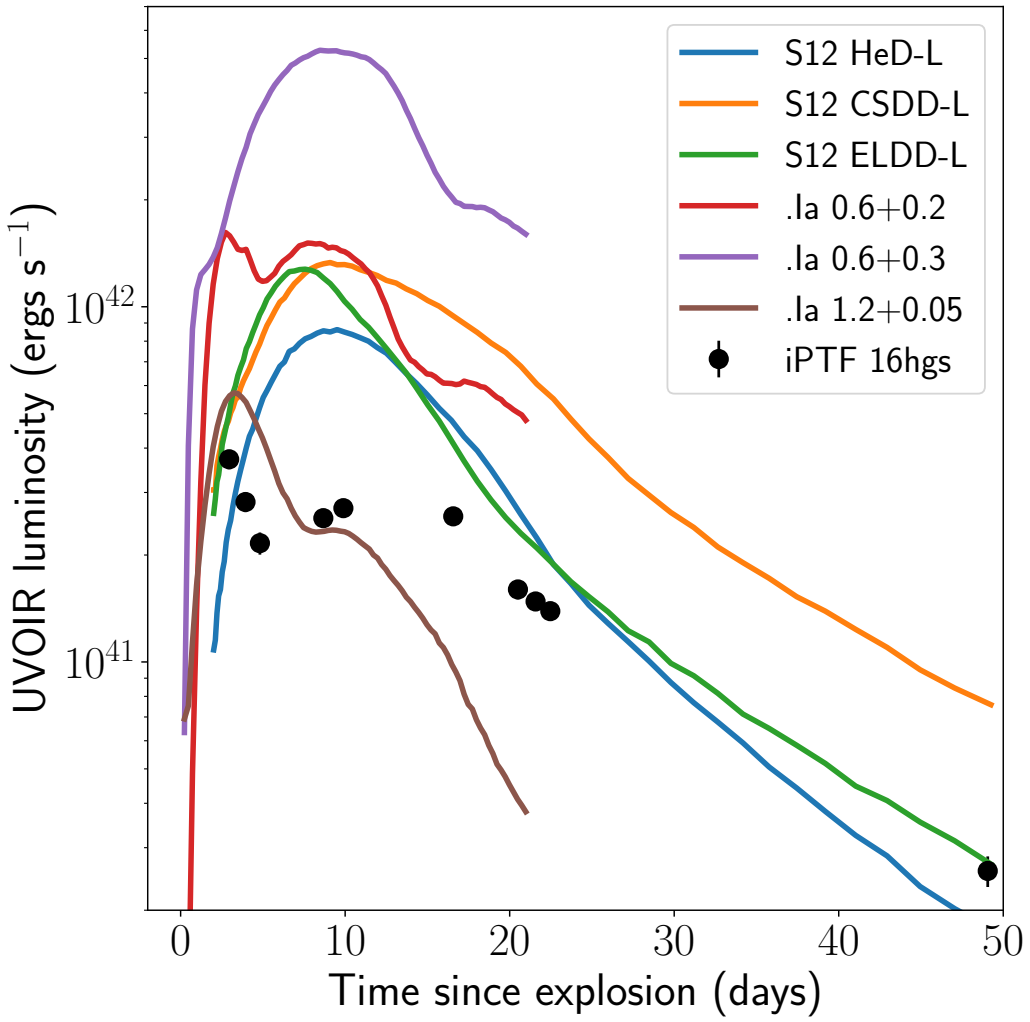

Figure 5.18: **Comparison of the pseudo-bolometric light curve of iPTF 16hgs to the bolometric light curve of models of He shell detonations (and double detonations) from Sim et al., 2012 (denoted as S12 models), and with .Ia detonation models of Shen et al., 2010 (denoted as .Ia models).** For the Sim et al., 2012 models, we show the low mass (L) models of only He shell detonations (HeD), converging shock (CS) double detonations and edge-lit (EL) double detonations. As shown, although the double-peaked behavior in iPTF 16hgs is reminiscent of the .Ia detonation models, they are either too luminous or too rapidly evolving compared to the overall light curve of iPTF 16hgs.

observations. Spectroscopically, they find that the peak photospheric spectra are likely to be dominated by absorption lines of incomplete He burning products such as Ti II and Ca II (see also Holcomb et al., 2013), and most notably, lack lines of Si and Mg. This is different from our observations, where the spectra can be well modeled by prominent features of He I, Mg II, Si II, and Ca II. While their spectra did not show He I lines, they did suggest that non-thermal excitation will likely lead to the production of He lines in these events (see also Dessart et al., 2015a; Waldman et al., 2011). For comparison, the .Ia detonation candidate OGLE-2013-SN-079 (Inserra et al., 2015) did exhibit prominent Ti II and Ca II lines near peak light, unlike the Ca-rich transient SN 2005E, as noted in Inserra et al., 2015. While the highlighted differences may appear problematic to this interpretation, we caution that the .Ia detonation models shown for comparison involved simple simulations in 1-D spherical symmetry and the nucleosynthetic outcome may differ in more realistic 3-D simulations.

A low luminosity core-collapse explosion?

We showed that the early peak of iPTF 16hgs can be well modeled by shock cooling of an extended progenitor star at the time of explosion. If the first peak was powered by shock cooling emission, the extended progenitor at the time of explosion would strongly argue for a core-collapse origin of the explosion. In fact, a core-collapse origin is plausible even if the early peak was radioactively powered. E.g., Bersten et al., 2013 invoked a similar ^{56}Ni clump near the surface to explain the double peaked light curve of SN 2008D, while Drout et al., 2016 also suggested outward ^{56}Ni mixing to explain the early blue bump in SN 2013ge.

In the case of a shock cooling first peak, the inferred parameters of the extended envelope ($M_e \approx 0.08$ M$_\odot$ and $R_e \approx 13$ R$_\odot$) provide important clues to the nature of the progenitor star. Since the Piro, 2015 models used for this analysis is simplified and ignores the density structure of the envelope, these numbers are likely to be correct only to an order of magnitude (Piro et al., 2017). We note that such extended envelopes have been previously inferred in several other stripped envelope SNe (e.g. Arcavi et al., 2017; Ben-Ami et al., 2015; Taddia et al., 2016), and are suggested to be associated with elevated mass loss prior to explosion, or formed due to binary interactions. In fact, studies of the pre-SN evolution of He stars suggest that they are

capable of swelling significantly before core-collapse (up to radii $\sim 10 - 100$ $R_\odot$), consistent with such a scenario (Woosley et al., 1995; Yoon et al., 2010).

The main peak of the light curve suggests an ejecta mass of 0.4 $M_\odot$ and ^{56}Ni mass of $\approx 8 \times 10^{-3}$ $M_\odot$, which is unusually low compared to the normal population of stripped envelope core-collapse SNe (Drout et al., 2011; Lyman et al., 2016a; Taddia et al., 2018). In particular, the low inferred ejecta mass would require significantly more stripping than observed in the typical population of stripped envelope SNe, either due to the presence of a compact companion or due to stripping by a companion in a very close orbit. Hence, we compare iPTF 16hgs to models of ultra-stripped SNe arising from highly stripped massive star progenitors in close He star - neutron star (NS) binaries (Tauris et al., 2013, 2015).

Moriya et al., 2017 presented the expected light curves and spectra of ultra-stripped (Fe core-collapse) SNe in the context of systems that lead to double neutron star systems. However, their models did not explore SN explosions with ejecta masses as large as 0.4 $M_\odot$ (as in iPTF 16hgs), although such ejecta masses are allowed by binary population synthesis models (Tauris et al., 2015). Thus, if iPTF 16hgs originated in an ultra-stripped SN explosion from a He star – compact object binary, this would require either an initially more massive He star or a wider He star – NS binary separation than the systems simulated in Moriya et al., 2017, in order to explain the larger progenitor mass at the time of explosion. Nevertheless, we note that simulations of ultra-stripped explosions in Suwa et al., 2015 did explore systems that produced ≈ 0.4 $M_\odot$ of ejecta, and found synthesized ^{56}Ni masses of $\approx 8 \times 10^{-3}$ $M_\odot$ in the explosion, very similar to our estimates for iPTF 16hgs.

While the majority of ultra-stripped SNe are expected to be of Type Ic, more massive progenitors (as would be the case for iPTF 16hgs) with larger He layers ($M_{He} \gtrsim 0.06$ $M_\odot$) may lead to He-rich Type Ib SNe (Hachinger et al., 2012; Moriya et al., 2017). Recently, Yoshida et al., 2017 also showed that the nucleosynthesis in ultra-stripped explosions may produce ejecta that are particularly rich in isotopes of Ca, suggesting that the ultra-stripped interpretation may explain the Ca-rich nebular spectra as well. It is also important to note that the larger ejecta mass and He-rich spectra of iPTF 16hgs would also be consistent with a core-collapse explosion in a close binary system of two non-degenerate massive stars (Yoon et al., 2010), where stripping by

a close non-degenerate companion can lead to a similar highly stripped progenitor that retains a large amount of He in its outer layers.

Interestingly, the low peak luminosity of iPTF 16hgs and the associated low inferred ^{56}Ni mass, together with the peculiar signatures of nucleosynthesis (i.e. Ca-rich nebular spectra) is also reminiscent of models of electron capture SNe. Such SNe are initiated by the loss of pressure due to electron captures on to ^{24}Mg and ^{20}Ne in a degenerate O-Ne-Mg core of a massive star (Nomoto, 1984). While only single stars in the mass range of 8 - 12 $M_\odot$ are expected to undergo such an outcome, the mass range may be significantly extended when considering binary interactions (Podsiadlowski et al., 2004). Since stars in this mass range do not produce massive enough winds to remove their outer H layers, a stripped envelope SN such as iPTF 16hgs would necessarily require a binary scenario to explain the observed SN. A similar scenario was also used to explain the Ca-rich SN 2005cz (Kawabata et al., 2010), although Perets et al., 2011 argue against a massive star scenario for this event based on the old stellar population in its environment and stringent limits on nearby star formation.

Kitaura et al., 2006 presented simulations of such electron capture SNe and found explosion energies and ^{56}Ni mass yields of $\sim 10^{50}$ ergs and $\sim 10^{-3}$ $M_\odot$. These are consistent with the properties of iPTF 16hgs within a factor of a few. We also compare iPTF 16hgs to the simulations of Moriya et al., 2016 (hereafter M16), who investigated the expected signatures of stripped-envelope ECSNe with binary population synthesis models at solar and sub-solar metallicity. Specifically, they performed population synthesis simulations of binary massive stars that led to ECSN progenitors either via the merger of two initially less massive stars or due to close (Case B or Case C) stripping of an initially massive star by a non-degenerate companion. Note that Tauris et al., 2015 also found ECSN progenitors in their simulations of He star – NS binaries, although the large stripping by the NS in a close orbit led to explosions that had significantly lower ejecta masses ($\lesssim 0.2$ $M_\odot$) than that inferred for iPTF 16hgs and those presented in M16.

At sub-solar metallicity of $Z = 0.004$, the ejecta mass of iPTF 16hgs is typical of the ejecta masses expected in these explosions, lying in the lower half of the distribution presented in M16. However, the peak bolometric luminosity ($\approx 3 \times 10^{41}$

ergs s^{-1}) is higher than that predicted by any of the models presented in M16, as the light curves presented in their work were much fainter (peak of $\approx 10^{41}$ ergs s^{-1}). We show a comparison of the bolometric light curves of stripped envelope ECSNe presented in M16 to iPTF 16hgs in Figure 5.19, for a model with 0.42 $M_\odot$ of ejecta (as derived from our Arnett fit) at a metallicity of $Z = 0.004$. As indicated earlier, the models presented in M16 included too little ^{56}Ni (2.5×10^{-3} $M_\odot$ for the shown light curves) to account for the (main) peak luminosity of iPTF 16hgs, so that the model prediction (solid blue curve) is much fainter than the data. We also show a comparison model to account for a higher ^{56}Ni mass by scaling the luminosity of the original model by a factor of ≈ 3.5. After adding a shock cooling component to the light curve (for $M_e = 0.05$ $M_\odot$ and $R_e = 10$ $R_\odot$) to account for the early declining emission, we find that the total predicted luminosity of the model (solid red curve) is consistent with the observations.

Taken at face value, we find that the explosion properties of iPTF 16hgs are consistent (within a factor of a few) to the expected properties of highly stripped-envelope ECSNe in binary systems. Although the association may be reasonable given the uncertainties in the explosion properties of ECSNe (Woosley et al., 2015), we reiterate that current models of these explosions cannot explain the relatively high luminosity of iPTF 16hgs. Nevertheless, Kawabata et al., 2010 argued that such low luminosity core-collapse explosions (as SN 2005cz) from lower mass progenitors are likely associated with unique nucleosynthetic signatures, in particular, a higher abundance of Ca with respect to O, consistent with the Ca-rich nebular phase spectra of SN 2005cz. Hence, the high [Ca II]/[O I] ratio in the nebular phase spectra of iPTF 16hgs would be consistent with a low luminosity electron capture explosion of a stripped massive star (Nomoto et al., 2013; Sukhbold et al., 2016; Wanajo et al., 2013; Woosley et al., 2007).

The local ISM constrained by radio observations

We have used the non-detection of radio emission in iPTF 16hgs to place stringent constraints on the environment of the progenitor using models of a spherical SN shock. Additionally, we have also used our radio limits to constrain the presence of a relativistic jet, as expected in some progenitor models for Ca-rich gap transients.

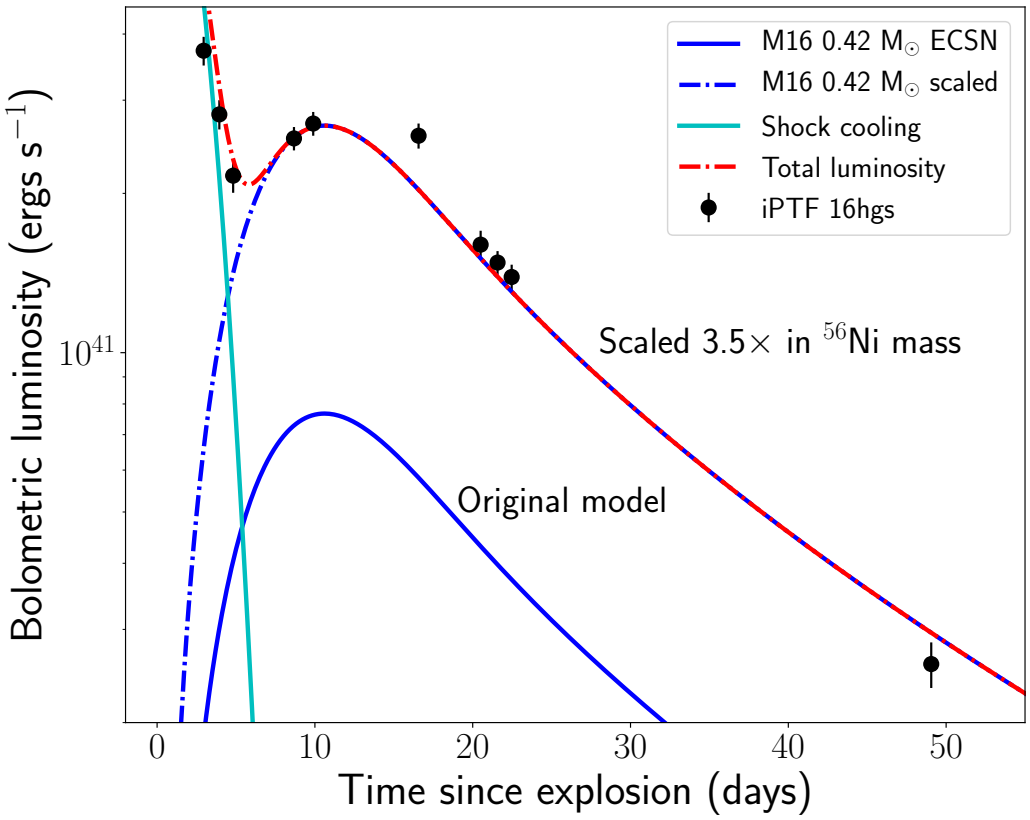

Figure 5.19: **Comparison of the bolometric light curve of iPTF 16hgs to a model of a stripped envelope ECSNe at a sub-solar metallicity of** $Z = 0.004$, as presented in Moriya et al., 2016 (M16). The solid blue line shows the original model in M16 with an ejecta mass of 0.42 $M_\odot$ and ^{56}Ni mass of 2.5×10^{-3} $M_\odot$. The blue dashed line shows the same model scaled in luminosity by a factor of 3.5 to account for a higher ^{56}Ni mass. The cyan line represents a shock cooling envelope model for an extended mass of $M_e = 0.05$ $M_\odot$ and radius of $R_e = 10$ $R_\odot$. The red line represents the total luminosity from the shock cooling and the scaled ECSN model.

A low density SN environment

We discuss the CSM environment of the progenitor in the case where iPTF 16hgs was purely powered by a spherical SN explosion. In this context, we note that core-collapse SNe exhibit a wide range of radio emission properties that reflect their diverse circumstellar mass-loss environments (e.g. Cao et al., 2013; Soderberg et al., 2005; van der Horst et al., 2011; Weiler et al., 2011). However, no Type Ia SNe, that likely share similar progenitor systems (i.e. WDs) as Ca-rich gap transients, have been detected in the radio band till date to very stringent limits. For

instance, Chomiuk et al., 2016 presented radio limits on a sample of Type Ia SNe and found that the radio non-detections constrained some of their environments to stringent limits of $\dot{M} \lesssim 10^{-9} \frac{v_{CSM}}{100\mathrm{km/s}}$ $\mathrm{M_\odot\ yr^{-1}}$. Chomiuk et al., 2016 also presented radio limits on the Ca-rich gap transients SN 2005E (Perets et al., 2010) and PTF 10iuv (Kasliwal et al., 2012) (in addition to some other 'Ca-rich' transients), and constrained their mass loss environments to $\lesssim 4 \times 10^{-7}$ $\mathrm{M_\odot\ yr^{-1}}$ and $\lesssim 10^{-5}$ $\mathrm{M_\odot\ yr^{-1}}$, respectively.

Taking standard values of the energy density fraction in the magnetic field of $\epsilon_B = 0.1$, we find that our radio limits constrain the mass loss environment of the progenitor to $\lesssim 2 \times 10^{-6} \frac{v_{CSM}}{100\mathrm{km/s}}$ $\mathrm{M_\odot\ yr^{-1}}$ for a wind-like CSM density profile, and to $n_e \lesssim 100$ $\mathrm{cm^{-3}}$ for a constant density environment. While these limits are comparable to those obtained previously for Type Ia SNe and Ca-rich gap transients, they also imply a very low density environment in the context of a core-collapse explosion. We show a comparison of the radio limits on iPTF 16hgs to the population of stripped and relativistic core-collapse SNe in Figure 5.20. As shown, these limits rule out radio emission similar to the majority of radio detected Type Ib/c SNe (see also Figure 16 in Drout et al., 2016 and Figure 16 in Milisavljevic et al., 2017), that typically exhibit radio luminosities of $\gtrsim 10^{26}$ ergs $\mathrm{s^{-1}\ Hz^{-1}}$. However, these limits are consistent with the low density environments of stripped envelope SNe like the radio faint SN 2007gr (Soderberg et al., 2010b) and SN 2002ap (Berger et al., 2002), along with the Type Ib/c SN 2013ge (Drout et al., 2016) that remained undetected in the radio band. Additionally, these limits also rule out radio emission similar to that of late-time interacting events like SN 2007bg (Salas et al., 2013) and SN 2014C (Anderson et al., 2017).

In the context of inferring the CSM environment of the progenitor, we also considered a scenario where the early peak in the optical light curve is powered by interaction of the ejecta with a dense CSM envelope around the progenitor. In order to power the early luminosity, we find that an ISM density $\rho \sim 3 \times 10^{-15}$ g $\mathrm{cm^{-3}}$ ($n_e \sim 10^9$ $\mathrm{cm^{-3}}$) is required for a constant CSM density environment, while a mass loss rate of $\dot{M} \sim 7 \times 10^{-5} \frac{v_{CSM}}{100\mathrm{km/s}}$ $\mathrm{M_\odot\ yr^{-1}}$ would be required for a constant mass loss environment. We note that this is at odds with CSM environment constraints derived from our late-time radio observations, which constrain the mass loss environment to $\dot{M} \lesssim 10^{-5}$ $\mathrm{M_\odot\ yr^{-1}}$ and $n_e \lesssim 10^3$ $\mathrm{cm^{-3}}$ for a constant density

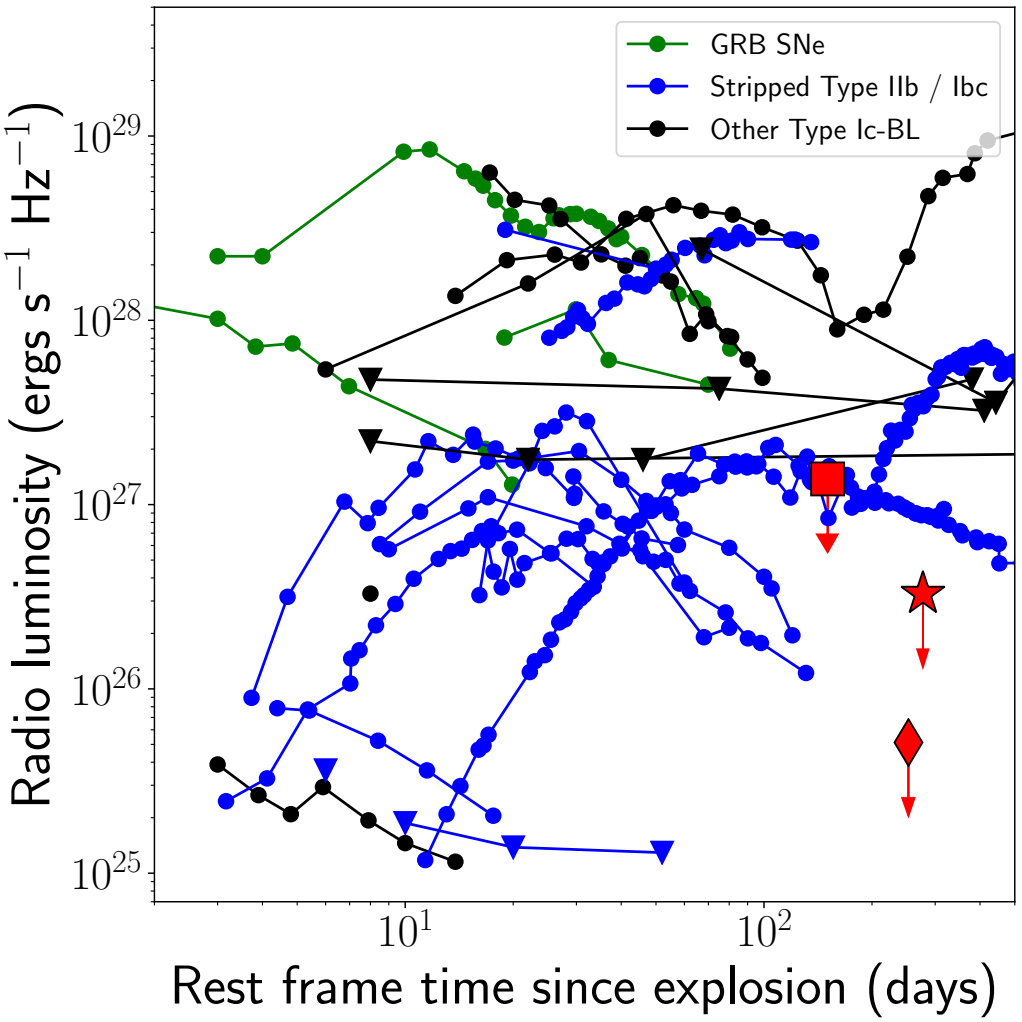

Figure 5.20: **Comparison of the radio luminosity limits on iPTF 16hgs (symbols in red) to the radio light curves of core-collapse SNe.** For the limits on iPTF 16hgs, the red square shows the AMI limit, the red star shows the GMRT limit, and the red diamond shows the VLA limit.

environment, even for a $\epsilon_B = 0.01$. Indeed, this would be consistent with the elevated pre-explosion mass loss episodes inferred from very early observations of both H-rich and H-poor core-collapse SNe (Gal-Yam et al., 2014; Yaron et al., 2017).

Limits on a tidal disruption scenario

Tidal detonations of low mass He WDs have been previously proposed as a potential progenitor channel for Ca-rich gap transients (Sell et al., 2015). In this context,

Foley, 2015 argued that the host offsets of Ca-rich gap transients appear to show a correlation with their radial velocity offsets (as inferred from the late-time nebular spectra) from their host galaxy, suggesting a nuclear origin for the progenitors of Ca-rich gap transients. This would be consistent, for instance, if a WD binary system (where the companion is a NS/BH) was hardened due to interaction with a central supermassive BH in the host galaxy, eventually leading to the tidal disruption of the WD (Sell et al., 2015).

However, Milisavljevic et al., 2017 argue that the radial velocity argument (based on the blueshifts of the [Ca II] emission lines in Foley, 2015) may be flawed since the [O I] velocities do not show these systematic offsets even if the [Ca II] do exhibit them. In Figure 5.9, we show the profiles of the [Ca II] $\lambda\lambda$ 7291, 7324 lines and the the [O I] $\lambda\lambda$ 6300, 6364 lines in the late-time spectra of iPTF 16hgs, as a function of velocity offset from 7306 Å and 6300 Å, respectively. It is interesting to note that the nebular emission features in iPTF 16hgs show no evidence of a systematic offset in either the [Ca II] or [O I] lines.

We also compare the predictions of the models of MacLeod et al., 2016 to our data, who predicted the photometric and spectroscopic signatures of tidal disruptions of 0.6 $M_\odot$ WDs by an IMBH. In general, there are major differences between the predictions and our data, specifically that the time scales of the predicted light curves are longer while the predicted spectroscopic signatures are inconsistent. This is not surprising since the detonation of a 0.6 CO $M_\odot$ WD produces more massive ejecta (and hence a slower evolving light curve) and different nucleosynthetic signatures (dominated by Si) compared to the He-rich spectra of iPTF 16hgs. Future modeling will be required to understand the properties of tidal disruptions of He-rich WDs, and if they can reproduce the observed signatures of iPTF 16hgs. Nevertheless, the first peak of the light curve remains to be explained in such a scenario, but could potentially be associated with an optical flare arising out of the initial rapid fall-back accretion on to the compact object.

As observed in some tidal disruption events of non-degenerate stars (e.g. Gezari et al., 2012), the production of a relativistic jet in the disruption was suggested to be a potential signature of such a progenitor channel (MacLeod et al., 2016; Sell et al., 2015). Based on our multi-wavelength data set on iPTF 16hgs, we place stringent

constrains on the presence of a relativistic jet in Section 5.5. In particular, we rule out the presence of a relativistic jet for near on-axis jet, unless the jet energy was very low ($\lesssim 10^{49}$ ergs, equivalent to $\lesssim 10^{-5}$ of the rest mass energy of a $0.4\,M_\odot$ WD).

Independently, we can try to place limits on the mass of the compact disrupting object using our X-ray limits on iPTF 16hgs. The accretion flare coincident with the WD disruption is expected to be several orders of magnitude above the Eddington rate (MacLeod et al., 2014, 2016; Rosswog et al., 2008), and hence the X-ray emission along the axis of the jet is likely to be super-Eddington and tracing the $\propto t^{-5/3}$ accretion rate evolution of the BH (Phinney, 1989). Along all other directions, the X-ray luminosity is likely to be at least the Eddington luminosity L_{Edd}, where

$$L_{Edd} \approx 10^{41} \frac{M_c}{10^3 M_\odot} \text{ergs s}^{-1} \tag{5.2}$$

and M_c is the mass of the compact object. Hence, the non-detection of X-ray emission in our *Swift* XRT observations constrains the mass of the compact object to be $M_c \lesssim 490\,M_\odot$. However, such an interpretation may be complicated by possible effects of reprocessing layers in the accreting system, that can reprocess the high energy emission into optical / UV light (e.g. Gezari et al., 2012; Hung et al., 2017; Miller, 2015).

Ca-rich transients from multiple progenitor channels?

Recent transient surveys have discovered a diverse population of events that can be classified as 'Ca-rich' based on their nebular phase spectra. Apart from the members of the class of Ca-rich gap transients, notable examples include iPTF 15eqv (Milisavljevic et al., 2017) which exhibited a high [Ca II]/[O I] ratio in its nebular phase spectra and hence was suggested to be 'Ca-rich', while its high luminosity and slow decline excludes it from the class of Ca-rich gap transients. Filippenko et al., 2003 and Perets et al., 2010 presented a set of events that appeared Ca-rich based on their nebular spectra, although no photometric information was available for comparison to Ca-rich gap transients.

Based on the general peculiarity of transients that exhibit strong [Ca II] emission in their nebular phase spectra, we searched the sample of spectroscopically classified stripped envelope SNe (Type IIb, Ib, or Ic) discovered by PTF and iPTF (based on

the compilation by Fremling et al., 2018) to look for objects that exhibit a high [Ca II]/[O I] ratio in their nebular phase spectra. We show our results in a plot of [Ca II]/[O I] ratio of the transient as a function of the phase from light curve peak in Figure 5.21 (similar to Figure 11 in Milisavljevic et al., 2017 and Figure 13 in Valenti et al., 2014). A major fraction of the events in this sample are Type Ic SNe, since these events were followed up to late times in the nebular phase. As shown, all the stripped envelope SNe in this sample exhibit low [Ca II]/[O I] ratio at all phases, consistent with the suggestion that the Ca-rich classification is not sensitively dependent on the phase of the transient (Lunnan et al., 2017).

The Ca-rich transients clearly stand out in this plot, occupying the phase space of high [Ca II]/[O I] ratio at early phases. Denoted as the star, iPTF 16hgs is also consistent with the other members of this class. A notable exception is iPTF 15eqv (denoted in yellow), which as mentioned earlier, exhibited a Ca-rich nebular phase spectrum, but was not a Ca-rich gap transient photometrically. The lowest [Ca II]/[O I] ratio in the sample of Ca-rich gap transients is that of SN 2012hn (Valenti et al., 2014), which exhibited a [Ca II]/[O I]$\approx$ 2.3 at a phase of $\approx$ 150 days. In this context, Milisavljevic et al., 2017 suggested that a [Ca II]/[O I] ratio of 2 separates the Ca-rich transients from the population of other stripped envelope SNe.

The class of Ca-rich gap transients, as defined by Kasliwal et al., 2012, includes a unique subset of the broader class of Ca-rich transients that was empirically defined to include many faint and fast evolving SNe that exhibited conspicuous [Ca II] emission in their early nebular phase spectra. In particular, the definition did not constrain the properties of the photospheric phase spectra of these sources, which is likely to be an important indicator of the nature of the explosion. Hence, objects like PTF 09dav (Sullivan et al., 2011) and PTF 12bho (Lunnan et al., 2017) that exhibit significantly different photospheric phase spectra may arise from different progenitor channels than the majority of this class, which appear to exhibit He-rich Type Ib-like spectra near peak light, similar to the prototype event SN 2005E (Perets et al., 2010).

The discovery of iPTF 16hgs adds further diversity to this class with its distinct double peaked light curve. If one were to invoke a similar progenitor channel for iPTF 16hgs compared to the old inferred progenitor systems of other Ca-rich gap transients, we find that a thermonuclear detonation event from a WD binary system

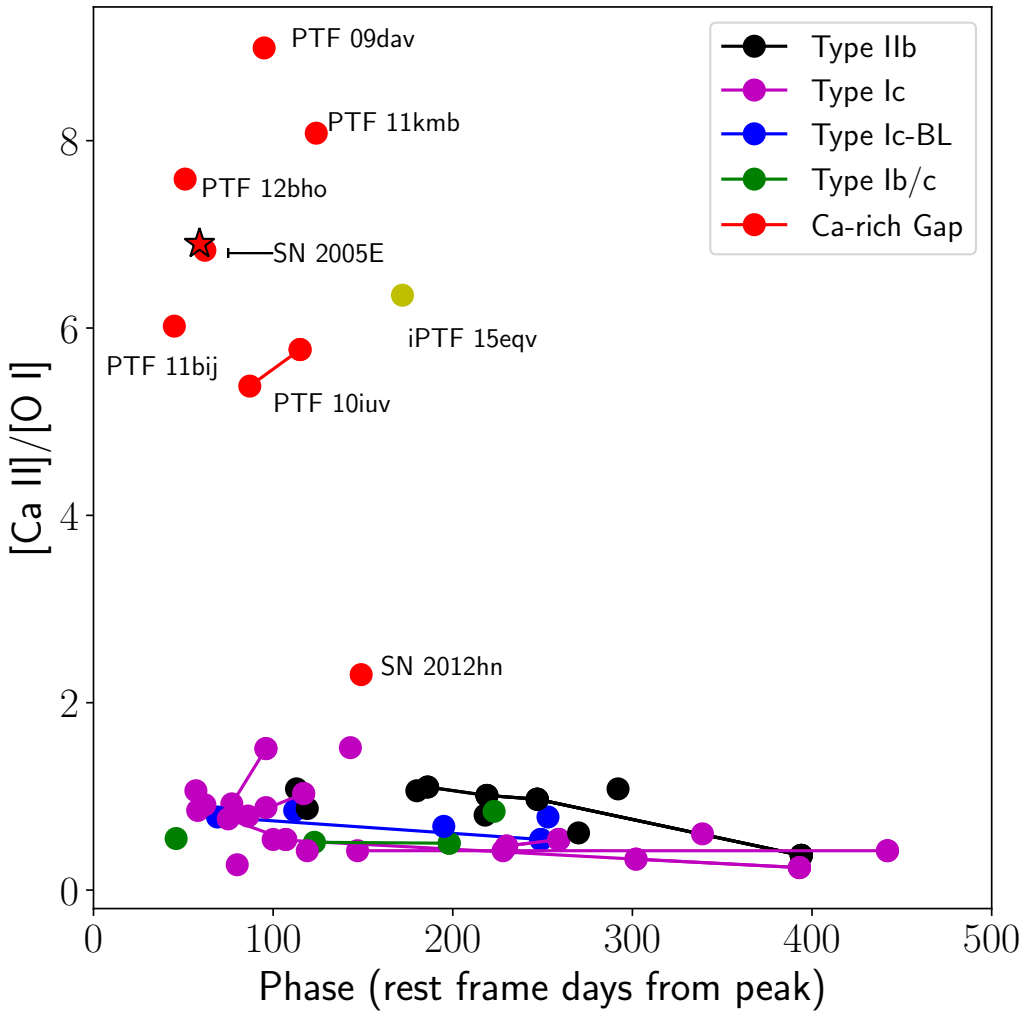

Figure 5.21: **Ca to O ratio as function of light curve phase for the PTF sample of stripped envelope SNe, together with previously known Ca-rich gap transients and iPTF 16hgs (denoted by the star).** The Ca-rich transients clearly occupy a unique phase space of high [Ca II]/[O I] in this plot.

could still be a viable explanation that unifies this explosion to the rest of the class. In this case, the light curve of iPTF 16hgs provides the first evidence of significant differences in the mixing of radioactive material in the detonation, providing strong constraints on the explosion mechanism. As the environment of the transient suggests its association with a young stellar population, this could perhaps also suggest that thermonuclear detonations occurring with shorter delay times lead to such highly mixed radioactive material in the explosion.

We also considered the scenario where the early emission in iPTF 16hgs could be powered by the interaction shock between the ejecta and a non-degenerate companion. An attractive property of this interpretation is that it would naturally explain the uniqueness of iPTF 16hgs in the class of Ca-rich gap transients, as this signature is expected to be prominent only if the observer is oriented along the direction of the companion. Based on this, Kasen, 2010 estimates that only 10% of Type Ia SNe should exhibit these early signatures. If Ca-rich gap transients arise from accreting WDs with non-degenerate companions, we would also expect only 1 in 10 of these transients to exhibit early excess emission, consistent with the discovery of iPTF 16hgs. However, our analysis of the companion interaction model suggests that the color and luminosity evolution of iPTF 16hgs are inconsistent with the models presented in Kasen, 2010. Future modeling will be required to understand if the assumptions of the companion interaction models for the massive ejecta in Type Ia SNe hold in low ejecta mass (and hence low optical depth) events with different ejecta compositions, as in iPTF 16hgs.

Another widely discussed channel for the broader class of Ca-rich gap transients that may be relevant for iPTF 16hgs is the disruption of a low mass WD by a NS or BH (MacLeod et al., 2016; Margalit et al., 2016; Metzger, 2012; Sell et al., 2015). However, it has also been suggested that such a merger likely leads to an associated radio transient powered by the interaction of either a relativistic jet or a fast wind outflow with the surrounding CSM (MacLeod et al., 2016; Margalit et al., 2016; Metzger, 2012). Based on our deep radio limits, we find that such a radio interaction signature can be hidden only if the explosion took place in a relatively clean environment ($n_e \lesssim 10^{-2}$ cm^{-3}) or if the jet energy was particularly low ($E \lesssim 10^{49}$ ergs), noting that the constraints are particularly stringent in the case of an on-axis event ($n_e \lesssim 10^{-6}$ cm^{-3}). If iPTF 16hgs arises from a similar progenitor channel as those of other Ca-rich gap transients, our observations provide strong evidence against the formation of relativistic jet-like outflows in these explosions.

Recent theoretical studies of the formation and evolution of systems leading to NS-WD mergers suggest that their rates are likely to be much lower than that inferred for Ca-rich gap transients ($\sim 30 - 90\%$ of the Type Ia SN rate) after accounting for the survey biases of PTF (Frohmaier et al., 2018; Toonen et al., 2018). The inferred rates would also be unusually high for scenarios involving tidal disruptions

of low mass He WDs by a NS or BH (Sell et al., 2015), in which case it would also be difficult to understand their preference for old stellar populations. Modeling of the physical properties of NS-WD mergers also suggest that they may not be able to explain the He-rich spectra of most Ca-rich gap transients and old environments (Zenati et al., 2019b; see also Margalit et al., 2016).

As noted in Lunnan et al., 2017, the host environments of Ca-rich gap transients are striking in light of their preference for hosts with old stellar populations in group and cluster environments. In particular, these differ substantially from the observed host properties of Type Ia SNe (which occur in both early and late-type galaxies; see discussion in Lunnan et al., 2017). In general, the older environments may be indicative of a delay-time distribution that extends out to much longer delay times than in the case of Type Ia SNe. While iPTF 16hgs was also found in a sparse galaxy group, its star forming dwarf host galaxy makes it stand out in this sample. Interestingly, the only other Ca-rich gap transient hosted in a star forming host galaxy was PTF 09dav, which was also a spectroscopically peculiar event compared to the other members of this class. Unlike the majority of Ca-rich gap transients that do not show any evidence of underlying host systems down to stringent limits that rule out the presence of a dwarf galaxy or globular cluster (Lunnan et al., 2017; Lyman et al., 2014, 2016b), iPTF 16hgs clearly occurred inside its host galaxy, and is thus robustly associated with a host system.

Regardless, the low metallicity and young stellar population of the host galaxy still provides important clues to the nature of the progenitor star. In this context, we note that the remote locations of these transients in the outskirts of galaxies (where the metallicity is likely lower) have been used to argue for low metallicity progenitors of these explosions (Yuan et al., 2013). If the low metallicity is indeed a driving factor leading to these peculiar explosions, it is not surprising that the majority of Ca-rich gap transients are found in the metal-poor halos of old galaxies. Although iPTF 16hgs was discovered at the smallest host offset of any known Ca-rich gap transient, it was found in a very low metallicity galaxy, and is thus consistent with the preference of these events for metal poor environments. In this context, it is also interesting to note that the host galaxy of SN 2005E (Perets et al., 2010), that was also discovered at a small projected offset, was a low metallicity galaxy (12 + log(O/H) $\approx$ 8.4; Milisavljevic et al., 2017), further strengthening the association of

these transients to metal-poor environments.

Nevertheless, given that there are examples of core-collapse SNe like iPTF 15eqv that exhibit high [Ca II]/[O I] ratio in their nebular phase spectra, and that iPTF 16hgs occurred in a star forming environment, it is indeed plausible that iPTF 16hgs is associated with a core-collapse explosion of a massive star. However, we reiterate that a core-collapse scenario can be ruled out for most members of this class based on their environments, and thus if a core-collapse scenario is true for iPTF 16hgs, it would require the existence of multiple progenitor channels for producing Ca-rich SNe, even though they appear quite homogeneous in terms of the SN properties. In this case, the low ejecta mass and low peak luminosity of the main peak makes it striking in the context of core-collapse explosions, suggesting its association with a highly stripped progenitor similar to those discussed in the context of stripped envelope electron capture explosions (Kitaura et al., 2006; Moriya et al., 2017; Tauris et al., 2015; Yoon et al., 2010). Although our radio limits suggest an unusually low density environment for the progenitor, the low final mass of the progenitor and the low metallicity of the progenitor environment may play a role in suppressing the formation of dense CSM environments by line-driven winds (Crowther, 2013; Langer, 2012; Smartt, 2009).

5.8 Summary & conclusions

In this paper, we have presented the discovery and multi-wavelength follow-up observations of iPTF 16hgs, a unique Ca-rich gap transient that exhibited a double-peaked light curve. The multi-wavelength properties of the transient can be summarized as follows.

- The light curve of the transient shows an initial blue decline, followed by rising to a second (main) peak on a timescale of $\approx$ 10 days. The properties of the second peak are well consistent with other known Ca-rich gap transients.
- The transient reached a peak r-band magnitude of $M_r \approx -15.65$, and to a bolometric luminosity of $\approx 3\times10^{41}$ ergs s^{-1}. On the other hand, the first peak was caught at discovery, declining from a bolometric luminosity of $\approx 4\times10^{41}$ ergs s^{-1}.
- Spectroscopically, the transient exhibited a He-rich peak photospheric spec-

trum with velocities of $\approx 8000 - 12000$ km s^{-1} similar to a number of other Ca-rich gap transients, while it subsequently exhibited an early transition to a nebular phase dominated by strong [Ca II] emission.

- No radio counterpart was detected in radio follow-up with the AMI, VLA and uGMRT down to 3σ upper limits on the radio luminosity of 1.4×10^{27} ergs s^{-1} Hz^{-1}, 5.1×10^{25} ergs s^{-1} Hz^{-1}, and 3.3×10^{26} ergs s^{-1} Hz^{-1} at 15 GHz, 10 GHz, and 1.2 GHz, respectively, at a phase of ≈ 250 days after the explosion. These are the deepest radio limits published till date on radio emission from any Ca-rich gap transient.

- X-ray follow-up with the *Swift* XRT did not detect an X-ray counterpart to a 3σ upper limit on the X-ray luminosity of $\approx 4.9 \times 10^{40}$ ergs s^{-1}.

Modeling the double-peaked light curve, we find that the main peak can be well described by a ^{56}Ni powered light curve with ≈ 0.4 M$_\odot$ of ejecta and 8×10^{-3} M$_\odot$ of ^{56}Ni. The first peak can be modeled either by ≈ 0.01 M$_\odot$ of ^{56}Ni mixed outwards into the surface of the progenitor star, or due to shock cooling of an extended envelope around the progenitor with a mass of 0.08 M$_\odot$ and radius of 13 R$_\odot$. We use the radio upper limits to constrain the environment of the progenitor, and find that the explosion occurred in a relatively 'clean' environment ($\dot{M} \lesssim 2 \times 10^{-6}$ M$_\odot$ yr^{-1} or $n_e \lesssim 150$ cm^{-3}) in the case of a standard spherical SN explosion. We also used these radio limits to place the first constraints on the presence of a relativistic jet as suggested in some models of Ca-rich gap transients, and find that the limits rule out a large parameter space of jet energies and ISM densities depending on the viewing angle of the observer.

We also presented the IFU observations of the host galaxy of iPTF 16hgs, which are the first such observations of a Ca-rich gap transient. These observations suggest that iPTF 16hgs occurred in the outskirts (at a projected offset of ≈ 6 kpc ≈ 1.9 R$_{\rm eff}$) of a star forming spiral dwarf galaxy at a significantly sub-solar metallicity of ≈ 0.4 Z$_\odot$. In particular, the young stellar population of the host galaxy and near the location of the transient is markedly different from the old environments of most Ca-rich gap transients. Hence, we find that both models of thermonuclear detonations on WDs (where the first peak is likely powered by outward mixed radioactive material) or the core-collapse of a highly stripped massive star (where the first peak is powered by cooling envelope emission or mixed radioactive material) are consistent with the

observations and the host environment.

Taken together, we find that although the distinct properties of iPTF 16hgs suggest that it may be an outlier in this observationally defined class, understanding the properties of this transient will be crucial to understand the physics of the broader class of Ca-rich explosions. Given the faint and fast evolving nature of these explosions, future and current wide-field transient surveys such as the Large Synoptic Survey Telescope and the Zwicky Transient Facility (Bellm et al., 2017) will be important to find more (and likely peculiar) examples of this intriguing class of explosions. This will shed light not only on their progenitors, but also help understand their distinct nucleosynthetic properties that likely play an important role in the chemical evolution of the universe (Frohmaier et al., 2018; Mulchaey et al., 2014).

We thank the referee Hagai Perets for a careful reading of the manuscript and providing valuable feedback for improving its content. We thank C. Steidel, E. Kirby, K. Shen, T. Moriya, L. Bildsten, D. Kasen, A. Horesh, and N. Stone for valuable discussions. We thank Ken Shen, Takashi Moriya and Stuart Sim for providing the comparison models presented in this paper. We thank Q. Ye, N. Blagorodnova, V. Ravi, S. Adams, and R. Lau for assisting with the observations presented in the paper.

The Intermediate Palomar Transient Factory project is a scientific collaboration between the California Institute of Technology, Los Alamos National Laboratory, the University of Wisconsin, Milwaukee, the Oskar Klein Center, the Weizmann Institute of Science, the TANGO Program of the University System of Taiwan, and the Kavli Institute for the Physics and Mathematics of the Universe. This work was supported by the GROWTH (Global Relay of Observatories Watching Transients Happen) project funded by the National Science Foundation under PIRE Grant No 1545949. GROWTH is a collaborative project between California Institute of Technology (USA), University of Maryland College Park (USA), University of Wisconsin Milwaukee (USA), Texas Tech University (USA), San Diego State University (USA), Los Alamos National Laboratory (USA), Tokyo Institute of Technology (Japan), National Central University (Taiwan), Indian Institute of Astrophysics (India), Indian Institute of Technology Bombay (India), Weizmann Institute of Science (Israel), The Oskar Klein Centre at Stockholm University (Sweden), Humboldt University (Germany), Liverpool John Moores University (UK).

Some of the data presented herein were obtained at the W.M. Keck Observatory, which is operated as a scientific partnership between the California Institute of Technology, the University of California and the National Aeronautics and Space Administration. The Observatory was made possible by the generous financial support of the W.M. Keck Foundation. The authors wish to recognize and acknowledge the very significant cultural role and reverence that the summit of Mauna Kea has always had within the indigenous Hawaiian community. We are most fortunate to have the opportunity to conduct observations from this mountain. These results made use of the Discovery Channel Telescope at Lowell Observatory. Lowell is a private, non-profit institution dedicated to astrophysical research and public appreciation of astronomy and operates the DCT in partnership with Boston University, the University of Maryland, the University of Toledo, Northern Arizona University, and Yale University. The upgrade of the DeVeny optical spectrograph has been funded by a generous grant from John and Ginger Giovale. We thank the staff of the Mullard Radio Astronomy Observatory for their invaluable assistance in the commissioning and operation of AMI, which is supported by Cambridge University and the European Research Council under grant ERC-2012-StG-307215 LODESTONE. The National Radio Astronomy Observatory is a facility of the National Science Foundation operated under cooperative agreement by Associated Universities, Inc. We thank the staff of the GMRT that made these observations possible. The GMRT is run by the National Center for Radio Astrophysics of the Tata Institute of Fundamental Research. Part of this research was carried out at the Jet Propulsion Laboratory, California Institute of Technology, under a contract with the National Aeronautics and Space Administration. YCP is supported by a Trinity College JRF.

Table 5.1: **Optical photometric follow-up of iPTF 16hgs (corrected for galactic extinction).** Upper limits indicated are 5σ upper limits in the respective bands.

MJD	Rest frame phase (days from explosion)	Filter	Magnitude	Instrument
57655.46	−35.50	*g*	> 20.42	P48
57662.97	−28.11	*g*	> 21.30	P48
57668.97	−22.21	*g*	> 20.84	P48
57681.36	−10.03	*g*	18.57 ± 0.08	P48
57682.37	−9.04	*g*	18.95 ± 0.09	P48
57683.22	−8.20	*g*	19.27 ± 0.12	P48
57684.36	−7.08	*g*	19.33 ± 0.17	P48
57687.10	−4.39	*g*	19.42 ± 0.02	P60

57688.40	−3.11	*g*	19.46 ± 0.04	P60
57694.37	2.76	*g*	19.74 ± 0.16	P48
57695.15	3.53	*g*	19.82 ± 0.05	P60
57696.33	4.69	*g*	19.98 ± 0.15	P48
57697.36	5.70	*g*	20.10 ± 0.16	P48
57698.21	6.54	*g*	20.43 ± 0.20	P48
57699.08	7.39	*g*	> 19.79	P60
57699.31	7.62	*g*	20.51 ± 0.16	P48
57700.25	8.54	*g*	20.70 ± 0.07	P60
57700.35	8.64	*g*	20.61 ± 0.28	P48
57701.19	9.47	*g*	20.86 ± 0.15	P60
57701.19	9.47	*g*	> 20.05	P48
57702.18	10.44	*g*	> 20.89	P60
57704.22	12.45	*g*	> 20.99	P60
57706.10	14.30	*g*	> 20.49	P60
57709.30	17.44	*g*	> 19.69	P60
57710.09	18.22	*g*	> 20.89	P60
57717.16	25.17	*g*	> 20.20	P48
57722.16	30.09	*g*	> 21.29	P60
57723.16	31.07	*g*	> 21.00	P48
57728.23	36.06	*g*	> 21.59	P60
57734.17	41.90	*g*	> 19.29	P60
57655.50	−35.46	*r*	> 20.23	P48
57663.01	−28.07	*r*	> 21.09	P48
57669.01	−22.17	*r*	> 20.63	P48
57681.32	−10.07	*r*	18.81 ± 0.10	P48
57682.33	−9.08	*r*	18.94 ± 0.09	P48
57683.26	−8.16	*r*	19.18 ± 0.12	P48
57687.09	−4.40	*r*	18.99 ± 0.02	P60
57687.32	−4.17	*r*	18.98 ± 0.11	P48
57688.39	−3.12	*r*	18.85 ± 0.03	P60
57694.33	2.72	*r*	18.76 ± 0.06	P48
57695.27	3.65	*r*	18.80 ± 0.07	P48
57696.30	4.66	*r*	18.86 ± 0.08	P48
57698.25	6.58	*r*	19.11 ± 0.07	P48
57699.08	7.39	*r*	19.26 ± 0.11	P60
57699.28	7.59	*r*	19.24 ± 0.09	P48
57700.25	8.54	*r*	19.40 ± 0.03	P60
57700.26	8.55	*r*	19.38 ± 0.03	P60
57700.30	8.59	*r*	19.44 ± 0.12	P48
57701.18	9.46	*r*	19.42 ± 0.04	P60
57701.23	9.51	*r*	19.46 ± 0.13	P48
57704.21	12.44	*r*	20.05 ± 0.10	P60
57706.10	14.30	*r*	20.17 ± 0.19	P60
57709.29	17.43	*r*	> 19.96	P60
57710.09	18.22	*r*	20.46 ± 0.22	P60
57711.13	19.24	*r*	20.61 ± 0.08	P60
57717.20	25.21	*r*	> 20.90	P48
57722.16	30.09	*r*	> 21.06	P60
57723.20	31.11	*r*	> 21.03	P48
57726.17	34.03	*r*	20.84 ± 0.31	P48
57728.23	36.06	*r*	21.57 ± 0.27	P60

57734.17	41.90	*r*	> 18.96	P60
57687.10	−4.39	*i*	18.79 ± 0.03	P60
57688.40	−3.11	*i*	18.63 ± 0.03	P60
57695.15	3.53	*i*	18.48 ± 0.03	P60
57699.08	7.39	*i*	18.94 ± 0.11	P60
57700.25	8.54	*i*	18.90 ± 0.03	P60
57700.26	8.55	*i*	18.92 ± 0.03	P60
57701.18	9.46	*i*	18.95 ± 0.04	P60
57702.17	10.43	*i*	19.08 ± 0.05	P60
57704.21	12.44	*i*	19.61 ± 0.08	P60
57706.10	14.30	*i*	19.64 ± 0.10	P60
57709.30	17.44	*i*	> 19.69	P60
57710.09	18.22	*i*	20.11 ± 0.15	P60
57711.13	19.24	*i*	20.22 ± 0.07	P60
57722.16	30.09	*i*	20.76 ± 0.20	P60
57728.23	36.06	*i*	20.87 ± 0.15	P60
57734.17	41.90	*i*	> 18.39	P60

Table 5.2: **Summary of spectroscopic observations of iPTF 16hgs.** The observation marked by * was in the form of a slit mask to measure the redshifts of potential host galaxies near the transient.

Observation Date	MJD	Rest frame phase (days from *r* peak)	Telescope + Instrument	Range (Observed Å)
2016 Oct 22.37	57683.36	−8.06	DCT + DeVeny	3600 – 7900
2016 Oct 26.21	57687.21	−4.28	P200 + DBSP	3500 – 10000
2016 Oct 31.29	57692.29	0.72	Keck I + LRIS	3500 – 10200
2016 Nov 28.32	57720.32	+28.28	Keck I + LRIS	3500 – 10000
2016 Dec 29.71*	57751.70	+59.13	Keck I + LRIS	3500 – 9900

Table 5.3: **Extinction corrected emission line fluxes in the spectrum of the nucleus of the host galaxy of iPTF 16hgs.** The fluxes were calculated by fitting a Gaussian profile to the emission line profiles, measuring the integrated flux under the profile.

Emission line	Rest wavelength (Å)	Flux (10^{-15} ergs cm^{-2} s^{-1})
Hα	6563	9.50 ± 0.37
Hβ	4865	1.58 ± 0.27
[S II]	6716	1.40 ± 0.08
[S II]	6731	1.08 ± 0.12
[N II]	6584	1.07 ± 0.14
[O II]	3727	8.27 ± 0.40
[O III]	5007	6.25 ± 0.41
[O III]	4959	1.86 ± 0.20

Table 5.4: **Redshifts of galaxies near iPTF 16hgs as measured from our spectroscopic mask observation.**

Object name	α (J2000)	δ (J2000)	Redshift	Offset (")
Obj1	$00^h50^m51.16^s$	$27°22'45.19''$	0.362	4.12
Obj2	$00^h50^m53.29^s$	$27°22'36.53''$	0.017	27.70
Obj3	$00^h50^m53.26^s$	$27°23'1.66''$	0.195	28.36
Obj4	$00^h50^m45.90^s$	$27°22'49.64''$	0.160	73.17
Obj5	$00^h50^m52.56^s$	$27°24'3.70''$	0.290	77.30
Obj6	$00^h50^m55.20^s$	$27°23'55.47''$	0.210	84.43
Obj7	$00^h50^m55.52^s$	$27°24'6.34''$	0.107	95.70
Obj8	$00^h50^m52.00^s$	$27°24'26.22''$	0.107	98.57
Obj9	$00^h50^m45.33^s$	$27°21'45.31''$	0.175	102.26
Obj10	$00^h50^m34.34^s$	$27°21'45.60''$	0.170	235.51
Obj11	$00^h50^m33.34^s$	$27°21'31.34''$	0.171	252.40
Obj12	$00^h50^m29.08^s$	$27°21'33.40''$	0.170	306.36

Chapter 6

CALCIUM RICH GAP TRANSIENTS FROM A POPULATION OF HELIUM SHELL EXPLOSIONS ON LOW MASS WHITE DWARFS

De, K. et al. (2020). "The Zwicky Transient Facility Census of the Local Universe. I. Systematic Search for Calcium-rich Gap Transients Reveals Three Related Spectroscopic Subclasses". In: *ApJ* 905.1, 58, p. 58. DOI: 10.3847/1538-4357/abb45c.

Kishalay De[1], Mansi M. Kasliwal[1], Anastasios Tzanidakis[1], U. Christoffer Fremling[1], Scott M. Adams[1], Robert Aloisi[2], Igor Andreoni[1], Ashot Bagdasaryan[1], Eric C. Bellm[3], Lars Bildsten[4,5], Christopher Cannella[1], David O. Cook[6], Alexandre Delacroix[7], Andrew Drake[1], Dmitry Duev[1], Alison Dugas[1,8], Sara Frederick[9], Avishay Gal-Yam[10], Daniel Goldstein[1], V. Zach Golkhou[3,11], Matthew J. Graham[1], David Hale[9], Matthew Hankins[1], George Helou[6], Anna Y. Q. Ho[1], Ido Irani[12], Jacob E. Jencson[13], David L. Kaplan[2], Stephen Kaye[7], S. R. Kulkarni[1], Thomas Kupfer[5], Russ R. Laher[6], Robin Leadbeater[14], Ragnhild Lunnan[15], Frank J. Masci[6], Adam A. Miller[16,17], James D. Neill[1], Eran O. Ofek[10], Daniel A. Perley[18], Abigail Polin[19,20], Thomas A. Prince[1], Eliot Quataert[19], Dan Reiley[7], Reed L. Riddle[7], Ben Rusholme[6], Yashvi Sharma[1], David L. Shupe[6], Jesper Sollerman[15], Leonardo Tartaglia[15], Richard Walters[7], Lin Yan[1], and Yuhan Yao[1]

[1]Cahill Center for Astrophysics, California Institute of Technology, 1200 E. California Blvd., Pasadena, CA 91125, USA
[2]Center for Gravitation, Cosmology, and Astrophysics, Department of Physics, University of Wisconsin-Milwaukee, P.O. Box 413, Milwaukee, WI 53201, USA
[3]DIRAC Institute, Department of Astronomy, University of Washington, 3910 15th Avenue NE, Seattle, WA 98195, USA
[4]Department of Physics, University of California, Santa Barbara, CA 93106, USA
[5]Kavli Institute for Theoretical Physics, University of California, Santa Barbara, CA 93106, USA
[6]IPAC, California Institute of Technology, 1200 E. California Blvd, Pasadena, CA 91125, USA
[7]Caltech Optical Observatories, California Institute of Technology, Pasadena, CA 91125, USA
[8]Institute for Astronomy, University of Hawai'i, 2680 Woodlawn Drive, Honolulu, HI 96822, USA
[9]Department of Astronomy, University of Maryland, College Park, MD 20742, USA
[10]Benoziyo Center for Astrophysics, The Weizmann Institute of Science, Rehovot 76100, Israel
[11]The eScience Institute, University of Washington, Seattle, WA 98195, USA
[12]Department of Particle Physics and Astrophysics, Weizmann Institute of Science, Rehovot 7610001, Israel
[13]Steward Observatory, University of Arizona, 933 North Cherry Avenue, Tucson, AZ 85721-0065, USA
[14]Three Hills Observatory, The Birches CA71JF, UK

[15]Department of Astronomy, The Oskar Klein Center, Stockholm University, AlbaNova, 10691 Stockholm, Sweden
[16]Center for Interdisciplinary Exploration and Research in Astrophysics (CIERA) and Department of Physics and Astronomy, Northwestern University, 2145 Sheridan Road, Evanston, IL 60208, USA
[17]The Adler Planetarium, Chicago, IL 60605, USA
[18]Astrophysics Research Institute, Liverpool John Moores University, IC2, Liverpool Science Park, 146 Brownlow Hill, Liverpool L3 5RF, UK
[19]Department of Astronomy, University of California, Berkeley, CA, 94720-3411, USA
[20]Lawrence Berkeley National Laboratory, Berkeley, California 94720, USA

Abstract

Using the Zwicky Transient Facility alert stream, we are conducting a large spectroscopic campaign to construct a complete, volume-limited sample of transients brighter than 20 mag, and coincident within 100″of galaxies in the Census of the Local Universe catalog. We describe the experiment design and spectroscopic completeness from the first 16 months of operations that classified 754 supernovae. We present results from a systematic search for Calcium rich gap transients in the sample of 22 low luminosity (peak absolute magnitude $M > -17$), hydrogen poor events found in the experiment. We report the detection of eight new events, and constrain their volumetric rate to be $\gtrsim 15 \pm 5\%$ of the SN Ia rate. Combining this sample with ten previously known events, we find a likely continuum of spectroscopic properties ranging from events with SN Ia-like features (Ca-Ia objects) to SN Ib/c-like features (Ca-Ib/c objects) at peak light. Within the Ca-Ib/c events, we find two populations distinguished by their red ($g - r \approx 1.5$ mag) or green ($g - r \approx 0.5$ mag) colors at r-band peak, wherein redder events show strong line blanketing features and slower light curves (similar to Ca-Ia objects), weaker He lines, and lower [Ca II]/[O I] in the nebular phase. Together, we find that the spectroscopic continuum, volumetric rates and striking old environments are consistent with the explosive burning of He shells on low mass white dwarfs. We suggest that Ca-Ia and red Ca-Ib/c objects arise from double detonation of He shells, while green Ca-Ib/c objects are consistent with low efficiency burning scenarios like detonations in low density shells or deflagrations.

6.1 Introduction

Calcium-rich gap transients represent an emerging population of faint and fast evolving supernovae identified by their conspicuous [Ca II] emission in nebular phase spectra (De et al., 2018a; Kasliwal et al., 2012; Lunnan et al., 2017; Perets et al., 2010; Sullivan et al., 2011; Valenti et al., 2014). Their photometric evolution is characterized by timescales and peak luminosities faster and fainter than those of typical core-collapse and thermonuclear supernovae (SNe), while their photospheric

phase velocities are largely similar to normal Type Ib/c SNe ($\sim$ 8000 km s^{-1}; see Filippenko, 1997; Gal-Yam, 2017 for a review). Yet, their most striking feature remains their preference for remote locations in the far outskirts of galaxies in old quiescent environments, in stark contrast to normal stripped envelope SNe which are found close to star formation (Lunnan et al., 2017; Perets et al., 2010). Together with the non-detection of any parent stellar populations in late-time imaging of the locations of these objects, their remote locations suggest that these transients arise from very old progenitors that may have traveled far away from their parent stellar population or were possibly formed in these remote locations (Lunnan et al., 2017; Lyman et al., 2014, 2016b; Perets, 2014; Yuan et al., 2013).

Their host offset distribution has been shown to be more skewed towards larger offsets than Type Ia SNe and even short gamma-ray bursts (Lunnan et al., 2017), while their hosts are preferentially found in group and cluster environments (Foley, 2015; Lunnan et al., 2017; Mulchaey et al., 2014). Shen et al., 2019 show that the radial offset distribution of the sample may be consistent with that of globular clusters, and potentially indicative of a progenitor population that has been kicked out of nearby globular clusters.

The progenitors of Calcium rich gap transients remain unknown to date, and are currently only constrained with circumstantial evidence. Specifically, their remote locations and old host environments point to old progenitors involving white dwarfs (WDs) in binary systems. Suggested channels include helium shell detonations on WDs (Bildsten et al., 2007; Dessart et al., 2015a; Meng et al., 2015; Shen et al., 2010; Sim et al., 2012; Waldman et al., 2011), double detonations of He shells on the surface of WDs (Polin et al., 2019, 2021; Sim et al., 2012), mergers of WDs with neutron stars (Bobrick et al., 2017; Margalit et al., 2016; Metzger, 2012; Toonen et al., 2018; Zenati et al., 2019b), tidal disruptions of WDs by intermediate mass black holes (Kawana et al., 2020; MacLeod et al., 2014, 2016; Rosswog et al., 2008; Sell et al., 2015, 2018), and even extreme core-collapse SNe from highly stripped massive stars (Moriya et al., 2017; Tauris et al., 2015); however their old environments make core-collapse SNe unlikely (Perets et al., 2011). If they arise from binary WD systems, Meng et al., 2015 show that the old environments and consequently long delay times constrain the progenitor binary to consist of low mass CO ($\lesssim 0.6\,M_\odot$) and He ($\lesssim 0.25\,M_\odot$) WDs.

Constraining their progenitors and rates is not only important for our understanding of these potentially common types of transients, but also to shed light on a likely

common end point in binary stellar evolution involving white dwarfs in binary systems, and their possible significant contribution to the enrichment of the intergalactic medium with Ca (Mernier et al., 2016; Mulchaey et al., 2014). Estimates of the volumetric rates of this population from previous transient experiments include an estimate of $7 \pm 5\%$ of the SN Ia rate from the Lick Observatory Supernova Search (LOSS; Li et al., 2011; Perets et al., 2010) and a lower limit of $\approx 3\%$ of the SN Ia rate from the Palomar Transient Factory (Kasliwal et al., 2012). A later estimate based on post-facto simulations of the detection efficiency and survey cadence of the Palomar Transient Factory suggests that their rates may be as high as $\approx 30\%$ of the SN Ia rate (Frohmaier et al., 2018). However, the known sample of objects were found largely by follow-up of isolated events outside of systematic SN classification efforts, leaving considerable uncertainty on the rates of the class.

The number of reported Ca-rich gap transients in the literature, as well as the diversity in their observed properties, have risen substantially in the last decade with large scale optical transient surveys. As per the name of the class, the detection of strong [Ca II] emission in the nebular phase spectra with high [Ca II]/[O I] ratio[1] is the primary criterion used to relate objects to the class of Ca-rich transients (De et al., 2018a; Milisavljevic et al., 2017; Valenti et al., 2014). In addition, Kasliwal et al., 2012 defined this class of 'gap' transients by their i) faint peak luminosity, ii) fast photometric evolution, iii) photospheric phase velocities similar to normal hydrogen-poor SNe ($\sim$ 8000 km s^{-1}) and iv) early evolution to the nebular phase, notably without any constraints on the photospheric phase spectra of the transient. These criteria are consistent with the prototype event of the class SN 2005E (Perets et al., 2010), which was also spectroscopically similar to Type Ib SNe near peak light.

There are seven other events in the class of Ca-rich gap transients that are spectroscopically similar to Type Ib/c SNe near peak light – SN 2007ke, SN 2010et, PTF 11bij (Kasliwal et al., 2012), SN 2012hn (Valenti et al., 2014), PTF 11kmb, PTF 12bho (Lunnan et al., 2017), and SN 2016hgs (De et al., 2018a). Other Type Ic SNe which show evidence of strong [Ca II] emission in the early nebular phase include iPTF 14gqr (De et al., 2018b), SN 2018kzr (McBrien et al., 2019) and SN 2019bkc (Chen et al., 2020; Prentice et al., 2020), although they were more luminous ($M_{peak} \lesssim -17.5$) than the typical Ca-rich gap transient. However, spectroscopic similarity to Type Ib/c SNe does not appear to be a defining characteristic

[1]Throughout this paper, we refer to the flux ratio of the forbidden [Ca II]$\lambda\lambda$7291, 7324 to [O I]λ6300, 6364 lines as [Ca II]/[O I].

of the class. Notable exceptions include PTF 09dav (Kasliwal et al., 2012; Sullivan et al., 2011) and SN 2016hnk (Galbany et al., 2019; Jacobson-Galan et al., 2019), which exhibit similarities to sub-luminous SN1991bg-like Type Ia SNe (Filippenko et al., 1992b) near peak light.

Similarly, iPTF 15eqv (Milisavljevic et al., 2017) was a peculiar hydrogen-rich SN IIb which exhibited high [Ca II]/[O I] ratio in nebular phase spectra, noting that it was luminous at peak and consistent with a core-collapse SN in a star forming environment. Another potential member of the class, SN 2005cz (Kawabata et al., 2010; Perets et al., 2011) exhibited high [Ca II]/[O I] ratio in its nebular phase spectrum; yet the lack of photometry around peak light precludes a confirmed association with this class of faint and fast evolving transients, as is the case for several candidates presented in Filippenko et al., 2003.

The large heterogeneity in the peak luminosity and spectroscopic appearance of objects likely points to a diversity in explosions that produce high [Ca II]/[O I] in their nebular phase spectra. Yet, the small number of total reported events ($\lesssim 10$) has prevented a holistic analysis of the spectroscopic and photometric properties of this class. Most previous studies have focused on one or two events, each of which have been suggested to be unique members of this emerging population which remains poorly understood. In particular, previous works have not characterized the nebular phase behavior of a systematically selected sample of low-luminosity hydrogen poor transients to be able to quantitatively place the photometric and spectroscopic properties of the class of Ca-rich gap transients in a broader context. Such an analysis with a large sample can yield vital clues to trends within the population and shed light on the underlying explosions. The aim of this paper is to systematically uncover and analyze this population of faint and fast evolving hydrogen-poor events that exhibit high [Ca II]/[O I] in nebular phase spectra.

While galaxy-targeted supernova surveys are sensitive to transients occurring close to their host galaxies, the known preference of these transients for large host offsets necessitates a wide-field search approach that is sensitive to transients at large projected offsets from their host galaxies. Given the faint peak luminosity ($M_r \approx -16$) and relatively low volumetric rates ($\sim 10\%$ of SN Ia rate) of these events, finding a large sample of events thus requires a sufficiently deep (depth $r \gtrsim 20$ mag to find events out to ≈ 150 Mpc) optical all sky survey with a cadence of $\lesssim 4$ d to detect these short lived events. At the same time, due to the large rate of higher redshift Type Ia SNe at this depth (~ 8500 yr^{-1} down to $r = 20$ mag limiting

magnitude; Feindt et al., 2019), finding a systematic sample of these local universe events requires a targeted approach to classify transients in the local universe by cross-matching transients to known nearby galaxies. Such an approach is now possible with large catalogs of galaxies with known spectroscopic redshifts like the Census of the Local Universe (CLU; Cook et al., 2019) catalog and GLADE (Dálya et al., 2018).

This paper presents the first in a series of publications from the Census of the Local Universe experiment of the Zwicky Transient Facility (ZTF; Bellm et al., 2019b; Graham et al., 2019). This paper provides an overview of the sample selection and spectroscopic completeness of this volume-limited experiment. Here, we focus on the identification of Ca-rich gap transients, specifically on the class of faint and hydrogen-poor transients that exhibit Ca-rich spectra in the nebular phase. We briefly describe the design of the experiment and sample selection in Section 6.2. Section 6.3 presents an analysis of the photometric and spectroscopic properties of the combined sample of transients from ZTF and the literature, specifically noting the presence of two spectroscopic classes and a continuum of properties across these classes. Using the controlled selection criteria of the experiment, we present an analysis of the host environments of these transients in Section 6.4, while Section 6.5 presents a discussion on the estimated volumetric rates of these events. In Section 6.6, we combine all of the results to constrain the progenitors of this class and summarize our conclusions in Section 6.7.

Calculations in this paper assume WMAP9 flat ΛCDM cosmology with $H_0 = 69.3$ km s^{-1} Mpc^{-1} and $\Omega_M = 0.286$ (Hinshaw et al., 2013). We use the median redshift independent distance estimates from the NASA Extragalactic Database (NED) for transients hosted in galaxies that have such measurements, and redshift derived distance estimates otherwise. For the redshift derived distance estimates in this local universe sample ($z < 0.05$), the typical uncertainty in the luminosity distance and projected offsets is $\lesssim 5\%$ for peculiar velocities $\lesssim 300$ km s^{-1}. Times reported are in UT throughout this paper.

6.2 Observations

The Census of the Local Universe Experiment

The Zwicky Transient Facility is a wide-field optical time domain survey running out of the 48-inch Schmidt telescope (P48) at Palomar observatory (Bellm et al., 2019b; Graham et al., 2019). With a field of view of 47 square degrees, the instrument

achieves median limiting magnitude of $r \approx 20.5$ mag in 30 s exposures of the sky and a survey speed of ≈ 3750 square degrees per hour (Dekany et al., 2016). ZTF observing time is divided into a public component (40%), a collaboration component (40%), and a Caltech component (20%). Bellm et al., 2019a provide an overview of the various ZTF surveys undertaken in the first year of operations, and the survey scheduling system designed to carry out operations to maximize volumetric survey speed.

The public component is a 3-day cadence $g + r$ survey of the entire northern sky ($\approx$ 34% of P48 time) together with a 1-day cadence $g + r$ survey of the Galactic plane ($\approx$ 6% of P48 time). The collaboration time was dedicated to high cadence ($3g + 3r$ per night) observations of ≈ 2500 square degrees and a slower cadence (≈ 4 d) i-band survey. The Caltech time was dedicated to a one night cadence $g + r$ survey of ≈ 3000 square degrees. Transients in the difference imaging pipeline (based on the ZOGY subtraction algorithm; Zackay et al., 2016) of ZTF (Masci et al., 2019) are reported and distributed in Avro alert packets[2] (Patterson et al., 2019), including photometry and metadata for the detected transient, as well as a 30-day history for the previous detections and non-detections.

The ZTF Census of the Local Universe (CLU) experiment has been designed to build up a spectroscopically classified sample of transients in the local universe (within 200 Mpc) by classifying all transients found coincident with galaxies in the Census of the Local Universe (CLU; Cook et al., 2019) catalog. The CLU catalog consists of ~ 234500 galaxies with previously known redshifts compiled from several previous spectroscopic surveys (called CLU-compiled; see Cook et al., 2019), along with additional nearby galaxies found in a wide, narrow-band (Hα) survey covering 3π of the northern sky with the Palomar 48-inch telescope (Cook et al., 2019).

The initial filter for the experiment used the CLU-compiled catalog together with ~ 1000 of the highest significance ($> 25\sigma$) candidates from the Hα survey. Starting from 2019 April 01, we initiated the use of the next data release which included a larger sample (≈ 38000 candidates with significance $> 3\sigma$) of high confidence nearby galaxies from the CLU Hα survey (see Cook et al., 2019 for a description). Based on the transient sample found in this experiment, we find that $\approx$ 1% of transients were hosted in the CLU Hα survey galaxies before the 2019 April 01 update, while $\approx$ 10% of transients were hosted in galaxies from the Hα catalog following the inclusion of the next data release.

[2] `https://avro.apache.org`

The CLU experiment was initiated on 2018 June 01 and we restrict the sample of transients in this paper to events saved until 2019 September 30. The sample selection for the transients was implemented as a part of a custom filter implemented on the GROWTH Marshal (Kasliwal et al., 2019), which is a web-portal for vetting and coordinating follow-up of transients. The selection criteria for ZTF alerts to be saved in the CLU experiment are as follows:

1. Each alert packet is spatially cross-matched to the CLU catalog of galaxies. The size of the spatial cross-match is set to $3 \times D_{25}$ where D_{25} is the isophotal major axis containing 25% of the total light of the galaxy, as contained in the CLU catalog. If a D_{25} radius is not available for the galaxy, a default cross-match radius of $280''$ was used[3]. The cross-matching was performed on the dedicated time domain astronomy server called `kowalski` at Caltech (Duev et al., 2019).

2. The alert candidate was produced as a positive candidate in the subtraction, i.e. the source flux has increased from the reference image.

3. The alert candidate has a real-bogus score (rbscore) of > 0.3 as classified by the ZTF machine learning algorithm (Mahabal et al., 2019). This choice produces a false negative rate of $< 3\%$ (Duev et al., 2019).

4. The alert candidate is at least $20''$away from a star brighter than 15.0 mag.

5. Alert candidates within $1''$of a known star in PS1 (Chambers et al., 2016) are rejected. The identification of stars is based on the machine learning based star/galaxy classification score presented in Tachibana et al., 2018, which is available for the three nearest sources in the ZTF alert packets. We use a `sgscore` threshold of 0.6, i.e. candidates within $1''$ of a PS1 source with `sgscore` > 0.6 are rejected.

6. The alert candidate was at least $2''$ away from the nearest solar system object and was detected at least twice in the survey separated by 50 mins. The former criterion removes known asteroids in the ZTF alert stream while the latter removes unknown solar system objects.

No further magnitude cut was applied to this transient stream. This filter produces typically $\approx$ 100 sources to be vetted by on-duty astronomers every day, which in-

[3] $280''$is $3\times$ the median D_{25} value of all galaxies in the CLU catalog.

volves an inspection of the science, reference and difference image cutouts contained in the ZTF alert packets. The human vetting is required to remove alerts from remaining stellar sources that pass the filter, remove variability from known AGN and identify remaining bogus sources before assigning appropriate spectroscopic follow-up. For 2018 and 2019, spectroscopic follow-up was exclusively limited to transients within 100″of the nearest CLU galaxy to remove the large amount of contamination of SNe in background galaxies. In addition, transients coincident with known background galaxies (with known spectroscopic redshifts or photo-z > 0.1) were excluded from the sample in order to avoid the large number of false positives from background AGN and Type Ia SNe.

As such, the experiment may be incomplete to transients occurring at very large projected offsets of $> 100''$ from their parent galaxies, corresponding to a physical projected distance of 100 kpc at 200 Mpc, 50 kpc at 100 Mpc, and 25 kpc at 50 Mpc. In addition, sources coincident with the nuclei of known Active Galactic Nuclei (AGN) and with long term history of variability are not assigned for follow-up. On average, 10 - 15 SNe are saved for spectroscopic follow-up every week, which were coordinated via source pages on the GROWTH Marshal. Starting from 2019 November 01, sources from the public ZTF data stream are reported to the Transient Name Server (TNS[4]) as soon as they are saved by a human scanner (De et al., 2019g).

All transients saved after this vetting process are systematically assigned for spectroscopic follow-up. We prioritized follow-up of sources that were brighter than or were going to peak at brighter than 20 mag (in either $r_{\rm ZTF}$ or $g_{\rm ZTF}$; see Bellm et al., 2019b), which was selected to be the target limiting magnitude for the experiment. Given the typical ZTF limiting magnitude of 20.5 mag, we did not apply any magnitude cuts to the filter to be able to track the photometric evolution and assign follow-up for transients peaking around 20 mag. Spectroscopic classifications were performed using a multi-tiered approach – i) sources brighter than 19 mag were assigned for spectroscopic follow-up on the robotic Spectral Energy Distribution Machine (SEDM; Blagorodnova et al., 2018) and ii) sources between 19 and 20 mag were assigned for spectroscopic follow-up on the Double Beam Spectrograph (DBSP; Oke et al., 1982) on the 200-inch Hale telescope (P200) at Palomar Observatory, and iii) sources fainter than 20 mag were assigned for lower priority follow-up on P200 + DBSP.

[4] https://wis-tns.weizmann.ac.il/

Sources assigned to the SEDM queue remain as follow-up targets for a duration of 7 days after which they are re-assigned to SEDM (if still brighter than 19 mag) or to P200 otherwise. Spectroscopic follow-up on P200 was required for bright sources (< 19 mag) when coincident with the nuclei of nearby galaxies, where host galaxy contamination was difficult to remove in the SEDM spectra. In cases where P200 classifications were not possible due to poor weather or due to large host contamination in P200 data for faint targets, we also used the Low Resolution Imaging Spectrometer (LRIS; Oke et al., 1995) on the Keck-I telescope for spectroscopic classifications.

The spectroscopic follow-up effort for bright sources ($m < 19$ mag) was coordinated with the Bright Transient Survey (BTS; Fremling et al., 2019) experiment which aims to classify all transients brighter than 19 mag in the ZTF public alert stream. Community follow-up for bright transients overlapping with BTS have also aided in the spectroscopic classification completeness of the sample. Classifications are done with the `SuperNova IDentification` (Blondin et al., 2007) (SNID) code by automatic execution on spectra produced by the SEDM automated pipeline (Rigault et al., 2019) and manual execution for all other instruments. For spectra contaminated by the underlying host light, we used `superfit` (Howell et al., 2005) to attempt host subtraction and derive a classification. The final classification is made by human inspection of the best-fit templates matched from SNID or `superfit`.

Spectroscopic completeness

The aim of the tiered approach to spectroscopic classification was to obtain high spectroscopic completeness for transients that peaked brighter than 20 mag in galaxies within the local universe. This magnitude limit corresponds to a luminosity completeness of $M < -16.5$ mag for all galaxies in the 200 Mpc volume of the CLU catalog and $M < -15$ mag for galaxies within 100 Mpc. However, given the galaxy targeted nature of the target selection, the experiment is not sensitive to transients that occur in nearby galaxies with previously unknown spectroscopic redshifts. Based on results from the ZTF BTS, the completeness (in terms of galaxy counts) of the compiled catalog is $\approx 80\%$ at the lowest redshifts and decreases to $\approx 50\%$ at the edge of the 200 Mpc volume (Fremling et al., 2019).

While effort was made to have complete spectroscopic classifications to a depth of ≈ 20 mag, classifications were not always possible due to several reasons. These include the difficulty of following up transients found close to the sun, classifying

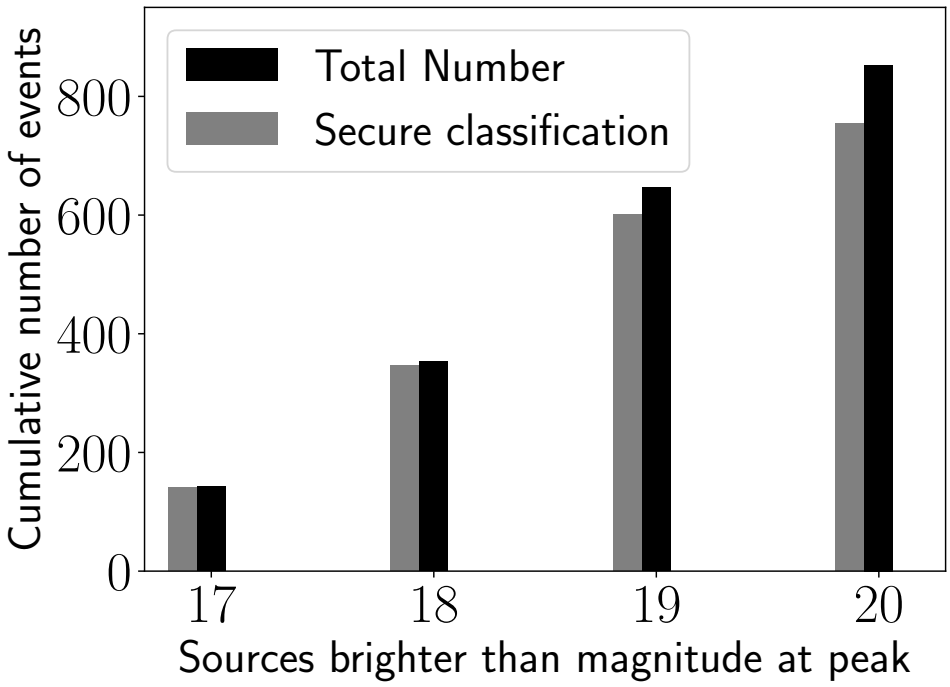

Figure 6.1: **Cumulative number of events that were saved (in black) and classified (in grey) as a function of the peak magnitude in the CLU sample of events.**

transients on the nuclei of bright galaxies (where low resolution SEDM spectra are dominated by host galaxy light) that faded before a scheduled run on the P200/Keck, and due to loss of P200/Keck time in periods of bad weather. We thus evaluate the spectroscopic completeness of the experiment in the first year of operations.

We restrict this sample to transients that were saved between[5] 2018 June 01 and 2019 September 30, and to sources detected in any of the public or internal collaboration surveys (note that the public survey has the largest footprint on the sky). We define our primary sample of sources such that they are detected at least twice, and peaked at a magnitude brighter than 20 mag in either the $r_{\rm ZTF}$ or $g_{\rm ZTF}$ filters. We require at least two detections of the transient separated by 50 minutes during the survey, as implemented in the alert filter. Multiple detections in the same filter on a single night were averaged to estimate the transient flux on each night.

A total of 852 candidate SNe were saved during this time period, out of which

[5]Accounting for observation gaps due to instrument maintenance and poor weather, this period contains a total of 390 nights of full or partial ZTF operations.

563 were also included in the BTS program. 754 out of these 852 events were reliably classified, while 98 were unclassified either due to the lack of follow-up spectroscopy or due to ambiguous classifications from spectroscopic data. As such, the spectroscopic completeness of the complete acquired sample is 88.5% for all transients that had at least one detection brighter than 20 mag. The corresponding classification completeness for $m_{\rm peak} < 19$ mag is 92.9%, $m_{\rm peak} < 18$ mag is 98.0%, and $m_{\rm peak} < 17$ mag is 98.6% for the entire experiment duration mentioned above. We show a cumulative plot of the number of sources saved and classified as a function of the peak magnitude in Figure 6.1.

Sample of Ca-rich gap transients

This work focuses on the sample of Ca-rich gap transients identified in this experiment in the aforementioned period of operations (i.e. between 2018 June 01 to 2019 September 30). Given the large number of supernovae that are classified as a part of the experiment, it is not possible to perform nebular phase spectroscopic follow-up of all events. We thus identified candidate Ca-rich gap transients with a simple selection criteria using photometry from the ZTF survey and peak-light spectroscopic properties (from the classification effort), focusing on the population of hydrogen-poor low luminosity events in the sample. Although the criteria were motivated by the known properties of the previous sample of events, we deliberately kept these minimal for candidate selection due to the uncertainties on the intrinsic properties of the class and the small number of previously reported events. The candidate selection criteria were:

1. The transient should have a peak luminosity (in $g_{\rm ZTF}$ or $r_{\rm ZTF}$ filter) fainter than $M = -17$ mag at the known redshift of the host galaxy (after correcting for Galactic extinction, but not possible host galaxy extinction). We require at least two detections on the rise of the light curve in the same filter to be able to constrain the peak luminosity.

2. The spectroscopic properties of the source should be consistent with a hydrogen-poor SN near peak light. We do not include any events that exhibit broad hydrogen features in their spectra (i.e. Balmer lines that are not emanating from the underlying host galaxy). We obtained at least one epoch of late-time (at $\gtrsim 30$ d after peak light) spectroscopy with DBSP and LRIS on the Keck-I telescope for events that passed (1) and this criterion.

Table 6.1: **Summary of the properties of the Ca-rich gap transients presented in this paper, together with the sample of events that passed the selection criteria based on peak light photometry and spectroscopy only, but did not exhibit high [Ca II]/[O I] in their nebular phase spectra.** The column Spec Type only refers to the spectroscopic appearance of the object near peak light. The Ca-rich objects are indicated with Ca in the Spec Type column. For cases where the object did not turn nebular even at the latest phases of spectroscopic follow-up, we indicate the [Ca II]/[O I] flux ratio with NN and indicate the phase of the latest available spectrum. In the case of SN 2018gwo (indicated with *), the object did not pass the primary selection criteria but is a likely Ca-rich gap transient when combined with publicly available photometry and nebular phase follow-up from our campaign. Details on the objects that did not pass the nebular phase criterion are discussed in Appendix 6.8, highlighting why each object was excluded from the Ca-rich sample. For one event (SN 2019gau), we do not detect the nebular emission features and hence denote the [Ca II]/[O I] ratio with –.

Object	RA J2000	Dec J2000	Spec Type	Peak r mag (Abs. Mag)	[Ca II]/ [O I]flux Value / Phase (days)	Redshift	Host Offset ($''$/ kpc)
ZTF 18aayhylv / SN 2018ckd	14h06m11.94s	+09°20′39.″33	Ca-Ib	−16.17	> 3.38 / +58	0.024	39.03 / 19.08
ZTF 18abmxelh / SN 2018lqo	16h28m43.26s	+41°07′58.″66	Ca-Ib	−16.21	> 12.5 / +49	0.033	23.25 / 15.46
ZTF 18abttsrb / SN 2018lqu	15h54m11.47s	+13°30′50.″87	Ca-Ib	−16.44	> 8.38 / +31	0.036	37.12 / 26.70
ZTF 18acbwazl / SN 2018gwo*	12h08m38.82s	+68°46′44.″42	Ca-Ic	< −16.0	5.16 / +53	0.008	54.20 / 8.56
ZTF 18acsodbf / SN 2018kjy	06h47m17.96s	+74°14′05.″90	Ca-Ib	−15.63	4.44 / +111	0.018	17.18 / 6.35
ZTF 19aaznwze / SN 2019hty	12h55m33.03s	+32°12′21.″70	Ca-Ib	−16.38	> 3.27 / +38	0.023	18.74 / 8.73
ZTF 19abrdxbh / SN 2019ofm	14h50m54.65s	+27°34′57.″59	Ca-Ia	−17.03	> 2.13 / +175	0.030	18.24 / 11.16
ZTF 19abwtqsk / SN 2019pxu	05h10m12.60s	-00°46′38.″63	Ca-Ib	−16.56	> 8.30 / +146	0.028	30.93 / 17.56
ZTF 19aamfupk / SN 2019ccm	04h41m05.36s	+73°40′23.″10	SN Ib	−16.40	1.18 / +207	0.015	14.73 / 4.54
ZTF 19aanfsmc / SN 2019txl	09h32m59.36s	+27°30′07.″80	SN Ib	−16.21	0.87 / +330	0.034	11.68 / 7.96
ZTF 19aasqseq / SN 2019txt	09h59m06.38s	+17°49′09.″99	SN Ib	−15.90	1.34 / +180	0.026	19.94 / 10.69
ZTF 19abgqruu / SN 2019mjo	00h06m59.83s	+03°27′39.″70	SN Ib-pec	−16.62	NN / +180	0.041	12.38 / 10.06
ZTF 18abdffeo / SN 2018dbg	14h17m58.86s	+26°24′44.″59	SN Ib/c	−16.65	NN / +22	0.015	2.01 / 0.61
ZTF 19aarrdoz / SN 2019txr	08h42m31.91s	+56°17′42.″19	SN Ib/c	−16.73	< 1 / +270	0.044	1.95 / 1.71
ZTF 18aboabxv / SN 2018fob	15h13m07.23s	+41°16′11.″07	SN Ic	−16.93	0.87 / +212	0.029	18.47 / 10.84
ZTF 19aadttht / SN 2019yz	15h41m57.30s	+00°42′39.″41	SN Ic	−16.63	0.59 / +242	0.006	34.17 / 4.54
ZTF 19aadwtoe / SN 2019abb	07h54m17.26s	+14°16′22.″42	SN Ic	−16.56	0.79 / +357	0.015	4.26 / 1.34
ZTF 19aailcgs / SN 2019ape	10h51m42.55s	+18°28′52.″62	SN Ic	−16.62	0.87 / +180	0.021	11.53 / 4.79
ZTF 19abhhdwf / SN 2019ouq	17h01m41.94s	+30°06′34.″43	SN Ic	−16.68	< 1 / +170	0.036	8.71 / 6.27
ZTF 18acushie / SN 2018kqr	08h50m03.60s	+55°10′09.″54	SN Ic-BL	−16.75	NN / +16	0.045	3.15 / 2.82
ZTF 19aavlfvn / SN 2019gau	14h38m10.42s	+10°08′04.″93	SN Ia	−16.75	– / +260	0.028	1.30 / 0.73
ZTF 19aawhlcn / SN 2019gsc	14h37m45.25s	+52°43′36.″28	SN Ia 02cx	−13.90	NN / +60	0.011	10.99 / 2.50
ZTF 19abalbim / SN 2019ttf	18h42m15.87s	+24°53′48.″99	SN Ia 02cx	−13.99	NN / +230	0.011	11.07 / 2.52

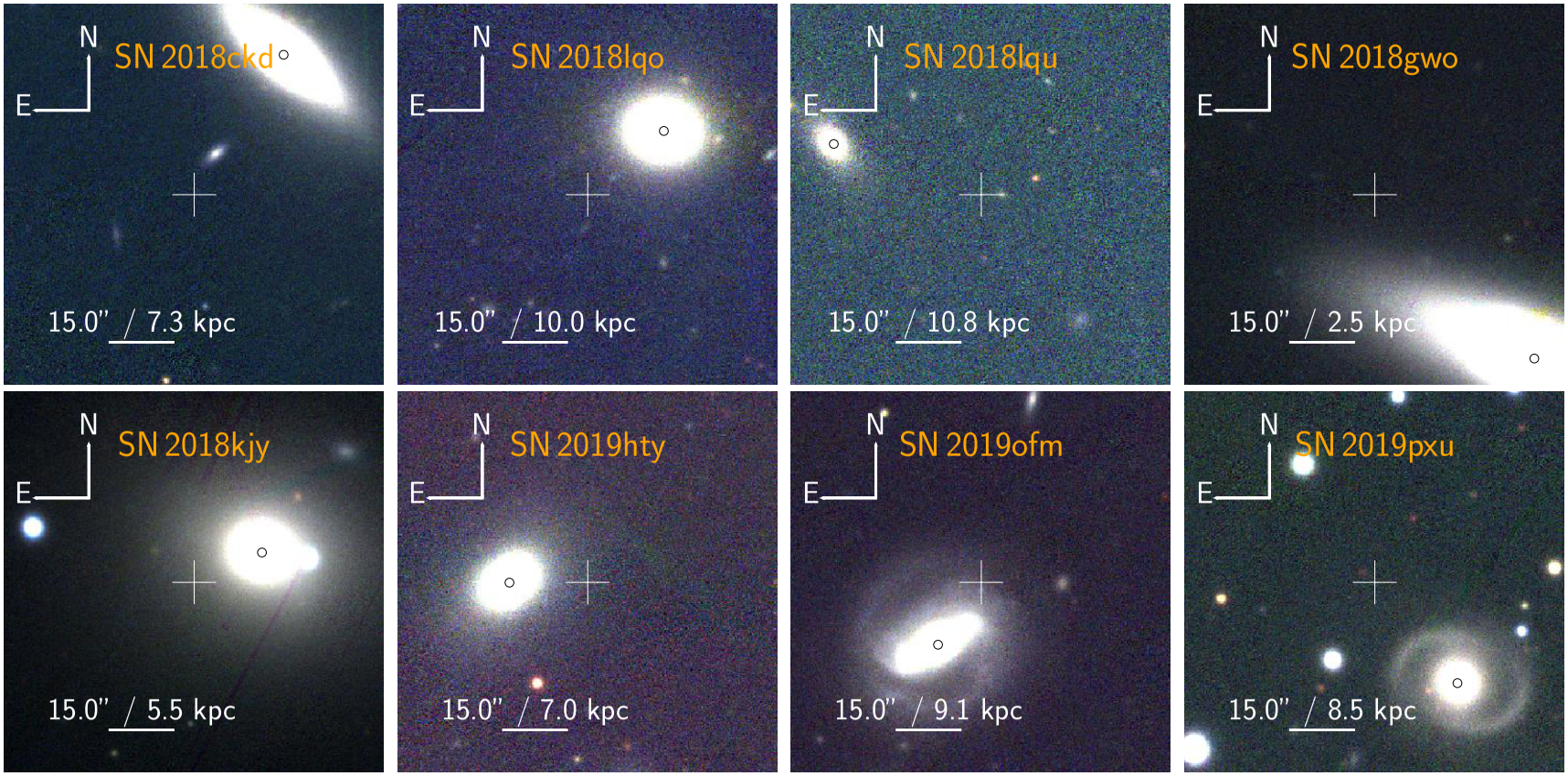

Figure 6.2: **RGB composite archival images of the locations of the 8 Ca-rich gap transients in the ZTF CLU sample.** Images were taken from the PS1 survey (Chambers et al., 2016). In each panel, the white cross-hair shows the location of the detected transient and the scale shows the projected angular size and physical scale at the redshift of the host galaxy. The apparent host galaxy is marked with a black circle at its core in each panel.

3. We require that the sources exhibit an early transition to the nebular phase, which we confirm by either the appearance of nebular emission lines and a fading continuum starting at +30 d from peak light or a complete transition to the nebular phase by $\approx$ 150 d after peak light.

4. As strong [Ca II] emission is the hallmark feature of this class, we require that the nebular phase spectrum should exhibit [Ca II]/[O I]$>$ 2 (De et al., 2018a; Milisavljevic et al., 2017) at any phase where the spectrum exhibits nebular emission lines.

Comparing the selection criteria to Kasliwal et al., 2012, we note that we do not select candidates based on the fast photometric evolution or photospheric phase velocities. This choice makes us more sensitive to events with larger diversity in ejecta masses and velocities. Applying selection criteria (1) and (2) to the sample of events in the volume limited experiment, we were left with 22 events which were followed up with spectroscopy in the nebular phase. Seven of these 22 sources were found to qualify the criterion for [Ca II]/[O I]$>$ 2 in the nebular phase, which defines the primary sample for this paper. In addition, we present observations of SN 2018gwo, a nearby Type Ic SN which was not detected in ZTF data before peak (due to a maintenance break in the month of October 2018), but was recovered on its radioactive decline tail. Combined with publicly available photometry and spectroscopy, we show that SN 2018gwo is a likely Ca-rich gap transient at a distance of 28 Mpc.

We apply the same selection criteria to the published literature sample of Ca-rich gap transients to include as our comparison sample. The set of ten literature events satisfying our cuts are SN 2005E, SN 2007ke, PTF 09dav, SN 2010et, PTF 11bij, SN 2012hn, PTF 11kmb, PTF 12bho, SN 2016hgs, and SN 2016hnk. We describe the initial detection to final classification of each of the individual objects in the sample of Ca-rich gap transients presented in this paper. We present a discussion of the properties of the remaining objects that passed the light curve criteria, but did not pass the nebular phase criterion in Appendix 6.8, specifically highlighting how we rule out the Ca-rich classification for each event. Henceforth, we refer all phases with respect to time of r-band peak (see Section 6.3).

SN 2018ckd / ZTF 18aayhylv

ZTF 18aayhylv (= SN 2018ckd) was first detected in the ZTF difference imaging pipeline on 2018 June 07.19 (MJD = 58276.19) at J2000 coordinates α = 14:06:11.95 and δ = 09:20:39.3, at a magnitude of $r = 19.39 \pm 0.09$ mag. The transient passed the filter on the GROWTH Marshal on 2018 June 10 (second detection) and was saved for spectroscopic follow-up. The transient was detected by the Catalina Realtime Transient Survey (CRTS; Drake et al., 2009) on 2018 June 12 and was reported to the TNS on the same date (Crts, 2018), and was assigned the IAU name AT 2018ckd. The transient was not detected in the ZTF alert production pipeline on 2018 June 01.31 to 5σ limit of $r \approx 19.82$ mag. However, the transient is detected at $\approx 4\sigma$ significance with $r \approx 20.25$ mag with forced photometry (see Section 6.2) at the transient location in the ZTF difference images (Masci et al., 2019). The last non-detection of the source in forced photometry was at 2018 May 29.31 down to a 5σ limit of $r \approx 19.65$ mag.

The transient was found in the outskirts of NGC 5463, a S0 galaxy at $z = 0.024$ (Figure 6.2), at a projected offset of $\approx 39\farcs0$ from the host center, corresponding to a physical separation of ≈ 19.1 kpc. We obtained a spectrum of ZTF 18aayhylv with DBSP on 2018 June 12, which exhibited P-Cygni features of He I and Ca II similar to Type Ib SNe. Subsequent photometry from ZTF and follow-up with the P60 + SEDM confirmed a faint and fast evolving (rise time $\lesssim 15$ d) light curve peaking at an absolute magnitude of $M \approx -16.0$ mag (Figure 6.3). A nebular phase spectrum of the source at $\approx +60$ d from r-band peak with LRIS on the Keck-I telescope showed strong [Ca II] emission lines with weak [O I] emission, confirming an early transition to the nebular phase and the classification of this source as a Ca-rich gap transient.

SN 2018lqo / ZTF 18abmxelh

ZTF 18abmxelh (= SN 2018lqo) was first detected in the ZTF difference imaging pipeline on 2018 August 10.18 (MJD = 58340.18) at J2000 coordinates α = 16:28:43.26 and δ = 41:07:58.7, at a magnitude of $r = 20.11 \pm 0.17$ mag. The transient passed machine learning thresholds on the GROWTH Marshal on 2018 August 16 and was saved for spectroscopic follow-up. We reported the transient to the TNS on 2019 October 28 (De, 2019a), leading to its IAU name of AT 2018lqo. With forced photometry on the ZTF difference images, we find that the transient was not detected on 2018 August 07.18 (MJD = 58337.18) down to a 5σ limit

of $r \approx 21.16$ mag. The transient exhibited an initial fading of ≈ 0.7 mag in ≈ 3 d following the first detection, followed by a rise to a peak ≈ 10 d later.

The transient was found in the outskirts of CGCG 224-043, an E-type galaxy at $z = 0.032$ (Figure 6.2), at a projected offset of $\approx 23\farcs2$, corresponding to a physical separation of ≈ 15.5 kpc. We obtained a spectrum of ZTF 18abmxelh with DBSP on 2018 August 21, which exhibited P-Cygni features of He I and Ca II similar to Type Ib SNe. Subsequent photometry from ZTF and follow-up with the P60 + SEDM indicated a faint and fast evolving (rise time $\lesssim 15$ d) light curve peaking at an absolute magnitude of $M \approx -16.1$ mag (Figure 6.3). A nebular phase spectrum of the source at $\approx +50$ d from r-band peak with LRIS on the Keck-I telescope showed strong [Ca II] emission lines, confirming a fast nebular phase transition and the classification of this source as a Ca-rich gap transient.

SN 2018lqu / ZTF 18abttsrb

ZTF 18abttsrb (= SN 2018lqu) was first detected in the ZTF difference imaging pipeline on 2018 September 03.13 (MJD = 58364.13) at J2000 coordinates α = 15:54:11.48 and δ = +13:30:50.9, at a magnitude of $r = 20.14 \pm 0.33$ mag. The transient was saved as a candidate supernova on its second detection on 2018 September 07, and assigned spectroscopic follow-up. We reported the transient to the TNS on 2019 November 06 (De, 2019b), leading to its IAU name of AT 2018lqu. With forced photometry on the ZTF difference images, we find that the transient was not detected on 2018 August 16.17 (MJD = 58346.17) down to a 5σ limit of $r \approx 21.16$ mag.

The transient was found in the outskirts of WISEA J155413.91+133102.4, a E-type galaxy at $z = 0.035$ (Figure 6.2), at a projected offset of $\approx 37\farcs1$, corresponding to a physical separation of ≈ 26.7 kpc. We obtained a spectrum of ZTF 18abttsrb with DBSP on 2018-09-12, which exhibited P-Cygni features of He I and Ca II similar to Type Ib SNe. Subsequent photometry from ZTF and follow-up with the P60 + SEDM indicated a faint and fast evolving (rise time $\lesssim 15$ d) light curve peaking at an absolute magnitude of $M \approx -16.4$ mag (Figure 6.3). A nebular phase spectrum of the source at $\approx +30$ d from r-band peak with LRIS on the Keck-I telescope showed strong [Ca II] and weak [O I] emission lines, confirming an early transition to the nebular phase and the classification of this source as a Ca-rich gap transient.

SN 2018gwo / ZTF 18acbwazl / Gaia 18dfp / PS 19lf

ZTF 18acbwazl (= SN 2018gwo) was first detected in the ZTF difference imaging pipeline on 2018 October 31.49 (MJD = 58422.49) at J2000 coordinates α = 12:08:38.83 and δ = +68:46:44.4, at a magnitude of $g = 19.20 \pm 0.17$ mag. Since the source was detected multiple times in the same night as part of the collaboration high cadence survey, the source was saved to the GROWTH Marshal on 2018 October 31. The source was detected by ZTF after a month-long gap in survey operations due to maintenance on the P48 camera. The source was first detected on 2018 September 28 by Wiggins, 2018 at 16.4 mag (clear filter) and reported to the TNS with the IAU Name AT 2018gwo, shortly after the sky region emerged from solar conjunction. An upper limit of 17 mag was reported on the previous night. A low resolution spectrum from the Three Hills Observatory was reported to the TNS on 2018 September 30 and 2018 October 06 by Leadbeater, 2018, consistent with a Type Ib/c SN with a reddened continuum near peak light, renaming this source to SN 2018gwo. Subsequent ZTF photometry showed that the source was detected by ZTF on its post peak decline tail. We obtained a spectrum of the source with P60 + SEDM on 2018 November 06, which exhibited a weak continuum with emerging broad [Ca II] and Ca II lines.

The transient was found in the outskirts of NGC 4128, a S0 galaxy at a distance (median reported in NED) of 28.6 Mpc (Figure 6.2), at a projected offset of $\approx 54\farcs2$ corresponding to a physical projected distance of ≈ 8.6 kpc. Although the transient was not detected by ZTF around peak light, we find the public observations combined with the later follow-up to be consistent with that of a Ca-rich gap transient. First, the initial detection and prior non-detection of the source reported by P. Wiggins suggest a fast rise to an absolute magnitude of $M \approx -16.0$ mag (in clear filter; Figure 6.3). The transient subsequently declined rapidly by ≈ 2 mags within ≈ 30 d after peak, confirming the faint peak luminosity and fast photometric evolution of the event. The peak light spectra together with the SEDM spectrum taken at ≈ 30 d are consistent with a Type Ib/c SN[6] in the photospheric phase, which exhibited a fast transition to the nebular phase. We obtained a follow-up spectrum of the transient with LRIS on the Keck-I telescope on 2018 Dec 04, which exhibited strong [Ca II] emission and weak [O I] emission, confirming the classification of this source of a Ca-rich gap transient.

[6] Although not used as a defining characteristic of the class, the only Type Ib/c SNe reported thus far in the outskirts of early-type galaxies are found to be Ca-rich gap transients.

SN 2018kjy / ZTF 18acsodbf / PS 18cfh

ZTF 18acsodbf (= SN 2018kjy) was first detected in ZTF difference imaging pipeline on 2018 December 03.36 (MJD = 58455.36) at J2000 coordinates α = 06:47:17.96 and δ = +74:14:05.9, at a magnitude of $r = 19.56 \pm 0.14$ mag. The transient was saved as a candidate supernova on its second detection on 2018 December 04, and assigned for spectroscopic follow-up. The transient was detected by the Pan-STARRS1 survey (Chambers et al., 2016) on 2018 December 17 and reported to TNS on 2018 December 22 (Chambers et al., 2018), acquiring the IAU name AT 2018kjy. With forced photometry on the ZTF difference images, we find three more lower significance detections up to ≈ 7 d before the first alert was issued. The last non-detection of the source was on 2018 November 19.48 (MJD = 58442.48) to a 5σ limit of $g \approx 20.45$ mag.

The transient was found in the outskirts of NGC 2256, an E-type galaxy at $z = 0.017$ (Figure 6.2), at a projected offset of $\approx 17\farcs2$, corresponding to a physical separation of $\approx$ 6.4 kpc. We obtained a spectrum of ZTF 18acsodbf with DBSP on 2018-12-14, which exhibited narrow P-Cygni features of He I, O I, and Ca II, and a reddened continuum similar to the Ca-rich gap transient PTF 12bho (Lunnan et al., 2017). Subsequent photometry from ZTF and follow-up with the P60 + SEDM confirmed a faint and fast evolving (rise time $\approx$ 17 d) light curve peaking at an absolute magnitude of $M \approx -15.6$ mag (Figure 6.3). Subsequent spectra of the source taken with Keck/LRIS +30 d and +120 d from peak show a fast transition to the nebular phase dominated by [Ca II] emission, confirming its classification as a Ca-rich gap transient.

SN 2019hty / ZTF 19aaznwze / ATLAS 19nhp / PS 19bhn

ZTF 19aaznwze (= SN 2019hty) was first detected in the ZTF difference imaging pipeline on 2019 June 14.18 (MJD = 58648.18) at J2000 coordinates α = 12:55:33.03 and δ = +32:12:21.7, at a magnitude of $g = 19.62 \pm 0.19$ mag. The transient passed machine learning thresholds on the GROWTH Marshal on 2019 June 20 and was saved for spectroscopic follow-up. The transient was detected by the ATLAS survey (Tonry et al., 2018) on 2019 June 19 (Tonry et al., 2019a) and reported to TNS on the same date, and assigned the IAU name AT 2019hty. With forced photometry on the ZTF difference images, we found an additional detection of the source on 2019 June 11.24 (MJD = 58645.24) at a magnitude of $g = 19.52 \pm 0.12$. The last non-detection of the source was on 2019 June 08.23

(MJD = 58642.23) to a 5σ limit of $r \approx 21.43$ mag.

The transient was found in the outskirts of WISEA J125534.50+321221.5, an E-type galaxy at $z = 0.023$ (Figure 6.2), at a projected offset of $\approx 18\farcs7$, corresponding to a physical separation of ≈ 8.7 kpc. We obtained a spectrum of ZTF 19aaznwze with SEDM and DBSP on 2019 July 01, which exhibited a Type Ib-like spectrum with a reddened continuum and a broad P-Cygni feature of the Ca NIR triplet. Photometric follow-up with SEDM and data from ZTF show a faint peak magnitude of $M \approx -16.1$ mag and a rise time of ≈ 15 d (Figure 6.3). We obtained an additional spectrum of the source with DSBP at ≈ 40 d from peak light, which showed broad emerging line of [Ca II] and weak [O I], confirming a fast transition to the nebular phase dominated by [Ca II] emission, and classifying this source as a Ca-rich gap transient.

SN 2019ofm / ZTF 19abrdxbh / ATLAS 19tjf

ZTF 19abrdxbh (= SN 2019ofm) was first detected in the ZTF difference imaging pipeline on 2019 August 20.15 (MJD = 58715.15) at J2000 coordinates α = 14:50:54.65 and δ = +27:34:57.6, at a magnitude of $g = 20.43 \pm 0.24$ mag. The transient met machine learning thresholds and was saved to the GROWTH Marshal on 2019 August 24. The ZTF detection was reported by the AMPEL (Nordin et al., 2019a) automatic stream to TNS on 2019 August 23 (Nordin et al., 2019b), acquiring the IAU name AT 2019ofm. With forced photometry on the ZTF difference images, we find an additional detection of the source on 2019 August 17.24 (MJD = 58712.24) at a magnitude of $r = 20.07 \pm 0.26$. The last non-detection of the source was on 2019 August 17.15 (MJD = 58712.15) to a 5σ limit of $g \approx 20.40$ mag.

The transient was found on top of the SB-type galaxy IC 4514 at $z = 0.030$ (Figure 6.2), at a projected offset of $\approx 18\farcs2$, corresponding to a physical offset of ≈ 11.2 kpc. We obtained a spectrum of the source with DBSP on 2019 August 27, which exhibited clear features of a 1991bg-like Type Ia SN at the host redshift. Following the first detection, the source rose to a peak absolute magnitude of $M_r \approx -16.6$ mag, suggesting a sub-luminous Type Ia SN consistent with the spectroscopic classification. We obtained a follow-up spectrum of the source with LRIS at ≈ 175 d after peak light, which showed that the source had transitioned to the nebular phase exhibiting [Ca II] as the only detectable broad feature in the spectrum. Together with the non-detection of iron-group features typically seen in 1991bg-like objects,

the strong [Ca II] feature suggested that SN 2019ofm was similar to the Ca-rich gap transients PTF 09dav and SN 2016hnk, thus classifying the source as a Ca-rich gap transient.

SN 2019pxu / ZTF 19abwtqsk / ATLAS 19uvg / PS 19fwq

ZTF 19abwtqsk (= SN 2019pxu) was first detected in the ZTF difference imaging pipeline on 2019 September 04.50 (MJD = 58730.50) at J2000 coordinates α = 05:10:12.61 and δ = −00:46:38.6, at a magnitude of $r = 20.09 \pm 0.20$ mag. The transient met machine learning thresholds and was saved to the GROWTH Marshal on 2019 September 22 on its third detection in the ZTF alert stream. The transient was detected by the ATLAS survey on 2019 September 10 (Tonry et al., 2019b) and reported on the same date to TNS, acquiring the IAU name AT 2019pxu. The field was not covered by the survey in > 30 d before the first detection, and hence we are unable to determine a recent upper limit from the first detection.

The transient was found in the outskirts of the spiral galaxy WISEA J051011.32-004702.5 at $z = 0.028$, at a projected offset of $\approx 30\farcs9$ (Figure 6.2), corresponding to a physical projected offset of ≈ 17.6 kpc. We obtained a peak light spectrum of the source with P200 + DBSP on 2019 October 03, which exhibited a Type Ib-like spectrum and a reddened continuum similar to the Ca-rich gap transient PTF 12bho. Subsequent photometry from ZTF and P60 + SEDM indicated a rise time of ≈ 17 d and a faint peak absolute magnitude of $M = -16.4$ mag. We obtained a follow-up spectrum with LRIS on 2019 October 27, which showed a faint continuum with emerging broad emission lines of [Ca II] and Ca II, confirming a fast nebular transition and the classification of the source as a Ca-rich gap transient.

Photometry

We obtained *gri* photometry of transients from data taken with the P48 ZTF camera (Bellm et al., 2019b), that were processed with the ZTF data processing system (Masci et al., 2019). Light curves were extracted using forced point spread function (PSF) photometry (Masci et al., 2019) at the location of the transient in the difference images, where the location was determined from the median position of the source reported in all alerts of the transient in the ZTF transient detection pipeline. We report detections of the transients in the forced photometry for epochs where the signal-to-noise ratio is higher than 3σ, while 5σ upper limits are reported for other epochs. We include data acquired in the public as well as the higher cadence internal

collaboration and Caltech surveys. In cases where the transient was covered by an internal survey and has more than one visit per night, we performed an inverse variance weighted binning of the flux measurements in bins of 2.5 d to improve the signal-to-noise ratio of the measurements. We perform the same binning for reporting upper limits, where we use inverse variance weighted flux uncertainty to report the 5σ upper limit for that epoch.

We obtained additional multi-color photometry near peak light with the SEDM rainbow camera on the Palomar 60-inch telescope, and the data were processed using the SEDM image reduction pipeline. Image subtraction against archival references from SDSS and PS1 were performed, and difference magnitudes were obtained using the pipeline described in Fremling et al., 2016. We show the photometric evolution of these transients near peak light in Figure 6.3, while the data are presented in Table 6.5. We correct the photometry for foreground Galactic extinction using the maps in Schlafly et al., 2011 and the extinction law of Cardelli et al., 1989, assuming $R_V = 3.1$.

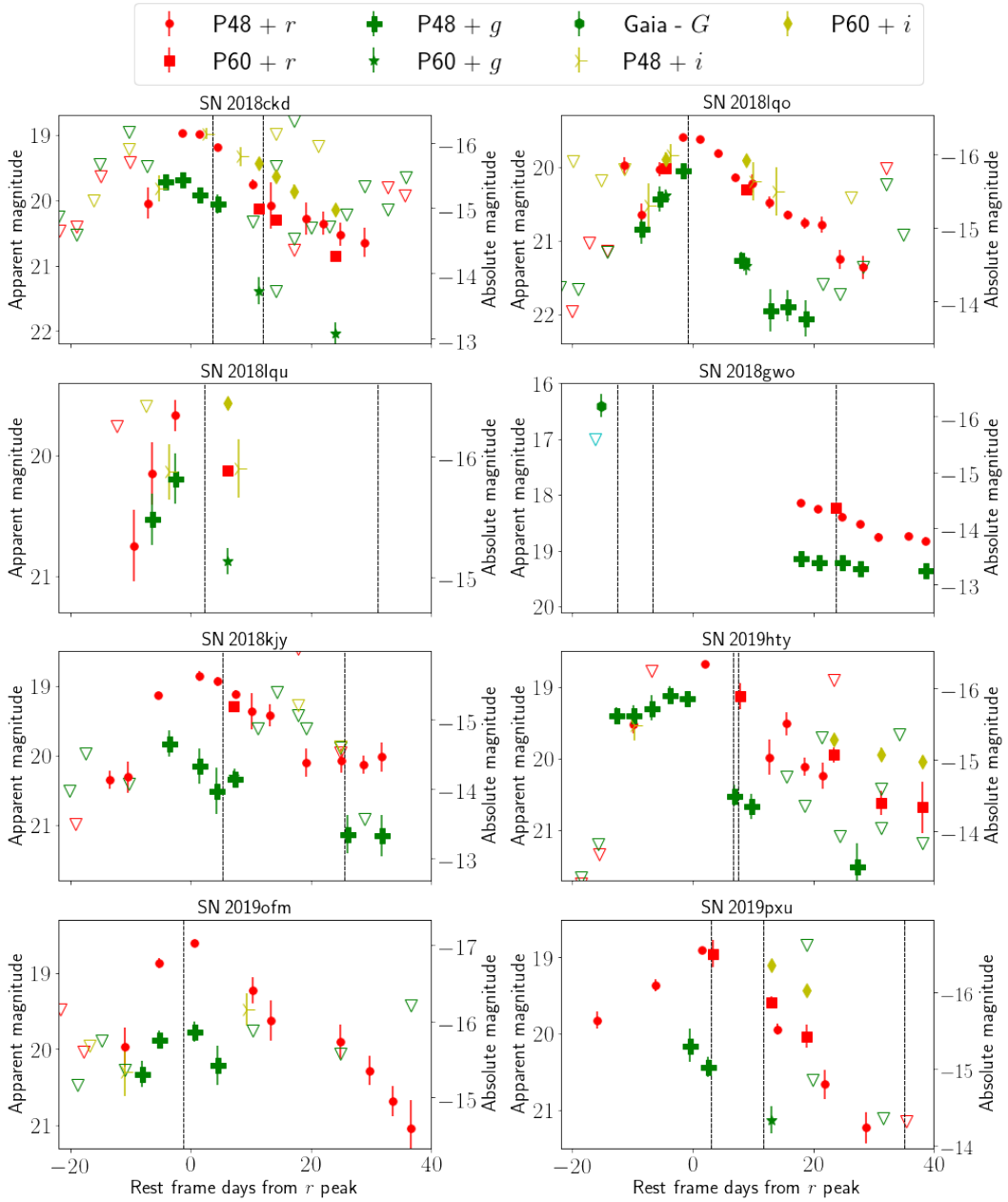

Figure 6.3: **Photometric evolution near peak light of the Ca-rich gap transients presented in this sample.** Time is presented with respect to the r-band light curve of the individual sources (corrected for Galactic extinction). Filled symbols denote detections from forced photometry on the ZTF difference images (see figure legend), while hollow inverted triangles denote 5σ upper limits at the position of the transient. Red points denote r-band photometry, green points denote g-band photometry, yellow points denote i-band photometry and cyan points denote photometry in the clear filter. The vertical dashed lines denote epochs of spectroscopy. For SN 2018gwo, we also show public TNS photometry from Gaia and Wiggins, 2018 (see legend).

Late-time imaging

We obtained additional late-time photometry of the transients with the Wafer Scale Imager for Prime (WASP) on the Palomar 200-inch telescope, which were reduced with the pipeline described in De et al., 2020b. We used LRIS on the Keck-I telescope for late-time imaging of some transients reported in this paper, and the data were reduced using the automated `lpipe` pipeline (Perley, 2019). Image subtraction was not necessary for the late-time imaging for most sources since the majority were far from their host galaxies, and we report aperture photometry measurements (accounting for aperture corrections) for these sources, calibrated against the PS1 (Chambers et al., 2016) catalog.

For sources where the photometry was deemed to be contaminated by host galaxy light from visual inspection (which was found to be true only for SN 2018kjy), we performed image subtraction using reference images from WASP obtained > 1 year after the peak of the transient light curve. The image subtraction was performed by first aligning the science image to the reference image by aligning the two images to the same system calibrated against Gaia DR2 (Gaia Collaboration et al., 2018). The alignment was performed by first extracting a source catalog for both the science and the reference image using `SExtractor` (Bertin, 2006) followed by astrometric alignment using the `scamp` code with Gaia DR2 as the reference catalog.

The images were then resampled to the same output grid using `Swarp` (Bertin et al., 2002) and flux scaled to a common zero-point. The image subtraction was performed using the `ZOGY` code (Zackay et al., 2016) using an input PSF model for the science and reference image using `PSFEx` (Bertin, 2011). Forced PSF photometry was performed on the generated difference image to estimate the flux and flux uncertainty at the transient position, including an additional Monte Carlo simulation of the PSF-fit flux variance across the difference images to account for uncorrected correlated noise in the difference image output.

However, we caution that in several cases, the latest images from LRIS show evidence of diffuse sources near the transient which we are unable to subtract due to the absence of a template (ideally acquired several hundred days after the latest observation), and thus report the host-contaminated aperture photometry fluxes only. As in the case of the ZTF photometry, we report detections of sources where the signal to noise ratio is higher than 3σ, and 5σ upper limits otherwise. The late-time photometric evolution for the sample is shown in Figure **??**. We discuss the local environments of the Ca-rich gap transients as observed in the late-time imaging in

Section 6.4.

Spectroscopy

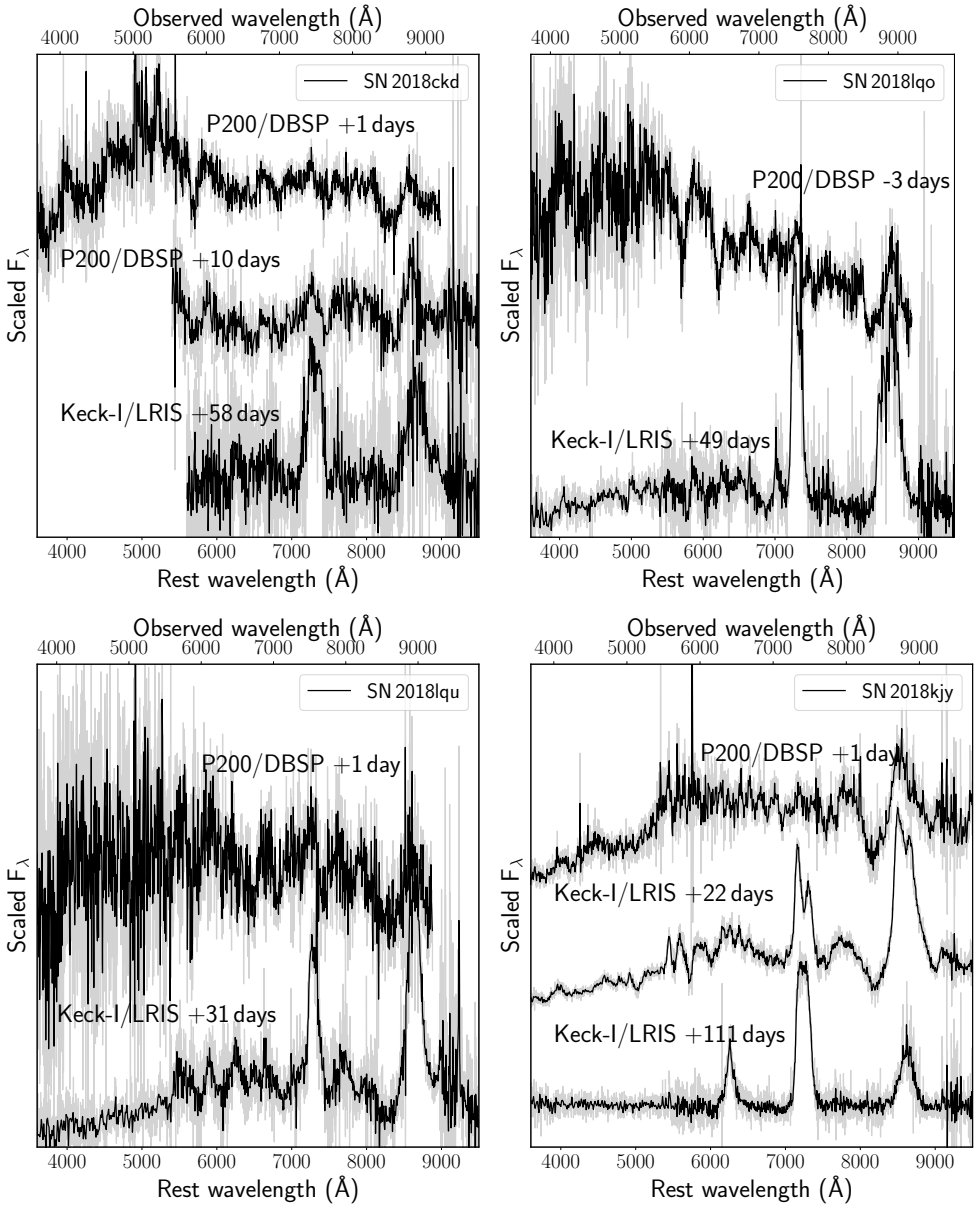

Figure 6.5: **Spectroscopic sequence of the sample of Ca-rich gap transients presented in this paper.** In each panel, the object name is indicated in the legend and the phase of the spectrum is denoted next to each spectrum with respect to the peak of the *r*-band light curve. The gray lines show the unbinned spectra while black lines show the same spectra binned to improve the signal-to-noise ratio.

Spectroscopic follow-up of transients near peak light was obtained as a part of the regular classification effort of the CLU experiment. Typically one spectrum was

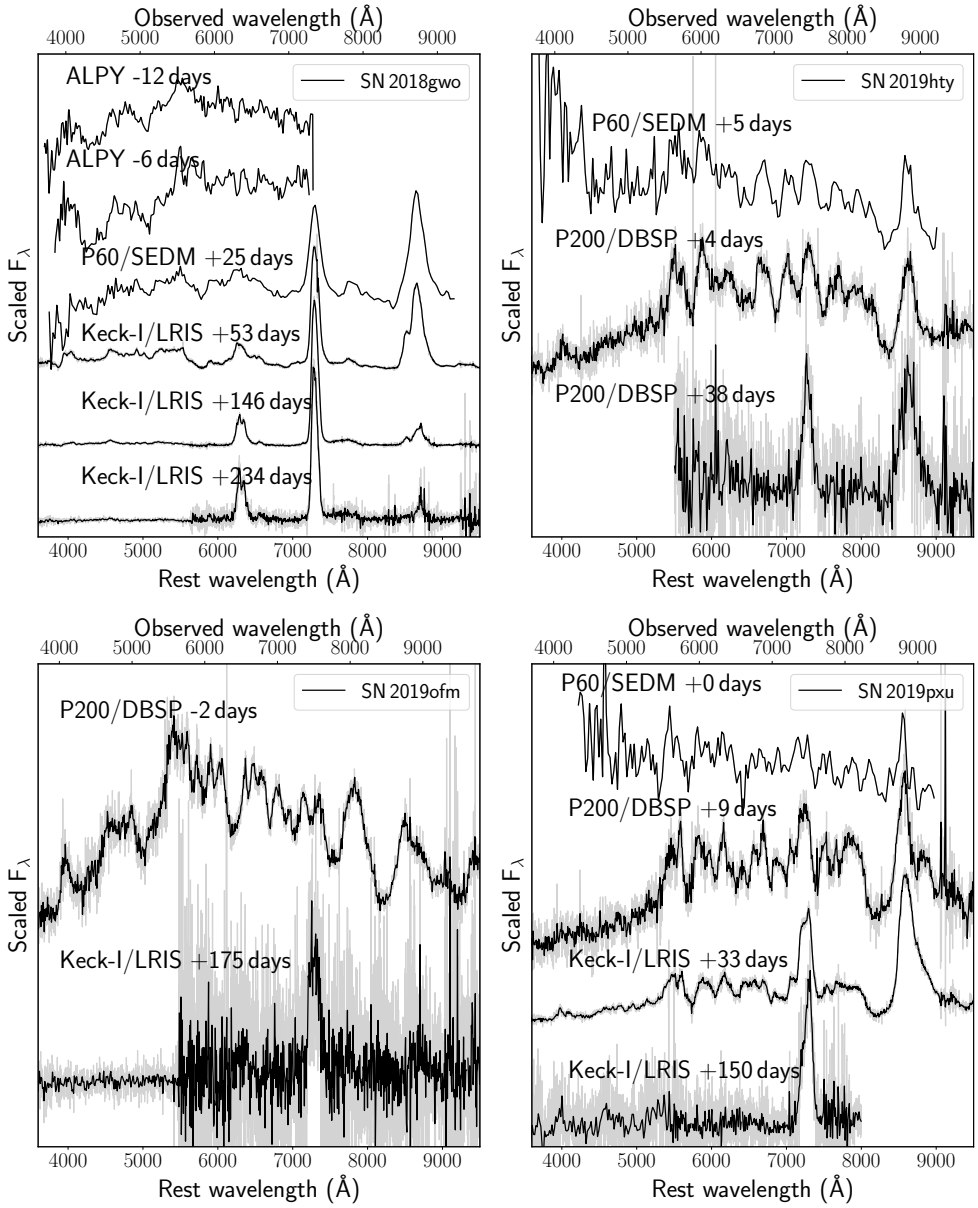

Figure 6.5: Continued.

obtained near peak light for initial spectroscopic classification and a sequence of nebular phase spectra were obtained starting at least ≈ 30 d after peak. The SED Machine spectrograph was used for spectroscopy for only two of these sources (SN 2018gwo and SN 2019hty) since they were typically too faint (> 19 mag) for SEDM spectroscopy. The SEDM data were reduced using the `pysedm` (Rigault et al., 2019) automatic pipeline. Peak light spectroscopy for the rest of the sample was obtained using the DBSP, and the data were reduced using the `pyraf-dbsp` pipeline (Bellm et al., 2016).

We obtained two epochs of spectroscopy of SN 2018gwo with the APLY200 spectrograph at Three Hills Observatory. The spectra were reduced using ISIS software[7]. The spectrum images were bias and dark subtracted, flat field corrected using a tungsten halogen lamp, corrected for geometric distortions, and the sky background subtracted before extracting the spectrum profile. The spectrum was wavelength calibrated using a Ne/Ar reference lamp and calibrated in relative flux using as a reference, a hot star (HD123299) from the MILES library of spectra[8] measured the same night at similar airmass. We obtained follow-up spectroscopy for some sources using the Alhambra Faint Object Spectrograph and Camera (ALFOSC) on the Nordic Optical Telescope (NOT). The NOT data were reduced using the `foscgui` pipeline[9].

Late-time nebular spectroscopy was obtained using LRIS on the Keck-I telescope starting from $\approx$ 30 d after peak light. For some sources, we obtained up to four epochs of nebular phase spectra using LRIS. The data were reduced using the automated `lpipe` pipeline. We present the complete list of spectroscopic observations in Table 6.6, while the spectra are presented in Figure 6.5. In addition, we use publicly available spectra from TNS for SN 2018gwo and some events in the control sample (Appendix 6.8). Spectra for the literature sample of events were obtained from WISEReP (Yaron et al., 2012) and attributed to the original source where relevant. All data presented in this paper will be publicly released on WISEReP and as an electronic supplement upon publication.

6.3 Analysis of the combined sample

Here, we present a combined analysis of the spectroscopic and photometric properties of the sample of Ca-rich gap transients presented in this paper with those in the literature sample of events that satisfy our selection criteria. We begin with a qualitative analysis of the spectroscopic properties, in particular, to highlight the existence of a continuum of spectroscopic characteristics in the full sample of events. We outline the procedures used for a quantitative analysis of the full sample of events, and present quantitative results on the photometric and spectroscopic properties of the sample to highlight trends across the continuum of spectroscopic properties. We use these results to discuss implications for the progenitor channels in Section 6.6.

[7] by C. Buil; `http://www.astrosurf.com/buil/isis-software.html`

[8] `http://miles.iac.es/`

[9] `http://graspa.oapd.inaf.it/foscgui.html`

Photospheric phase spectra

Since we aim to characterize the peak light spectral diversity in this section, we discuss objects where a medium resolution spectrum was available within ≈ 10 d of peak light – 16 of the total sample of 18 objects[10] have photospheric phase spectra acquired near the peak of the light curve. The photospheric phase spectra of this sample are diverse, and most notably separate into SN Ib/c-like (absence of a strong Si II line, with a continuum of He I line strengths) and SN Ia-like (with strong Si II lines) objects. This distinction is a natural parallel to the traditional classification scheme invoked for the broader population of hydrogen poor supernovae (Filippenko, 1997; Gal-Yam, 2017). We thus proceed by defining two spectroscopic classes within the sample of Ca-rich gap transients based on their similarity to either SNe Ib/c or SNe Ia near peak light – and refer to them as Ca-Ib/c and Ca-Ia objects. Within the photometric selection criteria defined in this experiment, the relative occurrence rate of the Ca-Ib/c to Ca-Ia objects are 6:1, although a true rate estimate would require incorporating the luminosity functions of the two classes (see Section 6.5).

The Ca-Ib/c class

In Figure 6.6, we plot the photospheric phase spectra of the Ca-Ib/c objects. Prominent spectral lines detected in the photospheric phase are marked, along with three optical lines of He I and their P-Cygni absorption regions due to the known similarity of these objects to Type Ib SNe at peak (Perets et al., 2010). The ZTF sample of events is dominated by Type Ib-like spectra near peak light (exhibiting He I λ5876, λ6678, and λ7065) in the photospheric phase spectra albeit with a range of line strengths and velocities. The He I λ6678 line is usually contaminated by the nearby Si II $\lambda\lambda 6347, 6371$ lines (De et al., 2018a; Kasliwal et al., 2012; Sullivan et al., 2011). Other common features in the peak light spectra include P-Cygni features of O I λ7774 and Ca II H&K and the NIR triplet. SN 2012hn is the only object that does not show any evidence for He I in its peak spectrum (Valenti et al., 2014). We also do not conclusively identify He I in the peak light spectrum of SN 2018gwo. We thus tentatively classify SN 2018gwo as a Ca-Ic although the low SNR and resolution of the peak spectrum precludes a definite classification.

Upon closer inspection, the set of peak light spectra shown in Figure 6.6 demarcates into two groups of events – one with events characterized by flat continua across the

[10] SN 2007ke and PTF 11bij are the only objects that do not have a peak light spectrum.

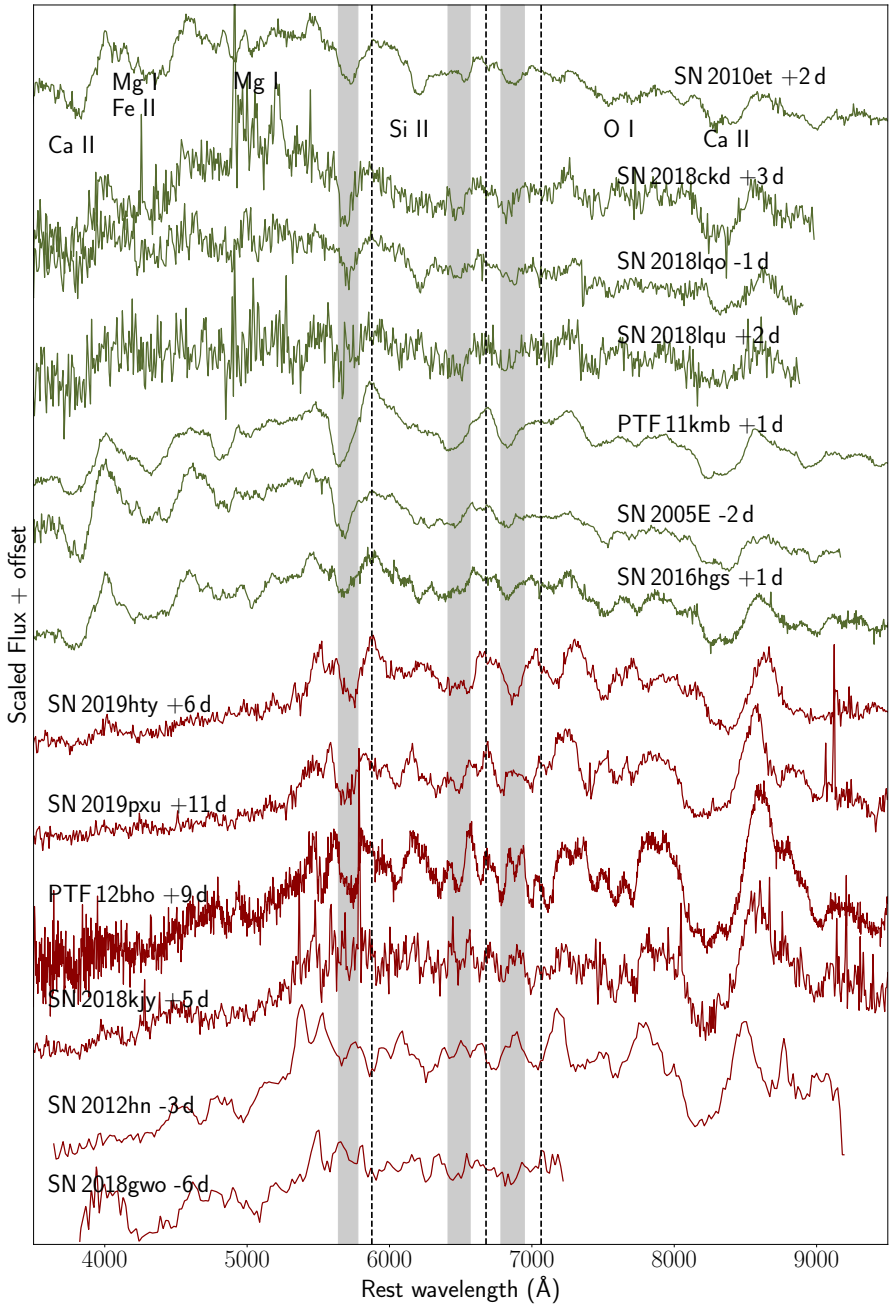

Figure 6.6: **Photospheric phase spectra of Ca-rich gap transients that exhibit SN Ib/c-like features (termed Ca-Ib/c objects) in the ZTF sample combined with the same for events in the literature.** The transient name and phase of the spectrum is indicated next to each spectrum. The spectrum color separates the two primary spectral types in the sample based on the shape of the continuum – the events plotted in green have peak spectra characterized by flat or green continua, while spectra in red show events that exhibit strong suppression of flux at bluer wavelengths thus exhibiting red continua. The solid dashed lines show the rest frame wavelengths of three optical He I lines, while the shaded bars show the expected P-Cygni absorption minima for velocities ranging from 5000 – 12000 km s^{-1}.

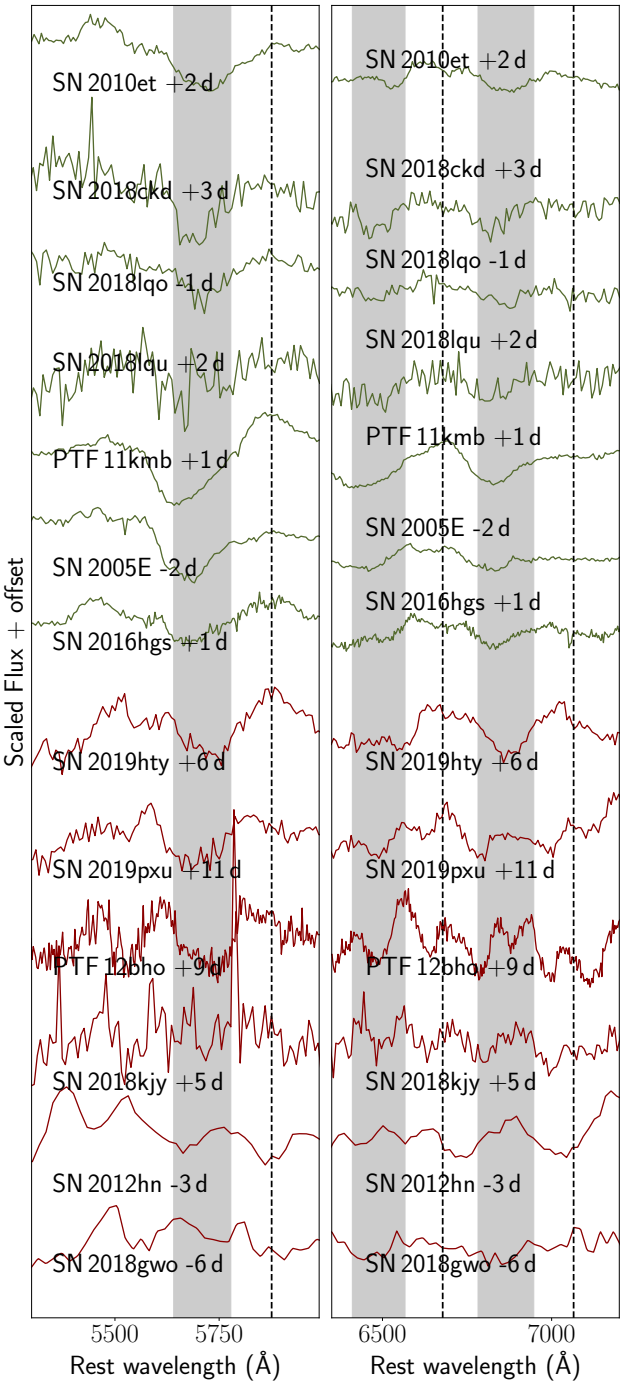

Figure 6.7: **Zoomed-in plots of the photospheric phase spectra of the Ca-Ib/c objects around the expected positions of He I transitions.** The left panel shows the region around the He I λ5876 line and the right panel shows the region including the He I λ6678 and λ7065 lines. The color coding of the spectra is the same as in Figure 6.6. The black dashed lines show the rest frame positions of the He I lines, while the grey shaded regions show the absorption region for the a velocity range of 5000 – 12000 km s^{-1}.

entire spectral range and one with events characterized by strong suppression of flux at bluer wavelengths and red continua. We indicate these two classes of events with different colors (dark green and red) in Figure 6.6, and throughout the rest of this manuscript. The spectra of events in the first class are relatively homogeneous, and show clear evidence of strong He I at normal photospheric velocities ($\approx 8000-11000$ km s^{-1}; see Section 6.3). Notably, these objects exhibit strong continuum in the blue side of the spectrum (below 5500 Å) and clear absorption features of Ca II, Mg I, and Fe II superimposed on the blue side continuum.

On the other hand, events in the latter group show strong suppression of the continuum flux in the blue side of the spectrum (below 5500 Å) producing a spectrum with redder colors. These exhibit a diverse range of line velocities, ranging from events with normal photospheric velocities (SN 2019pxu) to peculiar low velocity ($\approx$ 4000 – 6000 km s^{-1}) events such as PTF 12bho and SN 2018kjy. Absorption features of metals blue-wards of 5500 Å (Ca II, Mg I, and Fe II), are only weakly detected due to the strong suppression of flux in this region. Notably, SN 2012hn and SN 2018gwo in this group do not show evidence of He I (and hence would be Ca-Ic objects nominally), while SN 2018kjy exhibits only weak signatures of low velocity He I in its spectrum. Given the small number of events, it is unclear whether there is a continuum of events between these two types of objects. We proceed by referring to the two classes of objects as objects with green and red continua, respectively, and use the same color scheme as in Figure 6.6.

There is considerable diversity in the presence and strength of He lines in the peak light spectra of the Ca-Ib/c objects. The identification of He is a crucial aspect for understanding the progenitors of these explosions since the presence of He in the ejecta is indicative of a He-rich progenitor system. However, He lines visible in the optical region are non-thermally excited (Dessart et al., 2012; Hachinger et al., 2012) and hence their absence does not necessarily preclude the presence of He in the ejecta. The detection of He lines is dependent on the amount of ^{56}Ni mixing in the ejecta to be able to excite the He I transitions non-thermally and thus these lines also constrain on the mixing in the ejecta. While most of the Ca-Ib/c objects exhibit prominent and unambiguous He I lines in the optical, similar to the prototype event SN 2005E, these lines are difficult to unambiguously identify in peculiar events.

In Figure 6.7, we show zoomed in regions of the peak light spectra of the sample around the optical He I lines at 5876 Å, 6678 Å , and 7065 Å. The identification of He is complicated by the contamination of the He I 5876 Åline with the nearby Na

I line seen in SNe Ic, thus requiring the detection of multiple He I lines at similar velocities to conclusively confirm the presence of He. This necessitates a careful examination of the features around the other optical He I lines at 6678 Å and 7065 Å. We note that all the green Ca-Ib/c events exhibit unambiguous evidence of He I at similar velocities at all the optical transitions.

However, the family of events with red continua exhibit much more diverse properties around the He I transitions, which include peculiar events like SN 2012hn, PTF 12bho, and SN 2018kjy. Only SN 2019hty exhibits unambiguous P-Cygni absorption in all the He I lines and thus He can be confirmed. In the progression from SN 2019pxu to SN 2012hn, we see a gradual change in the strength and absorption depth of the He lines. Specifically, we note the appearance of an emission feature at the expected absorption position of the He I λ7065 line that gets stronger from SN 2019pxu to SN 2012hn. This emission feature was attributed to C II in the spectral modeling of SN 2012hn, although it could also be associated with Al II (De et al., 2018a; Kasliwal et al., 2010; Sullivan et al., 2011). In the same sequence of objects, the He I λ7065 line gets progressively weaker until it is not detected at all in SN 2012hn. The same trend is also detected in the He I λ6678 line, although the identification of He I λ6678 in SN 2012hn is complicated by the presence of the nearby Si II line. SN 2012hn does not show any evidence of He either in its optical or near-infrared spectra (Valenti et al., 2014). We thus find evidence of a continuum of He line strengths in these events, which range from events with strong He lines to very weak or absent He lines.

The Ca-Ia class

Figure 6.8 shows a comparison of the photospheric and nebular phase spectra of the three Ca-Ia objects in the sample, indicated by orange markers throughout this manuscript. These objects exhibit typical features of 1991bg-like objects defined by the strong Ti II trough in the blue side of the spectrum. In addition, all of these objects exhibit mild to strong line blanketing features short-wards of 5000 Å in the blue side of the spectrum. Such features are typically indicative of the outer ejecta being rich in Fe-group material that efficiently absorbs the blue flux (Nugent et al., 1997; Polin et al., 2019). We note that SN 2019ofm exhibits several similarities to the peak light spectrum of SN 2016hnk (although with lower line velocities), while PTF 09dav exhibits some different features and line strengths, some of which were attributed to rare elements like Sc II and Sr II in Sullivan et al., 2011. Although the

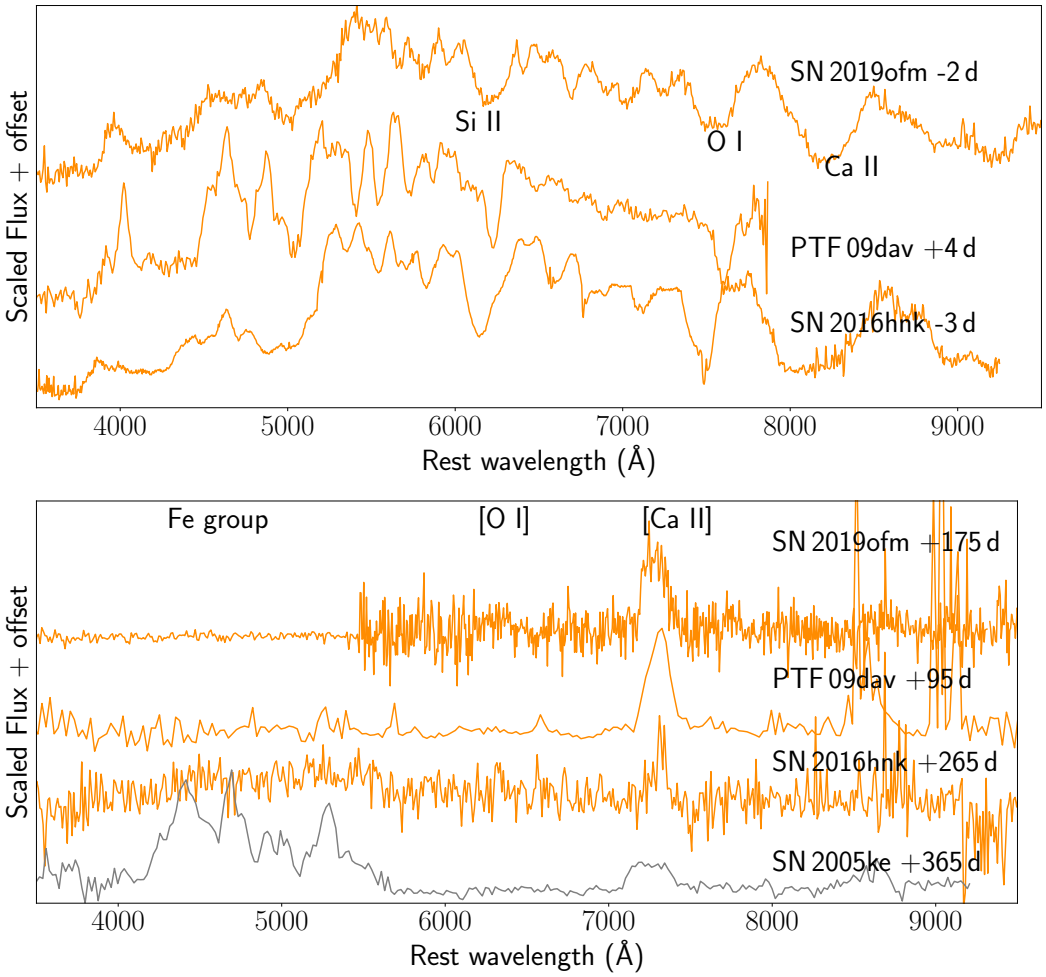

Figure 6.8: **Photospheric (top panel) and nebular (bottom panel) phase spectra of Ca-rich gap transients that exhibit SN Ia-like features (termed Ca-Ia objects) in the ZTF sample combined with the same for events in the literature.** The transient name and phase of the spectrum is indicated next to each spectrum. The prominent photospheric lines of Si II, O I, and Ca II are marked in the peak light spectra plot while the nebular lines of [O I], [Ca II], and Fe group elements are marked in the lower panel. In the lower panel, we also show a nebular phase spectrum of the SN 1991bg-like event SN 2005ke to highlight the differences between 1991bg-like objects and the Ca-rich objects in terms of the absence of Fe-group features in the blue part of the spectrum.

peak light spectra are broadly similar, such exotic elements were not required in the spectral modeling of SN 2016hnk in Galbany et al., 2019 and Jacobson-Galan et al., 2019, and hence is unlikely for SN 2019ofm given the spectral similarity between the two objects.

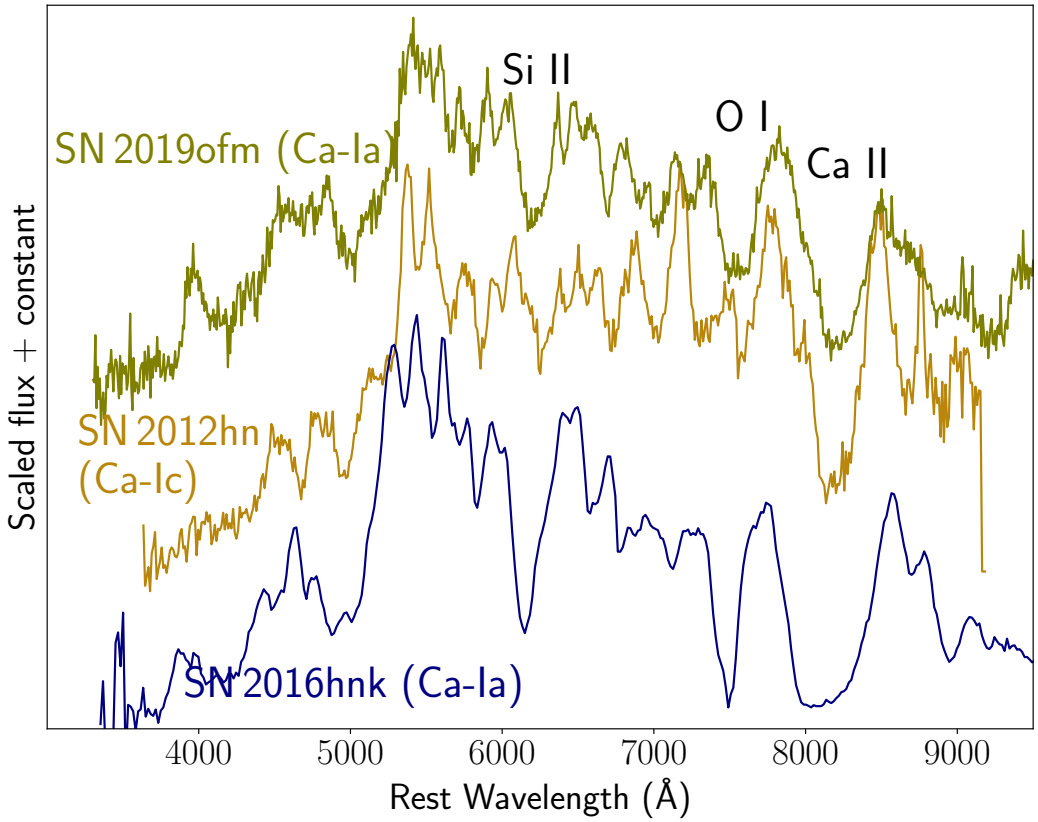

Figure 6.9: **Comparison of the peak light optical spectra of He poor Ca-Ib/c event SN 2012hn and the two Ca-Ia events SN 2016hnk and SN 2019ofm.** Prominent spectral features of Si II, O I, and Ca II are marked.

Given the lack of the prominent He lines in both the Ca-Ic objects and Ca-Ia objects, it is instructive to compare the peak light spectra of the two classes. In Figure 6.9, we plot the peak light spectrum of SN 2012hn – the only unambiguous Ca-Ic object in the sample along with the peak light spectra of two Ca-Ia objects SN 2019ofm and SN 2016hnk. It is worth noting the striking resemblance between the spectra of SN 2012hn and SN 2019ofm, barring the weaker strength of the Si II line in SN 2012hn (which leads to its Ca-Ic classification). Specifically, we find that although the velocities are different in the three objects, they show similar features over the entire optical spectrum. The only discrepancies are in the bluer part of the spectrum where the Ca-Ia objects show features from Fe group elements (near

$\approx$ 4000 Å). SN 2016hnk exhibits a very strong Si II line similar to normal / sub-luminous SNe Ia (Gal-Yam, 2017), while SN 2019ofm exhibits a weaker Si II line but with all the characteristic SN Ia features, and SN 2012hn exhibits the weakest Si II line and nearly the same spectral features as SN 2019ofm.

Sun et al., 2017 demonstrated that Type I SN subtypes (Ia/Ib/Ic) occupy different loci on the line depth diagram of Si II λ6150 Å and O I λ7774 Å measured in peak-brightness spectra (see their Figure 9). In order to quantitatively investigate the striking similarities between the Ca-Ia and Ca-Ic objects, we performed these measurements in a manner similar to that of Sun et al., 2017. SN 2016hnk exhibits a λ6150 line depth of $\approx$ 0.6 and a depth ratio of $\lambda6150/\lambda7774 \approx 0.75$, similar to 91bg-like SNe Ia in the Sun et al., 2017 sample. However, we find that SN 2019ofm exhibits a λ6150 line depth of $\approx$ 0.35 and a depth ratio of $\lambda6150/\lambda7774 \approx 0.83$ which is exactly at the SN Ia-SN Ic classification boundary suggested in that work.

Similarly, the peak spectrum of SN 2012hn exhibits a λ6150 depth of $\approx$ 0.3 and a depth ratio of $\lambda6150/\lambda7774 \approx 1.0$, which falls exactly on the classification boundary for SNe Ib/c in that sample. In particular, we note that SN 2019ofm and SN 2012hn occupy an empty phase space in the classification diagram of Sun et al., 2017 – with SN 2019ofm being a transitional Ia-Ic object and SN 2012hn being a transitional Ib-Ic object. We thus conclude that there may be a continuum of events leading from Ca-Ia to Ca-Ic to Ca-Ib objects based on their peak light photospheric spectral properties. We discuss this sequence together with the photometric and nebular phase properties in Section 6.6.

Photospheric velocities

For a quantitative comparison of the spectral features, we performed fits of the most prominent spectroscopic features of the combined sample of events, and list the derived parameters in Table 6.4. The aim of this exercise is to elucidate the photospheric velocity evolution of the most prominent spectral lines in these transients as they hold clues to the density structure of the ejecta and internal emission powering mechanism (Piro et al., 2014a; Sell et al., 2015). These velocity estimates are also necessary for quantitative estimates of the explosion kinetics (Arnett, 1982; Arnett et al., 1985). We follow procedures similar to those used in Liu et al., 2016 and Fremling et al., 2018 for normal stripped envelope SNe. He I is the most common spectral feature near peak light in the sample of Ca-Ib/c events, and hence we estimate the velocity of the He I λ5876 line by fitting a low order polynomial to the

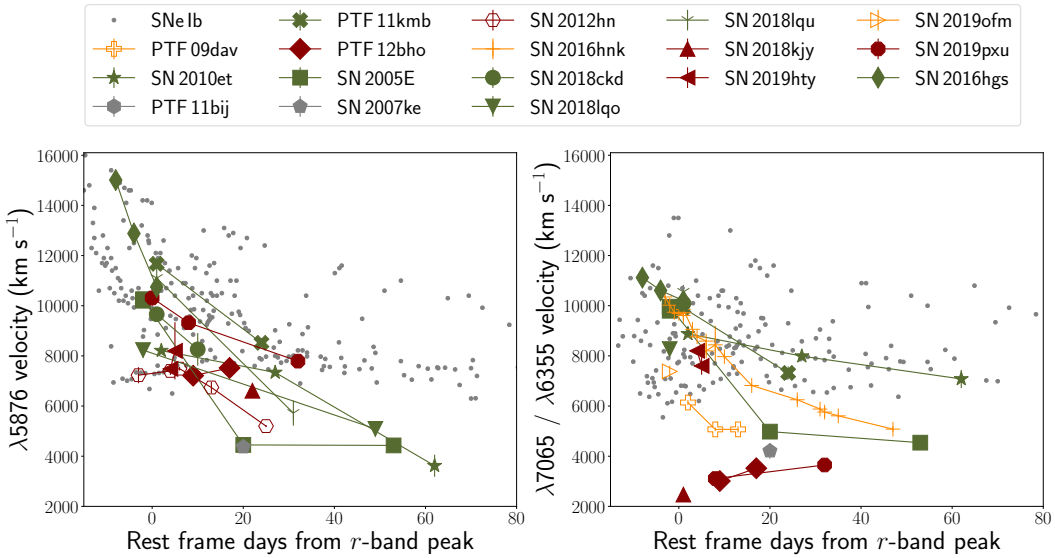

Figure 6.10: **Evolution of photospheric line velocity as a function of phase from r-band peak for the combined sample of Calcium rich gap transients discussed in this paper.** Points joined by solid lines represent the velocity evolution for the same object. We also plot the velocity evolution of the respective lines observed in normal SNe Ib in the sample of Liu et al., 2016, as gray dots in the background. Individual events are shown by markers as indicated in the legend, with their marker colors indicating whether they belong to the Ca-Ib/c class with green (shown in dark green) or red (shown in red) continua, or to the Ca-Ia class (shown in orange). The left panel shows the velocity evolution of the prominent He I λ5876 line in cases where it is unambiguously identified (with solid symbols), or the likely nearby Na I feature (for SN 2012hn in hollow symbols). The right panel shows the velocity evolution of the He I λ7065 feature for the Ca-Ib/c events and the Si II λ6355 feature for the Ca-Ia events.

flux around the line. We estimate the uncertainties in the velocity by Monte Carlo sampling of the flux in the relevant wavelength region.

We estimate the flux uncertainty by subtracting the smooth polynomial fit from the spectral data and compute the noise RMS as the standard deviation of the flux from the smoothed spectrum. We then add a Gaussian distribution of noise to the spectrum using the wavelength dependent flux RMS as the standard deviation, and compute the spectral fit parameters for the several realizations of the input spectrum. While O I λ7774 is also detected in most of the peak light spectra, we do not fit the absorption in this line since it appears to be uniformly contaminated by another nearby absorption feature (likely Mg II; e.g. De et al., 2018a; Valenti et al., 2014). We perform the same fitting for the He I λ7065 line in the spectra where it is detected in the Ca-Ib/c events, while the same is computed for the Si II λ6355 line in the case

of the Ca-Ia events.

The velocity estimates from fitting the He I λ5876 and λ7065 are largely consistent in the Ca-Ib/c events. However, the velocities and detection of He in the red events is complicated by several factors. While SN 2019hty shows unambiguous presence of both the He I lines we measure, the λ7065 line absorption in the other objects is contaminated by emission from a nearby blueward feature (see Figure 6.7), which could be associated with C II (Valenti et al., 2014) or Al II (De et al., 2018a; Kasliwal et al., 2012). Thus, the He I velocities are discrepant between the two lines for these objects. However, we report all these measurements for completeness.

SN 2012hn does not show clear signs of He I in its peak light spectra, and hence we compute the velocity for the nearby 5800 Å feature (suggested to be due to Na I or Cr II in Valenti et al., 2014) assuming that the peak of the feature near maximum light corresponds to the rest wavelength of the line. The low signal-to-noise ratio and resolution of the spectrum of SN 2018gwo does not allow us to conclusively identify He I, and hence we do not measure the corresponding velocities for these objects. SN 2018kjy exhibits a peculiar peak light spectrum with a large number of low-velocity ($\sim$ 2500 km s^{-1}) lines. While He I λ7065 is identifiable in the peak light spectrum, we caution that due to the large number of low velocity lines, we only tentatively identify He I λ5876 in the peak light spectrum.

In Figure 6.10, we plot the evolution of the prominent photospheric phase He I λ5876 and λ7065 (for the Ca-Ib/c events), and Si II λ6355 line (for the Ca-Ia events) velocities as a function of phase from r-band peak. For comparison, we also plot the evolution of the He I line velocities observed in the sample normal SNe Ib presented in Liu et al., 2016. The He I λ7065 velocity in most of the red events is much lower than in the events with green continua. As stated in Section 6.3, this discrepancy is due to blending of a nearby emission feature blue-wards of λ7065 that contaminates the velocity measurement, thus making the velocity evolution uncertain. SN 2018kjy stands out as a peculiar low velocity event as evident from the large number of narrow lines visible in its peak light spectrum (see Figure 6.5), exhibiting several similarities to the low velocity spectrum observed in PTF 12bho. SN 2012hn does not exhibit signatures of He I in its peak light spectrum and hence we show the velocity evolution of the nearby 5800 Å feature, likely associated with Na I.

It is worth noting the diversity of Si II λ6355 velocities in the Ca-Ia events – both PTF 09dav and SN 2019ofm exhibit lower (by $\approx$ 3000 km s^{-1}) velocities than

SN 2016hnk at peak ($\approx 11000\,\mathrm{km\,s^{-1}}$). The combined sample of photospheric phase velocities shows a consistent trend of decreasing velocities with time, consistent with a receding photosphere (in mass coordinates) in the SN ejecta. Comparing to the sample of normal Type Ib events in the comparison sample, we find that while the photospheric velocities are similar near peak light, the Ca-rich gap transients exhibit a much faster drop to low photospheric velocites around $\approx 20\,\mathrm{d}$ after peak light. A faster drop in photospheric phase velocities suggests that the photospheric line forming regions recede into the inner and slower layers of the ejecta faster than normal SNe Ib, consistent with the lower ejecta masses and faster transition to the optically thin nebular phase observed in these events.

Nebular phase spectra

The Ca-Ib/c class

In Figure 6.11, we show a comparison of the nebular phase spectra of the Ca-Ib/c class of objects. Despite the diversity in the photospheric phase colors and velocities, the nebular phase spectra are relatively homogeneous, and dominated by strong [Ca II] emission and weak [O I] emission (if [O I] is detected at all). The low velocity events SN 2018kjy and SN 2019pxu exhibit double-peaked lines near the [Ca II] doublet early in the nebular phase, similar to that observed in PTF 12bho (Lunnan et al., 2017), although later spectra exhibit a single unresolved [Ca II] feature. Since SN 2018gwo was a relatively nearby event at 30 Mpc, our nebular phase spectral sequence extends out to $\approx 235\,\mathrm{d}$, showing that [Ca II] emission continues to dominate the spectrum from the earliest to these very late phases and hence the Ca-rich classification is independent of the exact phase of the nebular spectrum. We note that the events with red continua SN 2012hn, SN 2018kjy, and SN 2018gwo exhibit relatively stronger [O I] lines relative to [Ca II], when compared with other objects observed at similar phases. SN 2012hn and SN 2018gwo are also notable for exhibiting clear signatures of Fe group elements around $4000 - 6000\,\text{Å}$ similar to late-time spectra of sub-luminous SNe Ia.

The Ca-Ia class

Figure 6.8 shows the nebular phase spectra for the Ca-Ia objects, which are dominated by [Ca II] lines. It is important to note the difference between the Ca-Ia objects and the class of 1991bg-like objects in the nebular phase – while 1991bg-like objects exhibit strong features of Fe-group elements in the blue part of the spectrum in the

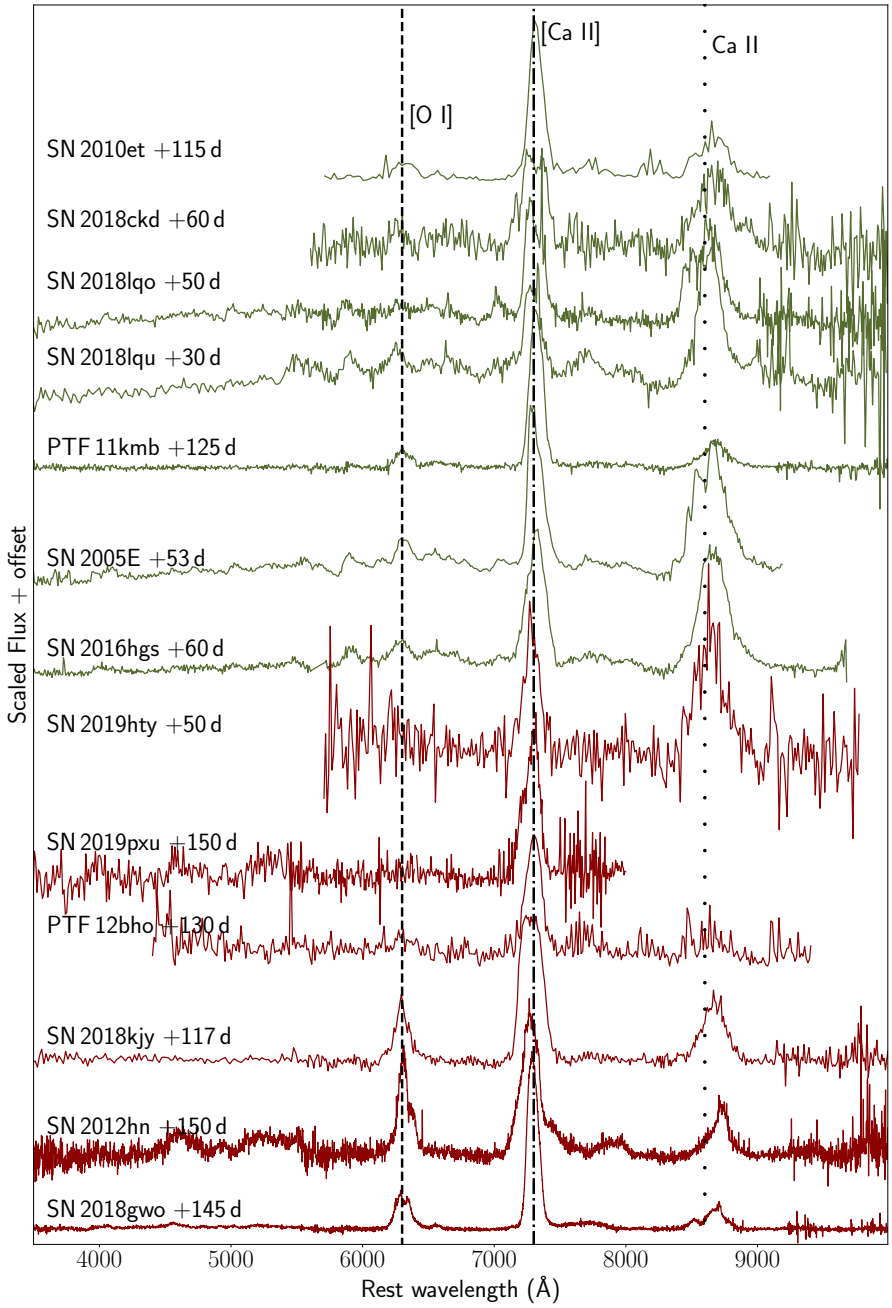

Figure 6.11: **Nebular phase spectra of the Ca-Ib/c events in the ZTF sample combined with the same for events in the literature.** The transient name and phase of the spectrum is indicated next to each spectrum. Color coding of the spectra are the same as in Figure 6.6. The prominent nebular lines of [O I], [Ca II], and Ca II are marked.

nebular phase, the Ca-Ia objects show nearly no signatures of such features in the blue-side spectra at similar phases. We demonstrate this by plotting a nebular phase spectrum of the 1991bg-like object SN 2005ke (Silverman et al., 2012) in Figure 6.8.

SN 2005ke also exhibits a strong emission feature at 7290 Å near [Ca II]; however this feature could be associated with [Fe II] and [Ni II] emission given the strong Fe group elements observed in the blue side of the spectrum (Flörs et al., 2020; see also Polin et al., 2021 who suggest that this feature is due to [Ca II]). Unlike the Ca-Ib/c objects, the Ca-Ia objects exhibit very weak or no [O I] emission in the nebular phase. The nebular phase spectrum of SN 2016hnk (Galbany et al., 2019) exhibits a narrow double-peaked feature at the [Ca II] line, and is noticably narrower than other objects[11]. However this could be due to the very late phase of the spectrum which is unavailable for the other, fainter objects in this class.

[Ca II]/[O I] ratio

In the nebular phase spectra of the combined sample of events, we fit a Gaussian to the [Ca II] and [O I] emission features to estimate their flux ratio. We compute the fluxes by fitting a single Gaussian (see e.g. Jerkstrand, 2017) to the respective line emission features. We do not compute the absolute flux in these lines as the spectro-photometric calibration is not available for several spectra in the literature[12]. Instead, we compute the [Ca II]/[O I] ratio for each spectrum. For several late-time spectra [O I] is barely or not detected. In such cases, we compute an upper limit on the [O I] flux by using the RMS of the flux around the expected position of the line center to compute a 1σ upper limit on the [O I] flux assuming that [Ca II] and [O I] lines have the same velocity width (this provides a lower limit on the [Ca II]/[O I] ratio). We estimate the uncertainties in the line ratios by computing the standard deviations in these quantities from 1000 Monte Carlo realizations of the spectra, where the samples are created by adding flux uncertainties in the same way as with the photospheric phase spectra. Table 6.6 lists the best fit parameters for the sample of events in this paper as well as all the published spectra in the literature.

We plot the evolution of the [Ca II]/[O I] ratio in these sources compared to a sample of nebular phase spectra of other types of stripped envelope SNe in ZTF in Figure 6.12. These spectra were obtained either as a part of confirmation spectra for the candidate Ca-rich gap transients identified from photometry or as a part of nebular phase follow-up of a volume-limited sample of stripped envelope SNe (C. Fremling et al., in prep.). The Ca-rich gap transients occupy a unique phase space in this plot

[11] However, the late-time spectrum of SN 2016hnk reported by Jacobson-Galan et al., 2019 does not show a clear double peak.

[12] Absolute calibration would also require contemporaneous photometry, which is largely unavailable.

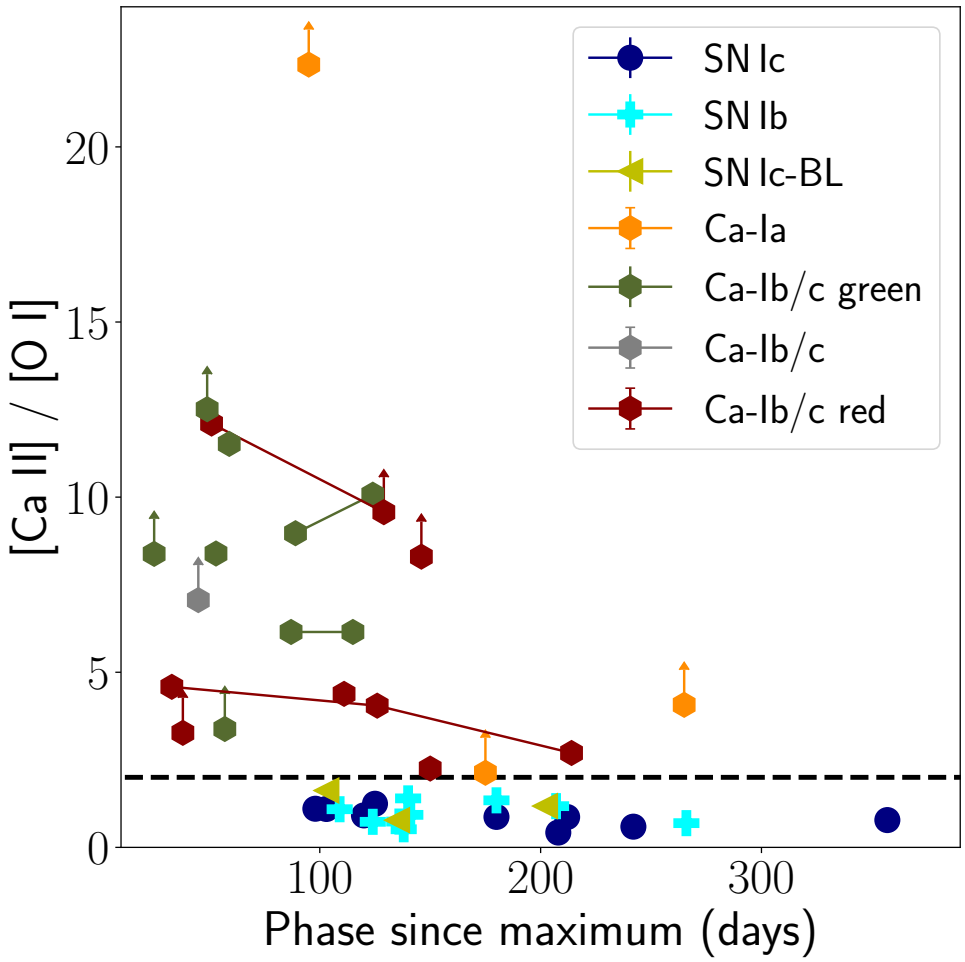

Figure 6.12: **[Ca II]/[O I] ratio for the Ca-rich gap transients and stripped envelope SNe in the ZTF volume limited experiment.** The black horizontal dashed line shows the [Ca II]/[O I] ratio defined as the threshold in this paper for classification as a Ca-rich transient. Symbols with upward arrows indicate lower limits on the [Ca II]/[O I] ratio where the [O I] feature is not detected with statistical significance. The Ca-rich events are indicated by hexagons with colors that reflect their peak light spectroscopic appearance as discussed in the text.

with high [Ca II]/[O I] at all phases in their evolution. We also show the threshold of [Ca II]/[O I] = 2 used to select the sample of Ca-rich gap transients in this paper, which clearly separates out the Ca-rich events from the normal events, which primarily occupy the phase space of [Ca II]/[O I] $\lesssim$ 1 at all phases. We note that several of the red Ca-Ib/c events exhibit relatively small [Ca II]/[O I] at all phases, where the [Ca II]/[O I] values are smaller by a factor of $\approx$ 2 when compared to the green Ca-Ib/c events. This trend is consistent with the qualitative analysis in Section

6.3 where we noted the stronger [O I] features in the red events. The [Ca II]/[O I] estimates result in lower limits for all the Ca-Ia events, suggesting that [O I] is not detected in the nebular phase spectra of these objects.

Photometric evolution

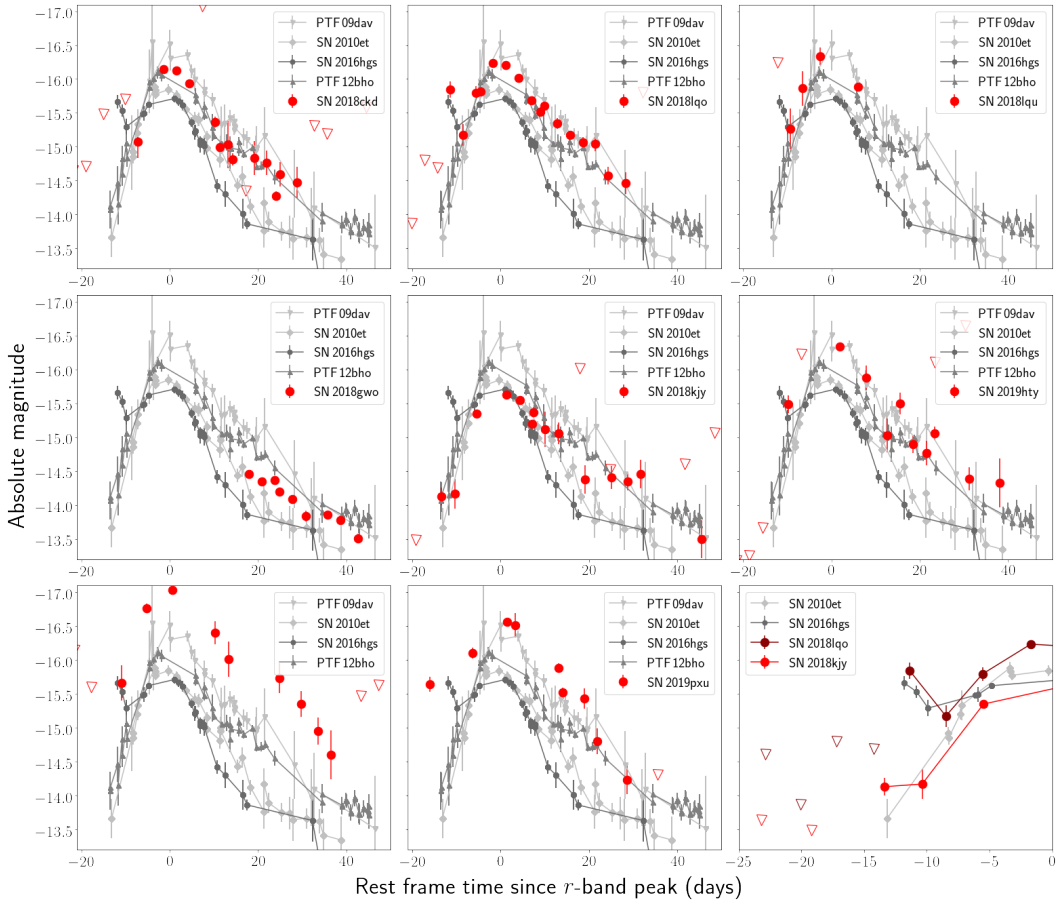

Figure 6.13: **Comparison of the r-band evolution of this sample of Ca-rich gap transients to some previously confirmed events** – PTF 09dav (Sullivan et al., 2006), SN 2010et (Kasliwal et al., 2012), PTF 12bho (Lunnan et al., 2017), and SN 2016hgs (De et al., 2018a). In each panel, the r-band photometry for the ZTF sample are presented as red points while the archival sources are plotted in shades of grey. The photometric evolution is shown as a function of rest-frame time from the best estimate of the r-band peak (except in the case of SN 2018gwo; see text). Inverted triangles denote 5σ upper limits. Bottom right panel: Comparison of the early time bumps seen in the light curves of some of the transients in the ZTF Ca-rich sample to that of the literature events SN 2016hgs (which exhibited an early time bump; De et al., 2018a) and SN 2010et (which exhibited a monotonic rise; Kasliwal et al., 2012).

In Figure 6.13, we compare the r-band light curves of the ZTF sample of Ca-rich

gap transients near peak light, to four characteristic light curves of the literature Ca-rich events PTF 09dav (Sullivan et al., 2011), PTF 10iuv (Kasliwal et al., 2012), PTF 12bho (Lunnan et al., 2017), and SN 2016hgs (De et al., 2018a). The comparison sample was chosen to encompass the diversity of photospheric phase spectral properties reported in the literature sample. The r-band light curves of the full ZTF sample are largely similar to the comparison sample, with the exception of SN 2019ofm and SN 2019pxu, which exhibit more luminous and broader light curves than the comparison objects. SN 2018lqo exhibits a prominent early time 'bump' of $\approx$ 1 mag compared to the light curve of SN 2010et. Excess emission is also marginally detected in the light curve of SN 2018kjy, although at much lower significance.

In the bottom right panel of Figure 6.13, we show a zoomed inset of the early r-band light curves of these two objects together with that of SN 2016hgs, which was previously reported as a peculiar Ca-rich gap transient with a prominent double-peaked light curve. For comparison, we plot the well-sampled light curve of SN 2010et, which shows a purely monotonic rise in its early light curve, as is found for all the other events in the full sample. The early excess emission in the light curve of SN 2018lqo is similar in luminosity and time scale to the early emission in SN 2016hgs. The early excess in SN 2018kjy is detected but of lower significance, and hence we do not discuss it further here. SN 2018gwo has no ZTF coverage near peak light, although the peak light photometry published on TNS and late time decay tail are consistent with the literature sample of events if we assume that the source was first detected $\approx$ 7 d before peak light. We caution, however, that we are unable to measure the time of peak or any other light curve parameter for this object due to the absence of photometry around peak.

Light curve parameters

We fit the light curve of each transient (in every filter available) around peak light (within 20 d of peak) with a low order polynomial (order 3 to 4) and derive parameters describing the light curve peak and timescale. We perform the same fitting for all multi-color photometry data available for the literature sample of Ca-rich gap transients. We use the functional fits to determine the times of peak in each filter, peak apparent and absolute magnitudes (m_p and M_p, respectively), and the characteristic rise time and decline time. We define the rise and decay time ($t_{r,1/2}$ and $t_{f,1/2}$) of the light curve as the time it takes to rise or decline to half flux from

peak light. In addition, we compute the characteristic decay of the light curve (in magnitudes) in 7 d from peak light, denoted by Δm_7.

We estimate uncertainties on these quantities by Monte Carlo sampling of the derived parameters from 1000 realizations of each light curve using the photometric uncertainties of each point in the light curve. We restrict our fitting to photometric bands that have at least one data point before peak light, since it is not possible to estimate the peak magnitude without a corresponding detection before peak. In addition, for sources that do not have photometry sampling the relevant time period of the rise or fall of the light curve, we do not compute the respective Δm_7, rise or fall times. For SN 2018gwo, photometry was not available around peak light, and hence we use the reported photometry near peak on the TNS (Wiggins, 2018) as a lower limit on the peak magnitude. In computing the peak apparent and absolute magnitude, we also correct the photometry of the literature events for Galactic extinction using the maps of Schlafly et al., 2011 and the extinction law of Cardelli et al., 1989 with $R_V = 3.1$.

We do not correct for any additional host galaxy extinction due to the absence of Na I D absorption in their spectra and the remote locations of these events. The only exception is SN 2012hn, for which we assume a host extinction of $E(B-V) = 0.2$ mag which was estimated from Na I D absorption in its spectra (Valenti et al., 2014). The best-fit parameters from the light curve fitting are given in Table 6.3.

Color evolution

Figure 6.14 shows the $g-r$ and $r-i$ color evolution of the complete sample of Ca-rich gap transients discussed in this paper. For comparison to other types of SNe, we also show the well-sampled color curves of the nearby SN Ia 2011fe (Nugent et al., 2011) and the SN Ib iPTF 13bvn (Cao et al., 2013). Ca-rich gap transients redden rapidly in $g-r$ color compared to SNe Ia, although the color evolution has a similar trend compared to the SN Ib iPTF13bvn. However, all the Ca-rich gap transients are redder than iPTF 13bvn in $g-r$ at similar epochs. The same trend is also seen in the $r-i$ color evolution. The $g-r$ evolution of both the Ca-Ib/c objects with red continua and the Ca-Ia objects are systematically redder than the Ca-Ib/c objects with green continua, consistent with the suppressed blue flux in the spectra of the the former objects. We note that the complete sample of Ca-rich gap transients occupies a narrow distribution around $g-r \approx 0.7$ mag near peak light, which we later use to simulate their light curves for estimation of volumetric rates

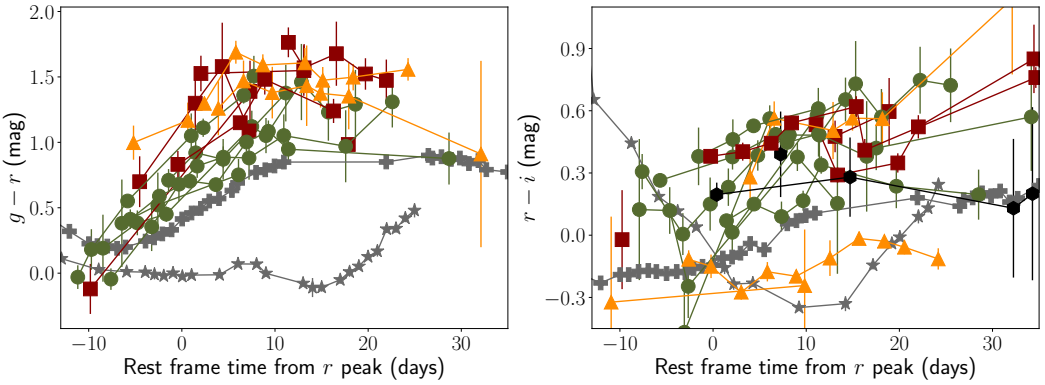

Figure 6.14: **Comparison of the $g-r$ and $r-i$ color curves of the known sample of Calcium rich gap transients**. Symbols are color coded by their spectroscopic membership of the green Ca-Ib/c (green circles), red Ca-Ib/c (red squares) or the Ca-Ia (orange triangles) class. For comparison, we also show the color evolution curves of the Type Ia SN 2011fe (Nugent et al., 2011) as dark gray stars and the Type Ib iPTF 13bvn (Cao et al., 2013) as dark gray crosses, which are systematically bluer in $g-r$ than the Ca-rich gap transients at similar epochs. Events in the combined sample without a peak light spectrum are shown in black circles.

from the ZTF survey (Section 6.5).

Luminosity, width, and color relationship

In Figure 6.15, we plot the peak r-band magnitude of the transients as a function of the decline in r-band in 7 d from peak (Δm_7) and time taken to fall to half the maximum flux ($t_{f,1/2}$). While some objects have well sampled light curves on the rise to estimate the time taken to rise from half-maximum in flux to maximum, the majority of literature events do not have well constrained pre-peak light curves, and hence we only plot the fall time from peak. We choose r-band as it is the most commonly available filter for the combined photometric sample and allows us to perform a homogeneous analysis on the largest number of objects. For comparison of this phase space to the general trend followed by thermonuclear SNe, we plot the same parameters for SNe Ia. We use the sample of ZTF SN Ia light curves published in Yao et al., 2019, and compute the same quantities using the fitting techniques mentioned above with the r band light curves. The distribution of these SNe Ia shows the expected luminosity – width relationship (the Phillips relation; Phillips, 1993) with more luminous events being systematically slower evolving[13]. In order

[13]Note that the canonical relationship for SNe Ia is defined using the magnitude decline in 15 d after peak in the B band versus peak absolute magnitude M_B.

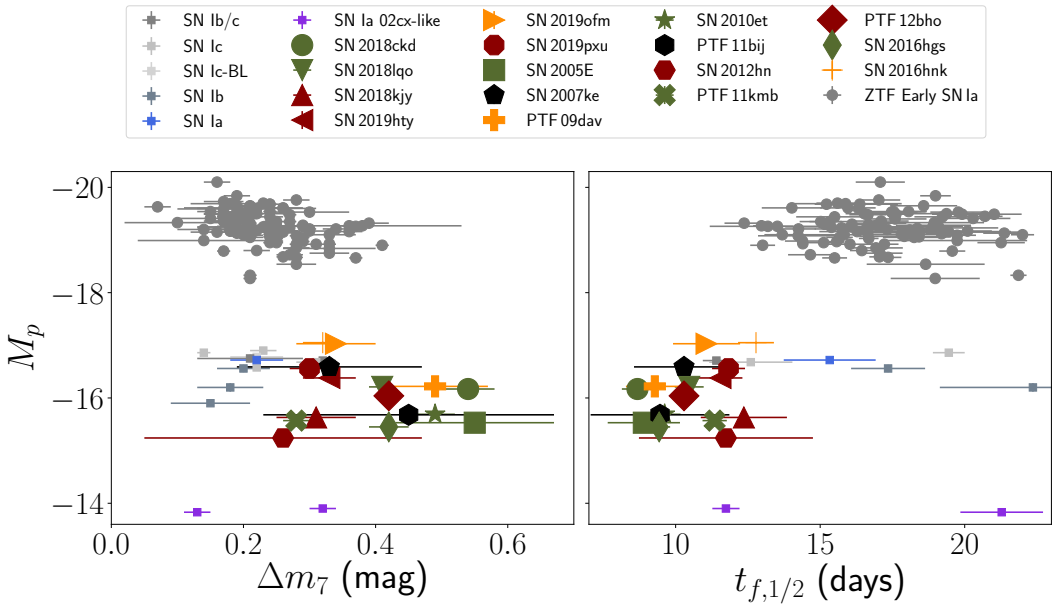

Figure 6.15: **Luminosity - width phase space for the r-band light curves of Calcium rich gap transients.** Symbols are shown with the object names in the legend. The individual events are colored by their spectral type at peak light. Green Ca-Ib/c events are indicated by green and those with reddened continua are indicated by red. Ca-Ia events are indicated in orange and marker symbols for all events are indicated in the legend. We are unable to constrain the peak light spectroscopic properties of SN 2007ke and PTF 11bij, and hence show these objects in black. For comparison, we plot the same phase space of timescales for the ZTF 2018 early SN Ia sample in Yao et al., 2019 in gray dots, together with the same parameters for objects in the control sample (in squares; indicated in the legend by their spectroscopic type at peak).

to investigate the presence of a luminosity-width relationship in the full sample of Ca-rich objects[14], we compute a Spearman correlation coefficient between the two pairs of plotted paramaters and find no significant evidence of correlation. The corresponding correlation coefficients are 0.25 between M_p and Δm_7 (p-value of 0.35) and -0.36 between M_p and $t_{f,1/2}$ (p value of 0.18), suggesting no statistically significant evidence of a correlation between these parameters.

We now examine possible differences in the photometric properties between the Ca-Ib/c and the Ca-Ia objects. Due to the absence of peak light spectroscopy for SN 2007ke and PTF 11bij, we are unable to ascertain the nature of the blue continuum at peak light; however, their early nebular phase spectra show lines characteristic

[14]We choose to conduct this analysis on Δm_7 against peak absolute magnitude in the r band M_r since the faint and fast declining Calcium rich gap transients usually lack photometry extending beyond $\approx$ 15 d from maximum

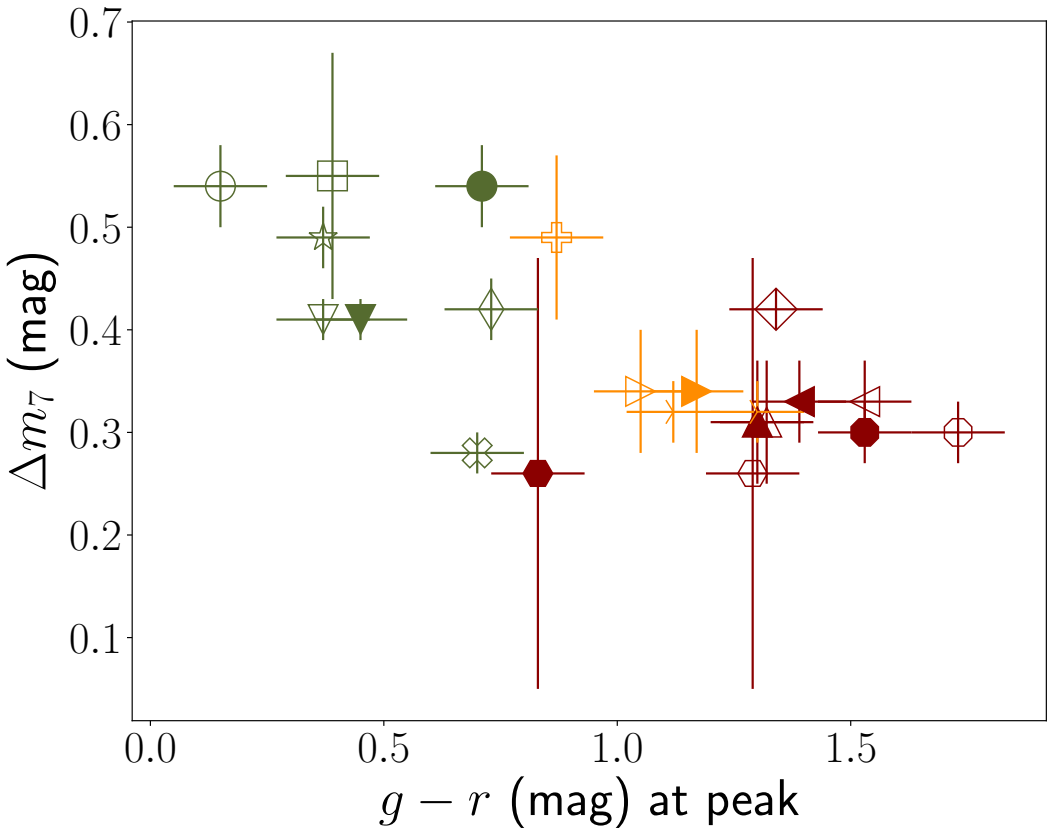

Figure 6.16: **Dependence of the rate of light curve evolution post-peak in r-band (Δm_7) on the transient $g - r$ color at peak.** The symbol color coding and markers are the same as those used in Figure 6.15. Hollow symbols indicate colors computed from spectro-photometry on observed spectra within $\approx$ 10 d of peak light, while solid symbols indicate colors derived from peak light photometry where available. The colors have been corrected for foreground Galactic extinction.

of SNe Ib/c suggesting their membership in the class of Ca-Ib/c objects. The peak luminosity distributions of the green and red events among the Ca-Ib/c objects are consistent with each other; however, the Ca-Ia objects are typically more luminous. The total number of events remain small to draw a conclusion on the statistical significance of the differences. Specifically, we note that Ca-Ib/c events with red continua exhibit systematically slower light curves than the Ca-Ib/c events with green continua, as shown by their smaller Δm_7 and larger $t_{f,1/2}$ values. A 2-sample Kolmogorov-Smirnov (KS) test suggests that the null hypothesis probability that the two sets of values are drawn from the same underlying population is $< 5\%$ for $t_{f,1/2}$ and $< 18\%$ for Δm_7. While only marginally significant due to the small number of events, we further examine this trend in Figure 6.16.

We show the dependence of Δm_7 as a function of the $g - r$ color of the transient

near peak light in Figure 6.16. The $g - r$ photometric colors at peak light are not available for several events in the combined sample, and hence we use both the spectro-photometric colors derived from peak light spectroscopy as well as photometric colors where available. Since the photometric colors are not always available at the same phase as the spectroscopy, there are differences between the derived photometric and spectro-photometric colors. The Ca-Ib/c events separate into two classes of events based on their $g - r$ colors, while Ca-Ia events exhibit colors intermediate between the two classes but redder than the green Ca-Ib/c events. Specifically, we note that Ca-Ib/c events with bluer $g - r$ colors at peak exhibit larger Δm_7 (faster photometric evolution) at peak, while the red Ca-Ib/c events are slower evolving, consistent with the trend observed in Figure 6.15. However, we caution against drawing conclusions about any correlations between these two parameters as the photometric and spectro-photometric colors were not available at the same phase in all cases. We find that the green and red events in the Ca-Ib/c sample are separated at $g - r \approx 1$ mag at peak light; the Ca-Ia objects also exhibit redder colors of $g - r > 1$ mag at peak, consistent with their line blanketed spectra.

Dependence on spectroscopic properties

In Figure 6.17, we plot the photopsheric velocity at peak light against the peak r-band magnitude of the sources to examine the dependence of the photospheric phase velocity on the peak luminosity of each event. In the case of SN 2018kjy, we are unable to measure the He line velocities directly due to the large number of narrow lines, and hence we estimate typical line velocities in the spectra from the P-Cygni absorption velocities of ≈ 4000 km s^{-1}. We do not find a clear dependence of the photospheric phase velocity on the peak luminosity of the events, but note that events with green continua have higher photospheric phase velocities compared to the red events.

The right panel of Figure 6.17 shows the dependence of the peak light photospheric velocity on the rate of decay of the light curve, Δm_7. As per the formalism for radioactively powered light curves laid down in Arnett, 1982, the peak light photospheric velocity and light curve evolution near peak are indicators of the ejecta mass in the explosion. We thus also plot lines of constant ejecta mass in the right panel to guide the eye to the range of ejecta masses in the sample. We construct these lines by creating analytic light curves using the formalism of Arnett, 1982 assuming two constant opacities of $\kappa = 0.07$ cm^2 g^{-1} (as relevant for Type Ib/c SNe; Cano,

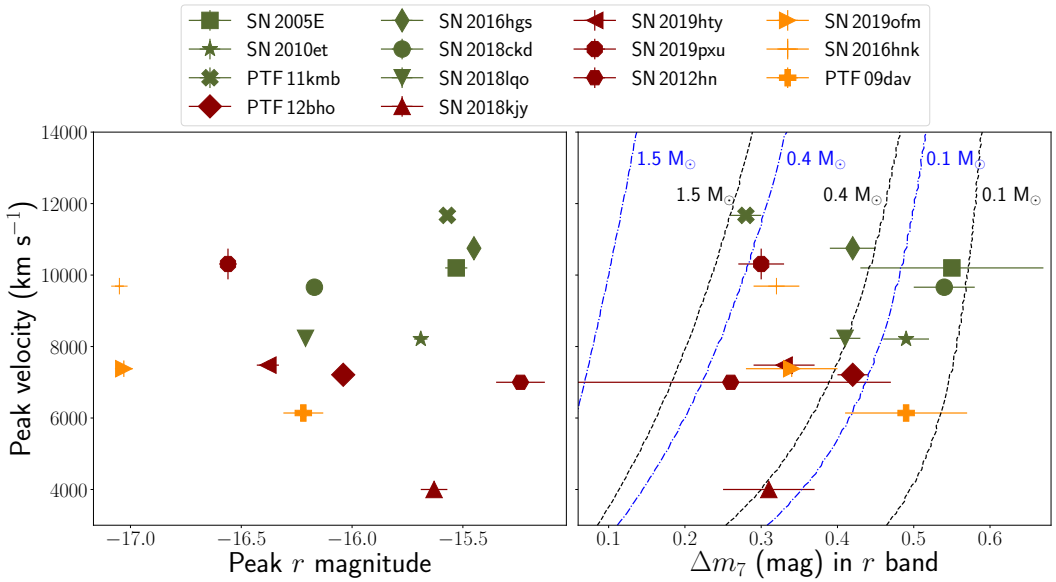

Figure 6.17: **Photospheric phase line velocities as a function of the light curve peak luminosity (in r band) and timescale of evolution (characterized by Δm_7) for the sample of Ca-rich gap transients analyzed in this paper.** We use the velocity of the He I λ5876 feature from the spectrum taken closest to the estimated time of peak light in r band (if available within 10 d of peak) for the Ca-Ib/c objects, and the Si II λ6355 velocity for the Ca-Ia objects. The left panel shows the peak velocity as a function of the peak r-band magnitude and the right panel shows the peak velocity as a function of Δm_7. The right panel also shows contours of constant ejecta mass computed using the analytical model of Arnett, 1982 to guide the eye on the range of ejecta masses found in the sample. We show the ejecta mass contours for two different optical opacities of $\kappa = 0.07$ cm^2 g^{-1} (black dashed lines) and $\kappa = 0.2$ cm^2 g^{-1} (blue dot-dashed lines).

2013; Taddia et al., 2018) and $\kappa = 0.2$ cm^2 g^{-1} (relevant for completely ionized hydrogen-free material). We caution however, that the Arnett diffusion model has several assumptions which may not be satisfied in these explosions (see Khatami et al., 2019 for a review). We do not find a dependence of the peak photospheric velocity on the light curve evolution near peak. It is important to note that the inferred ejecta masses can vary significantly depending on the assumed opacity. The majority of Ca-Ib/c events with green continua lie on contours of lower ejecta masses (between 0.1 and 0.4 M$_\odot$), while the red Ca-Ib/c and Ca-Ia events lie near larger ejecta masses (up to $\approx$ 1 M$_\odot$ for $\kappa = 0.07$ cm^2 g^{-1}, but $<$ 0.5 M$_\odot$ for $\kappa = 0.2$ cm^2 g^{-1}). However, we stress that redder events also likely have higher effective optical opacity in the ejecta than their green counterparts, as evident from the strong suppression of flux in the blue, which would suggest increased bound-bound opac-

ity from Fe group material. As such, this effect would decrease the ejecta masses inferred from assuming a constant opacity across all events.

Late-time photometric evolution

In Figure **??**, we show the late-time (> 40 d after r-band peak) photometric evolution of the sample of Ca-rich gap transients presented in this paper together with published photometry of events in the literature. While most of the late-time photometry presented here was obtained using targeted follow-up observations using the P60 + SEDM, P200 + WASP and Keck-I + LRIS, we also stacked several epochs (over up to 30 days) of the high cadence ZTF observations to derive flux limits at late times. Owing to its small distance, SN 2018gwo has good photometric follow-up from ZTF up to $\approx$ 100 d from the estimated peak time. We also show a numerically computed Arnett model (Arnett, 1982) for the decline rate expected from a radioactive powered light curve with ejecta mass of 0.5 $M_\odot$ and ^{56}Ni mass of 0.015 $M_\odot$. The model parameters were chosen based on the typical values found in previous studies (De et al., 2018a; Kasliwal et al., 2012; Perets et al., 2010; Valenti et al., 2014).

Compared to the expected ^{56}Ni decay tail shown in Figure **??**, the luminosity at late times is much fainter than the prediction from the Arnett model, while the decay slope is also steeper for these events. The characteristics are consistent with the fast rising light curves of these events, which suggest low ejecta masses and incomplete γ-ray trapping at late times. Figure **??** also shows the last deep photometric limits obtained using P200 and Keck for this sample of events, extending out to $\approx$ 1.5 years after peak light. Although SN 2018gwo is detected with Keck (owing to its small distance) out to $\approx$ 500 d after peak light, the very late-time follow-up photometry for all the objects could be potentially contaminated by underlying host systems. We discuss the presence of potential underlying host stellar systems from late-time imaging in Section 6.4.

6.4 Locations and host environments

Here, we examine the environments and host properties of the Ca-rich gap transients analyzed in this sample. The host environments of the literature sample of transients have been noted in several works previously for their preference of old environments located far away from their host galaxies, with no evidence for parent stellar populations at the location of the transients. (De et al., 2018a; Kasliwal et al.,

2012; Lunnan et al., 2017; Lyman et al., 2014, 2016b; Mulchaey et al., 2014; Perets et al., 2010; Perets et al., 2011; Shen et al., 2019; Yuan et al., 2013). Additionally, Yuan et al., 2013 find that the offset distribution of a subset of events in the literature sample was inconsistent with the stellar mass profiles of their host galaxies, while Yuan et al., 2013 and Shen et al., 2019 show that their offset distributions are consistent with globular clusters or old metal poor stellar populations. Frohmaier et al., 2018 show that the preference for large host offsets in the PTF sample cannot be explained by the reduced recovery efficiency on top of bright galaxies. However, all of the works were based on heterogeneous samples of events gathered from different surveys with diverse selection effects that are difficult to quantify. As the first unbiased systematic experiment to classify a large sample of Ca-rich gap transients, we perform a systematic analysis of their locations and host environments.

Host galaxy morphology

We begin with analyzing the host galaxy morphologies of these events. Our selection criteria for these events did not include any restrictions on the host galaxy type. Six out of the eight events in this sample were found in S0 / E early-type host galaxies (four out of the eight were in E type galaxies), and all of the events were found at projected galactocentric offsets > 6 kpc. Two events (SN 2019ofm and SN 2019pxu) were found in late-type galaxies, although at relatively large host offsets (11 and 17.5 kpc respectively, corresponding to host-normalized offsets of 2.1 and 4.5 R_e[15]). Notably, both the Ca-Ia objects SN 2016hnk and SN 2019ofm were found in late-type star forming galaxies, while PTF 09dav was found to be hostless in late-time imaging and the nearest galaxy with a known redshift was a star forming spiral ≈ 40 kpc from the transient location. However, we caution that PTF 09dav was close to several faint extended sources (see Figure 3 in Kasliwal et al., 2012) which could be nearby dwarf galaxies; it also showed Hα emission in its latest nebular phase spectrum, although it could be associated with circumstellar photo-ionized gas around the SN (Kasliwal et al., 2012).

Nevertheless, the preference of these transients for old host environments with large offsets is striking compared to other types of transients in the local universe. The preference for early type galaxies in this sample is reminiscent of that observed for 91bg-like SNe Ia (Howell, 2001; Neill et al., 2009; Perets et al., 2010; Taubenberger, 2017), albeit the preference of Ca-rich gap transients for early-type galaxies is more extreme than for these events. A total of 19 91bg-like SNe Ia were classified in the

[15] R_e is defined as the half-light radius of the apparent host galaxy.

CLU experiment in the span of time considered in this paper, out of which 10 events were found in early type galaxies while the rest were in late-type galaxies. The near equal distribution in early and late type galaxies for 91bg-like SNe Ia is consistent with the stellar mass distribution between early-type and late-type galaxies in the local universe (Bell et al., 2003; Kochanek et al., 2001).

Locations and offset distribution

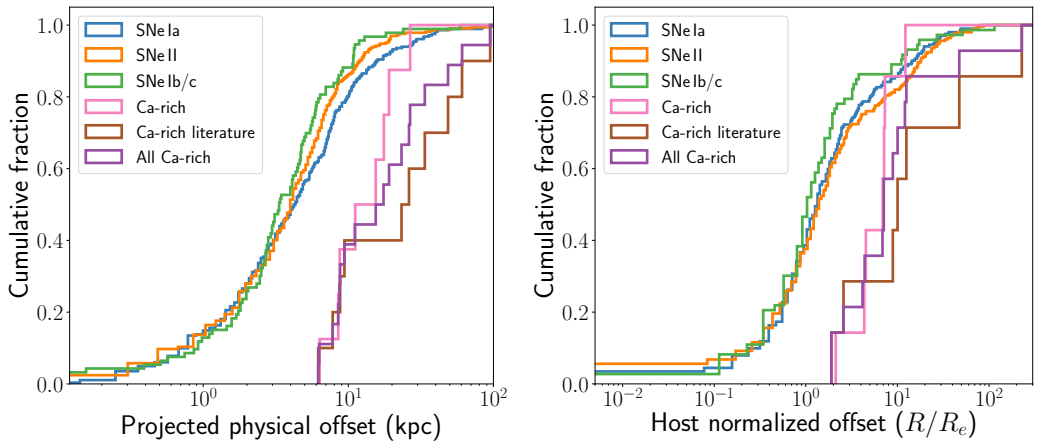

Figure 6.18: **Projected offset distribution of all transients in the CLU experiment.** The left panel shows the distribution in units of physical projected distance (kpc), while the right panel shows the distribution in host offset normalized by the half-light Petrosian radius of the host galaxy. The half-light Petrosian radii were derived from the Sloan Digitial Sky Survey (SDSS; Abolfathi et al., 2017) catalog, and hence are limited to transients occurring in the SDSS footprint.

In Figure 6.18, we compare the host offset distribution of the ZTF Ca-rich gap transients (both in physical projected distance and host-normalized distance) to the other types of SNe in the volume limited experiment – SNe Ia, SNe II and SNe Ib/c. The host offsets for each event in the sample are computed from the host galaxy in the CLU catalog, which was confirmed to be at the same redshift as the SN. As shown in Figure 6.18, SNe Ib/c show systematically smaller physical offsets than SNe II, while SNe II show systematically smaller offsets than SNe Ia. However, the Ca-rich gap transients exhibit a significantly skewed distribution of larger offsets (both in terms of physical offsets and host normalized offsets) than any of the object types in the comparison sample.

Using a two sample KS test, we can rule out the possibility that the entire population of SNe Ia and Ca-rich gap transients in the ZTF sample originate from the same underlying population at 99.9% confidence. For comparison, we also show the host

offset distribution of the literature sample of Ca-rich gap transients and the total combined sample of Ca-rich gap transients, whose distribution appears to extend out to larger galactocentric offsets. A KS test between the ZTF and literature sample of offsets does not indicate a statistically significant difference between the two distributions (p value of 0.28); regardless, the limitation of the CLU experiment to finding transients within 100″of their host galaxies prevents us from finding objects with very large host offsets. The consistent offset distributions justify the use of the full sample of offset distributions to estimate the incompleteness of the CLU sample (Section 6.5).

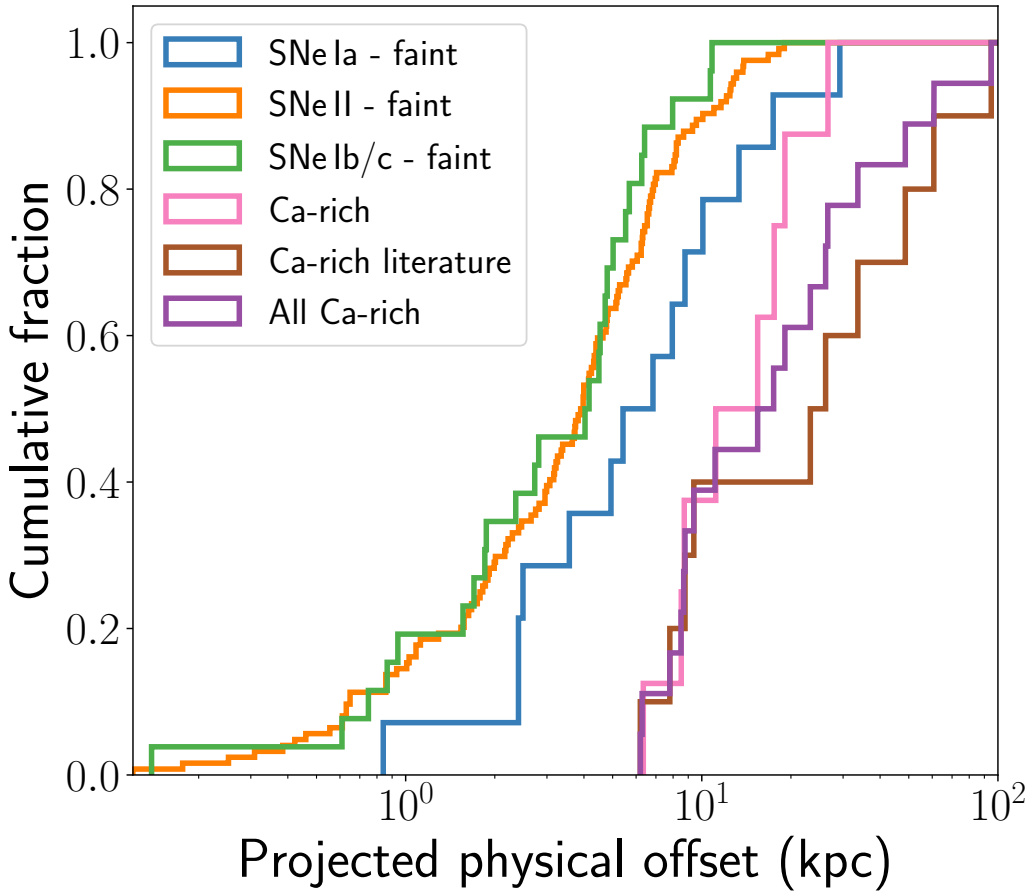

Figure 6.19: **Projected offset distribution of all faint transients that were detected at $M > -17$ in the CLU experiment.**

Several previous works have suggested that the lack of Ca-rich gap transients at small host offsets may be due to their faint light curves, which would make them difficult to detect on top of high surface brightness regions on galaxies (Foley, 2015). Frohmaier et al., 2017 presented the recovery efficiency for the PTF pipeline

as a function of the source magnitude and local surface brightness, demonstrating that the recovery efficiency is indeed lower in regions of high surface brightness. Yet, Frohmaier et al., 2018 showed that the preference of the small PTF sample of Ca-rich gap transients for large host offsets cannot be explained by the reduced recovery efficiency on bright galaxy backgrounds.

While the recovery efficiency for the ZTF pipeline is currently not available, we can empirically examine if the offset locations for the faint Ca-rich gap transients in the ZTF sample can be primarily explained by poor recovery efficiency on the cores of galaxies. In Figure 6.19, we show the projected offset distribution of all transients fainter than $M = -17$ mag in the CLU experiment. The offset distribution of the SNe II, SNe Ib/c and SNe Ia in this low luminosity sample extend from the smallest offsets at < 1 kpc to ≈ 30 kpc. Notably the Ca-rich gap transients continue to stand out with large host offsets of at least 5 kpc and extending out to ≈ 40 kpc. The skewed offset distribution of the Ca-rich gap transients even in this sample of low-luminosity transients suggests that low recovery efficiency of faint transients cannot completely explain the remote locations of these events.

We further compare the environments of 91bg-like SNe Ia to that of the Ca-rich gap transients. We plot the projected offset distributions of all SNe Ia, 91bg-like SNe Ia and Ca-rich gap transients in Figure 6.20. We also show the simulated radial distribution of globular clusters from Shen et al., 2019 for two difference Sersic indices. The literature sample analyzed in this paper includes the Ca-Ia events from the literature, in addition to the 'gold' sample in Shen et al., 2019. Thus, in plotting the radial offset distribution of the sample of Ca-rich events, we define our new 'gold' sample by adding the ZTF sample of events to the literature sample (including all the Ca-Ia objects, amounting to a total of 18 events).

We also define a new 'silver' sample by adding the ZTF sample of events to the silver sample in Shen et al., 2019, which included Ca-rich events without photometric constraints at peak light (amounting to a total of 24 events). 91bg-like SNe Ia show systematically smaller offsets than the Ca-rich gap transients in this sample, and systematically larger offsets compared to the full population of SNe Ia. A two sample KS test between the offset distribution of SN 91bg-like SNe Ia and the gold and silver samples of Ca-rich gap transients produce null hypothesis probabilities of being drawn from the same underlying population at $< 2.5\%$ and $< 10\%$ respectively. We conclude that the discrepancies between the environments of 91bg-like and Ca-rich events suggest that stellar mass alone does not dictate the rates of Ca-rich gap

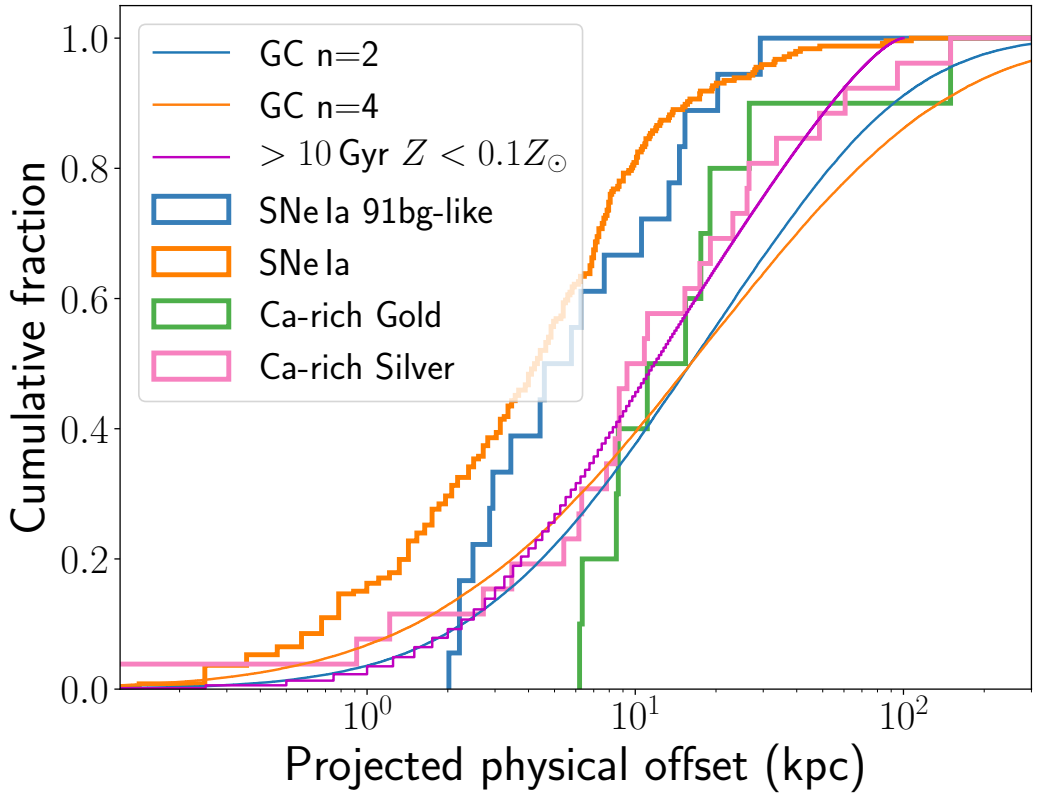

Figure 6.20: **Offset distribution comparison of the 'gold' and 'silver' samples of Calcium rich gap transients discussed in this paper to that of all SNe Ia and 91bg-like SNe Ia in the volume limited experiment.** Our gold sample includes the literature sample of events (which includes the gold sample discussed in Shen et al., 2019 in addition to the Ca-Ia objects discussed in this work) and the ZTF sample, while the silver sample includes the silver sample discussed in Shen et al., 2019 in addition to the ZTF sample of events. We also show the simulated offset distribution of globular clusters for two Sersic indices, as well as the offset distribution for old (> 10 Gyr), metal-poor ($Z < 0.1\ Z_\odot$) stars discussed in Shen et al., 2019.

transients. Long delay times and / or low metallicities in these remote environments of early type galaxies have thus been suggested to play an important role (Meng et al., 2015; Perets et al., 2010; Shen et al., 2019; Yuan et al., 2013).

In addition to being skewed towards larger offsets compared to the SNe Ia, the Ca-rich gold and silver samples exhibit offset distributions different than that of the globular clusters and old metal poor stars from the IllustrisTNG similations (Marinacci et al., 2018; Naiman et al., 2018; Nelson et al., 2019). Specifically, the gold sample distribution is skewed towards larger offsets than these two populations. However, the silver sample offset distribution is more consistent with both these distributions (consistent with the result in Yuan et al., 2013 and Shen et al., 2019), although there

are discrepancies at relatively large offsets. Notably, all of the Ca-rich gap transients found in this experiment were in 'rich' environments with $\gtrsim 10$ galaxies clustered near the nominal host, while Shen et al., 2019 find that 17% of globular cluster hosts are in rich clusters (see Section 6.4).

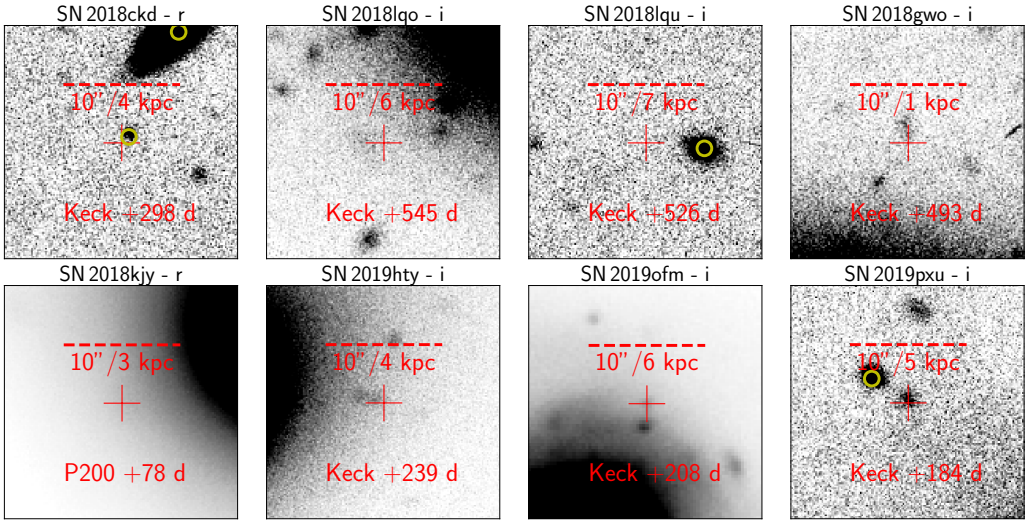

Figure 6.21: **Cutouts of the locations of the Ca-rich gap transients presented in this paper from late-time ground based imaging of the transient locations.** North is up and East is left in each cutout. The source name, filter and phase of observation, instrument used and physical scale of the image at the redshift of the transient is shown in each panel. The crosses show the location of the transient. Yellow circles mark locations of potential host systems also detected in pre-explosion archival imaging (see text).

We examine the deep late-time images of the locations of these transients to investigate if there is any evidence for underlying stellar populations at the locations of these transients. We show these images in Figure 6.21. SN 2018ckd shows clear evidence for a relatively bright point-like source (marked with a yellow circle) offset by < 1 kpc from the transient location. This source is also detected in archival imaging of the field in the Dark Energy Legacy Survey DR8 (Dey et al., 2019) at a magnitude of $r \approx 23.5$ mag and $g - r \approx 0.3$ mag, corresponding to an absolute magnitude of ≈ -11.5 mag if at the redshift of the transient. However, the source is unlikely to be a globular cluster as it is more luminous than nearly the entire known luminosity function of globular clusters (Harris, 1996). We oriented the slit to include the extended galaxy $\approx 10''$ to the north of SN 2018ckd (marked with a yellow circle) during nebular phase spectroscopy, and find it to be an unrelated background galaxy at $z = 0.1$, consistent with the photometric redshift of the object in SDSS.

An extended source is detected near the location of SN 2018lqu (marked with a yellow circle), although its redshift is unknown. If at the redshift of the transient, its magnitude of $r \approx 21.4$ would imply an absolute magnitude of $M_r \approx -14.5$ mag similar to a dwarf galaxy. SN 2018lqo, SN 2018gwo, and SN 2019hty show evidence of faint and extended sources underneath their locations, which likely contaminate our photometry measurements during very late-time imaging (Figure 6.21). However, we caution that the density of unrelated background sources at the depths of the late-time images (≈ 25 mag) is high (Hogg et al., 1997). Using the methodology of Bloom et al., 2002, we find that the chance coincidence probability of an unrelated ≈ 25 mag galaxy within a $5''$ radius of the transient is $\sim 50\%$, while the same for a $10''$ radius is $\sim 95\%$. Thus, the association of these sources to the transients can only be determined from deep spectroscopy in the future. SN 2018kjy is notable for the smallest host offset (≈ 6 kpc) in the ZTF sample, and is located within the halo of its host galaxy. SN 2019ofm is found to be on top of its spiral host galaxy, while SN 2019pxu is at a large offset from its spiral host and has a point source (marked with a yellow circle) within $5''$of its location ($M_r \approx -12.1$ mag if at the redshift of the transient). The latest Keck images of SN 2019ofm and SN 2019pxu still show the transient clearly. Future deep imaging for these events will help disentangle the potential host contamination in our latest photometry measurements, as well as allow inspection of potential underlying hosts.

Group and cluster environments

Given the large host offsets of the Ca-rich gap transient sample, we analyze the environments of the assumed host galaxies to check if they are part of a larger group or cluster that may explain the remote locations of these transients. Mulchaey et al., 2014, Lunnan et al., 2017 and De et al., 2018a performed a similar analysis on the literature sample of Ca-rich gap transients, and demonstrated that these objects preferred host galaxies in groups and clusters. For each transient, we construct the sample of nearby galaxies by selecting galaxies from the CLU catalog (with a previously known spectroscopic redshift) within a projected radius of 1 Mpc and a recession velocity difference of ± 3000 km s^{-1} from the location of the transient.

We emphasize that since galaxy catalogs are highly incomplete at the redshifts of these transients (Fremling et al., 2019; Kulkarni et al., 2018), these distributions are only lower limits to the true number of galaxies in the environments of these transients. We show the velocity histograms of the identified galaxies in Figure 6.22. As shown, the environments of the Ca-rich gap transient host galaxies are

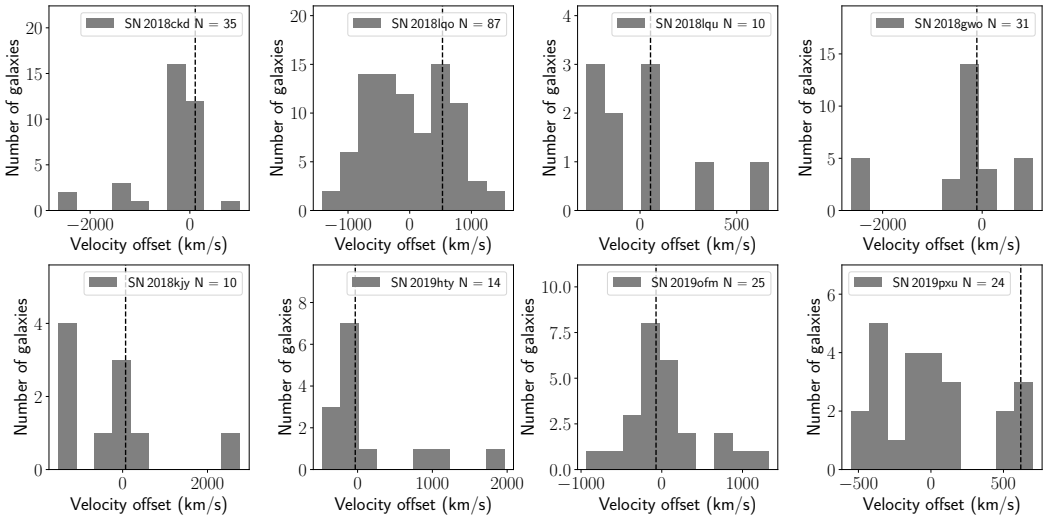

Figure 6.22: **Velocity distributions of galaxies in the environments of the ZTF Ca-rich gap transient sample, that have previously known spectroscopic redshifts in the CLU catalog.** In each distribution, we define zero velocity as the median of the redshift distribution of all the galaxies in the projected vicinity of the transient, and show the velocity of the assumed (nearest) host galaxy of the transient with a dashed line. The transient name and number of galaxies in each histogram is indicated in the legend.

largely dominated by groups and clusters with at least 10 known objects within the selection criteria defined above. SN 2018lqo is in the densest environment with 87 known nearby galaxies. We thus conclude that all of the transients in the ZTF sample are in group or cluster environments, consistent with that reported for the literature sample presented in Lunnan et al., 2017 and De et al., 2018a.

6.5 Volumetric rates in the local universe

In this section, we estimate the volumetric rates of Ca-rich gap transients using the ZTF CLU experiment. As a large scale systematic and controlled experiment, the volume-limited SN classification effort provides the first direct way to estimate the volumetric rates of this class within 200 Mpc due to its high spectroscopic completeness ($\approx 90\%$) down to the experiment limiting magnitude of 20 mag.

Demographics from the volume limited experiment

Since the volume-limited experiment has high spectroscopic classification completeness, a straightforward way to estimate the volumetric rates of Ca-rich gap transients relative to other SNe is by comparing the number of events. We perform this analysis by restricting the sample of transients in the CLU experiment to within

the volume where Ca-rich gap transients are detectable. Based on the luminosity function of known events discussed in Section 6.5, we find that the average Ca-rich gap transient (peaking at $M = -16$ mag) is detectable to 150 Mpc for a flux limit of $r = 20.0$ mag, which is the target limiting magnitude of the CLU experiment. Within the experiment duration mentioned above, a total of eight Ca-rich gap transients were detected along with 133 SNe Ia that were classified in the same volume. So, we can place a lower limit on the rates of Ca-rich gap transients of 6% of the volumetric rates of SNe Ia, or 1.5×10^{-6} Mpc^{-3} yr^{-1} (assuming the SN Ia rate to be 2.5×10^{-5} Mpc^{-3} yr^{-1}; Frohmaier et al., 2019). Note that this estimate is likely an underestimate of the true rate of Ca-rich gap transients since SNe Ia will be bright in the 150 Mpc volume (peaking at ≈ 17 mag) and so detectable during the survey for at least ≈ 100 d around peak, while the average Ca-rich gap transient in this volume is visible for $\approx 10 - 20$ d. In addition, our selection criteria requires the detection of each source on the rise to peak, which further limits the sample of fast evolving Ca-rich sample relative to the slow rising SNe Ia. A true estimate of the volumetric rate of Ca-rich gap transients thus requires a simulation of the cadence of the ZTF survey together with the characteristic luminosity evolution of a Ca-rich gap transient to be able to estimate the number of sources that pass our light curve selection criteria as a function of the input volumetric rate.

Luminosity function

We aim to derive the luminosity function of Ca-rich gap transients using the controlled sample of events from the CLU experiment. Due to the small number of events, we do not separate the spectroscopic sub-types discussed in this work while estimating luminosity functions and volumetric rates. In Figure 6.23, we show the observed histograms of the peak r-band magnitudes of the literature sample of Ca-rich objects and the ZTF sample of objects. The majority of the literature events exhibit peak magnitudes between $M = -16.5$ mag and $M = -15.5$ mag, while the ZTF sample shows a near uniform distribution between $M = -17$ mag and $M = -15.5$ mag. However, it is difficult to quantify the selection biases when combining the literature sample of events with the ZTF sample due to the diverse selection criteria of the surveys that detected the literature objects. In order to derive an unbiased luminosity function, we focus specifically on the ZTF sample of events. Despite being classified as part of a CLU experiment, most of the objects in the ZTF sample are not luminous enough to be detectable across the entire experiment volume (200 Mpc) for a limiting magnitude of $r = 20$ mag, and thus a volume

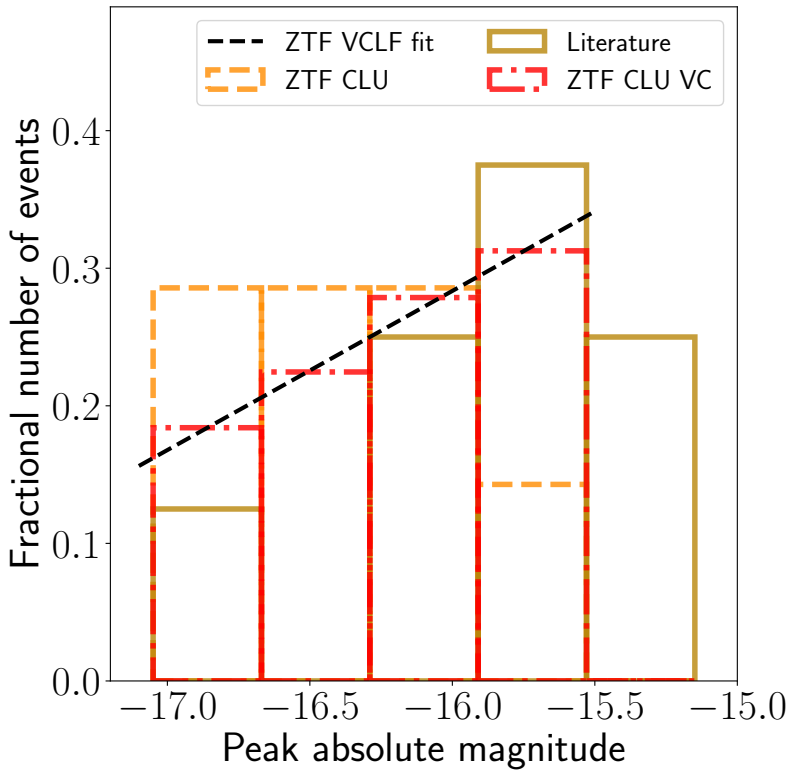

Figure 6.23: **Peak r-band absolute magnitude distribution of the literature sample of Ca-rich gap transients (gold solid) and the ZTF sample (orange dashed).** The dot-dashed distribution in red shows the volume corrected luminosity function (VCLF) of the ZTF sample, where a $\frac{1}{V_{max}}$ weighting was applied, with V_{max} being the maximum volume out to which the transient would be detected by the volume limited experiment. The black dashed line shows a linear fit to the volume-corrected luminosity function.

correction needs to be applied to recover the true luminosity function.

We show a volume-corrected luminosity function (VCLF) histogram of the ZTF Ca-rich sample in Figure 6.23. For each object, we apply a volume-correction of $\frac{1}{V_{max}}$ where V_{max} is the maximum volume out to which object would be detectable for a limiting magnitude of 20. For sources that would be detectable at > 200 Mpc, we set the relevant volume to 200 Mpc given the volume-limited nature of the experiment. The VCLF shows evidence of an increasing number of events down to the faintest event, and a simple linear polynomial describes the VCLF well. It is difficult to constrain the luminosity function below the faintest observed events, since it is unclear if there is a population of fainter events which would be detectable only within a very small volume (< 100 Mpc). Hence, for the purpose of the simulations, we restrict the observed function between $M = -17$ mag (the upper luminosity limit

for our sample) and $M = -15.3$ mag (faintest observed event SN 2012hn). We caution that the ZTF CLU experiment is not sensitive to transients brighter than $M = -17$ mag at peak due to the sample selection criteria, if such a population exists. Our rate estimates are thus limited to events peaking at $-15.3 > M > -17$.

Template light curve for a Ca-rich gap transient

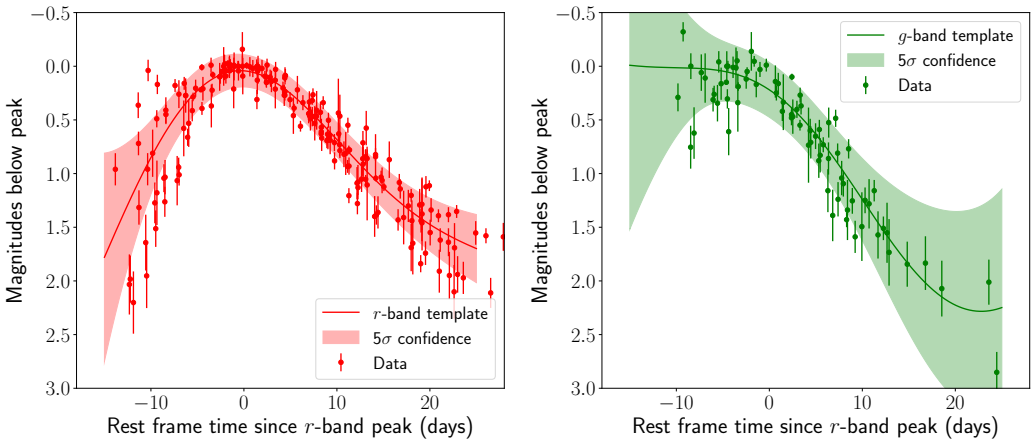

Figure 6.24: **r-band and g-band light curve templates for Ca-rich gap transients, normalized to peak magnitude.** The points with error bars show the observed light curves with 1σ error bars in the respective filters while the solid lines indicate the best-fit light curve from Gaussian process fitting. The shaded regions indicate the uncertainty intervals derived from the Gaussian process fitting, corresponding to 5σ confidence regions.

In order to provide a more robust estimate of the volumetric rates of Ca-rich gap transients, accounting for their low-luminosity light curves and the ZTF survey cadence, we start by constructing a template light curve of a Ca-rich gap transient in the r and g bands (which have the most photometric coverage) using the data available for the events in the combined sample. Since we are interested in the photometric evolution timescale of each event, we first normalize each light curve by its peak magnitude measured in the respective filter. Time is measured with respect to the best-fit r-band peak time. We then fit a Gaussian process model with a constant kernel to the normalized light curves in each filter to construct a normalized light curve template in the r and g filters.

We perform the fit in the phase space of magnitude versus time ranging from -15 d before r-band peak to $+25$ d after r-band peak, where there is photometric coverage for more than one object in both the filters. This produces the average peak-normalized template light curve and its uncertainty as a function of phase

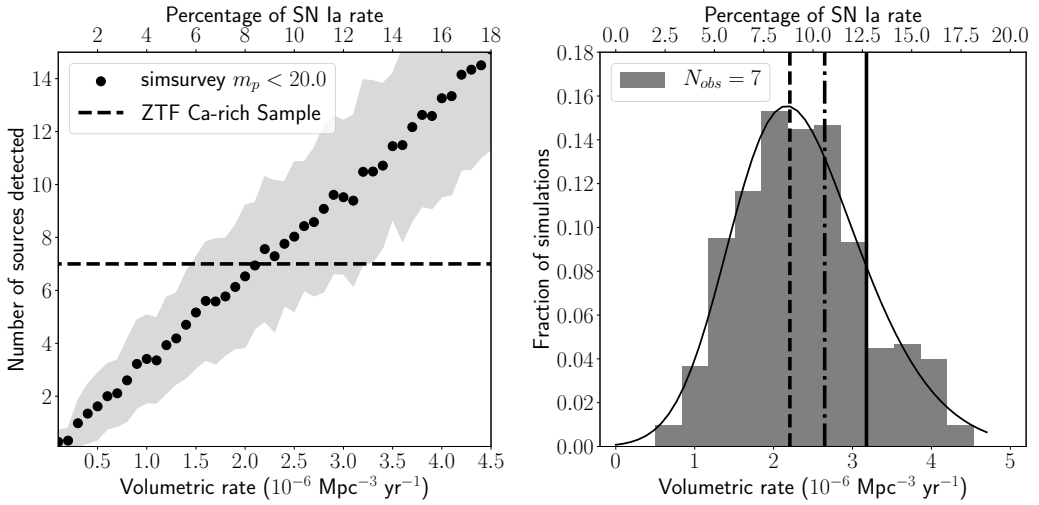

Figure 6.25: **Estimate of the volumetric rate of Ca-rich gap transients with simulations of the ZTF survey using the `simsurvey` code.** (Left panel) We show the number of sources passing our selection criteria for the CLU experiment as a function of the input volumetric rate (see text). The points and error bars are the mean and standard deviation of the number of transients recovered as a function of the volumetric rate, while the dashed black line shows the observed number of sources in the experiment. (Right panel) The fraction of simulations producing the observed number of transients as a function of the input volumetric rate. The dependence is fit with a skewed Gaussian distribution shown by the solid line, which we use to derive the best estimate of the volumetric rate and its confidence interval (see text). The dashed line shows the mean of the distribution, the dot-dashed line shows the rate after correcting for galaxy catalog incompleteness and the solid line shows the rate estimate after accounting for the transients missed beyond 100″ from their host galaxies.

from *r*-band maximum. We do not include photometry upper limits in the fit. In Figure 6.24, we show the peak normalized data and best fit templates together with their uncertainties for the two filters. In particular, we note that the sample of peak normalized light curves in both filters are fairly homogeneous around peak light (even though there is a dispersion in the peak magnitudes), suggesting that a single light curve template normalized to peak magnitude can well capture the shape of the light curve.

Simulations of the ZTF survey

Using the derived luminosity function and light curve templates for the class of Ca-rich gap transients, we estimate their volumetric rates in the local universe using the `simsurvey` code (Feindt et al., 2019). `simsurvey` is capable of simulating transient

light curves as would be observed by ZTF for a given input SN template (provided using the `sncosmo` package from Barbary et al., 2016), and an input survey tiling pattern and duration (termed as a survey plan). We use the best-fit r and g band templates to construct a `TimeSeriesSource` model in the `sncosmo` package to simulate the spectral evolution of a Ca-rich gap transient between 15 d before and 25 d after r-band peak. We then use the actual ZTF observing history between 2018 June 01 and 2019 September 30 in any of the public or collaboration surveys as the input survey plan. Since the ZTF reference images were created shortly before the start of the survey and extended well into the time period discussed here for some fields, we only consider pointings that were acquired at least 60 d after the end of reference creation to avoid contamination of the reference images by transient light.

We then simulate ZTF light curves of Ca-rich gap transients for a range of input volumetric rates, performing 100 simulations of the ZTF observing plan for each input rate. Based on the observed volume-corrected luminosity function, we fix the peak absolute magnitude distribution of the injected transients to be a linear function between $M = -15.3$ mag and $M = -17$ mag in r-band. We assume a color of $g - r = 0.7$ mag at r-band peak (based on the observed color evolution of the sample). Transients are injected out to a redshift of $z = 0.05$. In order to select transient candidates that would have passed the selection criteria defined in this experiment, we perform quality cuts on the simulated light curves as follows:

1. At least 2 detections of the source are required above signal-to-noise ratio (SNR) of 5 in either $g_{\rm ZTF}$ or $r_{\rm ZTF}$ filters.

2. The peak detected magnitude of the transient should be $m < 20$ in either $g_{\rm ZTF}$ or $r_{\rm ZTF}$ filters.

3. The transient is observed before peak such that there is at least one detection with SNR > 5 before the peak of the light curve in either $g_{\rm ZTF}$ or $r_{\rm ZTF}$ filters.

Applying this selection criteria to the sample presented in this paper, all but SN 2018gwo, which was recovered after peak light, satisfy the criteria. We use the average number of transients qualifying these cuts as the best estimate of the number of detected transients for each input volumetric rate, while the standard deviation of the number detected in the simulations is taken as the uncertainty. We show the expected number of detected transients as a function of the input volu-

metric rate in Figure 6.25. Figure 6.25 also shows the fraction of simulations that produce the observed number of transients as a function of the input volumetric rate.

Note that `simsurvey` is designed to inject simulated transients over the entire sky for a given input volumetric rate, while the CLU experiment is restricted to transients coincident within 100″of galaxies with known spectroscopic redshifts. Hence we denote the `simsurvey` derived rate as $r_{Ca,u,o}$ with the u subscript indicating uncorrected for the galaxy catalog completeness, and o indicating uncorrected for offset distribution. The distribution of the fraction of simulations (Figure 6.25) is well described by a skewed Gaussian function and we fit the fraction of simulations with this functional form to derive the best estimate of the volumetric rate and its 68% confidence interval similar to the procedure adopted by Frohmaier et al., 2018. We find a volumetric rate of

$$r_{Ca,u,o} = (2.21^{+1.01}_{-0.67}) \times 10^{-6}\mathrm{Mpc}^{-3}\mathrm{yr}^{-1}. \tag{6.1}$$

Here, we quote the mode of the probability distribution in Figure 6.25 as the most likely rate, while the median of the rate probability distribution is $2.40 \times 10^{-6}\,\mathrm{Mpc}^{-3}\,\mathrm{yr}^{-1}$. The uncertainty intervals correspond to central 68% confidence region, bounded by the 15.86 and 84.15 percentiles of the derived distribution. The most likely rate corresponds to $\approx 9^{+4}_{-3}$% of the SN Ia rate in the local universe ($\approx 2.5 \times 10^{-5}$ Mpc^{-3} yr^{-1}; Frohmaier et al., 2019).

In order to estimate the effect of incompleteness of galaxy catalogs in our estimate of the volumetric rate, we use the estimated redshift completeness factor (RCF) from the ZTF BTS (Fremling et al., 2019) as a function of the WISE W_1 (3.36 μm) magnitude and redshift of the host galaxies. Taking the observed distribution of redshift z and W_1 absolute AB magnitude M_{W1} (as obtained from the `Tractor` catalogs described in Lang et al., 2016) of the ZTF sample of Ca-rich gap transients, we weight each event by $\frac{1}{RCF(M_{W1},z)}$ for its host galaxy, and sum up over the sample of seven events relevant for the simulation. With this exercise, we find that the incompleteness of galaxy catalogs leads to an underestimate of the Ca-rich gap transient rate by $\approx$ 20%. Next, analyzing the full sample of 18 events, we find that 3 out of the 18 objects exhibited offsets larger than 100″ of their host galaxies, although we caution that it is hard to quantify the systematic biases associated with the literature events. Accounting for this effect would increase the inferred rate by another $\approx$ 20%. Adjusting for these incompleteness, we derive a rate of

$$r_{Ca} = (3.19^{+1.45}_{-0.96}) \times 10^{-6}\mathrm{Mpc}^{-3}\mathrm{yr}^{-1} \tag{6.2}$$

which is 13^{+6}_{-4}% of the volume-averaged SN Ia rate in the local volume.

Owing to the predominance of early type hosts in this sample, we also compare this rate against the SN Ia rate in early type galaxies. Li et al., 2011 report a luminosity-function averaged SN Ia rate in early type galaxies of ≈ 0.05 per 100 yr per 10^{10} $L_{\odot,K}$. Using the local K-band luminosity density in early type galaxies (Kochanek et al., 2001), we find the corresponding volumetric rate of SNe Ia in early type galaxies to be $\approx 1.1 \times 10^{-5}$ Mpc^{-3} yr^{-1}. Thus, the inferred rate of Ca-rich gap transients is ≈ 30% of the volume-averaged SN Ia rate in early type galaxies. We further note that the rate of SNe Ia in early type galaxies in cluster environments (Mannucci et al., 2008) is ≈ 40% lower than the volume-averaged rate per unit mass in Li et al., 2011. This suggests that the rate of Ca-rich gap transients in early type galaxies in clusters (which is true for nearly all events in our sample) is nearly ≈ 50% of the SN Ia rate in these environments.

However, we caution that this rate estimate is still strictly a lower limit as we did not include the detection efficiency of the ZTF image subtraction pipeline as a function of transient magnitude and underlying surface brightness. An accurate estimate of the true rate would require us to assign a probabilistic detection likelihood for each simulated detection, using measured detection efficiencies of the ZTF pipeline, which are currently not available. We thus proceed taking the derived rate as the first measured lower limit to the volumetric rate of Ca-rich gap transients from a large systematic volume-limited experiment.

The derived rate is consistent with those estimated by Perets et al., 2010 from LOSS and Kasliwal et al., 2012 from PTF. Frohmaier et al., 2018 presented the first quantitative analysis of the volumetric rates of Ca-rich gap transients using three events reported by PTF, incorporating the detection efficiency of the PTF pipeline as a function of transient magnitude and background surface brightness. They infer a rate that could be larger than in this work, of $\approx 30 - 90$% of the SN Ia rate in the local universe, although their estimate has large error bars owing to the small number of three events in the PTF sample.

6.6 Discussion

In this paper, we have presented observations and analysis of eight new Calcium rich gap transients classified as a part of the ZTF CLU experiment, nearly doubling the known sample of events in the literature. In Section 6.3 we demonstrated that the ZTF sample shares several similarities to ten events reported in the literature, while

also increasing the diversity of several observed properties among the combined sample. Utilizing the systematic selection criteria of the ZTF sample, we presented an analysis of the host environment properties (Section 6.4) and volumetric rates (Section 6.5) of the class. In this section, we gather all of these findings to discuss their constraints and implications on the progenitor channels for this class.

Spectroscopic sub-classes and correlations

In Section 6.3, we noted the existence of two classes of Ca-rich gap transients distinguished by their spectroscopic appearance at peak – the Ca-Ib/c events and the Ca-Ia events (see Table 6.2). We further found a possible continuum of peak light spectral characteristics within the Ca-Ib/c class, wherein the events evolve from green continua with strong P-Cygni features in the blue to events with featureless reddened continua at short ($\lesssim 5500$ Å) wavelengths. While the Ca-Ia events are distinguished by their strong Si II features at peak light, we demonstrated a continuum in the peak-light spectral features going from the Ca-Ia to Ca-Ic to Ca-Ib events. We briefly summarize them here:

1. Ca-Ib/c objects with green continua show strong optical He I features, while events with redder continua show a continuum of strong to weak to no He lines in their peak spectra (Figure 6.7).

2. He line velocities in red Ca-Ib/c events (≈ 7000 km s^{-1}) are lower than those observed in the green Ca-Ib/c events, which show high photospheric velocities of ≈ 10000 km s^{-1}.

3. Red Ca-Ib/c events exhibit slower evolving light curves (as quantified by $t_{f,1/2}$) compared to the green events, with a null hypothesis probability (that the two classes are drawn from the same underlying population of $t_{f,1/2}$) of $< 5\%$ (Figure 6.15). This dependence is corroborated by the $g-r$ color dependence of the photometric evolution (Δm_7) shown in Figure 6.16.

4. Red Ca-Ib/c events typically exhibit smaller [Ca II]/[O I] compared to green Ca-Ib/c events (by a factor of ≈ 2) at similar phases when the transient spectrum becomes optically thin (Figure 6.12).

5. Ca-Ia events exhibit more luminous light curves (peak absolute magnitude $M \lesssim -16.5$) than the Ca-Ib/c class, and have similar red spectroscopic colors / line blanketing and slow photometric evolution as the red Ca-Ib/c events (Figure 6.15).

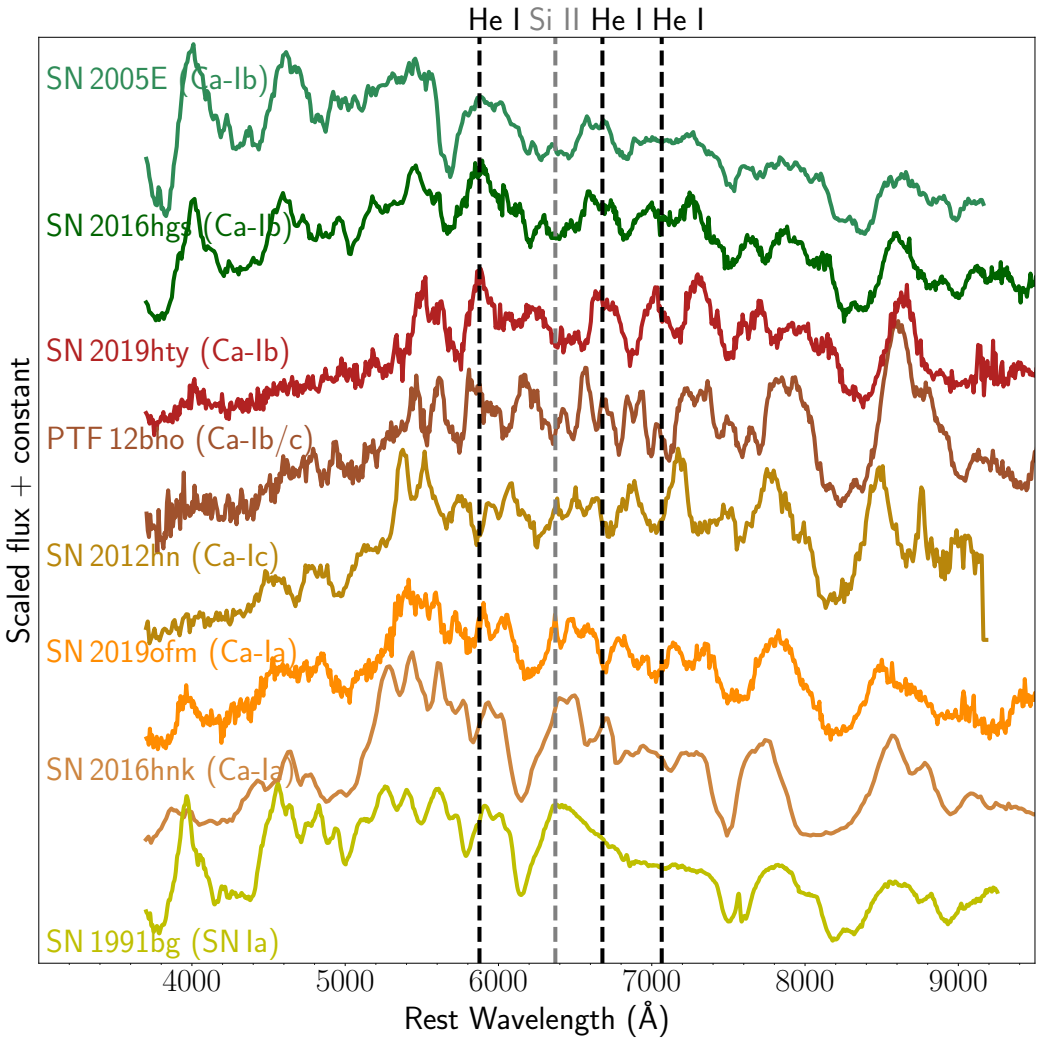

Figure 6.26: **A continuum of spectroscopic and photometric properties in the sample of Ca-rich gap transients.** For comparison, we also show a peak light spectrum of SN 1991bg, which shows striking similarities to the Ca-Ia objects. From bottom to top, we find a sequence of events that appear similar to SNe Ia-91bg at peak (Ca-Ia events) with strong Si II lines, to SNe Ib/c at peak (Ca-Ib/c events) with weak He lines and line-blanketed continua, to SNe Ib at peak (Ca-Ib events) with strong optical He I lines and no line blanketing. The colors reflect the photometric colors of the transient at peak. In general, going up the same sequence from bottom to top, the light curves become faster evolving while the peak $g - r$ colors become bluer. The black dashed lines show the rest wavelength of the optical He I lines and the gray dashed line shows the position strong Si II line at ≈ 6360 Å. Note the increasing depth and higher velocity of the Ca II NIR triplet going from the Ca-Ib to Ca-Ia events.

6. Although the strong Si II line distinguishes the Ca-Ia events from the Ca-Ib/c events, there are striking similarities between the Ca-Ia and Ca-Ib/c events with

redder continua, and we find evidence of a continuum of Si II line strengths going from Ca-Ia to Ca-Ib/c events (Figure 6.9).

Observable	Ca-Ia	Ca-Ib/c red	Ca-Ib/c green
Si II?	strong	strong to weak	weak
He I?	No	weak to strong	strong
V (10^3 km s^{-1})	6 – 10 (8)	4 – 10 (7)	8 – 12 (10)
Blanketed?	Yes	Yes	No
M_p (mag)	-16.2 – -17	-15.3 – -16.7	-15.5 – -16.2
Δm_7 (mag)	0.4	0.3	0.5
$g - r$ (mag)	1.0	1.5	0.4
[Ca II]/[O I]	No [O I]	2.5 - 10 (4)	7 - 13 (10)

Table 6.2: **Primary observational differences between the Ca-Ia and Ca-Ib/c objects, also highlighting differences between the green and red Ca-Ib/c objects.** The velocity row is indicated with V, and shows the range of observed peak velocities together with the typical value. The Peak mag and [Ca II]/[O I] row shows the range of peak absolute magnitudes in r-band and [Ca II]/[O I], respectively.

It is worth noting that even most Ca-Ib/c events exhibit weak but identifiable Si II lines blended with the nearby λ6678 He line (Section 6.3). We thus find evidence of a sequence in the Ca-rich gap transients going from Ca-Ia to red Ca-Ib/c to green Ca-Ib objects, potentially suggesting a continuum of underlying explosion conditions and progenitor systems. We show the corresponding spectroscopic sequence in Figure 6.26, where we plot the peak light spectra of a few representative members of the Ca-Ia and Ca-Ib/c class. In addition, we also show a peak light spectrum of SN 1991bg (Filippenko et al., 1992b), which shows several similarities to the Ca-Ia objects. Thus, the underlying cause for this continuum of spectroscopic appearance could provide a clue to the nature of these explosions. We tabulate and quantify the key observational differences between the different spectroscopic classes in Table 6.2. We now further this idea of a continuum of underlying progenitor systems as an explanation for the diversity observed in Ca-rich gap transients by probing physical explanations for this continuum.

Constraints on ejecta composition and mixing

Suppression of flux and features at short wavelengths can be explained as an outcome of line blanketing along the line of sight from Fe group material in the outer ejecta (e.g. Nugent et al., 1997; Woosley et al., 1994). Such features are often seen in peculiar thermonuclear SNe (De et al., 2019a), suggestive of Fe-group rich layers in the outer ejecta. The presence of such material is expected to produce redder colors in the transient (Kromer et al., 2010; Nugent et al., 1997; Polin et al., 2019)

while increasing the effective opacity of the ejecta due to increase in bound-bound opacity from Fe group material. The increased opacity can also produce slower evolving light curves if we assume that the underlying ejecta mass distribution is the same (see Figure 6.17; however, this is not expected to be dominant if the increased opacity is confined only to the outer layers of the ejecta).

The variety in the strengths and velocities of the optical He lines provides yet another clue to the underlying ejecta composition. Due to the high ionization temperature of He, the optical He lines may or may not be excited depending on the ejecta temperature and non-thermal excitation from radioactive material (Lucy, 1991). Dessart et al., 2012 show that non-thermal excitation from radioactive decay of ^{56}Ni is crucial for exciting optical He lines seen in the spectra of Type Ib/c SNe, thus suggesting that the SN Ib/c classification may be related to the amount of ^{56}Ni mixing into the He layer instead of the actual He content of the ejecta (but see also Hachinger et al., 2012). While highly mixed radioactive material in the He layer would produce strong optical He lines, they would also redden the transient color due to the presence of Fe group material in the outer layers. However, we do not observe this trend in the Ca-rich sample – events with redder continua exhibit weaker (or no) He lines, suggesting a reduction in the He content as the amount of Fe group elements increase in the outer ejecta. In addition, unlike the massive cores in core-collapse SNe, the low optical depth for γ-rays in these low ejecta mass explosions (see De et al., 2018b for a discussion) makes it difficult to hide non-thermal excitation of He.

While a continuum of Fe-group mass fraction in the outer ejecta appears to explain several of the observables, it does not explain the reason for such a continuum. This continuum could be associated with either a fundamental transition in the composition of the underlying ejecta, or be due to viewing angle effects. If the outer Fe group material is produced from He burning in the outer ejecta, one could explain these observations as a continuum of He burning efficiencies in the outer ejecta, wherein the outer ejecta become richer in Fe group elements (which cause the line blanketing) as the He burning is more complete, thus leading to weaker He lines (see Townsley et al., 2012 for recent work on partial burning of He shells).

Regardless, it is important to note that the change in the peak light continuum properties also appears to affect the appearance of the transient in the late-time nebular phase (its [Ca II]/[O I] ratio) when the ejecta are optically thin and viewing angle effects should be minimal. Both [Ca II] and [O I] are effective coolants of

SN ejecta at late-times (Fransson et al., 1989) being powered by ^{56}Co decay in the case of normal core-collapse SNe. Together, these observations suggest that the cooling in the inner ejecta becomes progressively dominated by [O I] as the outer ejecta become poorer in He content / richer in Fe group content. Although not discussed thus far, Figure 6.26 also shows a continuum in the depth and velocity of the prominent Ca II NIR triplet, wherein the absorption becomes deeper and moves to higher velocity over this sequence. Since Ca is a known He burning product (Townsley et al., 2012), this evolution in the Ca II NIR triplet may be associated with the He burning sequence discussed here.

For completeness, we can rule out dust extinction as a possible cause for this evolution, while dust reddening can suppress red continua, it cannot explain the lack of blue side SN ejecta features seen in the red Ca-Ib/c events. In addition, the remote locations of all of these events and the lack of detectable Na I D absorption in the spectra argue against host galaxy dust extinction.

Implications for the explosion mechanism

Models in the literature

Shen et al., 2019 summarizes the circumstantial evidence used to rule out several progenitor channels in the literature sample based on their environments, hosts, and volumetric rates. Owing to the striking similarities of the host demographics and environments of the ZTF sample and the literature events, our controlled experiment provides corroborating evidence for the preference of these transients for old environments. As in the literature sample, we find core-collapse SNe from massive stars as unlikely progenitor channels due to the prevalence of early type hosts and large offset locations with no signs of nearby star formation. On the other hand, the high inferred volumetric rates (lower limit of $\approx 15\%$ of the SN Ia rate) rule out progenitor channels with low expected volumetric rates such as He WD - neutron star mergers, where the field rate is $\sim 100\times$ lower (Toonen et al., 2018; see also Shen et al., 2019 for arguments against the viability of the high volumetric rates of these systems in globular clusters).

We thus consider explosive burning of He shells on white dwarfs as the strongest candidates for the cause of these events, and proceed by discussing the implications of our findings on the possible explosion conditions. Assuming that Ca-rich gap transients arise from He shell explosions on white dwarfs, we aim to constrain variations in the underlying progenitor configurations and / or the burning mechanisms

using the observed continuum of spectroscopic and photometric properties.

In the He shell detonation scenario, a shell of accreted He on the WD surface (accreted from a He-rich companion) can undergo dynamical burning for large shell masses, and detonate explosively to produce a thermonuclear transient (Bildsten et al., 2007; Iben et al., 1989; Shen et al., 2009; Sim et al., 2012; Woosley et al., 2011). Shen et al., 2010 presented calculations of the optical signatures of these events termed as '.Ia' supernovae, and Perets et al., 2010 suggested that the prototype Ca-rich transient SN 2005E was a result of such a detonation. However, the photometric evolution for the low ejecta mass ($\lesssim 0.2\,M_\odot$) models presented in Shen et al., 2010 were substantially faster than SN 2005E, leading Perets et al., 2010 to suggest that more massive shells could explain the slower light curve evolution.

Waldman et al., 2011 carried out explosive nucleosynthesis calculations of the shell detonation scenario with a 0.2 $M_\odot$ shell on a 0.45 $M_\odot$ CO WD, and demonstrated nucleosynthesis of a large amount of intermediate mass elements together with unburned He in the ejecta. Including non-thermal excitation effects, Dessart et al., 2015a showed that these events exhibit low-luminosity light curves, He spectroscopic signatures at peak light and [Ca II] emission in the nebular phase, and are thus consistent with Ca-rich gap transients. Yet, the relatively slow light curve evolution of most of the literature events required even more massive shells ($\gtrsim 0.2\ M_\odot$) than in these calculations if the underlying core is not detonated. In particular, Dessart et al., 2015a showed that the ratio of [Ca II]to [O I]emission depends not only on their relative abundance, but also on where the γ-rays from late-time radioactive decay are being deposited, as these lines are primary coolants of the regions of the ejecta where they exist. They further showed that the ejecta continued to cool predominantly through [Ca II] emission even if [O I] was present owing to the higher efficiency of [Ca II] cooling, thus pointing out the importance of mixing of radioactive material as well as the Ca and O regions in determining [Ca II]/[O I] in the nebular phase (Fransson et al., 1989).

Modifications to this scenario involving the detonation of the underlying CO core and the conditions required thereof have also been explored in the literature, first in the context of double detonation models for Type Ia supernovae (Livne et al., 1995; Nomoto, 1980, 1982a,b; Woosley et al., 1986, 1994). These initial models invoked thick He shells ($\sim 0.1\,M_\odot$) for this scenario and were largely ruled out due to the predicted red colors and strong line blanketing signatures found for these configurations (e.g. Nugent et al., 1997).

Later studies found that thin He shells (as low as $0.01\,M_\odot$) on relatively massive CO cores ($\gtrsim 0.8\ M_\odot$) can detonate the underlying white dwarf (Bildsten et al., 2007; Fink et al., 2010; Shen et al., 2010, 2014b), potentially producing luminous slow-evolving transients akin to normal and sub-luminous Type Ia SNe (Kromer et al., 2010; Polin et al., 2019; Sim et al., 2010; Woosley et al., 2011). Specifically, the slower evolving light curves in these models may be consistent with the Ca-rich gap transients; however, since the luminosity and timescale of these light curves increase with the underlying total mass (owing to higher Ni production from higher density cores), Ca-rich gap transients are likely associated with explosions on lower mass WDs in this scenario.

To this end, Sim et al., 2012 further extended these calculations to lowest mass CO WDs ($\approx 0.45\,M_\odot$) with thick He shells ($0.2\,M_\odot$) specifically to probe the parameter space for sub-luminous and fast evolving events like Ca-rich events. They find that secondary detonations are likely triggered for these shell masses (although there remain large uncertainties), and present a suite of simulations varying the extent and mechanism of the core detonation to demonstrate the corresponding effects on the nucleosynthetic signatures. They specifically note that their suite of models produce brighter transients (peak absolute magnitude $\lesssim -17$) than the prototype SN 2005E, and thus reproducing the properties would require lower yields of radioactive material that could be possible in lower density He shells (Shen et al., 2009; Woosley et al., 2011) or via significant pollution of the shell with C (Kromer et al., 2010).

Ca-rich gap transients from He shell explosions

Jacobson-Galan et al., 2019 suggested that the Ca-Ia object SN 2016hnk was consistent with the detonation of a thin ($\approx 0.02\,M_\odot$) He shell on a $\approx 0.8\,M_\odot$ WD. This interpretation was based on recent work by Polin et al., 2021 showing that the ejecta in double detonation events could cool predominantly through [Ca II] lines in the nebular phase (instead of the Fe group lines as in other SNe Ia) for low total (WD core + He shell) masses ($\lesssim 0.9\,M_\odot$), even if the Ca abundance in the ejecta is of the order of a few percent. This channel thus provides a promising scenario to explain the origins of the Ca-Ia objects, owing to their luminous and slow evolving light curves, strong line blanketing signatures with SN Ia-like spectra, and [Ca II] emission in the nebular phase. The observed diversity in the peak luminosities could then be associated with a range of white dwarf core masses.

Therefore, it is interesting to extend this mechanism to a continuum of He shell and CO core masses that may explain the diversity in the population of Ca-Ib/c events with double detonations. Unlike pure shell detonations that have had difficulty explaining the relatively slow evolving light curves of prototypical Ca-rich transients like SN 2005E and SN 2010et (see for example, Waldman et al., 2011 and Dessart et al., 2015a), double detonations predict slower evolving light curves compared to pure shell detonations due to the higher ejecta mass involved (Sim et al., 2012; Woosley et al., 2011). Noting that SN 2005E and SN 2010et belong to the class of green Ca-Ib/c events that have faster evolving light curves, the problem with slow evolution is even worse for the red Ca-Ib/c events that exhibit slower light curves similar to the Ca-Ia events (Figure 6.15), leading us to consider double detonations for the red Ca-Ib/c events.

Owing to the explosive burning of He-rich material, a common spectroscopic prediction of the He shell double detonation scenario is a transient marked by strong line blanketing features of Fe group material and Ti II (at early times when the photopshere is in the He detonation material), in addition to the intermediate mass elements produced from the core burning (Hoeflich et al., 1996; Holcomb et al., 2013; Kromer et al., 2010; Nugent et al., 1997; Polin et al., 2019; Woosley et al., 2011). Such signatures are also found in pure shell and double detonations on lower mass white dwarfs (Dessart et al., 2015a; Sim et al., 2012). While previous attempts to model the green Ca-Ib/c objects (Dessart et al., 2015a; Sim et al., 2012) have had difficulty accounting for the relatively blue colors of these transients at peak, the red colors, line blanketing, and slow evolution make the double detonation channel an attractive possibility for the red Ca-Ib/c events. The typically lower peak luminosity of the red Ca-Ib/c events would then require detonations on lower mass white dwarfs compared to the Ca-Ia events.

However, despite having un-burned He in the ejecta (Moore et al., 2013; Polin et al., 2019; Sim et al., 2012; Townsley et al., 2012), existing works on double detonations have not yet demonstrated whether He I lines can be reproduced as observed. On the other hand, Si II lines are the most conspicuous spectral features in these models as seen in the Ca-Ia objects. The red Ca-Ib/c events show weak but clear signatures of He, sometimes stronger than the Si II lines. We note that existing models have primarily explored this scenario with relatively higher mass white dwarfs ($\gtrsim 0.8\,M_{\odot}$), and without including non-thermal radiation effects required to excite He lines (Sim et al., 2012 explored lower mass WDs but without non-thermal

effects). Given the continuum of strong-to-weak He lines observed in the red Ca-Ib/c population, it is possible that these explosions constitute a range of shell burning efficiencies, and correspondingly He content in the ejecta depending on the pressure at the base of the shell at the time of ignition (Moore et al., 2013). Ca-Ia events would then represent the extreme end of this population where the He is nearly completely burnt to iron group elements.

In the nebular phase, red Ca-Ib/c objects often show strong [O I] emission, unlike the Ca-Ia events. If both the red Ca-Ib/c events and the Ca-Ia events arise from double detonations but with different underlying white dwarf masses, this provides observational evidence that the core burning becomes less efficient as one moves towards smaller core masses. A possible explanation is if the core detonation transitions from converging shock detonations in high mass cores to edge lit detonations (Livne et al., 1990, 1991; Nomoto, 1982a) at the base of the shell for lower mass white dwarfs. Owing to the lower density of the core in edge-lit detonations, Sim et al., 2012 show that these explosions produce incomplete burning of the core (thus lower Ni yields and fainter light curves) and larger amounts of O in the core, both consistent with the red Ca-Ib/c population. Alternatively, it is possible that a larger fraction of the Ni produced in the core detonation is convectively mixed into the O rich regions of the ejecta for lower mass white dwarf cores, thus producing stronger [O I] emission in the nebular phase.

Ca-Ib/c objects with green continua pose several problems to the general double detonation picture above, especially with regards to their bluer colors at peak without line blanketing signatures. The lack of these signatures suggests a scenario where the outer ejecta are not significantly enriched with Fe group elements, while their strong He line signatures indicate low He burning efficiency. Taken together with their systematically faster evolving light curves, these signatures likely point to a low efficiency burning mechanism that ejects a small amount of material. Although pure He shell detonation scenarios also predict line blanketed spectra (due to abundance of Ti II near the photosphere; e.g. Dessart et al., 2015a; Waldman et al., 2011), lower He burning efficiency has been shown to be achievable if the pressure at the base of the shell is lower (Moore et al., 2013; Perets et al., 2010). If so, the higher photospheric velocities, relatively fast photometric evolution and weak [O I] emission in the nebular phase are consistent with properties of green Ca Ib/c events (Dessart et al., 2015a; Waldman et al., 2011). The relatively low peak luminosity of this group (Table 6.2) then translates to a lower amount of radioactive material

synthesized in these shell-only explosions compared to double-detonations.

Alternatively, such low efficiency burning conditions may be achieved in pure shell deflagrations. The study of this mechanism is extremely limited at this time, but Woosley et al., 2011 show that these explosions produce slowly evolving sub-luminous light curves, but with low photospheric velocities (≈ 4000 km s^{-1}). However, that study was performed with 1D simulations which are poorly suited for deflagrations and future work is required to determine if higher velocities could be achieved to make this a plausible scenario.

We note that early excess emission has so far been clearly seen only in the green Ca-Ib/c objects SN 2016hgs and SN 2018lqo. If these explosions are indeed associated with He shell detonations or deflagrations, these observations suggest that the outer ejecta produced in the shell burning is enriched with short-lived isotopes (e.g. ^{48}Cr, ^{52}Fe, and ^{56}Ni with half-lives of 0.90 d, 0.35 d, and 6.07 d, respectively), as has been found in previous simulations of the pure shell detonation scenario (Shen et al., 2010). Although the early bump in iPTF 16hgs was potentially consistent with a core-collapse explosion from a giant He star (e.g. Woosley, 2019), the detection of this bump in SN 2018lqo in an old elliptical galaxy strongly argues against a core-collapse interpretation. Although most objects in the green Ca-Ib/c sample do not have well sampled early time light curves to detect this early emission, this phenomenon is clearly not ubiquitous in the Ca-Ib objects as demonstrated by the monotonic rise observed in the well sampled early light curve of SN 2010et (Figure 6.13).

Implications for the progenitor stellar populations

We have thus far discussed the implications of diversity in the photometric and spectroscopic properties of the Ca-rich gap transient population on the underlying explosion mechanism. Broadly, we find that the range of observed properties can be explained with scenarios involving explosive He burning on the surface of a CO WD. Specifically, the slowly evolving light curves of the Ca-Ia and red Ca-Ib/c objects are difficult to explain using scenarios involving pure shell detonations, and likely require relatively massive explosions that detonate the underlying core. On the other hand, the green Ca-Ib/c objects may be consistent with shell-only explosions with low He burning efficiency. We now extend this discussion to probe the implications of the environments of these transients on the inferred progenitors, i.e., white dwarfs accreting He from a companion. As noted in several previous works, this population

is distinguished from other classes of transients by their striking preference for large offsets from their passive host galaxies in predominantly group and cluster environments. These two trends generally point to old stellar populations with long delay times, and argue against channels which have a significant rate at short delay times ($\lesssim 1$ Gyr; Meng et al., 2015; Perets et al., 2010). We note that several objects in our combined sample (iPTF 16hgs, SN 2016hnk, and SN 2019ofm) were found in star forming environments, suggesting that there is a small but likely non-zero contribution at short delay times as well.

The pathways of stellar evolution to explosive burning of He shells have been explored in several previous works (Bauer et al., 2017; Bildsten et al., 2007; Brooks et al., 2015; Nomoto, 1982b; Shen et al., 2009; Woosley et al., 1994), with tight sdB + WD systems (Geier et al., 2013; Kupfer et al., 2017) and AM-CVn binaries (Nelemans et al., 2004) being possible well-observed evolutionary stages prior to the detonation. The observed formation rate of stable accreting AM-CVn systems in the Milky Way is $\sim 1.3 \times 10^{-4}$ yr^{-1} (Carter et al., 2013; Roelofs et al., 2007) or $\sim 2\%$ of the SN Ia rate in Milky-way like galaxies (Li et al., 2011). Bildsten et al., 2007 use this to estimate the rate of He shell detonations to be $2-6\%$ of the SN Ia rate in E/S0 galaxies assuming all AM-CVns detonate in a last flash. This rate is $\approx 3-7\times$ lower than our lower limit estimate for the volumetric rate of Ca-rich gap transients, and thus likely inconsistent. However, we cannot rule out the scenario where the green Ca-Ib events of the Ca-rich continuum discussed here originates in these explosions.

Similar detonation conditions can also be achieved in the case of mergers of He WDs with CO WDs (e.g. Pakmor et al., 2013), where a variety of detonation conditions could be achieved depending on how the He layer settles on the surface of the more massive WD (Dessart et al., 2015a; Fryer et al., 2010). The merger rate of He + CO WD binaries in the field for a Milky way-like galaxy is $\sim 3\times10^{-3}$ yr^{-1} (Brown et al., 2016) or $\approx 10\%$ of the SN Ia rate, suggesting that most He + CO WD binaries end up merging to produce thermonuclear transients or stable long-lived remnants (e.g. RCrB stars; Clayton, 1996; Schwab, 2019). The high rate of these mergers within Milky-Way like galaxies is however in contradiction with the preference of large offset distributions (long delay times) of the Ca-rich gap transient population (Shen et al., 2019). The measured rate in the halo (Brown et al., 2016) is only $\sim 10\%$ of the rate within the galaxy ($\sim 1\%$ of the SN Ia-rate) and hence inconsistent with our estimates for the Ca-rich population which reside in or outside their host halos.

With population synthesis calculations, Meng et al., 2015 suggested that the relatively high rates and long delay times of the Ca-rich gap transient population could be consistent with double WD binaries with a CO WD $\lesssim 0.6\,M_{\odot}$ and He WD $\lesssim 0.25\,M_{\odot}$, specifically highlighting the low mass as a key aspect of extending the delay time. This is consistent with our suggestion for low mass white dwarfs as the progenitor population, but the observed halo population of He-CO WD mergers remain too rare to explain the high rate (Brown et al., 2016). The measured rates are high enough such that there is one Ca-rich gap transient for every three SNe Ia in early type galaxies, suggesting that the progenitors must be nearly as common as the progenitors of SNe Ia.

Together, we find that the observed merger rates of WDs in He-rich accreting systems is too low in the field in the outskirts of galaxies to explain the high rates of Ca-rich gap transients. However, the interaction rate may be enhanced in dense stellar systems like globular clusters (see e.g. Pfahl et al., 2009; Samsing et al., 2017). Although such stellar systems are not detected exactly at the positions of known Ca-rich gap transients (Lunnan et al., 2017; Lyman et al., 2014, 2016b), Shen et al., 2019 suggest that these transients could be produced from being kicked out due to dynamical interactions inside dense stellar systems in the outskirts. Yuan et al., 2013 and Shen et al., 2019 argue that the locations and host environments are consistent with the globular cluster scenario; however, we continue to find that the number of Ca-rich gap transients at small offsets is too small compared to the globular cluster offset distribution in Shen et al., 2019. Additionally, the preference for rich cluster environments is even more extreme compared to globular clusters and remains to be explained.

Based on our deep late-time imaging observations of the transient locations, we find in 4 out of 8 cases evidence of faint and diffuse nearby or underlying stellar associations. We estimate the absolute magnitudes of these sources to be ≈ -9 mag to -11 mag at the redshift of the transient. A similar diffuse system was also detected in late-time imaging of PTF 11kmb (Lunnan et al., 2017). While we caution that the chance coincidence probability of background galaxies at this depth is high, we speculate about the implications of these being associated with the transient itself. Specifically, a population of such faint and ultra-diffuse galaxies have been detected in low surface brightness imaging surveys (Abraham et al., 2014) in nearby clusters. These systems appear to exhibit an overabundance (by nearly an order of magnitude) of globular clusters when compared to the expected numbers for their luminosity

(van Dokkum et al., 2016, 2017, 2018). Although work remains to be done to constrain the formation rate of double WD binaries in such dense stellar systems, it is an intriguing possibility that the offset locations of Ca-rich gap transients may be due to an overabundance of globular clusters in ultra-diffuse galaxies within nearby galaxy groups and clusters.

While Shen et al., 2019 point out that a relatively large fraction of WDs in globular clusters could be required to explain the estimated rate in Frohmaier et al., 2018, our lower rate estimates may provide a more viable solution to the problem. The locations of these transients in early type galaxies in predominantly rich cluster environments are indeed suggestive given that up to 30 – 70% of stellar light may be in intra-cluster light in these environments (D'Souza et al., 2014; Perets, 2014).

6.7 Summary

In this paper, we have presented the design and completeness of the Census of the Local Universe experiment of the Zwicky Transient Facility, aimed at assembling a spectroscopically complete sample of transients in the local universe within 200 Mpc. With a total sample of 754 spectroscopically classified SNe, we present the first systematic search for Ca-rich gap transients. Using simple and systematic selection criteria, we identified a sample of 22 low luminosity hydrogen-poor supernovae as candidate Ca-rich gap transients from the first 16 months of operations, which were followed up with nebular phase spectroscopy. We report the detection of eight Ca-rich gap transients in this sample, which we combine with the literature sample of ten events that pass the same selection criteria. We perform the first systematic study of the spectroscopic and photometric properties of this sample and identify several trends and correlations that have implications for the underlying explosions and progenitor systems. Summarizing these correlations, we find:

- Ca-rich gap transients broadly bifurcate into two classes based on their peak light spectroscopic similarity to SNe Ia (with strong Si II lines; Ca-Ia objects) and SNe Ib/c (without strong Si II lines; Ca-Ib/c objects).
- Ca-Ib/c objects show a bimodal population in peak light spectral properties based on their spectroscopic behavior bluewards of ≈ 5500 Å, wherein some events exhibit red continua and strong line blanketing of blue flux (Ca-Ib/c-red) while other events exhibit flat continua with clear P-Cygni absorption features of metals at short wavelengths (Ca-Ib/c-green). Ca-Ia objects always show line blanketed spectra at peak.

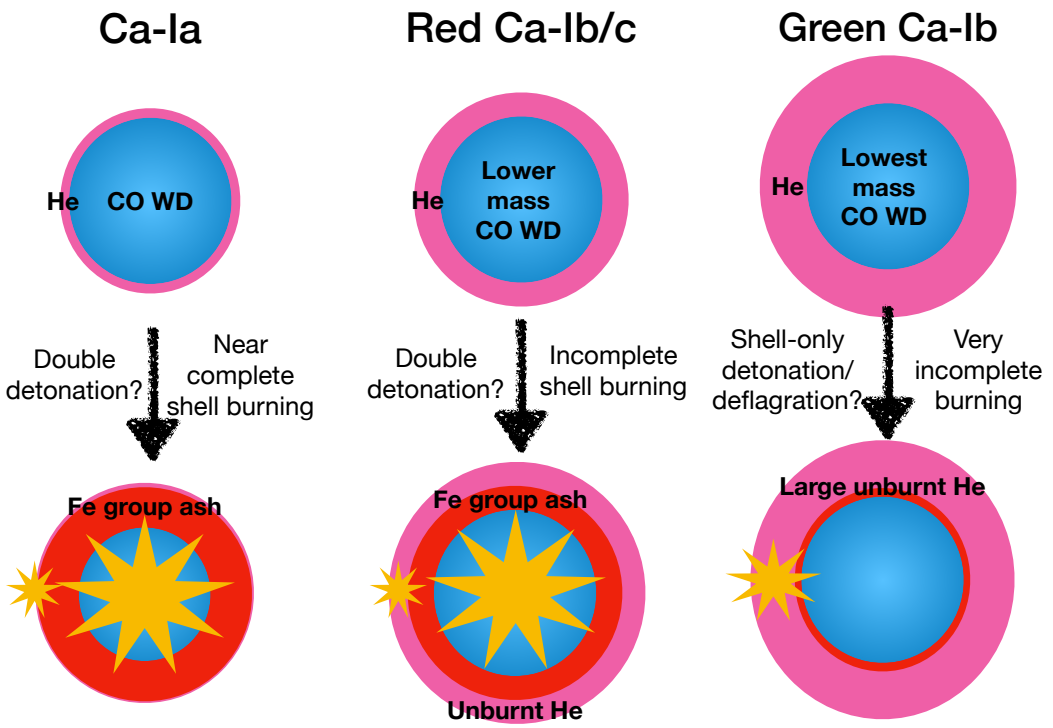

Figure 6.27: **A cartoon schematic of a possible progenitor and explosion mechanism sequence in WD and He shell masses that may explain the diversity of properties of the population of Ca-rich gap transients.** Double-detonation (involving a detonation in the shell followed by detonation in the core) with thin He shells and relatively massive WDs produce Ca-Ia objects, while double detonations on lower mass WDs produce red Ca-Ib/c objects. Pure shell detonations or deflagrations (involving only a detonation or deflagration in the shell) could explain the incomplete burning and bluer spectra of green Ca-Ib objects.

- Ca-Ia objects do not show any He lines, red Ca-Ib/c objects show a continuum from weak to strong He lines (velocity $\approx$ 7000 km s^{-1}), and green Ca-Ib/c objects always exhibit strong He lines at higher velocities of $\approx$ 10000 km s^{-1}.

- Photometrically, red Ca-Ib/c events with line blanketing signatures exhibit redder colors at peak and slower evolving light curves ($\Delta m_7 \approx 0.3$ mag) compared to green Ca-Ib/c events ($\Delta m_7 \approx 0.5$ mag), where Δm_7 is the decay of the r-band light curve in 7 days from peak light. Ca-Ia events also exhibit relatively slow photometric evolution compared to green Ca-Ib/c objects ($\Delta m_7 \approx 0.4$ mag).

- Ca-Ia objects do not show [O I] in the nebular phase, while red Ca-Ib/c objects

show stronger [O I] lines in the nebular phase relative to [Ca II] and green Ca-Ib/c objects shower weaker [O I] lines (higher [Ca II]/[O I] flux ratio) relative to red Ca-Ib/c objects.

- We find tentative evidence of a spectroscopic continuum of properties going from Ca-Ia to Ca-Ic to Ca-Ib objects, where Si II lines get weaker, He I lines get stronger, and line blanketing becomes less significant in the spectrum in moving along that sequence. Photometrically, the peak light colors get bluer while the light curve evolution becomes faster along this sequence.

We find that these spectroscopic properties and the corresponding trends can be broadly explained in scenarios involving the explosive burning of He shells on low mass white dwarfs ($\lesssim 0.8\,M_\odot$). The slowly evolving light curves and line blanketed spectra of the Ca-Ia and red Ca-Ib/c events are consistent with scenarios involving the double detonation of He shells on low mass white dwarfs where the efficiency of He burning in the outer ejecta is high. On the other hand, the strong He lines, higher velocities, and faster evolving light curves of the green Ca-Ib/c events suggest lower ejecta mass explosions likely involving He shell-only detonations with low He burning efficiency or even deflagrations. While the theoretical modeling of He shell explosions on low mass white dwarfs remains limited at this time, this data set together with the inferred correlations from the first systematic search for these explosions will be a useful benchmark for future modeling efforts.

The host environments of the sample are dominated by remote locations in the far outskirts of galaxies similar to what was found in previous studies, while the offset distribution are skewed towards large host offsets compared to globular clusters. The apparent host galaxies themselves are always found in rich group and cluster environments, and are likely an important clue to the progenitor channels. Using the systematic selection strategy of the experiment, together with the measured incompleteness of galaxy catalogs from the ZTF Bright Transient Survey, we infer the volumetric rates of these events to be at least $\approx 15 \pm 5\%$ of the local SN Ia rate. While the explosion scenarios require white dwarfs with He-rich donors, the observed rates of these systems are apparently too low in the field to explain their high volumetric rates. However, we note that the observed environments of these events in the outskirts of early type galaxies in clusters are strikingly different from the Galactic disk. We speculate that the rich host environments, offset locations, and faint nearby diffuse stellar associations in some events may point to a

contribution from dynamical interactions within ultra-diffuse stellar associations in galaxy clusters, that are found to be extremely rich in globular clusters (van Dokkum et al., 2016, 2017).

Our findings have broader implications for the population of thermonuclear supernovae in the local universe. While the double detonation scenario has been long proposed as a viable explosion triggering mechanism for Type Ia SNe, the strong line blanketing signatures produced by Fe group elements in the burning of the He shell have remained inconsistent for the broad population of normal Type Ia SNe (Hoeflich et al., 1996; Kromer et al., 2010; Nugent et al., 1997; Polin et al., 2019; Woosley et al., 2011). However, recent discoveries of peculiar SNe such as SN 2016jhr (Jiang et al., 2017) and SN 2018byg (De et al., 2019a) show that thin and thick He shell double detonations may indeed be realized in nature, but are intrinsically rare in the population. These transients were much more luminous at peak ($M \lesssim -18$) compared to the sample discussed here, consistent with the larger core masses ($\gtrsim 0.75\,M_{\odot}$) inferred for those objects. The Ca-Ia objects are then lower luminosity analogs of this family with relatively lower mass white dwarfs, while red Ca-Ib/c objects could be manifestations of He shell double detonations on the lowest mass white dwarfs. While it remains unclear if double detonations are realized for the lowest mass white dwarfs, the green Ca-Ib/c objects could potentially be manifestations of 'failed double-detonations' of the lowest mass white dwarfs in the universe that do not burn much of the progenitor He shell[16]. We summarize this possible progenitor sequence within Ca-rich gap transients in Figure 6.27.

Given the fast evolving light curves of Ca-rich gap transients, high cadence and wide-field time domain surveys will continue to be vital for unveiling large samples of these elusive events. With the combination of the flux-limited Bright Transient Survey (to estimate the redshift incompleteness of nearby galaxy catalogs; Fremling et al., 2019) and the volume-limited Census of the Local Universe experiment described in this work, we have demonstrated that focused experiments that spectroscopically classify a small fraction ($\lesssim 10\%$) of the total transient yield of a wide-field, all-sky survey like ZTF can yield statistically meaningful samples of transients that shed vital light on the underlying explosions and progenitor populations. As the current effort has been focused on a targeted search for these events in current (and incomplete) catalogs of nearby galaxies, the advent of heavily multiplexed spectrographs (e.g. DESI Collaboration et al., 2016; Kollmeier et al., 2017) aiming to complete galaxy

[16]See also Drout et al., 2011; Inserra et al., 2015; Kasliwal et al., 2010 for promising candidates for He shell-only detonation transients.

catalogs in the local universe will be vital for dedicated experiments to complete our census of transients in the local universe.

We thank H. Perets, K. Shen, E. S. Phinney, J. Fuller, D. Kasen, B. Margalit and S. Schulze for valuable discussions during this work. We thank M. Coughlin, S. Anand, A. Sagues Carracedo, L. Rauch, and U. Feindt for several discussions on the use of `simsurvey`.

This work was supported by the GROWTH (Global Relay of Observatories Watching Transients Happen) project funded by the National Science Foundation under PIRE Grant No 1545949. GROWTH is a collaborative project between California Institute of Technology (USA), University of Maryland College Park (USA), University of Wisconsin Milwaukee (USA), Texas Tech University (USA), San Diego State University (USA), University of Washington (USA), Los Alamos National Laboratory (USA), Tokyo Institute of Technology (Japan), National Central University (Taiwan), Indian Institute of Astrophysics (India), Indian Institute of Technology Bombay (India), Weizmann Institute of Science (Israel), The Oskar Klein Centre at Stockholm University (Sweden), Humboldt University (Germany), Liverpool John Moores University (UK) and University of Sydney (Australia). This research benefited from interactions at several ZTF Theory Network meetings, funded by the Gordon and Betty Moore Foundation through Grant GBMF5076.

Based on observations obtained with the Samuel Oschin Telescope 48-inch and the 60-inch Telescope at the Palomar Observatory as part of the Zwicky Transient Facility project. ZTF is supported by the National Science Foundation under Grant No. AST-1440341 and a collaboration including Caltech, IPAC, the Weizmann Institute for Science, the Oskar Klein Center at Stockholm University, the University of Maryland, the University of Washington, Deutsches Elektronen-Synchrotron and Humboldt University, Los Alamos National Laboratories, the TANGO Consortium of Taiwan, the University of Wisconsin at Milwaukee, and Lawrence Berkeley National Laboratories. Operations are conducted by COO, IPAC, and UW. SED Machine is based upon work supported by the National Science Foundation under Grant No. 1106171. The ZTF forced-photometry service was funded under the Heising-Simons Foundation grant 12540303 (PI: Graham). Some of the data presented herein were obtained at the W.M. Keck Observatory, which is operated as a scientific partnership between the California Institute of Technology, the University of California and the National Aeronautics and Space Administration. The Observatory was made possible by the generous financial support of the W.M. Keck

Foundation. The authors wish to recognize and acknowledge the very significant cultural role and reverence that the summit of Mauna Kea has always had within the indigenous Hawaiian community. We are most fortunate to have the opportunity to conduct observations from this mountain. Based on observations made with the Nordic Optical Telescope (operated by the Nordic Optical Telescope Scientific Association at the Observatorio del Roque de los Muchachos, La Palma, Spain, of the Instituto de Astrofisica de Canarias.)

AGY's research is supported by the EU via ERC grant No. 725161, the ISF GW excellence center, an IMOS space infrastructure grant, and BSF/Transformative and GIF grants, as well as The Benoziyo Endowment Fund for the Advancement of Science, the Deloro Institute for Advanced Research in Space and Optics, The Veronika A. Rabl Physics Discretionary Fund, Paul and Tina Gardner, Yeda-Sela, and the WIS-CIT joint research grant; AGY is the recipient of the Helen and Martin Kimmel Award for Innovative Investigation. AYQH is supported by a National Science Foundation Graduate Research Fellowship under Grant No. DGE-1144469 and by the GROWTH project funded by the National Science Foundation under PIRE Grant No. 1545949. RL is supported by a Marie Skłodowska-Curie Individual Fellowship within the Horizon 2020 European Union (EU) Framework Programme for Research and Innovation (H2020-MSCA-IF-2017-794467). Foscgui is a graphic user interface aimed at extracting SN spectroscopy and photometry obtained with FOSC-like instruments. It was developed by E. Cappellaro. A package description can be found at `http://sngroup.oapd.inaf.it/foscgui.html`.

Table 6.3: **Light curve fit parameters for the sample of Ca-rich gap transients presented in this paper, together with the fits for the literature sample of Ca-rich gap transients.** t_p denotes the time of peak in the respective filter, m_p denotes the peak apparent magnitude (corrected for Galactic extinction using the maps of Schlafly et al., 2011), M_p denotes the peak absolute magnitude, $t_{r,1/2}$ denotes the rise time to peak from half of the peak flux, and $t_{f,1/2}$ denotes the fall time from peak to half the peak flux. Δm_7 denotes the drop in magnitudes from time of peak to 7 d after peak. Photometry for some of the sources in the literature were obtained from the Open Supernova Catalog (Guillochon et al., 2017). The data were originally published in [1] Perets et al., 2010, [2] Sullivan et al., 2011, [3] Kasliwal et al., 2012, [4] Valenti et al., 2014, [5] Lunnan et al., 2017, [6] De et al., 2018a, and [7] Galbany et al., 2019. This table will be available in its entirety in machine-readable form.

Object	Filter	t_p MJD	m_p	M_p	$t_{r,1/2}$ (days)	$t_{f,1/2}$ (days)	Δm_7 (mag)	Ref.
SN 2018ckd	r	58277.67 ± 0.33	18.95 ± 0.02	−16.17	6.20 ± 0.29	8.68 ± 0.54	0.54 ± 0.04	This work
SN 2018ckd	g	58274.21 ± 1.31	19.69 ± 0.07	−15.43	...	10.17 ± 1.78	0.33 ± 0.19	This work
SN 2018ckd	i	58280.67 ± 0.66	19.00 ± 0.08	−16.12	7.88 ± 0.60	12.60 ± 1.07	0.33 ± 0.05	This work
SN 2018lqo	r	58351.92 ± 0.23	19.62 ± 0.02	−16.21	7.33 ± 0.25	10.47 ± 0.50	0.41 ± 0.02	This work
SN 2018lqo	g	58349.97 ± 0.35	20.09 ± 0.05	−15.73	5.80 ± 0.27	7.67 ± 0.41	0.64 ± 0.06	This work
SN 2018lqo	i	58353.41 ± 1.85	19.49 ± 0.17	−16.33	7.69 ± 1.76	11.04 ± 1.49	0.37 ± 0.14	This work
SN 2018lqu	r	58370.83 ± 2.27	19.57 ± 0.30	−16.44	7.40 ± 1.37	...	...	This work
SN 2018kjy	r	58460.93 ± 0.33	18.85 ± 0.06	−15.63	...	12.36 ± 1.49	0.31 ± 0.06	This work
SN 2018kjy	g	58458.18 ± 1.81	19.81 ± 0.25	−14.68	...	...	0.64 ± 0.46	This work
SN 2019hty	r	58657.90 ± 0.83	18.63 ± 0.05	−16.38	8.81 ± 0.78	11.55 ± 0.76	0.33 ± 0.04	This work
SN 2019hty	g	58653.44 ± 0.68	19.01 ± 0.08	−16.00	...	8.05 ± 0.84	0.59 ± 0.12	This work
SN 2019ofm	r	58723.58 ± 1.02	18.60 ± 0.04	−17.03	8.39 ± 1.14	11.07 ± 1.16	0.34 ± 0.06	This work
SN 2019ofm	g	58721.71 ± 1.65	19.69 ± 0.11	−15.94	...	...	...	This work
SN 2019pxu	r	58747.78 ± 0.48	18.90 ± 0.04	−16.56	...	11.83 ± 0.57	0.30 ± 0.03	This work
SN2005E	B	53387.15 ± 0.35	18.14 ± 0.13	−14.52	...	5.06 ± 1.26	...	[1]
SN2005E	V	53387.15 ± 0.51	17.51 ± 0.07	−15.15	...	7.93 ± 0.89	0.62 ± 0.12	[1]
SN2005E	R	53388.72 ± 0.71	17.13 ± 0.05	−15.53	...	8.90 ± 1.25	0.55 ± 0.12	[1]
SN2005E	I	53389.51 ± 1.32	16.73 ± 0.07	−15.93	...	...	0.39 ± 0.14	[1]
SN2007ke	R	54369.54 ± 1.82	17.77 ± 0.06	−16.59	...	10.29 ± 1.73	0.33 ± 0.14	[1]
PTF 09dav	r	55054.38 ± 0.78	19.86 ± 0.09	−16.22	6.26 ± 0.63	9.28 ± 1.00	0.49 ± 0.08	[2]
SN 2010et	r	55359.36 ± 0.25	19.03 ± 0.03	−15.69	6.30 ± 0.32	9.62 ± 0.55	0.49 ± 0.03	[3]
SN 2010et	g	55357.04 ± 0.39	19.56 ± 0.08	−15.15	...	8.01 ± 0.95	0.61 ± 0.11	[3]
SN 2010et	i	55361.86 ± 0.73	18.90 ± 0.04	−15.82	...	...	0.32 ± 0.05	[3]
PTF 11bij	r	55635.44 ± 1.60	20.28 ± 0.10	−15.68	...	9.46 ± 2.40	0.45 ± 0.22	[3]
SN2012hn	B	56031.06 ± 0.48	18.72 ± 0.06	−13.42	...	7.44 ± 1.02	0.69 ± 0.12	[4]
SN2012hn	V	56031.60 ± 0.63	17.15 ± 0.03	−14.99	...	...	0.32 ± 0.05	[4]
SN2012hn	R	56031.06 ± 0.84	16.59 ± 0.02	−15.55	...	15.23 ± 1.00	0.14 ± 0.05	[4]
SN2012hn	r'	56035.62 ± 2.94	16.90 ± 0.11	−15.24	...	11.74 ± 3.01	0.26 ± 0.21	[4]
SN2012hn	I	56037.90 ± 3.17	16.22 ± 0.01	−15.92	...	9.01 ± 3.17	0.40 ± 0.20	[4]
SN2012hn	G	56031.01 ± 0.80	17.45 ± 0.17	−14.69	...	9.31 ± 2.22	0.47 ± 0.27	[4]
SN2012hn	g'	56031.01 ± 0.83	17.45 ± 0.16	−14.69	...	9.31 ± 2.13	0.47 ± 0.24	[4]

PTF 11kmb	*r*	55800.73 ± 0.34	18.79 ± 0.01	−15.57	...	11.35 ± 0.42	0.28 ± 0.02	[5]
PTF 11kmb	*g*	55797.95 ± 1.01	19.37 ± 0.03	−14.99	...	10.41 ± 1.13	0.36 ± 0.09	[5]
PTF 12bho	*r*	55992.00 ± 0.25	18.99 ± 0.03	−16.04	6.97 ± 0.27	10.29 ± 0.35	0.42 ± 0.02	[5]
SN 2016hgs	*r*	57691.80 ± 0.24	18.91 ± 0.03	−15.45	...	9.43 ± 0.38	0.42 ± 0.03	[6]
SN 2016hgs	*g*	57683.22 ± 1.00	19.48 ± 0.10	−14.88	...	13.29 ± 0.98	0.25 ± 0.10	[6]
SN 2016hgs	*i*	57692.85 ± 0.21	18.54 ± 0.03	−15.82	...	9.47 ± 0.34	0.44 ± 0.03	[6]
SN2016hnk	*B*	57691.35 ± 0.60	18.92 ± 0.05	−15.31	...	7.00 ± 0.62	0.75 ± 0.09	[7]
SN2016hnk	*V*	57691.74 ± 0.74	17.46 ± 0.03	−16.77	...	...	0.39 ± 0.08	[7]
SN2016hnk	*r*	57692.78 ± 0.43	17.18 ± 0.02	−17.05	...	12.78 ± 0.62	0.32 ± 0.03	[7]
SN2016hnk	*i*	57691.34 ± 0.78	17.34 ± 0.03	−16.89	...	...	0.27 ± 0.06	[7]
SN2016hnk	*z*	57697.79 ± 2.42	17.38 ± 0.07	−16.85	...	...	0.09 ± 0.06	[7]
SN2016hnk	*g*	57695.27*	18.53 ± 0.04	−15.70	...	6.47 ± 2.25	0.76 ± 0.10	[7]

Table 6.4: **Spectral fit parameters for the sample of Ca-rich gap transients presented in this paper, together with the fits for the literature sample of Ca-rich gap transients.** For each spectrum, we measure both the He I λ5876 and λ7065 velocity (if detected) for the Ca-Ib/c events, and only the Si II λ6355 velocity for the Ca-Ia events. We indicate the line measured in brackets next to the velocity measurements for each spectrum phase. Values denoted by * indicate epochs where the signal-to-noise ratio of the spectrum was not high enough in the region of interest to measure the specific parameter. The velocity for SN 2012hn was measured using the feature near 5800 Åat peak light since it does not exhibit He signatures. For phases where the spectrum exhibited nebular emission features, we report the measured [Ca II]/[O I] ratio or lower limits in case [O I] is not detected (see text). Archival spectra were obtained from the WISEReP repository (Yaron et al., 2012). The data were originally published in [1] Perets et al., 2010, [2] Sullivan et al., 2011, [3] Kasliwal et al., 2012, [4] Valenti et al., 2014, [5] Lunnan et al., 2017, [6] De et al., 2018a, [7] Galbany et al., 2019, and [8] Jacobson-Galan et al., 2019. This table will be available in its entirety in machine-readable form.

Object	Phase (days)	V_1 (km s^{-1})	V_2 (km s^{-1})	[Ca II]/ [O I]	Ref.
SN 2018ckd	+1	9660 ± 110 (λ5876)	10090 ± 140 (λ7065)	...	This work
SN 2018ckd	+10	8260 ± 650 (λ5876)	...	...	This work
SN 2018ckd	+58	...	...	> 3.38	This work
SN 2018lqo	-2	8230 ± 150 (λ5876)	8270 ± 100 (λ7065)	...	This work
SN 2018lqo	+49	5090 ± 310 (λ5876)	...	> 12.51	This work
SN 2018lqu	+1	11100 ± 410 (λ5876)	10550 ± 280 (λ7065)	...	This work
SN 2018lqu	+31	5720 ± 500 (λ5876)	...*	> 8.38	This work
SN 2018gwo	+23	5150 ± 570 (λ5876)	...	...	This work
SN 2018gwo	+53	4780 ± 100 (λ5876)	6660 ± 80 (λ7065)	5.16 ± 0.08	This work
SN 2018gwo	+146	...	...	3.98 ± 0.06	This work
SN 2018gwo	+243	...	...	2.70 ± 0.08	This work
SN 2018kjy	+1	...*	2470 ± 170 (λ7065)	...	This work

SN 2018kjy	+22	6610 ± 90 (λ5876)	...	...	This work
SN 2018kjy	+111	...	...	4.44 ± 0.24	This work
SN 2019hty	+4	7480 ± 120 (λ5876)	8200 ± 50 (λ7065)	...	This work
SN 2019hty	+5	8200 ± 1140 (λ5876)	7600 ± 350 (λ7065)	...	This work
SN 2019hty	+38	...	...	> 3.27	This work
SN 2019ofm	-2	...	7380 ± 230	...	This work
SN 2019ofm	+168	...	...	> 2.15	This work
SN 2019pxu	+0	10310 ± 430 (λ5876)	...*	...	This work
SN 2019pxu	+8	9320 ± 100 (λ5876)	3110 ± 80 (λ7065)	...	This work
SN 2019pxu	+32	7790 ± 90 (λ5876)	3650 ± 180 (λ7065)	...	This work
SN 2019pxu	+146	...	...	> 8.30	This work
SN 2005E	-2	10200 ± 200 (λ5876)	9800 ± 80 (λ7065)	...	[1]
SN 2005E	-1	10260 ± 60 (λ5876)	9960 ± 60 (λ7065)	...	[1]
SN 2005E	+20	4450 ± 230 (λ5876)	4980 ± 60 (λ7065)	...	[1]
SN 2005E	+53	4430 ± 80 (λ5876)	4540 ± 150 (λ7065)	8.39 ± 0.26	[1]
SN 2007ke	+20	4370 ± 100 (λ5876)	4210 ± 310 (λ7065)	...	[1]
PTF 09dav	+2	...	6140 ± 100 (λ6355)	...	[2]
PTF 09dav	+8	...	5070 ± 70 (λ6355)	...	[2]
PTF 09dav	+13	...	5070 ± 120 (λ6355)	...	[2]
PTF 09dav	+88	...	...	> 22.35	[2]
SN 2010et	+2	8210 ± 70 (λ5876)	8880 ± 60 (λ7065)	...	[3]
SN 2010et	+27	7340 ± 110 (λ5876)	7990 ± 120 (λ7065)	...	[3]
SN 2010et	+62	3620 ± 440 (λ5876)	7080 ± 360 (λ7065)	...	[3]
SN 2010et	+87	...	...	6.15 ± 0.51	[3]
SN 2010et	+115	...	...	6.14 ± 1.36	[3]
PTF 11bij	+45	...	...	> 7.06	[3]
SN 2012hn	-3	7230 ± 320 (λ5800)	...	...	[4]
SN 2012hn	+4	7400 ± 160 (λ5800)	...	...	[4]
SN 2012hn	+6	7490 ± 70 (λ5800)	...	...	[4]
SN 2012hn	+13	6740 ± 220 (λ5800)	...	...	[4]
SN 2012hn	+25	5200 ± 40 (λ5800)	...	...	[4]
SN 2012hn	+150	...	...	2.25 ± 0.05	[4]
PTF 11kmb	+1	11670 ± 50 (λ5876)	9910 ± 40 (λ7065)	...	[5]
PTF 11kmb	+24	8520 ± 170 (λ5876)	7320 ± 260 (λ7065)	...	[5]
PTF 11kmb	+89	...	...	8.97 ± 0.30	[5]
PTF 11kmb	+124	...	...	10.07 ± 0.70	[5]
PTF 12bho	+9	7210 ± 170 (λ5876)	3010 ± 50 (λ7065)	...	[5]
PTF 12bho	+17	7520 ± 250 (λ5876)	3520 ± 300 (λ7065)	...	[5]
PTF 12bho	+51	...	...	12.10 ± 0.66 (λ5876)	[5]
PTF 12bho	+129	...	...	> 9.57	[5]
SN 2016hgs	-8	15010 ± 200 (λ5876)	11120 ± 310 (λ7065)	...	[6]
SN 2016hgs	-4	12880 ± 110 (λ5876)	10610 ± 400 (λ7065)	...	[6]
SN 2016hgs	+1	10750 ± 100 (λ5876)	10200 ± 90 (λ7065)	...	[6]
SN 2016hgs	+28	...	...	> 4.80	[6]
SN 2016hgs	+59	...	...	11.52 ± 4.37	[6]
SN 2016hnk	-3	...	10350 ± 60 (λ6355)	...	[7]
SN 2016hnk	-2	...	10020 ± 30 (λ6355)	...	[7]
SN 2016hnk	-1	...	9740 ± 20 (λ6355)	...	[7]
SN 2016hnk	+0	...	9690 ± 40 (λ6355)	...	[7]
SN 2016hnk	+1	...	9610 ± 90 (λ6355)	...	[7]
SN 2016hnk	+1	...	9720 ± 90 (λ6355)	...	[7]
SN 2016hnk	+1	...	9850 ± 130 (λ6355)	...	[7]

SN 2016hnk	+3	...	9060 ± 70 (λ6355)	...	[7]
SN 2016hnk	+4	...	8760 ± 50 (λ6355)	...	[7]
SN 2016hnk	+6	...	8590 ± 40 (λ6355)	...	[7]
SN 2016hnk	+6	...	8200 ± 160 (λ6355)	...	[7]
SN 2016hnk	+8	...	8440 ± 760 (λ6355)	...	[7]
SN 2016hnk	+10	...	7970 ± 110 (λ6355)	...	[7]
SN 2016hnk	+16	...	6820 ± 70 (λ6355)	...	[7]
SN 2016hnk	+26	...	6250 ± 140 (λ6355)	...	[7]
SN 2016hnk	+31	...	5880 ± 80 (λ6355)	...	[7]
SN 2016hnk	+32	...	5760 ± 210 (λ6355)	...	[7]
SN 2016hnk	+35	...	5610 ± 90 (λ6355)	...	[7]
SN 2016hnk	+47	...	5080 ± 110 (λ6355)	...	[7]
SN 2016hnk	+265	...	...	> 4.07	[8]

6.8 Appendix: Transients in the control sample

Here we discuss the photometric and spectroscopic properties of the transients that passed the selection criteria for follow-up, but did not exhibit high [Ca II]/[O I] ratio in their nebular phase spectra. We summarize the photometric and spectroscopic properties of these transients in Table 6.1. The control sample consists of 4 SNe Ib, 5 SNe Ic, 1 SN Ic-BL, 2 SNe Ib/c, and 3 SNe Ia. Figure 6.29 shows forced photometry light curves of these transients, while Figure 6.30 shows a collage of the spectroscopic data for each object. The complete log of the spectroscopic follow-up for these objects is presented in Table 6.6, which will be released on WISeREP together with the photometry upon publication. We plot the original reduced spectra for the spectroscopy epochs near peak light for each object. For the nebular phase spectra, we show the original reduced spectra for events that did not have a large host contamination. For other nebular spectra, we attempted to fit a polynomial to the underlying host continuum to subtract the host features and show the subtracted spectrum to highlight the broad nebular emission features of [O I] and [Ca II]. In cases where the host background was not smooth and had features sharper than ≈ 1000 Å (usually in the case of S0 / E type galaxies) such that the nebular emission features were not easily measurable, we attempted more careful host subtraction using `superfit` (Howell et al., 2005). In these cases, the spectra figures show the unsubtracted spectra, and the `superfit`-subtracted spectra are shown in Figure 6.28.

In addition to the objects discussed here, we note the case of the peculiar SN 2019ehk in the galaxy M100. SN 2019ehk was reported to the TNS by Grzegorzek, 2019 and an early spectrum was reported by Dimitriadis et al., 2019, which exhibited a reddened featureless continuum with 'flash'-ionized lines (see e.g. Gal-Yam et al.,

2014) of He II λ4686 and Hα. We obtained follow-up spectra of the event near peak light with DBSP, which showed a reddened continuum with strong photospheric He absorption features and weaker H features, similar to Type IIb SNe. Specifically, the peak light spectra show signatures of Hβ and Hγ absorption together with flat-bottomed feature near Hα blended with the nearby He I λ6678 line. The flat-bottomed Hα feature is characteristic of several well-studied Type IIb SNe like SN 2001ig (Silverman et al., 2009) and SN 2011dh (Marion et al., 2014). Curiously, this object shows strong [Ca II] lines in our early nebular phase spectrum from SEDM and LRIS, similar to several Ca-rich transients in this sample. However, the clear presence of H in the early flash spectra and at peak light exclude it from our sample. Additionally, the deep Na I D absorption detected in its spectrum suggests significant host reddening by $A_V \gtrsim 3$ mag, making it intrinsically luminous ($M_p \lesssim -17$). This object may be similar to the Type IIb iPTF 15eqv which exhibited high [Ca II]/[O I] in late-time spectra (Milisavljevic et al., 2017), and we defer the discussion of this object to future work.

Spectroscopic classification

We summarize the detection, environments, and properties of each transient in the control sample, and in particular, highlight how we exclude them from the group of Ca-rich gap transients. In the next section, we use this discussion to compare the properties of these transients to those in the Ca-rich sample.

SN 2019ccm was found on top of the spiral arm of a Sa-type galaxy at $z = 0.015$ and peaked at an absolute magnitude of $M_r \approx -16.4$ mag (without correcting for its host extinction). A spectrum taken at peak light shows characteristic features of a SN Ib at peak on the red side (the blue side spectrum was not recorded due to a readout issue on the LRIS detector), as well as a deep Na I D feature at the host redshift, suggesting that the low luminosity is partly due to host extinction. A LRIS spectrum taken ≈ 180 d after peak shows [O I]and [Ca II] emission of nearly equal strengths, ruling out a Ca-rich classification. We note that the [Ca II]/[O I] ratio (≈ 1.18) is likely overestimated because the significant host extinction would only increase the observed ratio.

SN 2019txl was found on the arm of a spiral galaxy at $z = 0.034$ and peaked at an absolute magnitude of $M_r \approx -16.2$ mag. The peak light spectrum shows typical features of a SN Ib at peak, together with clear Na I D absorption at the host redshift, confirming it as a reddened normal Type Ib SN. A nebular phase spectrum

taken ≈ +330 d from peak shows clear signatures of [O I]and [Ca II]emission with a [Ca II]/[O I]of ≈ 0.9 (without correcting for host extinction), thus excluding it from the Ca-rich sample.

SN 2019txt was found on the disk of a nearly edge-on disk galaxy at $z = 0.026$ and peaked at an absolute magnitude of $M_r \approx -15.9$ mag. The peak light spectrum is relatively noisy, but still clearly shows features of a Type Ib SN at peak, as well as prominent Na I D absorption at the host redshift, consistent with a reddened Type Ib SN. The nebular phase spectrum at ≈ 220 d from peak light shows clear [O I] and [Ca II] emission with [Ca II]/[O I] of ≈ 1.3 without host extinction correction, thus excluding it from the Ca-rich sample.

SN 2019mjo stands out as a peculiar SN Ib found in the outskirts of an elliptical galaxy at $z \approx 0.041$. Its peak light spectrum is reddened with strong He lines and it exhibits a very slow transition in spectroscopic properties. The source did not turn nebular even in our latest spectrum at ≈ +180 d from peak light, and hence does not satisfy our criterion for a fast nebular phase transition. We defer conclusions about the nature of this event to a forthcoming publication that will present the full dataset on this source (K. De et al., in prep.).

SN 2018dbg was found close to the nucleus of a grand spiral host galaxy at $z \approx 0.015$, peaking at an absolute magnitude of $M_r \approx -16.6$ mag. We were unable to secure a peak light spectrum of SN 2018dbg, but secured a spectrum at ≈ 35 d after peak, where the spectrum is still dominated by strong photospheric phase lines of O, Ca II and possibly He I. Using `superfit` (Howell et al., 2005) to subtract the underlying continuum, we find an excellent match to the spectrum of the Type Ib SN 1990U at ≈ +41 d after peak, consistent with the photometric phase (≈ +30 d). We thus classify it as a SN Ib/c. Since all Ca-rich gap transients start exhibiting strong nebular [Ca II] emission features at this phase, this object does not satisfy our early nebular phase transition criterion and is excluded from the sample.

SN 2019txr was found close to the nucleus of an irregular spiral galaxy at $z = 0.044$, and peaked at an absolute magnitude of $M_r \approx -16.7$ mag. The peak light spectrum is relatively noisy and we can only identify P-Cygni features of Ca II, O I and possibly He I; however, we classify it as a SN Ib/c due to the uncertain identification of He I. We cannot identify any Na I D absorption due to the noisy nature of the spectrum. We obtained a nebular phase spectrum at ≈ 270 d from peak, which we find to be dominated by host light. We visually identify a weak nebular emission peak around the [O I]transition, but the [Ca II] emission is not detected. We show

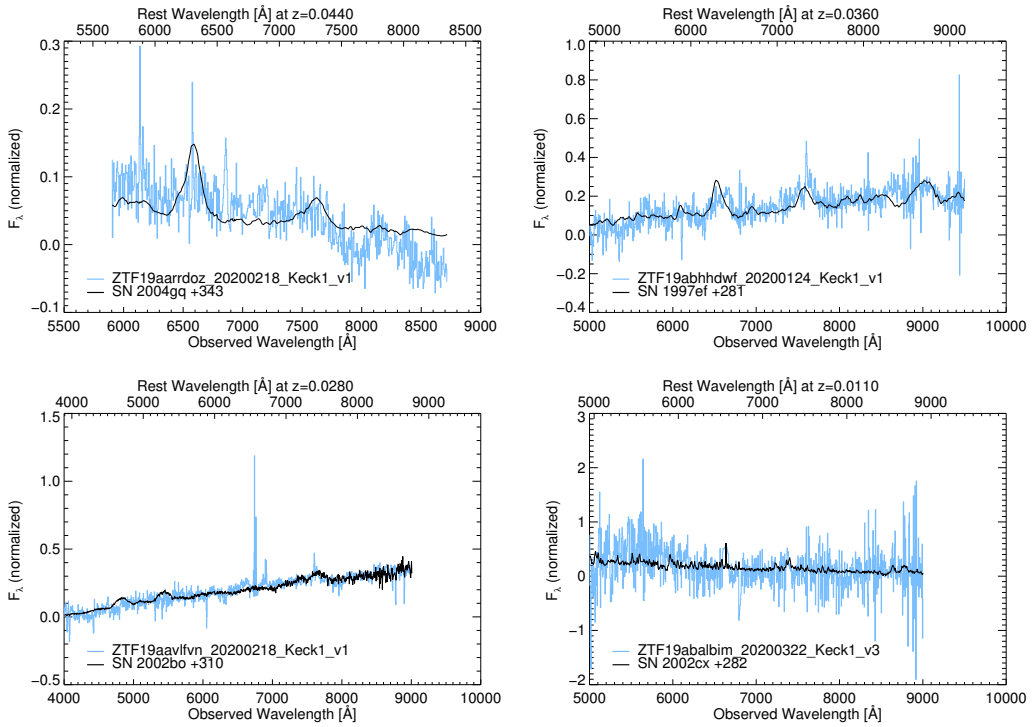

Figure 6.28: **Host-subtracted late-time spectra of events in the sample that were heavily contaminated by host galaxy light and thus required host-subtraction using `superfit`**. (Top Left) Late-time spectrum of SN 2019txr with host features subtracted using `superfit`. The observed host-subtracted spectrum is shown in blue, while the black line shows the best match spectrum of the Type Ib SN 2004gq at 297 d after peak. (Top right) Late-time spectrum of SN 2019ouq plotted with the late-time spectrum of Type Ic SN 1997ef at $\approx$ 270 d after peak light. (Bottom left) Host subtracted late-time spectrum of SN 2019gau at $\approx$ 270 d, compared against a late-time spectrum of the Type Ia SN 2002bo. However, we do not find a convincing match as several features in the subtracted spectrum are not well matched, and present the fit here for completeness. (Bottom right) Host-subtracted late-time spectrum of SN 2019ttf at $\approx$ 210 d compared to the late-time spectrum of SN 2002cx at $\approx$ 280 d.

a host-subtracted spectrum of the object matched with `superfit` with the Type Ib SN 2004gq $\approx$ 300 d after peak. Although the features are very weak, the host-subtracted spectrum shows the existence of a broad emission feature around [O I] and possible [Ca II]Ġiven the host dominated spectrum, we are unable to measure a [Ca II]/[O I], but use the detection of [O I] and the weak detection of the nearby [Ca II] line to constrain the [Ca II]/[O I] ratio to < 1, excluding it from the Ca-rich sample.

SN 2018fob was found on the spiral arm of a disk galaxy at $z = 0.029$, and peaked at an absolute magnitude of $M_r \approx -16.9$ mag. The peak light spectra do not show

any He signatures, and are consistent with a SN Ic. Na I D absorption is clearly detected at the host redshift, suggesting host extinction. The nebular phase spectrum at $\approx$ 210 d shows a strong [O I] line and a weak [Ca II] line with [Ca II]/[O I]$\approx$ 0.87, thus excluding it from our sample.

SN 2019yz is the lowest redshift object in this sample, and is consistent with a reddened SN Ic in the disk of UGC 09977 based on the prominent Na I D absorption in its peak light spectrum. The peak spectrum was obtained from TNS and was originally obtained by Burke et al., 2019. The light curve peaks at an observed absolute magnitude of $M_r \approx -16.63$ mag. The nebular phase spectrum at $\approx +210$ d shows strong [O I] emission with [Ca II]/[O I]$\approx$ 0.6, excluding it from our sample of Ca-rich events.

SN 2019abb was found on top of an irregular blue galaxy at $z = 0.015$, and peaked at an absolute magnitude of $M_r \approx -16.6$ mag. The peak light spectrum shows characteristic features of a SN Ic with no obvious He signatures, as well as clear Na I D absorption at the host redshift suggesting significant host extinction. A spectrum taken $\approx$ 60 d after peak still shows photospheric phase features suggesting slow spectral evolution. The nebular phase spectrum obtained at $\approx +350$ d is dominated by the underlying host, but clearly shows both the nebular [O I] and [Ca II] emission lines with [Ca II]/[O I]$\approx$ 0.8, thus excluding the object from our sample.

SN 2019ape was detected on top of a yellow early type galaxy at $z = 0.020$, and peaked at an absolute magnitude of $M_r \approx -16.6$ mag. Although the galaxy morphology is early-type, the SDSS as well as the SN spectra show clear Hα emission. The peak light spectrum is characteristic of a SN Ic with no He signatures. Na I D absorption is also detected in the peak light spectrum, confirming host reddening. The nebular phase spectrum taken at $\approx +280$ d shows clear [O I] and [Ca II] emission lines with [Ca II]/[O I]$\approx$ 0.9, thus excluding it from our sample. A complete analysis of this object will be presented in a forthcoming publication (I. Irani et al., in prep.).

SN 2019ouq was found in the disk of a nearly edge-on disk galaxy at $z = 0.036$, and peaked at an absolute magnitude of $M_r \approx -16.9$ mag. The peak light spectrum exhibits a highly reddened continuum but with clear broad P-Cygni features of O I and Ca II. Using `superfit` to subtract the host emission, we find that the peak spectrum is well matched to the Type Ic SN 1994I about 7 d after peak. The same fit suggests that an extinction of $A_V \approx 1$ mag is required to match the continuum. The nebular spectrum obtained at $\approx$ 170 d from maximum light is completely dominated

by the underlying host galaxy continuum, making it difficult to identify the nebular [O I] and [Ca II] features directly. We thus used `superfit` to subtract the host features and show a host-subtracted spectrum in Figure 6.28. As shown, the nebular phase spectrum is consistent with a late-time spectrum of the Type Ic SN 1997ef at $\approx$ 281 d. The host-subtracted late-time spectrum also shows similarities to the late-time spectra of the Type Ic SNe SN 2006aj and SN 1994I. In particular, the host subtracted spectrum exhibits a stronger [O I] line compared to the [Ca II] line, constraining [Ca II]/[O I]$\lesssim 1$, thus excluding it from the Ca-rich sample.

SN 2018kqr was detected inside a blue irregular galaxy at $z = 0.045$, and peaked at an absolute magnitude of $M_r \approx -16.8$ mag. The peak light spectrum shows broad features consistent with a SN Ic-BL around peak light. Na I D absorption is not clearly detected at the host redshift. We obtained a follow-up spectrum $\approx$ 16 d after peak light where the source still exhibited strong photospheric features consistent with a SN Ic. However, we were unable to obtain a follow-up nebular spectrum for this object. Nevertheless, the slow photospheric phase evolution of this evolution is consistent with a normal SN Ic, and excludes it from the Ca-rich sample discussed in this work.

SN 2019gau was detected close to the core of a disk galaxy at $z = 0.028$, and peaked at an absolute magnitude of $M_r \approx -16.8$ mag. A low resolution SEDM spectrum taken near peak shows a strong Si II line and the Ca II NIR triplet in P-Cygni absorption, leading to the SN Ia classification of this event. We obtained a late-time spectrum of the source at $\approx$ 260 d from peak, and find it to be dominated by the host galaxy light. We attempted host subtraction using `superfit`, but were unable to find a good match to the host subtracted features. For completness, we present the best-fit host subtracted spectrum in Figure 6.28 compared to the best match in `superfit` to the late time spectrum of SN 2002bo. Unlike the Ca-Ia objects that show strong [Ca II] emission and no [O I] emission, this host-subtracted spectrum does not show any strong [Ca II] emission, leading us to exclude it from the Ca-rich sample.

SN 2019gsc was detected inside an irregular blue galaxy at $z = 0.011$, and peaked at a faint absolute magnitude of $M_r = -13.90$ mag. Its peak light spectrum exhibits low velocity Si II lines similar to 02cx-like SNe Ia (Li et al., 2003), while its faint peak luminosity makes it similar to the lowest luminosity member SN 2008ha (Foley et al., 2009). Our spectrum taken at $\approx$ +30 d from peak shows that the spectrum is still photospheric and dominated by several low velocity P-Cygni features. Additional

data on SN 2019gsc has been published in Srivastav et al., 2020 and Tomasella et al., 2020, which show that the source does not turn nebular even up to ≈ 60 d from peak light, consistent with our data and with what is typically observed in this class (Foley et al., 2016). The absence of an early nebular phase transition excludes it from the Ca-rich sample.

SN 2019ttf was found on top of an irregular star forming galaxy at $z = 0.011$, and peaked at a faint absolute magnitude of $M_r = -14.0$ mag. The spectrum taken at $\approx +10$ d from peak shows low velocity lines similar to the 02cx-like SNe Ia SN 2008ha (Foley et al., 2009) and SN 2005hk (Phillips et al., 2007). Its low peak luminosity is similar to SN 2019gsc. We obtained a late-time spectrum of the object at ≈ 230 d, which was dominated by the underlying host galaxy light. We show a host-subtracted spectrum using `superfit` in Figure 6.28. The subtracted spectrum is relatively noisy, but we note two detected features of Na I and [Ca II] (near 5800Å and 7300Å, respectively) that are similar to SN 2002cx at a similar phase. As in the case of 02cx-like objects that do not become completely nebular at late times, we find a weak Na I P-Cygni profile, and thus exclude this object from the Ca-rich sample.

Candidate selection and false positives

In Section 6.2, we presented our selection criterion for identifying candidate Ca-rich gap transients in order to prioritize nebular phase follow-up. We now evaluate the merits and disadvantages of our selection scheme in the context of understanding the broader population of Ca-rich transients. We start with a comparison of our selection criteria to that of Kasliwal et al., 2012. Unlike that work, we did not select candidates based on their photometric evolution or spectroscopic velocities. This choice makes us sensitive to events with broader light curves such as SN 2019pxu, which appears to be a more luminous and slower evolving member of this class.

However, we do select events based on their peak luminosity, with a cutoff at $M = -17$ mag. We thus caution that certain spectroscopic sub-types may be underrepresented in this sample, e.g. the Ca-Ia events appear to exhibit systematically higher peak luminosity than the Ca-Ib/c events. Indeed, the only Ca-Ia object in the sample SN 2019ofm is also the faintest SN Ia in the CLU sample (barring the low velocity 08ha-like events), suggesting that Ca-Ia events discussed here could represent the tip of the Ca-rich sample in the broader 91bg-like SN Ia population. Resolving this issue would require a similar experiment targeting brighter SNe Ia,

which will inevitably include other known populations of faint SNe Ia.

As in Kasliwal et al., 2012, we do not select events based on their spectroscopic type at peak light. However, the low spectroscopic velocities in SN 2018kjy would not have passed the criteria in Kasliwal et al., 2012 since they required 'normal' photospheric phase velocities. Our follow-up campaign revealed that despite its peculiar low spectroscopic velocities at peak, the later evolution of SN 2018kjy establishes its membership in the class of Ca-rich gap transients. In the context of low velocity events, it is important to highlight the contamination of 02cx-like SNe Ia. Two of the events in the control sample were spectroscopically similar to 02cx-like objects near peak light (similar to SN 2008ha; Foley et al., 2009) with low spectroscopic velocities at peak (like SN 2018kjy). Yet unlike SN 2018kjy (and the rest of the Ca-rich class), their spectra do not turn nebular at late phases and exhibit a pseudo continuum of emission lines.

Next, we discuss the host environments of these events, re-iterating that our selection criteria was agnostic to the host type and environment. In comparison to the SNe Ib/c in the control sample (which were primarily found in star-forming late-type galaxies), a striking characteristic of the sample of the Ca-Ib/c objects is their preference for early type galaxies and old environments. SN 2019pxu is the only exception, but is still at a large projected offset of ≈ 18 kpc from its host, suggesting that spectroscopically classified SNe Ib/c in old environments could be used to select likely Ca-rich gap transients near peak light. Yet, SN 2019ape serves as an important exception to this trend as a SN Ic in an early type galaxy, suggesting that this criterion also has its own false positives despite producing a relatively high success rate (six out of seven SNe Ib/c in early type galaxies in this sample turned out to be Ca-rich events). However, nearly all the low luminosity SNe Ia in the sample (including two 02cx-like events) are in late-type galaxies – as such, the environment of the only Ca-Ia event in the sample SN 2019ofm is not exceptional.

In terms of the photometric and spectroscopic properties of the transients, the sample presented in this work was selected using the smallest possible selection criteria to identify these faint transients in the local universe. The final confirmation of a Ca-rich gap transient, however, is derived from nebular phase spectroscopy at late times. As such, it is instructive to examine if the confirmed sample of Ca-rich gap transients can be differentiated based on the peak light spectra and photometric evolution in order to guide future searches for these events. In Figure 6.15, we show the luminosity-width phase space of the control sample of transients compared to

the Ca-rich gap transients analyzed in the work. We make this comparison in order to examine if Ca-rich gap transients can be identified from their peak luminosity and light curve evolution near peak. As shown, a striking trend is that the control sample of objects exhibit systematically slower evolving light curves (smaller Δm_7 and larger $t_{f,1/2}$) than nearly the entire sample of Ca-rich gap transients, suggesting typically larger diffusion time and correspondingly larger ejecta masses in the control sample. Yet, the Ca-rich and control objects occupy a common phase space near $\Delta m_7 \approx 0.3$ and M_p between -16 and -17, noting that the fastest evolving objects in this sample are always Ca-rich. Thus, we conclude that while the fastest evolving Ca-rich gap transients $\Delta m_7 > 0.4$ can be identified with peak light photometry and spectroscopy, it is difficult to select a complete sample based on only these properties.

The broader light curves and low [Ca II]/[O I] of the Type Ib/c events in the control sample suggest that these events are likely consistent with being normal core-collapse SNe (Gal-Yam, 2017) that are extinguished by foreground dust. Indeed, the detection of prominent Na I D absorption from the host galaxy in nearly all of these events suggest that host extinction likely plays an important role in making these events appear sub-luminous at a peak similar to the Ca-rich events. The 02cx-like events (Li et al., 2003) are consistent with being very low luminosity members of the SN Iax class similar to the lowest luminosity member SN 2008ha (Foley et al., 2009). However, we did not have a high resolution spectrum of the only other Type Ia SN 2019gau at peak to ascertain the role of host extinction. At the same time, we were unable to securely identify nebular emission features in the late time spectrum of this object, leaving this as an inconclusive low luminosity SN Ia in the sample.

We examine the spectroscopic properties of the control sample to identify potential spectroscopic clues at peak light for identifying Ca-rich gap transients. Ca-Ib exhibit strikingly similar spectra to normal SNe Ib in the sample; however, the line blanketed spectra of the red Ca-Ib objects are uncommon in the control sample. The only objects in the control sample that also exhibit suppressed blue continua are SN 2019txl and SN 2019mjo. The former object also exhibits a strong Na I D absorption, suggesting that host extinction likely suppresses the blue continuum in this otherwise normal core-collapse SN. SN 2019mjo is a pecular SN Ib whose nature remains unclear, and we do not discuss its properties further here. Nevertheless, peculiar low velocity objects such as SN 2018kjr and PTF 12bho are not seen in the control sample, suggesting that the combination of low velocity and highly reddened continuum may be indicative of a Ca-rich object if its peak luminosity

can be constrained. The Ca-Ia objects with strongly line blanketed spectra are unique in the broader population of SNe Ia that exhibit blue continua at peak (see discussion in De et al., 2019a), and thus strong line blanketing with prominent Si II lines could be used to identify likely Ca-Ia candidates at peak. Given that all the above selection procedures are unable to yield a complete sample of Ca-rich gap transients, we conclude in general that nebular phase spectroscopy of systematically selected samples of low luminosity transients in the local universe with 8 – 10 m class telescopes will continue to be important for our census of these elusive transients.

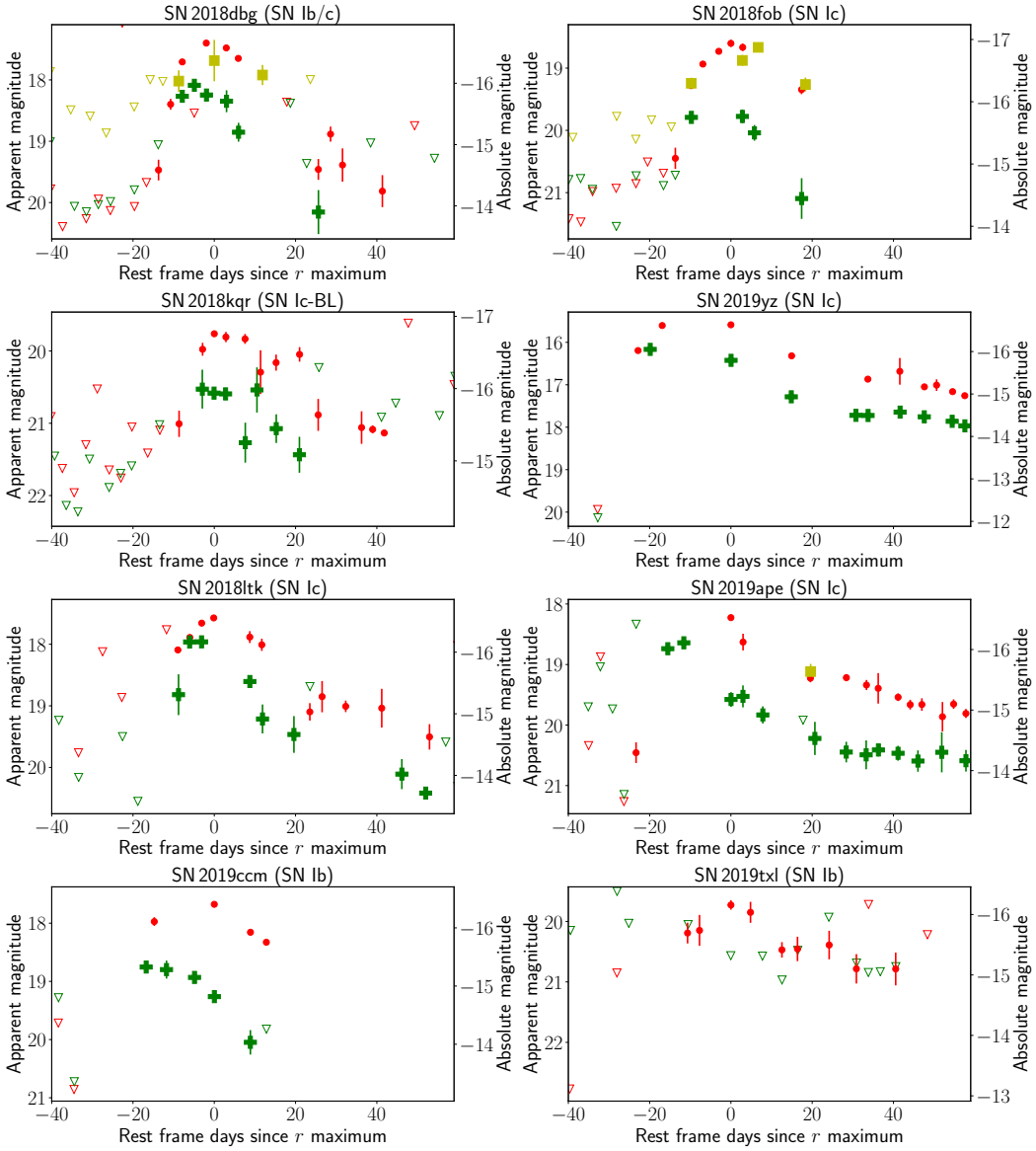

Figure 6.29: **Forced photometry light curves of each object in the control sample that did not pass the [Ca II]/[O I] threshold defined in the sample.** Each panel shows the photometric evolution near the peak for the transient indicated in the figure title. We include photometry in *gri* filters from ZTF and phase is defined with respect to time from *r*-band peak. Red circles denote *r*-band photometry, green plus symbols indicate *g*-band photometry, and yellow squares indicate *i*-band photometry. Hollow inverted triangles denote 5σ upper limits at the location of the transient.

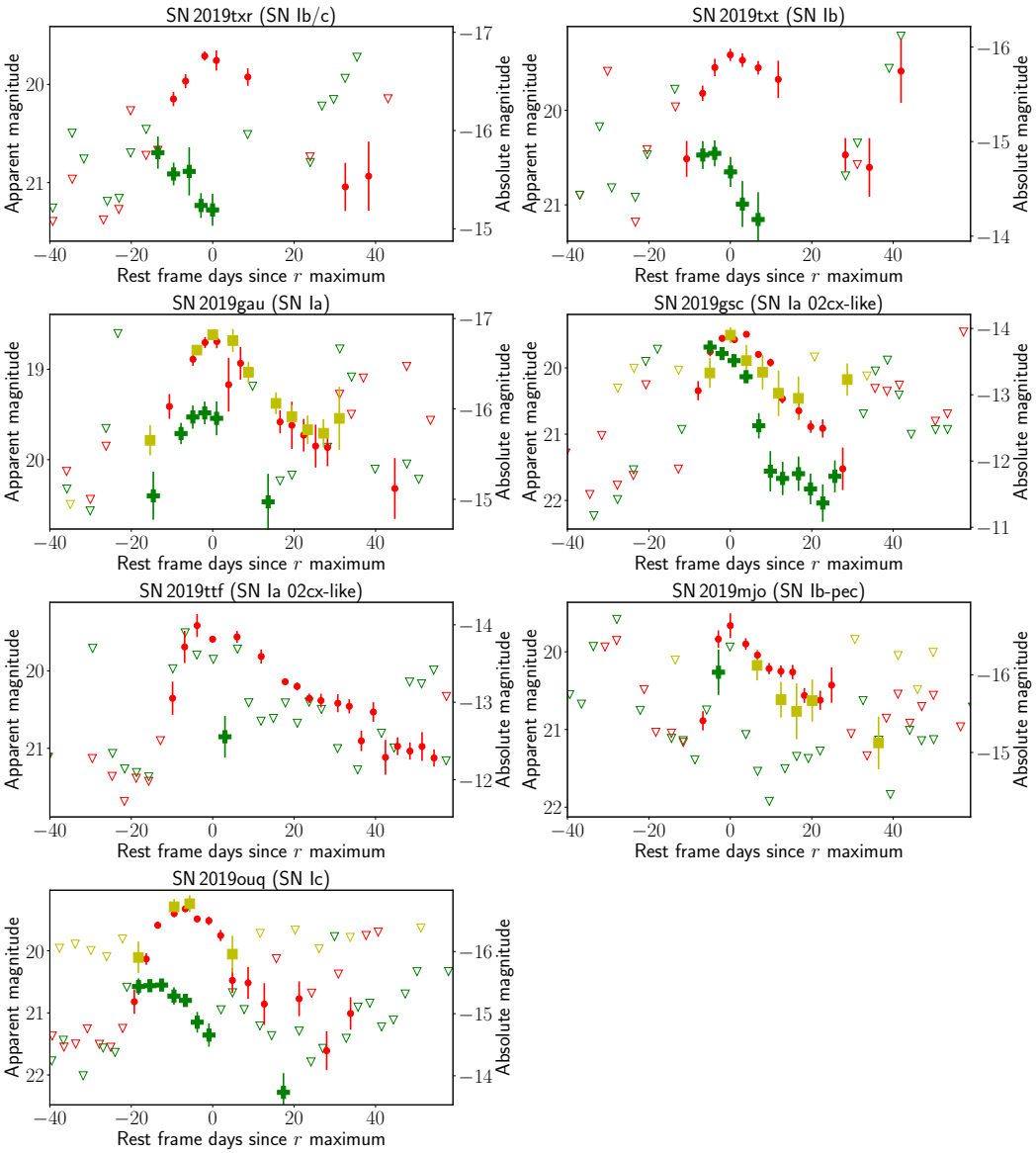

Figure 6.29: Continued.

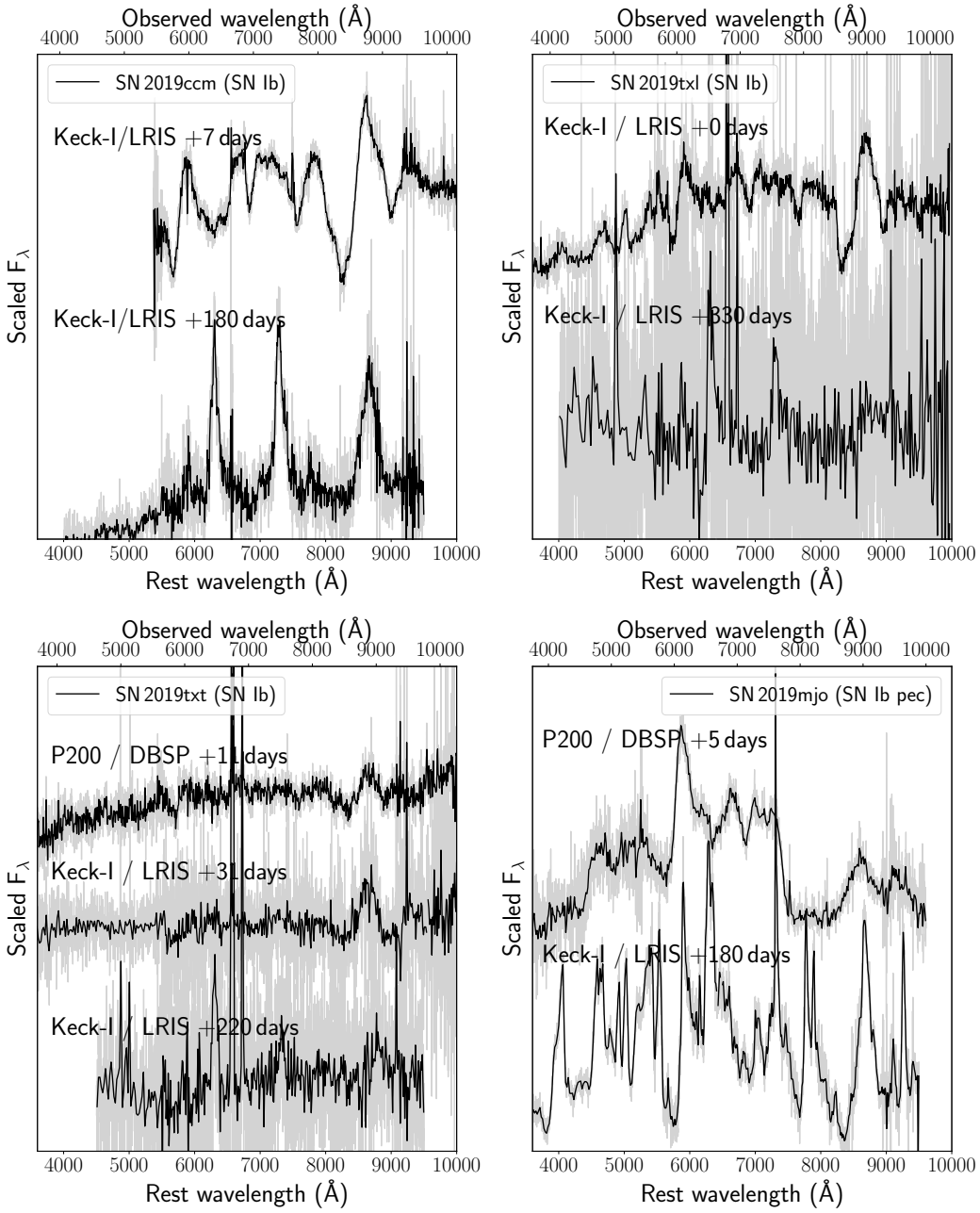

Figure 6.30: **Photospheric and nebular phase spectrum of objects in the control sample that did not pass either the early nebular phase transition criterion or the nebular phase [Ca II]/[O I] threshold defined in the sample.** See Appendix 6.8 for discussion. Each panel shows one object with its name and classification indicated in the legend. Gray lines show unbinned spectra while the black lines show spectra binned to improve the signal-to-noise ratio. The instrument used and phase of each spectrum is shown next to each spectrum.

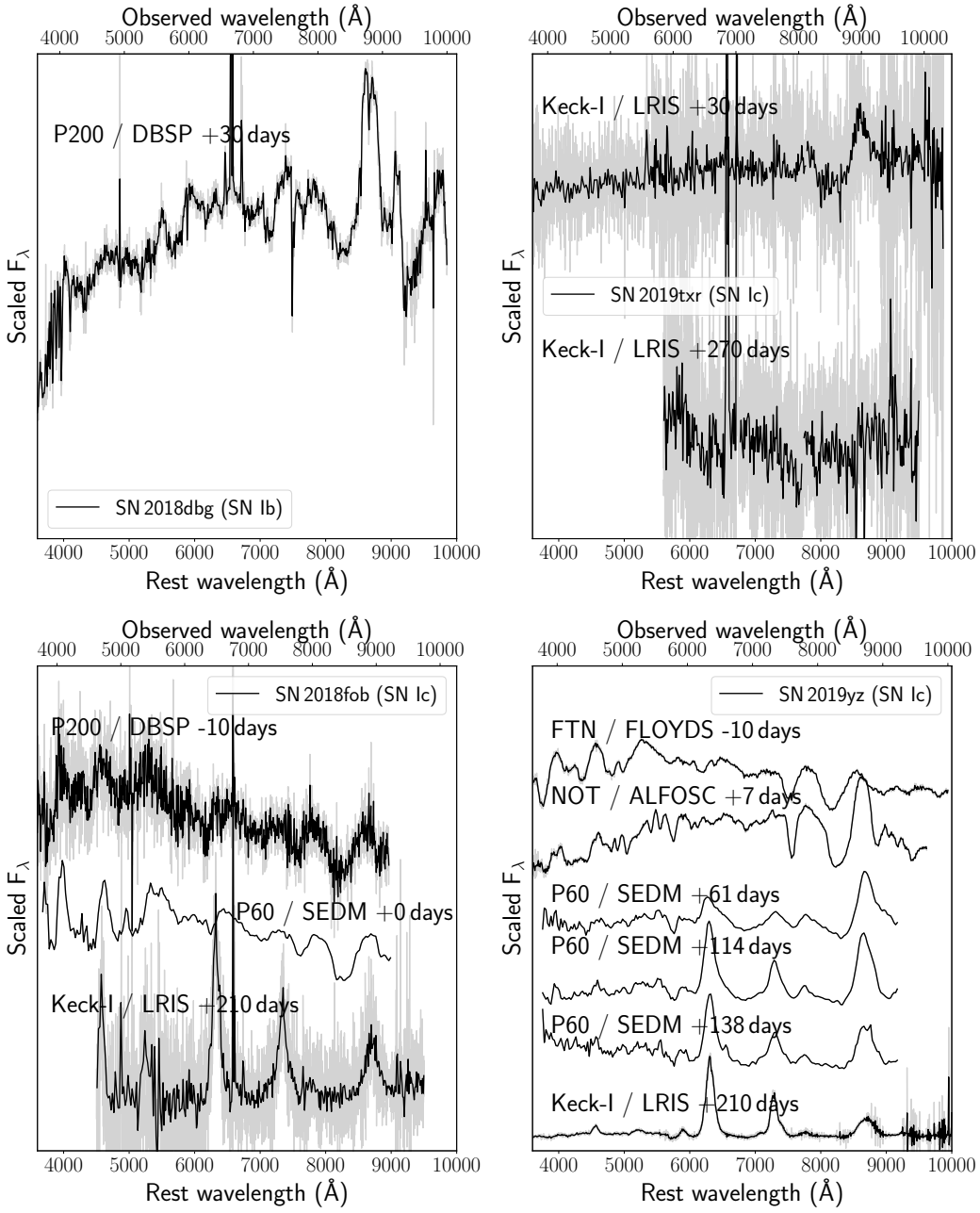

Figure 6.30: Continued.

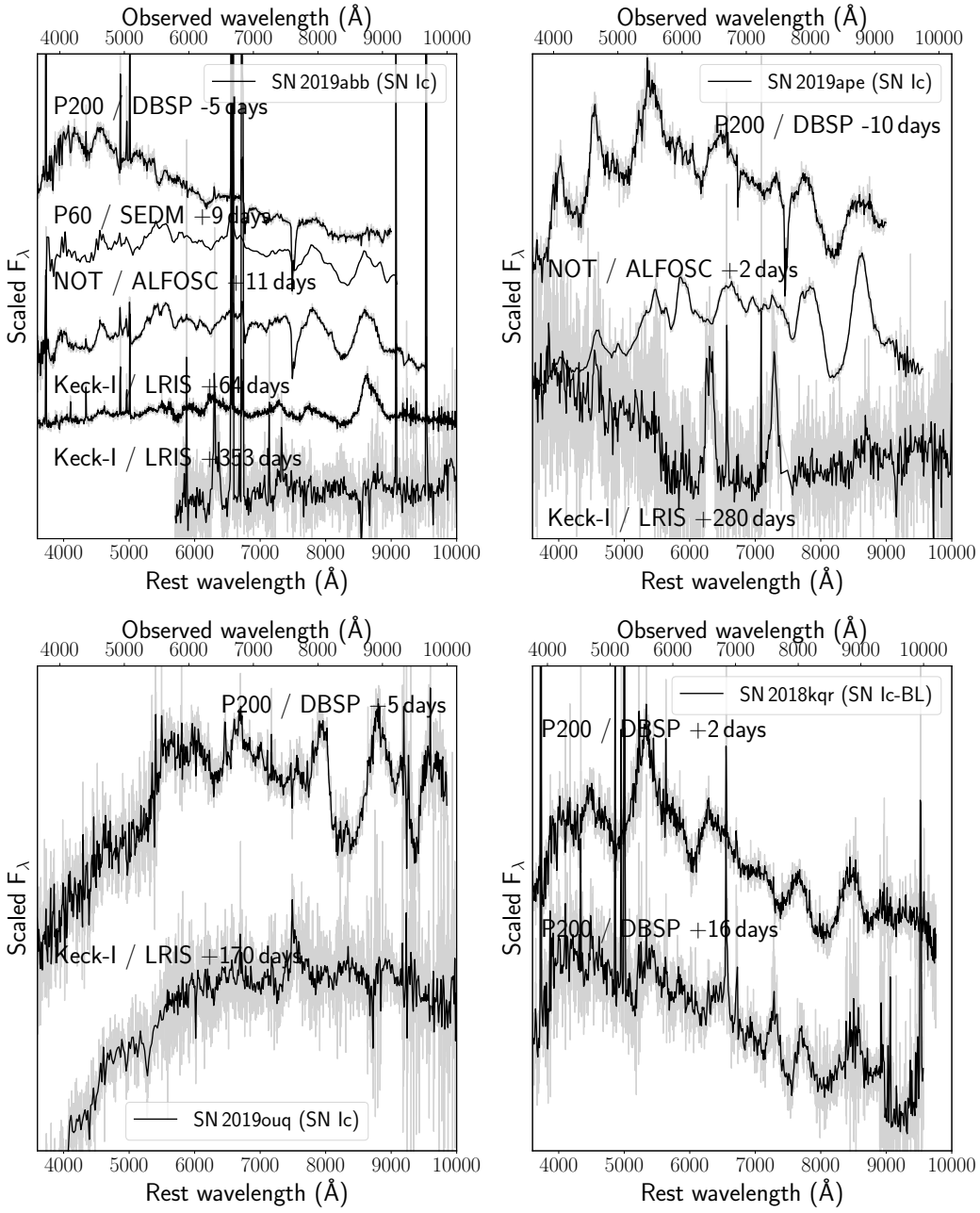

Figure 6.30: Continued.

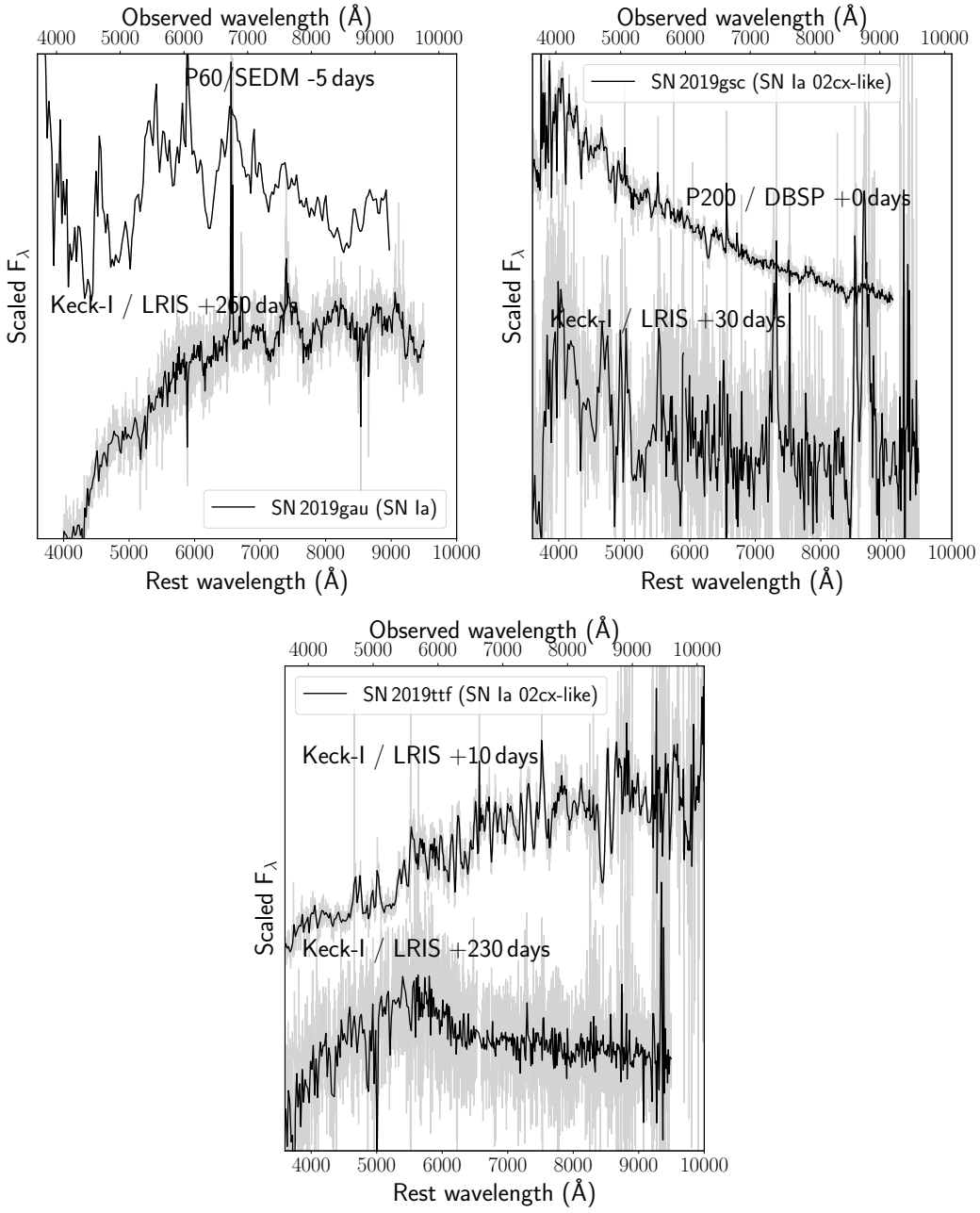

Figure 6.30: Continued.

Table 6.5: **Photometry of all the sources presented in this paper.** The photometry has not been corrected for Galactic extinction. Phases are indicated with respect to the time from the best-fit r-band peak. Upper limits are at 5σ confidence at the location of the transient. This table will be available in its entirety in machine-readable form upon publication.

Object	MJD	Rest frame phase (days from r peak)	Filter	Magnitude	Instrument
SN 2018ckd	58242.31	−34.53	r	> 20.53	P48+ZTF
SN 2018ckd	58245.34	−31.57	r	> 18.89	P48+ZTF
SN 2018ckd	58248.27	−28.71	r	> 20.95	P48+ZTF
SN 2018ckd	58255.26	−21.88	r	> 20.70	P48+ZTF
SN 2018ckd	58258.25	−18.96	r	> 20.64	P48+ZTF
SN 2018ckd	58262.30	−15.01	r	> 19.87	P48+ZTF
SN 2018ckd	58267.31	−10.12	r	> 19.65	P48+ZTF
SN 2018ckd	58270.32	−7.18	r	20.28 ± 0.24	P48+ZTF
SN 2018ckd	58276.19	−1.45	r	19.21 ± 0.03	P48+ZTF
SN 2018ckd	58279.17	1.46	r	19.23 ± 0.04	P48+ZTF
SN 2018ckd	58282.19	4.41	r	19.42 ± 0.04	P48+ZTF
SN 2018ckd	58285.17	7.32	r	> 18.28	P48+ZTF
SN 2018ckd	58288.24	10.32	r	19.99 ± 0.08	P48+ZTF
SN 2018ckd	58289.23	11.29	r	20.36 ± 0.07	P60+SEDM
SN 2018ckd	58291.24	13.25	r	20.32 ± 0.35	P48+ZTF
SN 2018ckd	58292.25	14.24	r	20.54 ± 0.09	P60+SEDM
SN 2018ckd	58295.24	17.16	r	> 21.00	P60+SEDM
SN 2018ckd	58297.27	19.14	r	20.52 ± 0.25	P48+ZTF
SN 2018ckd	58300.18	21.98	r	20.59 ± 0.18	P48+ZTF
SN 2018ckd	58302.25	24.00	r	21.08 ± 0.07	P60+SEDM
SN 2018ckd	58303.18	24.91	r	20.76 ± 0.18	P48+ZTF
SN 2018ckd	58307.17	28.81	r	20.88 ± 0.23	P48+ZTF
SN 2018ckd	58311.17	32.71	r	> 20.04	P48+ZTF
SN 2018ckd	58314.17	35.64	r	> 20.16	P48+ZTF
SN 2018ckd	58323.16	44.42	r	> 19.77	P48+ZTF
SN 2018ckd	58336.20	57.16	r	> 20.76	P48+ZTF
SN 2018ckd	58364.14	84.44	r	> 19.79	P48+ZTF
SN 2018ckd	58242.23	−34.61	g	> 20.44	P48+ZTF
SN 2018ckd	58245.27	−31.64	g	> 15.83	P48+ZTF
SN 2018ckd	58248.21	−28.77	g	> 20.75	P48+ZTF
SN 2018ckd	58255.21	−21.93	g	> 20.57	P48+ZTF
SN 2018ckd	58258.27	−18.95	g	> 20.85	P48+ZTF
SN 2018ckd	58262.26	−15.05	g	> 19.77	P48+ZTF
SN 2018ckd	58267.21	−10.21	g	> 19.27	P48+ZTF
SN 2018ckd	58270.24	−7.26	g	> 19.80	P48+ZTF
SN 2018ckd	58273.24	−4.33	g	20.02 ± 0.09	P48+ZTF
SN 2018ckd	58276.23	−1.41	g	20.00 ± 0.08	P48+ZTF
SN 2018ckd	58279.21	1.50	g	20.23 ± 0.11	P48+ZTF
SN 2018ckd	58282.23	4.45	g	20.37 ± 0.15	P48+ZTF
SN 2018ckd	58288.19	10.27	g	> 20.64	P48+ZTF
SN 2018ckd	58289.24	11.30	g	21.70 ± 0.21	P60+SEDM
SN 2018ckd	58292.19	14.18	g	> 19.80	P48+ZTF

SN 2018ckd	58292.25	14.24	*g*	> 21.70	P60+SEDM
SN 2018ckd	58295.17	17.09	*g*	> 19.10	P48+ZTF
SN 2018ckd	58295.24	17.16	*g*	> 20.90	P60+SEDM
SN 2018ckd	58298.17	20.02	*g*	> 20.73	P48+ZTF
SN 2018ckd	58301.26	23.04	*g*	> 20.72	P48+ZTF
SN 2018ckd	58302.25	24.00	*g*	22.36 ± 0.17	P60+SEDM
SN 2018ckd	58304.19	25.90	*g*	> 20.54	P48+ZTF
SN 2018ckd	58307.23	28.87	*g*	> 20.10	P48+ZTF
SN 2018ckd	58311.23	32.77	*g*	> 20.46	P48+ZTF
SN 2018ckd	58314.23	35.70	*g*	> 19.97	P48+ZTF
SN 2018ckd	58324.26	45.50	*g*	> 18.09	P48+ZTF
SN 2018ckd	58332.17	53.22	*g*	> 20.56	P48+ZTF
SN 2018ckd	58336.17	57.13	*g*	> 20.50	P48+ZTF
SN 2018ckd	58348.15	68.83	*g*	> 18.86	P48+ZTF
SN 2018ckd	58243.34	−33.53	*i*	> 20.03	P48+ZTF
SN 2018ckd	58247.15	−29.80	*i*	> 19.88	P48+ZTF
SN 2018ckd	58254.16	−22.96	*i*	> 19.95	P48+ZTF
SN 2018ckd	58261.17	−16.11	*i*	> 20.19	P48+ZTF
SN 2018ckd	58267.23	−10.20	*i*	> 19.40	P48+ZTF
SN 2018ckd	58272.34	−5.21	*i*	20.00 ± 0.20	P48+ZTF
SN 2018ckd	58280.39	2.66	*i*	19.16 ± 0.08	P48+ZTF
SN 2018ckd	58286.17	8.30	*i*	19.51 ± 0.15	P48+ZTF
SN 2018ckd	58289.24	11.30	*i*	19.61 ± 0.04	P60+SEDM
SN 2018ckd	58292.17	14.16	*i*	> 19.16	P48+ZTF
SN 2018ckd	58292.25	14.24	*i*	19.82 ± 0.06	P60+SEDM
SN 2018ckd	58295.24	17.16	*i*	20.05 ± 0.11	P60+SEDM
SN 2018ckd	58299.30	21.12	*i*	> 19.35	P48+ZTF
SN 2018ckd	58302.25	24.00	*i*	20.33 ± 0.05	P60+SEDM
SN 2018ckd	58576.6	298	*r*	> 26.00	Keck+LRIS
SN 2018ckd	58576.6	298	*g*	> 26.50	Keck+LRIS
SN 2018lqo	58311.19	−39.43	*r*	> 22.09	P48+ZTF
SN 2018lqo	58314.18	−36.53	*r*	> 22.08	P48+ZTF
SN 2018lqo	58319.22	−31.66	*r*	> 21.95	P48+ZTF
SN 2018lqo	58322.23	−28.74	*r*	> 21.66	P48+ZTF
SN 2018lqo	58325.22	−25.85	*r*	> 21.34	P48+ZTF
SN 2018lqo	58328.30	−22.87	*r*	> 21.24	P48+ZTF
SN 2018lqo	58331.18	−20.08	*r*	> 21.98	P48+ZTF
SN 2018lqo	58334.17	−17.18	*r*	> 21.05	P48+ZTF
SN 2018lqo	58337.19	−14.26	*r*	> 21.16	P48+ZTF
SN 2018lqo	58340.18	−11.36	*r*	20.01 ± 0.12	P48+ZTF
SN 2018lqo	58343.16	−8.48	*r*	20.68 ± 0.16	P48+ZTF
SN 2018lqo	58346.18	−5.56	*r*	20.06 ± 0.10	P48+ZTF
SN 2018lqo	58347.26	−4.51	*r*	20.04 ± 0.06	P60+SEDM
SN 2018lqo	58350.15	−1.71	*r*	19.62 ± 0.03	P48+ZTF
SN 2018lqo	58353.15	1.19	*r*	19.65 ± 0.03	P48+ZTF
SN 2018lqo	58356.21	4.15	*r*	19.84 ± 0.05	P48+ZTF
SN 2018lqo	58359.22	7.07	*r*	20.17 ± 0.05	P48+ZTF
SN 2018lqo	58361.14	8.93	*r*	20.34 ± 0.07	P60+SEDM
SN 2018lqo	58362.14	9.89	*r*	20.25 ± 0.12	P48+ZTF
SN 2018lqo	58365.14	12.80	*r*	20.51 ± 0.08	P48+ZTF
SN 2018lqo	58368.14	15.70	*r*	20.68 ± 0.06	P48+ZTF
SN 2018lqo	58371.14	18.61	*r*	20.79 ± 0.08	P48+ZTF

SN 2018lqo	58374.13	21.50	*r*	20.81 ± 0.11	P48+ZTF
SN 2018lqo	58377.13	24.40	*r*	21.28 ± 0.13	P48+ZTF
SN 2018lqo	58381.11	28.26	*r*	21.39 ± 0.16	P48+ZTF
SN 2018lqo	58385.18	32.20	*r*	> 20.05	P48+ZTF
SN 2018lqo	58311.24	−39.38	*g*	> 22.01	P48+ZTF
SN 2018lqo	58314.24	−36.48	*g*	> 21.82	P48+ZTF
SN 2018lqo	58317.35	−33.47	*g*	> 21.15	P48+ZTF
SN 2018lqo	58320.18	−30.73	*g*	> 21.44	P48+ZTF
SN 2018lqo	58323.29	−27.72	*g*	> 21.09	P48+ZTF
SN 2018lqo	58326.18	−24.92	*g*	> 21.01	P48+ZTF
SN 2018lqo	58329.18	−22.01	*g*	> 21.67	P48+ZTF
SN 2018lqo	58332.18	−19.11	*g*	> 21.69	P48+ZTF
SN 2018lqo	58337.18	−14.27	*g*	> 21.19	P48+ZTF
SN 2018lqo	58343.18	−8.46	*g*	20.88 ± 0.20	P48+ZTF
SN 2018lqo	58346.16	−5.58	*g*	20.47 ± 0.17	P48+ZTF
SN 2018lqo	58347.26	−4.51	*g*	20.43 ± 0.09	P60+SEDM
SN 2018lqo	58350.24	−1.63	*g*	20.08 ± 0.05	P48+ZTF
SN 2018lqo	58360.14	7.96	*g*	21.30 ± 0.11	P48+ZTF
SN 2018lqo	58361.14	8.93	*g*	21.38 ± 0.12	P60+SEDM
SN 2018lqo	58365.22	12.88	*g*	21.98 ± 0.28	P48+ZTF
SN 2018lqo	58368.20	15.76	*g*	21.92 ± 0.21	P48+ZTF
SN 2018lqo	58371.20	18.66	*g*	22.09 ± 0.25	P48+ZTF
SN 2018lqo	58374.19	21.56	*g*	> 21.62	P48+ZTF
SN 2018lqo	58377.19	24.46	*g*	> 21.76	P48+ZTF
SN 2018lqo	58381.17	28.32	*g*	> 21.40	P48+ZTF
SN 2018lqo	58385.12	32.14	*g*	> 20.28	P48+ZTF
SN 2018lqo	58388.12	35.04	*g*	> 20.96	P48+ZTF
SN 2018lqo	58312.19	−38.46	*i*	> 20.32	P48+ZTF
SN 2018lqo	58320.25	−30.66	*i*	> 20.01	P48+ZTF
SN 2018lqo	58325.31	−25.76	*i*	> 19.89	P48+ZTF
SN 2018lqo	58331.32	−19.94	*i*	> 19.95	P48+ZTF
SN 2018lqo	58336.16	−15.26	*i*	> 20.21	P48+ZTF
SN 2018lqo	58340.16	−11.38	*i*	> 20.05	P48+ZTF
SN 2018lqo	58344.32	−7.36	*i*	20.55 ± 0.30	P48+ZTF
SN 2018lqo	58347.26	−4.51	*i*	19.92 ± 0.10	P60+SEDM
SN 2018lqo	58348.18	−3.62	*i*	19.86 ± 0.15	P48+ZTF
SN 2018lqo	58361.15	8.94	*i*	19.93 ± 0.03	P60+SEDM
SN 2018lqo	58362.28	10.03	*i*	20.22 ± 0.26	P48+ZTF
SN 2018lqo	58366.28	13.90	*i*	20.35 ± 0.33	P48+ZTF
SN 2018lqo	58379.14	26.35	*i*	> 20.44	P48+ZTF
SN 2018lqo	58760.6	408	*r*	> 24.32	P200+WASP
SN 2018lqo	58760.6	408	*i*	> 24.15	P200+WASP
SN 2018lqo	58897.6	545	*g*	> 25.4	Keck+LRIS
SN 2018lqo	58897.6	545	*i*	> 25.1	Keck+LRIS
SN 2018lqu	58332.27	−37.23	*r*	> 20.27	P48+ZTF
SN 2018lqu	58339.15	−30.59	*r*	> 20.36	P48+ZTF
SN 2018lqu	58343.15	−26.72	*r*	> 20.49	P48+ZTF
SN 2018lqu	58346.17	−23.81	*r*	> 20.68	P48+ZTF
SN 2018lqu	58358.19	−12.20	*r*	> 19.96	P48+ZTF
SN 2018lqu	58361.14	−9.36	*r*	20.95 ± 0.30	P48+ZTF
SN 2018lqu	58364.13	−6.47	*r*	20.35 ± 0.26	P48+ZTF
SN 2018lqu	58368.13	−2.61	*r*	19.87 ± 0.13	P48+ZTF

SN 2018lqu	58377.13	6.08	*r*	20.33 ± 0.05	P60+SEDM
SN 2018lqu	58464.55	90.48	*r*	> 20.93	P48+ZTF
SN 2018lqu	58467.55	93.38	*r*	> 21.44	P48+ZTF
SN 2018lqu	58471.56	97.25	*r*	> 21.28	P48+ZTF
SN 2018lqu	58332.17	−37.32	*g*	> 20.95	P48+ZTF
SN 2018lqu	58336.23	−33.40	*g*	> 20.77	P48+ZTF
SN 2018lqu	58343.17	−26.70	*g*	> 21.03	P48+ZTF
SN 2018lqu	58346.15	−23.83	*g*	> 20.10	P48+ZTF
SN 2018lqu	58364.19	−6.41	*g*	20.80 ± 0.21	P48+ZTF
SN 2018lqu	58368.19	−2.55	*g*	20.46 ± 0.21	P48+ZTF
SN 2018lqu	58377.13	6.08	*g*	21.15 ± 0.11	P60+SEDM
SN 2018lqu	58332.16	−37.33	*i*	> 19.81	P48+ZTF
SN 2018lqu	58336.16	−33.47	*i*	> 19.73	P48+ZTF
SN 2018lqu	58345.16	−24.78	*i*	> 20.17	P48+ZTF
SN 2018lqu	58363.13	−7.43	*i*	> 19.74	P48+ZTF
SN 2018lqu	58367.14	−3.56	*i*	20.29 ± 0.23	P48+ZTF
SN 2018lqu	58377.13	6.08	*i*	19.72 ± 0.04	P60+SEDM
SN 2018lqu	58379.12	8.00	*i*	20.26 ± 0.24	P48+ZTF
SN 2018lqu	58760.6	390	*r*	> 23.8	P200+WASP
SN 2018lqu	58760.6	390	*i*	> 23.5	P200+WASP
SN 2018lqu	58897.6	527	*g*	> 25.5	Keck+LRIS
SN 2018lqu	58897.6	527	*i*	> 25.2	Keck+LRIS
SN 2018gwo	58422.52	17.88	*r*	18.22 ± 0.01	P48+ZTF
SN 2018gwo	58425.48	20.82	*r*	18.33 ± 0.01	P48+ZTF
SN 2018gwo	58428.47	23.79	*r*	18.31 ± 0.04	P60+SEDM
SN 2018gwo	58429.51	24.82	*r*	18.48 ± 0.02	P48+ZTF
SN 2018gwo	58432.51	27.80	*r*	18.59 ± 0.02	P48+ZTF
SN 2018gwo	58435.51	30.78	*r*	18.84 ± 0.08	P48+ZTF
SN 2018gwo	58440.53	35.76	*r*	18.82 ± 0.04	P48+ZTF
SN 2018gwo	58443.43	38.64	*r*	18.90 ± 0.07	P48+ZTF
SN 2018gwo	58447.45	42.63	*r*	19.17 ± 0.07	P48+ZTF
SN 2018gwo	58471.41	66.41	*r*	19.94 ± 0.06	P60+SEDM
SN 2018gwo	58472.45	67.44	*r*	20.26 ± 0.25	P48+ZTF
SN 2018gwo	58476.50	71.46	*r*	20.38 ± 0.22	P48+ZTF
SN 2018gwo	58486.49	81.37	*r*	20.46 ± 0.14	P48+ZTF
SN 2018gwo	58502.54	97.30	*r*	20.55 ± 0.31	P48+ZTF
SN 2018gwo	58422.49	17.85	*g*	19.23 ± 0.04	P48+ZTF
SN 2018gwo	58425.51	20.85	*g*	19.31 ± 0.02	P48+ZTF
SN 2018gwo	58429.47	24.78	*g*	19.31 ± 0.02	P48+ZTF
SN 2018gwo	58432.47	27.76	*g*	19.41 ± 0.03	P48+ZTF
SN 2018gwo	58443.49	38.70	*g*	19.46 ± 0.10	P48+ZTF
SN 2018gwo	58450.47	45.62	*g*	19.89 ± 0.14	P48+ZTF
SN 2018gwo	58461.49	56.56	*g*	20.08 ± 0.20	P48+ZTF
SN 2018gwo	58464.49	59.54	*g*	20.17 ± 0.09	P48+ZTF
SN 2018gwo	58467.47	62.50	*g*	> 18.59	P48+ZTF
SN 2018gwo	58471.41	66.41	*g*	20.40 ± 0.09	P60+SEDM
SN 2018gwo	58472.53	67.52	*g*	20.64 ± 0.14	P48+ZTF
SN 2018gwo	58476.55	71.51	*g*	> 20.10	P48+ZTF
SN 2018gwo	58480.51	75.44	*g*	20.49 ± 0.21	P48+ZTF
SN 2018gwo	58486.55	81.43	*g*	21.09 ± 0.30	P48+ZTF
SN 2018gwo	58491.46	86.30	*g*	> 20.36	P48+ZTF
SN 2018gwo	58494.49	89.31	*g*	21.08 ± 0.19	P48+ZTF

SN 2018gwo	58502.45	97.21	*g*	> 19.82	P48+ZTF
SN 2018gwo	58471.41	66.41	*i*	18.63 ± 0.03	P60+SEDM
SN 2018gwo	58486.32	81.20	*i*	18.93 ± 0.09	P60+SEDM
SN 2018gwo	58539.4	134	*g*	> 21.16	P200+WASP
SN 2018gwo	58539.4	134	*r*	21.71 ± 0.11	P200+WASP
SN 2018gwo	58539.4	134	*i*	20.20 ± 0.10	P200+WASP
SN 2018gwo	58897.6	492	*g*	25.0 ± 0.20	Keck+LRIS
SN 2018gwo	58897.6	492	*g*	24.5 ± 0.20	Keck+LRIS
SN 2018kjy	58422.39	−37.86	*r*	> 20.86	P48+ZTF
SN 2018kjy	58425.44	−34.86	*r*	> 21.24	P48+ZTF
SN 2018kjy	58428.28	−32.07	*r*	> 21.30	P48+ZTF
SN 2018kjy	58431.36	−29.05	*r*	> 21.26	P48+ZTF
SN 2018kjy	58434.35	−26.11	*r*	> 20.88	P48+ZTF
SN 2018kjy	58437.34	−23.17	*r*	> 21.23	P48+ZTF
SN 2018kjy	58441.36	−19.22	*r*	> 21.38	P48+ZTF
SN 2018kjy	58447.31	−13.38	*r*	20.74 ± 0.13	P48+ZTF
SN 2018kjy	58450.38	−10.36	*r*	20.70 ± 0.22	P48+ZTF
SN 2018kjy	58455.36	−5.47	*r*	19.52 ± 0.04	P48+ZTF
SN 2018kjy	58462.33	1.38	*r*	19.24 ± 0.07	P48+ZTF
SN 2018kjy	58465.47	4.46	*r*	19.32 ± 0.06	P48+ZTF
SN 2018kjy	58468.19	7.13	*r*	19.67 ± 0.05	P60+SEDM
SN 2018kjy	58468.49	7.43	*r*	19.50 ± 0.06	P48+ZTF
SN 2018kjy	58471.25	10.14	*r*	19.75 ± 0.26	P48+ZTF
SN 2018kjy	58474.32	13.15	*r*	19.81 ± 0.16	P48+ZTF
SN 2018kjy	58479.12	17.87	*r*	> 18.85	P60+SEDM
SN 2018kjy	58480.43	19.16	*r*	20.49 ± 0.21	P48+ZTF
SN 2018kjy	58486.18	24.80	*r*	> 20.34	P60+SEDM
SN 2018kjy	58486.47	25.09	*r*	20.46 ± 0.17	P48+ZTF
SN 2018kjy	58490.20	28.75	*r*	20.52 ± 0.13	P48+ZTF
SN 2018kjy	58493.28	31.78	*r*	20.41 ± 0.21	P48+ZTF
SN 2018kjy	58503.28	41.60	*r*	> 20.26	P48+ZTF
SN 2018kjy	58507.24	45.49	*r*	21.37 ± 0.28	P48+ZTF
SN 2018kjy	58510.28	48.48	*r*	> 19.80	P48+ZTF
SN 2018kjy	58513.41	51.55	*r*	> 20.91	P48+ZTF
SN 2018kjy	58522.22	60.21	*r*	21.60 ± 0.28	P48+ZTF
SN 2018kjy	58526.19	64.11	*r*	> 20.60	P48+ZTF
SN 2018kjy	58534.34	72.11	*r*	> 20.10	P48+ZTF
SN 2018kjy	58539.21	76.90	*r*	> 21.47	P48+ZTF
SN 2018kjy	58543.24	80.85	*r*	> 16.28	P48+ZTF
SN 2018kjy	58556.17	93.56	*r*	> 20.92	P48+ZTF
SN 2018kjy	58559.19	96.52	*r*	> 20.64	P48+ZTF
SN 2018kjy	58562.16	99.44	*r*	> 19.52	P48+ZTF
SN 2018kjy	58422.45	−37.80	*g*	> 21.14	P48+ZTF
SN 2018kjy	58425.36	−34.94	*g*	> 21.46	P48+ZTF
SN 2018kjy	58428.30	−32.05	*g*	> 21.94	P48+ZTF
SN 2018kjy	58431.45	−28.96	*g*	> 21.24	P48+ZTF
SN 2018kjy	58434.42	−26.04	*g*	> 20.88	P48+ZTF
SN 2018kjy	58437.45	−23.06	*g*	> 21.55	P48+ZTF
SN 2018kjy	58440.43	−20.14	*g*	> 21.03	P48+ZTF
SN 2018kjy	58443.23	−17.39	*g*	> 20.49	P48+ZTF
SN 2018kjy	58450.45	−10.29	*g*	> 20.92	P48+ZTF
SN 2018kjy	58457.28	−3.59	*g*	20.35 ± 0.19	P48+ZTF

SN 2018kjy	58462.46	1.50	*g*	20.67 ± 0.25	P48+ZTF
SN 2018kjy	58465.22	4.21	*g*	21.03 ± 0.33	P48+ZTF
SN 2018kjy	58468.19	7.13	*g*	20.82 ± 0.08	P60+SEDM
SN 2018kjy	58468.43	7.37	*g*	20.85 ± 0.14	P48+ZTF
SN 2018kjy	58472.24	11.11	*g*	> 20.12	P48+ZTF
SN 2018kjy	58475.53	14.34	*g*	> 19.60	P48+ZTF
SN 2018kjy	58479.12	17.87	*g*	> 19.94	P60+SEDM
SN 2018kjy	58480.49	19.21	*g*	> 20.12	P48+ZTF
SN 2018kjy	58486.18	24.80	*g*	> 20.41	P60+SEDM
SN 2018kjy	58486.18	24.80	*g*	> 20.41	P60+SEDM
SN 2018kjy	58487.45	26.05	*g*	21.65 ± 0.28	P48+ZTF
SN 2018kjy	58490.27	28.82	*g*	> 21.43	P48+ZTF
SN 2018kjy	58493.21	31.71	*g*	21.67 ± 0.30	P48+ZTF
SN 2018kjy	58505.24	43.53	*g*	> 20.83	P48+ZTF
SN 2018kjy	58509.22	47.44	*g*	> 21.28	P48+ZTF
SN 2018kjy	58512.39	50.55	*g*	> 18.93	P48+ZTF
SN 2018kjy	58522.17	60.16	*g*	> 20.67	P48+ZTF
SN 2018kjy	58526.43	64.34	*g*	> 20.64	P48+ZTF
SN 2018kjy	58534.24	72.01	*g*	> 20.13	P48+ZTF
SN 2018kjy	58538.26	75.96	*g*	> 21.37	P48+ZTF
SN 2018kjy	58547.28	84.82	*g*	> 21.15	P48+ZTF
SN 2018kjy	58558.14	95.49	*g*	> 20.70	P48+ZTF
SN 2018kjy	58561.21	98.51	*g*	> 20.22	P48+ZTF
SN 2018kjy	58479.13	17.88	*i*	> 19.57	P60+SEDM
SN 2018kjy	58486.18	24.80	*i*	> 20.16	P60+SEDM
SN 2018kjy	58486.18	24.80	*i*	> 20.16	P60+SEDM
SN 2018kjy	58539.4	78	*r*	> 22.64	P200+WASP
SN 2019hty	58628.33	−29.23	*r*	> 21.22	P48+ZTF
SN 2019hty	58633.17	−24.50	*r*	> 21.70	P48+ZTF
SN 2019hty	58636.22	−21.52	*r*	> 21.91	P48+ZTF
SN 2019hty	58639.18	−18.62	*r*	> 21.84	P48+ZTF
SN 2019hty	58642.23	−15.64	*r*	> 21.43	P48+ZTF
SN 2019hty	58648.19	−9.82	*r*	19.61 ± 0.13	P48+ZTF
SN 2019hty	58651.25	−6.82	*r*	> 18.87	P48+ZTF
SN 2019hty	58660.22	1.95	*r*	18.76 ± 0.03	P48+ZTF
SN 2019hty	58666.23	7.82	*r*	19.22 ± 0.18	P60+SEDM
SN 2019hty	58671.20	12.68	*r*	20.07 ± 0.25	P48+ZTF
SN 2019hty	58674.22	15.63	*r*	19.60 ± 0.16	P48+ZTF
SN 2019hty	58677.19	18.54	*r*	20.20 ± 0.13	P48+ZTF
SN 2019hty	58680.24	21.52	*r*	20.33 ± 0.18	P48+ZTF
SN 2019hty	58682.17	23.41	*r*	> 18.99	P60+SEDM
SN 2019hty	58682.19	23.43	*r*	20.04 ± 0.10	P60+SEDM
SN 2019hty	58689.19	30.27	*r*	> 18.45	P48+ZTF
SN 2019hty	58690.22	31.28	*r*	20.71 ± 0.17	P60+SEDM
SN 2019hty	58697.19	38.09	*r*	20.77 ± 0.36	P60+SEDM
SN 2019hty	58622.17	−35.26	*g*	> 20.19	P48+ZTF
SN 2019hty	58633.26	−24.41	*g*	> 21.85	P48+ZTF
SN 2019hty	58636.26	−21.48	*g*	> 21.95	P48+ZTF
SN 2019hty	58639.24	−18.57	*g*	> 21.79	P48+ZTF
SN 2019hty	58642.20	−15.67	*g*	> 21.32	P48+ZTF
SN 2019hty	58645.24	−12.70	*g*	19.52 ± 0.12	P48+ZTF
SN 2019hty	58648.18	−9.83	*g*	19.52 ± 0.14	P48+ZTF

SN 2019hty	58651.17	−6.90	*g*	19.41 ± 0.18	P48+ZTF
SN 2019hty	58654.24	−3.90	*g*	19.23 ± 0.12	P48+ZTF
SN 2019hty	58657.20	−1.01	*g*	19.28 ± 0.05	P48+ZTF
SN 2019hty	58665.20	6.81	*g*	20.64 ± 0.15	P48+ZTF
SN 2019hty	58668.19	9.74	*g*	20.79 ± 0.17	P48+ZTF
SN 2019hty	58674.20	15.61	*g*	> 20.38	P48+ZTF
SN 2019hty	58677.18	18.53	*g*	> 20.79	P48+ZTF
SN 2019hty	58680.18	21.46	*g*	> 19.83	P48+ZTF
SN 2019hty	58683.17	24.38	*g*	> 21.21	P48+ZTF
SN 2019hty	58686.17	27.32	*g*	21.63 ± 0.32	P48+ZTF
SN 2019hty	58690.20	31.26	*g*	> 20.55	P48+ZTF
SN 2019hty	58690.22	31.28	*g*	> 21.10	P60+SEDM
SN 2019hty	58693.25	34.24	*g*	> 19.78	P48+ZTF
SN 2019hty	58697.20	38.10	*g*	> 21.30	P60+SEDM
SN 2019hty	58716.15	56.63	*g*	> 19.81	P48+ZTF
SN 2019hty	58720.16	60.55	*g*	> 19.87	P48+ZTF
SN 2019hty	58648.29	−9.72	*i*	19.61 ± 0.20	P48+ZTF
SN 2019hty	58682.20	23.43	*i*	19.80 ± 0.07	P60+SEDM
SN 2019hty	58690.22	31.28	*i*	20.01 ± 0.09	P60+SEDM
SN 2019hty	58697.20	38.10	*i*	20.11 ± 0.08	P60+SEDM
SN 2019hty	58897.6	238	*g*	> 25.0	Keck+LRIS
SN 2019hty	58897.6	238	*i*	> 24.5	Keck+LRIS
SN 2019ofm	58684.19	−38.16	*r*	> 20.78	P48+ZTF
SN 2019ofm	58698.18	−24.58	*r*	> 20.30	P48+ZTF
SN 2019ofm	58701.16	−21.68	*r*	> 19.58	P48+ZTF
SN 2019ofm	58705.18	−17.78	*r*	> 20.13	P48+ZTF
SN 2019ofm	58712.24	−10.93	*r*	20.07 ± 0.26	P48+ZTF
SN 2019ofm	58718.15	−5.19	*r*	18.97 ± 0.07	P48+ZTF
SN 2019ofm	58724.16	0.64	*r*	18.70 ± 0.04	P48+ZTF
SN 2019ofm	58734.13	10.32	*r*	19.33 ± 0.17	P48+ZTF
SN 2019ofm	58737.18	13.28	*r*	19.72 ± 0.26	P48+ZTF
SN 2019ofm	58749.12	24.87	*r*	20.00 ± 0.22	P48+ZTF
SN 2019ofm	58754.12	29.72	*r*	20.38 ± 0.19	P48+ZTF
SN 2019ofm	58758.10	33.58	*r*	20.78 ± 0.20	P48+ZTF
SN 2019ofm	58761.11	36.51	*r*	21.13 ± 0.36	P48+ZTF
SN 2019ofm	58768.09	43.28	*r*	> 20.26	P48+ZTF
SN 2019ofm	58772.09	47.16	*r*	> 20.10	P48+ZTF
SN 2019ofm	58684.20	−38.15	*g*	> 21.04	P48+ZTF
SN 2019ofm	58691.22	−31.33	*g*	> 21.03	P48+ZTF
SN 2019ofm	58694.21	−28.43	*g*	> 21.02	P48+ZTF
SN 2019ofm	58698.20	−24.56	*g*	> 17.58	P48+ZTF
SN 2019ofm	58704.16	−18.77	*g*	> 20.60	P48+ZTF
SN 2019ofm	58708.18	−14.87	*g*	> 20.02	P48+ZTF
SN 2019ofm	58712.15	−11.02	*g*	> 20.40	P48+ZTF
SN 2019ofm	58715.16	−8.10	*g*	20.45 ± 0.17	P48+ZTF
SN 2019ofm	58718.16	−5.18	*g*	20.00 ± 0.11	P48+ZTF
SN 2019ofm	58724.17	0.65	*g*	19.90 ± 0.13	P48+ZTF
SN 2019ofm	58728.13	4.49	*g*	20.34 ± 0.26	P48+ZTF
SN 2019ofm	58734.16	10.35	*g*	> 19.89	P48+ZTF
SN 2019ofm	58749.13	24.88	*g*	> 20.19	P48+ZTF
SN 2019ofm	58761.10	36.50	*g*	> 19.55	P48+ZTF
SN 2019ofm	58706.16	−16.83	*i*	> 20.03	P48+ZTF

SN 2019ofm	58712.22	−10.95	*i*	20.37 ± 0.32	P48+ZTF
SN 2019ofm	58733.13	9.35	*i*	19.55 ± 0.21	P48+ZTF
SN 2019pxu	58730.50	−15.96	*r*	20.09 ± 0.11	P48+ZTF
SN 2019pxu	58740.47	−6.26	*r*	19.63 ± 0.08	P48+ZTF
SN 2019pxu	58748.46	1.51	*r*	19.17 ± 0.04	P48+ZTF
SN 2019pxu	58750.38	3.38	*r*	19.22 ± 0.18	P60+SEDM
SN 2019pxu	58760.37	13.09	*r*	19.85 ± 0.07	P60+SEDM
SN 2019pxu	58761.44	14.13	*r*	20.21 ± 0.07	P48+ZTF
SN 2019pxu	58766.34	18.90	*r*	20.30 ± 0.15	P60+SEDM
SN 2019pxu	58769.43	21.91	*r*	20.93 ± 0.19	P48+ZTF
SN 2019pxu	58776.42	28.71	*r*	21.50 ± 0.21	P48+ZTF
SN 2019pxu	58783.39	35.49	*r*	> 21.42	P48+ZTF
SN 2019pxu	58805.39	56.89	*r*	> 21.05	P48+ZTF
SN 2019pxu	58833.26	84.00	*r*	> 20.94	P48+ZTF
SN 2019pxu	58746.47	−0.43	*g*	20.51 ± 0.22	P48+ZTF
SN 2019pxu	58749.47	2.49	*g*	20.79 ± 0.13	P48+ZTF
SN 2019pxu	58758.45	11.23	*g*	> 22.20	P48+ZTF
SN 2019pxu	58760.37	13.09	*g*	21.49 ± 0.18	P60+SEDM
SN 2019pxu	58766.34	18.90	*g*	> 19.20	P60+SEDM
SN 2019pxu	58767.39	19.92	*g*	> 20.97	P48+ZTF
SN 2019pxu	58779.46	31.66	*g*	> 21.46	P48+ZTF
SN 2019pxu	58760.38	13.10	*i*	19.31 ± 0.03	P60+SEDM
SN 2019pxu	58766.34	18.90	*i*	19.64 ± 0.06	P60+SEDM
SN 2019pxu	58931.3	184	*g*	> 25.1	Keck+LRIS
SN 2019pxu	58931.3	184	*i*	22.83 ± 0.06	Keck+LRIS
SN 2018dbg	58270.30	−37.32	*r*	> 20.49	P48+ZTF
SN 2018dbg	58276.19	−31.51	*r*	> 20.36	P48+ZTF
SN 2018dbg	58279.24	−28.51	*r*	> 20.04	P48+ZTF
SN 2018dbg	58282.22	−25.58	*r*	> 20.23	P48+ZTF
SN 2018dbg	58285.19	−22.64	*r*	> 17.17	P48+ZTF
SN 2018dbg	58288.24	−19.64	*r*	> 20.16	P48+ZTF
SN 2018dbg	58291.24	−16.69	*r*	> 19.77	P48+ZTF
SN 2018dbg	58294.25	−13.72	*r*	19.57 ± 0.17	P48+ZTF
SN 2018dbg	58297.27	−10.74	*r*	18.49 ± 0.09	P48+ZTF
SN 2018dbg	58300.18	−7.88	*r*	17.80 ± 0.03	P48+ZTF
SN 2018dbg	58303.18	−4.92	*r*	> 18.64	P48+ZTF
SN 2018dbg	58306.17	−1.97	*r*	17.50 ± 0.03	P48+ZTF
SN 2018dbg	58311.17	2.96	*r*	17.57 ± 0.03	P48+ZTF
SN 2018dbg	58314.17	5.91	*r*	17.75 ± 0.05	P48+ZTF
SN 2018dbg	58326.28	17.84	*r*	> 18.46	P48+ZTF
SN 2018dbg	58334.16	25.61	*r*	19.56 ± 0.17	P48+ZTF
SN 2018dbg	58337.20	28.61	*r*	18.98 ± 0.12	P48+ZTF
SN 2018dbg	58340.19	31.55	*r*	19.48 ± 0.27	P48+ZTF
SN 2018dbg	58350.15	41.36	*r*	19.91 ± 0.26	P48+ZTF
SN 2018dbg	58358.19	49.29	*r*	> 18.84	P48+ZTF
SN 2018dbg	58273.25	−34.41	*g*	> 20.19	P48+ZTF
SN 2018dbg	58276.24	−31.47	*g*	> 20.28	P48+ZTF
SN 2018dbg	58279.22	−28.53	*g*	> 20.16	P48+ZTF
SN 2018dbg	58282.26	−25.54	*g*	> 20.11	P48+ZTF
SN 2018dbg	58288.22	−19.67	*g*	> 19.92	P48+ZTF
SN 2018dbg	58294.17	−13.79	*g*	> 19.19	P48+ZTF
SN 2018dbg	58300.19	−7.86	*g*	18.40 ± 0.06	P48+ZTF

SN 2018dbg	58303.20	−4.90	*g*	18.22 ± 0.05	P48+ZTF
SN 2018dbg	58306.22	−1.92	*g*	18.38 ± 0.06	P48+ZTF
SN 2018dbg	58311.23	3.02	*g*	18.48 ± 0.18	P48+ZTF
SN 2018dbg	58314.23	5.97	*g*	18.98 ± 0.15	P48+ZTF
SN 2018dbg	58327.16	18.72	*g*	> 18.51	P48+ZTF
SN 2018dbg	58331.24	22.73	*g*	> 19.49	P48+ZTF
SN 2018dbg	58334.18	25.63	*g*	20.28 ± 0.36	P48+ZTF
SN 2018dbg	58347.20	38.46	*g*	> 19.16	P48+ZTF
SN 2018dbg	58363.16	54.18	*g*	> 19.41	P48+ZTF
SN 2018dbg	58272.34	−35.31	*i*	> 18.56	P48+ZTF
SN 2018dbg	58277.17	−30.55	*i*	> 18.67	P48+ZTF
SN 2018dbg	58281.19	−26.59	*i*	> 18.94	P48+ZTF
SN 2018dbg	58288.17	−19.71	*i*	> 18.51	P48+ZTF
SN 2018dbg	58292.17	−15.76	*i*	> 18.07	P48+ZTF
SN 2018dbg	58295.33	−12.66	*i*	> 18.10	P48+ZTF
SN 2018dbg	58299.30	−8.75	*i*	18.09 ± 0.18	P48+ZTF
SN 2018dbg	58308.17	0.00	*i*	17.76 ± 0.34	P48+ZTF
SN 2018dbg	58320.21	11.87	*i*	17.99 ± 0.16	P48+ZTF
SN 2018dbg	58332.16	23.64	*i*	> 18.07	P48+ZTF
SN 2018fob	58322.25	−36.92	*r*	> 21.48	P48+ZTF
SN 2018fob	58325.22	−34.04	*r*	> 20.99	P48+ZTF
SN 2018fob	58331.19	−28.24	*r*	> 20.94	P48+ZTF
SN 2018fob	58336.21	−23.36	*r*	> 20.86	P48+ZTF
SN 2018fob	58339.16	−20.49	*r*	> 20.52	P48+ZTF
SN 2018fob	58343.15	−16.61	*r*	> 20.70	P48+ZTF
SN 2018fob	58346.18	−13.67	*r*	20.46 ± 0.17	P48+ZTF
SN 2018fob	58350.14	−9.82	*r*	19.29 ± 0.02	P48+ZTF
SN 2018fob	58353.14	−6.90	*r*	18.94 ± 0.02	P48+ZTF
SN 2018fob	58357.18	−2.98	*r*	18.74 ± 0.03	P48+ZTF
SN 2018fob	58360.24	0.00	*r*	18.61 ± 0.06	P48+ZTF
SN 2018fob	58363.23	2.90	*r*	18.67 ± 0.06	P48+ZTF
SN 2018fob	58378.13	17.39	*r*	19.35 ± 0.07	P48+ZTF
SN 2018fob	58322.19	−36.98	*g*	> 20.78	P48+ZTF
SN 2018fob	58325.19	−34.07	*g*	> 20.96	P48+ZTF
SN 2018fob	58331.24	−28.18	*g*	> 21.55	P48+ZTF
SN 2018fob	58336.24	−23.33	*g*	> 20.74	P48+ZTF
SN 2018fob	58343.17	−16.59	*g*	> 20.90	P48+ZTF
SN 2018fob	58346.16	−13.69	*g*	> 20.73	P48+ZTF
SN 2018fob	58350.24	−9.72	*g*	19.80 ± 0.06	P48+ZTF
SN 2018fob	58363.16	2.84	*g*	19.79 ± 0.11	P48+ZTF
SN 2018fob	58366.21	5.80	*g*	20.05 ± 0.13	P48+ZTF
SN 2018fob	58378.15	17.41	*g*	21.10 ± 0.33	P48+ZTF
SN 2018fob	58331.32	−28.11	*i*	> 19.78	P48+ZTF
SN 2018fob	58336.16	−23.40	*i*	> 20.15	P48+ZTF
SN 2018fob	58340.16	−19.52	*i*	> 19.84	P48+ZTF
SN 2018fob	58345.15	−14.67	*i*	> 19.95	P48+ZTF
SN 2018fob	58350.22	−9.74	*i*	19.25 ± 0.09	P48+ZTF
SN 2018fob	58363.14	2.81	*i*	18.88 ± 0.09	P48+ZTF
SN 2018fob	58367.14	6.70	*i*	18.67 ± 0.06	P48+ZTF
SN 2018fob	58379.12	18.35	*i*	19.27 ± 0.11	P48+ZTF
SN 2018kqr	58425.47	−37.38	*r*	> 21.64	P48+ZTF
SN 2018kqr	58428.51	−34.47	*r*	> 21.98	P48+ZTF

SN 2018kqr	58431.51	−31.60	*r*	> 21.31	P48+ZTF
SN 2018kqr	58434.45	−28.79	*r*	> 20.54	P48+ZTF
SN 2018kqr	58437.53	−25.84	*r*	> 21.66	P48+ZTF
SN 2018kqr	58440.53	−22.97	*r*	> 21.78	P48+ZTF
SN 2018kqr	58443.37	−20.25	*r*	> 21.07	P48+ZTF
SN 2018kqr	58447.42	−16.37	*r*	> 21.43	P48+ZTF
SN 2018kqr	58450.54	−13.39	*r*	> 21.11	P48+ZTF
SN 2018kqr	58455.48	−8.66	*r*	21.03 ± 0.18	P48+ZTF
SN 2018kqr	58461.53	−2.88	*r*	19.99 ± 0.09	P48+ZTF
SN 2018kqr	58464.53	0.00	*r*	19.78 ± 0.04	P48+ZTF
SN 2018kqr	58467.53	2.86	*r*	19.83 ± 0.07	P48+ZTF
SN 2018kqr	58472.45	7.58	*r*	19.85 ± 0.07	P48+ZTF
SN 2018kqr	58476.43	11.38	*r*	20.31 ± 0.30	P48+ZTF
SN 2018kqr	58480.43	15.21	*r*	20.18 ± 0.11	P48+ZTF
SN 2018kqr	58486.47	20.99	*r*	20.07 ± 0.10	P48+ZTF
SN 2018kqr	58491.26	25.57	*r*	20.90 ± 0.22	P48+ZTF
SN 2018kqr	58502.41	36.25	*r*	21.08 ± 0.23	P48+ZTF
SN 2018kqr	58505.25	38.97	*r*	21.10 ± 0.06	P48+ZTF
SN 2018kqr	58508.24	41.82	*r*	21.15 ± 0.04	P48+ZTF
SN 2018kqr	58514.41	47.73	*r*	> 19.63	P48+ZTF
SN 2018kqr	58426.47	−36.42	*g*	> 22.16	P48+ZTF
SN 2018kqr	58429.47	−33.56	*g*	> 22.25	P48+ZTF
SN 2018kqr	58432.45	−30.70	*g*	> 21.52	P48+ZTF
SN 2018kqr	58437.50	−25.87	*g*	> 21.91	P48+ZTF
SN 2018kqr	58440.45	−23.04	*g*	> 21.72	P48+ZTF
SN 2018kqr	58443.28	−20.33	*g*	> 21.61	P48+ZTF
SN 2018kqr	58450.47	−13.46	*g*	> 21.05	P48+ZTF
SN 2018kqr	58461.46	−2.94	*g*	20.55 ± 0.27	P48+ZTF
SN 2018kqr	58464.47	−0.06	*g*	20.61 ± 0.07	P48+ZTF
SN 2018kqr	58467.44	2.78	*g*	20.62 ± 0.09	P48+ZTF
SN 2018kqr	58472.51	7.63	*g*	21.29 ± 0.28	P48+ZTF
SN 2018kqr	58475.51	10.50	*g*	20.56 ± 0.31	P48+ZTF
SN 2018kqr	58480.47	15.25	*g*	21.10 ± 0.20	P48+ZTF
SN 2018kqr	58486.43	20.95	*g*	21.46 ± 0.25	P48+ZTF
SN 2018kqr	58491.44	25.75	*g*	> 20.25	P48+ZTF
SN 2018kqr	58507.52	41.14	*g*	> 20.94	P48+ZTF
SN 2018kqr	58511.17	44.63	*g*	> 20.75	P48+ZTF
SN 2018kqr	58522.43	55.40	*g*	> 20.92	P48+ZTF
SN 2019yz	58493.51	−32.79	*r*	> 20.40	P48+ZTF
SN 2019yz	58503.52	−22.84	*r*	16.65 ± 0.04	P48+ZTF
SN 2019yz	58509.49	−16.90	*r*	16.06 ± 0.01	P48+ZTF
SN 2019yz	58526.51	0.00	*r*	16.04 ± 0.01	P48+ZTF
SN 2019yz	58541.54	14.94	*r*	16.77 ± 0.01	P48+ZTF
SN 2019yz	58560.42	33.70	*r*	17.32 ± 0.02	P48+ZTF
SN 2019yz	58568.34	41.57	*r*	17.14 ± 0.31	P48+ZTF
SN 2019yz	58574.42	47.61	*r*	17.51 ± 0.02	P48+ZTF
SN 2019yz	58577.44	50.61	*r*	17.46 ± 0.14	P48+ZTF
SN 2019yz	58581.40	54.55	*r*	17.62 ± 0.03	P48+ZTF
SN 2019yz	58584.42	57.54	*r*	17.71 ± 0.02	P48+ZTF
SN 2019yz	58493.55	−32.75	*g*	> 20.75	P48+ZTF
SN 2019yz	58506.52	−19.86	*g*	16.78 ± 0.02	P48+ZTF
SN 2019yz	58526.54	0.04	*g*	17.04 ± 0.02	P48+ZTF

SN 2019yz	58541.46	14.86	*g*	17.90 ± 0.02	P48+ZTF
SN 2019yz	58557.46	30.76	*g*	18.33 ± 0.04	P48+ZTF
SN 2019yz	58560.48	33.76	*g*	18.34 ± 0.04	P48+ZTF
SN 2019yz	58568.40	41.63	*g*	18.26 ± 0.04	P48+ZTF
SN 2019yz	58574.40	47.59	*g*	18.37 ± 0.03	P48+ZTF
SN 2019yz	58581.30	54.45	*g*	18.47 ± 0.03	P48+ZTF
SN 2019yz	58584.45	57.57	*g*	18.58 ± 0.03	P48+ZTF
SN 2018ltk	58480.42	−33.42	*r*	> 19.83	P48+ZTF
SN 2018ltk	58486.45	−27.48	*r*	> 18.19	P48+ZTF
SN 2018ltk	58491.25	−22.75	*r*	> 18.93	P48+ZTF
SN 2018ltk	58502.42	−11.75	*r*	> 17.83	P48+ZTF
SN 2018ltk	58505.26	−8.95	*r*	18.16 ± 0.04	P48+ZTF
SN 2018ltk	58508.24	−6.02	*r*	17.96 ± 0.04	P48+ZTF
SN 2018ltk	58511.21	−3.09	*r*	17.72 ± 0.01	P48+ZTF
SN 2018ltk	58514.21	−0.14	*r*	17.64 ± 0.01	P48+ZTF
SN 2018ltk	58523.23	8.74	*r*	17.95 ± 0.10	P48+ZTF
SN 2018ltk	58526.23	11.70	*r*	18.07 ± 0.10	P48+ZTF
SN 2018ltk	58538.23	23.52	*r*	19.16 ± 0.14	P48+ZTF
SN 2018ltk	58541.29	26.53	*r*	18.92 ± 0.25	P48+ZTF
SN 2018ltk	58547.19	32.34	*r*	19.07 ± 0.09	P48+ZTF
SN 2018ltk	58556.19	41.21	*r*	19.10 ± 0.31	P48+ZTF
SN 2018ltk	58568.13	52.96	*r*	19.57 ± 0.21	P48+ZTF
SN 2018ltk	58475.51	−38.25	*g*	> 19.32	P48+ZTF
SN 2018ltk	58480.48	−33.37	*g*	> 20.25	P48+ZTF
SN 2018ltk	58491.43	−22.58	*g*	> 19.59	P48+ZTF
SN 2018ltk	58495.26	−18.80	*g*	> 20.64	P48+ZTF
SN 2018ltk	58505.42	−8.80	*g*	18.91 ± 0.33	P48+ZTF
SN 2018ltk	58508.19	−6.07	*g*	18.05 ± 0.02	P48+ZTF
SN 2018ltk	58511.17	−3.13	*g*	18.05 ± 0.03	P48+ZTF
SN 2018ltk	58523.24	8.75	*g*	18.69 ± 0.03	P48+ZTF
SN 2018ltk	58526.40	11.87	*g*	19.30 ± 0.23	P48+ZTF
SN 2018ltk	58534.25	19.60	*g*	19.55 ± 0.30	P48+ZTF
SN 2018ltk	58538.25	23.54	*g*	> 18.77	P48+ZTF
SN 2018ltk	58561.21	46.15	*g*	20.20 ± 0.24	P48+ZTF
SN 2018ltk	58567.17	52.02	*g*	20.50 ± 0.07	P48+ZTF
SN 2018ltk	58572.17	56.95	*g*	> 19.68	P48+ZTF
SN 2019ape	58502.52	−35.02	*r*	> 20.45	P48+ZTF
SN 2019ape	58505.51	−32.09	*r*	> 18.98	P48+ZTF
SN 2019ape	58511.39	−26.32	*r*	> 21.37	P48+ZTF
SN 2019ape	58514.44	−23.33	*r*	20.56 ± 0.17	P48+ZTF
SN 2019ape	58538.25	0.00	*r*	18.33 ± 0.03	P48+ZTF
SN 2019ape	58541.30	2.99	*r*	18.73 ± 0.14	P48+ZTF
SN 2019ape	58558.21	19.56	*r*	19.33 ± 0.07	P48+ZTF
SN 2019ape	58567.23	28.41	*r*	19.32 ± 0.06	P48+ZTF
SN 2019ape	58572.28	33.35	*r*	19.44 ± 0.08	P48+ZTF
SN 2019ape	58575.23	36.25	*r*	19.50 ± 0.25	P48+ZTF
SN 2019ape	58580.23	41.15	*r*	19.65 ± 0.06	P48+ZTF
SN 2019ape	58583.26	44.12	*r*	19.77 ± 0.08	P48+ZTF
SN 2019ape	58586.19	46.99	*r*	19.77 ± 0.10	P48+ZTF
SN 2019ape	58591.35	52.05	*r*	19.97 ± 0.24	P48+ZTF
SN 2019ape	58594.16	54.80	*r*	19.76 ± 0.08	P48+ZTF
SN 2019ape	58597.24	57.82	*r*	19.91 ± 0.07	P48+ZTF

SN 2019ape	58502.44	−35.09	*g*	> 19.84	P48+ZTF
SN 2019ape	58505.46	−32.13	*g*	> 19.18	P48+ZTF
SN 2019ape	58508.53	−29.13	*g*	> 19.88	P48+ZTF
SN 2019ape	58511.42	−26.29	*g*	> 21.29	P48+ZTF
SN 2019ape	58514.46	−23.32	*g*	> 18.48	P48+ZTF
SN 2019ape	58522.41	−15.52	*g*	18.88 ± 0.02	P48+ZTF
SN 2019ape	58526.42	−11.59	*g*	18.78 ± 0.05	P48+ZTF
SN 2019ape	58538.28	0.03	*g*	19.72 ± 0.12	P48+ZTF
SN 2019ape	58541.27	2.96	*g*	19.67 ± 0.18	P48+ZTF
SN 2019ape	58546.25	7.85	*g*	19.97 ± 0.14	P48+ZTF
SN 2019ape	58556.37	17.76	*g*	> 20.06	P48+ZTF
SN 2019ape	58559.33	20.67	*g*	20.36 ± 0.27	P48+ZTF
SN 2019ape	58567.21	28.38	*g*	20.59 ± 0.17	P48+ZTF
SN 2019ape	58572.21	33.29	*g*	20.63 ± 0.24	P48+ZTF
SN 2019ape	58575.27	36.29	*g*	20.55 ± 0.11	P48+ZTF
SN 2019ape	58580.21	41.12	*g*	20.61 ± 0.12	P48+ZTF
SN 2019ape	58585.20	46.02	*g*	20.74 ± 0.18	P48+ZTF
SN 2019ape	58591.18	51.88	*g*	20.59 ± 0.33	P48+ZTF
SN 2019ape	58558.27	19.62	*i*	19.20 ± 0.13	P48+ZTF
SN 2019ccm	58534.20	−38.37	*r*	> 20.22	P48+ZTF
SN 2019ccm	58538.11	−34.51	*r*	> 21.36	P48+ZTF
SN 2019ccm	58558.16	−14.76	*r*	18.47 ± 0.08	P48+ZTF
SN 2019ccm	58573.14	−0.00	*r*	18.18 ± 0.02	P48+ZTF
SN 2019ccm	58582.18	8.91	*r*	18.66 ± 0.05	P48+ZTF
SN 2019ccm	58586.14	12.81	*r*	18.83 ± 0.05	P48+ZTF
SN 2019ccm	58534.24	−38.32	*g*	> 19.95	P48+ZTF
SN 2019ccm	58538.18	−34.44	*g*	> 21.39	P48+ZTF
SN 2019ccm	58556.13	−16.76	*g*	19.42 ± 0.09	P48+ZTF
SN 2019ccm	58561.21	−11.75	*g*	19.47 ± 0.15	P48+ZTF
SN 2019ccm	58568.21	−4.86	*g*	19.60 ± 0.08	P48+ZTF
SN 2019ccm	58573.16	0.02	*g*	19.93 ± 0.09	P48+ZTF
SN 2019ccm	58582.16	8.88	*g*	20.72 ± 0.21	P48+ZTF
SN 2019ccm	58586.16	12.83	*g*	> 20.49	P48+ZTF
SN 2019txl	58534.36	−31.80	*r*	> 19.14	P48+ZTF
SN 2019txl	58538.24	−28.04	*r*	> 20.93	P48+ZTF
SN 2019txl	58541.27	−25.10	*r*	> 19.23	P48+ZTF
SN 2019txl	58556.20	−10.66	*r*	20.27 ± 0.17	P48+ZTF
SN 2019txl	58559.25	−7.72	*r*	20.23 ± 0.26	P48+ZTF
SN 2019txl	58562.34	−4.73	*r*	> 19.39	P48+ZTF
SN 2019txl	58567.23	0.00	*r*	19.81 ± 0.08	P48+ZTF
SN 2019txl	58572.21	4.82	*r*	19.93 ± 0.17	P48+ZTF
SN 2019txl	58575.21	7.72	*r*	> 19.41	P48+ZTF
SN 2019txl	58580.21	12.56	*r*	20.55 ± 0.13	P48+ZTF
SN 2019txl	58584.17	16.39	*r*	20.53 ± 0.20	P48+ZTF
SN 2019txl	58589.19	21.24	*r*	> 18.84	P48+ZTF
SN 2019txl	58592.23	24.18	*r*	20.47 ± 0.24	P48+ZTF
SN 2019txl	58599.15	30.87	*r*	20.86 ± 0.24	P48+ZTF
SN 2019txl	58602.24	33.86	*r*	> 19.80	P48+ZTF
SN 2019txl	58609.15	40.55	*r*	20.86 ± 0.27	P48+ZTF
SN 2019txl	58617.23	48.37	*r*	> 20.30	P48+ZTF
SN 2019txl	58538.27	−28.01	*g*	> 19.61	P48+ZTF
SN 2019txl	58541.26	−25.12	*g*	> 20.14	P48+ZTF

SN 2019txl	58556.34	−10.53	*g*	> 20.16	P48+ZTF
SN 2019txl	58567.21	−0.02	*g*	> 20.67	P48+ZTF
SN 2019txl	58575.26	7.76	*g*	> 20.68	P48+ZTF
SN 2019txl	58580.23	12.58	*g*	> 21.07	P48+ZTF
SN 2019txl	58584.23	16.45	*g*	> 20.58	P48+ZTF
SN 2019txl	58589.15	21.20	*g*	> 18.93	P48+ZTF
SN 2019txl	58592.15	24.10	*g*	> 20.03	P48+ZTF
SN 2019txl	58599.18	30.91	*g*	> 20.79	P48+ZTF
SN 2019txl	58602.21	33.83	*g*	> 20.95	P48+ZTF
SN 2019txl	58605.23	36.76	*g*	> 20.94	P48+ZTF
SN 2019txl	58609.19	40.58	*g*	> 20.85	P48+ZTF
SN 2019txr	58572.22	−34.49	*r*	> 21.10	P48+ZTF
SN 2019txr	58575.16	−31.67	*r*	> 18.95	P48+ZTF
SN 2019txr	58580.22	−26.83	*r*	> 21.52	P48+ZTF
SN 2019txr	58584.17	−23.04	*r*	> 21.41	P48+ZTF
SN 2019txr	58587.16	−20.17	*r*	> 20.41	P48+ZTF
SN 2019txr	58591.15	−16.36	*r*	> 20.86	P48+ZTF
SN 2019txr	58594.16	−13.47	*r*	> 20.81	P48+ZTF
SN 2019txr	58598.16	−9.64	*r*	20.29 ± 0.07	P48+ZTF
SN 2019txr	58601.27	−6.66	*r*	20.10 ± 0.07	P48+ZTF
SN 2019txr	58606.18	−1.96	*r*	19.85 ± 0.05	P48+ZTF
SN 2019txr	58609.16	0.90	*r*	19.89 ± 0.10	P48+ZTF
SN 2019txr	58617.22	8.62	*r*	20.06 ± 0.09	P48+ZTF
SN 2019txr	58633.18	23.91	*r*	> 20.88	P48+ZTF
SN 2019txr	58642.22	32.56	*r*	21.18 ± 0.24	P48+ZTF
SN 2019txr	58648.20	38.29	*r*	21.07 ± 0.35	P48+ZTF
SN 2019txr	58653.17	43.06	*r*	> 20.28	P48+ZTF
SN 2019txr	58572.18	−34.53	*g*	> 20.68	P48+ZTF
SN 2019txr	58575.20	−31.63	*g*	> 20.94	P48+ZTF
SN 2019txr	58581.20	−25.88	*g*	> 21.38	P48+ZTF
SN 2019txr	58584.22	−22.99	*g*	> 21.34	P48+ZTF
SN 2019txr	58587.18	−20.16	*g*	> 20.88	P48+ZTF
SN 2019txr	58591.17	−16.34	*g*	> 20.64	P48+ZTF
SN 2019txr	58594.18	−13.45	*g*	20.88 ± 0.16	P48+ZTF
SN 2019txr	58598.20	−9.60	*g*	21.10 ± 0.12	P48+ZTF
SN 2019txr	58602.20	−5.77	*g*	21.07 ± 0.25	P48+ZTF
SN 2019txr	58605.22	−2.88	*g*	21.42 ± 0.13	P48+ZTF
SN 2019txr	58608.18	−0.04	*g*	21.46 ± 0.16	P48+ZTF
SN 2019txr	58617.18	8.58	*g*	> 20.69	P48+ZTF
SN 2019txr	58633.22	23.94	*g*	> 20.98	P48+ZTF
SN 2019txr	58636.24	26.84	*g*	> 20.40	P48+ZTF
SN 2019txr	58639.22	29.69	*g*	> 20.34	P48+ZTF
SN 2019txr	58642.17	32.52	*g*	> 20.12	P48+ZTF
SN 2019txr	58645.21	35.42	*g*	> 19.91	P48+ZTF
SN 2019txr	58648.18	38.27	*g*	> 19.39	P48+ZTF
SN 2019txt	58567.23	−36.96	*r*	> 21.04	P48+ZTF
SN 2019txt	58574.21	−30.16	*r*	> 19.73	P48+ZTF
SN 2019txt	58581.23	−23.31	*r*	> 21.32	P48+ZTF
SN 2019txt	58584.19	−20.44	*r*	> 20.56	P48+ZTF
SN 2019txt	58591.34	−13.47	*r*	> 20.11	P48+ZTF
SN 2019txt	58594.16	−10.73	*r*	20.65 ± 0.19	P48+ZTF
SN 2019txt	58598.19	−6.80	*r*	19.96 ± 0.08	P48+ZTF

SN 2019txt	58601.26	−3.80	*r*	19.69 ± 0.09	P48+ZTF
SN 2019txt	58605.16	0.00	*r*	19.56 ± 0.06	P48+ZTF
SN 2019txt	58608.22	2.97	*r*	19.61 ± 0.07	P48+ZTF
SN 2019txt	58612.19	6.85	*r*	19.69 ± 0.07	P48+ZTF
SN 2019txt	58617.25	11.77	*r*	19.81 ± 0.20	P48+ZTF
SN 2019txt	58634.17	28.26	*r*	20.61 ± 0.18	P48+ZTF
SN 2019txt	58637.18	31.19	*r*	> 20.72	P48+ZTF
SN 2019txt	58640.22	34.16	*r*	20.74 ± 0.31	P48+ZTF
SN 2019txt	58648.20	41.93	*r*	19.73 ± 0.34	P48+ZTF
SN 2019txt	58567.21	−36.98	*g*	> 21.09	P48+ZTF
SN 2019txt	58572.21	−32.11	*g*	> 20.36	P48+ZTF
SN 2019txt	58575.26	−29.14	*g*	> 21.01	P48+ZTF
SN 2019txt	58581.21	−23.34	*g*	> 21.11	P48+ZTF
SN 2019txt	58584.23	−20.39	*g*	> 20.66	P48+ZTF
SN 2019txt	58591.19	−13.62	*g*	> 19.97	P48+ZTF
SN 2019txt	58598.23	−6.76	*g*	20.66 ± 0.15	P48+ZTF
SN 2019txt	58601.23	−3.83	*g*	20.64 ± 0.14	P48+ZTF
SN 2019txt	58605.21	0.05	*g*	20.84 ± 0.16	P48+ZTF
SN 2019txt	58608.21	2.96	*g*	21.18 ± 0.24	P48+ZTF
SN 2019txt	58612.18	6.83	*g*	21.34 ± 0.29	P48+ZTF
SN 2019txt	58634.20	28.29	*g*	> 20.88	P48+ZTF
SN 2019txt	58637.22	31.23	*g*	> 20.54	P48+ZTF
SN 2019txt	58645.20	39.01	*g*	> 19.75	P48+ZTF
SN 2019txt	58648.17	41.90	*g*	> 19.40	P48+ZTF
SN 2019gau	58606.34	−35.88	*r*	> 20.28	P48+ZTF
SN 2019gau	58612.34	−30.04	*r*	> 20.59	P48+ZTF
SN 2019gau	58616.30	−26.19	*r*	> 20.00	P48+ZTF
SN 2019gau	58619.32	−23.25	*r*	> 18.18	P48+ZTF
SN 2019gau	58632.28	−10.63	*r*	19.56 ± 0.14	P48+ZTF
SN 2019gau	58638.23	−4.85	*r*	19.04 ± 0.07	P48+ZTF
SN 2019gau	58641.28	−1.88	*r*	18.85 ± 0.06	P48+ZTF
SN 2019gau	58644.26	1.02	*r*	18.84 ± 0.07	P48+ZTF
SN 2019gau	58647.23	3.91	*r*	19.32 ± 0.30	P48+ZTF
SN 2019gau	58650.23	6.83	*r*	19.08 ± 0.18	P48+ZTF
SN 2019gau	58660.21	16.54	*r*	19.73 ± 0.13	P48+ZTF
SN 2019gau	58663.19	19.44	*r*	19.77 ± 0.26	P48+ZTF
SN 2019gau	58666.17	22.34	*r*	19.88 ± 0.18	P48+ZTF
SN 2019gau	58669.19	25.27	*r*	20.00 ± 0.24	P48+ZTF
SN 2019gau	58672.19	28.20	*r*	20.01 ± 0.21	P48+ZTF
SN 2019gau	58675.24	31.16	*r*	> 19.43	P48+ZTF
SN 2019gau	58678.21	34.05	*r*	> 19.65	P48+ZTF
SN 2019gau	58681.24	37.01	*r*	> 19.25	P48+ZTF
SN 2019gau	58689.18	44.72	*r*	20.47 ± 0.34	P48+ZTF
SN 2019gau	58692.18	47.65	*r*	> 19.12	P48+ZTF
SN 2019gau	58695.19	50.58	*r*	> 17.98	P48+ZTF
SN 2019gau	58698.18	53.48	*r*	> 19.72	P48+ZTF
SN 2019gau	58701.16	56.38	*r*	> 17.64	P48+ZTF
SN 2019gau	58606.42	−35.80	*g*	> 20.53	P48+ZTF
SN 2019gau	58612.29	−30.09	*g*	> 20.77	P48+ZTF
SN 2019gau	58616.27	−26.21	*g*	> 19.86	P48+ZTF
SN 2019gau	58619.27	−23.30	*g*	> 18.81	P48+ZTF
SN 2019gau	58628.21	−14.59	*g*	20.60 ± 0.27	P48+ZTF

SN 2019gau	58635.21	−7.78	*g*	19.91 ± 0.12	P48+ZTF
SN 2019gau	58638.19	−4.89	*g*	19.73 ± 0.13	P48+ZTF
SN 2019gau	58641.19	−1.97	*g*	19.68 ± 0.12	P48+ZTF
SN 2019gau	58644.19	0.95	*g*	19.74 ± 0.19	P48+ZTF
SN 2019gau	58653.28	9.79	*g*	> 19.39	P48+ZTF
SN 2019gau	58657.19	13.60	*g*	20.67 ± 0.31	P48+ZTF
SN 2019gau	58660.19	16.52	*g*	> 20.44	P48+ZTF
SN 2019gau	58663.21	19.46	*g*	> 20.37	P48+ZTF
SN 2019gau	58672.18	28.19	*g*	> 20.06	P48+ZTF
SN 2019gau	58675.30	31.22	*g*	> 18.98	P48+ZTF
SN 2019gau	58678.25	34.10	*g*	> 19.29	P48+ZTF
SN 2019gau	58684.21	39.89	*g*	> 20.31	P48+ZTF
SN 2019gau	58692.20	47.67	*g*	> 20.25	P48+ZTF
SN 2019gau	58695.21	50.60	*g*	> 20.42	P48+ZTF
SN 2019gau	58698.20	53.50	*g*	> 16.56	P48+ZTF
SN 2019gau	58607.28	−34.96	*i*	> 20.61	P48+ZTF
SN 2019gau	58627.42	−15.36	*i*	19.90 ± 0.17	P48+ZTF
SN 2019gau	58639.21	−3.90	*i*	18.90 ± 0.05	P48+ZTF
SN 2019gau	58643.21	0.00	*i*	18.73 ± 0.05	P48+ZTF
SN 2019gau	58648.29	4.94	*i*	18.80 ± 0.13	P48+ZTF
SN 2019gau	58652.23	8.78	*i*	19.15 ± 0.12	P48+ZTF
SN 2019gau	58659.17	15.53	*i*	19.49 ± 0.12	P48+ZTF
SN 2019gau	58663.17	19.42	*i*	19.64 ± 0.13	P48+ZTF
SN 2019gau	58667.17	23.31	*i*	19.78 ± 0.16	P48+ZTF
SN 2019gau	58671.17	27.20	*i*	19.82 ± 0.15	P48+ZTF
SN 2019gau	58675.17	31.10	*i*	19.66 ± 0.35	P48+ZTF
SN 2019gsc	58605.39	−34.50	*r*	> 22.02	P48+ZTF
SN 2019gsc	58608.35	−31.57	*r*	> 21.13	P48+ZTF
SN 2019gsc	58612.23	−27.74	*r*	> 21.88	P48+ZTF
SN 2019gsc	58616.19	−23.82	*r*	> 21.73	P48+ZTF
SN 2019gsc	58619.33	−20.71	*r*	> 20.36	P48+ZTF
SN 2019gsc	58627.37	−12.76	*r*	> 21.64	P48+ZTF
SN 2019gsc	58632.28	−7.90	*r*	20.45 ± 0.14	P48+ZTF
SN 2019gsc	58635.26	−4.96	*r*	19.86 ± 0.07	P48+ZTF
SN 2019gsc	58638.24	−2.01	*r*	19.66 ± 0.02	P48+ZTF
SN 2019gsc	58641.29	1.01	*r*	19.68 ± 0.03	P48+ZTF
SN 2019gsc	58644.27	3.95	*r*	19.60 ± 0.03	P48+ZTF
SN 2019gsc	58647.24	6.90	*r*	19.91 ± 0.05	P48+ZTF
SN 2019gsc	58650.24	9.87	*r*	20.03 ± 0.06	P48+ZTF
SN 2019gsc	58653.19	12.78	*r*	20.57 ± 0.07	P48+ZTF
SN 2019gsc	58657.27	16.81	*r*	20.76 ± 0.13	P48+ZTF
SN 2019gsc	58660.24	19.75	*r*	20.99 ± 0.09	P48+ZTF
SN 2019gsc	58663.20	22.69	*r*	21.02 ± 0.14	P48+ZTF
SN 2019gsc	58668.18	27.61	*r*	21.63 ± 0.32	P48+ZTF
SN 2019gsc	58676.21	35.55	*r*	> 20.42	P48+ZTF
SN 2019gsc	58679.19	38.50	*r*	> 20.46	P48+ZTF
SN 2019gsc	58682.24	41.52	*r*	> 20.37	P48+ZTF
SN 2019gsc	58691.17	50.35	*r*	> 20.91	P48+ZTF
SN 2019gsc	58694.18	53.33	*r*	> 20.80	P48+ZTF
SN 2019gsc	58698.18	57.28	*r*	> 19.57	P48+ZTF
SN 2019gsc	58606.39	−33.51	*g*	> 22.38	P48+ZTF
SN 2019gsc	58612.27	−27.69	*g*	> 22.13	P48+ZTF

SN 2019gsc	58616.24	−23.77	*g*	> 21.68	P48+ZTF
SN 2019gsc	58619.25	−20.79	*g*	> 20.05	P48+ZTF
SN 2019gsc	58622.18	−17.89	*g*	> 19.87	P48+ZTF
SN 2019gsc	58628.22	−11.92	*g*	> 21.08	P48+ZTF
SN 2019gsc	58635.23	−4.99	*g*	19.83 ± 0.06	P48+ZTF
SN 2019gsc	58638.19	−2.05	*g*	19.93 ± 0.02	P48+ZTF
SN 2019gsc	58641.19	0.91	*g*	20.04 ± 0.03	P48+ZTF
SN 2019gsc	58644.20	3.89	*g*	20.28 ± 0.07	P48+ZTF
SN 2019gsc	58647.34	7.00	*g*	21.02 ± 0.19	P48+ZTF
SN 2019gsc	58650.20	9.83	*g*	21.70 ± 0.30	P48+ZTF
SN 2019gsc	58653.26	12.85	*g*	21.81 ± 0.25	P48+ZTF
SN 2019gsc	58657.20	16.75	*g*	21.74 ± 0.26	P48+ZTF
SN 2019gsc	58660.18	19.70	*g*	21.97 ± 0.23	P48+ZTF
SN 2019gsc	58663.23	22.71	*g*	22.18 ± 0.28	P48+ZTF
SN 2019gsc	58666.22	25.67	*g*	21.78 ± 0.24	P48+ZTF
SN 2019gsc	58673.30	32.67	*g*	> 20.84	P48+ZTF
SN 2019gsc	58676.30	35.64	*g*	> 20.19	P48+ZTF
SN 2019gsc	58679.28	38.59	*g*	> 20.03	P48+ZTF
SN 2019gsc	58682.18	41.45	*g*	> 20.56	P48+ZTF
SN 2019gsc	58685.20	44.44	*g*	> 21.15	P48+ZTF
SN 2019gsc	58691.22	50.39	*g*	> 21.08	P48+ZTF
SN 2019gsc	58694.22	53.36	*g*	> 21.08	P48+ZTF
SN 2019gsc	58698.20	57.30	*g*	> 19.01	P48+ZTF
SN 2019gsc	58612.33	−27.64	*i*	> 20.39	P48+ZTF
SN 2019gsc	58616.32	−23.68	*i*	> 20.09	P48+ZTF
SN 2019gsc	58627.43	−12.70	*i*	> 20.12	P48+ZTF
SN 2019gsc	58635.18	−5.03	*i*	20.16 ± 0.23	P48+ZTF
SN 2019gsc	58640.31	0.04	*i*	19.59 ± 0.12	P48+ZTF
SN 2019gsc	58644.25	3.94	*i*	19.97 ± 0.24	P48+ZTF
SN 2019gsc	58648.28	7.92	*i*	20.15 ± 0.26	P48+ZTF
SN 2019gsc	58652.24	11.84	*i*	20.47 ± 0.34	P48+ZTF
SN 2019gsc	58657.18	16.72	*i*	20.54 ± 0.33	P48+ZTF
SN 2019gsc	58661.18	20.68	*i*	> 19.92	P48+ZTF
SN 2019gsc	58669.30	28.71	*i*	20.26 ± 0.24	P48+ZTF
SN 2019gsc	58674.18	33.54	*i*	> 20.21	P48+ZTF
SN 2019ttf	58619.41	−37.47	*r*	> 18.92	P48+ZTF
SN 2019ttf	58627.40	−29.57	*r*	> 21.69	P48+ZTF
SN 2019ttf	58632.32	−24.70	*r*	> 21.92	P48+ZTF
SN 2019ttf	58635.36	−21.69	*r*	> 22.25	P48+ZTF
SN 2019ttf	58638.30	−18.79	*r*	> 21.95	P48+ZTF
SN 2019ttf	58641.40	−15.72	*r*	> 21.99	P48+ZTF
SN 2019ttf	58644.32	−12.83	*r*	> 21.46	P48+ZTF
SN 2019ttf	58647.33	−9.85	*r*	20.91 ± 0.21	P48+ZTF
SN 2019ttf	58650.33	−6.89	*r*	20.25 ± 0.21	P48+ZTF
SN 2019ttf	58653.41	−3.84	*r*	19.98 ± 0.15	P48+ZTF
SN 2019ttf	58657.27	−0.02	*r*	20.15 ± 0.01	P48+ZTF
SN 2019ttf	58663.34	5.98	*r*	20.12 ± 0.08	P48+ZTF
SN 2019ttf	58669.33	11.91	*r*	20.38 ± 0.09	P48+ZTF
SN 2019ttf	58675.29	17.80	*r*	20.70 ± 0.03	P48+ZTF
SN 2019ttf	58678.25	20.73	*r*	20.76 ± 0.05	P48+ZTF
SN 2019ttf	58681.27	23.72	*r*	20.92 ± 0.06	P48+ZTF
SN 2019ttf	58684.18	26.59	*r*	20.95 ± 0.09	P48+ZTF

SN 2019ttf	58688.36	30.73	*r*	20.98 ± 0.12	P48+ZTF
SN 2019ttf	58691.20	33.54	*r*	21.02 ± 0.09	P48+ZTF
SN 2019ttf	58694.20	36.50	*r*	21.47 ± 0.13	P48+ZTF
SN 2019ttf	58697.18	39.45	*r*	21.09 ± 0.13	P48+ZTF
SN 2019ttf	58700.19	42.43	*r*	21.68 ± 0.22	P48+ZTF
SN 2019ttf	58703.18	45.39	*r*	21.54 ± 0.11	P48+ZTF
SN 2019ttf	58706.26	48.44	*r*	21.60 ± 0.11	P48+ZTF
SN 2019ttf	58709.27	51.41	*r*	21.54 ± 0.19	P48+ZTF
SN 2019ttf	58712.25	54.36	*r*	21.69 ± 0.11	P48+ZTF
SN 2019ttf	58715.33	57.41	*r*	> 20.89	P48+ZTF
SN 2019ttf	58627.48	−29.49	*g*	> 20.46	P48+ZTF
SN 2019ttf	58632.42	−24.60	*g*	> 21.82	P48+ZTF
SN 2019ttf	58635.44	−21.61	*g*	> 22.02	P48+ZTF
SN 2019ttf	58638.37	−18.71	*g*	> 22.07	P48+ZTF
SN 2019ttf	58641.43	−15.69	*g*	> 22.12	P48+ZTF
SN 2019ttf	58647.40	−9.79	*g*	> 20.73	P48+ZTF
SN 2019ttf	58650.46	−6.76	*g*	> 20.26	P48+ZTF
SN 2019ttf	58653.36	−3.89	*g*	> 20.55	P48+ZTF
SN 2019ttf	58657.44	0.15	*g*	> 20.60	P48+ZTF
SN 2019ttf	58660.34	3.01	*g*	21.60 ± 0.27	P48+ZTF
SN 2019ttf	58663.44	6.08	*g*	> 20.47	P48+ZTF
SN 2019ttf	58666.24	8.85	*g*	> 21.17	P48+ZTF
SN 2019ttf	58669.28	11.86	*g*	> 21.40	P48+ZTF
SN 2019ttf	58672.35	14.90	*g*	> 21.37	P48+ZTF
SN 2019ttf	58675.34	17.85	*g*	> 21.17	P48+ZTF
SN 2019ttf	58678.30	20.78	*g*	> 21.43	P48+ZTF
SN 2019ttf	58681.23	23.68	*g*	> 21.16	P48+ZTF
SN 2019ttf	58684.29	26.71	*g*	> 21.25	P48+ZTF
SN 2019ttf	58688.30	30.67	*g*	> 21.76	P48+ZTF
SN 2019ttf	58693.29	35.61	*g*	> 22.03	P48+ZTF
SN 2019ttf	58699.19	41.44	*g*	> 21.56	P48+ZTF
SN 2019ttf	58702.33	44.55	*g*	> 21.75	P48+ZTF
SN 2019ttf	58706.19	48.36	*g*	> 20.90	P48+ZTF
SN 2019ttf	58709.15	51.30	*g*	> 20.92	P48+ZTF
SN 2019ttf	58712.17	54.28	*g*	> 20.74	P48+ZTF
SN 2019ttf	58715.24	57.32	*g*	> 21.91	P48+ZTF
SN 2019mjo	58652.46	−30.78	*r*	> 20.21	P48+ZTF
SN 2019mjo	58655.44	−27.91	*r*	> 20.12	P48+ZTF
SN 2019mjo	58662.46	−21.16	*r*	> 20.76	P48+ZTF
SN 2019mjo	58665.46	−18.29	*r*	> 21.30	P48+ZTF
SN 2019mjo	58669.44	−14.46	*r*	> 21.32	P48+ZTF
SN 2019mjo	58672.46	−11.56	*r*	> 21.43	P48+ZTF
SN 2019mjo	58677.48	−6.73	*r*	21.15 ± 0.12	P48+ZTF
SN 2019mjo	58681.43	−2.94	*r*	20.10 ± 0.11	P48+ZTF
SN 2019mjo	58684.49	0.00	*r*	19.93 ± 0.16	P48+ZTF
SN 2019mjo	58688.44	3.79	*r*	20.17 ± 0.07	P48+ZTF
SN 2019mjo	58691.42	6.66	*r*	20.31 ± 0.07	P48+ZTF
SN 2019mjo	58694.40	9.52	*r*	20.48 ± 0.07	P48+ZTF
SN 2019mjo	58697.42	12.43	*r*	20.52 ± 0.07	P48+ZTF
SN 2019mjo	58700.42	15.31	*r*	20.53 ± 0.09	P48+ZTF
SN 2019mjo	58703.42	18.19	*r*	20.83 ± 0.10	P48+ZTF
SN 2019mjo	58707.46	22.08	*r*	20.89 ± 0.12	P48+ZTF

SN 2019mjo	58710.38	24.88	*r*	20.70 ± 0.23	P48+ZTF
SN 2019mjo	58715.38	29.68	*r*	> 21.32	P48+ZTF
SN 2019mjo	58719.43	33.58	*r*	> 21.61	P48+ZTF
SN 2019mjo	58724.38	38.33	*r*	> 21.12	P48+ZTF
SN 2019mjo	58727.33	41.16	*r*	> 20.81	P48+ZTF
SN 2019mjo	58730.38	44.09	*r*	> 21.19	P48+ZTF
SN 2019mjo	58733.40	47.00	*r*	> 20.97	P48+ZTF
SN 2019mjo	58736.40	49.88	*r*	> 20.83	P48+ZTF
SN 2019mjo	58739.38	52.74	*r*	> 19.35	P48+ZTF
SN 2019mjo	58743.34	56.55	*r*	> 21.23	P48+ZTF
SN 2019mjo	58646.45	−36.55	*g*	> 21.03	P48+ZTF
SN 2019mjo	58649.47	−33.65	*g*	> 20.29	P48+ZTF
SN 2019mjo	58655.48	−27.87	*g*	> 19.94	P48+ZTF
SN 2019mjo	58661.48	−22.11	*g*	> 21.11	P48+ZTF
SN 2019mjo	58669.46	−14.44	*g*	> 21.47	P48+ZTF
SN 2019mjo	58672.43	−11.59	*g*	> 21.50	P48+ZTF
SN 2019mjo	58675.45	−8.69	*g*	> 21.75	P48+ZTF
SN 2019mjo	58678.44	−5.81	*g*	> 21.11	P48+ZTF
SN 2019mjo	58681.46	−2.91	*g*	20.62 ± 0.29	P48+ZTF
SN 2019mjo	58684.40	−0.08	*g*	> 20.30	P48+ZTF
SN 2019mjo	58688.46	3.82	*g*	> 21.42	P48+ZTF
SN 2019mjo	58691.46	6.70	*g*	> 21.90	P48+ZTF
SN 2019mjo	58694.46	9.58	*g*	> 22.28	P48+ZTF
SN 2019mjo	58698.46	13.42	*g*	> 21.86	P48+ZTF
SN 2019mjo	58701.45	16.30	*g*	> 21.71	P48+ZTF
SN 2019mjo	58704.42	19.16	*g*	> 21.73	P48+ZTF
SN 2019mjo	58707.43	22.05	*g*	> 21.64	P48+ZTF
SN 2019mjo	58710.46	24.96	*g*	> 19.51	P48+ZTF
SN 2019mjo	58718.41	32.60	*g*	> 20.99	P48+ZTF
SN 2019mjo	58722.42	36.44	*g*	> 21.50	P48+ZTF
SN 2019mjo	58725.39	39.30	*g*	> 22.20	P48+ZTF
SN 2019mjo	58730.33	44.05	*g*	> 21.37	P48+ZTF
SN 2019mjo	58733.37	46.97	*g*	> 21.50	P48+ZTF
SN 2019mjo	58736.46	49.94	*g*	> 21.49	P48+ZTF
SN 2019mjo	58739.50	52.86	*g*	> 19.46	P48+ZTF
SN 2019mjo	58743.40	56.61	*g*	> 19.16	P48+ZTF
SN 2019mjo	58670.41	−13.53	*i*	> 20.31	P48+ZTF
SN 2019mjo	58691.34	6.58	*i*	20.38 ± 0.19	P48+ZTF
SN 2019mjo	58697.44	12.44	*i*	20.82 ± 0.23	P48+ZTF
SN 2019mjo	58701.43	16.28	*i*	20.97 ± 0.36	P48+ZTF
SN 2019mjo	58705.42	20.12	*i*	20.83 ± 0.27	P48+ZTF
SN 2019mjo	58716.33	30.59	*i*	> 20.05	P48+ZTF
SN 2019mjo	58722.38	36.41	*i*	21.38 ± 0.34	P48+ZTF
SN 2019mjo	58727.37	41.21	*i*	> 20.25	P48+ZTF
SN 2019mjo	58732.33	45.97	*i*	> 20.69	P48+ZTF
SN 2019mjo	58736.33	49.81	*i*	> 20.21	P48+ZTF
SN 2019mjo	58743.46	56.67	*i*	> 19.30	P48+ZTF
SN 2019ouq	58660.32	−36.53	*r*	> 21.75	P48+ZTF
SN 2019ouq	58663.31	−33.65	*r*	> 21.70	P48+ZTF
SN 2019ouq	58666.27	−30.79	*r*	> 21.46	P48+ZTF
SN 2019ouq	58669.33	−27.84	*r*	> 21.71	P48+ZTF
SN 2019ouq	58672.23	−25.04	*r*	> 21.75	P48+ZTF

SN 2019ouq	58675.25	−22.11	*r*	> 21.45	P48+ZTF
SN 2019ouq	58678.22	−19.25	*r*	21.02 ± 0.20	P48+ZTF
SN 2019ouq	58681.27	−16.31	*r*	20.33 ± 0.09	P48+ZTF
SN 2019ouq	58684.18	−13.50	*r*	19.79 ± 0.05	P48+ZTF
SN 2019ouq	58688.36	−9.46	*r*	19.60 ± 0.06	P48+ZTF
SN 2019ouq	58691.19	−6.73	*r*	19.52 ± 0.04	P48+ZTF
SN 2019ouq	58694.21	−3.82	*r*	19.69 ± 0.03	P48+ZTF
SN 2019ouq	58697.18	−0.95	*r*	19.72 ± 0.07	P48+ZTF
SN 2019ouq	58700.18	1.95	*r*	19.95 ± 0.09	P48+ZTF
SN 2019ouq	58703.17	4.83	*r*	20.68 ± 0.20	P48+ZTF
SN 2019ouq	58707.16	8.69	*r*	20.72 ± 0.26	P48+ZTF
SN 2019ouq	58711.28	12.67	*r*	21.06 ± 0.34	P48+ZTF
SN 2019ouq	58714.35	15.63	*r*	> 20.33	P48+ZTF
SN 2019ouq	58720.15	21.22	*r*	20.97 ± 0.28	P48+ZTF
SN 2019ouq	58723.33	24.30	*r*	> 20.88	P48+ZTF
SN 2019ouq	58727.15	27.98	*r*	21.81 ± 0.31	P48+ZTF
SN 2019ouq	58730.13	30.86	*r*	> 20.58	P48+ZTF
SN 2019ouq	58733.23	33.85	*r*	21.21 ± 0.26	P48+ZTF
SN 2019ouq	58737.19	37.67	*r*	> 19.95	P48+ZTF
SN 2019ouq	58740.26	40.65	*r*	> 19.90	P48+ZTF
SN 2019ouq	58660.17	−36.67	*g*	> 21.71	P48+ZTF
SN 2019ouq	58665.21	−31.81	*g*	> 22.28	P48+ZTF
SN 2019ouq	58670.28	−26.91	*g*	> 21.83	P48+ZTF
SN 2019ouq	58673.31	−23.99	*g*	> 21.91	P48+ZTF
SN 2019ouq	58676.31	−21.10	*g*	> 20.86	P48+ZTF
SN 2019ouq	58679.29	−18.22	*g*	20.84 ± 0.13	P48+ZTF
SN 2019ouq	58682.19	−15.42	*g*	20.83 ± 0.08	P48+ZTF
SN 2019ouq	58685.17	−12.54	*g*	20.82 ± 0.09	P48+ZTF
SN 2019ouq	58688.30	−9.52	*g*	21.00 ± 0.14	P48+ZTF
SN 2019ouq	58691.23	−6.70	*g*	21.07 ± 0.08	P48+ZTF
SN 2019ouq	58694.23	−3.80	*g*	21.42 ± 0.17	P48+ZTF
SN 2019ouq	58697.20	−0.92	*g*	21.63 ± 0.19	P48+ZTF
SN 2019ouq	58700.27	2.04	*g*	> 21.22	P48+ZTF
SN 2019ouq	58703.20	4.86	*g*	> 20.94	P48+ZTF
SN 2019ouq	58706.17	7.73	*g*	> 21.22	P48+ZTF
SN 2019ouq	58710.17	11.59	*g*	> 21.48	P48+ZTF
SN 2019ouq	58713.15	14.47	*g*	> 21.63	P48+ZTF
SN 2019ouq	58716.17	17.38	*g*	22.55 ± 0.31	P48+ZTF
SN 2019ouq	58720.15	21.23	*g*	> 21.56	P48+ZTF
SN 2019ouq	58723.17	24.14	*g*	> 22.06	P48+ZTF
SN 2019ouq	58726.15	27.02	*g*	> 21.84	P48+ZTF
SN 2019ouq	58729.15	29.92	*g*	> 20.04	P48+ZTF
SN 2019ouq	58732.13	32.79	*g*	> 21.68	P48+ZTF
SN 2019ouq	58735.12	35.68	*g*	> 21.18	P48+ZTF
SN 2019ouq	58738.12	38.58	*g*	> 21.11	P48+ZTF
SN 2019ouq	58741.12	41.48	*g*	> 21.49	P48+ZTF
SN 2019ouq	58744.14	44.38	*g*	> 21.38	P48+ZTF
SN 2019ouq	58747.14	47.29	*g*	> 20.96	P48+ZTF
SN 2019ouq	58750.14	50.18	*g*	> 20.60	P48+ZTF
SN 2019ouq	58659.18	−37.63	*i*	> 20.11	P48+ZTF
SN 2019ouq	58663.18	−33.77	*i*	> 20.05	P48+ZTF
SN 2019ouq	58667.18	−29.91	*i*	> 20.15	P48+ZTF

SN 2019ouq	58671.18	−26.05	*i*	> 20.25	P48+ZTF
SN 2019ouq	58675.22	−22.15	*i*	> 19.96	P48+ZTF
SN 2019ouq	58679.26	−18.25	*i*	20.26 ± 0.26	P48+ZTF
SN 2019ouq	58683.30	−14.35	*i*	> 19.04	P48+ZTF
SN 2019ouq	58688.34	−9.48	*i*	19.44 ± 0.12	P48+ZTF
SN 2019ouq	58692.31	−5.65	*i*	19.39 ± 0.14	P48+ZTF
SN 2019ouq	58703.16	4.83	*i*	20.21 ± 0.30	P48+ZTF
SN 2019ouq	58710.24	11.66	*i*	> 19.87	P48+ZTF
SN 2019ouq	58719.15	20.26	*i*	> 19.82	P48+ZTF
SN 2019ouq	58725.23	26.13	*i*	> 20.12	P48+ZTF
SN 2019ouq	58733.14	33.77	*i*	> 19.94	P48+ZTF
SN 2019ouq	58747.11	47.26	*i*	> 19.10	P48+ZTF
SN 2019ouq	58751.12	51.12	*i*	> 19.78	P48+ZTF

Table 6.6: **Log of spectroscopic observations of all objects presented in this paper.** † denotes spectra which did not have high enough signal-to-noise ratio to detect features.

Object	Observation Date (UTC)	MJD	Phase (days from *r* peak)	Telescope + Instrument	Range Å	Resolution $\lambda/\delta\lambda$
SN 2018ckd	2018-06-12	58281.3	+3	P200 + DBSP	3500 - 10000	1000
SN 2018ckd	2018-06-21	58290.2	+12	P200 + DBSP	3500 - 10000	1000
SN 2018ckd	2018-08-08	58338.3	+57	Keck-I + LRIS	3500 - 10000	1000
SN 2018ckd	2019-04-03	58576.5	+291	Keck-I + LRIS	3500 - 10000†	1000
SN 2018lqo	2018-08-21	58351.2	-1	P200 + DBSP	3500 - 10000	1000
SN 2018lqo	2018-10-12	58403.3	+49	Keck-I + LRIS	3500 - 10000	1000
SN 2018lqu	2018-09-12	58373.1	+2	P200 + DBSP	3500 - 10000	1000
SN 2018lqu	2018-10-12	58403.2	+31	Keck-I + LRIS	3500 - 10000	1000
SN 2018gwo	2018-09-30	58391.8	-12	THO + ALPY	3700 - 7500	100
SN 2018gwo	2018-10-06	58397.8	-6	THO + ALPY	3700 - 7500	100
SN 2018gwo	2018-11-06	58428.5	+23	P60 + SEDM	3800 - 9200	100
SN 2018gwo	2018-12-04	58456.6	+51	Keck-I + LRIS	3500 - 10000	1000
SN 2018gwo	2019-03-07	58549.5	+143	Keck-I + LRIS	3500 - 10000	1000
SN 2018gwo	2019-06-03	58637.3	+230	Keck-I + LRIS	3500 - 10000	1000
SN 2018kjy	2018-12-14	58466.3	+5	P200 + DBSP	3500 - 10000	1000
SN 2018kjy	2019-01-04	58487.4	+25	Keck-I + LRIS	3500 - 10000	1000
SN 2018kjy	2019-04-03	58576.2	+113	Keck-I + LRIS	3500 - 10000	1000
SN 2019hty	2019-07-01	58665.2	+6	P200 + DBSP	3500 - 10000	1000
SN 2019hty	2019-07-02	58666.2	+7	P60 + SEDM	3800 - 9200	100
SN 2019hty	2019-08-04	58699.2	+40	P200 + DBSP	3500 - 10000	1000
SN 2019ofm	2019-08-27	58722.3	-1	P200 + DBSP	3500 - 10000	1000
SN 2019ofm	2020-02-18	58897.5	+168	Keck-I + LRIS	3500 - 10000	1000
SN 2019pxu	2019-09-24	58750.4	+3	P60 + SEDM	3800 - 9200	100
SN 2019pxu	2019-10-03	58759.5	+11	P200 + DBSP	3500 - 10000	1000
SN 2019pxu	2019-10-27	58783.5	+35	Keck-I + LRIS	3500 - 10000	1000
SN 2019pxu	2020-02-18	58897.3	+146	Keck-I + LRIS	3500 - 10000	1000
SN 2018dbg	2018-08-04	58334.0	+22	P200 + DBSP	3500 - 10000	1000
SN 2018fob	2018-08-21	58351.0	-8	P200 + DBSP	3500 - 10000	1000
SN 2018fob	2018-08-31	58361.0	+0	P60 + SEDM	3800 - 9200	100
SN 2018fob	2019-04-03	58576.0	+209	Keck-I + LRIS	3500 - 10000	1000

SN 2018kqr	2018-12-14	58466.3	+1	P200 + DBSP	3500 - 10000	1000
SN 2018kqr	2018-12-27	58479.2	+14	P200 + DBSP	3500 - 10000	1000
SN 2019yz	2019-02-20	58534.2	+7	NOT + ALFOSC	3800 - 9500	300
SN 2019yz	2019-04-15	58588.2	+61	P60 + SEDM	3800 - 9200	100
SN 2019yz	2019-06-08	58642.0	+114	P60 + SEDM	3800 - 9200	100
SN 2019yz	2019-07-02	58666.0	+138	P60 + SEDM	3800 - 9200	100
SN 2019yz	2019-09-26	58752.2	+224	Keck-I + LRIS	3500 - 10000	1000
SN 2019abb	2019-01-26	58509.2	-4	P200 + DBSP	3500 - 10000	1000
SN 2019abb	2019-02-09	58523.0	+9	P60 + SEDM	3800 - 9200	100
SN 2019abb	2019-02-10	58524.9	+11	NOT + ALFOSC	3800 - 9500	300
SN 2019abb	2019-04-06	58579.2	+64	Keck-I + LRIS	3500 - 10000	1000
SN 2019abb	2020-01-24	58872.0	+353	Keck-I + LRIS	3500 - 10000	1000
SN 2019ape	2019-02-12	58526.4	-13	P200 + DBSP	3500 - 10000	1000
SN 2019ape	2019-03-01	58543.1	+2	NOT + ALFOSC	3800 - 9500	300
SN 2019ape	2019-12-03	58820.0	+274	Keck-I + LRIS	3500 - 10000	1000
SN 2019ccm	2019-04-06	58579.2	+6	Keck-I + LRIS	3500 - 10000	1000
SN 2019ccm	2019-09-28	58754.0	+178	Keck-I + LRIS	3500 - 10000	1000
SN 2019txl	2019-04-06	58579.0	+11	Keck-I + LRIS	3500 - 10000	1000
SN 2019txl	2020-02-18	58897.0	+318	Keck-I + LRIS	3500 - 10000	1000
SN 2019txr	2019-06-04	58638.0	+28	Keck-I + LRIS	3500 - 10000	1000
SN 2019txr	2020-02-18	58897.0	+276	Keck-I + LRIS	3500 - 10000	1000
SN 2019txt	2019-05-13	58616.0	+10	P200 + DBSP	3500 - 10000	1000
SN 2019txt	2019-06-04	58638.0	+31	Keck-I + LRIS	3500 - 10000	1000
SN 2019txt	2020-01-24	58872.0	+259	Keck-I + LRIS	3500 - 10000	1000
SN 2019gau	2019-06-04	58638.9	-4	P60 + SEDM	3500 - 10000	100
SN 2019gau	2020-02-18	58897.0	+260	Keck-I + LRIS	3500 - 10000	1000
SN 2019gsc	2019-06-04	58638.2	-2	P200 + DBSP	3500 - 10000	1000
SN 2019gsc	2019-07-04	58668.0	+27	Keck-I + LRIS	3500 - 10000	1000
SN 2019ttf	2019-07-04	58668.0	+10	Keck-I + LRIS	3500 - 10000	1000
SN 2019ttf	2020-03-22	58930.0	+269	Keck-I + LRIS	3500 - 10000	1000
SN 2019mjo	2019-08-01	58696.0	+7	P200 + DBSP	3500 - 10000	1000
SN 2019mjo	2020-01-24	58872.0	+176	Keck-I + LRIS	3500 - 10000	1000
SN 2019ouq	2019-08-04	58699.3	+6	P200 + DBSP	3500 - 10000	1000
SN 2019ouq	2020-01-24	58872.0	+173	Keck-I + LRIS	3500 - 10000	1000

Part III: A wide-field infrared view of compact objects in the dynamic and optically obscured Galactic plane

Chapter 7

PALOMAR GATTINI-IR: SURVEY OVERVIEW, DATA PROCESSING SYSTEM, ON-SKY PERFORMANCE, AND FIRST RESULTS

De, K. et al. (2020). "Palomar Gattini-IR: Survey Overview, Data Processing System, On-sky Performance and First Results". In: *PASP* 132.1008, 025001, p. 025001. DOI: 10.1088/1538-3873/ab6069. arXiv: 1910.13319 [astro-ph.IM].

Kishalay De[1], Matthew J. Hankins[1], Mansi M. Kasliwal[1], Anna M. Moore[2], Eran O. Ofek[3], Scott M. Adams[1], Michael C. B. Ashley[4], Aliya-Nur Babul[5], Ashot Bagdasaryan[1], Kevin B. Burdge[1], Jill Burnham[6], Richard G. Dekany[6], Alexandre Delacroix[6], Antony Galla[2], Timothee Greffe[6], David Hale[6], Jacob E. Jencson[1,7], Ryan M. Lau[8], Ashish Mahabal[1], Daniel McKenna[6], Manasi Sharma[9], Patrick L. Shopbell[1], Roger M. Smith[6], Jamie Soon[2], Jennifer Sokoloski[10], Roberto Soria[11], and Tony Travouillon[2]

[1]Cahill Center for Astrophysics, California Institute of Technology, 1200 E. California Blvd., Pasadena, CA 91125, USA
[2]Research School of Astronomy and Astrophysics, Australian National University, Canberra, ACT 2611, Australia
[3]Department of Particle Physics & Astrophysics, Weizmann Institute of Science, Rehovot 76100, Israel
[4]School of Physics, University of New South Wales, Sydney NSW 2052, Australia
[5]Department of Astronomy, Columbia University, 550 West 120th Street, New York, NY 10027, U.S.A.
[6]Caltech Optical Observatories, California Institute of Technology, Pasadena, CA 91125, USA
[7]Steward Observatory, University of Arizona, 933 North Cherry Avenue, Tucson, AZ85721-0065, USA
[8]Institute of Space & Astronautical Science, Japan Aerospace Exploration Agency, 3-1-1 Yoshinodai, Chuo-ku, Sagamihara, Kanagawa 252-5210, Japan
[9]Department of Physics, Pupin Hall, Columbia University, New York, NY 10027, USA
[10]Columbia Astrophysics Laboratory, Columbia University, 550 West 120th Street, New York, NY 10027, USA
[11]National Astronomical Observatories, Chinese Academy of Sciences, Beijing 100012, China

Abstract

Palomar Gattini-IR is a new wide-field, near-infrared robotic time domain survey operating at Palomar Observatory. Using a 30 cm telescope mounted with a H2RG detector, Gattini-IR achieves a field of view of 25 sq. deg. with a pixel scale of 8.7″ in J-band. Here, we describe the system design, survey operations, data processing system, and on-sky performance of Palomar Gattini-IR. As a part of the

nominal survey, Gattini-IR scans $\approx$ 7500 square degrees of the sky every night to a median 5σ depth of 15.7 AB mag outside the Galactic plane. The survey covers $\approx$ 15000 square degrees of the sky visible from Palomar with a median cadence of 2 days. A real-time data processing system produces stacked science images from dithered raw images taken on the sky, together with PSF-fit source catalogs and transient candidates identified from subtractions within a median delay of $\approx$ 4 hours from the time of observation. The calibrated data products achieve an astrometric accuracy (RMS) of $\approx 0.7''$ with respect to Gaia DR2 for sources with S/N > 10, and better than $\approx 0.35''$ for sources brighter than $\approx$ 12 Vega mag. The photometric accuracy (RMS) achieved in the PSF-fit source catalogs is better than $\approx$ 3% for sources brighter than $\approx$ 12 Vega mag and fainter than the saturation magnitude of $\approx$ 8.5 Vega mag, as calibrated against the 2MASS catalog. The detection efficiency of transient candidates injected into the images is better than 90% for sources brighter than the 5σ limiting magnitude. The photometric recovery precision of injected sources is 3% for sources brighter than 13 mag, and the astrometric recovery RMS is $\approx 0.9''$. Reference images generated by stacking several field visits achieve depths of $\gtrsim$ 16.5 AB mag over 60% of the sky, while it is limited by confusion in the Galactic plane. With a field of view $\approx 40\times$ larger than any other existing near infrared imaging instrument, Gattini-IR is probing the reddest and dustiest transients in the local universe such as dust obscured supernovae in nearby galaxies, novae behind large columns of extinction within the galaxy, reddened micro-lensing events in the Galactic plane, and variability from cool and dust obscured stars. We present results from transients and variables identified since the start of the commissioning period.

7.1 Introduction

Optical time domain astronomy has undergone a revolution in the last two decades due to the advent of wide field of view (FOV) telescopes equipped with large format CCD detectors. Combined with improvements in detector technology (faster readout and higher quantum efficiency), computing capabilities, and the lower cost of detectors per pixel, several surveys have tiled large portions of the sky to provide exquisite time domain coverage of the optical variable sky over a large parameter space of areal coverage, depth, cadence, and color. Examples include the Sloan Digital Sky Survey (SDSS; York et al., 2000), Skymapper (Keller et al., 2007), the Catalina Real-time Transient Survey (CRTS; Drake et al., 2009), the Palomar Transient Factory (PTF; Law et al., 2009), PanSTARRS (Kaiser et al., 2010), the All

Sky Automated Survey for Supernovae (ASASSN; Shappee et al., 2014), Evryscope (Law et al., 2015), the Dark Energy Survey (DES; Dark Energy Survey Collaboration et al., 2016) the Asteroid Terrestrial-impact Last Alert System (ATLAS; Tonry et al., 2018), and the Zwicky Transient Facility (ZTF; Bellm et al., 2019b).

The first near infrared (NIR) sky survey was carried out as a part of the Two Micron Sky Survey (TMSS; Neugebauer et al., 1969) that covered 70% of the sky and produced a catalog of $\sim$ 5700 sources. It was followed by its deeper successor three decades later with the Two Micron All Sky Survey (2MASS; Skrutskie et al., 2006), which surveyed the entire sky in J, H, and Ks bands down to a depth of $\approx$ 16, 15, and 14 Vega mag, respectively (for sources with a Signal-to-Noise ratio (SNR) of $\approx$ 10). The Deep Near-Infrared Survey of the Southern sky (DENIS; Epchtein et al., 1999) also surveyed the southern sky to depths of 16.5 and 14 Vega mag in J abnd Ks bands respectively. The UKIRT Infrared Deep Sky Survey performed a deeper survey of a smaller fraction of the sky ($\sim$ 7500 square degrees) to a depth of $K \approx 18.5$ Vega mag (Warren et al., 2007). The VISTA hemisphere survey (VHS; McMahon et al., 2013), when combined with data from the public VISTA surveys, will produce a deep NIR map of the entire southern sky down to $J \approx 20.2$ Vega mag and $Ks \approx 18.1$ Vega mag. In the mid-infrared, the Wide-field Infrared Survey Explorer (WISE) all-sky survey (Wright et al., 2010) created maps of the entire sky from 3.4 μm to 22 μm with 5σ point source sensitivities ranging from $\approx$ 14 AB mag (at 22 μm) to $\approx$ 19 AB mag (at 3.6 μm).

However, the time domain sky in the NIR remains largely unexplored due to limitations posed by the high sky background and detector technology. The brightness of the sky in the NIR wavebands arises from OH emission lines from the atmosphere, making ground based imaging limited by the high sky background noise. At the same time, the high cost of suitable detectors for the NIR (relative to optical CCD sensors) hinders the development of large format detectors that can perform fast imaging of large areas of the sky. Limited by the small FOV of most infrared imaging instruments, transient searches at these wavelengths have been largely limited to pencil beam surveys targeting small regions of the sky to hunt for variable and explosive events. For instance, a number of surveys have targeted luminous infrared galaxies (LIRGs) in the local universe at NIR wavelengths to search for supernovae (SNe) obscured by dust and hidden from optical surveys (e.g., Cresci et al., 2007; Kankare et al., 2008, 2012; Kool et al., 2018; Mannucci et al., 2003, 2007; Mattila et al., 2007; Miluzio et al., 2013) owing to the high amount of star formation and

dust in these galaxies. In the mid-infrared, the Spitzer Space Telescope (Gehrz et al., 2007; Werner et al., 2004) has been used to conduct targeted surveys of variables (e.g., Boyer et al., 2015; Freedman et al., 2011; Kozłowski et al., 2010; Rebull et al., 2014) and transient phenomena (e.g., Fox et al., 2011; Fox et al., 2012; Jencson et al., 2019; Kasliwal et al., 2017). The Near-Earth Object WISE (NEOWISE; Mainzer et al., 2011) mission initially used enhanced data processing from the primary WISE all-sky survey to find solar system objects. It was subsequently repurposed as an all-sky time domain survey to study solar system objects through their mid-infrared emission (Mainzer et al., 2014).

Given the relatively high cost of infrared detectors per pixel, two approaches have been proposed to probe the time domain sky at these wavelengths – i) the use of fast optics to achieve a large pixel scale and field of view and ii) the use of alternative and cheaper semi-conductor detector technology (relative to HgCdTe). In the former case, the large pixel scale produces under-sampled point spread functions (PSFs) that can be reconstructed in data processing while suffering a degradation in sensitivity due to the high sky background (Moore et al., 2016). The latter case takes advantage of the high sky background in the NIR to be able to use lower cost InGaAs detectors that have higher read noise and dark current, and can be operated at higher temperatures (Simcoe et al., 2019).

Here, we present Palomar Gattini-IR, a recently commissioned NIR time domain survey at Palomar Observatory in southern California, which serves as a working demonstration of the former approach to NIR time domain astronomy. Using a small 30-cm telescope housed in a clam-shell dome, Palomar Gattini-IR achieves a field of view of 25 square degrees and surveys $\approx$ 7500 square degrees every night to a median depth of $\approx$ 16 AB mag in J band outside the Galactic plane. This produces an unprecedented 2 night cadence NIR coverage of the entire visible sky from Palomar (see Moore et al., 2019 for an overview).

This paper describes the instrument, survey modes, and data processing system for the survey, along with on-sky performance and results from the survey commissioning phase on transients and variable science. Section 7.2 summarizes the telescope optics, detector and its housing, and readout electronics. Table 7.1 provides a summary of the instrument specifications, and the nominal sky survey. Section 7.3 describes the robotic observing system and its performance. Section 7.4 describes the data processing system designed to deliver science quality data products and transient candidates in real-time. Section 7.5 describes the on-sky performance of

the instrument derived from commissioning data. Section 7.6 provides an overview of the first results on infrared transients and variables identified since the start of commissioning operations. Section 7.7 summarizes the survey status and planned developments.

7.2 Hardware

Telescope and mount

The requirement of a large areal survey speed required the use of a fast focal beam to achieve a large field view when feeding the single, moderate-sized detector that we had available for the project (Section 7.2). The aperture of the telescope was set to 30 cm by a requirement of a single epoch 5 point source sensitivity of $\approx$ 16.0 – 16.5 AB mag in J band. Gattini-IR uses a 30 cm aperture, f/1.44 catadioptric optical telescope assembly (OTA) with 6 all-spherical elements, commercially available as the Terebizh TEC300VT by Telescope Engineering Inc. The optical design was evaluated for performance at J band combined with the 18 micron pixel size of the available detector. Fortuitously, with only a slight detector focus adjustment, sub-pixel performance was simulated to be possible across the entire field over a temperature range from 0 to 30 degree Celsius over a maximum field of 7 degrees, corresponding to a detector size of 52 mm (Moore et al. 2016). The OTA was assembled and tested to be diffraction limited on-axis at a wavelength of 633 nm prior to delivery to Caltech. The telescope, mount, and cryogenic system are located inside a clam-shell dome at Palomar Observatory, which also houses a compute server controlling the robotic observing system ('scheduler node' hereafter).

However, design specifications of sub-pixel imaging and athermal focus quality over the entire detector plane have not been achieved during on-sky tests (Section 7.5). The original focusing mechanism relies on three variable screws that have to be manually adjusted to the optimal focus. The manual operation makes it difficult to settle such a fast telescope on a stable position. In addition, temporal variations in the image quality as a function of ambient temperature are not corrected dynamically during nightly operation or even revisited at regular intervals. This issue will be corrected in the final quarter of 2019 with the addition of a robotic focusing mechanism. The system is based around a circular flexure element that is pre-stressed against three linear actuators. This design provides a level of anti-backlash to the system as well as helps with variable gravity vector effects during operation at various zenith angles. The three linear actuators will be remotely controlled and adjusted on regular basis to optimize the image PSF. The focus has been fully tested

in the laboratory and gives a focus range of motion of 3 mm and a resolution of 10 μm.

The telescope and the cryogenic system housing the detector are attached to a GM3000 HPS robotic equatorial mount made by 10Micron Technology. The mount is designed to support up to 100 kg of instrument weight with a slew speed of up to 12°/s. A pointing model was constructed for the mount after telescope installation and mount balancing, using a sample of 100 bright stars placed randomly across the visible sky. The resulting pointing model produces RMS residuals of $\approx 12''$ (≈ 1.5 native detector pixels).

Detector

Gattini-IR uses an engineering grade 2K × 2K Hawaii-2RG (H2RG) detector from Teledyne with a cut-off at 1.7 μm to be capable of J-band imaging and avoid the thermal infrared background beyond 2 μm. The pixel size is 18 μm, which provides a pixel scale on sky of $8.73''$ / pixel and a field of view of $4.96° \times 4.96°$ when attached to the F/1.44 focal beam of the telescope. The mean quantum efficiency in J band is $\approx 70\%$ (Blank et al., 2011). The gain and read noise of the detector were measured in the laboratory and found to be $\approx 4.5\,e^-$/ADU and $25\,e^-$, respectively. The read noise together with the measured J band sky background with the instrument (at least $\sim 1000\,e^-$/s/pixel) allows for background limited imaging in exposures as short as ≈ 1 second (the minimum allowed by the detector electronics). The detector does not have a shutter mechanism and is thus parked horizontally (facing the dome walls) during daytime and poor weather conditions.

The detector non-linearity was measured using a constant light source in the laboratory and found to be $< 3\%$ up to 30,000 counts (136,000 e^-), which we nominally adopt as the linearity limit for the purposes of the data processing system. The detector saturates at $\approx 36,000$ counts ($\approx 160000\,e^-$). The number of hot pixels in the detector are measured periodically using darks inside the telescope dome. Due to the absence of a shutter mechanism, darks are periodically acquired in the presence of observatory staff by covering the telescope tube with an aluminum coated cap and recording images. Due to the high background in our imaging application, the requirement for low dark current is not substantial. Nevertheless, the detector has been found to exhibit dark current levels of $\approx 0.9\,e^-$/s under nominal operating conditions while hot pixels amount to 0.1% of the detector pixels.

Dead (non-linear and unresponsive) pixels are identified in the array using sky

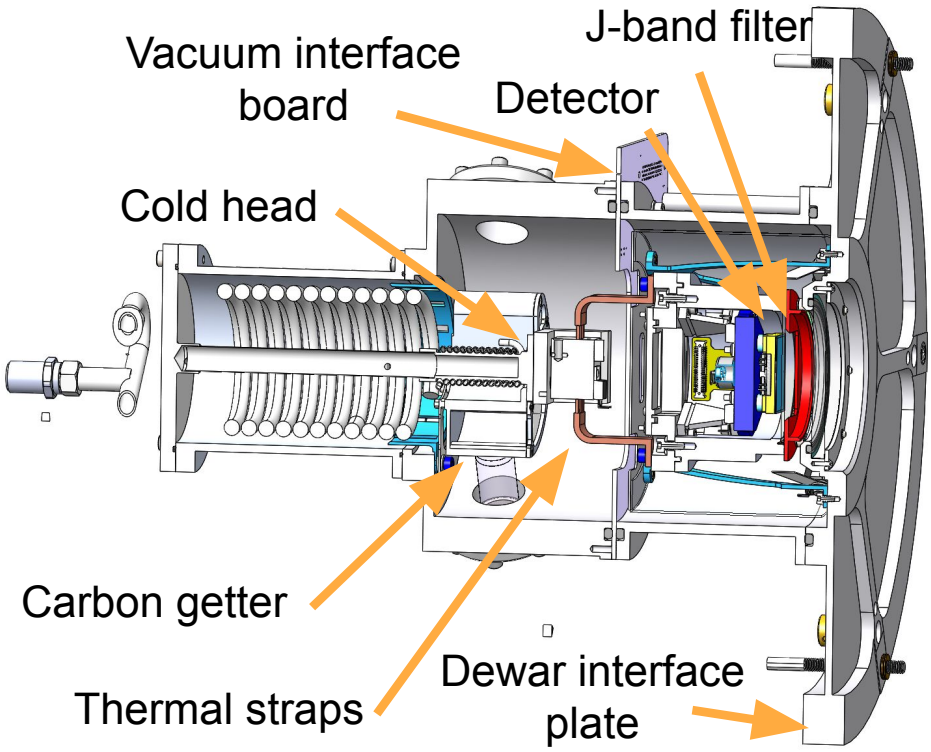

Figure 7.1: **Layout of the Gattini cryostat system**

flats with different exposure times taken during twilight at the start and end of every observing night. Dead pixels amount to $\approx$ 2.7% of the total number of pixels in the detector, including the intentionally non-responsive reference pixels that are 4 pixels deep on each edge of the detector. In addition, the detector has a triangular corner region of lower QE (measuring 700×740 pixels on the perpendicular sides, amounting to $\approx$ 12.4% of the detector area) due to the absence of an anti-reflection (AR) coating that was layered on the rest of the detector during a previous experimental phase. The region missing the AR coating was left to experimentally measure the change of the QE due to the presence of the AR coating, and has been verified to have a different zero-point (i.e. lower sensitivity) from the rest of the detector in commissioning data.

Readout electronics

The detector is read out using a detector controller system supplied by Astronomical Research Cameras, Inc. (ARC). The ARC controller chassis houses four 8-channel infrared video processor boards, a clock driver board, and a 250 MHz fiber optic timing board. Each video board contains eight identical video processors, with each

Table 7.1: **Summary of the Gattini observing system**

Survey characteristics	
Telescope	TEC300VT 30 cm
Location	33° 21′ 21″ N, 116° 51′ 54″ W
	Altitude 1712 m (Palomar Observatory)
Camera field dimensions	$4.96° \times 4.96°$
Camera field of view	24.7 square degrees
Light sensitive area	24.0 square degrees (97.2% fill factor)
Filters	Gattini-J
Median image quality	FWHM 1.2 to 2.1 pixels
Median sensitivity	15.7 AB mag outside Galactic plane ($\|b\| > 20°$)
(64.8 s, 5σ)	15.3 AB mag in the Galactic plane ($\|b\| < 20°$)

Detector array	
Make	Teledyne HAWAII2RG with 1.7μm cutoff
Size	2048×2048 pixels
Pixel size	18 μm/pixel
Plate scale	8.73″/pixel
Gain	4.54 e^-/ADU
Readout noise	25 e^-
Dark current	0.9 $e^- s^{-1}$
Typical sky background	4500 $e^- s^{-1}$
Readout channels	32
Linearity	$< 3\%$ up to 30,000 ADUs (136,000 e^-)
Saturation	$\approx$ 160000 e^-

processor consisting of multiple stages having adjustable gains and offsets and an 18-bit analog-to-digital (A/D) converter. Together, these four 8-channel video boards read all 32 outputs of the H2RG simultaneously. The video boards also contain programmable DC supplies to supply the bias voltages to the detector. The clock driver board translates digital input signals into analog output signals for driving the clocks required to control the H2RG detector. The fiber optic timing board contains a digital signal processor (DSP) which generates the timing waveforms and communicates between the ARC controller and the host computer using a duplex fiber optic link to a PCIe interface board in the host.

The H2RG detector is read out non-destructively using conventional readout, though the pixel time has been reduced from what is typically used because previous studies (Wizinowich et al., 2014) have shown improved noise performance. The pixel readout time is 6 μs, which represents 2 μs settling and 4 μs integration per pixel. The line overhead of 21 μs contains "pre-charge" pulses required by the H2RG as

well as pulses required for initializing the ARC controller's video board electronics. This amounts to a minimum frame time of about 834 ms.

Detector housing

The Gattini-IR cryostat is a custom built in-house fabricated assembly that was designed to minimize weight and volume by using 6061-T6 aluminum (Figure 7.1). The H2RG detector is mounted to a molybdenum block to match the CTE of the detector package which is cooled to about 100K by using a Brooks Poly Cold Compact Compressor charged with P-14 refrigerant. The cold head cools the activated carbon "getter" and heat is conducted away from the detector by using three braided copper thermal straps. In addition, the vacuum volume uses two room-temperature zeolite desiccants, freshly baked before pumping down the vacuum volume. Electrical connections to the vacuum volume is accomplished with the Vacuum Interface board (VIB) that carries both the detector and thermal management wiring.

Two heaters are used – a low power heater to stabilize the detector temperature, and a higher power (up to 50W, currently set to 8W) heater near the entrance window to guard against dew. The latter was installed towards the end of the commissioning period to remedy the accumulation of condensation on the window plate during periods of high humidity. The H2RG detector is optically filtered by a cold, J band interference filter. The dewar is connected to the compressor by 50 feet of armored flex hose with particular attention paid to maximizing the bend radius in an effort to protect the system from fatigue failure due to the observing cadence and all-sky motion envelope needed for Gattini-IR. To prevent the compressor from becoming too cold in the winter, a wooden enclosure with a thermostat controlled fan surrounds the compressor and uses the compressor waste heat to maintain the box temperature at 21° C.

7.3 Robotic observing system

The observing system (OS) for Gattini-IR serves as a primary control interface for the telescope, dome, mount, and detector. The OS runs on a single compute server inside the telescope dome at Palomar, hosting an Intel Xeon E5-2620V3 2.4 GHz processor with 6 cores (12 threads) and 32 GB of RAM. Figure 7.2 gives an overview of the interlinking between the OS and the data reduction server at Caltech, and the subsequent flow to science quality data products, human vetting, and follow-up.

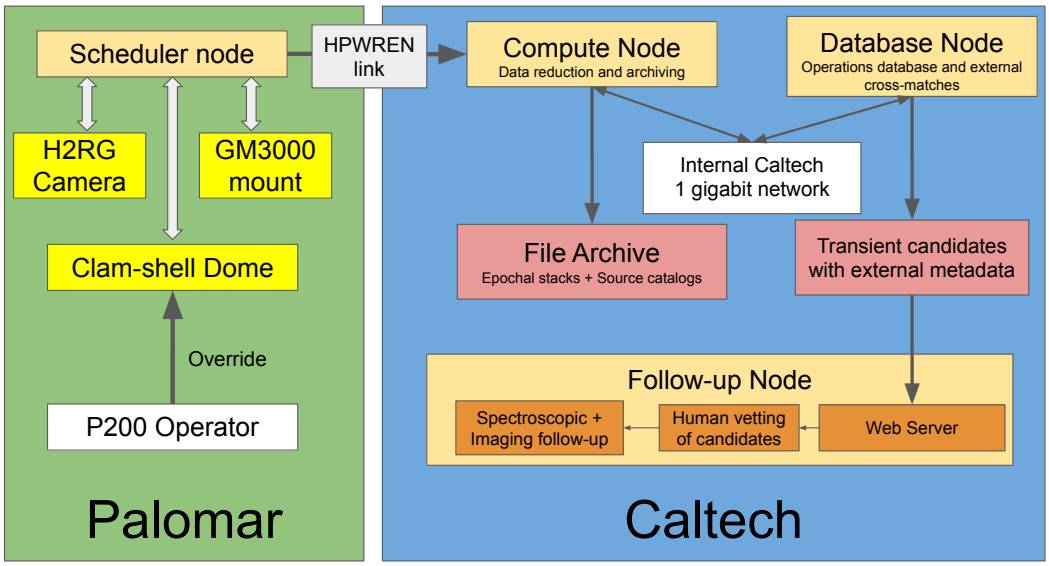

Figure 7.2: **Overview of the Gattini observing, data reduction, and follow-up system.** The green box on the left shows the observing components located at Palomar Observatory, while the blue box on the right shows the data reduction and follow-up components housed at Caltech. The light yellow boxes show the various computing servers involved in the observation scheduling, data reduction, and archiving. The observing hardware components (in light yellow) – telescope, camera, and dome are controlled with the scheduler node at Palomar. The operator at the Palomar 200-inch telescope is capable of overriding the dome status in case of poor observing conditions, which halts the scheduler operations. The compute node at Caltech is responsible for real-time data processing, while the database node hosts the PSQL server for metadata archiving and transient candidates. The compute node and data base node are linked with the internal Caltech 1-gigabit network. The red boxes show the long term science products produced in the data processing system – calibrated science images, source catalogs, and transient candidates with external cross-match metadata. The follow-up node represents an independent web server at Caltech which allows human vetting of candidates for spectroscopic and imaging follow-up downstream.

Scheduler and nominal survey operations

Nightly operations are controlled by an automated telescope scheduler adapted from the publicly-available software[1] for the Zwicky Transient Facility (Bellm et al., 2019a). Unless the Palomar 200-inch telescope operator sets a weather override, the scheduler opens the dome and observes nightly between the times of nautical twilight. The celestial sphere north of -28 degrees is divided into 1329 fields with overlaps of $6'$ between fields. The fields are separated by an average of $\approx 4.86^\circ$ in

[1] https://github.com/ZwickyTransientFacility/ztf_sim

the N-S direction and up to $\approx 4.9^\circ$ in the E-W direction, depending on declination. Under nominal survey operations, Gattini-IR observes fields over the entire visible celestial sphere from Palomar Observatory.

Each field visit consists of a set of 8 dithered exposures with an exposure time of 8.1 s each (total exposure time of 64.8 seconds per field visit). Multiple dithers were required to facilitate longer exposure times on the bright sky background, and to allow PSF reconstruction in data processing (Section 7.4) using the `Drizzle` algorithm (Fruchter et al., 2002). The amplitude of the dither is set to $\approx 3'$, which is randomized by a uniform distribution of $1'$ amplitude to sample random sub-pixel phases for individual point sources. Figure 7.3 shows a distribution of the pointing RMS in the RA and Dec direction for fields distributed over the sky. As the dither amplitude is larger than the typical pointing RMS and median offset, the entire field region is covered during the dither sequence. A minimum number of 8 dithers was selected to obtain uniform coverage of the sub-sampled pixels across the drizzled images such that $\sigma_w/m_w < 0.15$ in the output drizzled images (Gonzaga et al., 2012), where σ_w is the standard deviation of the output weight image from image reconstruction using `Drizzle` and m_w is the median weight. The exposure time per dither and number of dithers were balanced as a trade-off between maximizing the volumetric survey speed and cadence over the sky (Section 7.3).

The scheduler currently employs a greedy algorithm that minimizes slew time and airmass while prioritizing fields that have not been observed as recently. This is done by selecting for the next field for observation that has the highest value of the following metric:

$$\frac{t_{\mathrm{exp}} + t_{\mathrm{OH_{min}}}}{t_{\mathrm{exp}} + t_{\mathrm{OH}}} \times \Delta t^{0.1} \times \frac{z_{\mathrm{min}}}{z} \mathrm{HA_{weight}} \tag{7.1}$$

where t_{exp} is the exposure time (in seconds), t_{OH} is the overhead (in seconds, including slew, settle, and camera initialization/readout) to slew from the current field to the next, $t_{\mathrm{OH_{min}}}$ is the minimum field slew overhead measured in operations, Δt is the time since the field was last observed (in days), z is the airmass, z_{min} is the minimum observable airmass allowed by the mount, and $\mathrm{HA_{weight}}$ is a weight factor based on the hour angle of the field. The exposure time and overhead factors serve to maximize the areal survey rate and the Δt prioritizes fields in proportion to the time elapsed since the prior observation. The airmass factors are used to encourage observations to occur at the local meridian. The hour angle factor prioritizes setting fields because this would maximize the single-pass sky coverage with the original survey rate which was intended to be faster than sidereal. Figure 7.4 shows a

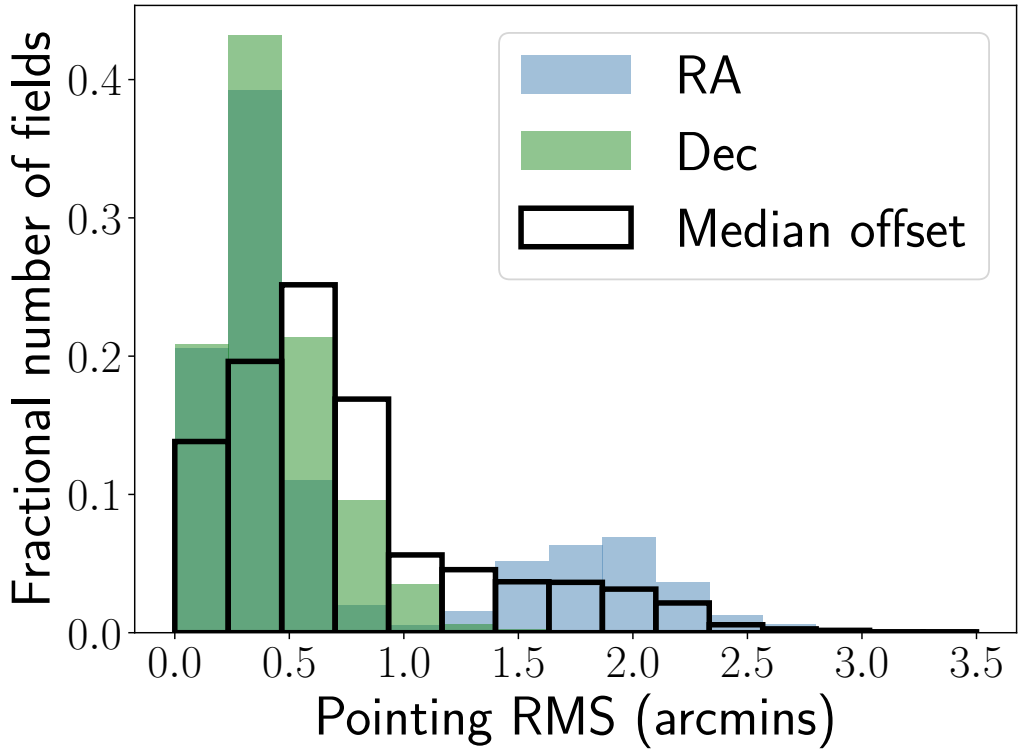

Figure 7.3: **Histogram of the pointing RMS residuals of the mount across fields over the entire sky – both in the RA axis and in the Dec axis.** The white blocks show the distribution of the median total offset across all fields in the sky.

distribution of the slew distances and observation airmasses from data taken during six months of the commissioning period using this scheduling algorithm. As shown, the scheduling algorithm prioritizes observations that minimize the slew distance and airmass of the observation.

The primary overhead during observing sequences is the time taken to move between individual dither positions in a dither sequence given the settling time of the mount, since the detector readout time is small (≈ 0.9 s). Figure 7.5 shows a distribution of the time between the start of subsequent dithered exposures in dither sequences taken over several nights. The distribution has a narrow peak around the median time of ≈ 13.0 s, including the exposure time of 8.1 s amounting to a dither overhead of $\approx 60\%$. Figure 7.5 also shows a distribution of the time between the start of exposures of successive fields during a night, which includes the exposure time inside the field (64.8 s), the time taken to dither between dither positions inside the field, and the slew time to the next field. The distribution also has a sharp peak near the median time of ≈ 115 s. Figure 7.6 shows a distribution of the observing

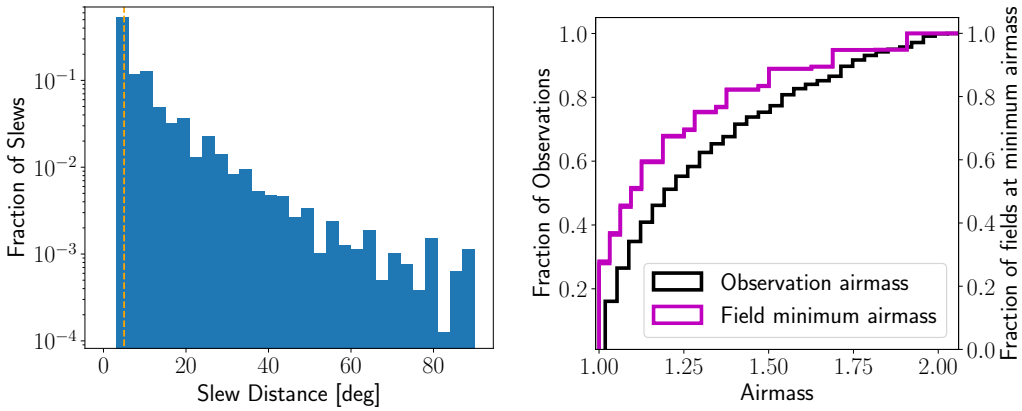

Figure 7.4: **Performance of Gattini-IR scheduler in terms of slew distance and observed airmass**. (Left) Distribution of slew distances for the nominal survey over the course of six months of the commissioning period. The scheduler prioritizes field slews that involve smaller slews. The dashed orange line shows the average field spacing of 4.9°. (Right) Cumulative distribution of airmass for observations taken during the commissioning period. 80% of observations are performed at airmass < 1.6 owing to the prioritization of fields at low airmass. The magenta line shows the cumulative distribution of minimum airmass in the Gattini-IR field grid, to compare the performance of the scheduler to the theoretical best possible in terms of airmass.

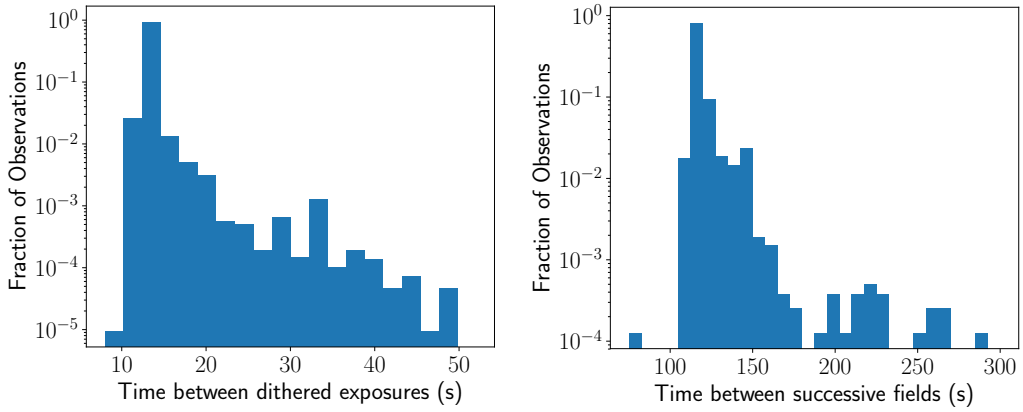

Figure 7.5: **Performance of Gattini-IR scheduler in terms of time between dithered exposures and time between successive field visits**. (Left) Distribution of times between successive dithers in a field visit, including the nominal exposure time of 8.1 s. The median time between start of exposures is 13.0 s, accounting for the overhead due to dithering the telescope. (Right) Distribution of the time between the start of observations of successive field visits in nightly operations. The elapsed time includes the total exposure time (64.8 s), dithers between exposures, and the slew across the successive fields. The median time between the start of successive field observations is 113.0 s, accounting for the dithers inside each field and the time to slew between successive fields.

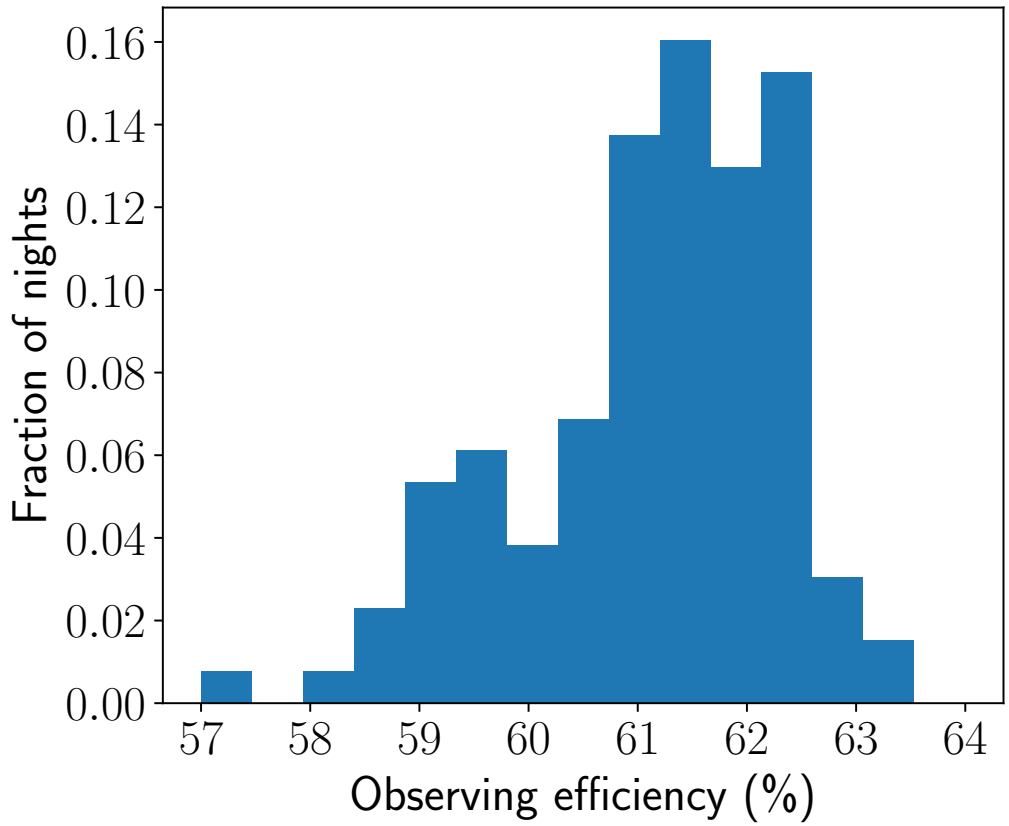

Figure 7.6: **Distribution of the observing efficiency of the Robotic Observing System on nights during the commissioning phase.** The median observing efficiency is ≈ 61%, accounting for the overheads due to the readout time, dithers inside each field, and slewing between fields (Section 7.3).

efficiency of the system, defined as the total exposure time in a night as a fraction of the time the telescope was observing. The overall observing efficiency distribution has a median of ≈ 61%, accounting for all the overheads for dithers and slewing between fields.

Volumetric survey speed and cadence

We show the volumetric survey speed (Bellm, 2016) for a Type Ia SN (peaking at $M = -19$) as a function of the exposure time per dither in Figure 7.7, for different choices of the number of dithers folding in the measured dither and field slew overheads. The volumetric survey speed increases with a smaller number of dithers, and hence we select 8 dithers as a minimum to support the PSF re-construction downstream. For the choice of 8 dithers per field, the exposure time that maximizes the volumetric survey speed is ≈ 17s per dithered exposure, and a corresponding

areal survey rate of $\approx$ 470 sq. deg. hr^{-1} with an all sky cadence of $\approx$ 4 nights. Adopting an exposure time of $\approx$ 8.1s (equal to 9 times the default frame readout time) instead, we found the volumetric survey speed to be only $\approx$ 5% smaller, while providing an areal survey speed of $\approx$ 800 sq. deg. hr^{-1}. This configuration allows coverage of the entire visible sky ($\approx$ 15000 square degrees) over two nights (assuming an average of $\approx$ 9 hours per night). On the other hand, increasing the cadence to cover the entire sky over a single night would require reducing the exposure time per dither to be $<$ 2 seconds, where the volumetric survey speed would be 50% smaller than the maximum volumetric speed.

We thus adopt eight dithers of 8.1 s each as the nominal observing strategy for the survey. The choice of all sky coverage is motivated by the aim of performing a completely untargeted time domain survey as the first infrared counterpart to ongoing optical time domain surveys. The 2-day cadence enables early discovery and follow-up of supernovae in nearby galaxies and large amplitude transients such as classical nova outbursts within the Galaxy. This cadence also allows the survey to obtain well sampled NIR light curves of these transients, while building up a large number ($\approx$ 100) of epochs for variable star science in each year of operations. Figure 7.8 shows a distribution of the average cadence over the visible sky for a typical month of observing. The cadence is $<$ 3 nights for 90% of visible fields in the sky, while the median cadence is two days (for $\approx$ 60% of fields). A small fraction of fields (8%) near the north celestial pole have typically shorter cadence of $\approx$ 1 day owing to their longer visibility during the night. The higher cadence in these fields allows the survey to probe the phase space of shorter timescale phenomena in the infrared time domain sky. Figure 7.9 shows the sky distribution of the cumulative number of field visits since the start of the survey commissioning period. Fields near the north pole have the largest number of visits due to their long visibility window from Palomar Observatory.

Target of Opportunity observations

The scheduler is designed to respond to target of opportunity (ToO) triggers to respond to time critical events such as gravitational wave triggers and neutrino alerts. ToO requests are submitted as a list of fields to be observed for a specified integration time. In the case of gravitational wave and neutrino triggers, the field tiling is optimally determined using the algorithm presented in Coughlin et al., 2019a and forwarded to the scheduling system via the GROWTH Marshal (Kasliwal et al., 2019), including a start and expiry date for the request. A `cron` job on the

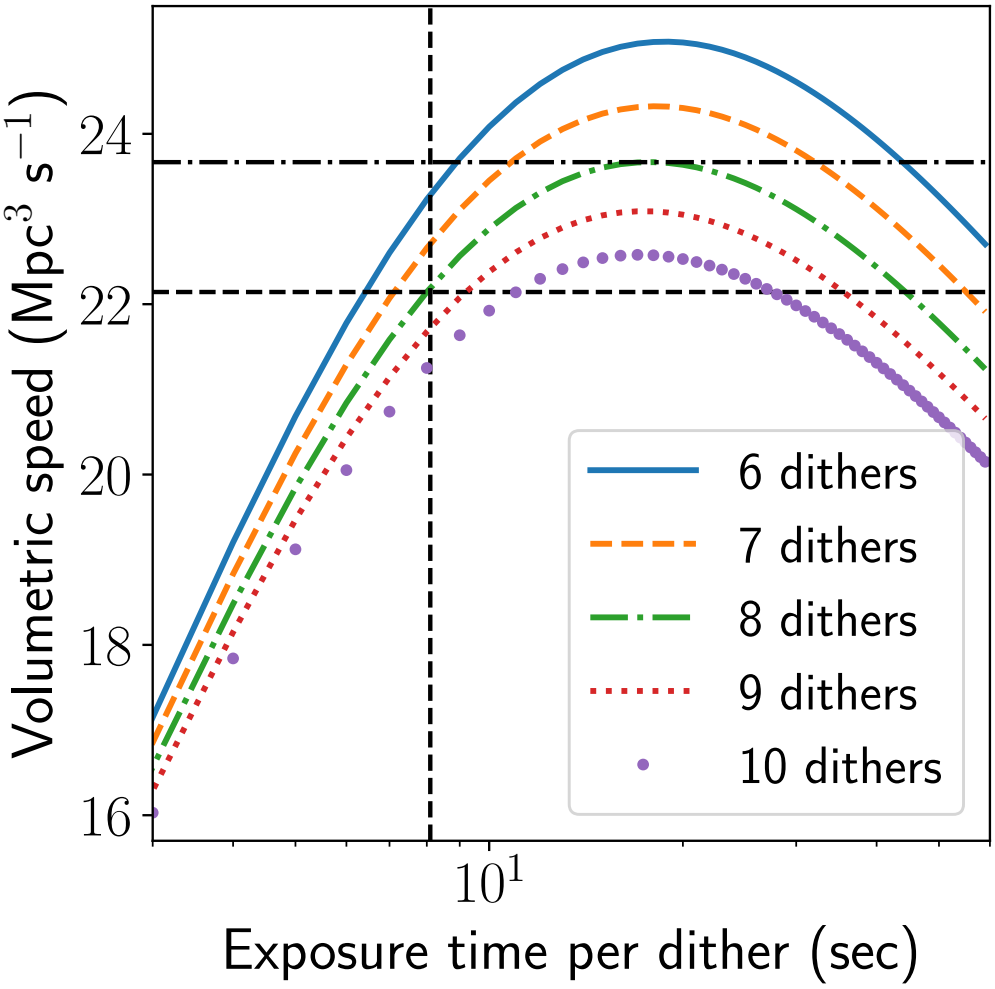

Figure 7.7: **Volumetric survey speed of the Gattini observing system for a fiducial Type Ia SN peaking at $M = -19$, assuming a limiting magnitude of 16 AB mag.** The survey speed is plotted as a function of the exposure time per dither folding in the overheads for dithering and slewing across fields. The different line styles correspond to different number of dithers as indicated in the legend. The horizontal and vertical dashed black lines correspond to the survey strategy adopted for the survey, while the black dot-dashed line shows the maximum volumetric survey speed possible for the adopted number of 8 dithers.

scheduler server periodically checks for new ToO requests every 5 minutes. In case a new ToO request is found, the scheduler interrupts the nightly survey after finishing the set of dithers on the field being observed.

Once triggered, the ToO scheduler checks if the list of requested fields in the ToO are observable (above airmass 2.5). If this condition is satisfied, the telescope slews

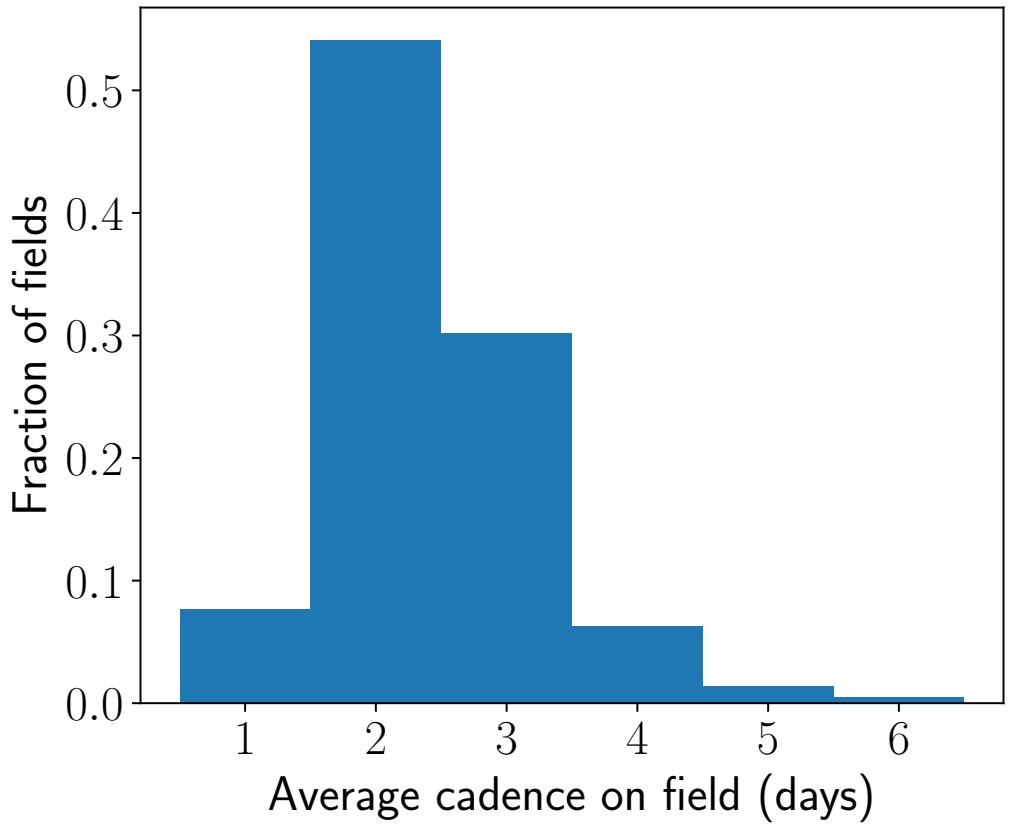

Figure 7.8: **Distribution of the average cadence per field (in days) for the visible sky in the month of September 2019.** The cadence is $\approx 1-3$ days over $\approx 90\%$ of visible fields while it is shorter (≈ 1 day) for fields near the north celestial pole due to their longer visibility.

to the field and begins dithered exposures of the nominal 8.1 s exposure time such that the total integration time equals the requested exposure time on the field. Each field in the submitted ToO is observed until no more observable fields are left, after which the scheduler resumes the nightly survey. The list of fields in each submitted ToO is checked every 5 minutes until all the fields in the ToO are observed or the ToO has reached its expiry date.

7.4 Data processing system

In this section, we describe the Gattini Data Processing System (GDPS), a highly parallelized real-time data reduction system running at Caltech to support fast delivery of science quality data products from the survey. Figure 7.2 provides an overview of the flow of data from the scheduler node at Palomar to the GDPS at Caltech. Figure 7.10 provides an overview of the data reduction within the GDPS. The

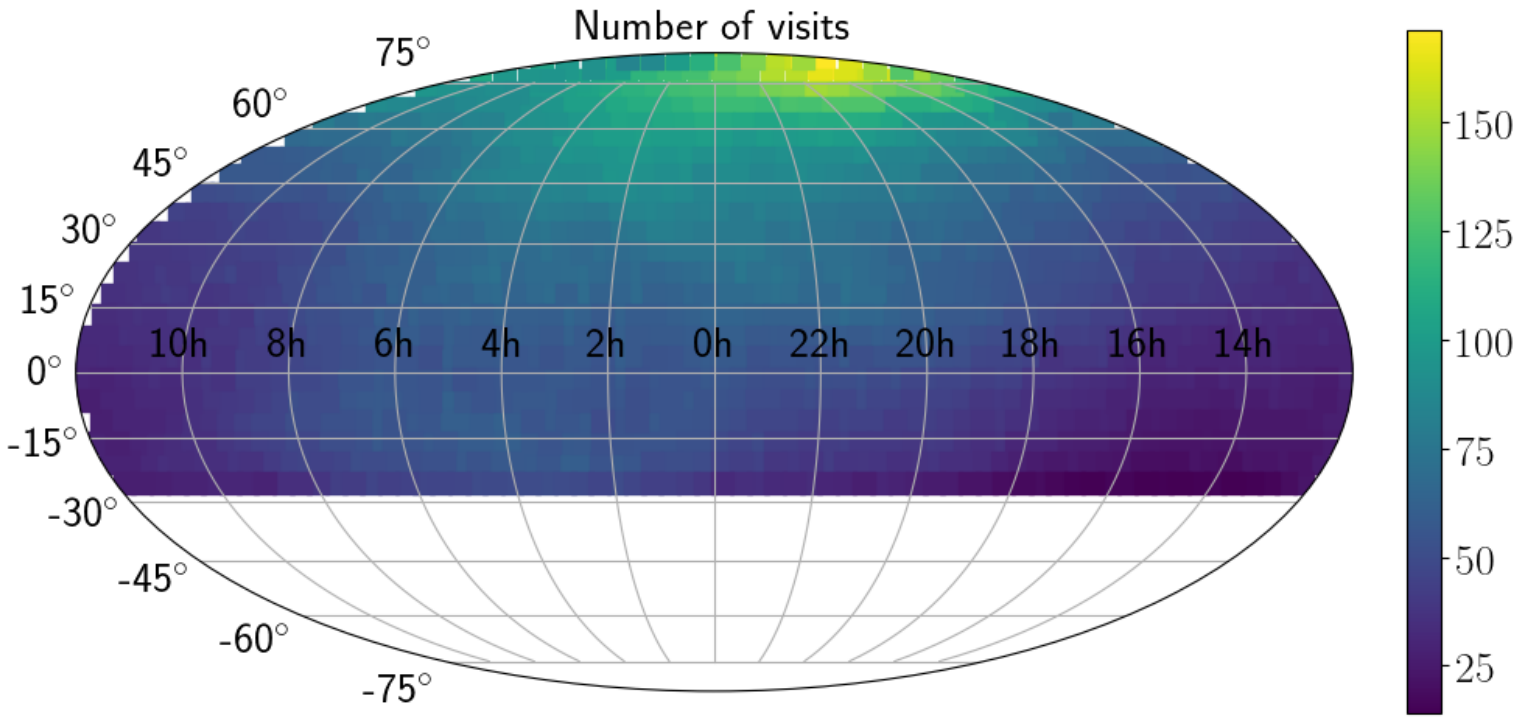

Figure 7.9: **Sky distribution of the cumulative number of field visits since the start of the commissioning period, as of 2 October 2019.** Fields near the north pole were visited the largest number of times due to their long visibility window from Palomar Observatory.

GDPS was developed completely in `python` and uses open source tools available from several `python` packages and the Astromatic suite of software (Bertin, 2006, 2011; Bertin et al., 1996). The GDPS is supported by a `Postgre-SQL` (PSQL) based database (DB) system[2] storing metadata for every step in the image reduction process. The code was derived from a multi-purpose near-infrared image reduction pipeline developed originally for the Wide field infrared camera (WIRC) on the Palomar 200-inch telescope (and later adapted to several other small field-of-view optical and near-infrared imagers), which we briefly describe in Appendix 7.8.

The basic requirements for the pipeline were to deliver science quality data products, including calibrated science images from raw images taken on sky, and transient candidates from difference imaging in real-time to support timely follow-up observations of transients. In addition, the GDPS monitors quality metrics for data taken during nightly operations and maintains DBs to allow for long-term storage and efficient access of data products generated from the system. The metrics are used to support light curve generation on epochal stacks and difference images. Although the epochal stacked images, calibrated source catalogs, and difference photometry are the primary data products for users, we also store a number of intermediate files to support auxiliary day-time tasks such as reference building, sky-flat generation, and dead pixel masking.

The pipeline was developed to run on a dual unit Intel Xeon E5-2620V4 2.1 GHz computing node ('compute node' hereafter) with a total of 16 cores (32 threads) and 64 GB of RAM, heavily utilizing parallelized operations to speed up processing during night-time operations. The `PSQL` DB is hosted on another server ('database node' hereafter) that was initially designed for testing purposes, and hosts an Intel Xeon E5-2620V3 2.4 GHz processor with 6 cores (12 threads) and 32 GB of RAM. Tables on the DB node are updated in real-time across the internal Caltech 1-gigabit network during nightly operations (Figure 7.2), and are backed up to a remote server on a daily basis. These two servers support the data reduction system in addition to the scheduler node, which runs the night time scheduler controlling the dome, telescope, and camera operations.

Processing architecture

Figure 7.10 provides an overview of the data processing flow within the GDPS. The data reduction flow for the system proceeds in five steps – i) image pre-processing, ii)

[2] `https://www.postgresql.org/`

astrometric solutions, iii) stacking of dithered exposures, iv) photometric solutions and v) difference imaging, which are performed sequentially when a new set of raw images are received. Although each step is performed sequentially on the raw incoming data, the processing of multiple observed fields within each step is parallelized with 30 threads to support the requirement of real-time processing.

Overall, the GDPS is controlled by a watchdog program that looks for new incoming images from the telescope and performs the data reduction through each of the steps mentioned above, while recording metadata for raw and intermediate data products at each step of the pipeline. At the end of the night, the watchdog accumulates the metadata and quality metrics for the data acquired during the night, including nightly sky coverage, image depths, and PSF quality, while performing accountability checks on the number of files received and ingested through each step in the pipeline. These metrics are sent to the members of the project in a summary email. We summarize the processing architecture below and provide detailed descriptions in the following sections.

- Raw data received from the scheduler node are initially de-trended and then digitally split into four quadrants of 1044×1044 pixels each (corresponding to a size of $2.5^\circ \times 2.5^\circ$ on sky), including an overlap (of 10 pixels = $87''$) between the common edges to avoid missing sources that are split between the quadrant edges (Section 7.4).

- An astrometric solution is derived for all the image quadrants produced from a single field visit i.e., 32 images from 8 dithers in four quadrants in the nominal observing strategy[3] (Section 7.4).

- The astrometric solutions are used to stack the processed images (Section 7.4) on a per-quadrant basis resampled to a pixel scale half of the raw pixel scale of the detector (thus producing stacks which are 2088×2088 pixels in size) using the Drizzle algorithm (Fruchter et al., 2002).

- The stacked quadrant images are again digitally split up into four sub-quadrants containing 1044×1044 resampled pixels each ($\approx 1.25^\circ \times 1.25^\circ$ on sky), including the same overlap between the sub-quadrants (of $87''$ or 20 pixels in drizzled images). Figure 7.11 shows the layout of the detector plane with

[3]Since the observing strategy involves acquiring multiple dithered exposures (8 nominally) over a single field, the subsequent processing (astrometry, stacking, photometry, and difference imaging) proceeds only after all of the dithers for a given field have been received from the scheduler node.

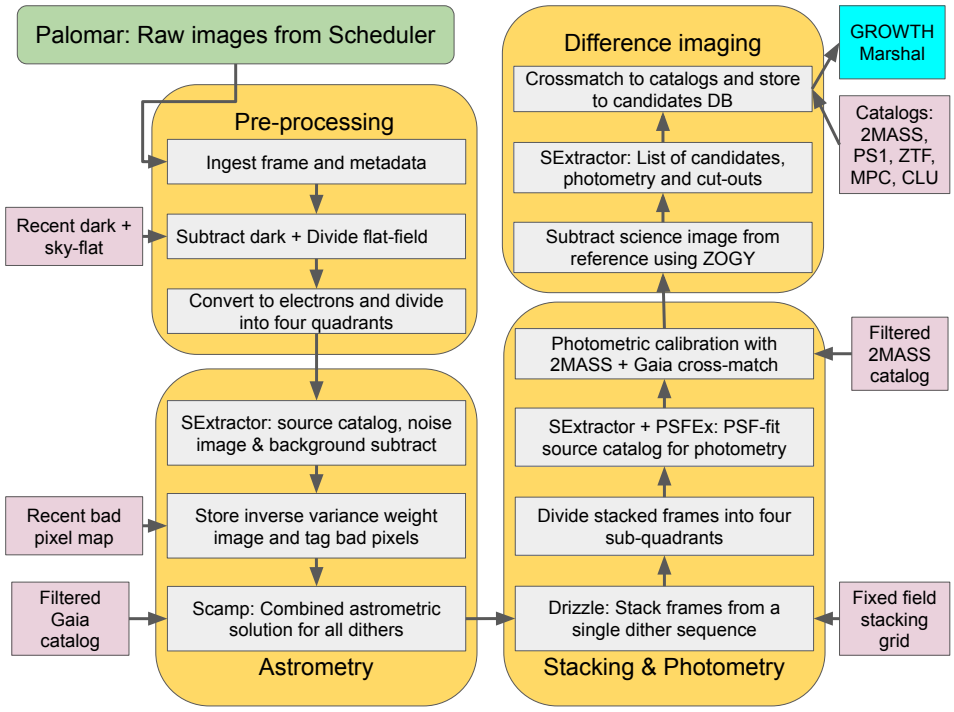

Figure 7.10: **General reduction flow for the Gattini data reduction system.** Boxes in yellow show the two automatic codes that perform the observing and reductions – the data reduction robot and the scheduler. Boxes in grey show the major steps in the data reduction flow, while boxes in cyan show external input catalogs to facilitate various processing steps. Green boxes show the major outputs from the pipeline – PSF-fit light curve catalog and subtraction candidates.

respect to the sky. Photometric solutions are derived on the split sub-quadrants (Section 7.4).

- Transient candidates are identified from difference imaging using the ZOGY algorithm (Zackay et al., 2016). These sources are passed through a machine learning (ML) classifier and cross-matched to several all-sky catalogs and known solar system objects from the Minor Planet Center. Candidates are subsequently uploaded to a web-portal for human vetting (Section 7.4).

The step-wise design for splitting up the raw images into 16 sub-images as the final products was motivated by several reasons that were tested during the commissioning phase:

1. Typical images exhibit a large variation of the PSF and sky-background over the large $5^\circ \times 5^\circ$ field of view, and hence better photometric solutions and

difference imaging is obtained by splitting up the image into smaller sections covering 1/16 of the total detector area, where the PSF and background are locally uniform.

2. Splitting up the raw images into four quadrants before the astrometric solution derivation produces images that are small enough such that the distortion in the field is small but also large enough so that a sufficient number of sources remains to derive a robust solution (this is particularly important under non-ideal observing conditions with low sky transparency). Dividing the images into 16 pieces at the start of the processing (before astrometry) increased both the failure rate and processing time for the reductions.

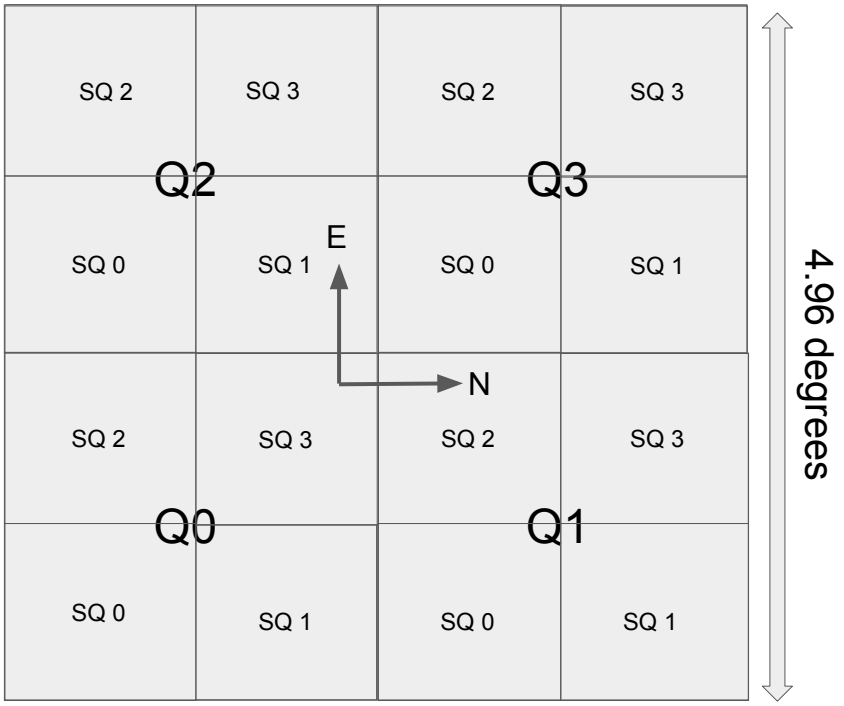

Figure 7.11: **Detector layout for the Gattini quadrants and sub-quadrants.**

Data transfer

Raw images from Gattini are recorded as FITS images, along with comprehensive header information including meteorological conditions (temperature, pressure, humidity, wind speed/direction) and ephemeris information (airmass, sun and moon positions, estimated sky brightness). A quick astrometric and photometric solution is performed to allow real-time correction of the telescope position and an estimate of the sky transparency. The raw FITS images contain 2048×2048 pixels stored as

2 byte short integers, resulting in an image size of $\approx$ 8.1 MB each. The total amount of raw data acquired in a full night of observing is $\approx$ 20 GB. Raw data are robotically acquired by the observing system under safe observing conditions and saved to disk on the scheduler node inside the telescope dome. Subsequently, the observing system transfers the images to the data processing server housed at Caltech (using an `rsync`-based synchronization running every minute) via the NSF-funded High Performance Wireless Research and Education Network (HPWREN) administered by the University of California San Diego. The volume of raw data is small enough to be transferred in real-time to Caltech (transfer time of $\lesssim$ 1 second per image compared to the image acquisition time of $\approx$ 10 seconds).

Image pre-processing

The metadata for the raw images are ingested into the `PSQL` DB followed by de-trending of the raw images. De-trending involves subtraction of the most recently acquired dark frame from the raw image followed by flat-fielding with the most recently made sky flat (Section 7.4) by querying metadata for calibration frames stored in the DB. Images are then digitally split into four overlapping quadrants, with an overlap size of 10 pixels (corresponding to $\approx 1.5'$ on sky) between quadrants sharing common edges. The image quadrants are stored to disk and metadata are recorded to the DB. Since the data processing was designed such that each quadrant corresponds to a fixed position in sky coordinates, the position of each quadrant has to be rotated by 180° depending on the side of the meridian of the equatorial mount i.e., the raw image is rotated by 180° for all images taken on the rising side of the meridian, while the orientation is left as is for observations taken on the setting side of the mount (Figure 7.11).

The pre-processed quadrants are stored as 32-bit floating point numbers, and are fed to the Astromatic package SExtractor (Bertin et al., 1996) to create a source catalog for the image and produce a corresponding background subtracted image. The detection threshold for point sources is set to 5σ in the de-trended image using the prescription in Zackay et al., 2017. Background subtraction is performed using a spatial median filter using a box size of 32×32 pixels ($\approx 5 \times 5'$ on sky) to remove the bright spatially varying background in J band. The source catalog is saved to support astrometric calibration in the subsequent steps. A background RMS map is also generated during the same SExtractor run and saved to disk with locations of known bad pixels (see Section 7.4) masked. The background RMS maps are used to generate inverse variance weight maps for stacking individual dithers into a single

image.

Astrometric calibration

Astrometric calibration is performed with respect to the Gaia DR2 catalog (Gaia Collaboration et al., 2018), using the pre-exisiting cross-match table between 2MASS and Gaia DR2 available as a part of the Gaia DR2 release (Marrese et al., 2019). The list of astrometric calibrators are stored as pre-partitioned static binary FITS tables ordered by field numbers since the observing is performed on a fixed sky grid. Only sources with 2MASS J magnitudes between 7 and 13 are used for astrometric calibration. In order to select a pure sample of stars (i.e. point sources), we require that all astrometric calibrators have a non-zero proper motion ($> 3\sigma$) in the Gaia DR2, do not have a corresponding counterpart in the 2MASS Extended source catalog (Jarrett et al., 2000), and are not confused in the Gaia - 2MASS cross-match solutions (i.e., `number_of_mates = 0` and `number_of_neighbours = 1`). Figure 7.12 shows a distribution of the number of astrometric calibrators per field quadrant, showing a minimum of a few hundred astrometric calibrators.

All image quadrants acquired as part of a single dither sequence on a field are astrometrically solved in a single run of `Scamp` (Bertin, 2006). For the nominal observing strategy of 8 dithers per field[4], this involves the solution of 32 image quadrants per execution of `Scamp`. The astrometry is solved to derive a common astrometric solution for all the dithers in a given quadrant using a third order distortion solution. The distortion coefficients are stored using the *TPV* convention and written to the headers of the image quadrants, and recorded in the DB. Images for which the astrometric solutions fail are not processed further downstream. Astrometric failures are nearly zero for 70% of nights, while the highest observed failure rate can be $\approx 25\%$ for images acquired through clouds and non-photometric conditions. We discuss the accuracy of the astrometric solutions in Section 7.5.

Stacking

Image quadrants acquired in each dither sequence are stacked using the `Drizzle` algorithm (Fruchter et al., 2002). Briefly, Drizzle resamples input images on to a user specified output grid with the option of shrinking each pixel by a user-defined parameter called `pixfrac`. `pixfrac` specifies the linear fraction by which each side of the input pixels are shrunk before co-addition. While smaller values of `pixfrac` produce sharper PSFs, smaller values of `pixfrac` result in uneven coverage in the

[4]Larger number of dithers may be used for targeted observations of ToO fields.

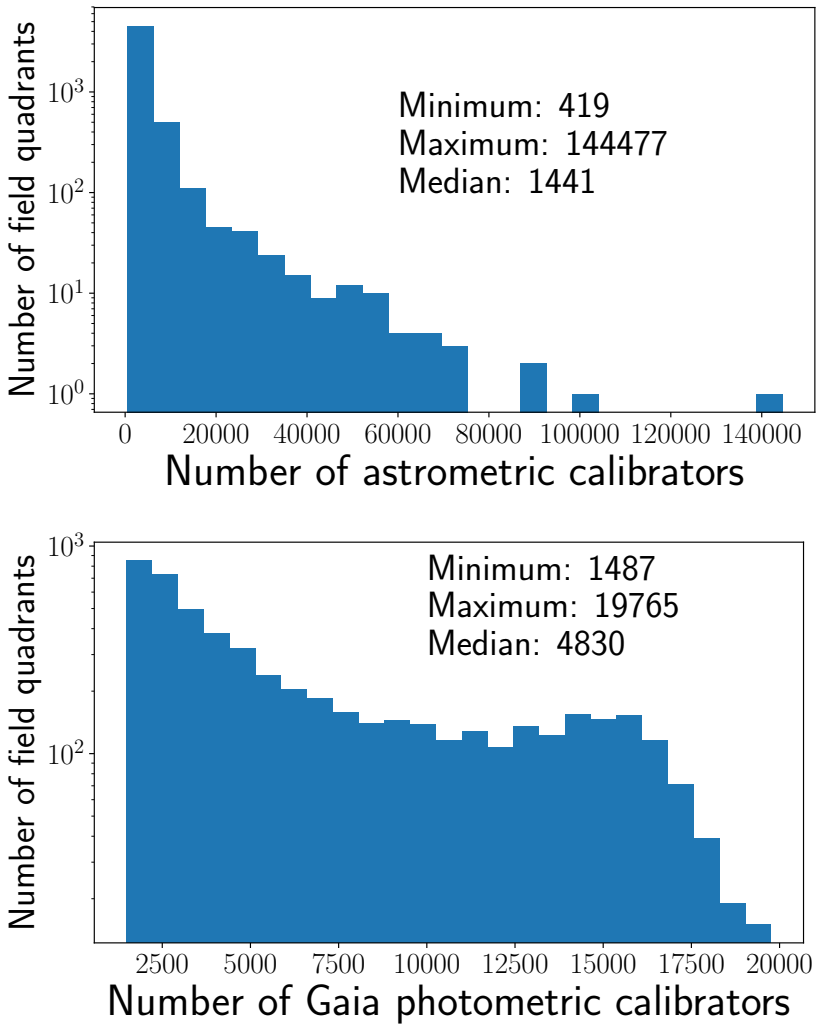

Figure 7.12: **Statistics of astrometric and photometric calibrators used in the Gattini-IR data processing system**. (Top) Histogram of number of astrometric calibrators per field quadrant, based on the Gattini pointing grid. (Bottom) Histogram of number of photometric calibrators per field quadrant, selecting sources that are isolated (no sources in 2MASS within 12″). The selection criteria for the calibrators are given in the text.

output pixels if the dithers are not placed ideally. The pixel scale of the output grid is determined by the `scale` parameter, which determines the linear size of the output pixels with respect to the input pixels. `Drizzle` also produces an output weight image, which reflects the number of images that were sampled into each pixel during the resampling. In order to reduce artifacts associated with pixel shrinking and uneven coverage, Gonzaga et al., 2012 recommend $\sigma_w/m_w < 0.15$, where σ_w is the standard deviation in the resampled weight image and m_w is the median of the

resampled weight image.

In the GDPS, the input images are resampled on to a fixed output grid with a pixel size half of the native pixels ($\approx 4.3''$), corresponding to a `scale` of 0.5. The output grid is determined from the fixed sky grid of fields using astrometric solutions of on-sky images from the telescope. We use a `pixfrac` parameter of 0.9 that controls the shrinkage of the pixels before resampling on to the output grid (i.e., the raw pixels are shrunk to 90% of the size on each side before adding on the output grid). Smaller values of `pixfrac` produce uneven coverage over the smaller pixels in the output grid, resulting in a larger dispersion in the weight over the output pixels (see Gonzaga et al., 2012 for a discussion). As the mount pointing is not accurate enough to provide sub-pixel pointing adjustments during the dither sequence, we resort to using a random sampling of sub-pixel phases during the dither sequence. A `pixfrac` of 0.9 was found to be adequate to produce Nyquist sampled images that are limited by the focusing of the optics.

The astrometry-solved and background subtracted input quadrant images are resampled to the fixed output WCS grid using a `python` implementation of the `Drizzle` algorithm[5]. In order to remove effects from cosmic rays, hot pixels, moving planes, and satellites, the `Drizzle` code was modified to perform sigma-clipping on the resampled images to reject outliers on a per-pixel basis. The stacking of the images is performed using a sigma-clipped (at 2.5σ), inverse-variance weighted mean of the resampled input images. The stacked image quadrants are then split further into four sub-quadrants for photometry and image-subtraction downstream. The splitting is done as shown in Figure 7.11, including a 20 pixel (10 raw pixel) overlap between the sub-quadrants, while transforming the WCS between the parent quadrant and child sub-quadrants. Both the resampled image sub-quadrants and their corresponding weight images are stored on disk as floating point 32-bit images for long term archiving in a single Multi-Extension FITS image, and quality metrics are recorded in the DB.

Photometric calibration

Photometric calibration is performed against the 2MASS point source catalog (Cutri et al., 2003) cross-matched to Gaia DR2, using a subset of the sources that were used for astrometric calibration. The photometric catalog includes additional filters to select a list of isolated stars with J magnitudes between 9 and 16 that are not

[5] `https://github.com/spacetelescope/drizzle`

saturated in images. 'Isolated' stars were defined to be sources that did not have any neighbors in 2MASS (regardless of any cuts in the astrometric catalog) within a radius of 12″ (3 Gattini drizzled pixels) to avoid confused sources. The stacked image sub-quadrants are fed as inputs to the photometric calibration pipeline. Figure 7.12 shows a distribution of the number of photometric calibrators per field quadrant. As in the case of the astrometric calibrators, the photometric calibrators are also stored as static pre-partitioned FITS binary tables per field on sky.

The stacked image sub-quadrants are fed as inputs to the photometric calibration pipeline, which first creates a SExtractor catalog of detected sources along with a set of 15×15 pixel cutouts for each detected source. The SExtractor catalog is fed to PSFEx (Bertin, 2011) to generate a PSF model of 15×15 drizzled pixels using the sources detected in the field. The PSF model is saved to disk for supporting difference imaging further downstream. The PSFEx model is then fed to a second run of SExtractor to generate a PSF-fit photometry catalog for the drizzled stack. Aperture corrections are computed between PSF-fit magnitudes and apertures of different sizes and recorded in the FITS headers. The PSF-fit catalog is used to select a list of unsaturated sources for photometric calibration, that are at least 40 pixels away from the edges of the image, and with SExtractor parameter `FLAGS` = 0 and `FLAGS_MODEL` = 0 and `SNR` > 10. The crossmatch proceeds only if there are at least 5 good cross-matched sources in the image.

The instrumental PSF and catalog magnitudes are fit with a linear solution of the form:

$$m_{\mathrm{TM,\,J}} - m_{\mathrm{ins}} = ZP + c\,(m_{\mathrm{TM,\,J}} - m_{\mathrm{TM,\,H}}) \tag{7.2}$$

where $m_{\mathrm{TM,\,J}}$ and $m_{\mathrm{TM,\,H}}$ are the 2MASS magitudes in J and H filters, respectively, m_{ins} is the instrumental magnitude, ZP is the zero-point of the image and c is the color coefficient to convert from the Gattini system to the 2MASS (TM) system. The solution is derived by fitting a linear polynomial to the magnitude differences as a function of the source color (so the intercept is the zero-point and the slope is color coefficient). The extreme outliers (1 percentile) in the fit are eliminated first and a solution is derived. Subsequently, outliers that are more than 4 sigma away (typically < 2% of the total number of stars) from the best-fit solution are clipped again and the final solution is re-derived. The photometric solution is recorded in the header of the image sub-quadrant and the DB, including quality metrics for data quality filtering. The PSF-fit source catalog is saved to disk and used to support light curve generation for sources detected across multiple-epochs. We discuss the

accuracy of the photometric solutions in Section 7.5.

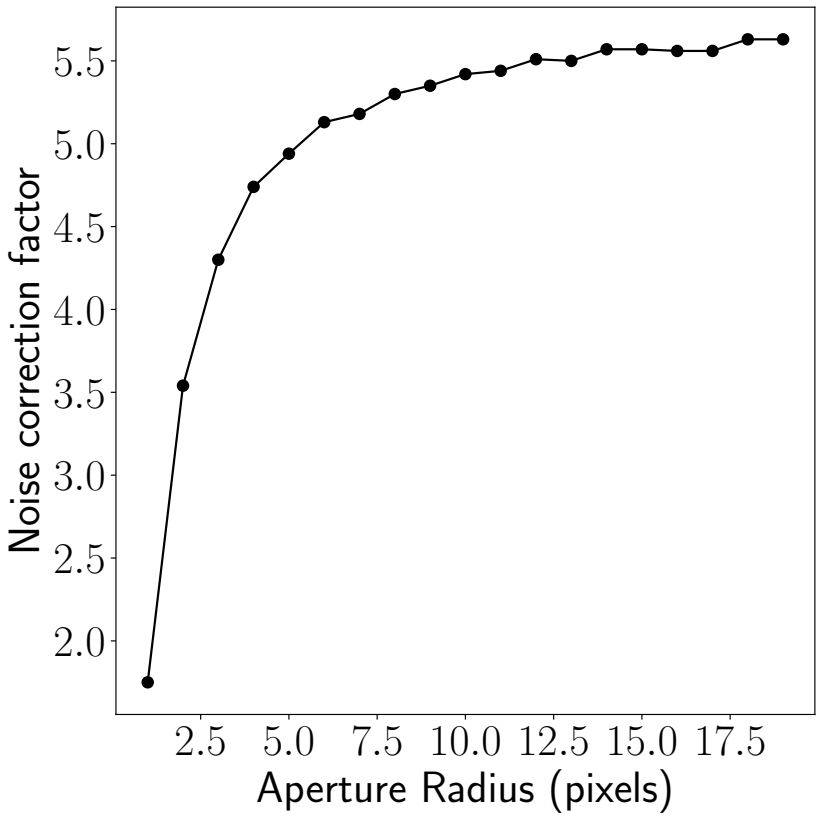

Figure 7.13: **Correction of correlated noise in the drizzled images produced by the Gattini-IR data processing system**. Noise correction (multiplication) factor as function of aperture size for typical Gattini drizzled images, as derived from Monte Carlo simulations.

Image depths and correlated noise

The pixel reconstruction and resampling procedure used in `Drizzle` leads to correlated noise between adjacent pixels in the output image. The noise correlation leads to underestimation of the photometric uncertainties in the PSF-fit source catalogs, and correspondingly, an overestimation of the depths of the images. In order to estimate the correction to the noise RMS in the images due to correlated noise, we use the prescription used for the WISE survey[6]. The GDPS uses simulated white noise images that are drizzled to an output grid using the same dither pattern, `pixfrac` and `scale` parameters as in the GDPS operations to correct for the correlated pixel noise in the output photometric catalogs, estimates of image depths, and the noise in the difference images produced downstream.

[6] `http://wise2.ipac.caltech.edu/staff/fmasci/ApPhotUncert_corr.pdf`

Briefly, a Monte-Carlo simulation is performed for estimating the PSF-flux uncertainty correction by calculating PSF-fit fluxes at random locations in the simulated drizzled images using the PSF model for the input image. The variance in these measurements are then compared to the flux uncertainties expected from uncorrelated pixel noise, and a noise RMS rescaling factor is computed to inflate the uncertainties for the PSF-fit photometry fluxes. The same simulation is used to estimate the correction for the aperture photometry fluxes by measuring the aperture summed fluxes at random locations in the simulated drizzled images and computing the rescaling factor expected from uncorrelated noise. Figure 7.13 shows the estimated scaling of the noise RMS of the image as a function of the aperture size used for photometry. The correction factor increases for large aperture sizes, but flattens beyond a radius of ≈ 5 pixels due to the correlation length of the resampling process. The correction factors are used to correct the estimated limiting magnitude of the epochal stacked images and stored in the FITS headers of the calibrated image sub-quadrants and the DB.

Difference imaging and transient extraction

Photometrically calibrated science images are fed to the image differencing pipeline if a good quality reference image exists for the field and if the photometric solution quality flags suggest that the image was acquired under good observing conditions (see Section 7.5). The difference imaging pipeline starts by preparing the input science and reference images by cross-matching the PSF-fit source catalogs to compute the relative flux-scaling and astrometric uncertainty between the two images. Since both the science and reference images are resampled on to the same fixed sky grid, only a spatial differential background is subtracted from the input images before subtraction with the ZOGY algorithm (Zackay et al., 2016). The science and reference image uncertainty maps, the corresponding PSF models, and the astrometric registration uncertainty are fed as additional inputs to the image subtraction.

The uncertainty maps are prepared by computing robust standard deviations (background noise) of the science and reference images and scaling them in regions of the image with low weight (smaller number of dithers) to inflate the noise maps accordingly. Source noise from the sources in the science and reference image are added to the uncertainty maps. Since the images fed into the ZOGY *do not* have uncorrelated pixel noise (due to the resampling performed by Drizzle), the uncertainty (RMS) maps are multiplied with the RMS scaling factor derived for scaling the PSF-fit photometric uncertainties. This factor reflects the noise correlation over the size

scale of a PSF and hence is appropriate for the match filtering performed to produce the Scorr image, which denotes the statistical significance for point source detection (Zackay et al., 2016). A saturated source mask is generated using a 25-pixel box at the location of any sources in the science image with pixel values above 0.95 times the saturation limit of the image. We adopt a lower value than true saturation to account for non-linearity effects near the saturation limit. An additional mask for bright sources in the field is prepared by querying the 2MASS point source catalog for sources brighter than 5th magnitude in the field. The size of the mask is adjusted such that brighter stars have larger masks around them, ranging from 81 pixel box masks for 5th magnitude sources to 181 pixel box masks for sources brighter than magnitude 0. A final bright source mask is produced by combining the saturation mask and the bright source mask from the 2MASS catalog.

The image subtraction produces a difference image, a difference image PSF, and a corresponding Scorr image (Equation 25 in Zackay et al., 2016), which is a match-filtered S/N image optimized for point source detection. An initial quality check of the Scorr image is performed to ensure the ZOGY run did not fail before proceeding (i.e., there are not a significant number of NANs in the image[7]). Further quality checks of the subtraction are determined later in the pipeline using candidate counts. The final bright source mask is applied to the difference and Scorr image to remove saturation artifacts. The Scorr image is then fed to SExtractor to generate a list of sources with S/N > 5 in the match-filtered image, corresponding to sources that have peak Scorr values of >= 5 in at least one pixel. The candidates are filtered to exclude image pixels with low weights (e.g., if the dither pattern did not sample the edge of a field uniformly, or if the region of the image is populated with many bad pixels). Additionally, candidates within 20 pixels of the edges of the image are excluded since they are already included in the adjoining sub-quadrant (or field) due to the overlap between the images earlier in the processing.

Quality metrics for the candidates are computed to detect bad subtractions from PSF-variation and astrometric residuals. Bad subtractions from positive-negative (yin-yang) residuals are found to be particularly severe in parts of the field where there are large gradients in the PSF. This arises due to a combination of poorly defined source positions in the presence of elongated and asymmetric PSFs, which leads to systematic residuals in the astrometric solution. Combined with the poor quality of PSF matching during the subtraction cross-convolution, this can produce

[7]Occasionally 'good' quality Scorr images can have NANs values due to edge effects. For these data, we adopt a more aggressive edge masking at the location of the bad values before proceeding.

a large number of subtraction artifacts, unless filtered appropriately. We thus use the following criteria[8]:

1. The ratio of magnitudes measured in a 4-pixel aperture and 8-pixel aperture is required to be between [0.4,1.5] for a candidate to be saved. This criterion rejects yin-yang residuals resulting from large PSF variation across the images, as well as hot pixels.

2. The ratio of the sum of pixels over the sum of their absolute values in a 3×3 median filtered image using a 7×7 pixel cutout centered at the source location is required to be ≥ 0.4 for a candidate to be saved. This criterion is effective at rejecting yin-yang residuals from a large PSF variation in the images. An additional ratio of pixel sums using a variable box size which depends on the image FWHM, PSF asymmetry, and relative astrometric uncertainty at the source location is also calculated and stored for later filtering.

3. The number of pixels 5-σ below the median value of the difference image contained in a 9×9 pixel box centered at the source location is determined. Candidates are rejected if the count is > 1 and the ratio of pixel sums with variable box size in #2 is < 0.8. This cut is only applied for sources with measured magnitudes > 10 to avoid rejecting bright sources which can produce significant 'ringing' in the difference image as a result of the noise decorrelation process in ZOGY.

4. The ratio of the flux of the candidate in the difference image and the reference image. Cross matching between sources in the difference and reference images is performed using a variable radius that is a function of the image FWHM, PSF asymmetry, and relative asymmetric uncertainty at the source location. No cuts are performed solely using this metric.

Values for these metrics were determined by performing tests with injected fake sources, which is described in section 7.5. This process is also performed for the corresponding negative difference and Scorr image to find sources that have faded from the reference image. An additional filtering of positive-negative source pairs is performed to remove extended residuals caused by astrometric residuals or extreme

[8]These criteria were tested and modifies starting from the prescription used for the ZTF pipeline in Masci et al., 2019, and presented in `https://irsa.ipac.caltech.edu/data/ZTF/docs/ztf_pipelines_deliverables.pdf`

cases of PSF-variation between the new and reference image. Cross matching between the positive and negative source catalog is performed using a variable radius that is a function of the image FWHM, PSF asymmetry, and relative asymmetric uncertainty at the source location. Candidates are discarded if a positive-negative cross match is found and the ratio of the source flux in the difference image and reference image (item 4) is less than 1. Together, these quality metrics reject $\approx 75\%$ of total candidates generated on a typical night.

PSF-fit fluxes are measured for each source in the Scorr image by fitting the difference image PSF model on the location of the source detected in `SExtractor`. The position of the source is refined in the fit by χ^2 minimization of the residuals from the PSF model. Although the ZOGY algorithm is designed to produce difference images with uncorrelated pixel noise, this does not hold in cases where the input images have correlated noise in them. Hence, in order to correctly estimate the difference photometric uncertainties, we perform a Monte Carlo simulation by estimating the variance of PSF-fit fluxes over a simulated difference image containing only noise, and scale the PSF-fit photometric uncertainties from the difference image accordingly. As an additional filter of bad quality candidates, we require the absolute value of the difference between the measured PSF-fit magnitude and 8-pixel aperture magnitude to be ≤ 0.4. Last, a final quality check is performed on the difference image using the total number of 'good' candidates, both positive and negative, found as compared to the total number of objects in the source catalog of the science image. If this value is > 0.2, the image is flagged as poor quality and no candidates are saved. Otherwise, the values for aperture photometry, PSF fitting, and other quantities described in this section are recorded in the DB for downstream filtering. Image cutouts (61×61 pixels; $4.4'$ on each side) are recorded in the DB around the location of the source in the science, reference, and difference image for machine learning based classification, and human vetting externally.

Machine Learning classification

To automatically distinguish between an astrophysical source and image subtraction artifacts, we use a Machine Learning (ML) based real-bogus (RB) classification scheme. The GDPS uses a real-bogus classifier scheme implemented through supervised Deep Learning where features are extracted from an input set of candidate sources using many-layered perceptrons (artificial neural networks). The Deep Learning based classifier design was adopted from the classification system implemented for the Zwicky Transient Facility (Duev et al., 2019; Mahabal et al., 2019).

The classifier was trained by assembling a training set of separately labeled real and bogus data by human classifiers. Bogus candidates were compiled using a labeling scheme on Zooniverse, a citizen science web portal which allows setup of individual projects usually pertaining to classification and data visualization[9]. Real sources were selected based on a sample of known variable stars, supernovae, and asteroids found with human vetting during the commissioning period.

We used a two-layer Convolutional Neural Network (CNN) for our Deep Learning model, as CNNs are commonly used in analyzing visual imagery and have numerous benefits over standard multi-layer perceptrons (Krizhevsky et al., 2012). This model is implemented using the TensorFlow package (Abadi et al., 2016) and the high-level Keras API[10]. The model has two convolutional layers, one flatten layer, and two fully-connected layers. The first convolutional layer uses 32 3×3 filters with a Refined Linear Unit (ReLU) activation function, and is followed by a maxpooling layer of size 2×2. The second convolutional layer uses 64 5×5 filters with a ReLU activation function, and is followed by a maxpooling layer of size 4x4. Dropout layers with rates of 0.25 are included after each convolutional layer to minimize over-fitting. After a flatten layer, there is one fully-connected layer of size 32 with a ReLU activation function, followed by a dropout layer of rate 0.40. The final output layer is a fully-connected layer with a sigmoid activation function for binary classification (real or bogus), amounting to a total of 5 layers.

The model is trained and run on stacks of images of size $61 \times 61 \times 3$, consisting of science, reference, difference cutouts (of size 61×61 each). We utilized a training/validation/test split of a 72%/8%/20%. While training the model, we used a batch size of 30 and utilized the early stop method at 20 epochs as there was no improvement in validation accuracy and an increase in validation loss past that point. We used K-fold cross validation technique with k=10 to reduce bias and prevent over-fitting. The performance of the model was evaluated using the following metrics: accuracy on the test set of 0.975, a Matthews correlation coefficient of 0.949, and an F1 score of 0.977. Figure 7.14 presents the normalized confusion matrices for the model, showing a false positive rate (FPR) under 5% and false negative rate (FNR) under 1.5%. The ML model has been deployed for regular use after extensive testing on unseen survey data. A complete description of the ML architecture will be presented in a forthcoming publication (M. Sharma et al., in prep.).

[9] `https://www.zooniverse.org/`

[10] `https://keras.io/`

The ML model is currently being tested on unseen data and will be refined before final deployment.

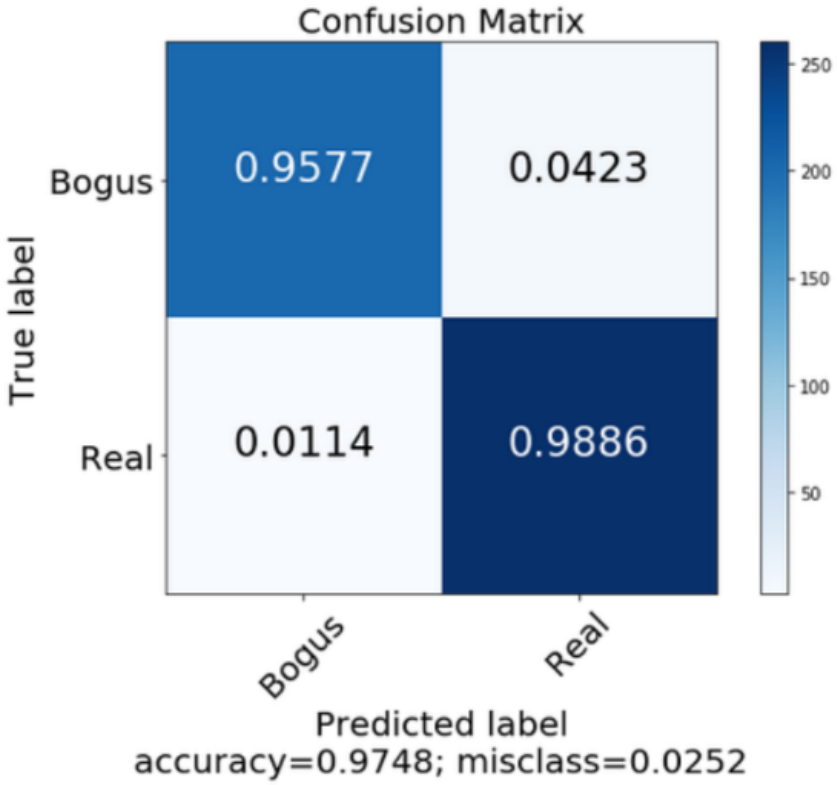

Figure 7.14: **Confusion matrix for the deep learning based real-bogus classification system used in the subtraction pipeline of the GDPS.**

External cross-matches and human vetting

Transient sources recorded in the DB are cross-matched to external catalogs for supporting follow-up prioritization using a dedicated database server at Caltech (Duev et al., 2019). In order to filter variable stars, extracted sources are cross-matched to the 2MASS point source catalog (Cutri et al., 2003) and the distances and J magnitudes of the three nearest sources are recorded. The same is recorded for the three nearest sources in the reference image for the respective field sub-quadrant. Sources are also cross-matched to the PS1 DR2 catalog (Chambers et al., 2016) including the star-galaxy classification scheme described in Tachibana et al., 2018, to store the distances, magnitudes and star-galaxy classification score of the three nearest objects. Additional recorded metadata include cross-matches to known solar system objects using the `astcheck`[11] utility, the ZTF public alert

[11] `https://www.projectpluto.com/astcheck.htm`

archive (Masci et al., 2019), the Census of the Local Universe (CLU) catalog of nearby galaxies (Cook et al., 2019), Gaia DR2, and previously known objects in SIMBAD.

The cross-matches are performed on the database node and recorded in the DB, which is accessible across the Caltech internal network for subsequent human filtering and vetting. Human vetting is performed via a dedicated scanning page on the GROWTH marshal (Kasliwal et al., 2019) showing the science, reference, and difference image cutouts of detected sources together with their metadata. The scanning page is created via read-access to the DB on the database node, and allows the user to enable several metadata-based filters on the detected transients, including the distance to the nearest 2MASS source (to reject variable stars), ML real-bogus score, the presence of a ZTF counterpart, and proximity to a nearby galaxy in the CLU catalog. Candidates are assigned a survey name once they are saved by a human scanner, and are followed up with imaging and spectroscopy via requests on the GROWTH Marshal.

Offline tasks

Reference image generation

Reference images are generated per field sub-quadrant and serve as a historical average snapshot of the sky over the duration when the images were acquired for creating the reference. Difference imaging in the nightly operations are performed against the reference image for each field sub-quadrant. Reference images in the GDPS are created using a minimum of 40 dithered images (5× the number of images for the nominal survey) on the field. The minimum number of images was set by the requirement to quickly build up references after a large period of poor weather during the commissioning period of the GDPS and trigger validation of the image subtraction and transient extraction pipelines. As more images are acquired over the first year of GDPS operations, higher quality references are expected to be built by the end of the first year.

The input images that are stacked into the reference co-add are filtered for several quality cuts by querying the historical record of images in the DB. These include quality cuts on the astrometric and photometric solutions (e.g., to reject images affected by clouds or high humidity), the limiting magnitudes of the images, and a moon-phase dependent cut on the moon distance of the observation (i.e., distance cuts are relaxed near new moon, but strict near full moon). Since the FWHM of

the images are limited by the quality of the instrumental focus and not by the local seeing at the time of the observations, we do not put additional cuts on the FWHM of the images. Since the quality of the PSF focus changes from one side of the mount to the other (as the detector rotates with respect to the plane of the sky), both in terms of PSF FWHM (from 1.4 to 2.1 pixels) and ellipticity / orientation (from 0.02 to 0.25), the possibility of generating a separate set of reference images for each side of the mount is being investigated.

Reference images creation is triggered at the end of the night for fields that *do not* already have reference images. If the number of image quadrants that pass the quality cuts for reference generation is larger than the minimum number, the pipeline proceeds with reference image creation. In this process, the input images and their corresponding noise variance maps are flux-scaled to a common zero-point, and then individually drizzled to the pre-fixed drizzle field grid on the sky using the same `scale` and `pixfrac` parameters as the nightly survey stacks. The resampled images are combined as a sigma-clipped weighted mean of the input images, where the weighting is done with the scaled inverse variance maps. The sigma-clipping removes cosmic rays and artificial tracks from satellites and planes. The stacked image is stored to disk and metadata recorded to the DB.

The reference image is fed to the same photometric calibration pipeline described in Section 7.4, and a PSF model and photometric solution is derived for the stacked image, recorded to the DB, and stored in the FITS header. As in the case of the epochal source catalogs, the photometric calibration produces a PSF-fit source catalog and aperture corrections for the reference image, which are used as seeds for generating light curves of all sources detected in the epochal stacks.

Flat image and dead pixel mask generation

The pixel to pixel responsivity of the detector (with respect to unity median over the image) is corrected using a flat image for the detector. Flat calibrations are generated using science exposures taken on sky during the night – after applying quality cuts for the image counts, moon distance, and local humidity. The flat generation pipeline is executed at the end of every night to query a list of raw images that satisfy these cuts and are ordered by increasing humidity to select images taken during lowest humidity. The flat generation proceeds only if there are at least 200 images that satisfy the quality selection criteria.

The most recent dark image is subtracted from each of the raw sky images, the

input images are normalized by their own median, and the flat image is created as a σ-clipped median (at 2.5σ) of the normalized images to reject outliers from stars, satellites, and other sources on sky. The new flat images are saved to disk and their metadata are recorded to the DB along with a quality flag. A pixel-wise σ and 'count' image storing the number of pixels that contributed to the median are also recorded to disk and metadata recorded to DB. Nightly data reduction proceeds by querying the most recent good quality flat image constructed out of sky images, which usually corresponds to the sky flat constructed from images taken the previous night in the absence of bad weather.

The robotic scheduler was designed to acquire sky images with different exposure times (4 s and 8 s nominally) at the start and end of each night to support the creation of dead pixel masks. At the end of the night, the robotic watchdog queries for dead pixel calibration images taken within the last 2 weeks, and mask creation proceeds only if at least 100 good quality images are available in this time range. If available, the calibration images are normalized and median combined separately for the two exposure times and divided. The ratio image of the two exposure times are used to flag unresponsive and non-linear pixels by measuring the distribution of pixels in the ratio image. A dead pixel mask is created from this distribution flagging pixels that are more than nσ away from unity. The dead pixel mask and its corresponding ratio image is stored to disk, and the metadata are recorded to the DB and the FITS headers. The nightly operations use the most recently constructed dead pixel mask for flagging bad pixels in the reduced images.

Dark image and hot pixel map generation

The thermal background of the detector is corrected using a dark image frame. Since the telescope and detector do not have a robotic shutter system, darks are acquired by observatory staff by manually covering the telescope tube with a cap back-coated with aluminum foil. Images of the dark optical beam are recorded with the same exposure time as used in the survey operations and then fed to the dark calibration pipeline. The dark calibration is created as a σ-clipped median of the input dark frames, with 20 input frames at a time. The median dark image is recorded to disk along with a 'count' image denoting the number of images that survived the σ-clipping in each pixel and a σ-image (corresponding to the standard deviation of the pixel values across multiple dark frames) after the pixel clipping.

The median dark frame generated is used to flag hot pixels in the detector that

have dark current levels more than 20σ larger from the median dark current in the detector. The 20σ cut is used since the high background imaging application of the detector does not require exceptionally low dark current, whereas the cut removes the worst outlier hot pixels. Pixels where the measured σ (i.e., the standard deviation across multiple dark frames) in the dark frames is more than $5\times$ the median σ in the constructed dark are also flagged as these are noisy pixels. The final hot pixel mask is created as a logical OR between the high dark current and noisy pixels, and recorded to disk. Quality metrics and metadata for the median dark frame and hot pixel masks are stored to the FITS headers and recorded to the DB. The nightly operations use the most recently acquired dark frame and hot pixel mask for data calibration.

Match file generation

Light curves for every source detected in the single epoch field visits are stored in HDF5 format using match files, one for every field sub-quadrant. These are created using the reference image source catalog as seeds for cross-matching detected sources across multiple visits of the same field. The files are generated manually (usually once a month) during day time when the processors are not occupied with night time processing. The pipeline proceeds by querying the complete list of stacked images for a given field that were acquired under photometric conditions, and uses the PSF-fit source catalog from the reference image as 'seeds' for sources to be detected in the single epoch images. It then cross-matches every source detected in the single epoch stack (from the PSF-fit source catalogs) to the source catalog for the reference image to perform associations between sources and build up a complete light curve using every visit for the respective field.

The match file product stores the photometric measurements along with metadata for every exposure that contributed to the match file in multiple tables inside the output HDF5 file. The tables include an *exposures*, *sources*, and *sourcedata* table. The *exposures* table stores metadata and observing conditions for every field visit that contributed to the match file, while the *sources* table contains photometric measurements and quality flags of all sources detected in the reference image for that field sub-quadrant. Additionally, the *sources* table stores statistics for the light curve of each source (if detected in the single epochs), including the average scatter, minimum, maximum, and number of detections. The *sourcedata* table contains individual photometric measurements of every source in the reference image that

is detected in any single epoch image, storing the photometric measurements and quality flags. Each row in the *sourcedata* table is associated with a unique object in the *sources* table by a unique index in the *sources* table to allow for light curve generation for each source.

7.5 On-sky performance

The development period for the GDPS ended in June 2019, and the system was deployed for full survey operations on 2019 July 02. We discuss the on-sky performance of the survey using all data acquired in the month of August 2019.

Real-time pipeline success rate and latency

Figure 7.15 shows a distribution of the success rate of the real-time pipeline processing in producing i) photometrically calibrated stacked data products on disk, and ii) in producing a usable subtraction for transient extraction. The success rate distribution was measured from all nights in August 2019. The median success rate of the production of photometrically calibrated stacks is 99.2%, while it is 99.4% for subtractions and transient extraction. The primary issue affecting the success rate of photometric stacks was observations taken under non-photometric conditions (e.g., through clouds, or through high humidity) leading to a significant fraction of astrometry and photometry failures (up to $\approx$ 30% of images on one of the nights in this period). The situation with regard to periods of high humidity is expected to improve with the recent installation of a window heater to avoid the accumulation of condensation.

Figure 7.15 also shows a distribution of the elapsed time between the end of a field observation at the telescope and i) a photometrically calibrated stacked image being available on disk and ii) availability of transient candidates in the DB for human vetting. The median time between the end of an observation and the generation of a photometrically calibrated image is $\approx$ 2 hours, while all images are generally processed within $\approx$ 4 hours from the end of an observation. Transient candidates are available within a median time of $\approx$ 3.8 hours, although the distribution of elapsed time has a long tail extending out to $\approx$ 12 hours. This primarily occurs due to fields in the Galactic plane where the high source density leads to the detection of a large number of candidates that strain the subsequent steps of PSF-fitting, photometry and external cross-matches. However, all candidates are available well before the start of the next night (the pipeline completes no later than noon of the following day on a typical night), and thus the processing is well suited for human vetting of transient

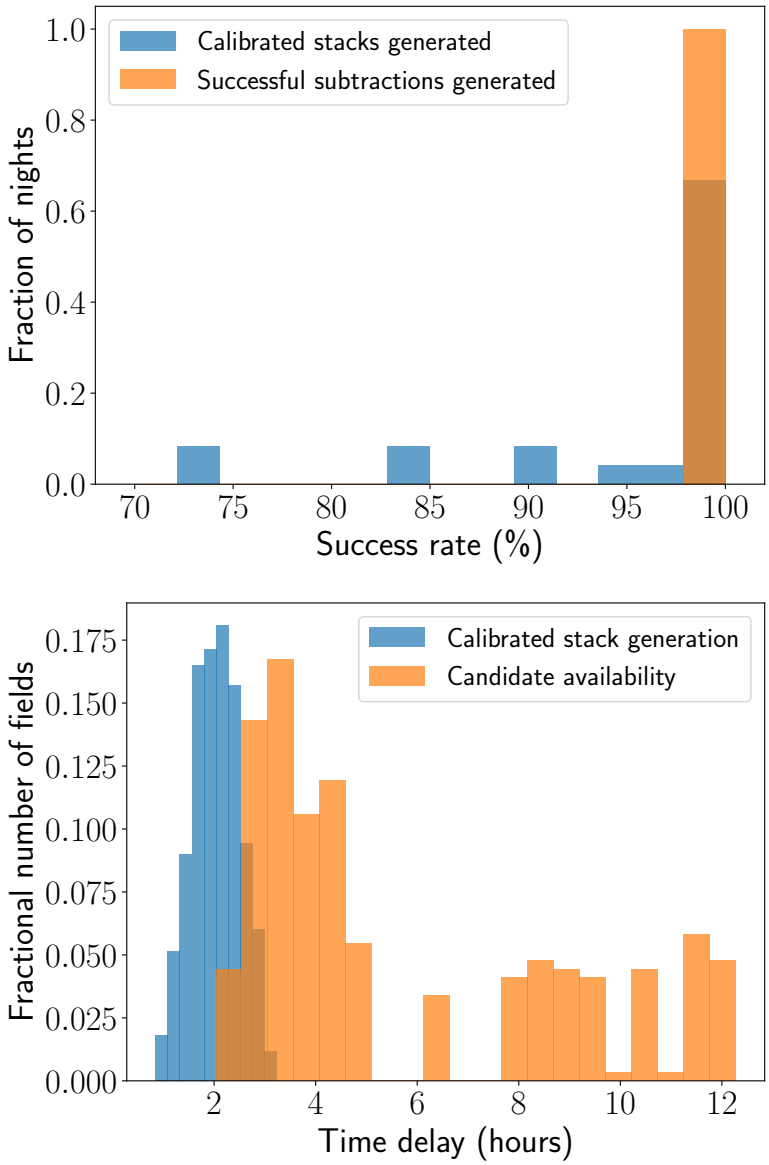

Figure 7.15: **Success rate and time delay of data products delivered by the GDPS.** (Top) Distribution of the percentage success rate of data flow from raw images to photometrically calibrated stacks and transient candidates, as derived from data acquired in the month of August 2019. Primary causes for failure of the pipeline are observations taken under non-photometric conditions through clouds or at times of high humidity. (Bottom) Distribution of elapsed time between the end of field observation and the availability of photometrically calibrated stacks and transient candidates on the database server at Caltech. The median time for the availability of calibrated stacks is $\approx$ 2 hours, while the same for transient candidates is $\approx$ 3.8 hours.

candidates within a day of the observation and subsequent follow-up assignment. By

benchmarking the data processing rate, we find that the time delays are limited by the availability of compute power so that the system processes data $\approx 1.5\times$ slower than the data acquisition rate. Thus, the complete data processing chain takes $\approx 12-13$ hours to complete for a typical $\approx 8-9$ hour observing night, leading to the median ≈ 4 hour delay between data acquisition and candidate availability.

Astrometric accuracy

The astrometric calibration method described in Section 7.4 leads to astrometric solutions which have typical accuracies of $\approx 0.8''$ (≈ 0.1 pixels) over the entire sky. Figure 7.16 (left panel) shows the distribution of the astrometric RMS (per axis) achieved over a range of airmasses and observing conditions during all nights in the month of August 2019, as measured from the astrometric solutions of the native images (after de-trending) using `Scamp` for sources with S/N > 10. We show an equivalent plot for the stacked images produced using `Drizzle` on the right panel of Figure 7.16, plotting the distribution of the median radial separation of sources detected in the Drizzled images cross-matched to the Gaia DR2 reference catalog. The median radial separation is $\approx 0.7''$.

Note that Figure 7.16 shows the astrometric accuracy of *all* sources detected above SNR > 10, where the astrometric measurements are prone to Poisson errors of centroiding for sources near SNR $\approx$ 10. The true achievable precision is higher for the case of brighter sources and is depicted in Figure 7.17, showing the median radial separation of sources from the reported Gaia DR2 position as a function of the source magnitude, both for a high Galactic latitude and a low Galactic latitude field. For sources brighter than $\approx$ 13 Vega mag, the astrometric precision achievable is better than $\approx 0.4''$ (0.05 native pixels) and is representative of the achievable astrometric precision. The astrometric precision is likely limited by the measurement of accurate source positions in the presence of asymmetric and variable PSFs in the final stacked images.

Photometric accuracy

Section 7.4 describes the photometric calibration procedure for stacked images against the 2MASS catalog. Figure 7.18 shows the distribution of the difference between 2MASS and Gattini calibrated magnitudes (including the zero-point and a color term) measured from the epochal PSF-fit source catalogs for a stacked field sub-quadrant. The residuals are plotted as a function of the source magnitude combined over 20 visits of a high and low Galactic latitude field, respectively. The left panels

show the distributions for a high Galactic latitude field (low source density) and the right panels are for a low Galactic latitude field (high source density). The photometric scatter RMS increases for fainter sources and up to $\approx 20\%$ for sources near the 5σ limiting magnitude. The orange squares denote the median residual in bins of 1 magnitude, which show evidence of a small systematic deviation at the brightest and faintest ends of the distribution, likely due to uncorrected non-linearity in the detector pixel response.

The bottom panels show the dependence of the median flux RMS residuals against 2MASS as a function of the source magnitude, binned into groups of 1 magnitude. The best achievable photometric accuracy is $\approx$ 3% (30 mmag) at the bright end (brighter than $\approx$ 11 mag), while it is better than $\approx$ 5% for sources brighter than $\approx$ 13mag. The scatter is believed to be largely dominated by errors in background estimation, flat-fielding, and PSF fitting over the field sub-quadrant (note that the PSF variation over a single field sub-quadrant can be significant at the edges of the focal plane).

Sensitivity and image quality

The $N\sigma$ limiting magnitude of each stacked image can be estimated using either an estimate of the median background RMS in the image and the size of the PSF, or measuring the observed magnitudes for sources in a narrow range of SNR around $N\sigma$. The GDPS measures the limiting magnitude of each image using both methods, while including the corrections for correlated noise in the image pixels (Section 7.4). Figure 7.19 shows the relative flux uncertainty for sources detected in a single epoch field visit of a high Galactic latitude field (left) and a low Galactic latitude field (right). The 5σ limiting magnitude corresponds to a relative flux uncertainty of 20%. The vertical red dashed lines correspond to the limiting magnitude estimated using the background RMS and PSF size information, while the horizontal red dashed line marks the location of 20% flux uncertainty. The intersection of the two lines overlap with the contour of sources in the flux uncertainty plane suggesting consistent limiting magnitude estimates from the two methods.

As seen in Figure 7.19, the depth of the image for the low Galactic latitude field is shallower than that for the high Galactic latitude field as a result of confusion noise in regions of very high source density, given the large pixel scale of the detector. Confusion noise generally degrades the limiting magnitudes (estimated using the the magnitude of sources near SNR = 5) of observations in the Galactic plane fields.

In Figure 7.20, we show a distribution of the 5σ limiting magnitudes of images taken over nights in August 2019 near the Galactic plane ($|b| < 20°$) and outside the plane ($|b| > 20°$). The median 5σ limiting magnitude of images outside the plane is $\approx$ 15.7 AB mag, while the same for low Galactic latitude fields is $\approx$ 15.3 AB mag. The low Galactic latitude fields show a long tail in the distribution extending to shallow limiting magnitudes, corresponding to the most crowded fields in the Galactic plane.

The limiting magnitude of the stacked field sub-quadrants also depends on its position in the plane of the detector due to large variations in the PSF size and shape across the detector. Larger PSFs lead to shallower limiting magnitudes given the high sky background. The top panels in Figure 7.21 show the variation of the PSF FWHM and ellipticity measured as a function of position on the detector, averaged over all nights of observations in August 2019. Sub-pixel image quality has not been achieved with the designed optical system. In the absence of a focusing mechanism (due to be installed in 2019), variations in the PSF FWHM and ellipticity have been observed as a function of the ambient temperature. The typical PSF FWHM size is $\approx 12 - 14''$ ($\approx 1.5 - 1.7$ detector pixels), although it is worse (up to $\approx 17'' \approx 2$ detector pixels) at the edges of the focal plane. As a result, the use of `Drizzle` with an output pixel scale half of the native pixel scale has been adequate to reconstruct Nyquist sampled images.

The lower panels in Figure 7.21 show the median limiting magnitude (including both low and high Galactic latitude observations) and zero-point as a function of position in the detector plane. The zero-point of the detector is largely uniform across the plane except for the bottom right corner, where the zero-point (sensitivity) is lower by $\approx$ 0.05 mag due to the absence of a AR coating. The distribution of limiting magnitude as a function of position in the detector plane is influenced by a combination of the local zero-point and PSF size, such that larger zero-points and smaller PSF FWHMs lead to deeper limiting magnitudes. Since the sky background from the PSF footprint is the dominant noise contribution limiting the image depths, the depths of the images are expected to improve with the installation of a focus mechanism in the second half of 2019.

Reference images

Section 7.4 discusses the generation of reference images by stacking all exposures of a given field acquired under photometric conditions. Although reference im-

age availability was limited during the commissioning phase of the survey due to extended periods of bad weather and poor observing conditions, reference maps were re-built at the end of June 2019 with data acquired between November 2018 and June 2019. The resulting reference maps have 99.3% coverage of the visible sky from Palomar and the sky distribution of the reference limiting magnitudes are shown in Figure 7.22. The number of images stacked in each field varies between 40 individual dithers (5× the nominal survey field visits) and 300 individual dithers, with fields near the north pole having the largest number of images stacked due to their near continuous visibility from Palomar Observatory. The resulting limiting magnitudes of the reference stacks vary between ≈ 14.5 AB mag in crowded regions in the Galactic plane (where the depths are limited by confusion) to ≈ 18 AB mag outside the plane. The reference images are deeper than 16.5 AB mag for 60% of the sky.

Difference images and transient recovery

After applying the quality cuts to the candidates generated from the subtractions, the difference imaging pipeline typically generates ≈ 25000 candidates each night (median ≈ 7 candidates per sub-quadrant), noting that the total number of candidates generated can have a large dispersion depending on the Galactic plane coverage and total observing time (which changes over the year). In order to evaluate the efficacy of the difference imaging pipeline, we performed various tests with injected fake sources. First, a set of test data was created using a copy of the nightly survey data. A total of 992 fake sources were inserted in these images using a PSF model for the image generated using PSFex and scaled to a specific magnitude. The magnitude of the fake sources were randomly drawn from a uniform brightness distribution between 0 and 5 magnitudes above the limiting magnitude of the science image. The positions for the fake sources were randomly drawn from a uniform distribution of x and y coordinates in the image, with checks to ensure that sources were not placed in low-weight portions of the maps (i.e., regions near the edge which were not sampled by at least half the dithers of the dither sequence). The subtraction pipeline was run on these test images to check the fractional source recovery, which are shown in Figure 7.23.

Injected sources which were missed by the pipeline can be broadly characterized into six groups: sources that were flagged as saturated (2), sources that were coincident with the masked area of a nearby bright star (11), sources masked as possible artifacts from the missing AR coating on a corner of the detector (23), sources which failed to

achieve a peak Scorr value of 5 (38), sources contained in images that failed quality criteria for candidate extraction (2), and sources that were initially detected but cut as part of candidate filtering criteria (17). The values listed after each category indicate the number of missed sources in that category. In total, 899 sources out of 992 possible sources were recovered, yielding an overall recovery fraction of 90.6%.

The recovered magnitude for the injected sources were compared with their injected magnitude to ensure consistency. Additionally, the coordinates of the injected sources were compared with their corresponding recovered candidate coordinates. The results of these tests can be found in Figures 7.25 and 7.26. The photometric precision for sources brighter than 13th Vega mag is $\approx$ 3%, while the astrometric RMS is 0.9″ in each axis for all recovered sources (down to S/N = 5).

In addition to the first set of test data, we performed a second evaluation of the subtraction pipeline to assess its efficacy for finding sources in close proximity to nearby galaxies. An additional set of test data was generated using the same procedure described above, except that the positions for the fake sources were randomly selected to be within a 30″ radius from nearby galaxies that are part of the Census of the Local Universe (CLU; Cook et al., 2019) catalog. The subtraction pipeline was run on this test data to check the rate of injected sources recovered as a function of the surface brightness at the location of the injected source. The test yielded what was at first an unexpected result, because the sky background level at J-band dominates over the galaxy light. This makes the 'standard' test of surface brightness vs. recovery somewhat more difficult to interpret. Overall, the performance of this test was comparable to the earlier randomly placed fake sources. The pipeline found 366 out of 382 possible sources. This slightly improved rate of 95.8 % sources found is likely due to the fact that CLU galaxies are found in regions where the J-band source density is not particularly high, unlike the Galactic plane fields which were included in the first test. Regions with high source densities make transient detection much more difficult because the data is typically not as deep due to the effects of confusion and there is higher chance of being masked by coincidence. Taking these into account, the improved performance of the second test makes sense and bodes well for finding transients in nearby galaxies with Palomar Gattini-IR.

7.6 First results

Commissioning operations of Palomar Gattini IR started in November 2018 and continued until the end of June 2019. The quality of the data taken during the first few months was affected by extended periods of bad weather and high humidity, during which the data processing and transient discovery system were extensively tested and modified to produce better quality data products. As the data reduction procedures were finalized, data from the start of the survey were re-processed to produce the complete baseline of observations available from the acquired data. Survey operations of Palomar Gattini-IR began on 2019 July 02, to survey the entire celestial sphere visible from Palomar Observatory. We present initial science results from transients and variables detected in the commissioning phase. Candidates detected each night are accessible from the GROWTH Marshal (Kasliwal et al., 2019) where they are vetted by an on-duty astronomer on the following day for assignment of follow-up optical / NIR imaging and spectroscopy with the Palomar 200-inch telescope using the optical Double Beam Spectrograph (DBSP) and the NIR Triple Spectrograph (TripleSpec). Follow-up is prioritized for sources coincident with nearby galaxies in the CLU catalog (candidate supernovae in nearby galaxies), host-less transients (candidate novae or dwarf novae), and large amplitude variables (candidate flaring stellar sources such as young stellar objects).

Transient science

Since the start of the commissioning period, several bright supernovae and extra-galactic transients were recovered in the Gattini transient stream. These include the SNe II 2018hna, 2019hsw, and SN Ia 2019np. In addition, large amplitude NIR flaring was detected from several high redshift blazars, a subset of which were followed up with optical / NIR spectroscopy on the Palomar 200-inch telescope. In Figure 7.27, we show a collage of the J band light curves and spectra of extragalactic transients detected in the commissioning phase. SN 2018hna was reported by K. Itagaki to the Transient Name Sever (TNS) early in the commissioning phase of Gattini-IR and brightened to be detectable in the NIR soon after explosion. Gattini observed the field as a part of regular survey operations with photometry capturing the entire rise to the radioactive peak and subsequent decline of this SN 1987A-like Type II SN (Figure 7.27, top left panel). SN 2019hsw (ASASSN 19pn / PGIR 19jg) is a Type II SN at 25 Mpc detected in the Gattini-IR commissioning data, and shows a slow J band decline at early time (Figure 7.27, top left panel). The SN went close to the sun soon after discovery and was not covered as a part of the nightly Gattini-IR

observations. SN 2019np (PGIR 19ayh) was a nearby Type Ia SN reported to TNS (Itagaki, 2019) and subsequently detected in Gattini data. Only two detections of the SN were recovered due to an extended period of poor weather surrounding the detection of the SN. PGIR 19c is a large amplitude flaring blazar (B1420+326) detected as a transient over several weeks of operations (Figure 7.27, top right panel). The fast variability and large amplitude flaring detected in the Gattini-IR data were announced via the Astronomer's Telegram (De et al., 2019d). Gattini-IR detected a new NIR flare of the blazar CTA 102 (Figure 7.27, top right panel), which was saved with the internal name PGIR 19ayd and announced publicly (De et al., 2019c).

Figure 7.27 also shows light curves of several Galactic transients detected in the data – highly reddened Galactic novae AT 2019qwf and AT 2019owg (Figure 7.27, bottom left panel), the outbursting X-ray binary MAXI J1820+07 / ASASSN-18ey (Tucker et al., 2018; the NIR brightening was reported in Hankins et al., 2019a), and the dwarf nova PGIR 19tf (Figure 7.27, bottom right panel). AT 2019qwf (PGIR 19brv) was first discovered and reported as a bright ($\approx$ 11 mag) NIR transient at Galactic latitude of 0.2 degrees by Gattini-IR, and classified as a Galactic nova with optical spectroscopy (**DeA2019**). Another reddened classical nova AT 2019owg (initially reported as Gaia 19dum to TNS) was detected as a bright NIR transient (at $\approx$ 8th mag), close to the saturation magnitude of the instrument (De et al., 2019b). Between July and September 2019, Gattini-IR detected a total of four Galactic classical novae – V3890 Sgr, Gaia 19dum/AT 2019owg, PGIR 19brv/AT 2019qwf, and V2860 Ori. Both MAXI J1820+07 and MAXI J1807+32 were detected as NIR transients coincident with a brightening detected in the optical wavebands. After re-processing older data taken during initial commissioning, a previous outburst of MAXI J1820+07 in 2019 was also recovered. Several recurrent outbursts from the dwarf nova Ay Lyr (PGIR 19tf) were detected in the commissioning, and are shown in Figure 7.27. Gattini-IR detected a reddened binary microlensing event in the Galactic plane (PGIR 19btb / Gaia 19dqj / AT 2019odt) which was announced in De et al., 2019e.

Figure 7.27 also shows a collage of optical (from P60 + SED Machine / P200 + DBSP) and NIR spectra (from P200 + TripleSpec) obtained for these transients detected during the commissioning phase. PGIR 19jg and PGIR 19hj exhibit typical features of Type II SNe, including broad P-Cygni lines of H, He, O I, and Fe II. A peak light spectrum of PGIR 19ayh shows typical features of Type Ia SNe near peak – Si II, S II, Ca II, and Fe II. PGIR 19brv (AT 2019qwf) was followed up

with rapid low resolution spectroscopy on the SED Machine spectrograph on the Palomar 60-inch telescope (Blagorodnova et al., 2018). The spectrum showed a reddened continuum and strong emission lines of H and O, classifying this source as a reddened Galactic classical nova (De et al., 2019f). We also obtained a NIR spectrum of the reddened Galactic nova AT 2019owg, which shows broad emission lines of He and H along with strong emission lines of O I. The NIR spectrum of Ay Lyr (PGIR 19tf) shows several narrow absorption lines of H, typical of dwarf nova outbursts.

Given the large field of view of Gattini, it has also been performing targeted follow-up of the localization regions of several alerts announced by LIGO/Virgo in O3. Gattini has demonstrated the capability to tile large fractions of the error regions of the localization regions, ranging from 32% of the poorly localized single detector detection of LIGO/Virgo S190425z (Coughlin et al., 2019b), and of the localization region of the candidate NS-BH mergers S190426c (92%; Hankins et al., 2019b,c) and S190814bv (89.5%; Hankins et al., 2019d). In the case of S190426c, Gattini tiled the localization region a total of ≈ 20 times over the course of one week after the merger, while each field in the localization region of S190814bv was observed for $\approx$ 2.5 hours during one week after the merger. Given the longer timescale ($\sim$ 1 week) of the infrared emission in kilonova counterparts (Kasen et al., 2017), stacking multiple epochs of data will allow the first constraints on infrared emission from compact binary mergers *independent* of optical searches.

Variable science

As a part of nominal survey operations, Gattini-IR will obtain J-band light curves of sources brighter than J $\approx$ 16 AB mag. The photometric measurements from these observations are readily available in the epochal PSF-fit source catalogs, which are cross-matched across epochs to produce match files for every detected source. In order to demonstrate the quality of light curves and the variable science potential of Gattini, we ran a blind period search algorithm on all sources detected more than 30 times. In Figure 7.28, we show a sample of periodic variables recovered from the blind period search, some of which already had known variable counterparts in SIMBAD. These include a candidate short period ($\approx$ 6 hour) eclipsing binary, an RR-Lyrae type variable showing a distinct saw-tooth shaped light curve, a Cepheid variable, and a BY Draconis type variable, demonstrating the photometric quality of the data and the capability for blind period searches.

Figure 7.29 also shows light curves of Galactic variables that were detected in the subtraction pipeline – a candidate brown dwarf and a known Young Stellar Object (YSO). While the brown dwarf is undetected in the optical due to its red color, the variability from the YSO is undetected in the optical due to extinction. Operating in J band, Gattini will probe variability in the coolest and dustiest stars in the galaxy (such as brown dwarfs and asymptotic giant branch stars) that are bright in the infrared but faint in the optical. It will also be particularly sensitive to stellar variability in the most dust extinguished lines of sight in the Galactic plane where optical time domain surveys become insensitive.

7.7 Summary

Palomar Gattini-IR is a new wide-field (25 square degree field of view) NIR time domain survey using a 30 cm telescope at Palomar Observatory. Gattini-IR operates in J band with a H2RG detector and a pixel scale of $\approx 8.7''$. Under the nominal survey, Gattini-IR scans the entire northern sky to a median 5σ depth of 16 AB mag (outside the Galactic plane) with a median cadence of two nights. We presented the performance of the robotic scheduling system that runs the survey. The observing system scans $\approx$ 7500 degrees of the sky every night with a median observing efficiency of $\approx$ 60%. We outline the design and operations of a real-time data processing system that produces science quality stacked and calibrated images from dithered raw images taken on sky, as well as transient candidates identified from subtractions. The calibrated science images are delivered within a median time of $\approx$ 2 hours from the end of an observation while transient candidates are delivered within a median time of $\approx$ 4 hours.

The median astrometric accuracy of the stacked images (calibrated to Gaia DR2) is $\approx 0.7''$for sources with SNR $>$ 10, while it is close to $\approx 0.3''$for sources brighter than 13 mag. The achieved photometric precision (calibrated against 2MASS) is $\approx$ 3% for sources brighter than 12 mag. Reference images were generated for the entire visible sky at the start of survey operations, and cover 99.3% of the visible sky with 60% of the reference image coverage having depths $>$ 16.5 AB mag. As with the epochal science images, the reference image depths are limited by confusion noise near the Galactic plane. The efficiency of transient detection was estimated using fake sources injected into the data stream and found to be $\approx$ 90% for sources down to the 5σ limiting magnitude. The photometric recovery precision (RMS) for injected sources is 3% for transients brighter than 13 Vega mag, while the astrometric recovery precision (RMS) is $\approx 0.9''$.

Survey operations for Palomar Gattini-IR began in July 2019, marking the end of the commissioning period. While the quality of the data during the commissioning period was affected by long periods of high humidity and bad weather causing condensation on a window in the OTA, this issue has been fixed with the recent installation of a window heating mechanism. Additionally, the planned installation of an automated focus mechanism is expected to yield better image quality and image depths moving into the second half of the first year survey. Additional planned improvements include using 'sample up the ramp' to read out the detector, which will increase the dynamic range of the instrument for bright sources by 2.5 magnitudes.

With the largest field of view of any NIR imaging instrument, Gattini-IR is a pathfinder of time domain astronomy in the NIR. In addition to the stream of known optically bright transients and variables, Gattini will be sensitive to the reddest and dustiest explosions in the nearby universe and the stellar variability from the most dust extinguished regions of the galaxy that are inaccessible to current optical time domain surveys. As a demonstration of the science capabilities, we present sample results from transients and large amplitude variables detected since the start of the commissioning period. Gattini-IR is already discovering dust extinguished novae in the Galactic plane, and is expected to be sensitive to transients behind large columns of extinction within the galaxy where optical time domain surveys lose sensitivity. Over the course of the nominal two year survey, Gattini-IR will explore the phase space of transients and variables in the dynamic infrared sky for the first time with an untargeted, all-sky sampling at two day cadence. As the first working demonstration for wide-field NIR time domain astronomy, Gattini-IR will lead the way for future IR time domain experiments like WINTER at Palomar Observatory (Simcoe et al., 2019), and DREAMS (Soon et al., 2018) at Siding Spring Observatory.

We thank A. Fruchter, F. Masci, S. R. Kulkarni, C. Steidel and M. J. Graham for valuable discussions on this work. We thank the anonymous referee for a careful reading of the manuscript that significantly helped improve the quality of the manuscript. MMK and EO acknowledge the US-Israel Bi-national Science Foundation Grant 2016227. MMK and JLS acknowledge the Heising-Simons foundation for support via a Scialog fellowship of the Research Corporation. MMK and AMM acknowledge the Mt Cuba foundation. J. Soon is supported by an Australian Government Research Training Program (RTP) Scholarship. SED Machine is based upon work supported by the National Science Foundation under Grant No. 1106171.

KD and MJH thank the hospitality of the astrophysics group at the Weizmann Institute of Science, Rehovot, Israel, where part of this work was carried out. This work was supported by the GROWTH (Global Relay of Observatories Watching Transients Happen) project funded by the National Science Foundation under PIRE Grant No 1545949. GROWTH is a collaborative project between the California Institute of Technology (USA), University of Maryland College Park (USA), University of Wisconsin Milwaukee (USA), Texas Tech University (USA), San Diego State University (USA), University of Washington (USA), Los Alamos National Laboratory (USA), Tokyo Institute of Technology (Japan), National Central University (Taiwan), Indian Institute of Astrophysics (India), Indian Institute of Technology Bombay (India), Weizmann Institute of Science (Israel), The Oskar Klein Centre at Stockholm University (Sweden), Humboldt University (Germany), Liverpool John Moores University (UK), and University of Sydney (Australia).

The High Performance Wireless Research & Education Network (HPWREN; `https://hpwren.ucsd.edu`) is a project at the University of California, San Diego and the National Science Foundation (grant numbers 0087344 (in 2000), 0426879 (in 2004), and 0944131 (in 2009)). This publication makes use of data products from the Two Micron All Sky Survey, which is a joint project of the University of Massachusetts and the Infrared Processing and Analysis Center/California Institute of Technology, funded by NASA and the National Science Foundation. This work has made use of data from the European Space Agency (ESA) mission Gaia (`https://www.cosmos.esa.int/gaia`),processed by the Gaia Data Processing and Analysis Consortium (DPAC, `https://www.cosmos.esa.int/web/gaia/dpac/consortium`). Funding for the DPAC has been provided by national institutions, in particular the institutions participating in the Gaia Multilateral Agreement. This work has also made use of the Pan-STARRS1 (PS1) Surveys (`http://www.ifa.hawaii.edu/pswww/`) and the PS1 public science archive (`https://panstarrs.stsci.edu`).

7.8 Appendix: General purpose optical / NIR image reduction pipeline

We provide a brief description of the general purpose optical / NIR image reduction pipeline developed initially for optical (WASP) and NIR (WIRC) imaging instruments on the Palomar 200-inch. The code is highly modular to allow support for a large range of optical and NIR instruments, and was subsequently updated to support data from MOSFIRE on the Keck-I telescope and the FOURSTAR camera on the Magellan telescope. The code is written completely in `python`, using several

functions from `astropy` and the Astromatic suite of software for source extraction, astrometry, and stacking. The code will be publicly released on `github` for general use. The parameters of the reduction are controlled using a configuration file that can be modified for custom reductions. We outline the various implemented steps implemented for the reduction of optical / NIR data.

1. The code uses the headers of the raw files to create a log for all images recorded in the night. This log is used to generate a list of science and calibration exposures to be processed.

2. A master dark image is created using darks found in the list of calibration frames. The master dark is subtracted from all the images prior to processing.

3. A master flat image is created using either dome flats (if available) or sky frames (using the bright sky background in the NIR). Since individual exposures can contain extended galaxies[12] (if the observing program involves a nearby galaxy) which do not reflect the flatness of the detector, the pipeline runs `SExtractor` to generate a list of detected sources, and checks for large extended sources in the field occupying more than 20% of the image. If an extended galaxy is detected, the specific image is not used in the flat-field generation. Images with no large extended sources are marked to be included in the flat-field generation.

4. The pipeline generates a first-pass flat-field by performing a median combination of the sky frames, which is used to flat-field all the target exposures. In case separate dome flats or twilight flats are available, those images are used to generate a median combined flat frame.

5. For each science exposure, the pipeline uses a median combination of the nearest sky (without extended sources) exposures to create a sky image which is subtracted from the science frame.

6. Following the generation of flat-fielded and sky-subtracted science frames, the code proceeds to generating a preliminary astrometric solution using the initial WCS from the image header using the `autoastrometry`[13] code, with 2MASS (or SDSS, if available) as the reference catalog. The initial astrometric solution only includes a distortion free CD matrix.

[12]The nominal observing strategy in such cases is to interleave the target exposures with sky exposures outside the galaxy field.

[13]`http://www.astro.caltech.edu/~dperley/programs/autoastrometry.py`

7. The `scamp` code is then used to derive a refined astrometric solution using Gaia DR2 as the reference catalog including a 3rd order distortion solution in the field. Given the small field of view (few arc-minutes) of most imaging instruments, the two-step astrometric solution (fitting distortions in the second pass astrometry after obtaining an initial solution) was found to have a higher success rate for astrometric calibration.

8. The astrometric solutions are used to generate a first-pass stacked image using the `Swarp` package. `Sextractor` is run on the first pass image to generate a list of detected sources.

9. The source map from the first pass stacked image is used to mask sources in the individual images by mapping positions in the stacked image to the individual science images. The master flat-field image (in case the flat-field was generated using sky images) and sky frames are then re-generated for the individual target exposures.

10. The science images are flat fielded and sky subtracted again using the new flat and sky images and then stacked using the existing astrometric solution using `Swarp`. This stacked image serves as the final stacked image product.

11. A photometric solution is derived on the final stacked image using the relevant catalog for the observed filter. `PSFEx` is used to generate a PSF model and corresponding PSF zero-points followed by aperture corrections for several apertures. The photometric solution is written to the header of the final stacked image product.

In the case of optical instruments, dome flats are directly used for producing flat field calibrations and a median spatial filter is used for sky subtraction.

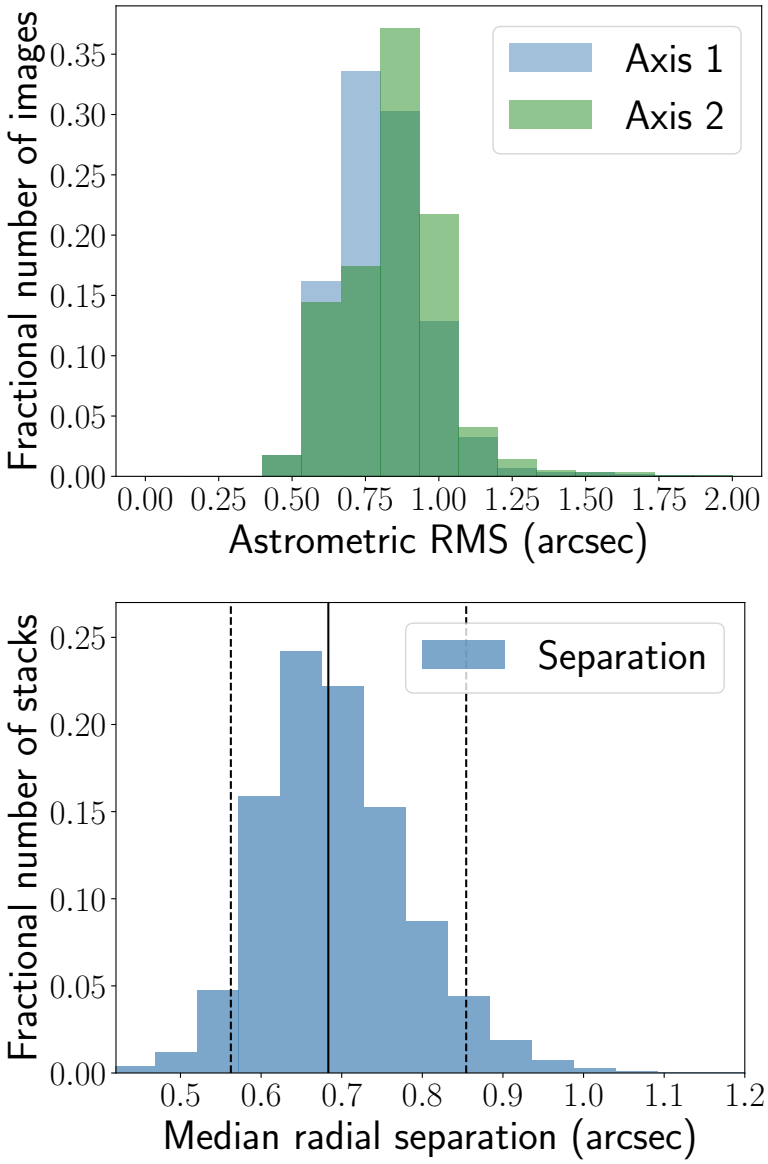

Figure 7.16: **The astrometric quality of the GDPS data products.** (Top) Distribution of the astrometric RMS derived from the scamp catalog fit for sources with S/N $>$ 10, using all images taken over all nights in the month of August 2019. (Bottom) Distribution of the radial RMS offset between cross-matched sources in drizzled stacks and the photometric catalog. The solid line is the median radial separation, while the dashed lines show the 5th and 95th percentiles of the radial separation distribution.

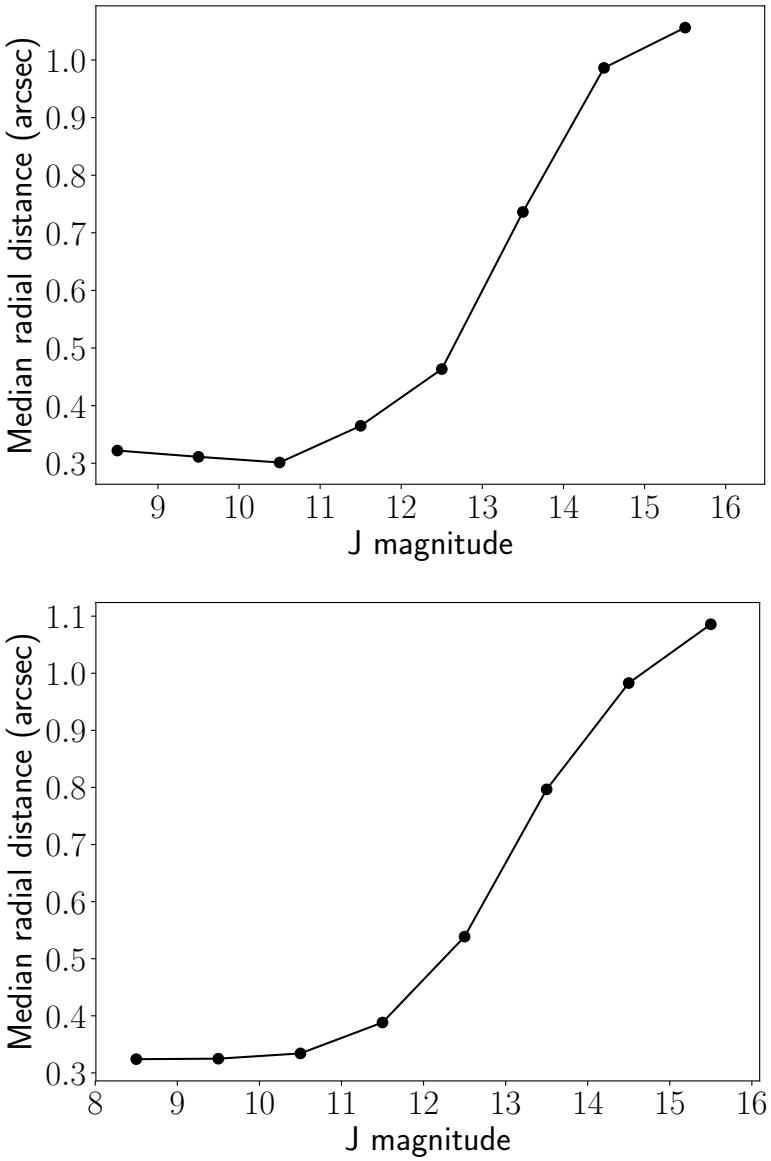

Figure 7.17: **Astrometric precision achieved in GDPS as a function of source brightness, in high and low Galactic latitude fields**. Median radial astrometric distance with respect to Gaia DR2 as a function of the J Vega magnitude of sources down to SNR = 5. The left plot was created from the astrometric solutions for 20 field visits of a high Galactic latitude field while the right plot corresponds to the same for 20 field visits of a low Galactic latitude field. The astrometric accuracy for sources brighter than ≈ 12 Vega mag is better than $\approx 0.4''$ (0.05 native pixels).

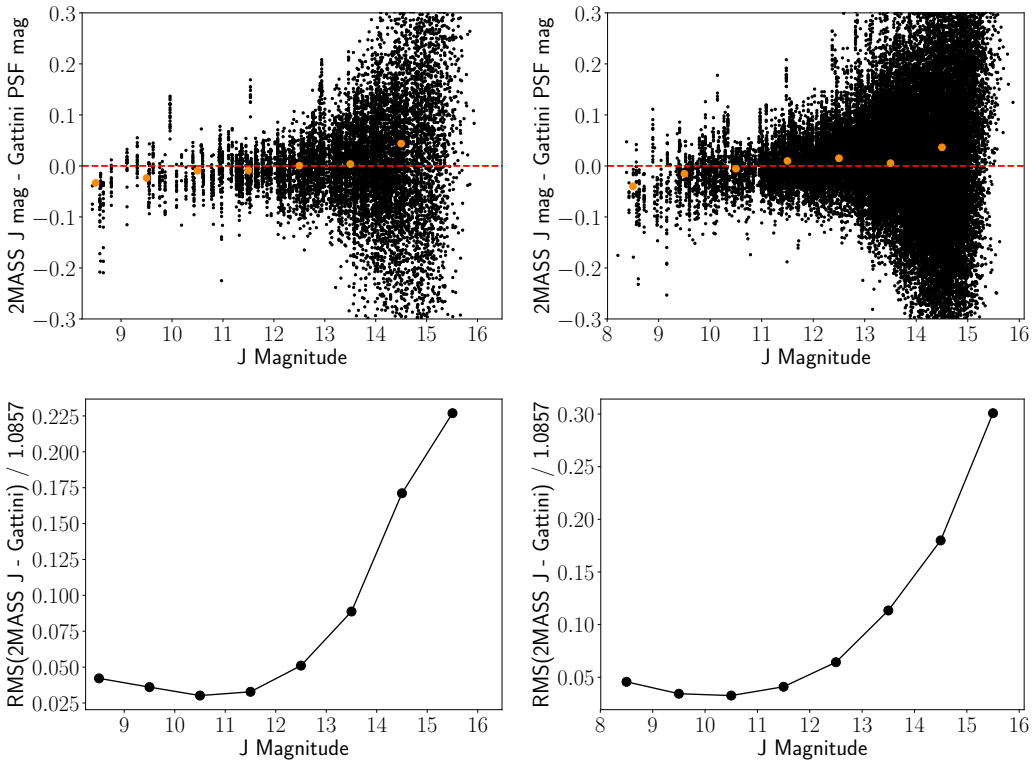

Figure 7.18: **Photometric precision of GDPS data products in high and low Galactic latitude fields.** (Top) Difference between 2MASS and Gattini J band magnitudes, as a function of J band magnitude, from the photometric solutions derived in the GDPS. The left panel shows a high Galactic latitude field and the right panel shows a low Galactic latitude field, compiled from 20 visits of each field. The orange dots denote the median deviation in bins of 1 magnitude, showing evidence of a small systematic shift at the brightest and faintest ends. (Bottom) Relative flux RMS between 2MASS and Gattini as a function of source magnitude. The relative flux RMS is estimated from the magnitude RMS, and then normalizing by 1.0857. The left and right panels are for the same single epoch fields shown in the upper panels.

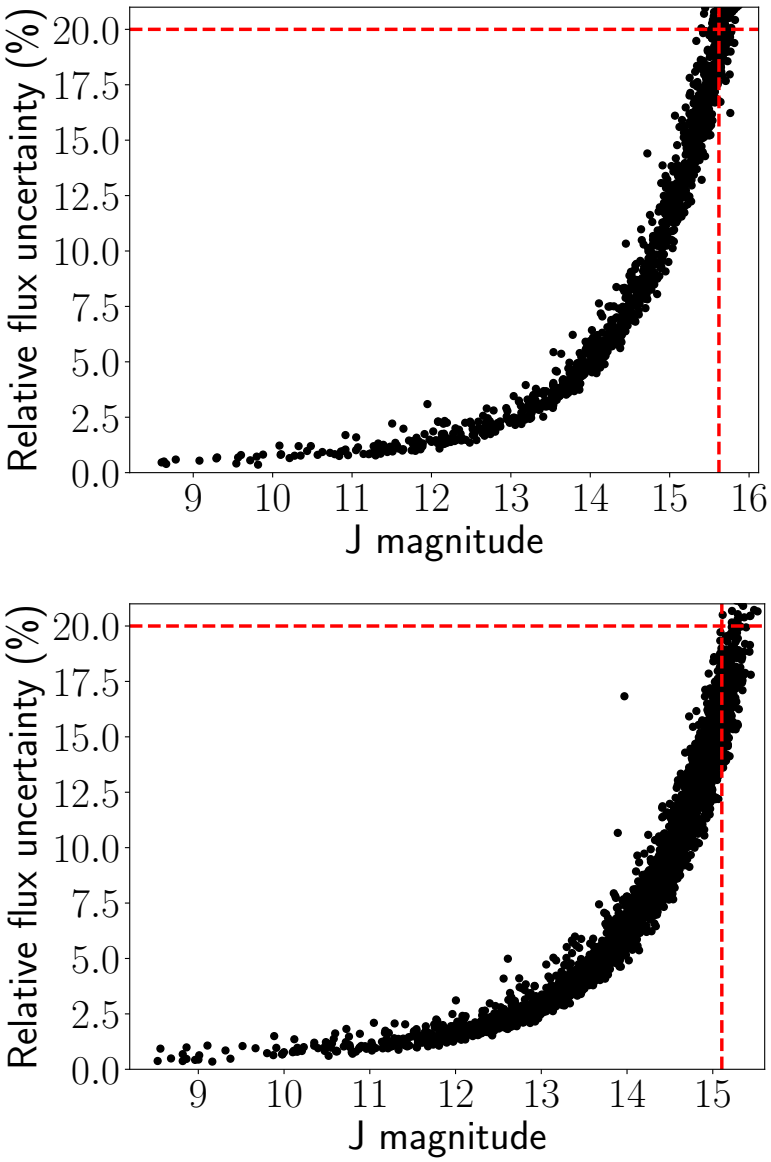

Figure 7.19: **Relative flux uncertainty as a function of source magnitude from single epoch PSF-fit source catalogs in the drizzled stacked images.** The red dashed vertical lines show the limit corresponding to SNR = 5 estimated from the background RMS, and are consistent with that estimated from 20% flux uncertainty of the detected sources, indicated by the red dashed horizontal lines. The top plot is for a high Galactic latitude field and the bottom is for a low Galactic latitude field.

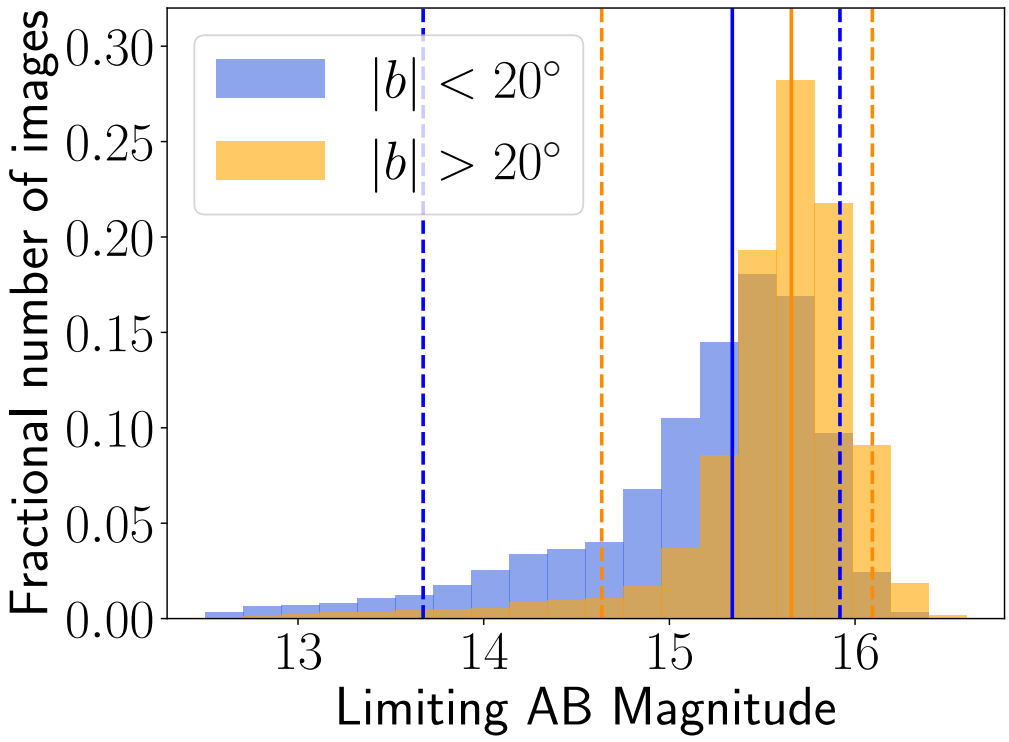

Figure 7.20: **Distribution of 5σ limiting magnitudes for low (blue) and high (orange) Galactic latitude fields for all observations taken in August 2019.** The limiting magnitudes were estimated using the magnitudes of sources detected in a narrow range of SNR around 5. The orange solid vertical line denotes the median limiting magnitude for the high Galactic latitude fields, while the two dashed lines denote the 5th and 95th percentile limiting magnitudes. The blue vertical lines correspond to the same statistics for the low Galactic latitude fields.

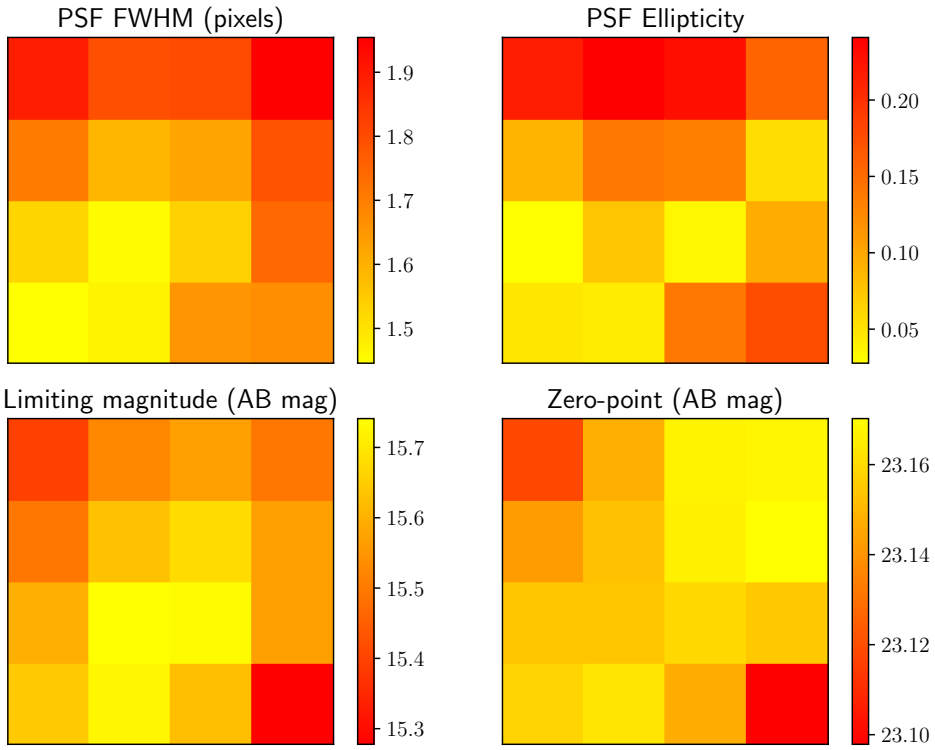

Figure 7.21: **PSF and zero-point variation around the Gattini focal plane, derived from all data taken in August 2019.** (Top left) PSF FWHM variation around the focal plane in units of native detector pixels. (Top right) PSF ellipticity variation around the focal plane. (Bottom left) Median limiting magnitude as a function of position in the focal plane. (Bottom right) AB zero-point as a function of position in the detector plane.

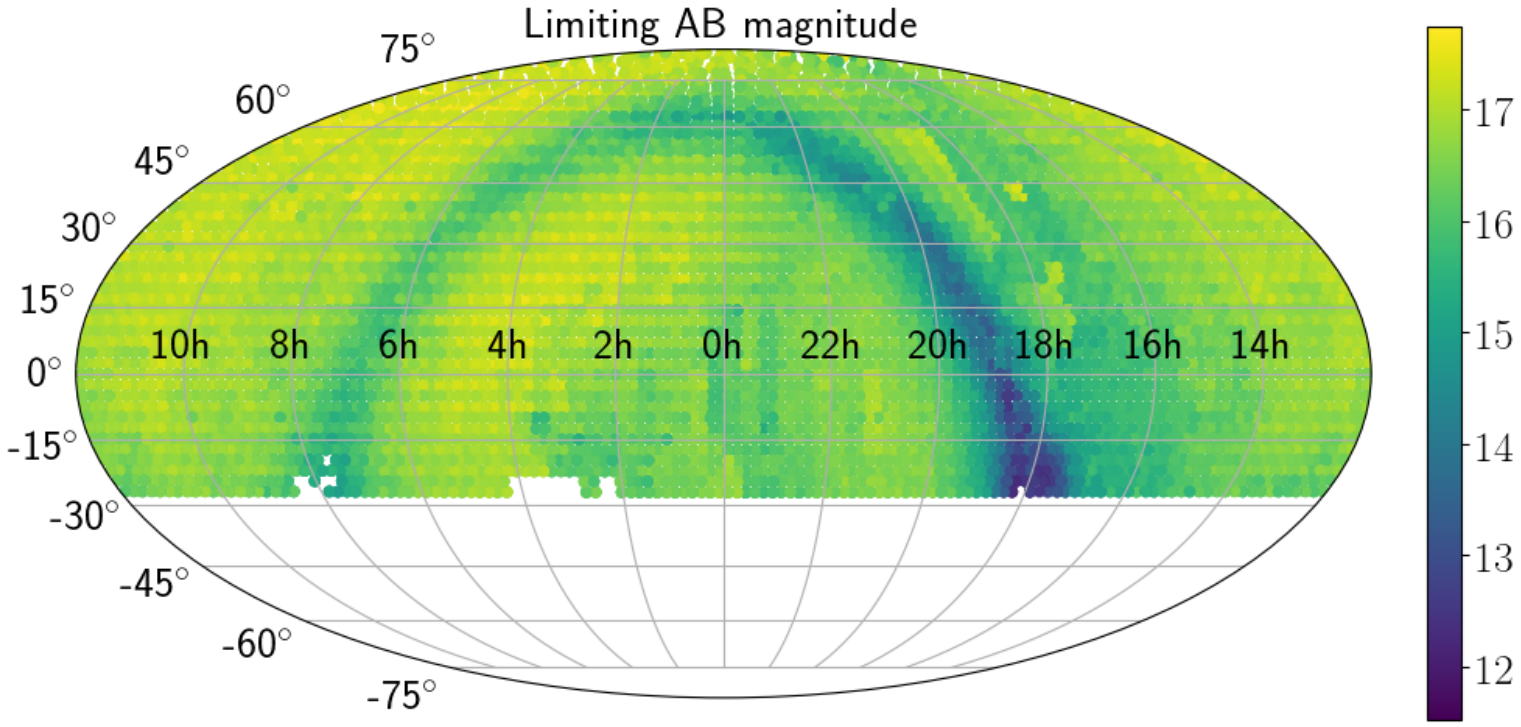

Figure 7.22: **Distribution of the depths of reference images as a function of sky position**. The depth map is shown as of June 2019 (just before the start of survey operations in July 2019). The deepest reference images achieve depths of ≈ 18 AB mag, while the depths are limited by confusion noise in the Galactic plane.

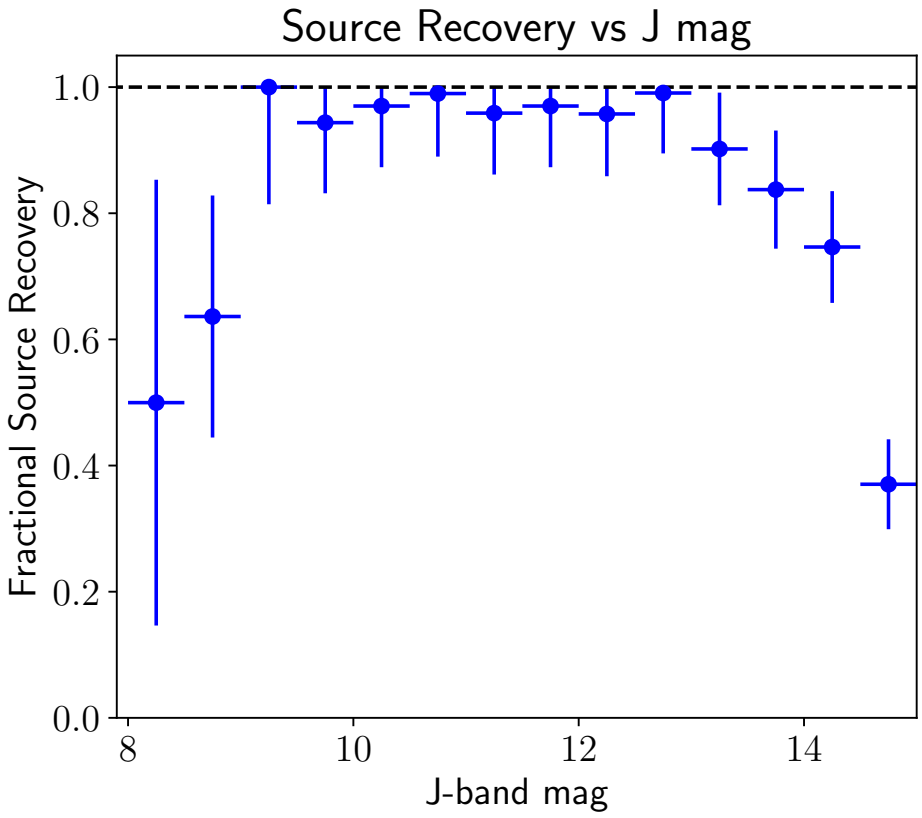

Figure 7.23: **Fractional recovery of injected sources as a function of their J-band magnitude.** The y error bars assume counting statistics for the number of sources in each bin. The black dashed line indicates the maximum possible fractional recovery value.

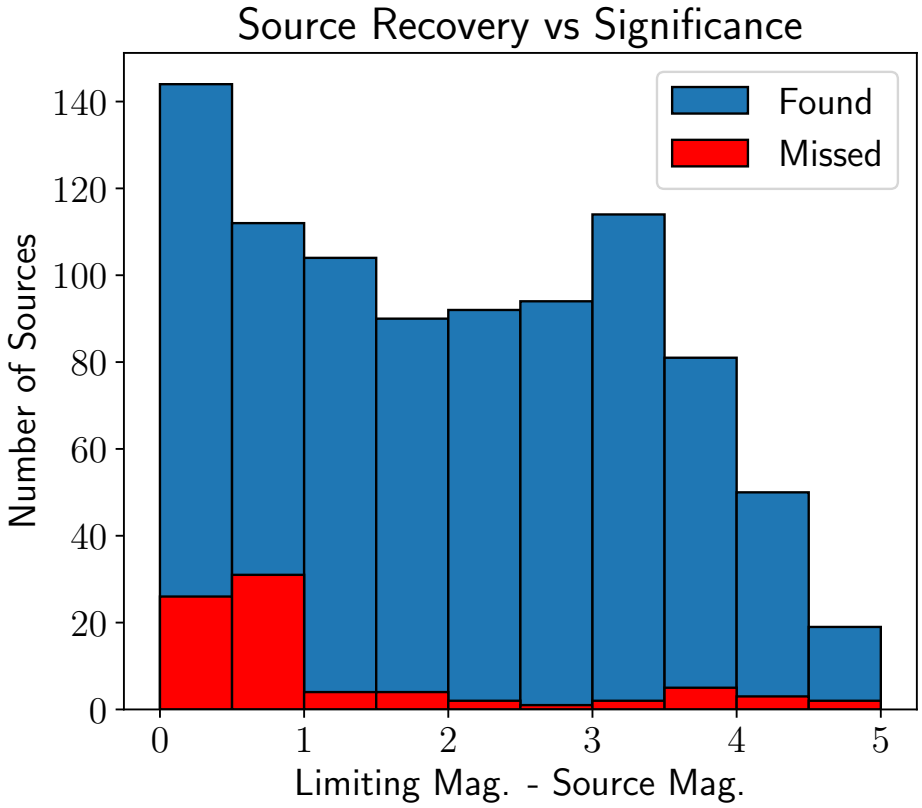

Figure 7.24: **Histogram of recovered and missed sources binned by the difference of the source magnitude and limiting magnitude of the image.** These data are the same from Figure 7.23.

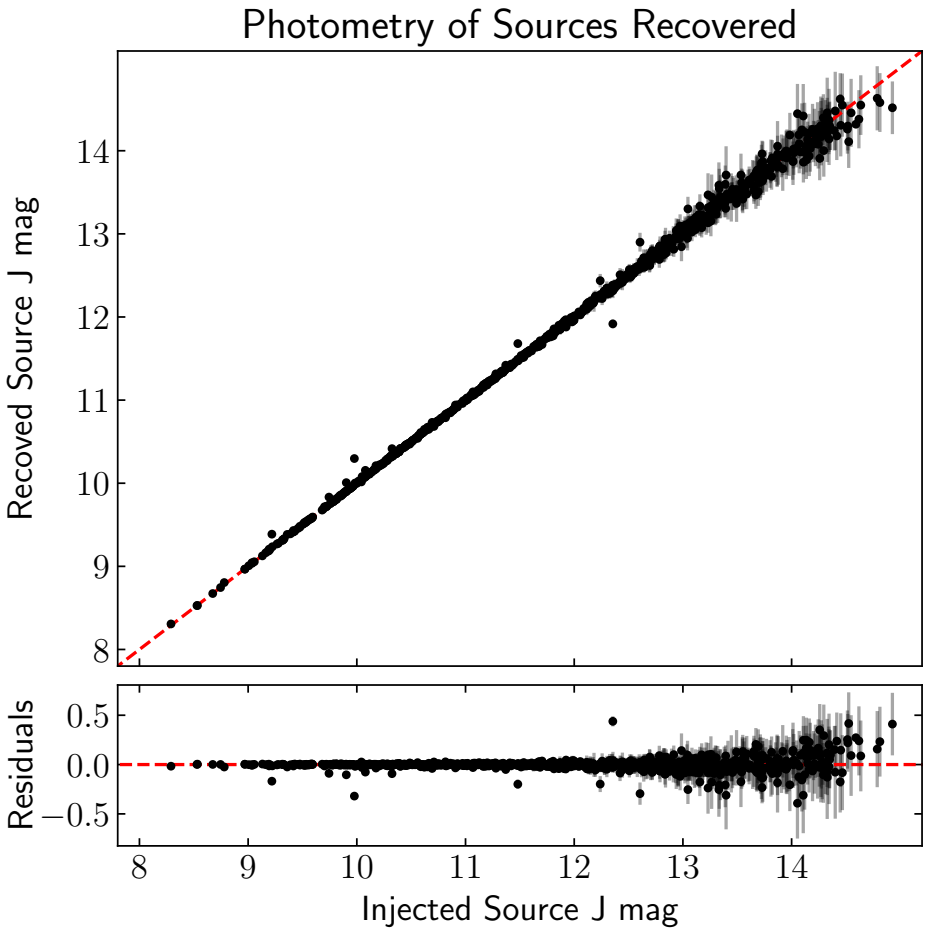

Figure 7.25: **Injected vs. recovered magnitude of sources by the subtraction pipeline.** The dashed red line in the top plot shows x=y, which the data generally follows. The bottom panel shows the source residuals with the red dashed line indicating the zero level.

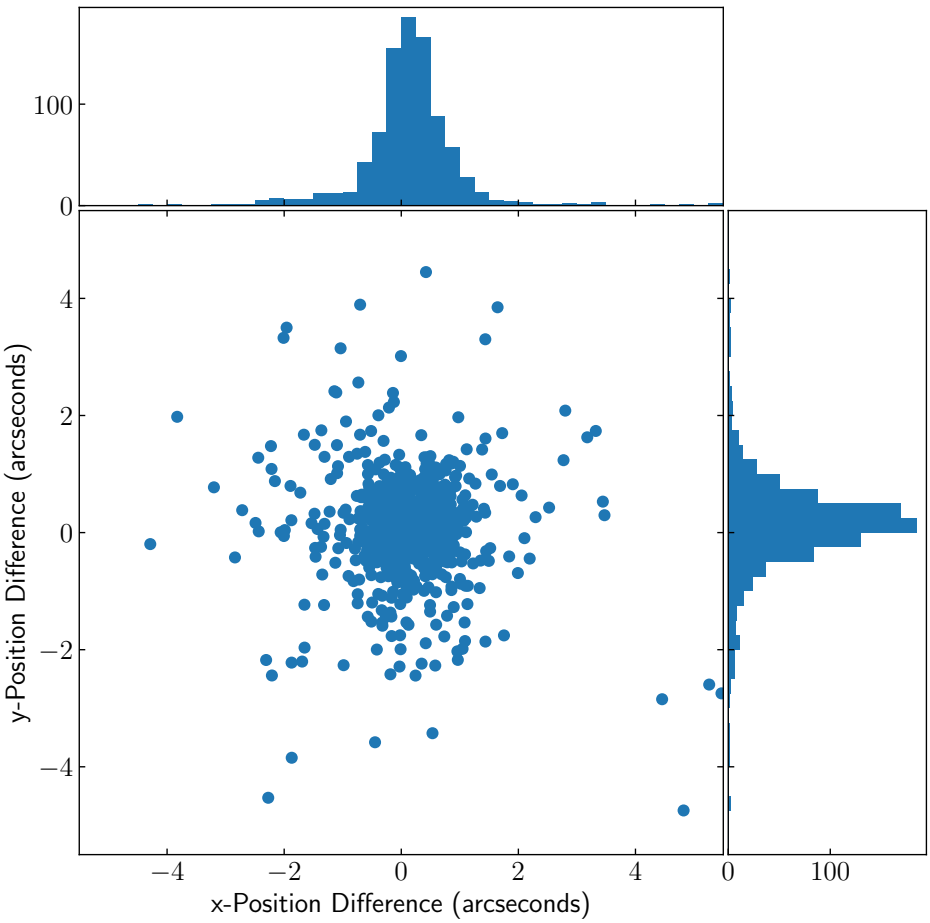

Figure 7.26: **The astrometric precision of recovered candidates in the GDPS subtraction pipeline.** The central scatter plot shows the difference of the injected source position and the recovered source position. The histograms show the values for the scatter plot with respect to the x and y directions.

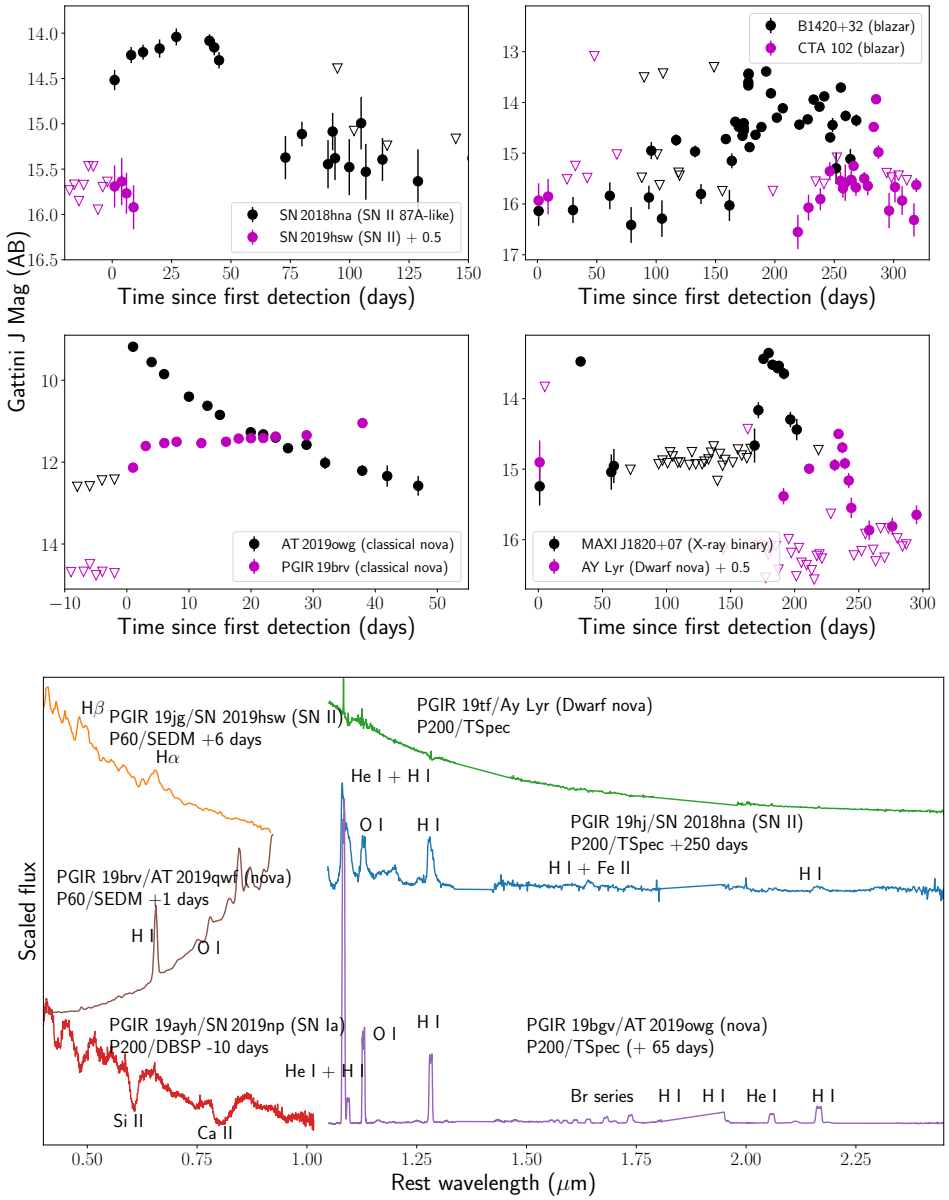

Figure 7.27: **Light curves and spectra of transients detected by Gattini-IR near the commissioning phase**. (Top panel) Collage of light curves of extragalactic and Galactic transients detected with Gattini. Circles denote detections while inverted triangles are 5σ upper limits. The extragalactic transients include the Type II SN 1987A-like SN 2018hna (PGIR 19hj) and Type II SN 2019hsw (PGIR 19jg), as well as the large amplitude flaring blazars B21420+32 (PGIR 19c) and CTA 102 (PGIR 19ayd). The Galactic transients include the reddened classical novae PGIR 19brv (AT 2019qwf) and PGIR 19bgv (AT 2019owg), a flaring X-ray binary MAXI J1820+07 (PGIR 19auj), and a recurrent dwarf nova Ay Lyr (PGIR 19tf). (Lower panel) Optical and NIR spectra obtained as follow-up for some of these sources, marking the prominent spectral lines in each source. In addition, we show an optical spectrum of the Type Ia SN 2019np (PGIR 19ayh).

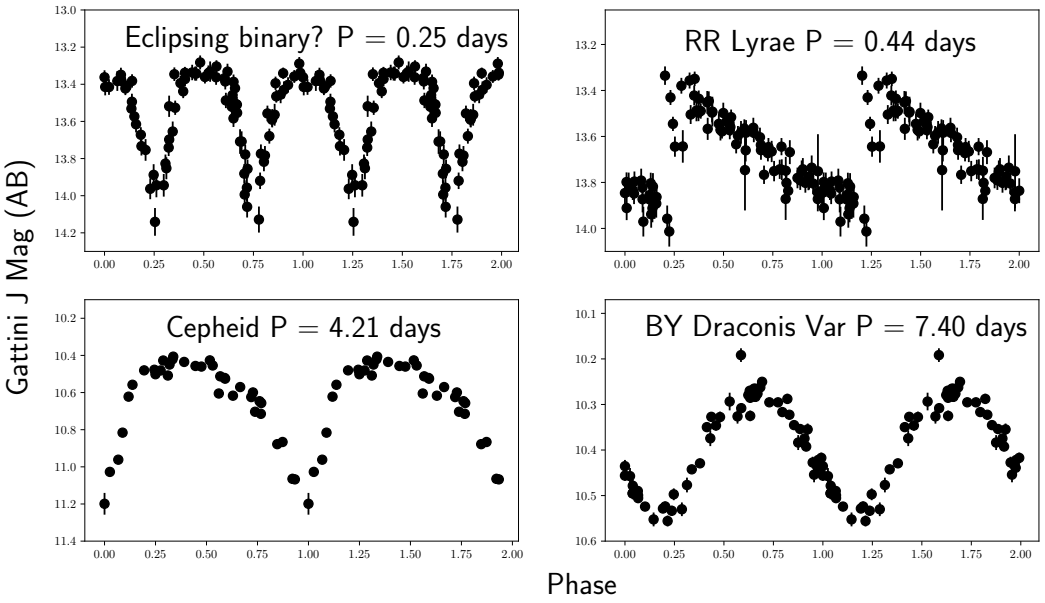

Figure 7.28: **Periodic variables recovered in the Gattini data.** The periods were recovered by running a blind period finding algorithm on match file products generated by GDPS, and folding at the best period. This figure represents a sample of periodic sources recovered in the period search. All sources apart from the top left panel had previous classifications in SIMBAD, while the top left panel represents a candidate eclipsing binary with a short period of 0.12 days.

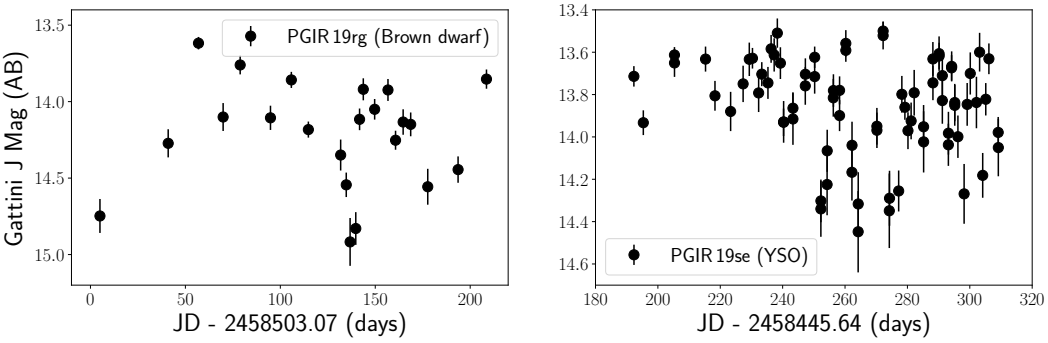

Figure 7.29: **Large amplitude Galactic variables identified as transients in the subtraction pipeline.** The left panel shows a M3.3 type brown dwarf reported in Dawson et al., 2014. The right panel shows large amplitude variability from a candidate YSO PGIR 19se, for which the classification was confirmed with optical spectroscopy on the Palomar 200-inch telescope.

Chapter 8

A POPULATION OF HEAVILY REDDENED, OPTICALLY MISSED NOVAE FROM PALOMAR GATTINI-IR: CONSTRAINTS ON THE GALACTIC NOVA RATE

De, K. et al. (2021). "A Population of Heavily Reddened, Optically Missed Novae from Palomar Gattini-IR: Constraints on the Galactic Nova Rate". In: *ApJ* 912.19, 20, p. 20. DOI: 10.3847/1538-4357/abeb75. arXiv: 2101.04045 [astro-ph.HE].

Kishalay De[1], Mansi M. Kasliwal[1], Matthew J. Hankins[2], Jennifer Sokoloski[3], Scott M. Adams[1], Michael C. B. Ashley[4], Aliya-Nur Babul[5], Ashot Bagdasaryan[1], Alexandre Delacroix[6], Richard G. Dekany[6], Timothee Greffe[6], David Hale[6], Jacob E. Jencson[1,7], Viraj R. Karambelkar[1], Ryan M. Lau[8], Ashish Mahabal[1], Daniel McKenna[6], Anna M. Moore[9], Eran O. Ofek[10], Manasi Sharma[11], Roger M. Smith[6], Jamie Soon[9], Roberto Soria[12], Gokul Srinivasaragavan[1], Samaporn Tinyanont[13], Tony Travouillon[9], Anastasios Tzanidakis[1], and Yuhan Yao[1]

[1]Cahill Center for Astrophysics, California Institute of Technology, 1200 E. California Blvd., Pasadena, CA 91125, USA
[2]Arkansas Tech University, Russellville, AR 72801, USA
[3]Columbia Astrophysics Laboratory, Columbia University, 550 West 120th Street, New York, NY 10027, USA
[4]School of Physics, University of New South Wales, Sydney NSW 2052, Australia
[5] Department of Astronomy, Columbia University, 550 West 120th Street, New York, NY 10027, U.S.A.
[6] Caltech Optical Observatories, California Institute of Technology, Pasadena, CA 91125, USA
[7]Steward Observatory, University of Arizona, 933 North Cherry Avenue, Tucson, AZ85721-0065, USA
[8]Institute of Space & Astronautical Science, Japan Aerospace Exploration Agency, 3-1-1 Yoshinodai, Chuo-ku, Sagamihara, Kanagawa 252-5210, Japan
[9]Research School of Astronomy and Astrophysics, Australian National University, Canberra, ACT 2611, Australia
[10]Department of Particle Physics & Astrophysics, Weizmann Institute of Science, Rehovot 76100, Israel
[11]Department of Physics, Pupin Hall, Columbia University, New York, NY 10027, USA
[12]National Astronomical Observatories, Chinese Academy of Sciences, Beijing 100012, China
[13]University of California Santa Cruz, 1156 High St, Santa Cruz, CA 95064

Abstract

The nova rate in the Milky Way remains largely uncertain, despite its vital importance in constraining models of Galactic chemical evolution as well as understanding progenitor channels for Type Ia supernovae. The rate has been previously estimated in the range of $\approx 10-300\,\mathrm{yr}^{-1}$, either based on extrapolations from a handful of very

bright optical novae or the nova rates in nearby galaxies; both methods are subject to debatable assumptions. The total discovery rate of optical novae remains much smaller ($\approx 5-10\,\mathrm{yr}^{-1}$) than these estimates, even with the advent of all-sky optical time domain surveys. Here, we present a systematic sample of 12 spectroscopically confirmed Galactic novae detected in the first 17 months of Palomar Gattini-IR (PGIR), a wide-field near-infrared time domain survey. Operating in J-band ($\approx 1.2\,\mu$m) that is significantly less affected by dust extinction compared to optical bands, the extinction distribution of the PGIR sample is highly skewed to large extinction values ($>$ 50% of events obscured by $A_V \gtrsim 5$ mag). Using recent estimates for the distribution of Galactic mass and dust, we show that the extinction distribution of the PGIR sample is commensurate with dust models. The PGIR extinction distribution is inconsistent with that reported in previous optical searches (null hypothesis probability $< 0.01\%$), suggesting that a large population of highly obscured novae have been systematically missed in previous optical searches. We perform the first quantitative simulation of a 3π time domain survey to estimate the Galactic nova rate using PGIR, and derive a rate of $\approx 43.7^{+19.5}_{-8.7}\,\mathrm{yr}^{-1}$. Our results suggest that all-sky near-infrared time-domain surveys are well poised to uncover the Galactic nova population.

8.1 Introduction

A nova outburst arises from a thermonuclear runaway on the surface of a white dwarf caused by unstable nuclear burning in a degenerate layer accreted from a companion (Bode et al., 2008; Chomiuk et al., 2020; Della Valle et al., 2020; Starrfield et al., 2016). As factories for the nucleosynthesis of elements as well as crucial phases in the evolution of binary low mass stars, the total rate and demographics of novae in the Milky Way are important to constrain the chemical evolution of the Galaxy. Nucleosynthesis in novae (see Gehrz et al., 1998 and José et al., 2006 for reviews) plays a crucial role in the synthesis of isotopes like ^{7}Li, ^{22}Na, ^{26}Al and ^{15}N (Prantzos, 2012; Romano et al., 2003). Novae have also been long suggested as possible progenitors of Type Ia supernovae (Shafter et al., 2015; Soraisam et al., 2015; Starrfield et al., 2020a; Starrfield et al., 2020b), especially with the discovery of rapidly recurrent novae such as M31N 2008-12a (Darnley et al., 2014; Henze et al., 2015a,b; Tang et al., 2014). Such recurrent novae likely contain very massive white dwarfs imminent for a complete thermonuclear supernova in $\lesssim 10^6$ years (Hillman et al., 2016; Kato et al., 2014), thus providing unique windows into the still poorly understood progenitors of Type Ia supernovae (see Darnley et al., 2020;

Maoz et al., 2014 for a review).

Despite its importance, the nova rate in the Galaxy remains observationally poorly constrained. Previous estimates for the Galactic nova rate primarily use two classes of techniques. One class uses the observed extragalactic nova rate from nearby galaxies to scale to the Milky Way's estimated K-band luminosity, resulting in rates over a range of $\approx 10 - 50\,\mathrm{yr}^{-1}$ (Ciardullo et al., 1990; Darnley et al., 2006; Della Valle, 1992; della Valle et al., 1994b; Shafter et al., 2000; van den Bergh, 1991). Unlike direct rate measurements of Galactic novae, the extragalactic estimates suffer from uncertainties in the differences between the star formation history, structure, and stellar population of the Milky Way and external galaxies (della Valle et al., 1994a; della Valle et al., 1994b; Shafter, 2002).

The second class of techniques uses the statistics of a handful of bright and nearby Galactic novae to extrapolate the rate to the entire Galaxy, resulting in estimates in a large range of $\approx 30 - 300\,\mathrm{yr}^{-1}$ (Allen, 1954; Hatano et al., 1997; Liller et al., 1987; Ozdonmez et al., 2018; Shafter, 1997, 2017; Shafter, 2002; Sharov, 1972). However, all previous estimates are subject to the poorly quantified selection effects of the discovery of even the brightest optical novae (e.g. Schaefer, 2014; Shafter, 2017). More recently, Mróz et al., 2015 presented a list of likely nova candidates[1] in the Galactic bulge from the Optical Gravitational Microlensing Experiment (OGLE; Udalski et al., 1992) survey, and used it to estimate a bulge rate of $13.8 \pm 2.6\,\mathrm{yr}^{-1}$.

Based on models of the distribution of mass and dust in the Galaxy, Shafter, 2017 suggest that the the number of detectable novae in optical surveys (to a depth of $\approx 17\,\mathrm{mag}$) should be $50^{+31}_{-23}\,\mathrm{yr}^{-1}$ depending on the assumed completeness for the brightest novae ($m < 2$; see their Figure 8 and see also Hatano et al., 1997). Despite the emergence of wide-field optical surveys that can routinely survey the entire sky to this depth, the discovery rate of novae[2,3] has remained much smaller at $\approx 5 - 10\,\mathrm{yr}^{-1}$. Thus, either the nova rate in the Milky Way has been grossly overestimated, or a large fraction of novae are missed or misidentified in optical searches (e.g. Hounsell et al., 2010). Alternatively, since the optical rate estimates are critically subject to uncertainties regarding the distribution of obscuring dust, many novae could be highly reddened and undetectable in optical searches (e.g. Hounsell et al., 2011). In particular, we note that recent estimates of the Galactic

[1] Most candidates in their sample were not confirmed with spectroscopy, and thus have contamination from other types of large amplitude variables like dwarf novae.

[2] `https://asd.gsfc.nasa.gov/Koji.Mukai/novae/novae.html`

[3] `https://github.com/Bill-Gray/galnovae/blob/master/galnovae.txt`

dust distribution (Green et al., 2019) reveal rich structures that are not captured by the simple double-exponential models used in previous works.

Given the extreme dust obscuration in the optical bands (Cardelli et al., 1989), the lower effects of extinction in the near-infrared (NIR[4]) bands make them ideally suited to search for these eruptions. However, large area surveys in the NIR bands have been prohibitively expensive due to the bright sky foreground as well as the high cost of detectors. The Vista Variables in the Via Lactea (VVV; Catelan et al., 2011) survey was one of the largest such experiment carried out previously, involving a deep (to $K \approx 18$ mag) and slow ($\approx 10-30$ epochs per year) time domain survey of a fraction of the southern Galactic bulge and disk. In particular, they reported ≈ 20 dust obscured nova candidates (e.g. Contreras Pena et al., 2017a,b; Saito et al., 2012, 2013a,b) from their search. However, these candidates were not confirmed with real-time spectroscopic follow-up due to their discovery in archival images, and likely contain contamination from large amplitude young stellar object outbursts and foreground dwarf novae (Contreras Pena et al., 2017a).

In this paper, we present a sample of 12 spectroscopically confirmed novae detected in the first 17 months of the Palomar Gattini-IR (PGIR) NIR time domain survey (De et al., 2020b; Moore et al., 2019). PGIR is a robotic, wide-field time domain survey at Palomar observatory using a 25 sq. deg. J-band camera to survey the entire northern visible sky ($\delta > -28.9°$; ≈ 15000 sq. deg.) at a cadence of ≈ 2 nights. We use this sample together with detailed simulations of the PGIR survey to construct the first constraints on the Galactic nova rate using a NIR discovery engine. In Section 8.2, we describe the techniques for identification of large amplitude transients in the PGIR transient stream and the sample of identified novae. In Section 8.3, we compare the extinction distribution of the PGIR nova sample to that in previous optical samples to highlight a population of highly obscured novae that have been systematically missed in optical searches. In Section 8.4, we present detailed simulations of the PGIR survey and detection efficiency of the PGIR pipeline to present constraints on the Galactic nova rate. In Section 8.5, we discuss the assumed parameters for the specific nova rates, luminosity function, and luminosity-width relationships in the context of variations in the derived nova rate. We conclude with a summary of our findings in Section 8.6.

[4]For the rest of this work, we refer to wavelengths $1-3\mu$m as NIR bands.

8.2 Candidate selection

The median 5σ sensitivity of PGIR is 14.8 Vega mag ($\approx$ 15.7 AB mag; De et al., 2020b) outside the Galactic plane. The sensitivity is limited by confusion to $\approx 1-2$ mag shallower in the Galactic plane due to the large ($\approx 8.7''$) pixel scale of the detector (2048×2048 pixels). The typical saturation magnitude for the detector was $\approx$ 8.5 Vega mag until May 2020; a modification of the readout electronics improved the dynamic range to $\approx$ 6.0 Vega mag at the bright end for later data (De et al., 2020a). A dedicated data processing system produces science quality stacked images together with transient candidates identified from subtractions against template images (using the ZOGY algorithm; Zackay et al., 2016) in real-time. Following a deep-learning based machine-learning classification system, the transient candidates are vetted by human scanners on a daily basis for photometric and spectroscopic follow-up.

Identification of nova candidates

This work considers survey data acquired in the first 17 months of the survey – between 2 July 2019 (the start date of the survey when the reference image construction was completed) and 30 Nov 2020 (the end of the 2020 Galactic bulge season in the northern hemisphere). We carried out a systematic search for large amplitude transients in the PGIR stream to search for Galactic novae. Candidate transients were identified as sources with at least three positive detections (i.e., the source flux has increased from the reference image) satisfying the following criteria:

1. Detected with signal-to-noise ratio (SNR) $>$ 8 without saturation. We require that the detection epochs should be separated by $>$ 1 day to eliminate contamination from solar system objects.

2. A real-bogus classification score $RB > 0.5$, that has been tested to produce a false positive rate of 1.6% and a false negative rate of 1.4% (De et al., 2020b).

3. The transient is either hostless (i.e., no known 2MASS counterpart within a radius of 10 arcsec) or has a large amplitude (i.e., is at least 3 mags brighter than any 2MASS counterparts within a radius of 10 arcsec). The choice of the amplitude and radius were defined to exclude the large contamination from variable stars in the Galactic plane given the coarse pixel scale ($\approx$ 8.7 arcsec) of the PGIR detector.

These selection criteria result in an average of $\approx 50-100$ candidates per night to be examined with human vetting. The majority of false positives arise from astrometric

residuals on bright stars in parts of the detector where the point spread function is elongated and sub-optimal (see discussion of image quality variation in De et al., 2020b).

Confirmation and Follow-up

All transients that pass these criteria were cross-matched against external catalogs for prior known classifications. In addition, we identified large amplitude regular/semi-regular variables using independent criteria based on known variable counterparts in archival Wide-field Infrared Survey Explorer (WISE; Mainzer et al., 2011, 2014) images. These sources will be presented as separate publications focusing on R Coronae Borealis variables (Karambelkar et al., 2020) and Young Stellar Objects (Hankins et al., 2020, Hankins et al. in prep.). For sources determined to be bonafide eruptive transients, we assigned photometry and spectroscopy using the Spectral Energy Distribution Machine (SEDM; Blagorodnova et al., 2018) spectrograph mounted on the Palomar 60-inch telescope for rapid confirmation and characterization. The SEDM data were reduced using the automated `pysedm` pipeline (Rigault et al., 2019). In cases where the source was heavily reddened or in very crowded fields preventing a reliable spectrum from SEDM, we used optical / NIR spectroscopy on larger telescopes for classification.

A total of 44 large amplitude transients passed our selection criteria and human vetting. 11 sources were determined to be active galactic nuclei known from prior surveys, 3 were classified as bright extragalactic supernovae (e.g. De et al., 2020i; to be presented in Srinivasaragavan et al. in prep.), 7 sources were determined to be outbursts of young stellar objects (e.g. Hankins et al., 2020, presented in Hillenbrand et al., 2021 and Hankins et al. in prep.) and 1 source was a previously known low mass X-ray binary in outburst (Hankins et al., 2019a). We identified 2 microlensing events using their characteristic photometric evolution (e.g. De et al., 2019e; to be presented in Mroz et al. in prep.)

In particular, dwarf novae (Warner, 1995) from cataclysmic variables bear striking photometric similarities to nova outbursts and represent a contaminant in this search. Despite being substantially more abundant than novae, their relatively low luminosity ($M \approx 3-5$ at peak) distinguishes them from nova outbursts. We thus reject transients that have a peak apparent magnitude fainter than that expected for the lowest luminosity novae ($M \approx -4$ at peak) at the farthest edge of the Galaxy (distance modulus of ≈ 16.5) after accounting for the integrated J-band extinction

PGIR Name	Variable	RA J2000	Dec J2000	MJD First Det.	Peak J Vega mag	Phot-class	Spec-class	$A_{V,c}$ mag	$A_{V,s}$ mag	$A_{V,t}$ mag
PGIR 20ekz	V3731 Oph	17:38:35.1	-25:19:02.9	58685.25	8.71 ± 0.01	S-class?	He/N?	6.4	–	5.5
PGIR 19bte	V2860 Ori	6:09:57.4	12:12:24.8	58735.52	12.07 ± 0.03	D-class	He/N	1.0	1.7 (K 7699)	2.1
PGIR 19bgv	V569 Vul	19:52:08.2	27:42:21.1	58716.28	8.42 ± 0.01	S-class	He/N	8.9	10.0 (K 7699)	9.6
PGIR 19brv	V2891 Cyg	21:09:25.5	48:10:51.9	58743.25	8.83 ± 0.01	F-class	Fe-II	7.3	12.2 (K 7699)	12.1
PGIR 19fai	V3890 Sgr	18:30:43.1	-24:01:10.5	58744.14	9.92 ± 0.01	–	Symbiotic	–	1.9 (Na D1)	1.5
PGIR 20dcl	V659 Sct	18:39:59.7	-10:25:43.1	58904.56	7.59 ± 0.01	J-class	Hybrid	2.9	4.0 (K 7699)	5.7
PGIR 20duo	V2000 Aql	18:43:53.4	0:03:51.7	58981.34	10.38 ± 0.01	S-class	Fe-II	9.4	–	8.4
PGIR 20dsv	V6567 Sgr	18:22:45.2	-19:36:02.6	59001.43	9.01 ± 0.01	O-class	Fe-II	4.6	4.3 (DIB 5780)	4.7
PGIR 20eig	V2029 Aql	19:14:27.0	14:44:32.0	59043.26	10.41 ± 0.02	C-class	Fe-II	6.1	5.7 (DIB 5780)	5.9
PGIR 20emj	V1391 Cas	0:11:42.8	66:11:19.1	59076.48	8.04 ± 0.01	D-class	Fe-II	4.7	4.6 (DIB 5780)	4.0
PGIR 20evr	V6593 Sgr	17:54:59.9	-21:22:41.3	59124.11	6.98 ± 0.01	–	Fe-II	4.2	–	4.7
PGIR 20fbf	V1112 Per	04:29:18.7	+43:54:21.5	59180.22	6.22 ± 0.01	D-class	R-Hybrid	2.3	2.4 (K 7699)	2.1

Table 8.1: **Summary of novae detected in the first 17 months of the PGIR survey**. See Appendix 8.7 for details. The column MJD Detection denotes the first detection of the nova in PGIR difference images, while the Peak J Mag denotes the brightest J magnitude in the nova light curve (note that the PGIR survey may have missed the peak light curve for some novae). The Phot-Class and Spec-Class columns denote the photometric and spectroscopic classes of the nova based on the classification schemes of Strope et al., 2010 and Williams, 1992, respectively. We caution that the light curve parameters and classifications are limited by the photometric coverage available for each nova. The $A_{V,c}$ and $A_{V,s}$ columns indicate the estimated extinction towards the nova using the photometric color and spectroscopic methods, respectively, while the $A_{V,t}$ column indicates the total Galactic extinction along this direction estimated in Schlafly et al., 2011. For each spectroscopic reddening measurement, we indicate the absorption feature used to estimate the reddening. We caution that the high extinction inferred towards most events lie in a regime beyond the well-calibrated range for these features.

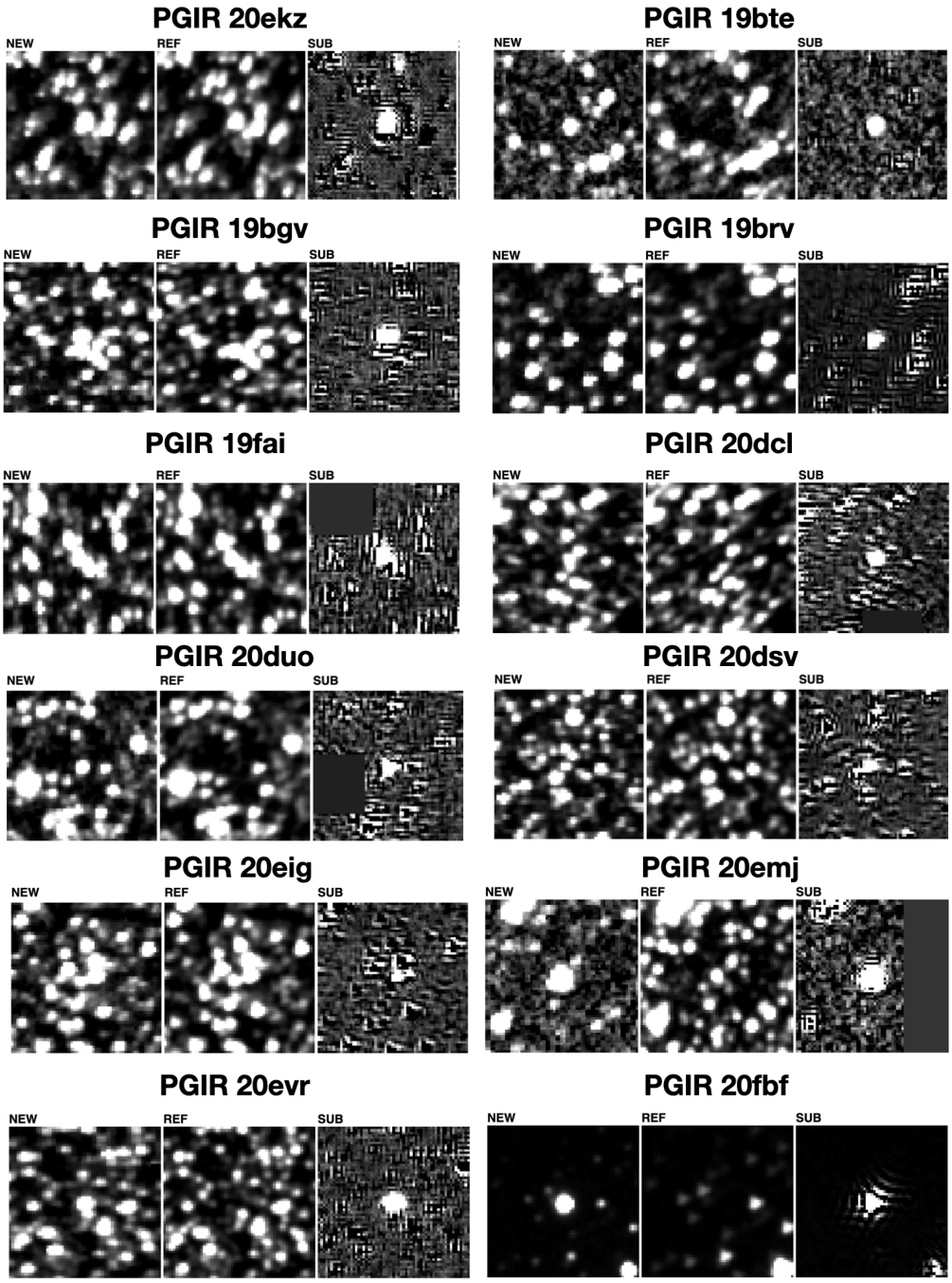

Figure 8.1: **Cutout triplets of science (new), reference (ref), and difference (sub) images of novae detected in the the first 17 months of the PGIR survey.** The name of the nova is indicated on top of each triplet. The novae are clearly detected as bright transients at the center of the subtracted image in each panel. The variation in the image quality for different sources is due to the variation of the optical point spread function across the detector plane (De et al., 2020b).

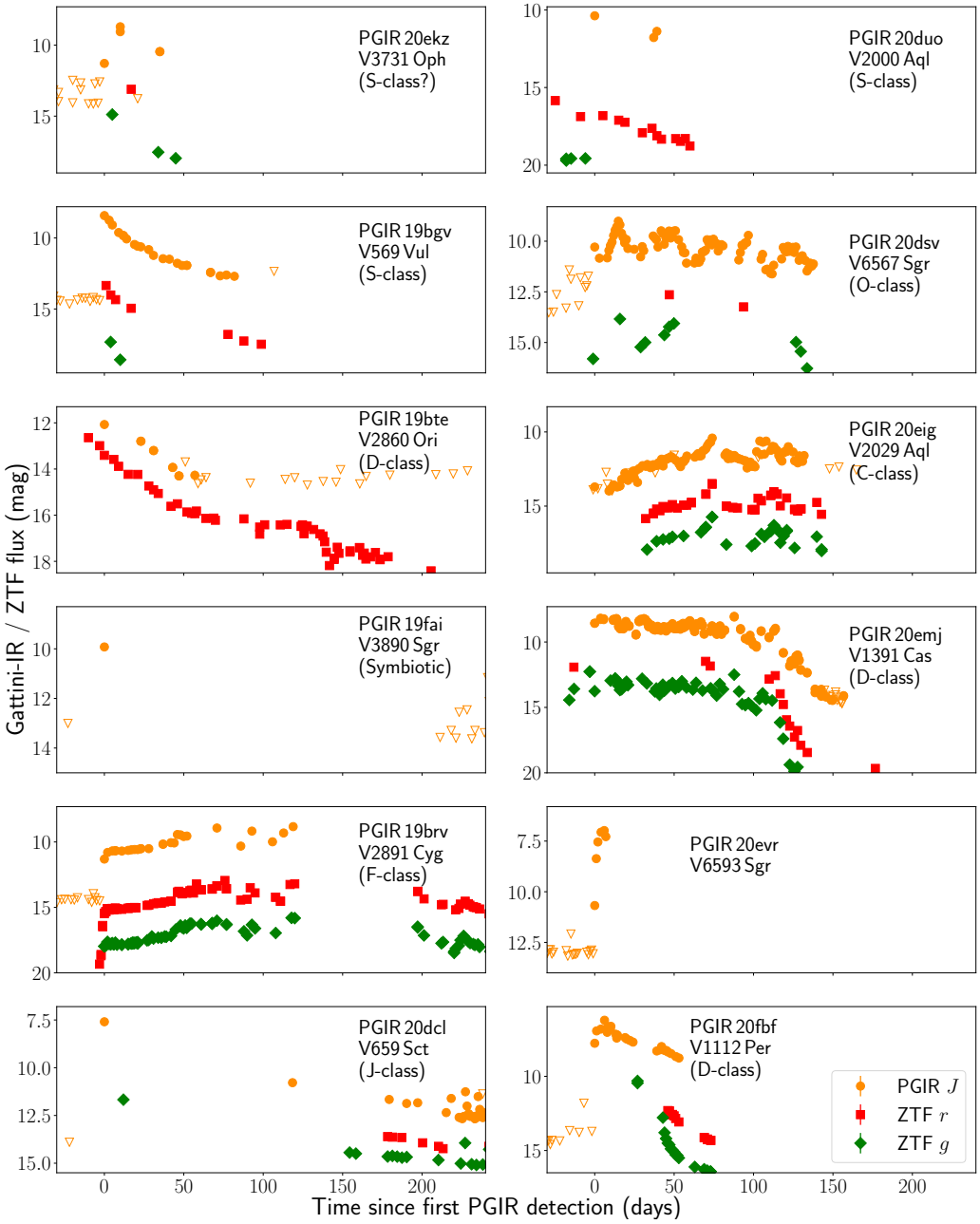

Figure 8.2: **Multi-color light curves of the PGIR nova sample from Gattini-IR (J-band as orange circles) and ZTF (g-band as green diamonds and r-band as red squares).** Hollow inverted triangles show 5σ upper limits from PGIR. In each panel, the name of the nova is shown along with its photometric class based on the classification scheme in Strope et al., 2010. The lack of post-peak photometric data precludes a classification for PGIR 20evr.

along the line of sight (Schlafly et al., 2011). We further used archival classifications from SIMBAD as well as data from other time domain surveys (e.g., prior eruptions

detected in the optical) to reject these objects[5]. Together, we identified a total of 9 dwarf nova outbursts in our search. Appendix 8.7 summarizes two previously unknown dwarf novae that we followed up and confirmed with spectroscopy.

In this paper, we focus on the sample of 12 spectroscopically confirmed novae found from this search. Eleven out of the 12 novae discussed here were selected using the criteria discussed above; the only exception is the 2019 eruption of the symbiotic-like recurrent nova V3890 Sgr (Page et al., 2020; Schaefer, 2010). The eruption of V3890 Sgr was detected in its early stages in the PGIR data, but did not pass our selection criteria due to saturation of the detector near peak brightness, and we include it here for completeness. In cases where the nova was first identified in PGIR survey data, the detection and spectroscopic confirmation were immediately announced to the community via the Transient Name Server[6] and The Astronomer's Telegram (De et al., 2019f, 2020d,e,g,h).

Detection images of identified PGIR novae are shown in Figure 8.1 and their light curves shown in Figure 8.2. Table 8.1 summarizes the properties of novae discussed in this paper, while Appendix 8.7 presents a brief summary of the initial identification and properties of each nova. All the novae presented here were identified and followed up in real-time during the eruption, with the exception of V3731 Oph, which was confirmed with a late-time spectrum in September 2019 from an archival search of early PGIR survey data (De et al., 2020f). Our search detected all but one nova reported publicly in the PGIR observing footprint during the survey period considered. The confirmed nova V670 Ser (Aydi et al., 2020a; Taguchi et al., 2020) was not detected due to its eruption shortly after solar conjunction when PGIR was not observing the field.

We accumulated multi-color photometry of each nova by performing forced photometry on the PGIR difference images, and accumulated publicly available r-band and g-band data from the Zwicky Transient Facility optical time domain survey (Bellm et al., 2019b; Masci et al., 2019). Figure 8.2 shows a collage of the optical/NIR light curves of the novae presented here. We classify the light curves using the combined optical and NIR dataset based on the scheme presented in Strope et al., 2010 and discuss features of individual objects in Appendix 8.7. As shown in Figure 8.2,

[5]In order to ensure that recurrent novae were not mistaken as repeating dwarf nova outbursts, we confirmed the classification of all sources that were bright enough to be novae at the farthest edge of the Galaxy by examining publicly available reports and spectra.

[6]`https://wis-tns.org`

the PGIR nova sample consists of diverse photometric classes encompassing all the types discussed in Strope et al., 2010.

In order to determine spectroscopic classifications of confirmed novae (Williams, 1992), we obtained medium resolution optical and infrared spectroscopic follow-up (see Figure 8.3) using the Palomar 200-inch telescope (P200) at Palomar observatory, the NASA Infrared Telescope Facility (IRTF) and Keck-I telescopes at Mauna Kea, and the 2.3 m telescope at Siding Spring Observatory (SSO). The P200 data were acquired using the optical Double Spectrograph (DBSP; Oke et al., 1982) and near-infrared Triple spectrograph (TSpec; Herter et al., 2008). The DBSP data were reduced using the `pyraf-dbsp` pipeline (Bellm et al., 2016) while the TSpec data were reduced using the `spextool` (Cushing et al., 2004) and `xtellcor` (Vacca et al., 2003) packages. The IRTF data were acquired with the SpeX instrument (Rayner et al., 2003) in the SXD mode ($\approx 0.7 - 2.5\mu$m) as part of programs 2020A111 and 2020B087 (PI: K. De). The data were reduced using the `spextool` (Cushing et al., 2004) and `xtellcor` (Vacca et al., 2003) packages. The Keck spectrum of PGIR 20ekz was acquired using the Low Resolution Imaging Spectrometer (LRIS; Oke et al., 1995) and was reduced using the `lpipe` package (Perley, 2019). The SSO data were acquired using the Wide-field Spectrograph (WiFeS; Dopita et al., 2010) on the ANU 2.3 m telescope and reduced using the PyWiFeS pipeline (Childress et al., 2014).

8.3 The extinction distribution

A striking feature of the PGIR novae is the abundance of highly reddened novae (as is evident from both photometry and spectroscopy; Figures 8.2, 8.3). We thus compare this sample to previous optically selected nova samples by deriving extinction estimates for each object using both photometric and spectroscopic methods.

Extinction from photometric color evolution

As in several previous works (e.g. Hachisu et al., 2014, 2016), we use the photometric color evolution of novae to estimate the line-of-sight extinction. While there is some uncertainty on the exact template phase as well as color during the eruption, the intrinsic color of novae has been estimated to be $B-V \approx 0.0-0.2$ mag (Hachisu et al., 2014; Miroshnichenko, 1988; van den Bergh et al., 1987) and consistent with the colors of A5V stars (Shafter et al., 2009). For objects in our sample with multi-color photometry, we use the intrinsic colors of A5V stars from Kraus et al., 2007 of $(g-J)_0 = 0.35$ mag and $(r-J)_0 = 0.42$ mag to estimate extinctions using

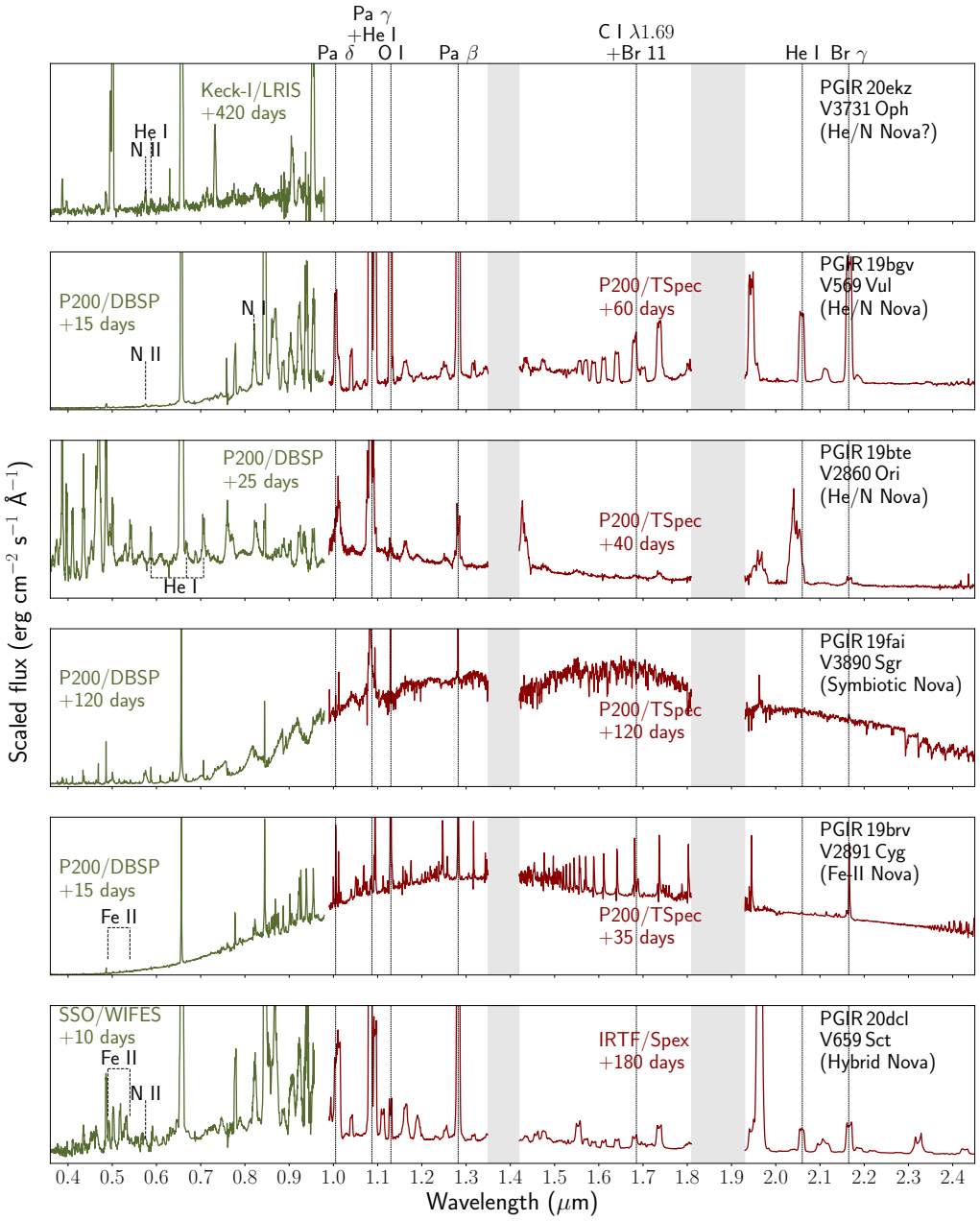

Figure 8.3: **Medium resolution optical and near-infrared spectra of the sample of novae discussed in this work.** Bands of low atmospheric transmission in the NIR are blocked out as shaded bands. In each panel, we indicate the instrument used and the phase of the spectrum with respect to the date of first detection in Table 8.1. We show the name(s) of the nova along with their spectroscopic classification according to the scheme of Williams, 1992. In each panel, we also highlight the primary spectroscopic features used to identify the nova type (R. Williams, priv. comm.), with the exception of V3890 Sgr which is a known symbiotic-like recurrent nova (Schaefer, 2010). See Appendix 8.7 for more details.

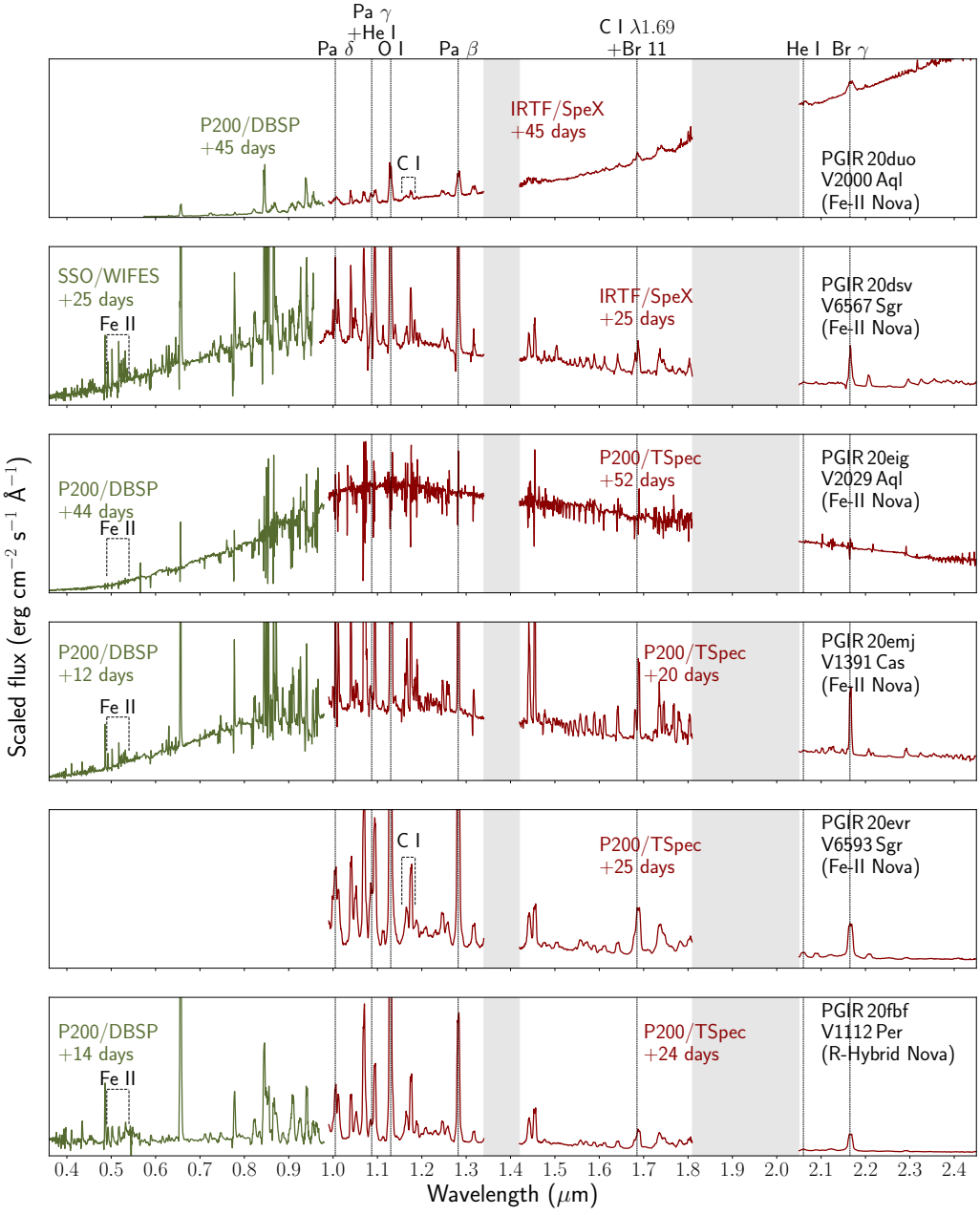

Figure 8.3: Continued.

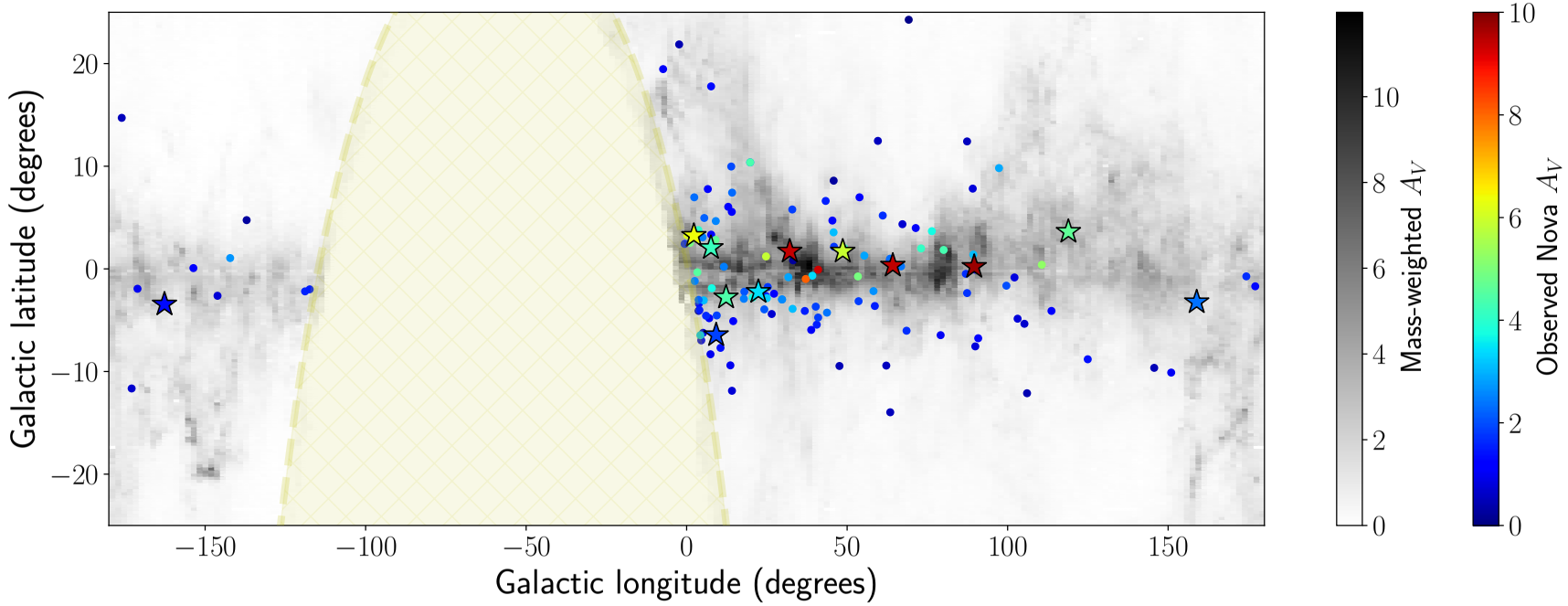

Figure 8.4: **Sky distribution of the PGIR nova sample (in galactic coordinates) shown as stars together with previous optical nova samples (in circles) from Ozdonmez et al., 2016 and Ozdonmez et al., 2018.** In the background, we overlay a grey-shaded map of the mass-weighted dust distribution (see text) in the Galaxy using the Milky Way mass model from Cautun et al., 2020 and dust distribution from Green et al., 2019. For each nova, we also show the inferred extinction towards the nova indicated by the rainbow color bar on the right. For the PGIR novae, we use the average of the extinction estimated from photometric and spectroscopic methods. The yellow shaded region lies south of the $\delta = -28.9°$ viewing limit of PGIR, and is not included in the Green et al., 2019 maps (which are based on PS1 images).

a Cardelli et al., 1989[7] extinction law as

$$\begin{aligned} A_V &= 1.06\,E(g-J) = 1.75\,E(r-J) \\ &= 1.06\,((g-J)-(g-J)_0) = 1.06\,((g-J)-0.35) \\ &= 1.75\,((r-J)-(r-J)_0) = 1.75\,((r-J)-0.42) \end{aligned} \tag{8.1}$$

where $(g-J)$ and $(r-J)$ are the observed nova colors near peak. We expect an uncertainty of ≈ 0.2 mag using this method, based on the spread in estimated values of the intrinsic $B-V$ color. The extinctions derived using this method are given in Table 8.1.

Extinction from spectroscopic features

As in previous works (e.g. Ozdonmez et al., 2016, 2018), we use the equivalent widths of the Na I D ($\lambda\lambda$5890.0, 5895.9 Å) and K I (λ7699 Å) lines to estimate the line-of-sight extinction to each nova using the calibration in Munari et al., 1997. We also search for absorption from the diffuse interstellar band (DIB) features to constrain the extinction using previously established relations (Yuan et al., 2012). In several cases, the novae exhibit broad/P-Cygni features in the Na and K lines precluding measurements of the interstellar features given our relatively low resolution spectra. Hence, we attempt to use the DIB features in these objects. We note that the K I line has been shown to be more sensitive at higher extinctions unlike the Na I lines which saturate beyond $E(B-V) \gtrsim 1.5$ mag (Munari et al., 1997); hence, we use the K I lines where detected. Regardless, the highly reddened nature of most of these sources ($E(B-V) \gtrsim 1.5$ mag) require extrapolation of the nominal relationships beyond their previously established range. The derived extinctions are given in Table 8.1 and a description of the derived extinction values are given in Appendix 8.7.

Consistency of the extinction estimates

As shown in Table 8.1, the estimates derived using the photometric and spectroscopic methods are generally consistent with each other in cases where the spectroscopic features are not saturated ($A_V \lesssim 5.0$ mag). We further examined distances for the quiescent counterparts in the Gaia EDR3 catalog (Bailer-Jones et al., 2020), and identified possible counterparts for only four of the twelve novae. For V2860 Ori, the counterpart is clearly identified with a parallax-based distance of $\approx 3.4-6.4$ kpc, corresponding to an estimated extinction of $A_V \approx 1.6-2.0$ mag (Green et al., 2019),

[7]Throughout this paper, we assume $R_V = A_V/E(B-V) = 3.1$ to relate the extinction across the optical and NIR bands.

consistent with our estimate. The bright symbiotic counterpart of V3890 Sgr has a reported distance of $\approx 6.1 - 8.9$ kpc, corresponding to $A_V \approx 1.6$ mag. For the case of V6593 Sgr and V1112 Per, we derive distance-based extinctions of $A_V \approx 2.3 - 3.5$ mag and $A_V \approx 1.1 - 1.5$ mag, respectively, which are somewhat lower than the photometric/spectroscopic estimates. However, given the large uncertainties in the distance estimates, it is difficult to ascertain the significance of differences in extinction estimates of $E(B-V) \lesssim 0.2$ mag.

Table 8.1 also shows the total integrated extinction expected along this line of sight from the maps of Schlafly et al., 2011. For some of the novae (e.g. V3731 Oph, V2000 Aql, V1391 Cas), the inferred extinctions are marginally larger (by $\lesssim 15\%$) than the total estimated extinction along the line of sight. Given the limited calibration of the nova extinction estimates at very high extinction values, we are unable to quantify the significance of the differences; we thus suggest that the inferred extinction towards the novae are largely consistent with interstellar dust extinction.

Comparison to optically discovered novae

We compare the derived extinction distribution of this sample to previous optically selected objects. We refer to the work of Ozdonmez et al., 2016 and Ozdonmez et al., 2018, who accumulated a complete sample of extinction estimates (see Appendix of Ozdonmez et al., 2016 for details of individual objects) of (≈ 180) optically discovered novae with photometric or spectroscopic measurements until 2018. In Figure 8.4, we show the sky distribution of the optically discovered novae compared to the PGIR nova sample, colored by the inferred extinction towards each nova. Figure 8.4 also shows the estimated mass-weighted dust extinction along the line of sight (see Section 8.3), in particular, noting the complex dust structures that correlate with the inferred extinction towards the novae.

Unlike the PGIR sample that is concentrated towards heavily extincted regions near the Galactic plane, Figure 8.4 shows that previous optically discovered novae appear to preferentially populate higher galactic latitudes while also exhibiting lower extinction. The relative scarcity of optically discovered novae near the central Galactic plane is surprising since the stellar mass density is the highest in this region, and already suggests that the heavy dust extinction prevents optical discovery in this region. In order to quantify this striking bias, we compare the cumulative distribution of the extinction (A_V) for previous optically selected novae to the PGIR sample in Figure 8.5. As shown, the distribution for the PGIR sample is distinctively skewed

towards larger extinction values compared to the optical sample. Performing a Kolmogorov-Smirnov (KS) test as well as an Anderson-Darling (AD) test between the optical and PGIR NIR samples (both photometric and spectroscopic estimates), we find that the null-hypothesis probability of being drawn from the same underlying population is $< 0.01\%$. This provides strong evidence that the PGIR sample uniquely probes a population of highly reddened novae that have been largely missed in previous optical searches.

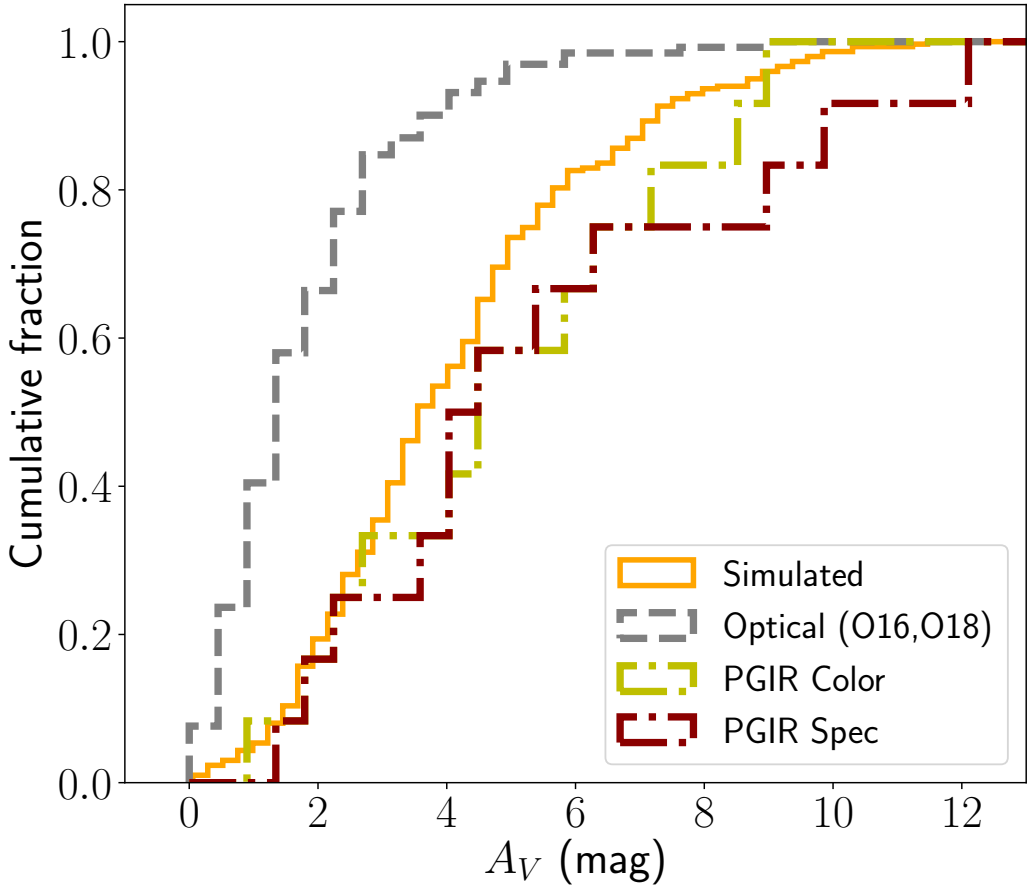

Figure 8.5: **Comparison of the extinction (A_V) distribution of the PGIR sample (both photometric color and spectroscopic absorption estimates) of novae to that in previous optically selected samples**. The optical samples consist of a total of 131 objects from Ozdonmez et al., 2016 (O16) and Ozdonmez et al., 2018 (018). We only include optically selected novae in the footprint accessible to PGIR for comparison. In cases where reliable spectroscopic estimates are not available, we use the color-based extinction estimates in the spectroscopic distribution curve (see Table 8.1). Also shown is the expected extinction distribution derived assuming that the novae trace the stellar mass distribution in the Galaxy, and using 3D dust distribution models from Green et al., 2019.

Simulated estimate for the Galaxy

We now compare the extinction distribution in Figure 8.5 to realistic models for the Milky Way. We use recent estimates of the stellar mass distribution from Cautun et al., 2020 calibrated to Gaia DR2, that consists of three distinct components – a bulge, a thin disk, and a thick disk (Bissantz et al., 2002; Jurić et al., 2008; McMillan, 2017). We use the derived parameters in Tables 1 and 2 of Cautun et al., 2020 for a contracted halo model. We utilize the mass distribution together with the Galactic dust distribution using the `Bayestar2019` model from Green et al., 2019 to estimate a mass-weighted extinction sky map from Earth. The mass weighted map is created by averaging the three dimensional extinction map along each line of sight over distances ranging from 0.1 kpc to 100 kpc weighted by the stellar mass density at each distance. The resulting distribution is shown in Figure 8.4, exhibiting rich structures in the dust distribution along the Galactic plane. Assuming novae roughly trace the Galactic stellar mass distribution, the mass weighted extinction map indicates the typical expected extinction towards novae along each line of sight.

We then create a simulated population of 1000 novae that are randomly placed in the Galaxy with the spatial probability weighted by the Galactic stellar mass distribution model. For each nova in the simulated population, we estimate the extinction towards the nova using its Galactic position and the three dimensional extinction map from Green et al., 2019. We use the prescribed relationship between the `Bayestar2019` reddening and the visual extinction A_V given in Green et al., 2019. The distribution of extinction estimates (limited to $\delta > -30^\circ$ covered by the PS1 maps) for this simulated population is shown in Figure 8.5. As shown, the distribution observed for the optically selected population is preferentially skewed to low extinction values while realistic estimates for the Galaxy suggest that more than 50% of novae should be obscured by $A_V \gtrsim 4$ mag. On the other hand, we find that the PGIR distribution exhibits the expected high extinction tail with $> 50\%$ of events obscured by $A_V \gtrsim 5$ mag, and thus commensurate with the expected distribution.

This result bolsters our suggestion that previous optical searches have likely missed a large population of highly reddened (and optically faint) novae. Alternatively, some reddened novae could be misidentified as dwarf novae in optical searches and not followed up with spectroscopy. This holds true in the case of the nova V6567 Sgr which was independently reported as a dwarf nova candidate by the ASASSN survey[8], and in the case of V2000 Aql which was independently reported by the

[8] `http://www.astronomy.ohio-state.edu/asassn/transients.html`

MASTER survey (Pogrosheva et al., 2020) as a faint Galactic optical transient, and not followed up with spectroscopy before the bright NIR detection. However, recent work by Kawash et al., 2021 suggests that it is unlikely that misidentified dwarf nova outbursts in the ASASSN sample can explain the large dearth of reddened novae in optical searches, suggesting that highly reddened novae have been undetected in optical searches.

8.4 The Galactic rate of novae

Having demonstrated that previous optical searches have likely missed a large fraction of novae, we turn to using the unique sensitivity of PGIR to dust obscured novae to constrain the Galactic rate. We proceed by using the 11 novae that passed the selection criteria for our search (Nova V3890 Sgr did not pass our selection criteria), and estimate the Galactic rate assuming a simple model where novae trace the stellar mass distribution in the Galaxy. We discuss this assumption together with other additional effects in Section 8.5.

The pipeline detection efficiency

Since the nova sample was identified using the candidates generated by the PGIR transient detection pipeline, we first quantify its detection efficiency. The overall detection efficiency has been demonstrated to be high, recovering $> 90\%$ of sources down to the 5σ limiting magnitude (De et al., 2020b). However, the efficiency is known to vary as a function of sky position due to varying amounts of source crowding and confusion given the large pixel scale of the detector. In order to quantify these biases, we selected 137 fields[9] distributed across galactic longitude in $0^\circ < l < 180^\circ$ and galactic latitudes in $-30 < b < 30^\circ$ to inject artificial sources into the images over a range of magnitudes. Since the detection efficiency is roughly constant at $|b| \geq 30^\circ$, we restrict our analysis to $|b| \leq 30^\circ$.

Figure 8.6 shows the sky positions of the fields where we injected artificial sources. For each selected field, we injected 200 artificial sources over a random selection of epochs, and distributed between the respective limiting and saturation magnitude. The artificial sources were injected in accordance with our nova identification criteria of requiring a detection at > 3 mags brighter than the nearest 2MASS source within $10''$ (if any). The images were then processed through the PGIR subtraction pipeline, and the detection efficiency (fraction of sources recovered) was quantified as a function of the relative brightness of the injected source with respect to the 5σ

[9]The entire sky north of $\delta = -28.9^\circ$ is divided into 1329 PGIR fields.

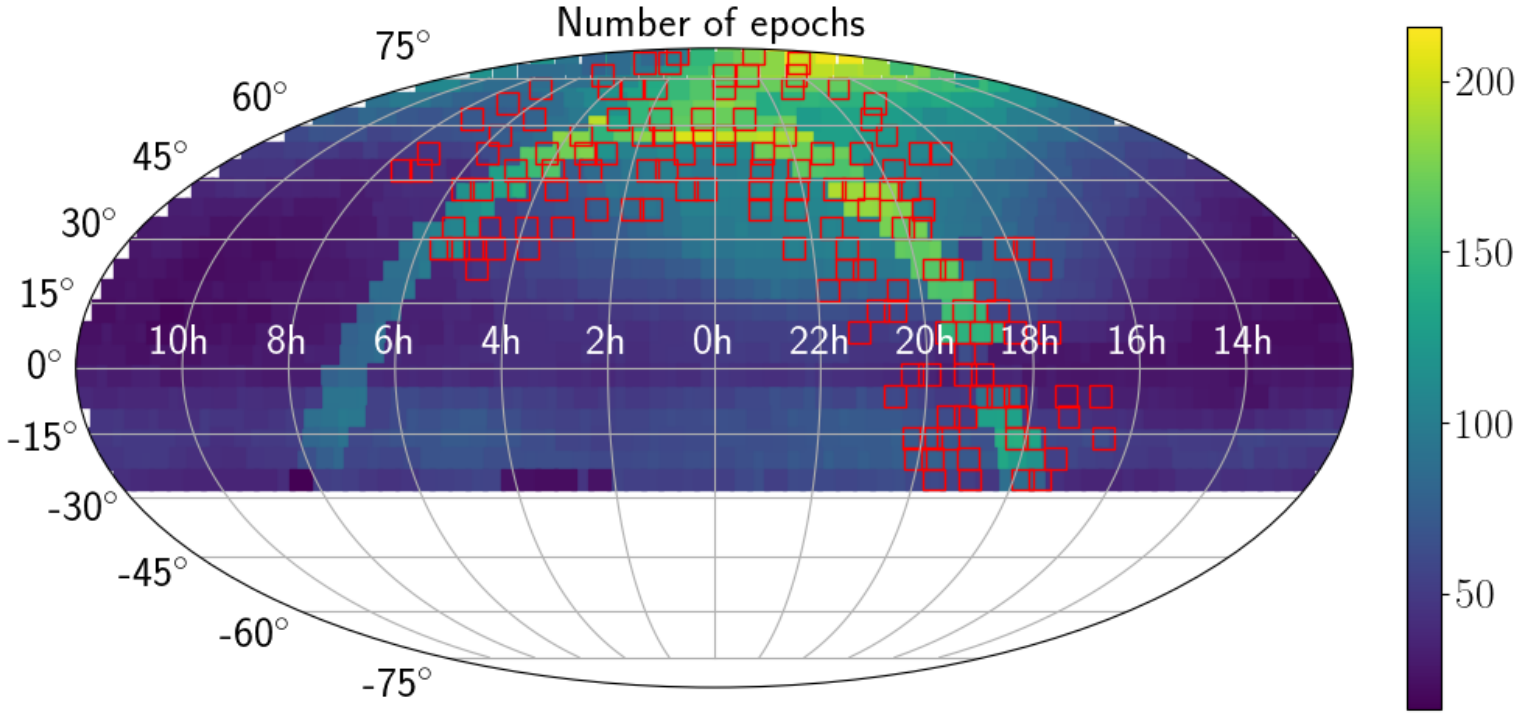

Figure 8.6: **All-sky distribution of the number of epochs of observations from PGIR during the first 17 months of the survey.** Fields at higher declination have larger number of epochs due to longer visibility over the year. Fields in the galactic plane also received a large number of visits due to a dedicated 1-day cadence observing program of the Galactic plane in 2020. The red squares show the sky positions of the fields where we carried out artificial source recovery tests.

limiting magnitude of the image. Figure 8.7 shows the resulting recovery efficiency for a low and high Galactic latitude field. While the recovery efficiency is consistently high ($> 95\,\%$) at high latitudes, it is lower ($\approx 60 - 80\%$) at lower Galactic latitudes due to confusion (De et al., 2020b).

Survey pointing simulations

We simulate the recovery efficiency of novae in PGIR data utilizing the actual observing schedule together with the derived recovery efficiency of the PGIR subtraction pipeline. As in Shafter, 2017, the peak magnitudes of the novae are drawn from the observed luminosity function of novae in M31 where the distance is very well constrained – a normal distribution with a mean peak luminosity of $M = -7.2$ mag and a standard deviation of $\sigma_M = 0.8$ mag. For each nova with a peak luminosity, we estimate the rate of decline of the nova light curve using the Maximum Magnitude Rate of Decline (MMRD; Mclaughlin, 1945; Zwicky, 1936) relationship between the nova luminosity and speed from Ozdonmez et al., 2018. We discuss possible deviations from the assumption of a universal luminosity function and MMRD in Section 8.5.

Figure 8.6 shows the number of epochs of observations of PGIR as a function of sky position for the duration of the survey considered here. We simulate the actual survey pointing schedule of PGIR to estimate if a simulated nova would have been detectable in our data given its light curve shape and extinction along the line of sight. A nova is detected in a simulated survey epoch if its brightness and sky location satisfy the same criteria we used to identify novae in the PGIR stream (Section 8.2). For epochs that pass the detection criteria, we randomly assign a detection or non-detection weighted by the derived detection efficiency (as a function of the brightness of the nova relative to the image limiting magnitude; Figure 8.7) for the spatially nearest field. As in the real candidate identification criteria, we require at least three epochs of detections with SNR$>$ 8 to classify a nova as recoverable in the PGIR survey.

Monte-Carlo rate estimate

Using the framework for simulating the recovery of novae, we carry out a Monte Carlo simulation of the number of novae detectable in 17 months of the PGIR survey as a function of the input Galactic rate. For each input rate r_0, we create a population of N novae that are randomly placed in the Galaxy with a spatial probability weighted by the Galactic stellar mass distribution (Section 8.3). The

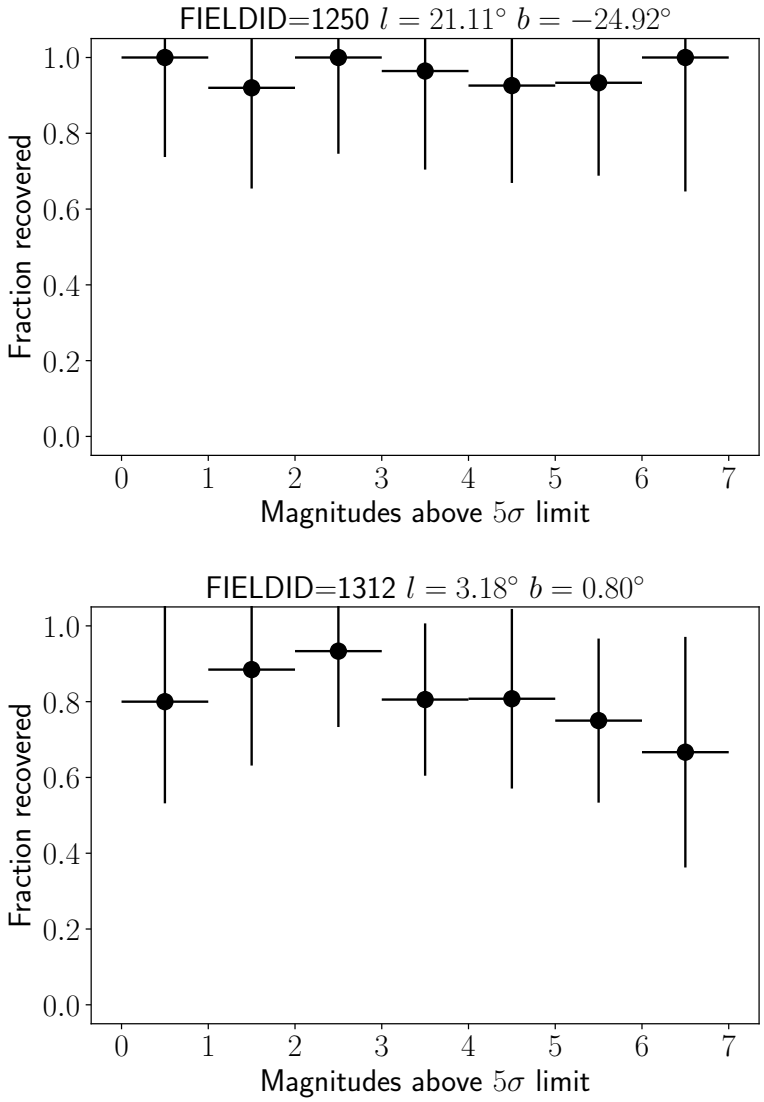

Figure 8.7: **The detection efficiency of fake transient sources injected into the PGIR science images**. We show the efficiency for two fields – at high galactic latitude (top) and low galactic latitude (bottom). The panel titles show the PGIR field ID, galactic longitude (l) and latitude (b). We quantify the recovered fraction as a function of the difference between the fake magnitude and estimated limiting magnitude for the image (as a proxy for the expected signal-to-noise of the source) – such that 0 mag difference corresponds to sources exactly at the limiting magnitude, while larger values correspond to brighter transient sources. For high galactic latitudes (top), the recovery efficiency is roughly uniform at $\approx 95 - 100\%$ for all sources brighter than the 5σ limiting magnitude. The recovery efficiency is reduced (typically $\approx 85\%$) at low latitudes due to confusion noise; the efficiency drops to $< 80\%$ near the 5σ limit due to photon noise from nearby sources and at the bright end due to saturation induced by the bright stellar background.

number of novae N is randomly drawn from a Poisson distribution with a mean of $\lambda = r_0 * t_s$, where t_s is the survey simulation duration in years:

$$P(N, \lambda) = \frac{\lambda^N}{N!} e^{-\lambda}. \tag{8.2}$$

We use the Galactic location of each simulated nova to calculate its sky position as viewed from Earth. The eruption times are randomly selected within the considered survey duration assuming a uniform distribution, which are then used to estimate its J-band brightness as a function of time. Using the recovery criteria given in Section 8.4 for an input nova sky location and light curve shape, we estimate the number of novae that would be detectable amongst the injected N novae. Typical causes for simulated novae going undetected include proximity to the Sun (PGIR does not actively cover fields near solar conjunction, as in the case of V670 Ser), location in a very dense field that prevents detection above the bright background, or if they are too bright to saturate the detector (as in the case of V3890 Sgr). We consider the detection efficiency in further detail in Section 8.5.

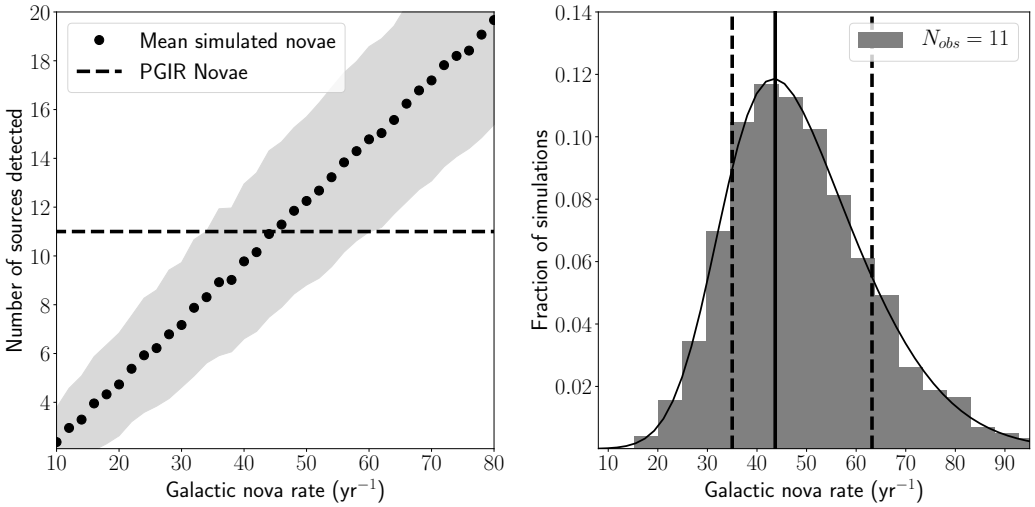

Figure 8.8: **Estimation of the Galactic nova rate with Monte-Carlo simulations of the PGIR survey**. (Left) Simulated number of novae detectable in 17 months of the PGIR survey, as a function of the Galactic nova rate. Black circles show the mean number of novae detected for an input rate while the shaded region corresponds to the measured standard deviation. The black dashed line shows the actual number of detected novae in PGIR. (Right) Distribution of the fraction of simulations that reproduce the observed number of PGIR novae as a function of the input Galactic rate. The solid black line shows the best-fit skewed Gaussian distribution, the black vertical solid line shows the best-fit rate, and the black vertical dashed lines show the 68% confidence interval for the estimate.

We repeat this simulation for 1000 iterations of each input Galactic nova rate ranging from $2\,\mathrm{yr}^{-1}$ to $100\,\mathrm{yr}^{-1}$. For each input nova rate, we record the mean number of novae detected in the PGIR simulations as well as its standard deviation to estimate the uncertainty. Figure 8.8 shows the number of novae recovered in the first 17 months of the PGIR survey simulation as a function of the input Galactic rate. Similarly to the rate estimation procedure discussed in De et al., 2020c, we estimate the best-fit rate and its confidence interval by creating a distribution of the fraction of simulations that produce the observed number of novae (= 11) as a function of the global rate. We fit a skewed normal function to this distribution to estimate a Galactic rate (with 68% confidence intervals)

$$r_{0,u} = 43.7^{+19.5}_{-8.7}\ \mathrm{yr}^{-1} \tag{8.3}$$

where $r_{0,u}$ is the Galactic rate assuming that the specific nova rate and luminosity function is uniform for the bulge and disk populations. We discuss possible variations in our assumptions and how they affect our rate estimates in Section 8.5.

8.5 Discussion

Using a sample of 12 spectroscopically confirmed novae detected in the PGIR survey, we have thus far demonstrated that the near-infrared sensitivity of PGIR has enabled the identification of a large population of highly obscured novae that have been systematically missed in previous optical searches. Unlike all previous estimates of the Galactic nova rate that suffer from poorly quantified completeness estimates, we derive an estimate of the Galactic nova rate combining i) a detailed quantification of the detection efficiency of the survey and ii) Monte Carlo simulations of the PGIR survey pointing schedule. In this section, we discuss the detection efficiency of the PGIR survey for novae in different parts of the galaxy, and revisit possible variations in the assumptions regarding the underlying population.

Detection efficiency for disk and bulge novae

Here, we examine the detection efficiency of novae as a function of Galactic position, as imposed by our selection criteria in the PGIR sample. For a simulated population of 1000 novae distributed by the Galactic stellar mass density, we show in Figure 8.9 the Galactic x-y positions of the novae colored by their recovery in the survey. The majority of novae at $l < 0^\circ$ are not detectable by the PGIR survey due to their location in the southern hemisphere at $\delta < 30^\circ$. For $l > 0^\circ$, the sensitivity of PGIR

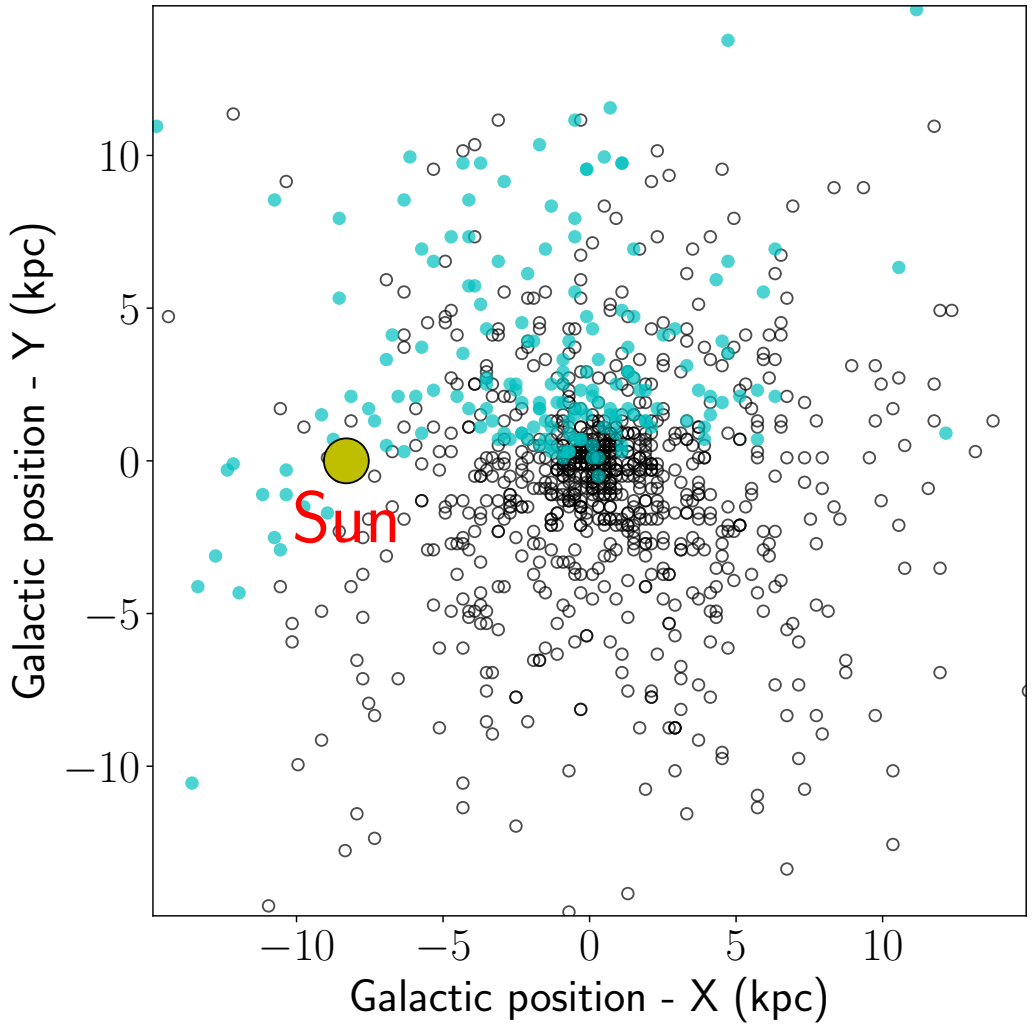

Figure 8.9: **Nova detection capability in the PGIR survey as a function of galactic position.** For a simulated population of 1000 novae, the cyan circles show eruptions that are detectable with the survey schedule and selection criteria while the black empty circles show the un-detected novae. Novae at $Y \lesssim 0\,\mathrm{kpc}$ are undetectable because they lie at Galactic longitude $l < 0^\circ$ that is largely invisible from Palomar. The position of the sun is shown as the yellow circle.

through regions of high dust extinction allows the detection of novae in the central regions of the Galaxy as well as behind the Galactic bulge.

Overall, our selection criteria with PGIR recover $\approx 17\%$ of all novae injected into our simulation, and $\approx 36\%$ of novae visible in the PGIR observing footprint. Using the same framework, we estimate that the PGIR recovery efficiency for disk novae was $\approx 18\%$ of all eruptions, while the same for bulge novae was $\approx 13\%$ owing to its location further in the southern hemisphere. Similarly, the recovery efficiency

of disk and bulge novae in the footprint visible to PGIR is estimated to be $\approx 35\%$ and $\approx 27\%$, respectively. We estimate that $\approx 6\%$ of novae would be saturated in the data based on our model, consistent with the one event (V3890 Sgr; out of a total of 12 events in active PGIR fields) that did not pass our selection criteria. Thus, the dynamic range of PGIR is well suited to detect most novae ($J \approx 6 - 14$ mag), but would miss very nearby and bright eruptions. This was seen in the case of the very bright nova KT Eridani (Hounsell et al., 2010) that was missed at the time of eruption, as well as in the case of nova V598 Puppis that was first detected as a bright X-ray source (Read et al., 2007) and subsequently confirmed as a nova (Torres et al., 2007).

Next, we compare the predictions of our assumed model for the relative contributions of disk and bulge novae with the observed statistics. Since we nominally assume the nova rate to scale with the stellar mass density, bulge novae constitute $\approx 20\%$ (the bulge mass fraction in our assumed mass model from Cautun et al., 2020) of the eruptions. When combined with the recovery efficiencies for the respective populations, we expect $\approx 1 - 2$ bulge novae and $\approx 10 - 11$ disk novae during our survey duration. For comparison, we note that at least 7 out of the 11 ($\gtrsim 65\%$) novae in our rate sample can be certainly associated to the disk population based on their sky locations (see Figure 8.4), while the rest are consistent with being bulge novae in terms of projected sky location.

As discussed in Hatano et al., 1997, without accurate distance estimates, many novae apparently in the bulge could be foreground disk novae. Due to the long-lived light curves of most objects in our sample, we do not yet have measurements of most of their decline times (t_3, the time to decline by 3 mags by peak). However, for the well sampled light curve of apparent bulge nova V659 Sct, we note that the distance estimated from the MMRD would be $\approx 4 - 5$ kpc, and thus consistent with a disk population rather than the bulge. Similarly, the very slow nova V6567 Sgr is likely to be relatively low luminosity and hence a foreground event. While we do not have extensive photometric coverage of V6593 Sgr due to its proximity to the sun at the time of eruption, data from the AAVSO International Database[10] suggests a moderately fast nova with $t_3 \approx 35$ days similar to V3731 Oph ($t_3 \approx 40$ days). V6593 Sgr also has a tentative Gaia counterpart with an estimated distance in a relatively uncertain range of $\approx 2 - 6$ kpc. As such, we suggest that these two moderately fast novae (V6593 Sgr and V3731 Oph) may have distances consistent

[10] www.aavso.org

($\approx 6-9$ kpc) with the bulge, making the number of bulge novae commensurate with our nominal model predictions.

Luminosity function and light curve shape

Our rate estimate was derived assuming a luminosity function represented by a normal distribution with a peak absolute magnitude of $M = -7.2 \pm 0.8$ mag, based on the luminosity function of novae in M31 (Shafter, 2017). However, several previous works have highlighted possible differences between the luminosity function of M31 and Milky Way novae, as well as differences between disk and bulge novae. Shafter et al., 2009 and Ozdonmez et al., 2018 have suggested that Milky Way novae are more luminous than M31 novae with an absolute magnitude distribution of $M_V = -7.9 \pm 0.8$ mag, although Shafter, 2017 suggests that this conclusion may be biased by bright Galactic disk novae that are easier to find. In order to quantify the effect of a possibly brighter population of Milky Way novae, we carried out our Monte Carlo simulations assuming the suggested Galactic luminosity function and find a marginally higher resulting nova rate of $51.2^{+20.3}_{-10.6}$ yr^{-1}. Although we expect brighter novae to be easier to detect in a simulated survey (producing a lower inferred rate for a fixed number of observed novae), the inferred rate is higher in these simulations since the faster evolution of bright novae are harder to recover in the survey.

Next, we discuss possible differences between the bulge and disk nova populations. Duerbeck, 1990, della Valle et al., 1992, and Della Valle et al., 1998 have shown evidence of likely different disk and bulge populations distinguished by their light curve speed and spectroscopic classification, wherein luminous ($M_V = -8 \pm 0.8$ mag) and fast He/N novae preferentially appear in the disk population while slow and faint ($M_V = -7 \pm 0.8$ mag) novae preferentially appear in the bulge population. The differences have been attributed to differing underlying stellar populations since more massive WDs in the disk are expected to produce faster, luminous outbursts (Livio, 1992; Shara, 1981). We quantified the effect of possible differing populations by carrying out our simulations with these two distinct populations of novae. The resulting rate estimate is marginally higher at $52.9^{+25.0}_{-10.1}$ yr^{-1}, but still consistent with our estimate assuming a uniform nova population.

Next, we discuss the validity of the assumed maximum absolute magnitude relation with decline time (MMRD). Specifically, multiple recent studies have questioned the validity of the MMRD utilizing high cadence observations of extragalactic novae

where interstellar absorption is much less severe and uncertain. Kasliwal et al., 2011 presented evidence for a class of faint and fast novae in M31 that deviated from the MMRD relationship, and consistent with the predictions of Yaron et al., 2005. Similar conclusions were reported from *Hubble Space Telescope* observations of M87 (Shara et al., 2016, 2017) and later observations of M31 by the Palomar Transient Factory (Cao et al., 2012).

Using Gaia DR2 observations of old Galactic novae, Schaefer, 2018 has suggested that the MMRD relationship should not be used owing to its poor consistency, although Selvelli et al., 2019 do find evidence for the MMRD (see also Della Valle et al., 2020). Given the general uncertainty regarding the MMRD, we note that a population of faint and fast Galactic novae would further increase the inferred Galactic rate owing to the difficulty in detecting them in magnitude-limited samples. Although the true fraction of these novae has not been quantified yet, $\approx$ 25% of novae presented in the sample of Shara et al., 2016 were shown to be faint and fast, suggesting that our estimate of the Galactic nova rate may be underestimated by at least a similar fraction, subject to differences in the stellar populations.

Comparison to previous estimates

Previous estimates for the Galactic nova rate have primarily used the rate in the very local solar neighborhood to derive the local outburst rate density (although without a rigorous quantification of the completeness), followed by extrapolation to the entire galaxy (e.g. Ozdonmez et al., 2018; Shafter, 2017). Figure 8.10 summarizes our rate measurement in comparison to previous estimates. Our rate estimates are consistent with the work of Hatano et al., 1997 and the most recent work of Shafter, 2017, although smaller than that estimated by Ozdonmez et al., 2018. Compared to the Galactic bulge rate of $13.8 \pm 2.6\,\mathrm{yr}^{-1}$ from Mróz et al., 2015, the estimated bulge rate in our model would be $\approx 8.8^{+4.0}_{-1.8}\,\mathrm{yr}^{-1}$, and marginally smaller than their estimate. Our estimates are inconsistent with the high rates ($> 100\,\mathrm{yr}^{-1}$) estimated from the early work of Allen, 1954 and Sharov, 1972 using all-sky statistics of Galactic novae known at the time.

When compared to extra-galactic estimates, our derived rate is generally higher than those estimated in previous works in the range of $\approx 10 - 40\,\mathrm{yr}^{-1}$. These underestimates likely arise from underestimation of the nova rate in external galaxies. For instance, Mróz et al., 2016 have shown that the nova rate in the Magellanic clouds is $\approx 2 - 3\times$ higher than estimated from the K-band luminosity using the

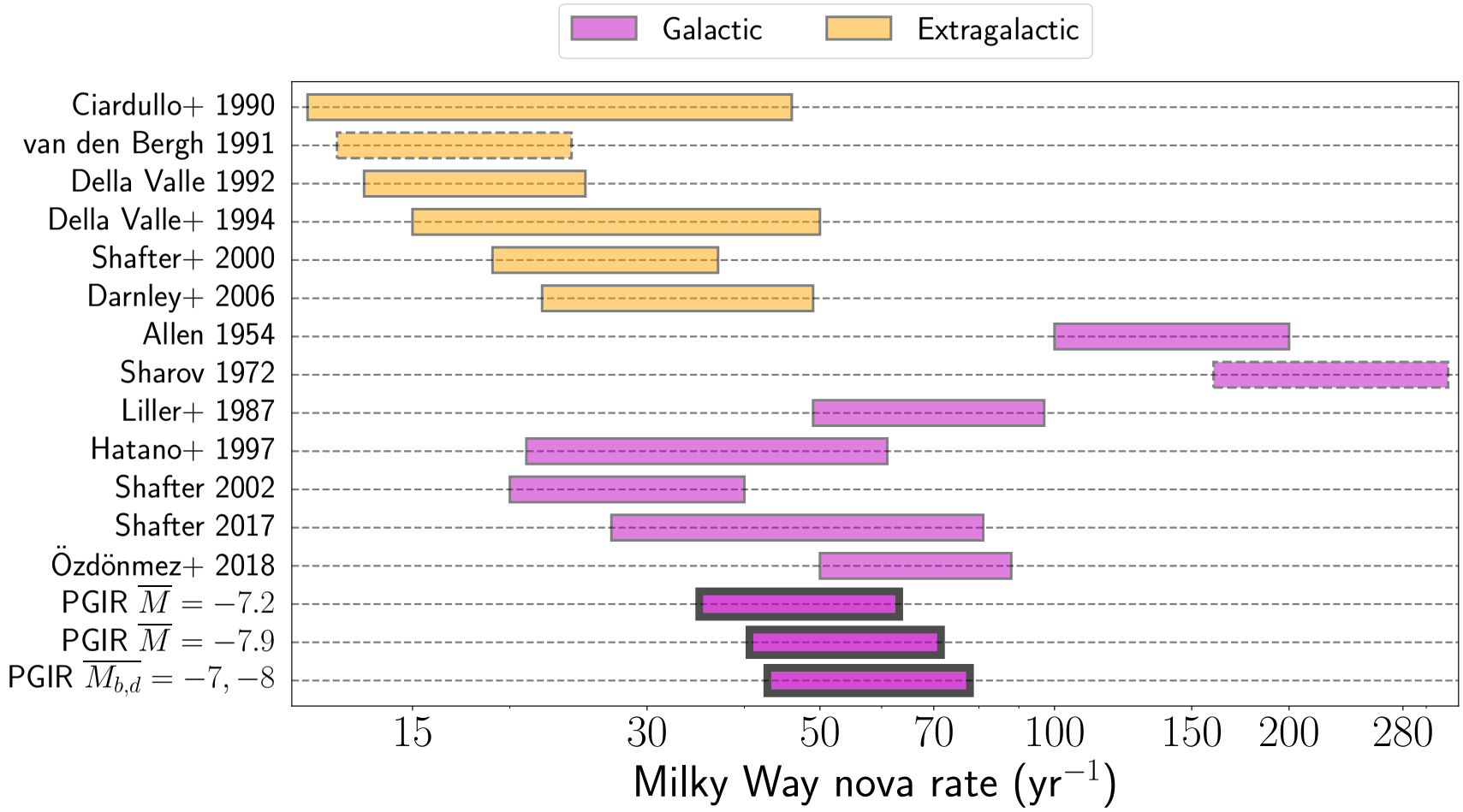

Figure 8.10: **Comparison of previously published nova rate estimates for the Milky Way to that estimated from the PGIR sample.** Yellow bars indicate estimates from extrapolation of nova rates of nearby galaxies while magenta bars indicate those from samples of Galactic novae. Bars with dashed edges indicate values without published uncertainty estimates where we nominally assign a factor of 2 uncertainty. For the PGIR sample, we show the estimated range for three assumed luminosity functions: $M = -7.2 \pm 0.8$ mag (as for M31 novae), $M = -7.9 \pm 0.8$ mag (as suggested for Galactic novae) and in the case of two different luminosity functions in the bulge ($M_b = -7.0 \pm 0.8$ mag) and disk ($M_d = -8 \pm 0.8$ mag).

OGLE survey. A similar high specific rate was inferred for M87 in the work of Shara et al., 2016. While our estimate for the bulge rate is strikingly similar to that extrapolated from the M31 bulge by Darnley et al., 2006, our estimate for the disk rate in the Milky Way ($\approx 34.2^{+15.5}_{-6.9}\,\mathrm{yr}^{-1}$) is higher (but consistent within error bars) than their estimate of $\approx 20^{+14}_{-11}\,\mathrm{yr}^{-1}$. The differences may be attributed to the different disk-to-bulge ratio in our model (constrained by recent Gaia DR2 data) compared to Darnley et al., 2006 together with differences in the stellar populations of the two galaxies. Indeed, the bulge population in M31 is known to be a more prolific contribution (per unit stellar light; Capaccioli et al., 1989; Ciardullo et al., 1987; Darnley et al., 2006; Shafter et al., 2001) to its nova rate as well as the stellar mass of the galaxy (disk-to-bulge luminosity ratio of ≈ 2; Shafter, 2002).

On the other hand, bulge rate estimates from Mróz et al., 2015 together with previous works (Hatano et al., 1997; Shafter, 2017; Shafter, 2002) have suggested that disk novae likely represent the majority of the nova outburst rate in the Milky Way. While our nominal model assumes a constant nova production rate per unit stellar mass and does appear to reproduce the observed number statistics, we are unable to further constrain the relative bulge-to-disk nova production rate due to low number statistics. Given the high extinction towards the bulge region, a larger sample of PGIR novae combined with upcoming datasets from NIR wide-field surveys in the southern hemisphere (with better visibility of the bulge) would be ideally suited to constrain the relative rates.

8.6 Summary

In this paper, we have presented a systematically selected sample of 12 spectroscopically confirmed novae detected in the first 17 months of the PGIR wide-field NIR survey. With $> 50\%$ of events obscured by $A_V \gtrsim 5$ mag, this sample contains some of the most highly dust extinguished novae that have been spectroscopically confirmed in the literature. We use this sample to perform the first quantitative simulations of a time domain survey to directly constrain the Galactic nova rate. We summarize our findings below.

- Comparing the extinction distribution of PGIR novae (derived from both photometric and spectroscopic tracers) to previously reported optical novae, we find the PGIR novae to be highly skewed towards large extinction values and inconsistent with the optical sample at $> 99.99\%$ confidence.

- We create a simulated population of novae distributed by the stellar mass density in the Galaxy and estimate the extinction distribution towards the eruptions using recent 3D dust maps from Green et al., 2019. We find the resulting extinction distribution to be commensurate with PGIR novae, suggesting that previous optical searches have likely missed or misidentified a large fraction of novae.

- We carry out detailed simulations of the PGIR pipeline detection efficiency together with the survey pointing schedule to estimate the Galactic nova rate. Using a simulated population of novae weighted by the stellar mass density and luminosity function (peak absolute magnitude $M = -7.2 \pm 0.8$ mag), we estimate the Galactic nova rate to be $43.7^{+19.5}_{-8.7}$ yr^{-1}.

- We further examined possible differences in our assumptions regarding the underlying luminosity function as well as differing bulge and disk populations. We derive marginally higher, but consistent rate estimates of $51.2^{+20.3}_{-10.6}$ yr^{-1} if Milky Way novae are characterized by a brighter luminosity function ($M = -7.9 \pm 0.8$ mag). On the other hand, if disk and bulge novae have differing luminosity functions ($M = -8 \pm 0.8$ mag and $M = -7 \pm 0.8$ mag, respectively), we derive an integrated rate of $52.9^{+25.0}_{-10.1}$. The presence of faint and fast novae, as reported in some extra-galactic searches, would increase the inferred nova rate; our estimate thus serves as a lower limit.

- Our rate estimates are generally consistent with previous estimates extrapolated from novae only in the local solar neighborhood. However, our estimates are higher than those derived via extrapolations from nearby galaxies, which we attribute to the previous underestimation of the specific nova rate in external galaxies as well as differences in assumptions regarding the relative contribution of bulge and disk novae.

Although all-sky optical surveys have consistently found only $5 - 10$ novae per year, our estimates are consistent with previous suggestions (which extrapolate the rate in the local solar neighborhood) of a Galactic rate of $\approx 50\,\mathrm{yr}^{-1}$. Given the evidence for a population of highly reddened novae detected in PGIR that have been systematically missed in optical searches, our results suggest that the discrepancy in the observed rates arises due to dust obscuration preventing the discovery of most events in the optical bands. Wide and shallow NIR surveys are thus ideally suited to provide a complete census of the Galactic nova population. In particular, the

lower effects of dust extinction in the NIR allow for easy discrimination between the abundance of faint (and nearby) dwarf novae and dust extinguished novae that are rarer but luminous in the NIR bands.

These results bode well for upcoming NIR surveys like the Dynamic REd All-sky Monitoring Survey (DREAMS; Soon et al., 2020), the Wide-field Infrared Transient Explorer (WINTER; Simcoe et al., 2019), and the Prime Focus Infrared Microlensing Experiment (PRIME). In particular, the finer pixel scale of these instruments as well as the southern locations of DREAMS and PRIME are suited to provide exquisite NIR statistics of novae in the highly dust extinguished and crowded southern Galactic bulge. Combining this population with the broader disk population from PGIR would provide accurate constraints on the long standing question of the relative bulge and disk nova rates in the Milky Way.

We thank R. Williams for assistance with the identification of the NIR spectroscopic features. We thank the anonymous referee for a careful reading of the manuscript and providing several constructive suggestions to improve its quality. We thank M. Darnley, A. Shafter, M. Shara, R. D. Gehrz, L. Bildsten, E. S. Phinney and S. R. Kulkarni for valuable feedback on this work. We acknowledge with thanks the variable star observations from the AAVSO International Database contributed by observers worldwide and used in this research.

Palomar Gattini-IR (PGIR) is generously funded by Caltech, the Australian National University, the Mt Cuba Foundation, the Heising Simons Foundation, and the Binational Science Foundation. PGIR is a collaborative project among Caltech, Australian National University, University of New South Wales, Columbia University and the Weizmann Institute of Science. MMK acknowledges generous support from the David and Lucille Packard Foundation. MMK and EO acknowledge the US-Israel Bi-national Science Foundation Grant 2016227. MMK and JLS acknowledge the Heising-Simons foundation for support via a Scialog fellowship of the Research Corporation. MMK and AMM acknowledge the Mt Cuba foundation. J. Soon is supported by an Australian Government Research Training Program (RTP) Scholarship.

The SED Machine is based upon work supported by the National Science Foundation under Grant No. 1106171. Some of the data presented here were obtained with the Visiting Astronomer facility at the Infrared Telescope Facility, which is operated by the University of Hawaii under contract 80HQTR19D0030 with the National Aeronautics and Space Administration. Some of the data presented herein were

obtained at the W.M. Keck Observatory, which is operated as a scientific partnership among the California Institute of Technology, the University of California and the National Aeronautics and Space Administration. The Observatory was made possible by the generous financial support of the W.M. Keck Foundation. The authors wish to recognize and acknowledge the very significant cultural role and reverence that the summit of Mauna Kea has always had within the indigenous Hawaiian community. We are most fortunate to have the opportunity to conduct observations from this mountain.

This work was supported by the GROWTH (Global Relay of Observatories Watching Transients Happen) project funded by the National Science Foundation under PIRE Grant No 1545949. GROWTH is a collaborative project among the California Institute of Technology (USA), University of Maryland College Park (USA), University of Wisconsin Milwaukee (USA), Texas Tech University (USA), San Diego State University (USA), University of Washington (USA), Los Alamos National Laboratory (USA), Tokyo Institute of Technology (Japan), National Central University (Taiwan), Indian Institute of Astrophysics (India), Indian Institute of Technology Bombay (India), Weizmann Institute of Science (Israel), The Oskar Klein Centre at Stockholm University (Sweden), Humboldt University (Germany), Liverpool John Moores University (UK), and University of Sydney (Australia).

8.7 Appendix: Summary of individual objects

Nova V3731 Oph

The transient PGIR 20ekz was recovered in an archival search for large amplitude transients (using the criteria described in Section 8.2) in early survey data from the month of 2019 July (De et al., 2020d). The source was also detected as a fast reddened transient ZTF 19abgnhzj in ZTF public data, but was missed and not followed up during the eruption. We obtained a late-time optical spectrum of the source using Keck-I + LRIS on 2020-09-15 ($\approx$ 420 days from peak) which confirmed its classification as a highly reddened nova in the nebular phase. Due to the large diversity in nebular phase features of novae, we are unable to confidently constrain the spectroscopic type; however, taking the detection of He I, [N II], [Ne III] 3869/3968, [O II] 7325, and [S III] 9069 (Figure 8.3; similar to the very fast He/N nova V838 Her in Williams et al., 1994) together with the fast evolving light curve, we tentatively suggest a He/N classification. The limited photometric coverage precludes a definitive identification of the photometric class; we suggest only a tentative S-type classification based on the post-peak decline observed in the

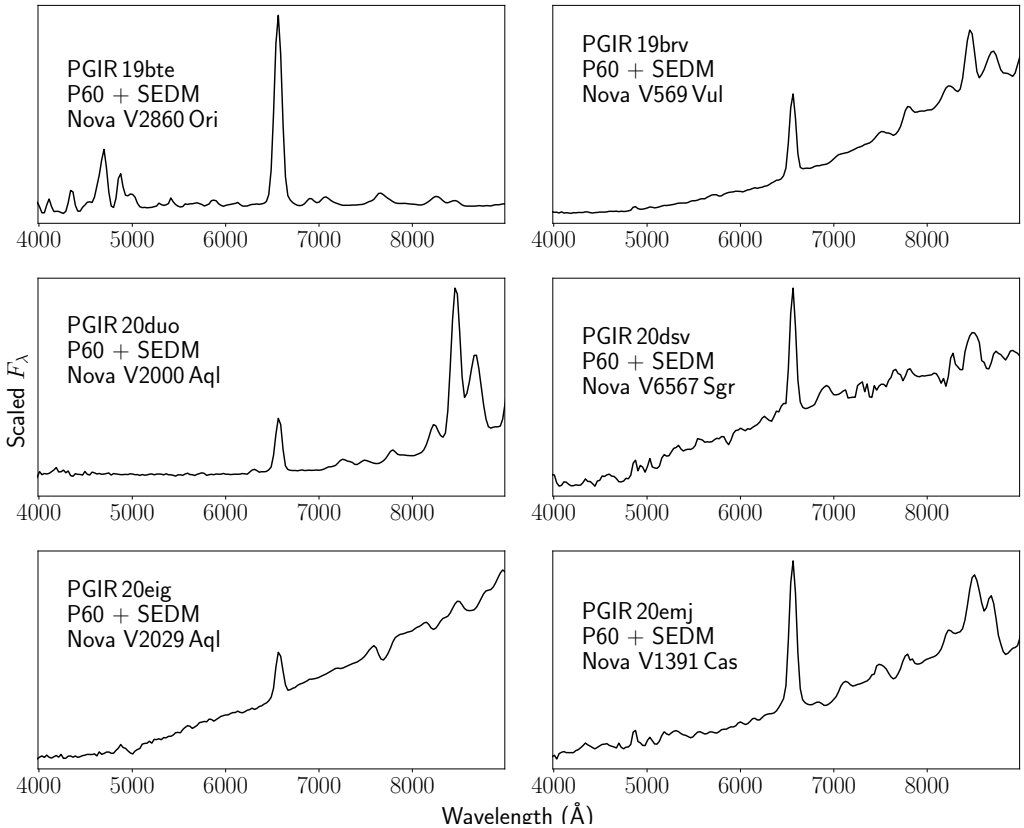

Figure 8.11: **Rapid ultra-low resolution confirmation spectra of PGIR novae obtained with the SED Machine Spectrograph.** Each spectrum (denoted with the nova name) shows strong Hα emission together with multiple emission features of O I, confirming the nova classifications.

data. Due to the absence of continuum emission in the late-phase spectrum, we are unable to detect any spectroscopic features to estimate the reddening; we thus use the color evolution of the nova for our estimate.

Nova V2860 Ori

The nova V2860 Ori was first discovered by Shigehisa Fujikawa in Kan'onji, Kagawa, Japan as PNV J06095740+1212255 on UT 2019 August 07, and classified by Aydi et al., 2019a as fast classical nova. The transient was recovered in PGIR data as PGIR 19bte with our selection criteria, and confirmed with rapid SEDM spectroscopy (Figure 8.11). With follow-up optical and NIR spectroscopy on the P200, we confirm its classification as a He/N nova based on the detection of He I and N II features with broad, flat-topped emission profiles (Figure 8.3). Combining the photometric coverage from PGIR and ZTF, we find a smooth decline in the nova light curve followed by a dramatic dip from dust formation at $\approx$ 150 days after outburst,

suggesting a D-type photometric class. Using the detect K I λ7699 absorption feature in the DBSP spectrum, we estimate an extinction of $E(B-V) \approx 0.55$ mag.

Nova V569 Vul

The nova V569 Vul was first reported by the Gaia survey (Hodgkin et al., 2019) on UT 2019 August 24 and spectroscopically confirmed as a highly reddened classical nova (Aydi et al., 2019b; Zielinski et al., 2019). Due to the highly reddened nature of the source, the nova was recovered as a very bright J-band transient (PGIR 19bgv) in the PGIR data, and brighter than the nominal non-linearity limit (≈ 8.5 mag) for the first two epochs. We obtained spectroscopic follow-up of the source using P200 and classified the source as a fast He/N nova based on the detection of He I and N II features with flat-topped emission profiles (Figure 8.3). The extremely red color of the outburst (Figure 8.2) suggests a large extinction ($A_V \approx 10$ mag), and is consistent with the high reddening we measure from the optical spectrum using the K I λ7699 absorption line. The light curve exhibits a smooth decline from the outburst peak, and consistent with a S-type photometric class.

Nova V2891 Cyg

The nova V2891 Cyg was first discovered by the PGIR survey as the transient PGIR 19brv (De et al., 2019f) on UT 2019 September 17 and confirmed with rapid spectroscopic follow-up on the Palomar 60-inch telescope (Figure 8.11). The nova exhibited a smooth rise to peak followed by at least a ≈ 100 day bumpy plateau, suggesting a F-type photometric class. With higher resolution spectroscopic follow-up on the P200, we detect a highly reddened spectrum with Fe II features and P-Cygni line profiles (Figure 8.3), suggesting a Fe II-type spectroscopic classification. Both the highly reddened colors as well as the K I λ7699 spectroscopic feature suggest a very high reddening – we estimate a reddening of $A_V \approx 7.5$ mag from the colors and higher estimate of $A_V \approx 12$ mag from the K I feature. We caution that the K I feature has not been calibrated at such high extinctions and likely saturates in this regime.

Nova V3890 Sgr

The nova V3890 Sgr is a known recurrent nova (Schaefer, 2010) with the 2019 eruption (Strader et al., 2019) detected in PGIR data (as PGIR 19fai). Owing to the saturation of the bright eruption in survey data, it does not pass our selection criteria (Section 8.2) and is not included for our rate estimates. We obtained

optical and NIR spectroscopy of the transient with P200, and detected broad Hα and higher Balmer emission from the nova, together with clear absorption features from the stellar companion (Figure 8.3). With very high resolution spectroscopy of the 2019 eruption, Munari et al., 2019 estimated a line-of-sight extinction of $E(B-V) \approx 0.62$ mag, which we use in our work.

Nova V659 Sct

The nova V659 Sct was discovered by the ASASSN survey (Stanek et al., 2019) on 2019 October 29, and confirmed with optical spectroscopy shortly thereafter (Williams et al., 2019). The nova was detected around the time of peak eruption in PGIR data, but was brighter than the nominal non-linearity limit until it went into solar conjunction. The nova subsequently passed our selection criteria as PGIR 20dcl and was followed up with optical and NIR spectroscopy with SSO and IRTF. Based on the detection of Fe II features as well as N II / He I features in the optical spectra (Figure 8.3), we classify the source as a hybrid nova. The nova exhibited a smooth photometric decline until > 200 days after eruption, followed by a phase of erratic bumps on top of the smooth decline. We thus obtain a photometric classification of a J-type nova based on its light curve. Using the detection of K I λ7699 absorption in the optical spectrum, we estimate a reddening of $A_V \approx 4.0$ mag, similar to that estimated from the photometric colors.

Nova V2000 Aql

The nova V2000 Aql (= PGIR 20duo) was first detected in the PGIR data on UT 2020 May 12, and identified as a nova candidate on its second detection on 2020 June 18. We obtained rapid spectroscopic follow-up of the source using SEDM (Figure 8.11) to confirm a nova classification (De et al., 2020g). The source had been previously reported as a faint hostless transient by the MASTER survey (Pogrosheva et al., 2020), but not followed up until the PGIR identification. Combining PGIR data with public ZTF data, we find the nova to be highly reddened with $g - J \approx 10$ mag. While the first observation of the nova was after a seasonal gap in PGIR data, the ZTF data constrained the eruption to have occurred ≈ 40 days before the first PGIR detection. With optical and NIR spectroscopic follow-up, we find evidence of a highly reddened nova of the Fe-II type based on the clear detection of C I lines (Figure 8.3) in the NIR spectra (Banerjee et al., 2012). We classify the photometric behavior of the nova as a S-type object based on the smooth decline seen in the NIR and optical data. Due to the highly reddened nature of the source, we do not

detect any clear extinction features in the optical spectra, and hence constrain the reddening using only the photometric colors to be $A_V \approx 9.5$ mag.

Nova V6567 Sgr

The nova V6567 Sgr (= PGIR 20dsv) was discovered by PGIR on 2020 June 01 (De et al., 2020h) and confirmed with rapid SEDM spectroscopy (Figure 8.11). Using optical spectroscopy shortly after eruption, we classify the nova as Fe-II type based on the detection of multiple Fe features in the optical spectra and P-Cygni line profiles (Figure 8.3). The nova exhibits a slow decline superimposed with oscillations with a period of ≈ 30 days leading to its photometric classification as a O-type nova. Using the clear detection of the DIB λ5780 absorption in its optical spectrum, we estimate a spectroscopic reddening of ≈ 4.5 mag, consistent with that estimated from its photometric colors.

Nova V2029 Aql

The nova V2029 Aql was discovered in PGIR data on UT 2020 July 13 (De et al., 2020e), and confirmed with SEDM spectroscopy on 2020 August 02 (Figure 8.11). The nova (PGIR 20eig) exhibited a peculiar light curve with a relatively smooth rise for ≈ 50 days since eruption followed by a smooth drop in brightness. The smooth decline for ≈ 30 days was interrupted by rapid oscillations in its light curve over ≈ 1 day timescales (Babul et al., 2020). Based on the cusp-like peak in the light curve, we suggest its photometric type as a C-class nova. We obtained optical and NIR spectroscopy of the nova, which suggest a Fe-II type classification based on the very low ($\approx 400\,\mathrm{km\,s^{-1}}$) P-Cygni line velocities and clearly detected Fe II features (Figure 8.3). Using the DIB λ5780 feature in the optical spectra, we estimate a reddening of $A_V \approx 6.0$ mag, consistent with the photometric color estimate.

Nova V1391 Cas

The nova V1391 Cas was discovered on 2020 July 27 UT by S. Korotkiy as part of the NMW survey, and classified as a classical nova with spectroscopic follow-up (Sokolovsky et al., 2020). The nova was detected in PGIR data on 2020 August 15 as PGIR 20emj, and confirmed with a SEDM spectrum (Figure 8.11). With higher resolution optical and NIR spectroscopic observations, we obtain a spectroscopic classification as a Fe II nova based on the detection of Fe II features and P-Cygni line profiles in the optical spectra (Figure 8.3). The nova light curve exhibited a smooth decline for ≈ 120 days after eruption before a dramatic drop in brightness

accompanied by the reddening of its colors. We attribute this transition to dust formation, classifying this source a D-type nova. The onset of dust formation is detected on a timescale similar to that seen for dust formation in the recent bright D-type nova V5668 Sgr (Gehrz et al., 2018),which also show a similar pre-dust-formation light curve. Using the detection of the DIB λ5780 absorption feature, we estimate a spectroscopic reddening of $A_V \approx 4.5$ mag consistent with the estimate derived from photometric colors.

Nova V6593 Sgr

The nova V6593 Sgr was detected in the PGIR data on UT 2020 October 02 (as PGIR 20evr) and independently reported as a nova candidate by the BrATS survey on UT 2020 October 03 (Jacques et al., 2020). The bright NIR transient was subsequently confirmed as a Fe-II type classical nova with optical spectroscopy (Aydi et al., 2020b). Owing to the short visibility of the nova before solar conjunction, PGIR only covered the rise of the nova light curve to peak, while we obtained only one higher resolution NIR spectrum of the source with P200. The NIR spectrum shows strong features of C I (Figure 8.3), consistent with the classification as a Fe-II type nova (Banerjee et al., 2012). We used the photometric color of the source obtained with an image from the P60 SED Machine camera to estimate an extinction of $A_V \approx 4$ mag.

Nova V1112 Per

Nova V1112 Per was discovered on UT 2020 November 25 as TCP J04291884+4354232 by Seiji Ueda (Kushiro, Hokkaido, Japan) and confirmed with optical spectroscopy by Munari et al., 2020. The nova was detected as a bright NIR transient in PGIR data as PGIR 20fbf, and followed up with optical and NIR spectroscopy on the P200. Based on the detection of multiple Fe II lines and P-Cygni line profiles in the optical spectrum (Figure 8.3), we classify the source as a Fe II nova. However, rapid early-time spectroscopic monitoring of the nova has revealed 'reverse hybrid' (R-Hybrid) behavior (Borthakur et al., 2020; Munari et al., 2020) wherein the nova transitioned from a He/N appearance to Fe II appearance (seen at the epochs of our spectra) in a sense opposite to that seen in hybrid novae (Williams, 1992). Following a smooth decline from the peak, the nova exhibited signatures of dust formation (hence classified as D-class) via rapid reddening of its optical-NIR color in the combined multi-color light curve. We estimate an extinction of $A_V \approx 2.5$ mag using the J-band data from PGIR with optical photometry reported by Munari et al.,

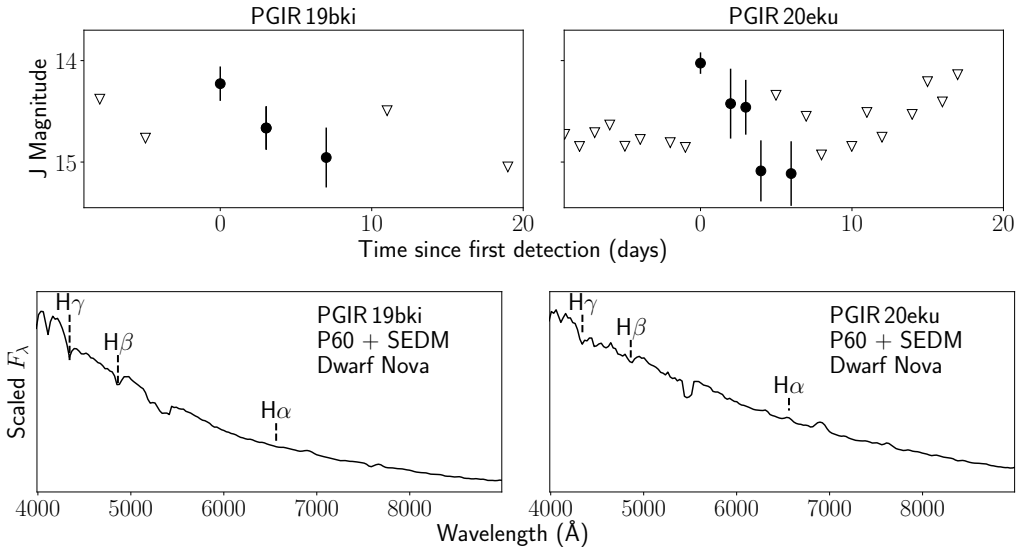

Figure 8.12: **Light curves and spectra of dwarf novae detected and followed up as part of the PGIR nova search.** The top panel shows the light curves of PGIR 19bki and PGIR 20eky, while the lower panel shows follow-up confirmation spectra from the SED Machine. The spectra show clear signs of weak Hα features in emission and higher Balmer features in absorption, confirming their classification as dwarf nova outbursts.

2020, and consistent with the spectroscopic estimate derived using the K I λ7699 absorption line in the optical spectrum.

Dwarf nova PGIR 19bki

The transient PGIR 19bki was discovered by PGIR on UT 2019 September 12 at coordinates RA = 19:53:46.5, Dec = -07:48:38. The source was identified as a fast fading large amplitude transient (Figure 8.12) without any history of prior outbursts in other time domain surveys or in SIMBAD, suggesting a possible classical nova outburst. Rapid spectroscopic follow-up on P60 + SEDM revealed a blue and largely featureless spectrum characterized by weak Hα emission and higher order Balmer absorption features (Figure 8.12). We thus classify the source as a dwarf nova outburst.

Dwarf nova PGIR 20eku

The transient PGIR 20eku was discovered by PGIR on UT 2020 August 04 at coordinates RA = 03:52:37.9, Dec = +47:51:05.9. The source was identified as a fast fading large amplitude transient (Figure 8.12) without any history of prior outbursts in other time domain surveys or in SIMBAD, suggesting a possible classical nova

outburst. Rapid spectroscopic follow-up on P60 + SEDM revealed a blue and largely featureless spectrum characterized by weak Hα emission and higher order Balmer absorption features (Figure 8.12). We thus classify the source as a dwarf nova outburst.

Chapter 9

CONSTRAINING THE X-RAY – INFRARED SPECTRAL INDEX OF SECOND TIMESCALE FLARES FROM SGR 1935+2154 WITH PALOMAR GATTINI-IR

De, K. et al. (2020). "Constraining the X-Ray-Infrared Spectral Index of Second-timescale Flares from SGR 1935+2154 with Palomar Gattini-IR". In: *ApJL* 901.1, L7, p. L7. DOI: 10.3847/2041-8213/abb3c5. arXiv: 2007.02978 [astro-ph.HE].

Kishalay De[1], Michael C. B. Ashley[2], Igor Andreoni[1], Mansi M. Kasliwal[1], Roberto Soria[3,4], Gokul P. Srinivasaragavan[1], Ce Cai[5,6], Alexander Delacroix[7], Tim Greffe[7], David Hale[7], Matthew J. Hankins[1], Chengkui Li[5], Daniel McKenna[7], Anna M. Moore[8], Eran O. Ofek[9], Roger M. Smith[7], Jamie Soon[8], Tony Travouillon[8], and Shuangnan Zhang[5,6]

[1]Cahill Center for Astrophysics, California Institute of Technology, 1200 E. California Blvd. Pasadena, CA 91125, USA
[2]School of Physics, University of New South Wales, Sydney NSW 2052, Australia
[3]National Astronomical Observatories, Chinese Academy of Sciences, Beijing 100012, China
[4]Sydney Institute for Astronomy, The University of Sydney, Sydney, NSW 2006, Australia
[5]Key Laboratory of Particle Astrophysics, Institute of High Energy Physics, Chinese Academy of Sciences, 19B Yuquan Road, Beijing 100049, China
[6]University of Chinese Academy of Sciences, Chinese Academy of Sciences, Beijing 100049, China
[7]Caltech Optical Observatories, California Institute of Technology, Pasadena, CA 91125, USA
[8]Research School of Astronomy and Astrophysics, Australian National University, Canberra, ACT 2611, Australia
[9]Department of Particle Physics & Astrophysics, Weizmann Institute of Science, Rehovot 76100, Israel

Abstract

The Galactic magnetar SGR 1935+2154 has been reported to produce the first example of a bright millisecond duration radio burst (FRB 200428) similar to the cosmological population of fast radio bursts (FRBs). The detection of a coincident bright X-ray burst represents the first observed multi-wavelength counterpart of a FRB. However, the search for similar emission at optical wavelengths has been hampered by the high inferred extinction on the line of sight. Here, we present results from the first search for second-timescale emission from the source at near-infrared (NIR) wavelengths using the Palomar Gattini-IR observing system in *J*-

band, enabled by a novel detector read-out mode that allows short exposure times of ≈ 0.84 s with 99.9% observing efficiency. With a total observing time of ≈ 12 hours ($\approx$ 47728 images) during its 2020 outburst, we place median $3\,\sigma$ limits on the second-timescale NIR fluence of $\lesssim 18$ Jy ms (13.1 AB mag). The corresponding extinction corrected limit is $\lesssim 125$ Jy ms for an estimated extinction of $A_J = 2.0$ mag. Our observations were sensitive enough to easily detect a NIR counterpart of FRB 200428 if the NIR emission falls on the same power law as observed across its radio to X-ray spectrum. We report non-detection limits from epochs of four simultaneous X-ray bursts detected by the Insight-*HXMT* and *NuSTAR* telescopes during our observations. These limits provide the most stringent constraints to date on fluence of flares at $\sim 10^{14}$ Hz, and constrain the fluence ratio of the NIR emission to coincident X-ray bursts to $R_{\rm NIR} \lesssim 0.025$ (fluence index $\gtrsim 0.35$).

9.1 Introduction

The source SGR 1935+2154 was discovered in 2014 as a short (≈ 0.2 s) burst (Stamatikos et al., 2014) by the Burst Alert Telescope on board the Neil Gehrels Swift Observatory (Gehrels et al., 2004). Subsequent follow-up in the X-ray wavebands revealed that the object was a new member of the class of Soft Gamma-ray Repeaters (SGRs) originating from a Galactic magnetar with a spin period of ≈ 3.24 s, period derivative of $\dot{P} \approx 1.43 \times 10^{-11}$ s s^{-1}, characteristic age of ≈ 3600 years, and surface magnetic field of $\sim 2 \times 10^{14}$ G (Israel et al., 2016). The source is coincident with the center of the supernova remnant G57.2+0.8 (Kozlova et al., 2016; Sun et al., 2011; Zhong et al., 2020; Zhou et al., 2020) at a distance of ≈ 10 kpc. For an assumed distance of 10 kpc, the energy released in the discovery burst was $\approx 3.6 \times 10^{37}$ erg in the observed energy range of $15 - 150$ keV, based on a refined analysis of the burst spectrum reported in Lien et al., 2014. Pulsed radio emission has so far remained undetected at radio bands (Israel et al., 2016; Lin et al., 2020b; Surnis et al., 2016; Younes et al., 2017). In the optical and near-infrared (NIR) regime, a possible faint ($H \approx 24$ mag) counterpart has been identified in follow-up imaging with the Hubble Space Telescope (Levan et al., 2018).

Since its discovery, the source has sporadically gone into outbursts over the last few years (Lin et al., 2020a), with the most recent being reported as a "forest" of X-ray bursts detected during 27-28 April 2020 (Palmer et al., 2020; Younes et al., 2020). Following the onset of the outburst, an unprecedented bright millisecond duration radio burst (hereafter FRB 200428) was detected from the source by the Canadian Hydrogen Intensity Mapping Experiment (CHIME; The CHIME/FRB

Collaboration et al., 2020) and STARE2 (Bochenek et al., 2020) telescopes, with an energy release that was $\sim$ 1000$\times$ brighter than any known radio burst from a Galactic source. The radio burst was accompanied by a bright hard X-ray counterpart detected by the INTEGRAL (Mereghetti et al., 2020), AGILE (Tavani et al., 2020), Konus-Wind (Ridnaia et al., 2020) and HXMT (Li et al., 2020a) space telescopes. The large luminosity of the radio burst is only a factor of $\approx$ 40 smaller than that of the weakest extragalactic Fast Radio Bursts (FRBs; Cordes et al., 2019; Petroff et al., 2019) observed at cosmological distances till date, providing evidence that active SGRs could produce bright radio bursts akin to FRBs.

The simultaneous detection of the X-ray burst provides the first evidence of a multi-wavelength counterpart for FRBs. Thus, several optical facilities performed follow-up observations of the source to detect and constrain the presence of optical counterparts coincident with radio/X-ray bursts (Lin et al., 2020b; Niino et al., 2020). However, the location of the source in the Galactic plane together with the high observed X-ray column density ($\sim 2 \times 10^{22}$ cm^{-2}; Israel et al., 2016; Li et al., 2020a; Younes et al., 2017) suggests a large line-of-sight optical extinction towards the source ($A_V \approx 7 - 10$ mag). In the case of FRB 200428, no optical counterpart was detected in a simultaneous observation by the BOOTES telescope (Lin et al., 2020b) to an extinction corrected fluence limit of $\lesssim$ 4400 Jy ms. However, the inferred extinction in the NIR is substantially smaller, and expected to be $\approx$ 30% of the optical in J-band.

Palomar Gattini-IR (PGIR) is a new wide-field NIR time domain survey scanning the entire Northern sky every two nights to a median depth of $J \approx 15.7$ AB mag (De et al., 2020b; Moore et al., 2019). With the implementation of a new detector readout mode that allows for fast (exposure time $\approx$ 0.84 s) and continuous (duty cycle $\approx$ 100%) exposures of the sky, we initiated targeted follow-up observations of the source. In this paper, we describe the PGIR follow-up campaign and constraints from simultaneous NIR observations of SGR 1935+2154 at the times of detected X-ray bursts. Section 9.2 describes the observing strategy and resulting observation schedule. In Section 9.3, we describe the methods used to analyze the acquired data, and Section 9.4 uses the non-detection of NIR bursts to constrain the fluence ratios of multi-wavelength counterparts of X-ray bursts from SGR 1935+2154. We conclude with a summary of our results, and prospects for future searches in Section 9.5.

9.2 Observations

Following the detection of the train of X-ray bursts from SGR 1935+2154 (Palmer et al., 2020) and FRB 200428 (Bochenek et al., 2020; The CHIME/FRB Collaboration et al., 2020), we triggered targeted observations of the source using PGIR on UT 2020 May 01. Due to the short expected emission timescale for counterparts from X-ray/radio bursts from the source ($\lesssim$ 1 s) as well as the background noise limited nature of NIR imaging with this instrument (see Table 1 in De et al., 2020b), we used the shortest possible exposure time allowed by the standard readout scheme (1.65 s) used in survey operations with an observing efficiency of 30% including dithers. Following this initial epoch, we significantly increased our observing efficiency, as well as our sensitivity to short timescale flares, by using a newly implemented readout mode of the H2RG detector array in Palomar Gattini-IR (De et al., 2020b). In this new mode, the detector is read out and digitized continuously while exposing on the sky, with an effective exposure time equivalent to the frame readout time of $\approx$ 0.84 s (see Appendix 9.6 for details).

Table 9.1 provides a summary of all the observing epochs on the source, including the readout mode used and the placement of the source in the large field of view. While the initial observations were designed to monitor the source for the total duration of its night time visibility from Palomar ($\approx$ 4.5 hours below airmass of 2) near the peak of its outburst, subsequent epochs in the second half of May 2020 were coordinated with the published visibility windows of the source with the Insight-*HXMT* satellite[1] and the CHIME telescope (K. Smith, pers. comm.).

9.3 Data analysis

The location of the source in a dense region of the Galactic plane together with the large pixel scale and under-sampled PSFs of the Gattini observing system present several challenges to the data reduction procedure, which were modified and adapted from the nominal survey mode. Appendix 9.7 provides a detailed summary of the reduction process adopted for this data set. Figure 9.1 shows an example triplet of a fast readout science frame centered at the location of the source, the corresponding reference image, and the resulting difference image. We were able to obtain high quality difference images in all the epochs, which show only background noise fluctuations and residual astrometric/Poisson noise from nearby bright stars.

Figure 9.2 shows a time series of the measured difference flux during one of the

[1] Published at `http://enghxmt.ihep.ac.cn/dqjh.jhtml`

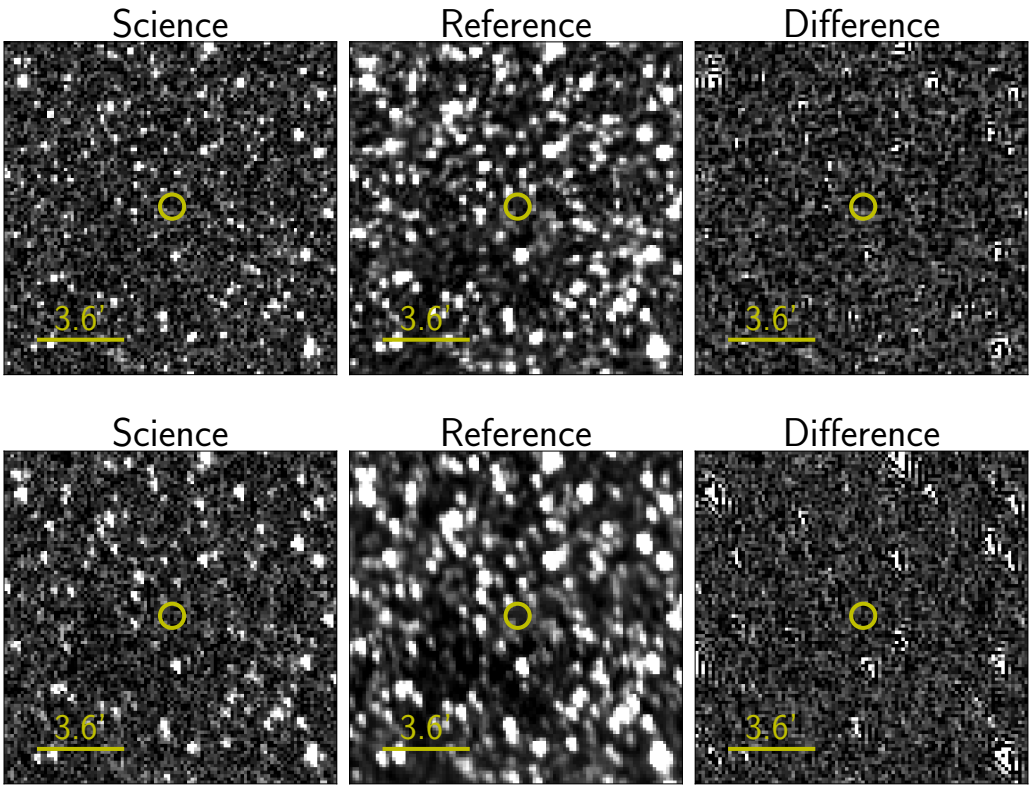

Figure 9.1: **Cutouts of the location of SGR 1935+2154 observed with the PGIR fast readout mode**. Example cutouts of a science (left column), reference (middle column), and difference image (right column) acquired in our observing sequence. North is up and East is left in each panel. The top and bottom rows show examples of the subtractions with the source placed in different parts of the focal plane with differing PSFs – the top row shows the case where the source was placed in the best part of the detector with approximately symmetric PSFs, while the lower row shows the same in a poorer region of the focal plane with elongated PSFs. In both cases, the difference image produced using ZOGY (Zackay et al., 2016) only shows residual astrometric noise and Poisson noise from nearby bright stars, with no statistically significant transient emission detected at the location of SGR 1935+2154 (yellow circle).

observing sessions[2]. In order to estimate the uncertainty and signal-to-noise ratio of the flux measurements, we measured the standard deviation of the fluxes in a running window of 200 observations around each image in the sequence. The measured flux scatter exceeds the propagated noise terms by $\approx$ 10% due to the presence of unaccounted noise terms such as correlated noise between the pixels

[2]The measured flux in counts was converted to mJy using the *2MASS* zero-points published at `https://old.ipac.caltech.edu/2mass/releases/allsky/doc/sec6_4a.html`. The corresponding $J = 0$ flux density is 1594 Jy.

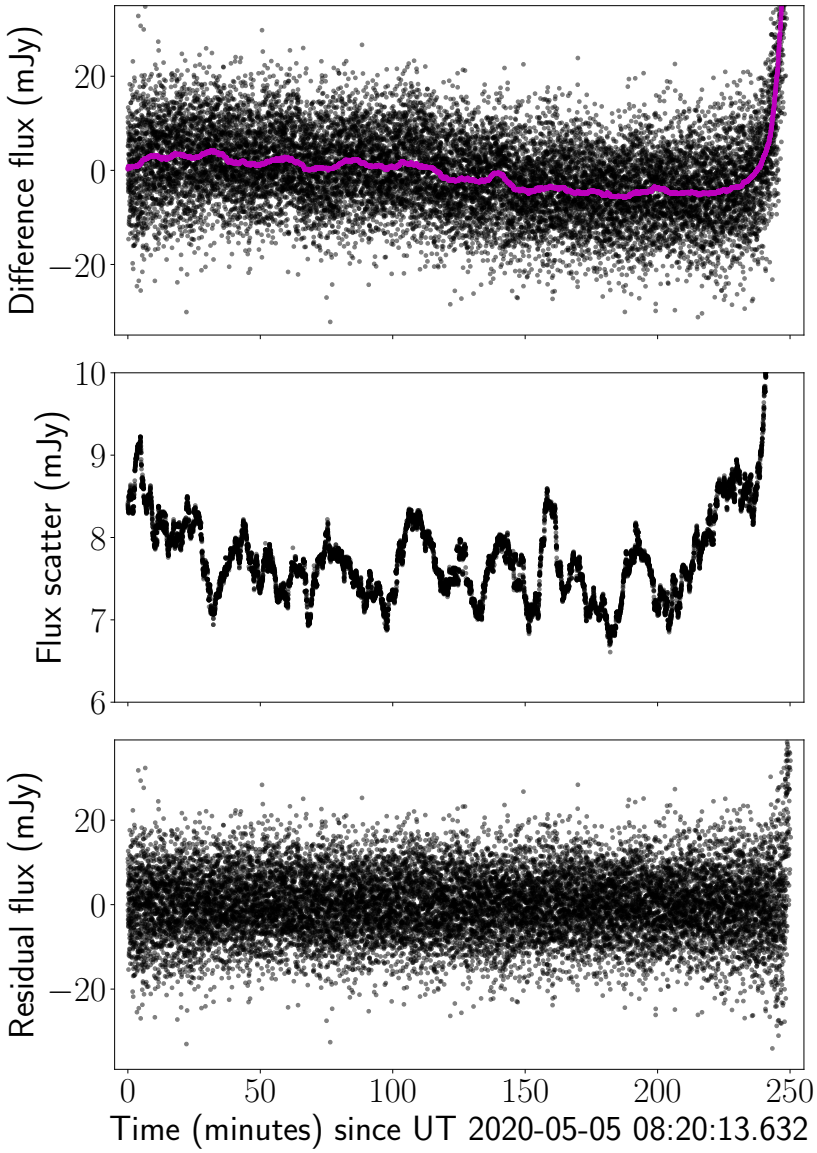

Figure 9.2: **Example of method used to search for second-timescale emission from SGR 1935+2154 using Gattini-IR data taken on UT 2020 May 05**. (Top panel) Forced photometry time series of fluxes measured at the location of the source in the difference images, with each dot representing a single image and the magenta lines representing a running median of fluxes measured in a window of 200 images in each side. The large increase in the background at the end of the observation is due to the approach of 12 degree twilight at the end of the observation. (Middle panel) Measured standard deviation in fluxes at the location of the source using the same window size as in the running median of the top panel. Noise variations due to the time variable airglow in J band is clearly visible. (Bottom panel) Residual flux obtained from subtracting the longer timescale airglow variations (shown in magenta in the top panel) from the observed flux.

introduced during the resampling process. The measured flux uncertainty exhibits temporal variations of the order of $\approx 20\%$ over the duration of the night, reflecting the variation in the foreground J-band sky brightness.

In addition to random scatter introduced due to time variable airglow in the J-band sky, the measured fluxes also show slow temporal variations (over time scales of tens of minutes) in the median (see Figure 9.2) that correlate with the changing scatter from the sky background, thus arising from imperfect background subtraction with the changing sky background. Since this effect introduces a slow temporal trend, we subtract it using a running median around each image since we aim to detect short timescale flares (~ 1 s) from the source. The resulting residual time series is shown in Figure 9.2, and is consistent with Gaussian noise in the flux measurements.

9.4 Results

Correlated variability between X-ray and NIR emission has been detected in several known Galactic magnetars, but over timescales of days to years (e.g. Israel et al., 2005; Rea et al., 2004; Tam et al., 2004). Fast optical flaring over timescales of a few seconds has also been observed in a candidate Galactic soft gamma-ray repeater (Castro-Tirado et al., 2008; Stefanescu et al., 2008). In the case of SGR 1935+2154, a probable faint NIR counterpart (at $H \approx 24$ mag) was identified with a deep Hubble Space Telescope exposure during its 2015 – 2016 outbursts (Levan et al., 2018), where the IR emission was shown to be enhanced during periods of the X-ray outburst. However, it was suggested that the lack of a direct correlation between the NIR – X-ray fluxes disfavors a disk reprocessing scenario for the NIR emission, and was likely more consistent with a magnetospheric origin of both the emission components (Levan et al., 2018). Here, we focus instead on the detection and limits on second-timescale flares in the NIR, which remain so far observationally unconstrained from this source.

Over the duration of ≈ 12 hours of observations (Table 9.1), we identified no reliable detections in the NIR time series at a flux level above $3\,\sigma$ from the background noise, beyond that expected from Gaussian noise. The median observed $3\,\sigma$ fluence limit on NIR bursts is ≈ 20 Jy ms (uncorrected for line-of-sight extinction). In order to constrain potential multi-wavelength counterparts, we searched all available public reports of X-ray and radio bursts from the source within our observing time intervals. A total of four X-ray bursts were reported by the *HXMT* (Li et al., 2020b)[3] and

[3]The updated list of bursts are available at `http://enghxmt.ihep.ac.cn/bfy/331.jhtml`

NuSTAR (Borghese et al., 2020) satellites during our observations. Table 9.2 provides an overview of the X-ray bursts reported during our observations. Notably, no significant emission was found detected around the reported epochs of four X-ray bursts. Below, we use the derived limits from our observations to constrain the fluence ratio of NIR bursts when compared to both the coincident X-ray bursts as well as the observed X-ray to radio spectrum of FRB 200428.

Extinction along the line of sight

Israel et al., 2016 find the neutral hydrogen column density ($n_{\rm H}$) along the line of sight to be $n_{\rm H} = (1.6 \pm 0.2) \times 10^{22}\,{\rm cm}^{-2}$ using XMM-Newton spectra fitted by a two-component power-law (PL) and blackbody (BB) model, from which we obtain an attenuation $A_V = 7.2 \pm 0.9$ mag (Guver et al., 2009) and $A_J = 2.0 \pm 0.3$ mag (Rieke et al., 1985). This extinction value is consistent with $1.82 < A_J < 1.97$ mag obtained using 3D dust map based on Pan-STARRS 1, Gaia, and 2MASS optical/NIR data (Green et al., 2019) assuming a distance of 8–12 kpc, although these dust maps suffer the lack of bright M-dwarf stars observable at these distances. For $A_J = 2.0 \pm 0.3$ mag, the corresponding median limits on the intrinsic fluence of the bursts will be $\approx 85 - 150$ Jy ms (within a factor of two). For the rest of this work, we assume an extinction of $A_J = 2.0$ mag towards the source, noting that the exact value does not significantly affect our constraints below due to the smaller effect of extinction in the NIR.

Constraints on the NIR fluence ratio from coincident X-ray bursts

In Table 9.2, we list the X-ray bursts reported from *HXMT* and *NuSTAR* during our observing sequence, together with the reported X-ray fluences from *HXMT* and our measured difference image flux and corresponding $3\,\sigma$ limit on the NIR fluence[4]. We note that the expected dispersion delay between X-ray and optical pulses for the reported DM of $\approx$ 330 pc cm^{-3} (Bochenek et al., 2020; The CHIME/FRB Collaboration et al., 2020; Zhang et al., 2020) is $\sim 10^{-11}$ s and thus not important for our observations. However, since a delay between the X-ray and optical emission could arise as a result of the intrinsic emission mechanism, we show in Figure 9.3 the measured difference flux in a window of $\approx$ 6 minutes centered on the times of the reported X-ray bursts[5].

[4]In order to be consistent with reported X-ray bursts, we define fluence as $\mathcal{F} = \nu f_\nu \delta t$ where ν is the observed frequency, f_ν is the spectral flux density, and δt is the exposure time for our data.

[5]For comparison, we note that the X-ray and radio emission observed in FRB 200428 was coincident within a maximum conservative uncertainty of $\approx$ 0.5 s, and shorter than our exposure

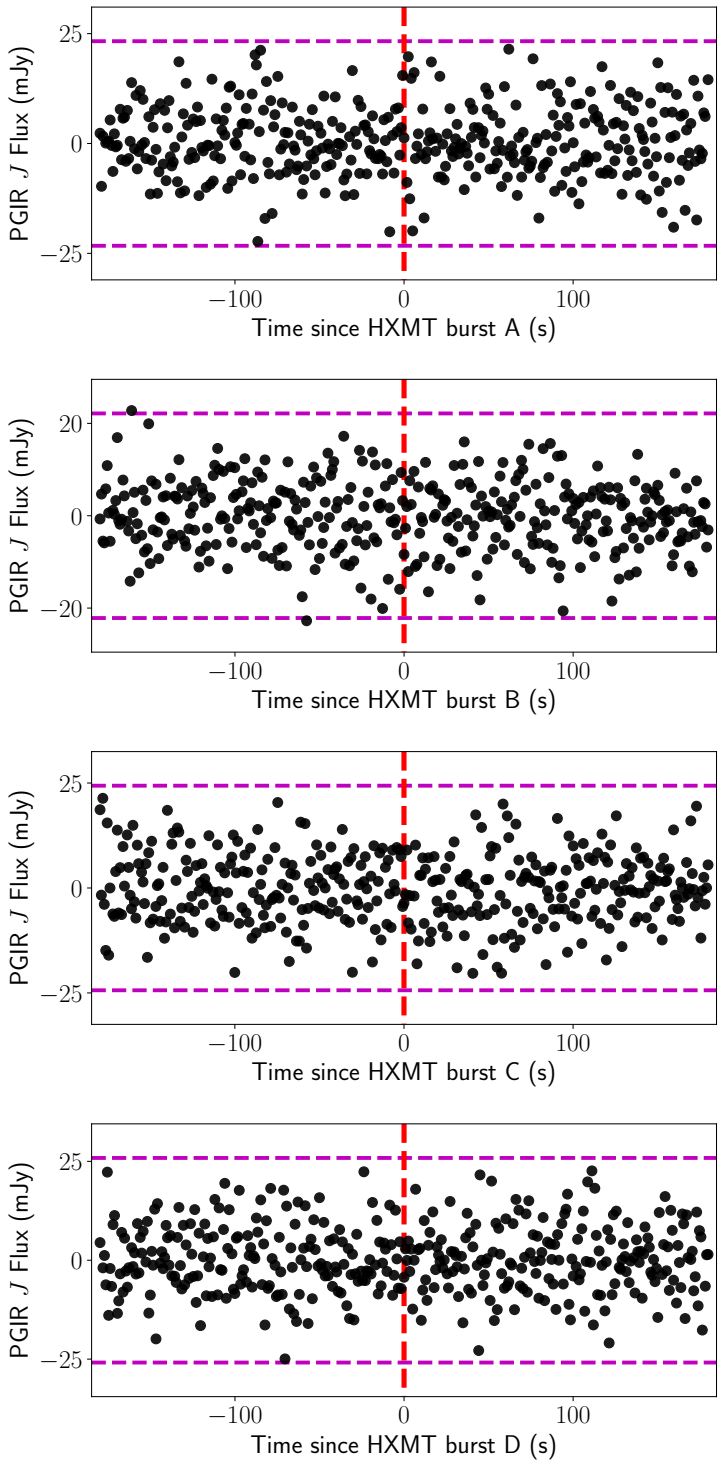

Figure 9.3: **Difference flux time series from PGIR around the time of reported X-ray bursts from SGR 1935+2154.** Time series of difference flux measurements over 360 s intervals centered on the times of known X-ray bursts listed in Table 9.2. The burst numbering indicated are the same as those in Table 9.2. The red vertical line shows the time of the reported burst, while the magenta horizontal dashed lines show the $3\,\sigma$ noise levels around the time of observation. No significant emission is detected at the $3\,\sigma$ level around the reported times of the X-ray bursts.

No significant emission is identified within this time window of the reported X-ray bursts and we list the derived limits on the NIR fluence of the bursts in Table 9.2. Combining the J-band flux limits from the epochs of the four X-ray bursts, we obtain a 3σ limit on the NIR fluence of 2.9×10^{-11} erg cm^{-2}. However, we caution that these bursts exhibit diversity in their X-ray spectral characteristics and hence their NIR fluence ratios may not be derived from the same population. The strongest simultaneous constraint on the NIR to X-ray fluence ratio ($R_{\rm NIR}$) is derived from the brightest burst (Burst B), where the non-detection of NIR emission constrains $R_{\rm NIR} \lesssim 2.5 \times 10^{-2}$ after correcting for extinction. For comparison, we note that the extinction corrected $R_{\rm NIR}$ for longer term correlated X-ray - NIR outbursts (over $\sim$ days – weeks) observed in Galactic magnetars range from typical values of $\sim 10^{-4}$ (as seen for SGR 1935+2154 as well as some other X-ray pulsars; Levan et al., 2018; Rea et al., 2004; Tam et al., 2004) to $\sim 10^{-2}$ (for the IR counterpart of SGR 1806-20; Israel et al., 2005).

Comparison to the multi-wavelength properties of FRB 200428

As the only other X-ray burst from SGR 1935+2154 that has been reported with a multi-wavelength (radio) counterpart, we compare the NIR limits to the observed spectral energy distribution (SED) of FRB 200428. The striking time coincidence between two X-ray pulses observed in the X-ray burst associated with FRB 200428 (Li et al., 2020a; Mereghetti et al., 2020) with the two radio pulses detected by CHIME (The CHIME/FRB Collaboration et al., 2020) potentially suggest a common emission source extending from the X-ray to radio frequencies. Li et al., 2020a show that the HXMT X-ray burst associated FRB 200428 was characterized with a hard power law spectrum with a photon index of $\Gamma \approx 1.5$, corresponding to a flux density dependence of $f_\nu \propto \nu^{-0.5}$ and fluence dependence of $\mathcal{F} \propto \nu^{0.5}$. In particular, they show that the observed STARE2 fluence at ~ 1.4 GHz can be explained by a single power law in f_ν extending from X-ray-to-radio frequencies (see also Ridnaia et al., 2020).

In Figure 9.4, we show the observed fluence of FRB 200428 as a function of frequency, which suggests a fluence dependence of approximately $\mathcal{F} \propto \nu^{0.46}$. In addition, Figure 9.4 shows the observed fluences of the X-ray bursts reported within our observing session along with our NIR fluence limits. While the spectrum of the X-ray burst for FRB 200428 remains unconstrained below ~ 1 keV, Figure 9.4 shows that our observations had the sensitivity to detect (at $\sim 30\,\sigma$ confidence) a

time.

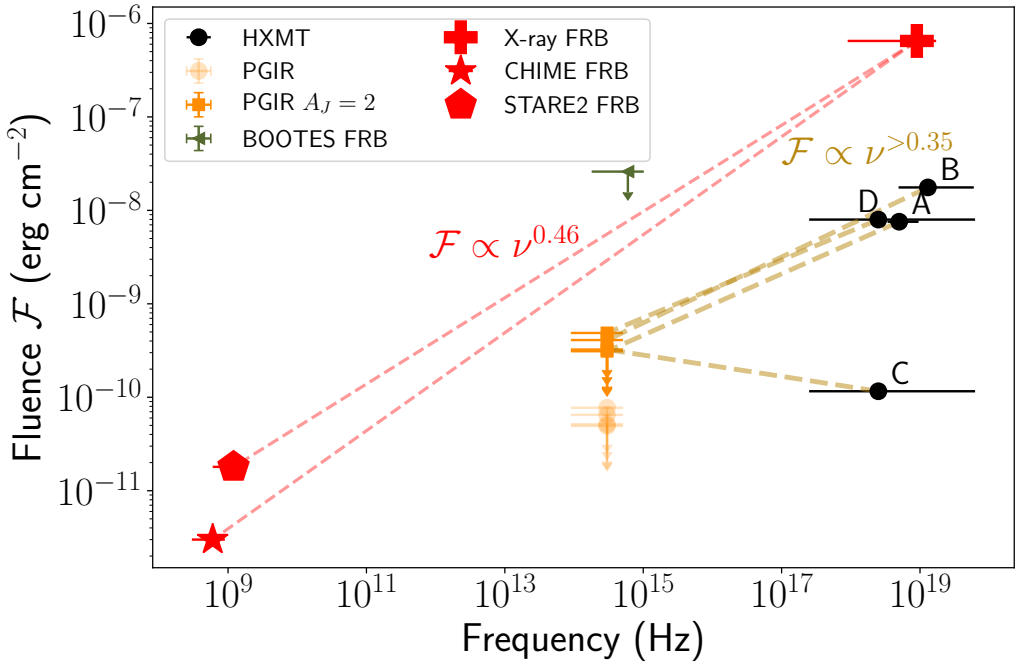

Figure 9.4: **Constraints on the NIR fluence of X-ray bursts from SGR 1935+2154 based on limits from Palomar Gattini-IR.** For comparison, we show the observed X-ray and radio fluence of FRB 200428 (in red) detected by CHIME and STARE2 in coincidence with a hard X-ray burst detected by HXMT, INTEGRAL, AGILE, and Konus-Wind. Optical limit from the BOOTES telescope for FRB 200428 is also shown. Limits from the PGIR campaign are shown in orange, with transparent circles showing raw limits, while solid squares show extinction corrected limits for $A_J = 2.0$ mag. The four X-ray bursts detected by *HXMT* and *NuSTAR* during the PGIR observing sessions (labels indicated as per Table 9.2) are shown with yellow dashed lines connecting the corresponding NIR limits. For each X-ray burst, we place the fluence at the frequency corresponding to the peak of the fluence spectrum ($= \nu f_\nu$) observed in the X-rays (and its uncertainty). The estimated fluence peak for bursts A and B are consistent with the observed spectrum of the bursts from NuSTAR observations (Borghese et al., 2020), where the fluence is observed to rise up to at least ~ 20 keV. In the case of burst C and D, the fluence spectrum was not well constrained and hence are placed nominally at 10 keV with error-bars spanning the full HXMT sensitivity range. The observed fluence index for FRB 200428, and constraints derived for the X-ray bursts are shown.

NIR counterpart of FRB 200428 if PGIR was observing at the time of the burst and the emission was characterized by a continuous power law extending from X-ray to radio frequencies. We note that the BOOTES limit from Lin et al., 2020b does not rule this out. However, we caution that the observed radio spectrum of FRB 200428 shows signatures of narrow bandwidth fluctuations (Bochenek et al., 2020; The CHIME/FRB Collaboration et al., 2020). Hence, the SED of FRB 200428 may not be consistent with a single power law extending from X-ray to radio frequencies, although propagation effects may affect this interpretation.

We compare this fluence index (β) to the expected NIR emission from the coincident X-ray bursts within our observing sessions. Here we refer to the fluence index as the exponential factor β of the observed fluence that scales as $\mathcal{F} \propto \nu^{\beta}$. The strongest constraints on the fluence index are derived from the brightest burst (Burst B), for which the fluence index is constrained to $\beta > 0.35$. The corresponding constraint on the spectral index α of f_ν is $\alpha > -0.65$. The derived limit on the fluence index is not constraining enough to rule out a NIR counterpart for these X-ray bursts with the same spectral behavior as that of FRB 200428, although it is within a factor of ≈ 1.5 from the estimated fluence index of FRB 200428. The non-detection is consistent with radio constraints derived from the non-detection of radio bursts by FAST of 29 bursts from SGR 1935+2154 detected by Fermi-GBM (Lin et al., 2020b), who derive deep limits of ~ 0.03 Jy ms at 1.25 GHz for these bursts. These non-detections require much steeper X-ray to radio fluence indices ($\beta > 1.2$) for the majority of bursts from SGR 1935+2154, suggesting that our limits in the NIR would not be deep enough to detect possible counterparts of the majority of bursts.

Comparison to theoretical models

Recent works have aimed to constrain several proposed models for FRBs to explain the observed occurrence of FRB 200428 simultaneously with the bright X-ray burst (e.g. Lu et al., 2020; Margalit et al., 2020). These models primarily revolve around two scenarios – one where the X-ray/radio emission is generated inside the neutron star magnetosphere via coherent curvature radiation (e.g. Cordes et al., 2016; Kumar et al., 2017; Lu et al., 2018; Pen et al., 2015) or via coherent maser processes produced at shock interaction of relativistic ejecta with circumstellar material (e.g. Beloborodov, 2019; Lyubarsky, 2014; Margalit et al., 2020; Metzger et al., 2019). In particular, the X-ray, optical/NIR and radio emission may not be generated at the same location near the neutron star in several of these scenarios. Since the theoretical predictions for multi-wavelength counterparts are not well constrained

enough to interpret our upper limits directly, we only briefly compare them to our NIR observational data.

Chen et al., 2020 provide a summary of the predictions for the fluence in the aforementioned models. In the case of the relativistic shock interaction model by Beloborodov, 2019, if the the blast wave strikes a wind bubble in the tail of a previous flare, a bright optical flare could result with an optical-to-radio fluence ratio of $\mathcal{F}_{\rm opt}/\mathcal{F}_{\rm radio} \lesssim 10^5$ (Chen et al., 2020). If some X-ray bursts from SGR 1935+2154 during the PGIR campaign were accompanied by a radio burst similar to FRB 200428, then we have the corresponding prediction of $R_{\rm NIR} \lesssim 0.1$ for $\mathcal{F}_{\rm radio}/\mathcal{F}_{\rm X\text{-}ray} \sim 10^{-6}$ (as observed by STARE2; Bochenek et al., 2020) and $R_{\rm NIR} \lesssim 0.01$ for $\mathcal{F}_{\rm radio}/\mathcal{F}_{\rm X\text{-}ray} \sim 10^{-7}$ (as observed by CHIME; The CHIME/FRB Collaboration et al., 2020). Our upper limits are thus comparable to these model predictions for the brighter X-ray bursts. On the other hand, for the curvature radiation model of Lu et al., 2018, the NIR/optical (or higher-frequency) emission from the coherently emitting particles is expected to be very faint. The transient event may be accompanied by incoherent emission processes inside the magnetosphere, and the maximum possible NIR flux from any incoherent emission processes from an emitting volume of radius $r = 10^8 r_8$ cm and plasma temperature $T = 10^8 T_8$ K is given by

$$\mathcal{F}_{max} \sim (h\nu/kT)^3 \sigma T^4 (r/D)^2 \tag{9.1}$$

$$\sim 10^{-13} T_8 r_8^2 \,\mathrm{erg\,cm^{-2}\,s^{-1}} \tag{9.2}$$

where $D \sim 9$ kpc is the distance to the source. We see that the NIR/optical emission from within the magnetosphere is undetectable in our observations for burst duration $\lesssim 1$ s.

9.5 Summary

We have presented results from a targeted follow-up campaign to search for second timescale NIR flares from the Galactic magnetar SGR 1935+2154 using Palomar Gattini-IR. The observations were enabled with a recently implemented detector read-out mode that allows for high time resolution readout of the detector array with nearly 100% observing efficiency. We found no significant counterparts for second timescale flares from the source above a median 3 σ fluence limit of ≈ 20 Jy ms. This non-detection, together with the relatively low inferred extinction towards the source at NIR wavelengths ($A_J \approx 2.0 \pm 0.3$ mag) allows us to place the most stringent extinction-corrected constraints till date on second-timescale flares from

the source of $\approx 85 - 150$ Jy ms at optical/NIR wavelengths ($\nu \sim 10^{14}$ Hz). The NIR limit corresponds to an energy $E \lesssim 3 \times 10^{36}$ erg at a distance of 9 kpc (Zhong et al., 2020), and is within an order of magnitude of that reported in the radio for FRB 200428 at 1.25 GHz ($\approx 2 \times 10^{35}$ erg; Bochenek et al., 2020). It is also several orders of magnitude deeper than reported optical limits from nearby well-localized FRBs ($\sim 10^{43-46}$ erg; Andreoni et al., 2020; Hardy et al., 2017).

A total of four X-ray bursts were detected by the *HXMT* and *NuSTAR* telescopes within our continuous observing campaign, although no NIR counterparts were detected. The non-detection of NIR emission around these bursts constrain the NIR to X-ray fluence ratio to $R_{\rm NIR} \lesssim 2.5 \times 10^{-2}$. Comparing these fluence limits to the radio/X-ray fluence observed in FRB 200428, we show that our observations were sensitive enough to detect a NIR counterpart at a significance of $\sim 30\,\sigma$ if PGIR was observing at the time of FRB 200428 and the NIR emission falls on the same power law suggested for the radio/X-ray emission. The non-detection of NIR emission associated with the brightest X-ray burst within our observation time constrains the X-ray to NIR fluence index of the burst to be $\beta > 0.35$ (spectral index $\alpha > -0.65$).

As Palomar Gattini-IR performs the first all-sky untargeted time domain survey of the dynamic infrared sky at timescales of days to years over the survey duration, these observations further demonstrate a unique new capability of this instrument to probe the infrared time domain sky at second timescales. Although the instrument uses a small (30 cm) telescope with coarse pixels that severely limit its sensitivity due to the bright J-band foreground, these observations prove the scientific utility of specialized NIR detector read-out modes in finding large amplitude second-timescale flares from dust-obscured sources in the Galactic plane. This advocates for a systematic exploration of this hitherto unexplored phase space, which is possible with PGIR not only for single sources (as demonstrated in this work) but for large patches of the sky, enabled by the instrument's large field of view.

We thank the Insight/HXMT team for their kind co-operation in co-ordinating observations and quickly providing fluence estimates. We thank K. Smith for cooperation regarding the CHIME observability windows. We thank C. Bochenek, W. Lu, V. Ravi, and S. R. Kulkarni for valuable discussions on this work.

Palomar Gattini-IR (PGIR) is generously funded by Caltech, Australian National University, the Mt Cuba Foundation, the Heising Simons Foundation, and the Binational Science Foundation. PGIR is a collaborative project between Caltech, Australian National University, University of New South Wales, Columbia University,

and the Weizmann Institute of Science. This work was supported by the GROWTH (Global Relay of Observatories Watching Transients Happen) project funded by the National Science Foundation under PIRE Grant No 1545949. GROWTH is a collaborative project between the California Institute of Technology (USA), University of Maryland College Park (USA), University of Wisconsin Milwaukee (USA), Texas Tech University (USA), San Diego State University (USA), University of Washington (USA), Los Alamos National Laboratory (USA), Tokyo Institute of Technology (Japan), National Central University (Taiwan), Indian Institute of Astrophysics (India), Indian Institute of Technology Bombay (India), Weizmann Institute of Science (Israel), The Oskar Klein Centre at Stockholm University (Sweden), Humboldt University (Germany), Liverpool John Moores University (UK), and University of Sydney (Australia).

9.6 Appendix: Fast readout mode

Conventional readout in the H2RG array requires one frame scan to reset and measure the resulting initial offset (including random errors) and a second frame to measure the final value (Figure 9.5, upper). The signal is then the difference of these two frames. At the fastest frame rate (with no delay between frames), the duty cycle drops to 50%. To address this deficiency, we altered the readout sequence such that immediately after the signal readout in a given line, the line is reset and the baseline for next frame is digitized before preceding to the next line (Figure 9.5, lower). Signal is then being recorded except during the interval between signal and post-reset level samples, i.e., dead time has been reduced from the time to scan through the entire frame to the time to read just one line.

Given the high sky noise, we were able to reduce signal sampling time so that pixel time was reduced from typical $\approx 6-7\,\mu$s to $3.1\,\mu$s. With two samples per pixel per frame, the frame time is then 0.848039 s. The dead time between reading final sample and the next post-reset sample $\approx 200\,\mu$s. The first exposure in a sequence still requires two frames, with the first frame establishing the post reset level. The duty cycle for an N frame sequence is then

$$\frac{N-1}{N} \times \frac{0.848039 - 0.0002}{0.848039} \tag{9.3}$$

which approaches 99.98% for long exposure sequences. Anomalous behavior due to self heating variations were avoided by clocking the detector continuously. The camera was set up to read continuously and store data in a ten frame circular buffer

in the computer's memory with the only distinction between "idling" and exposing being whether the data was written to disk.

9.7 Appendix: Data reduction

While the nominal survey mode operations in Gattini-IR use the `Drizzle` (Fruchter et al., 2002) technique to reconstruct the under-sampled PSFs by stacking several dithered images taken on the sky, our requirement for high time resolution at the native image readout timescale makes it unsuitable for this application. We thus modified our default data processing pipeline to perform detrending, astrometry, photometry, and subtractions on individual images at the native pixel scale of the detector, which we describe below.

Flat-field generation and image detrending

A master flat-field was created for the read-out mode using a median combination of 400 sky images across several observing nights in order to calibrate the pixel-to-pixel response of the array in the new readout mode. Using images acquired during a wide range of times ensures that temporal structures in the sky background variation do not affect the resulting flat-field. Each acquired image (2048×2048 pixels) was flat-fielded using the derived flat-field, and only 1/16 of the full image (512×512 pixels; hereafter referred to as a sub-quadrant as per the terminology in De et al., 2020b) containing the target of interest was retained for further processing. Retaining a smaller portion of the image containing the source leads to a large reduction in the variation of the PSF across the image, thus producing better quality astrometric and photometric solutions, as well as subtractions downstream.

Astrometry, photometry, and reference image generation

An astrometric and photometric solution for the sub-quadrant was derived using relatively bright and isolated stars in the field. The calibration was performed using the same techniques as in the regular Gattini observing system and using the same reference catalog, which is calibrated astrometrically to *Gaia* DR2 and photometrically to the *2MASS* point source catalog. The astrometric solutions achieved typical RMS of $\approx 1.0 - 1.2''$($\lesssim 1/8$ of a pixel), while the photometric solutions have typical uncertainties on the zero-point of $\approx 1\%$ as calibrated from ~ 100 stars in each image.

Due to the location of the source in a dense region of the Galactic plane (see Figure 9.1) and the highly non-stationary background limited by confusion noise, direct

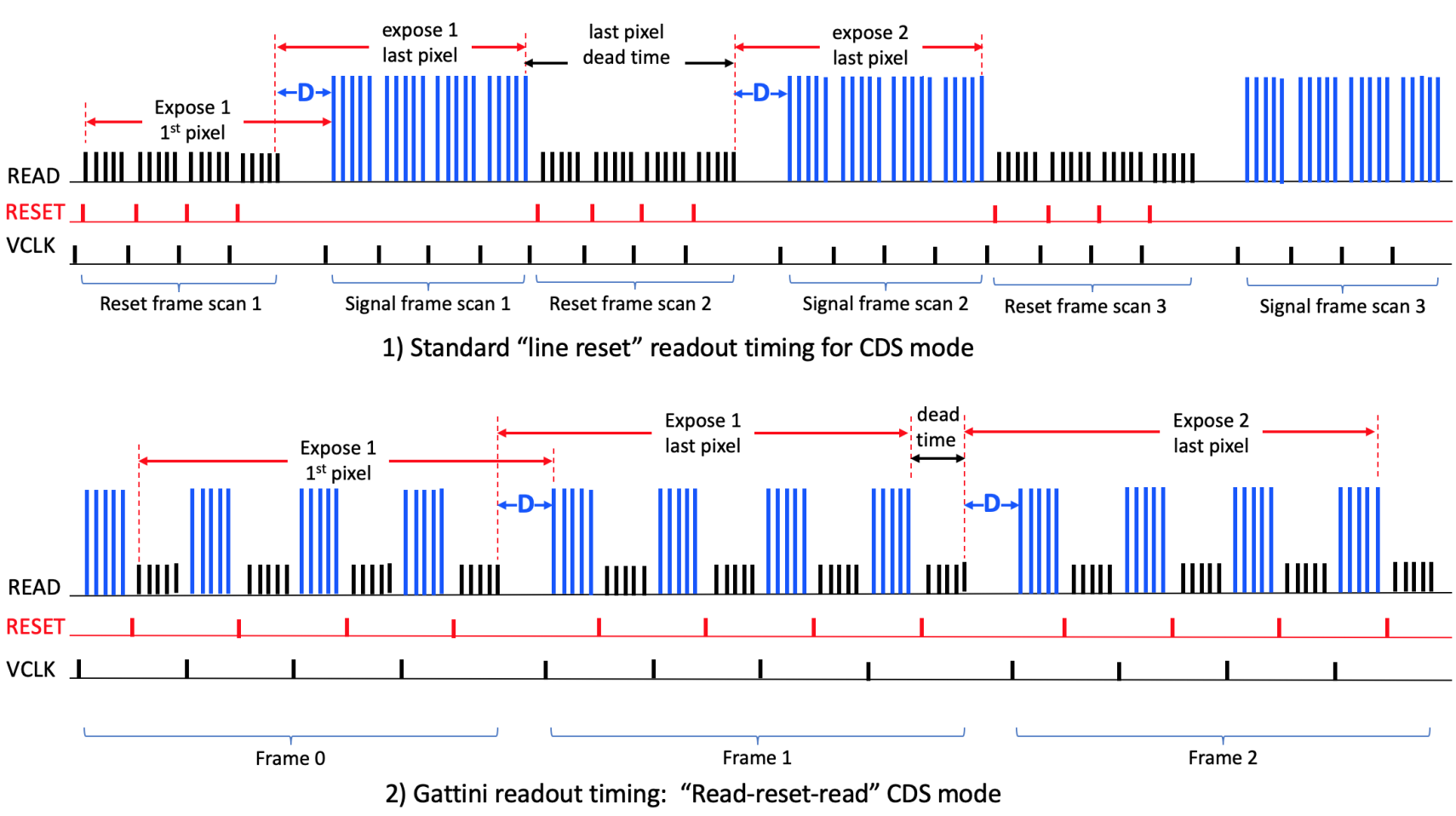

Figure 9.5: **Difference between a conventional H2RG readout scheme and the readout technique used in the new continuous fast readout mode of the H2RG array in PGIR.** In each panel, we show the time sequence of pixel reset and signal readout for a hypothetical detector of 20 pixels (4 rows with 5 pixels per row). Three horizontal lines in each panel indicate the reset and readout sequence. The top horizontal line in each panel (labeled as READ) shows progression of the pixel readout in each row, with short black vertical lines showing a post-reset pixel readout, and long blue vertical lines showing a post-expose pixel signal readout (the sky signal is thus the difference between these two values). Red vertical lines on the second horizontal line (labeled as RESET) mark the time of reset for each row of pixels, while black vertical lines on the third horizontal line (labeled as VCLK) mark the start time of signal readout for each row. In (1), the timing of pixel reads, reset, and vertical clock for conventional Correlated Double Sampling (CDS) is shown, where each row is reset, then digitized to establish a baseline. All baseline samples are acquired before reading the frame again to record signal levels. Light falling on the detector between the reading signal of one exposure and the baseline of the next is not recorded resulting in only 50% exposure duty cycle when exposure delay (D) is set to zero for continuous readout. In (2), we show the PGIR fast readout mode, where the signal is read, then the row is reset and baseline samples are acquired before advancing to the next row. Dead time is thus reduced from a full frame scan time to the time to read one row. The signal samples in the first frame and the baseline samples in the last are discarded.

aperture photometry measurements on un-subtracted images are not well-suited for deriving accurate constraints on the source flux. We thus created for each observing night, a deep median stack of 400 sub-quadrants to serve as a reference image with nearly identical PSF as the science images taken each night. Since the reference stack was produced as a median combination as implemented in `Swarp` (Bertin et al., 2002; at the same pixel scale as that of the science images), we do not expect any short timescale emission to contaminate the reference image.

Difference imaging and forced photometry

Each reduced sub-quadrant was processed through image subtraction by resampling the respective reference image (one for each night) to the coordinate grid of the science frame. The resampled reference frame was then flux-scaling to each science frame using common cross-matched stars in the two images. The typical astrometric registration uncertainty between the cross-matched stars was $\approx 0.1 - 0.15$ pixels, while the corresponding flux scaling certainty was $\lesssim 5\%$. Image subtraction was performed using the ZOGY algorithm (Zackay et al., 2016), including the propagation of noise uncertainties from the science and reference images to produce an uncertainty image for each produced difference image (as in De et al., 2020c). The flux and its uncertainty at the location of the source was measured directly from the difference images by performing a weighted flux measurement using the difference image PSF at the location of the target in the difference image and the corresponding uncertainty image.

ID	UT Start	UT End	Mode	Exp. time (s)	N	Total exposure (s)	Duty cycle (%)	$3\,\sigma$ limit (mJy/Jy ms)
1	2020-05-01 08:24:38.9	2020-05-01 12:34:53.6	I	1.65	2722	4491.3	29.9	9/16
2*	2020-05-02 07:49:45.5	2020-05-02 12:34:14.1	II	0.84	18009	15127.6	89.7	25/21
3*	2020-05-05 08:20:13.7	2020-05-05 12:31:09.0	II	0.84	15917	13370.3	89.7	23/19
4	2020-05-23 11:23:09.0	2020-05-23 11:38:27.3	III	0.84	1084	910.6	99.9	16/13
5	2020-05-24 06:57:05.3	2020-05-24 07:29:43.4	III	0.84	2310	1940.4	99.9	19/16
6†	2020-05-24 11:09:27.4	2020-05-24 11:34:12.3	III	0.84	1706	1433.0	97.3	21/18
7	2020-05-28 06:13:49.2	2020-05-28 07:13:34.7	III	0.84	4229	3552.4	99.9	18/15
8†	2020-05-31 09:01:30.0	2020-05-31 09:39:32.9	III	0.84	1751	1470.8	64.6	62/52

Table 9.1: **Summary of observing sessions of SGR 1935+2154 with PGIR**. The Mode column refers to the observing configuration of the system during the respective epoch. Mode I indicates the use of the standard observing mode of the survey including dithers between exposures and lower observing efficiency. Mode II indicates the fast readout mode discussed in the text. Both Mode I and II had the telescope aligned to the default observing grid and the source placed away from the best focused part of the field (see discussion of PSF variation in De et al., 2020b). Mode III indicates the fast readout mode with the source placed in the best focused part of the detector leading to better sensitivity. N denotes the number of images that produced good quality subtractions in the session. The duty cycle is a conservative lower limit for the first pixel read out in each detector channel. The limiting flux denotes the median limiting flux in the individual exposures at the location of the source as measured from the observed scatter of fluxes in the difference image. Data acquired during epochs marked by * were affected by a bug in the readout that repeated every 10th exposure in the sequence (i.e. every 9th and 10th exposure were identical), leading to a reduced duty cycle. Epochs marked by † were affected by intermittent clouds leading to a reduced observing duty cycle. Difference flux measurements and their uncertainties will be released as an electronic supplement upon publication.

ID	Instrument	Trigger time (UT)	Duration (s)	X-ray fluence (erg cm^{-2})	Obs Start (UT Day)	Obs End (UT Day)	Diff. Fluence (erg cm^{-2})	$3\,\sigma$ limit (erg cm^{-2})
A	*HXMT*/*NuSTAR*	2020-05-02 10:17:26.00	0.076	7.56×10^{-9}	10:17:25.90	10:17:26.74	2.69×10^{-12}	4.93×10^{-11}
B†	*HXMT*/*NuSTAR*	2020-05-02 10:25:25.80	0.415	1.76×10^{-8}	10:25:25.07	10:25:26.77	-3.64×10^{-11}	6.49×10^{-11}
C	*HXMT*	2020-05-02 10:46:20.85	0.077	1.16×10^{-10}	10:46:20.12	10:46:20.96	-7.64×10^{-12}	5.14×10^{-11}
D†	*HXMT*	2020-05-05 12:09:29.75	0.039	7.97×10^{-9}	12:09:28.94	12:09:30.65	-1.81×10^{-11}	7.73×10^{-11}

Table 9.2: **List of X-ray bursts reported by high energy instruments within the Gattini-IR observing sequences.** The Fluence column denotes the fluence reported by the *HXMT* satellite, while the duration denotes their T_{90} measurement. The Obs start and Obs end column denotes the start and end of the exposure that contained the trigger time of the X-ray burst, with respect to the start of the UT day (00:00:00). The Diff. fluence and $3\,\sigma$ limit column denote the IR fluence computed from the difference flux and the corresponding $3\,\sigma$ limit. For bursts denoted by †, the duration of the burst was covered by two consecutive and continuous exposures in the sequence, in which case we reported a weighted flux measurement between the two exposures and its corresponding uncertainty. The IR flux measurements have not yet been corrected for extinction since that is model dependent.

Chapter 10

SUMMARY AND THE NEXT FRONTIER

I finish this thesis summarizing the progress made with regards to the questions laid at the outset, and highlight open questions and the way forward. I particularly illuminate exciting opportunities with the Vera Rubin Observatory's (VRO) Legacy Survey of Space and Time (LSST; Ivezić et al., 2019), which is arguably going to be the largest time domain experiment of this decade. LSST will carry out a wide-field survey covering $\approx 18,000\,\mathrm{deg}^2$ in six filters from u to y-band to a single epoch depth of ≈ 24.5 mag. Its combination of depth and sky coverage will be an unprecedented leap towards probing the population of low luminosity transients in the local universe. ZTF Phase-II is already in operation. The focus of the CLU experiment has now shifted exclusively to characterizing low luminosity transients (peak absolute magnitude $\gtrsim -17$) down to the survey depth of ≈ 20.5 mag. This modification is expected to increase the yields of the faintest thermonuclear and core-collapse SNe, and prepare for the upcoming fire hose of faint transients from LSST.

To this end, clever filters and careful vetting will be required to select nearby events. Experience from the ZTF CLU and Bright Transient Survey (BTS; Fremling et al., 2019) experiment has clearly demonstrated that eliminating background SNe is a highly non-trivial task without spectroscopic redshifts. Given that the completeness of galaxy catalogs has been quantified to be only $\lesssim 50\%$ in the local (< 200 Mpc) universe by the ZTF BTS, upcoming large spectroscopic redshift catalogs from highly multiplexed spectrographs are going to be revolutionary for targeted searches of nearby transients with LSST. The Dark Energy Spectroscopic Instrument (DESI) is already in operation, and going to obtain redshifts of ≈ 10 million galaxies brighter than $r \approx 19.5$ mag. When combined with these redshift catalogs, the exquisite depth of LSST will enable statistical studies of transients down to $M \approx -12$ within 200 Mpc, albeit largely for relatively slow evolving events due to the slower cadence. In addition, there is a great opportunity for combining the depth of LSST with the near nightly cadence coverage of the entire sky from shallow time domain surveys to study extremely young supernovae.

10.1 The emerging population of ultra-stripped SNe

The properties of iPTF 14gqr (Chapter 2) can be reasonably explained by an ultra-stripped SN in a close binary system – in particular, with early time data that uniquely point to a highly stripped He star progenitor that underwent intense mass loss prior to explosion. Ejecting only $\approx 0.2\,M_\odot$ of material in the explosion, iPTF 14gqr arguably represents the most extreme end of the spectrum of stripped massive stars that undergo a collapse. Based on the models in Tauris et al., (2015), the extremely low ejecta mass points to a highly compact orbit of the companion (orbital period ~ 0.1 day), and the system may represent the first observed instance of the birth of a compact neutron star binary system that will merge within a Hubble time.

On the other hand, the properties of SN 2019dge (ejecta mass of $\approx 0.4\,M_\odot$; Yao et al., 2020b) suggest a likely wider orbit (orbital period $\sim 1-10$ days) that may result in analogs of binary NS systems in our Galaxy that have merger timescales longer than the age of the universe (Tauris et al., 2017). Finally, SN 2019ehk (Chapter 3) represents a less extreme case of a highly stripped SN (ejecta mass $\approx 0.6\,M_\odot$) from a low mass ($\approx 9-10\,M_\odot$) progenitor, that lost nearly all of its H envelope to stripping in a relatively compact orbit (orbital period ~ 10 days). Nonetheless, the progenitor was likely stripped by a main sequence companion in a tight orbit, and resulted in the formation of a compact NS – main sequence binary. Such binaries have been suggested to be progenitors of NS – WD systems that could be detectable in gravitational waves with LISA, and merge within a Hubble time (Toonen et al., 2018). Figure 10.1 presents a schematic that summarizes the new insights into the explosive lives of high mass binaries that form NSs in compact binary systems.

With the beginning of ZTF Phase-II covering the visible sky at a higher cadence of 2 days, the discovery potential for these faint rapidly evolving events has increased dramatically. In order to select these events more efficiently, we need to particularly pay close attention to faint and rapidly evolving SNe co-incident with nearby galaxies. With a larger sample of events, the distribution of ejecta masses combined with nebular phase spectroscopy (to constrain the progenitor zero-age mass) will provide exquisite constraints on the distribution of orbital periods and companion types. With the detection of gravitational waves from merging NSs expected to become routine (~ 1 per month) in future LIGO/Virgo observing runs, comparing the demographics of merging NSs to ultra-stripped SNe will ultimately reveal the formation channels.

The signatures of dense CSM ubiquitously observed in these events offer unique

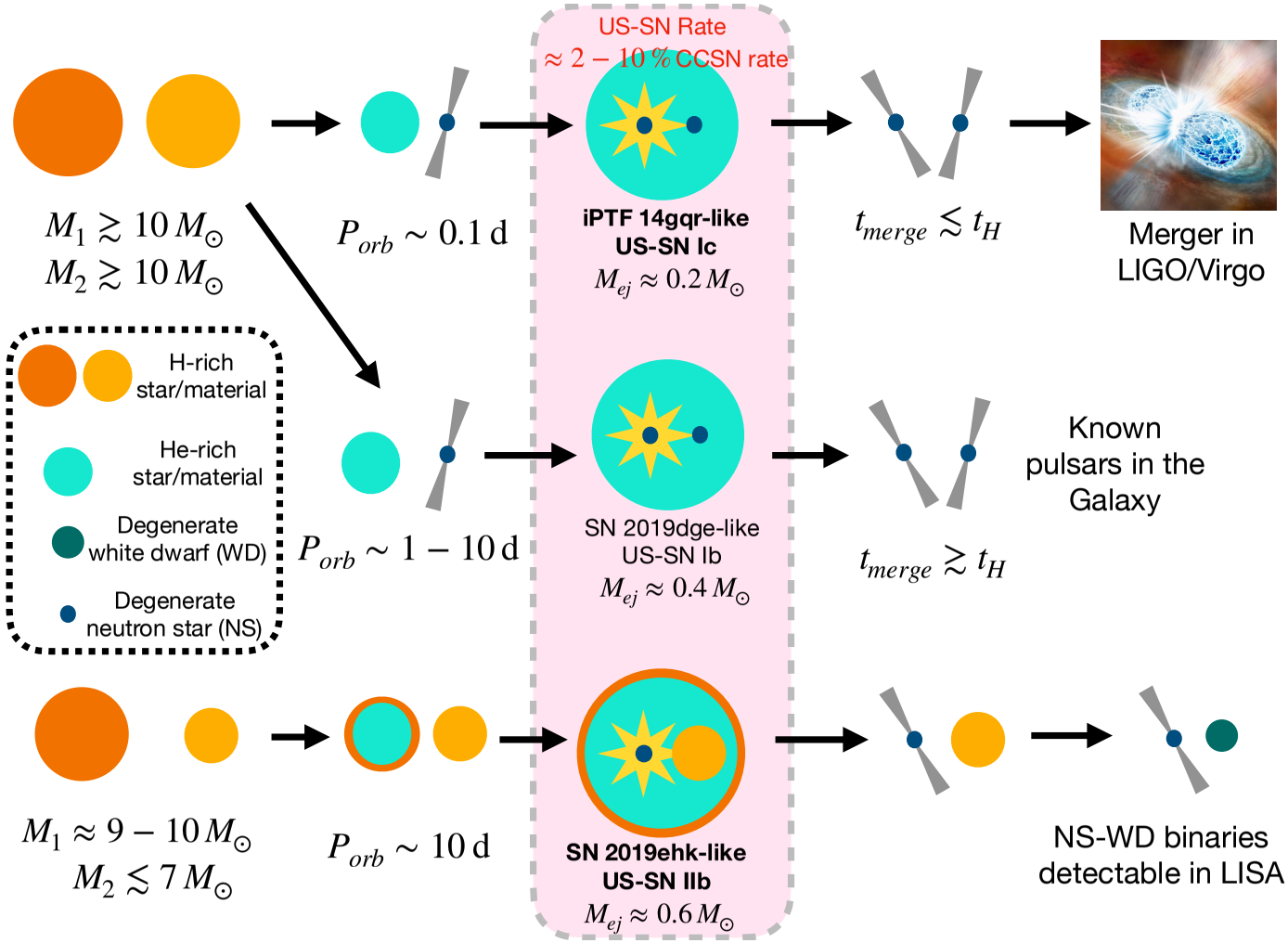

Figure 10.1: **The formation of neutron stars in compact binary systems starting from massive binaries**. The left box indicates the symbols used to depict different types of astrophysical systems. Ultra-stripped SNe (USSNe) from massive stellar binaries with a range of orbital periods and companion types may explain the diversity of the observed SN properties, leading to neutron stars in compact binary systems. The sizes of the spheres of the main sequence stars reflect their masses (not to scale). The phenomena shown in pink boxes indicate stages that were directly constrained based on the work in this thesis.

insights into the final nuclear processes and energy transport in these extremely low mass cores, and is emerging as an important topic for theoretical exploration (Wu et al., 2021). At the same time, the vigorous pre-explosion expansion could have important consequences for the merger times of the resulting binary system (Dewi et al., 2002; Laplace et al., 2020). Assuming the estimated rate of ultra-stripped SNe, ≈ 1 event per year should be expected within 50 Mpc, where upcoming surveys like LSST may be able to directly detect the pre-supernova outburst. Finally, identifying the progenitors of ultra-stripped SNe within the Galaxy (Götberg et al., 2020) offer promising new avenues. The extremely hot helium star progenitors emit most of their radiation in the UV bands where sky surveys have been limited (especially near the Galactic plane). Upcoming surveys like ULTRASAT (Sagiv et al., 2014), Dorado and UVEX may finally be able to uncover this population.

10.2 The explosive lives and fates of helium-accreting WDs

The properties of SN 2018byg (Chapter 4), together with its striking similarities to the class of Ca-Ia type of Ca-rich transients (SN 2016hnk and SN 2019ofm; Chapter 6), provide strong evidence that He shell detonations are indeed realized in nature. Detailed modeling of SN 2018byg and SN 2016hnk (Jacobson-Galán et al., 2020b) as helium shell double detonation SNe provide further confirmation of a diversity of shell masses on relatively massive ($\approx 0.75\,M_\odot$) WDs – with SN 2018byg having a massive ($\approx 0.15\,M_\odot$) shell and SN 2016hnk having a thin shell ($\lesssim 0.05\,M_\odot$). Noting the striking continuum of properties with the rest of the class of Ca-rich transients (the Ca-Ic and Ca-Ib objects), the complete diversity can be reasonably explained by a a family of helium shell explosions on low mass white dwarfs. The evidence for largely incomplete He burning in the Ca-Ib objects may suggest that the shell burning perhaps remains as a subsonic deflagration on the lowest mass WDs, and thus both He shell detonations and deflagrations may be realized in nature. Together, these results suggest that the long sought He shell detonation mechanism for Type Ia SNe are indeed realized in nature, but in a fainter and faster class of explosions that are nearly as common.

Detailed modeling of these elusive explosions is likely to be a ripe frontier for progress in our understanding of explosive He shell burning. The regime of low mass white dwarfs with thick He shells has been scarcely modeled in the literature. Previous studies have primarily focused on higher mass WDs (due to their applicability for Type Ia SNe), and largely without including non-thermal excitation of He lines. Current work is in progress to quantify the presence of He lines (A.

Polin, private comm.) when He is abundant in the ejecta. To complement these efforts, confirmation of the tantalizing observed correlations between peak light and nebular phase properties of a large sample would be particularly useful to constrain the nucleosynthetic properties as a function of WD mass and their role in chemical enrichment (Frohmaier et al., 2018; Mulchaey et al., 2014).

While the remote and old environments still remain to be completely explained, it is worth noting that most Ca-Ia objects are found in star forming galaxies, while Ca-Ib and Ca-Ic's are almost exclusively found in old, passive galaxies. Perhaps, this host preference points to an underlying division in the progenitor channels – wherein the Ca-Ia objects arise from more massive CO WDs with sdB companions in younger environments, while the Ca-Ib and Ca-Ic objects represent lower mass WDs accreting from He WDs in old environments. Perets et al., (2021) have suggested that this preference can be explained by the large amount of intra-cluster light in early type galaxies; deep and wide-field imaging of nearby early type clusters could direct test this suggestion.

For the brighter He shell detonations like SN 2018byg, their distinctive color evolution compared to other thermonuclear SNe is likely to provide a powerful way of selecting them in photometric time domain surveys. Such an approach would be particularly powerful in the era of LSST, subject to the currently uncertain cadence strategies. While the current Deep Wide Fast survey only revisits the same sky once every $\approx$ 15 days in the same filter, inter-filter visits can occur every $\approx$ 3 days. Perhaps, if the survey scheduling strictly enforces inter-filter visits in a blue (say g-band) followed by a red (say r-band) within $\approx$ 3 days, finding these events would be relatively easier by selecting extragalactic transients with very red $g - r$ color evolution similar to SN 2018byg. Such an exercise could make these events detectable out to $\approx$ 2 Gpc in LSST, possibly paving the way for population studies with just photometry (which can already constrain the He shell and WD core mass). For events in the local universe, serendipitous early-time detections with LSST would provide exquisite constraints on the early bumps from the shell radioactive decay. The nominal cadence of LSST would also be ideally suited to track the late-time radioactive decay of all nearby SNe, in particular, to detect signatures of peculiar, long-lived isotopes (e.g. ^{44}Ti) that have been long predicted in these events (Waldman et al., 2011). In preparation, we are already undertaking dedicated late-time follow-up of all faint hydrogen-poor SNe in ZTF with the Las Cumbres Observatory (Brown et al., 2013) robotic telescope network (PI: K. De).

10.3 Compact binaries in the Milky Way

Looking towards Galactic analogs of the progenitor systems, the powerful combination of Gaia and current photometric time domain surveys (and in the future, LSST) are well placed to discover i) short period CO + He WD binaries that are direct progenitors of the He accreting systems (e.g. Burdge et al., 2020) and ii) new outbursting AM-CVn binaries that are already undergoing accretion (e.g. Ramsay et al., 2018). The commissioning and initial science operations (Chapter 7) of PGIR has already opened up a vast array of avenues to probing stellar variability in the largely dust obscured Galactic plane. The potential for high cadence IR surveys in the Galactic plane have already been demonstrated with the results from the PGIR nova search program, that provided the first quantitative estimate of the Galactic nova rate (Chapter 8). And to sum up the diversity of fates of He-accreting WDs, PGIR enabled the identification of the first systematic infrared-variability selected sample of dust obscured R Coronae Borealis variables (Karambelkar et al., 2020), suggested to be stable merger products of CO and He white dwarfs (Clayton, 1996).

While the specific nova rates in the bulge and disk appear to be consistent with each other in the Milky Way, the M31 bulge has been shown to be a much more prolific nova producer compared to its disk. Upcoming wide-field IR surveys in the Galactic bulge and plane (see Section 10.4) together with LSST[1] in the redder filters could provide strong constraints on the specific rates. Finally, LSST could measure pre-explosion orbital periods of novae to constrain the effect of the eruption on the long term binary evolution. Figure 10.2 presents a summary of the progress in our understanding of low mass compact binaries, enabled by the work in this thesis. Together, these endeavors help set the landscape for astrophysical population studies in the upcoming era of mHz gravitational wave astronomy with LISA.

10.4 New opportunities on the horizon

I conclude by discussing new opportunities for synergies between upcoming optical/infrared time domain surveys and the rich emerging landscape of multi-wavelength all-sky surveyors. Within our own Galaxy, PGIR has set the stage for the wide-field exploration of the dynamic and optically obscured Galactic plane. The PGIR fast readout mode opens up exciting possibilities to study second-timescale IR variability from obscured Galactic sources – not only for targeted searches (as done in the case of SGR 1935+2154; Chapter 9), but wide-field untargeted searches

[1]Note that current work is in progress to discuss the inclusion of the Galactic plane and bulge in the Deep Wide Fast survey (Strader et al., 2018)

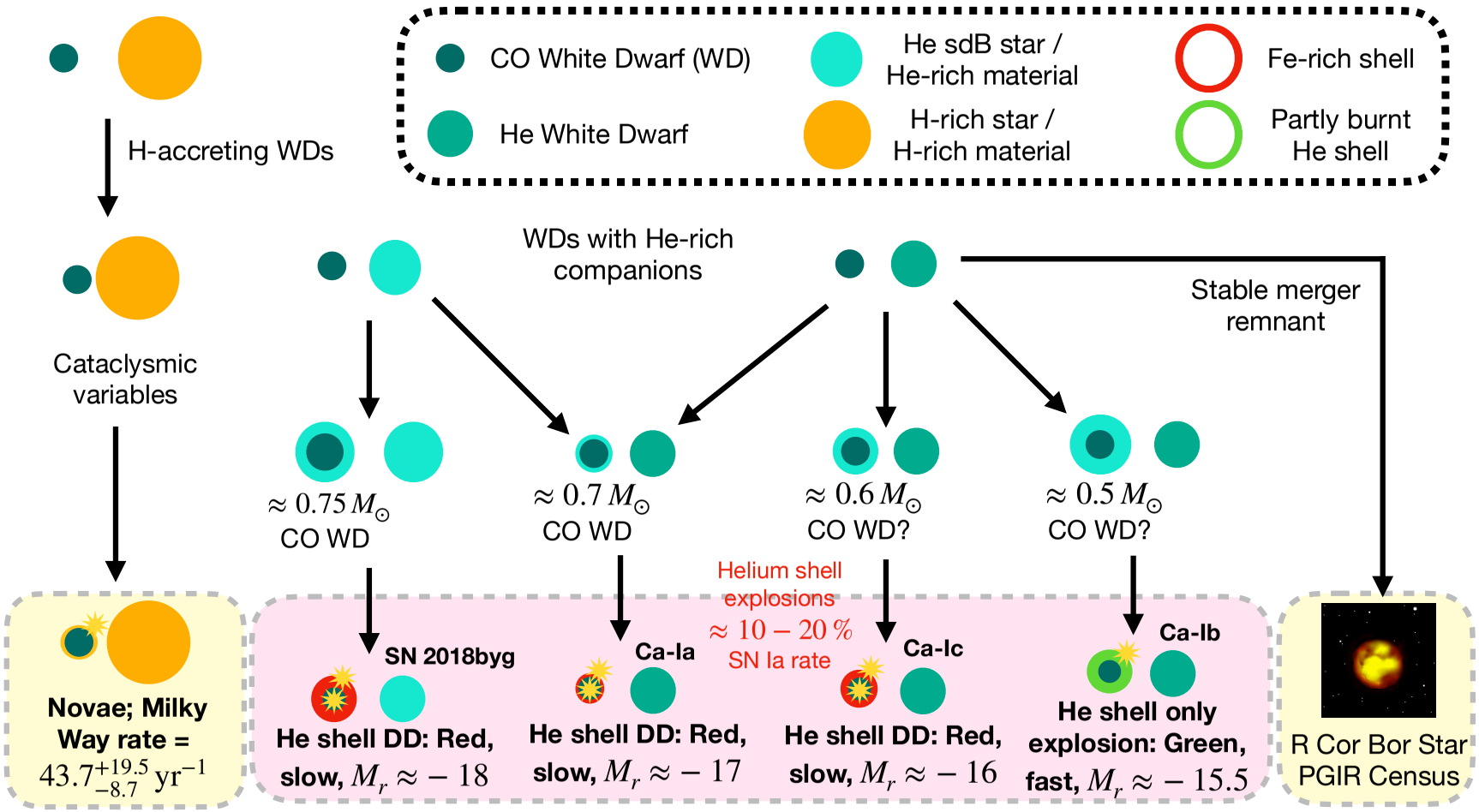

Figure 10.2: **Evolution of low mass binaries leading to a plethora of explosive phenomena from accreting WDs**. The top panel shows the symbols used for the different kinds of astrophysical systems. The phenomena shown inside the pink boxes have been studied as part of the ZTF CLU experiment presented in this thesis, while phenomena shown in yellow boxes show new results from PGIR that are either directly presented in this thesis (bold) or enabled by the PGIR survey.

in this largely uncharted territory. Coordinated observing campaigns with high energy X-ray/γ-ray instruments (which by design are generally wide-field, similar to PGIR) could systematically detect IR counterparts of the fastest timescale high energy phenomena like magnetar flares (Kaspi et al., 2017) and Supergiant Fast X-ray Transients (Romano, 2015). With the substantially larger dynamic range of the short exposure mode, nightly patrols of the Galactic plane with PGIR will prepare for the unprecedented science possible with the next Galactic supernova, that is likely to be heavily obscured by dust (Adams et al., 2013).

While the high cost of conventional HgCdTe detectors has long limited the construction of large format IR cameras for surveys, alternative detector technologies based on InGaAs that can achieve background limited imaging even with higher dark current (Simcoe et al., 2019) are now driving the IR time domain revolution. The Wide-field Infrared Transient Explorer (WINTER; Lourie et al., 2020) survey at Palomar Observatory and the Dynamic Red All-sky Monitoring Survey (DREAMS; Soon et al., 2020) at Siding Springs Observatory will be the first IR imaging surveys to employ these detectors. Finally, the next decade will see the launch of the Nancy Grace Roman Space Telescope[2] operating in the near-infrared, that will conduct an unprecedented high cadence, microlensing survey of the Galactic bulge. In preparation, the Prime Focus Infrared Microlensing Experiment (PRIME) is scheduled to begin operations at the South African Astronomical Observatory in 2021. Together, these surveys will be capable of surveying the entire Galaxy in the IR every night.

While substantial progress has been made concerning the explosive lives of WDs and NSs, stellar mass BHs still remain elusive – not only in terms of their formation in stellar deaths, but even their demographics in our Galactic backyard. Indeed, one of the primary obstacles is that BHs are by definition, dark objects, and hence the presence of a companion in a compact orbit is almost a necessity to discover BHs via their gravitational influence. There are only $\approx$ 20 confirmed BHs in the Galaxy, with all but one discovered via luminous X-ray accretion outburst from a low mass companion (Corral-Santana et al., 2016). To this end, the revolutionary depth of the ongoing eROSITA X-ray survey (Predehl et al., 2021) and the VLA Sky Survey (Lacy et al., 2020) hold great potential for finding and characterizing accreting compact objects in the Milky Way. Independently, IR surveys can lead the way in expanding the population of known BHs in the Milky Way by i) discovering the IR transient counterparts of accretion outbursts independent of the shallow sensitivity

[2] https://roman.gsfc.nasa.gov/

of all-sky X-ray monitors (e.g. Yao et al., 2020a), ii) characterizing the IR variability in a large sample of Galactic plane X-ray/radio sources (e.g. Maccarone et al., 2019) and iii) searching for isolated BHs in microlensing events in the Galactic plane (e.g. Wyrzykowski et al., 2016).

Combining the demographics of explosive transients in the local universe with a multi-wavelength census of compact objects in the Milky Way, the holy grail of a complete road-map of the local stellar graveyard is on the horizon.

BIBLIOGRAPHY

Abadi, M. et al. (2016). "TensorFlow: Large-Scale Machine Learning on Heterogeneous Distributed Systems". In: *arXiv e-prints*, arXiv:1603.04467, arXiv:1603.04467. arXiv: 1603.04467 [cs.DC].

Abbott, B. P. et al. (2017a). "GW170817: Observation of Gravitational Waves from a Binary Neutron Star Inspiral". In: *Physical Review Letters* 119.16, 161101, p. 161101. DOI: 10.1103/PhysRevLett.119.161101. arXiv: 1710.05832 [gr-qc].

Abbott, B. P. et al. (2017b). "Multi-messenger Observations of a Binary Neutron Star Merger". In: *ApJL* 848, L12, p. L12. DOI: 10.3847/2041-8213/aa91c9. arXiv: 1710.05833 [astro-ph.HE].

Abolfathi, B. et al. (2017). "The Fourteenth Data Release of the Sloan Digital Sky Survey: First Spectroscopic Data from the extended Baryon Oscillation Spectroscopic Survey and from the second phase of the Apache Point Observatory Galactic Evolution Experiment". In: *ArXiv e-prints*. arXiv: 1707.09322.

Abraham, R. G. et al. (2014). "Ultra-Low Surface Brightness Imaging with the Dragonfly Telephoto Array". In: *PASP* 126.935, p. 55. DOI: 10.1086/674875. arXiv: 1401.5473 [astro-ph.IM].

Adams, S. M. et al. (2013). "Observing the Next Galactic Supernova". In: *ApJ* 778.2, 164, p. 164. DOI: 10.1088/0004-637X/778/2/164. arXiv: 1306.0559 [astro-ph.HE].

Allen, C. W. (1954). "Whole-sky statistics of celestial objects". In: *MNRAS* 114, p. 387. DOI: 10.1093/mnras/114.4.387.

Almgren, A. S. et al. (2010). "CASTRO: A New Compressible Astrophysical Solver. I. Hydrodynamics and Self-gravity". In: *ApJ* 715, pp. 1221–1238. DOI: 10.1088/0004-637X/715/2/1221. arXiv: 1005.0114 [astro-ph.IM].

Amaro-Seoane, P. et al. (2012). "Low-frequency gravitational-wave science with eLISA/NGO". In: *Classical and Quantum Gravity* 29.12, 124016, p. 124016. DOI: 10.1088/0264-9381/29/12/124016. arXiv: 1202.0839 [gr-qc].

Anderson, G. E. et al. (2017). "The peculiar mass-loss history of SN 2014C as revealed through AMI radio observations". In: *MNRAS* 466, pp. 3648–3662. DOI: 10.1093/mnras/stw3310. arXiv: 1612.06059 [astro-ph.HE].

Anderson, J. P. et al. (2012). "Progenitor mass constraints for core-collapse supernovae from correlations with host galaxy star formation". In: *MNRAS* 424, pp. 1372–1391. DOI: 10.1111/j.1365-2966.2012.21324.x. arXiv: 1205.3802.

Andreoni, I. et al. (2020). "Zwicky Transient Facility constraints on the optical emission from the nearby repeating FRB 180916.J0158+65". In: *arXiv e-prints*, arXiv:2005.06273, arXiv:2005.06273. arXiv: 2005.06273 [astro-ph.HE].

Arcavi, I. et al. (2010). "Core-collapse Supernovae from the Palomar Transient Factory: Indications for a Different Population in Dwarf Galaxies". In: *ApJ* 721, pp. 777–784. DOI: 10.1088/0004-637X/721/1/777. arXiv: 1004.0615.

Arcavi, I. et al. (2011). "SN 2011dh: Discovery of a Type IIb Supernova from a Compact Progenitor in the Nearby Galaxy M51". In: *ApJL* 742, L18, p. L18. DOI: 10.1088/2041-8205/742/2/L18. arXiv: 1106.3551.

Arcavi, I. et al. (2017). "Constraints on the Progenitor of SN 2016gkg from Its Shock-cooling Light Curve". In: *ApJL* 837, L2, p. L2. DOI: 10.3847/2041-8213/aa5be1. arXiv: 1611.06451 [astro-ph.HE].

Arnett, W. D. (1982). "Type I supernovae. I - Analytic solutions for the early part of the light curve". In: *ApJ* 253, pp. 785–797. DOI: 10.1086/159681.

Arnett, W. D. et al. (1985). "Hubble's constant and exploding carbon-oxygen white dwarf models for Type I supernovae". In: *Nature* 314, p. 337. DOI: 10.1038/314337a0.

Asplund, M. et al. (2009). "The Chemical Composition of the Sun". In: *ARAA* 47, pp. 481–522. DOI: 10.1146/annurev.astro.46.060407.145222. arXiv: 0909.0948 [astro-ph.SR].

Aydi, E. et al. (2019a). "SOAR spectroscopic classification of PNV J06095740+1212255 as a very fast classical nova". In: *The Astronomer's Telegram* 13027, p. 1.

Aydi, E. et al. (2019b). "Spectroscopic classification of Gaia19dum as a highly reddened classical nova". In: *The Astronomer's Telegram* 13068, p. 1.

Aydi, E. et al. (2020a). "Classification of TCP J18104219-1534184 as a classical nova". In: *The Astronomer's Telegram* 13517, p. 1.

Aydi, E. et al. (2020b). "SALT spectroscopic classification of PNV J17545999-2122401 as a classical nova". In: *The Astronomer's Telegram* 14064, p. 1.

Babul, A. et al. (2020). "Strong J-band variability but no radio or X-ray emission from Nova PGIR20eig". In: *The Astronomer's Telegram* 14165, p. 1.

Bailer-Jones, C. A. L. et al. (2020). "Estimating distances from parallaxes. V: Geometric and photogeometric distances to 1.47 billion stars in Gaia Early Data Release 3". In: *arXiv e-prints*, arXiv:2012.05220, arXiv:2012.05220. arXiv: 2012.05220 [astro-ph.SR].

Banerjee, D. P. K. et al. (2012). "Near-infrared properties of classical novae: A perspective gained from Mount Abu Infrared Observatory". In: *Bulletin of the Astronomical Society of India* 40, p. 243. arXiv: 1306.0343 [astro-ph.SR].

Barbary, K. et al. (2016). *SNCosmo: Python library for supernova cosmology*. ascl: 1611.017.

Bauer, E. B. et al. (2017). "Electron Captures on ^{14}N as a Trigger for Helium Shell Detonations". In: *ApJ* 845, 97, p. 97. DOI: 10.3847/1538-4357/aa7ffa. arXiv: 1707.05394 [astro-ph.SR].

Becker, A. (2015). *HOTPANTS: High Order Transform of PSF ANd Template Subtraction*. ascl: 1504.004.

Bell, E. F. et al. (2003). "The Optical and Near-Infrared Properties of Galaxies. I. Luminosity and Stellar Mass Functions". In: *ApJS* 149.2, pp. 289–312. DOI: 10.1086/378847. arXiv: astro-ph/0302543 [astro-ph].

Bellm, E. C. et al. (2019a). "The Zwicky Transient Facility: Surveys and Scheduler". In: *PASP* 131.6, p. 068003. DOI: 10.1088/1538-3873/ab0c2a. arXiv: 1905.02209 [astro-ph.IM].

Bellm, E. C. (2016). "Volumetric Survey Speed: A Figure of Merit for Transient Surveys". In: *PASP* 128.966, p. 084501. DOI: 10.1088/1538-3873/128/966/084501. arXiv: 1605.02081 [astro-ph.IM].

Bellm, E. C. et al. (2016). *pyraf-dbsp: Reduction pipeline for the Palomar Double Beam Spectrograph*. DOI: 10.1088/1538-3873/128/966/084501. ascl: 1602.002 (astro-ph.IM).

Bellm, E. C. et al. (2019b). "The Zwicky Transient Facility: System Overview, Performance, and First Results". In: *PASP* 131.995, p. 018002. DOI: 10.1088/1538-3873/aaecbe. arXiv: 1902.01932 [astro-ph.IM].

Bellm, E. et al. (2017). "The unblinking eye on the sky". In: *Nature Astronomy* 1, 0071, p. 0071. DOI: 10.1038/s41550-017-0071. arXiv: 1705.10052 [astro-ph.IM].

Beloborodov, A. M. (2019). "Blast Waves from Magnetar Flares and Fast Radio Bursts". In: *arXiv e-prints*, arXiv:1908.07743, arXiv:1908.07743. arXiv: 1908.07743 [astro-ph.HE].

Ben-Ami, S. et al. (2015). "Ultraviolet Spectroscopy of Type IIb Supernovae: Diversity and the Impact of Circumstellar Material". In: *ApJ* 803, 40, p. 40. DOI: 10.1088/0004-637X/803/1/40. arXiv: 1412.4767 [astro-ph.HE].

Beniamini, P. et al. (2016). "Formation of double neutron star systems as implied by observations". In: *MNRAS* 456, pp. 4089–4099. DOI: 10.1093/mnras/stv2903. arXiv: 1510.03111 [astro-ph.HE].

Benn, C. et al. (2008). "ACAM: a new imager/spectrograph for the William Herschel Telescope". In: *Ground-based and Airborne Instrumentation for Astronomy II*. Vol. 7014. Proceedings of SPIE, p. 70146X. DOI: 10.1117/12.788694.

Benvenuto, O. G. et al. (2017). "Close Binary Stellar Evolution and Supernovae". In: *Handbook of Supernovae*. Cham: Springer International Publishing, pp. 1–22. ISBN: 978-3-319-20794-0. DOI: 10.1007/978-3-319-20794-0_124-1. URL: https://doi.org/10.1007/978-3-319-20794-0_124-1.

Berger, E. et al. (2002). "The Radio Evolution of the Ordinary Type Ic Supernova SN 2002ap". In: *ApJL* 577, pp. L5–L8. DOI: 10.1086/344045. eprint: astro-ph/0206183.

Bersten, M. C. et al. (2013). "Early Ultraviolet/Optical Emission of The Type Ib SN 2008D". In: *ApJ* 767, 143, p. 143. DOI: 10.1088/0004-637X/767/2/143. arXiv: 1303.0638 [astro-ph.SR].

Bertin, E. (2006). "Automatic Astrometric and Photometric Calibration with SCAMP". In: *Astronomical Data Analysis Software and Systems XV*. Ed. by C. Gabriel et al. Vol. 351. Astronomical Society of the Pacific Conference Series, p. 112.

Bertin, E. (2011). "Automated Morphometry with SExtractor and PSFEx". In: *Astronomical Data Analysis Software and Systems XX*. Ed. by I. N. Evans et al. Vol. 442. Astronomical Society of the Pacific Conference Series, p. 435.

Bertin, E. et al. (2002). "The TERAPIX Pipeline". In: *Astronomical Data Analysis Software and Systems XI*. Ed. by D. A. Bohlender et al. Vol. 281. Astronomical Society of the Pacific Conference Series, p. 228.

Bertin, E. et al. (1996). "SExtractor: Software for source extraction." In: *A&AS* 117, pp. 393–404. DOI: 10.1051/aas:1996164.

Bhattacharya, D. et al. (1991). "Formation and evolution of binary and millisecond radio pulsars". In: *Physics Reports* 203, pp. 1–124. DOI: 10.1016/0370-1573(91)90064-S.

Bianchi, L. et al. (2014). "VizieR Online Data Catalog: GALEX-GR6/7 data release (Bianchi+ 2014)". In: *VizieR Online Data Catalog* 2335.

Bianco, F. B. et al. (2014). "Multi-color Optical and Near-infrared Light Curves of 64 Stripped-envelope Core-Collapse Supernovae". In: *ApJS* 213, 19, p. 19. DOI: 10.1088/0067-0049/213/2/19. arXiv: 1405.1428 [astro-ph.SR].

Bianco, F. B. et al. (2016). "Monte Carlo method for calculating oxygen abundances and their uncertainties from strong-line flux measurements". In: *Astronomy and Computing* 16, pp. 54–66. DOI: 10.1016/j.ascom.2016.03.002. arXiv: 1505.06213 [astro-ph.IM].

Bida, T. A. et al. (2014). "First-generation instrumentation for the Discovery Channel Telescope". In: *Ground-based and Airborne Instrumentation for Astronomy V*. Vol. 9147. Proc. SPIE, 91472N. DOI: 10.1117/12.2056872.

Bildsten, L. et al. (2007). "Faint Thermonuclear Supernovae from AM Canum Venaticorum Binaries". In: *ApJL* 662, pp. L95–L98. DOI: 10.1086/519489. eprint: astro-ph/0703578.

Bissantz, N. et al. (2002). "Spiral arms, bar shape and bulge microlensing in the Milky Way". In: *MNRAS* 330.3, pp. 591–608. DOI: 10.1046/j.1365-8711.2002.05116.x. arXiv: astro-ph/0110368 [astro-ph].

Blagorodnova, N. et al. (2018). "The SED Machine: A Robotic Spectrograph for Fast Transient Classification". In: *PASP* 130.3, p. 035003. DOI: 10.1088/1538-3873/aaa53f. arXiv: 1710.02917 [astro-ph.IM].

Blank, R. et al. (2011). "The HxRG Family of High Performance Image Sensors for Astronomy". In: *Solar Polarization 6*. Ed. by J. R. Kuhn et al. Vol. 437. Astronomical Society of the Pacific Conference Series, p. 383.

Blondin, S. et al. (2007). "Determining the Type, Redshift, and Age of a Supernova Spectrum". In: *ApJ* 666.2, pp. 1024–1047. DOI: 10.1086/520494. arXiv: 0709.4488 [astro-ph].

Bloom, J. S. et al. (2002). "The Observed Offset Distribution of Gamma-Ray Bursts from Their Host Galaxies: A Robust Clue to the Nature of the Progenitors". In: *AJ* 123.3, pp. 1111–1148. DOI: 10.1086/338893. arXiv: astro-ph/0010176 [astro-ph].

Bobrick, A. et al. (2017). "Mass transfer in white dwarf-neutron star binaries". In: *MNRAS* 467.3, pp. 3556–3575. DOI: 10.1093/mnras/stx312. arXiv: 1702.02377 [astro-ph.HE].

Bochenek, C. D. et al. (2020). "A fast radio burst associated with a Galactic magnetar". In: *arXiv e-prints*, arXiv:2005.10828, arXiv:2005.10828. arXiv: 2005.10828 [astro-ph.HE].

Bode, M. F. et al. (2008). *Classical Novae*. Vol. 43.

Boquien, M. et al. (2009). "Collisional Debris as Laboratories to Study Star Formation". In: *AJ* 137, pp. 4561–4576. DOI: 10.1088/0004-6256/137/6/4561. arXiv: 0903.3403 [astro-ph.CO].

Borghese, A. et al. (2020). "The X-ray reactivation of the radio bursting magnetar SGR 1935+2154". In: *arXiv e-prints*, arXiv:2006.00215, arXiv:2006.00215. arXiv: 2006.00215 [astro-ph.HE].

Borthakur, S. et al. (2020). ""'Reverse hybrid" behavior of Nova Per 2020 = TCP J04291888+4354233". In: *The Astronomer's Telegram* 14230, p. 1.

Boyer, M. L. et al. (2015). "An Infrared Census of Dust in nearby Galaxies with Spitzer (DUSTiNGS). I. Overview". In: *ApJS* 216.1, 10, p. 10. DOI: 10.1088/0067-0049/216/1/10. arXiv: 1411.4053 [astro-ph.GA].

Brooks, J. et al. (2015). "AM Canum Venaticorum Progenitors with Helium Star Donors and the Resultant Explosions". In: *ApJ* 807, 74, p. 74. DOI: 10.1088/0004-637X/807/1/74. arXiv: 1505.05918 [astro-ph.SR].

Brown, P. J. et al. (2009). "Ultraviolet Light Curves of Supernovae with the Swift Ultraviolet/Optical Telescope". In: *AJ* 137, pp. 4517–4525. DOI: 10.1088/0004-6256/137/5/4517. arXiv: 0803.1265.

Brown, T. M. et al. (2013). "Las Cumbres Observatory Global Telescope Network". In: *PASP* 125, p. 1031. DOI: 10.1086/673168. arXiv: 1305.2437 [astro-ph.IM].

Brown, W. R. et al. (2016). "Most Double Degenerate Low-mass White Dwarf Binaries Merge". In: *ApJ* 824.1, 46, p. 46. DOI: 10.3847/0004-637X/824/1/46. arXiv: 1604.04269 [astro-ph.SR].

Bruzual, G. et al. (2003). "Stellar population synthesis at the resolution of 2003". In: *MNRAS* 344, pp. 1000–1028. DOI: 10.1046/j.1365-8711.2003.06897.x. eprint: astro-ph/0309134.

Burdge, K. B. et al. (2020). "A Systematic Search of Zwicky Transient Facility Data for Ultracompact Binary LISA-detectable Gravitational-wave Sources". In: *ApJ* 905.1, 32, p. 32. DOI: 10.3847/1538-4357/abc261. arXiv: 2009.02567 [astro-ph.SR].

Burke, J. et al. (2019). "Global SN Project Transient Classification Report for 2019-01-24". In: *Transient Name Server Classification Report* 2019-1232, p. 1.

Burrows, D. N. et al. (2005). "The Swift X-Ray Telescope". In: *Space Science Reviews* 120, pp. 165–195. DOI: 10.1007/s11214-005-5097-2. eprint: astro-ph/0508071.

Cano, Z. (2013). "A new method for estimating the bolometric properties of Ibc supernovae". In: *MNRAS* 434, pp. 1098–1116. DOI: 10.1093/mnras/stt1048. arXiv: 1306.1488 [astro-ph.SR].

Cao, Y. et al. (2012). "Classical Novae in Andromeda: Light Curves from the Palomar Transient Factory and GALEX". In: *ApJ* 752.2, 133, p. 133. DOI: 10.1088/0004-637X/752/2/133. arXiv: 1201.2393 [astro-ph.SR].

Cao, Y. et al. (2013). "Discovery, Progenitor and Early Evolution of a Stripped Envelope Supernova iPTF13bvn". In: *ApJL* 775, L7, p. L7. DOI: 10.1088/2041-8205/775/1/L7. arXiv: 1307.1470 [astro-ph.SR].

Cao, Y. et al. (2015a). "A strong ultraviolet pulse from a newborn type Ia supernova". In: *Nature* 521, pp. 328–331. DOI: 10.1038/nature14440. arXiv: 1505.05158 [astro-ph.SR].

Cao, Y. et al. (2015b). "iPTF independent discovery and classification of PSN J10520833+3256394". In: *The Astronomer's Telegram* 8428, p. 1.

Cao, Y. et al. (2016). "Intermediate Palomar Transient Factory: Realtime Image Subtraction Pipeline". In: *PASP* 128.11, p. 114502. DOI: 10.1088/1538-3873/128/969/114502. arXiv: 1608.01006 [astro-ph.IM].

Capaccioli, M. et al. (1989). "Properties of the Nova Population of M31". In: *AJ* 97, p. 1622. DOI: 10.1086/115104.

Cardelli, J. A. et al. (1989). "The relationship between infrared, optical, and ultraviolet extinction". In: *ApJ* 345, pp. 245–256. DOI: 10.1086/167900.

Carter, P. J. et al. (2013). "A search for the hidden population of AM CVn binaries in the Sloan Digital Sky Survey". In: *MNRAS* 429.3, pp. 2143–2160. DOI: 10.1093/mnras/sts485. arXiv: 1211.6439 [astro-ph.SR].

Castro-Tirado, A. J. et al. (2008). "Flares from a candidate Galactic magnetar suggest a missing link to dim isolated neutron stars". In: *Nature* 455.7212, pp. 506–509. DOI: 10.1038/nature07328. arXiv: 0809.4231 [astro-ph].

Catelan, M. et al. (2011). "The Vista Variables in the Via Lactea (VVV) ESO Public Survey: Current Status and First Results". In: *RR Lyrae Stars, Metal-Poor Stars, and the Galaxy*. Ed. by A. McWilliam. Vol. 5, p. 145. arXiv: 1105.1119 [astro-ph.GA].

Cautun, M. et al. (2020). "The milky way total mass profile as inferred from Gaia DR2". In: *MNRAS* 494.3, pp. 4291–4313. DOI: 10.1093/mnras/staa1017. arXiv: 1911.04557 [astro-ph.GA].

Cenko, S. B. et al. (2006). "The Automated Palomar 60 Inch Telescope". In: *PASP* 118, pp. 1396–1406. DOI: 10.1086/508366. eprint: astro-ph/0608323.

Chambers, K. C. et al. (2016). "The Pan-STARRS1 Surveys". In: *arXiv e-prints*, arXiv:1612.05560, arXiv:1612.05560. arXiv: 1612.05560 [astro-ph.IM].

Chambers, K. C. et al. (2018). "Pan-STARRS1 Transient Discovery Report for 2018-12-22". In: *Transient Name Server Discovery Report* 2018-2068, p. 1.

Chen, P. et al. (2020). "The Most Rapidly Declining Type I Supernova 2019bkc/ATLAS19dqr". In: *ApJL* 889.1, L6, p. L6. DOI: 10.3847/2041-8213/ab62a4. arXiv: 1905.02205 [astro-ph.HE].

Chevalier, R. A. (1982). "Self-similar solutions for the interaction of stellar ejecta with an external medium". In: *ApJ* 258, pp. 790–797. DOI: 10.1086/160126.

Chevalier, R. A. (1998). "Synchrotron Self-Absorption in Radio Supernovae". In: *ApJ* 499, pp. 810–819. DOI: 10.1086/305676.

Childress, M. et al. (2014). *PyWiFeS: Wide Field Spectrograph data reduction pipeline*. ascl: 1402.034.

Chomiuk, L. et al. (2020). "New Insights into Classical Novae". In: *arXiv e-prints*, arXiv:2011.08751, arXiv:2011.08751. arXiv: 2011.08751 [astro-ph.HE].

Chomiuk, L. et al. (2016). "A Deep Search for Prompt Radio Emission from Thermonuclear Supernovae with the Very Large Array". In: *ApJ* 821, 119, p. 119. DOI: 10.3847/0004-637X/821/2/119. arXiv: 1510.07662 [astro-ph.HE].

Ciardullo, R. et al. (1987). "The Spatial Distribution and Population of Novae in M31". In: *ApJ* 318, p. 520. DOI: 10.1086/165388.

Ciardullo, R. et al. (1990). "The Nova Rate in the Elliptical Component of NGC 5128". In: *AJ* 99, p. 1079. DOI: 10.1086/115397.

Cid Fernandes, R. et al. (2005). "Semi-empirical analysis of Sloan Digital Sky Survey galaxies - I. Spectral synthesis method". In: *MNRAS* 358, pp. 363–378. DOI: 10.1111/j.1365-2966.2005.08752.x. eprint: astro-ph/0412481.

Clayton, G. C. (1996). "The R Coronae Borealis Stars". In: *PASP* 108, p. 225. DOI: 10.1086/133715.

Contreras Pena, C. et al. (2017a). "A population of eruptive variable protostars in VVV". In: *MNRAS* 465.3, pp. 3011–3038. DOI: 10.1093/mnras/stw2801. arXiv: 1602.06267 [astro-ph.SR].

Contreras Pena, C. et al. (2017b). "Infrared spectroscopy of eruptive variable protostars from VVV". In: *MNRAS* 465.3, pp. 3039–3100. DOI: 10.1093/mnras/stw2802. arXiv: 1602.06269 [astro-ph.SR].

Contreras, C. et al. (2010). "The Carnegie Supernova Project: First Photometry Data Release of Low-Redshift Type Ia Supernovae". In: *AJ* 139, pp. 519–539. DOI: 10.1088/0004-6256/139/2/519. arXiv: 0910.3330.

Cook, D. O. et al. (2019). "Census of the Local Universe (CLU) Narrowband Survey. I. Galaxy Catalogs from Preliminary Fields". In: *ApJ* 880.1, 7, p. 7. DOI: 10.3847/1538-4357/ab2131. arXiv: 1710.05016 [astro-ph.GA].

Cordes, J. M. et al. (2016). "Supergiant pulses from extragalactic neutron stars". In: *MNRAS* 457.1, pp. 232–257. DOI: 10.1093/mnras/stv2948. arXiv: 1501.00753 [astro-ph.HE].

Cordes, J. M. et al. (2019). "Fast Radio Bursts: An Extragalactic Enigma". In: *ARA&A* 57, pp. 417–465. DOI: 10.1146/annurev-astro-091918-104501. arXiv: 1906.05878 [astro-ph.HE].

Corral-Santana, J. M. et al. (2016). "BlackCAT: A catalogue of stellar-mass black holes in X-ray transients". In: *A&A* 587, A61, A61. DOI: 10.1051/0004-6361/201527130. arXiv: 1510.08869 [astro-ph.HE].

Corsi, A. et al. (2016). "Radio Observations of a Sample of Broad-line Type IC Supernovae Discovered by PTF/IPTF: A Search for Relativistic Explosions". In: *ApJ* 830, 42, p. 42. DOI: 10.3847/0004-637X/830/1/42. arXiv: 1512.01303 [astro-ph.HE].

Coughlin, M. W. et al. (2019a). "2900 Square Degree Search for the Optical Counterpart of Short Gamma-Ray Burst GRB 180523B with the Zwicky Transient Facility". In: *PASP* 131.4, p. 048001. DOI: 10.1088/1538-3873/aaff99. arXiv: 1901.11385 [astro-ph.HE].

Coughlin, M. W. et al. (2019b). "GROWTH on GW190425: Searching thousands of square degrees to identify an optical or infrared counterpart to a binary neutron star merger with the Zwicky Transient Facility and Palomar Gattini IR". In: *arXiv e-prints*, arXiv:1907.12645, arXiv:1907.12645. arXiv: 1907.12645 [astro-ph.HE].

Cox, A. N. (2000). *Allen's astrophysical quantities*.

Cresci, G. et al. (2007). "A NICMOS search for obscured supernovae in starburst galaxies". In: *A&A* 462, pp. 927–931. DOI: 10.1051/0004-6361:20065364. eprint: astro-ph/0610783.

Crowther, P. A. (2007). "Physical Properties of Wolf-Rayet Stars". In: *ARAA* 45, pp. 177–219. DOI: 10.1146/annurev.astro.45.051806.110615. eprint: astro-ph/0610356.

Crowther, P. A. (2013). "On the association between core-collapse supernovae and H ii regions". In: *MNRAS* 428, pp. 1927–1943. DOI: 10.1093/mnras/sts145. arXiv: 1210.1126 [astro-ph.SR].

Crts, N. M. W. (2018). "SNHunt Transient Discovery Report for 2018-06-12". In: *Transient Name Server Discovery Report* 2018-804, p. 1.

Cushing, M. C. et al. (2004). "Spextool: A Spectral Extraction Package for SpeX, a 0.8-5.5 Micron Cross-Dispersed Spectrograph". In: *PASP* 116, pp. 362–376. DOI: 10.1086/382907.

Cutri, R. M. et al. (2003). *2MASS All Sky Catalog of point sources.*

Dálya, G. et al. (2018). "GLADE: A galaxy catalogue for multimessenger searches in the advanced gravitational-wave detector era". In: *MNRAS* 479.2, pp. 2374–2381. DOI: 10.1093/mnras/sty1703. arXiv: 1804.05709 [astro-ph.HE].

Darbha, S. et al. (2010). "Nickel-rich outflows produced by the accretion-induced collapse of white dwarfs: light curves and spectra". In: *MNRAS* 409, pp. 846–854. DOI: 10.1111/j.1365-2966.2010.17353.x. arXiv: 1005.1081 [astro-ph.HE].

Dark Energy Survey Collaboration et al. (2016). "The Dark Energy Survey: more than dark energy - an overview". In: *MNRAS* 460.2, pp. 1270–1299. DOI: 10.1093/mnras/stw641. arXiv: 1601.00329 [astro-ph.CO].

Darnley, M. J. et al. (2006). "Classical novae from the POINT-AGAPE microlensing survey of M31 - II. Rate and statistical characteristics of the nova population". In: *MNRAS* 369.1, pp. 257–271. DOI: 10.1111/j.1365-2966.2006.10297.x. arXiv: astro-ph/0509493 [astro-ph].

Darnley, M. J. et al. (2014). "A remarkable recurrent nova in M 31: The optical observations". In: *A&A* 563, L9, p. L9. DOI: 10.1051/0004-6361/201423411. arXiv: 1401.2905 [astro-ph.SR].

Darnley, M. J. et al. (2020). "On a century of extragalactic novae and the rise of the rapid recurrent novae". In: *Advances in Space Research* 66.5, pp. 1147–1168. DOI: 10.1016/j.asr.2019.09.044. arXiv: 1909.10497 [astro-ph.SR].

Davies, M. L. et al. (2009). "Follow-up observations at 16 and 33GHz of extragalactic sources from WMAP 3-yr data: I - Spectral properties". In: *MNRAS* 400, pp. 984–994. DOI: 10.1111/j.1365-2966.2009.15518.x. arXiv: 0907.3707.

Dawson, P. et al. (2014). "Near-infrared spectroscopy of young brown dwarfs in upper Scorpius". In: *MNRAS* 442.2, pp. 1586–1596. DOI: 10.1093/mnras/stu973. arXiv: 1405.3842 [astro-ph.SR].

De, K. (2019a). "ZTF Transient Discovery Report for 2019-10-28". In: *Transient Name Server Discovery Report* 2019-2208, p. 1.

De, K. (2019b). "ZTF Transient Discovery Report for 2019-11-07". In: *Transient Name Server Discovery Report* 2019-2307, p. 1.

De, K. et al. (2018a). "iPTF 16hgs: A Double-peaked Ca-rich Gap Transient in a Metal-poor, Star-forming Dwarf Galaxy". In: *ApJ* 866.1, 72, p. 72. DOI: 10.3847/1538-4357/aadf8e. arXiv: 1806.10623 [astro-ph.HE].

De, K. et al. (2019a). "ZTF 18aaqeasu (SN2018byg): A Massive Helium-shell Double Detonation on a Sub-Chandrasekhar-mass White Dwarf". In: *ApJL* 873.2, L18, p. L18. DOI: 10.3847/2041-8213/ab0aec. arXiv: 1901.00874 [astro-ph.HE].

De, K. et al. (2020a). "Constraining the X-Ray-Infrared Spectral Index of Second-timescale Flares from SGR 1935+2154 with Palomar Gattini-IR". In: *ApJL* 901.1, L7, p. L7. DOI: 10.3847/2041-8213/abb3c5. arXiv: 2007.02978 [astro-ph.HE].

De, K. et al. (2020b). "Palomar Gattini-IR: Survey Overview, Data Processing System, On-sky Performance and First Results". In: *PASP* 132.1008, 025001, p. 025001. DOI: 10.1088/1538-3873/ab6069. arXiv: 1910.13319 [astro-ph.IM].

De, K. et al. (2020c). "The Zwicky Transient Facility Census of the Local Universe. I. Systematic Search for Calcium-rich Gap Transients Reveals Three Related Spectroscopic Subclasses". In: *ApJ* 905.1, 58, p. 58. DOI: 10.3847/1538-4357/abb45c.

De, K. et al. (2018b). "A Hot and Fast Ultra-stripped Supernova that Likely Formed a Compact Neutron Star Binary". In: *Science* 362.6411, pp. 201–206. DOI: 10.1126/science.aas8693. arXiv: 1810.05181 [astro-ph.HE].

De, K. et al. (2019b). "Bright NIR detections of the reddened classical nova Gaia19dum / AT2019owg from Palomar Gattini-IR". In: *The Astronomer's Telegram* 13074, p. 1.

De, K. et al. (2019c). "Detection of a new large NIR flare of the gamma ray blazar CTA 102 with Palomar Gattini-IR". In: *The Astronomer's Telegram* 13051.

De, K. et al. (2019d). "Large amplitude near-infrared flaring of B2 1420+32 detected with Palomar Gattini-IR". In: *The Astronomer's Telegram* 12941, p. 1.

De, K. et al. (2019e). "Palomar Gattini-IR NIR detection of a reddened Galactic binary microlensing event PGIR 19btb / AT 2019odt / Gaia 19dqj". In: *The Astronomer's Telegram* 13186, p. 1.

De, K. et al. (2019f). "Palomar Gattini-IR NIR discovery and classification of a highly reddened galactic classical nova PGIR19brv / AT2019qwf". In: *The Astronomer's Telegram* 13130, p. 1.

De, K. et al. (2019g). "Public reports of transients from the Zwicky Transient Facility volume limited experiment". In: *The Astronomer's Telegram* 13262, p. 1.

De, K. et al. (2020d). "Palomar Gattini-IR archival discovery of the bright NIR transient PGIR20ekz/AT2019aafo: Spectroscopic confirmation of a highly reddened Galactic nova missed in 2019". In: *The Astronomer's Telegram* 14014, p. 1.

De, K. et al. (2020e). "Palomar Gattini-IR discovery and classification of the bright NIR transient PGIR20eig/AT2020qpq as a highly reddened Galactic nova". In: *The Astronomer's Telegram* 13914, p. 1.

De, K. et al. (2020f). "Palomar Gattini-IR early detection of the young and bright Galactic nova candidate AT2020urz / BraTS-SON-T2-020 / PGIR20evr". In: *The Astronomer's Telegram* 14062, p. 1.

De, K. et al. (2020g). "Palomar Gattini-IR NIR detection and classification of a highly reddened Galactic classical nova PGIR20duo / AT2020kvq / MASTER OTJ184353.33+000350.9". In: *The Astronomer's Telegram* 13817, p. 1.

De, K. et al. (2020h). "Palomar Gattini-IR NIR discovery and classification of a highly reddened Galactic classical nova PGIR20dsv / AT2020lrv". In: *The Astronomer's Telegram* 13790, p. 1.

De, K. et al. (2020i). "Palomar Gattini-IR NIR discovery of a candidate young supernova PGIR20eid / AT2020qmp in UGC07125 at 12 Mpc". In: *Transient Name Server AstroNote* 147, p. 1.

Dekany, R. et al. (2016). "The Zwicky Transient Facility Camera". In: *Ground-based and Airborne Instrumentation for Astronomy VI*. Vol. 9908. Proc. SPIE, p. 99085M. DOI: 10.1117/12.2234558.

Della Valle, M. (1992). "Nova Rate in M33 and in the Galaxy". In: *Cataclysmic Variable Stars*. Ed. by N. Vogt. Vol. 29. Astronomical Society of the Pacific Conference Series, p. 292.

Della Valle, M. et al. (1998). "The Spectroscopic Differences between Disk and Thick-Disk/Bulge Novae". In: *ApJ* 506.2, pp. 818–823. DOI: 10.1086/306275.

Della Valle, M. et al. (2020). "Observations of galactic and extragalactic novae". In: *A&A Rev.* 28.1, 3, p. 3. DOI: 10.1007/s00159-020-0124-6. arXiv: 2004.06540 [astro-ph.SR].

della Valle, M. et al. (1994a). "The nova rate in galaxies of different Hubble types." In: *A&A* 287, pp. 403–409.

della Valle, M. et al. (1992). "On the possible existence of two classes of progenitors for classical novae." In: *A&A* 266, pp. 232–236.

della Valle, M. et al. (1994b). "On the nova rate in the Galaxy". In: *A&A* 286, pp. 786–788.

DESI Collaboration et al. (2016). "The DESI Experiment Part I: Science,Targeting, and Survey Design". In: *arXiv e-prints*, arXiv:1611.00036, arXiv:1611.00036. arXiv: 1611.00036 [astro-ph.IM].

Dessart, L. et al. (2020). "Radiative-transfer modeling of nebular-phase type II supernovae. Dependencies on progenitor and explosion properties". In: *arXiv e-prints*, arXiv:2007.02243, arXiv:2007.02243. arXiv: 2007.02243 [astro-ph.SR].

Dessart, L. et al. (2011). "Core-collapse explosions of Wolf-Rayet stars and the connection to Type IIb/Ib/Ic supernovae". In: *MNRAS* 414, pp. 2985–3005. DOI: 10.1111/j.1365-2966.2011.18598.x. arXiv: 1102.5160 [astro-ph.SR].

Dessart, L. et al. (2012). "On the nature of supernovae Ib and Ic". In: *MNRAS* 424, pp. 2139–2159. DOI: 10.1111/j.1365-2966.2012.21374.x. arXiv: 1205.5349 [astro-ph.SR].

Dessart, L. et al. (2014). "Constraints on the explosion mechanism and progenitors of Type Ia supernovae". In: *MNRAS* 441, pp. 532–550. DOI: 10.1093/mnras/stu598. arXiv: 1310.7747 [astro-ph.SR].

Dessart, L. et al. (2015a). "One-dimensional non-LTE time-dependent radiative transfer of an He-detonation model and the connection to faint and fast-decaying supernovae". In: *MNRAS* 447, pp. 1370–1382. DOI: 10.1093/mnras/stu2520. arXiv: 1411.7397 [astro-ph.SR].

Dessart, L. et al. (2015b). "Radiative-transfer models for supernovae IIb/Ib/Ic from binary-star progenitors". In: *MNRAS* 453, pp. 2189–2213. DOI: 10.1093/mnras/stv1747. arXiv: 1507.07783 [astro-ph.SR].

Dessart, L. et al. (2016). "Inferring supernova IIb/Ib/Ic ejecta properties from light curves and spectra: correlations from radiative-transfer models". In: *MNRAS* 458, pp. 1618–1635. DOI: 10.1093/mnras/stw418. arXiv: 1602.06280 [astro-ph.SR].

Dewi, J. D. M. et al. (2002). "The evolution of naked helium stars with a neutron star companion in close binary systems". In: *MNRAS* 331, pp. 1027–1040. DOI: 10.1046/j.1365-8711.2002.05257.x. eprint: astro-ph/0201239.

Dewi, J. D. M. et al. (2003). "The late stages of evolution of helium star-neutron star binaries and the formation of double neutron star systems". In: *MNRAS* 344, pp. 629–643. DOI: 10.1046/j.1365-8711.2003.06844.x. eprint: astro-ph/0306066.

Dey, A. et al. (2019). "Overview of the DESI Legacy Imaging Surveys". In: *AJ* 157.5, 168, p. 168. DOI: 10.3847/1538-3881/ab089d. arXiv: 1804.08657 [astro-ph.IM].

Dimitriadis, G. et al. (2019). "Transient Classification Report for 2019-04-30". In: *Transient Name Server Classification Report* 2019-675, L1, p. 1. DOI: 10.3847/2041-8213/aaedb0. arXiv: 1811.10061 [astro-ph.HE].

Dopita, M. A. et al. (2016). "Chemical abundances in high-redshift galaxies: a powerful new emission line diagnostic". In: *Ap&SS* 361, 61, p. 61. DOI: 10.1007/s10509-016-2657-8. arXiv: 1601.01337.

Dopita, M. et al. (2010). "The Wide Field Spectrograph (WiFeS): performance and data reduction". In: *Ap&SS* 327.2, pp. 245–257. DOI: 10.1007/s10509-010-0335-9. arXiv: 1002.4472 [astro-ph.IM].

Drake, A. J. et al. (2009). "First Results from the Catalina Real-Time Transient Survey". In: *ApJ* 696.1, pp. 870–884. DOI: 10.1088/0004-637X/696/1/870. arXiv: 0809.1394 [astro-ph].

Drout, M. R. et al. (2011). "The First Systematic Study of Type Ibc Supernova Multi-band Light Curves". In: *ApJ* 741, 97, p. 97. DOI: 10.1088/0004-637X/741/2/97. arXiv: 1011.4959.

Drout, M. R. et al. (2013). "The Fast and Furious Decay of the Peculiar Type Ic Supernova 2005ek". In: *ApJ* 774, 58, p. 58. DOI: 10.1088/0004-637X/774/1/58. arXiv: 1306.2337 [astro-ph.HE].

Drout, M. R. et al. (2016). "The Double-peaked SN 2013ge: A Type Ib/c SN with an Asymmetric Mass Ejection or an Extended Progenitor Envelope". In: *ApJ* 821, 57, p. 57. DOI: 10.3847/0004-637X/821/1/57. arXiv: 1507.02694 [astro-ph.HE].

D'Souza, R. et al. (2014). "Parametrizing the stellar haloes of galaxies". In: *MNRAS* 443.2, pp. 1433–1450. DOI: 10.1093/mnras/stu1194. arXiv: 1404.2123 [astro-ph.GA].

Duerbeck, H. W. (1990). "Galactic Distribution and Outburst Frequency of Classical Novae". In: *IAU Colloq. 122: Physics of Classical Novae*. Ed. by A. Cassatella et al. Vol. 369, p. 34. DOI: 10.1007/3-540-53500-4_90.

Duev, D. A. et al. (2019). "Real-bogus classification for the Zwicky Transient Facility using deep learning". In: *MNRAS* 489.3, arXiv:1907.11259, pp. 3582–3590. DOI: 10.1093/mnras/stz2357. arXiv: 1907.11259 [astro-ph.IM].

Eldridge, J. J. et al. (2006). "Implications of the metallicity dependence of Wolf-Rayet winds". In: *A&A* 452, pp. 295–301. DOI: 10.1051/0004-6361:20065001. eprint: astro-ph/0603188.

Elmhamdi, A. (2011). "Oxygen Issue in Core Collapse Supernovae". In: *Acta Astronomica* 61.2, pp. 179–198. arXiv: 1109.2318 [astro-ph.CO].

Elmhamdi, A. et al. (2006). "Hydrogen and helium traces in type Ib-c supernovae". In: *A&A* 450.1, pp. 305–330. DOI: 10.1051/0004-6361:20054366. arXiv: astro-ph/0512572 [astro-ph].

Epchtein, N. et al. (1999). "A preliminary database of DENIS point sources". In: *A&A* 349, pp. 236–242.

Faber, S. M. et al. (2003). "The DEIMOS spectrograph for the Keck II Telescope: integration and testing". In: *Instrument Design and Performance for Optical/Infrared Ground-based Telescopes*. Ed. by M. Iye et al. Vol. 4841. Proceedings of SPIE, pp. 1657–1669. DOI: 10.1117/12.460346.

Fang, Q. et al. (2019). "A hybrid envelope-stripping mechanism for massive stars from supernova nebular spectroscopy". In: *Nature Astronomy* 3, pp. 434–439. DOI: 10.1038/s41550-019-0710-6.

Feindt, U. et al. (2019). "simsurvey: estimating transient discovery rates for the Zwicky transient facility". In: *Journal of Cosmology and Astroparticle Physics* 2019.10, 005, p. 005. DOI: 10.1088/1475-7516/2019/10/005. arXiv: 1902.03923 [astro-ph.IM].

Ferdman, R. D. et al. (2013). "The Double Pulsar: Evidence for Neutron Star Formation without an Iron Core-collapse Supernova". In: *ApJ* 767, 85, p. 85. DOI: 10.1088/0004-637X/767/1/85. arXiv: 1302.2914 [astro-ph.SR].

Filippenko, A. V. (1997). "Optical Spectra of Supernovae". In: *ARA&A* 35, pp. 309–355. DOI: 10.1146/annurev.astro.35.1.309.

Filippenko, A. V. et al. (1990). "The type IC (helium-poor Ib) supernova 1987M - Transition to the supernebular phase". In: *AJ* 100, pp. 1575–1587. DOI: 10.1086/115618.

Filippenko, A. V. et al. (1992a). "The peculiar Type IA SN 1991T - Detonation of a white dwarf?" In: *ApJL* 384, pp. L15–L18. DOI: 10.1086/186252.

Filippenko, A. V. et al. (1992b). "The subluminous, spectroscopically peculiar type IA supernova 1991bg in the elliptical galaxy NGC 4374". In: *AJ* 104, pp. 1543–1556. DOI: 10.1086/116339.

Filippenko, A. V. et al. (1995). "The Type IC Supernova 1994I in M51: Detection of Helium and Spectral Evolution". In: *ApJL* 450, p. L11. DOI: 10.1086/309659.

Filippenko, A. V. et al. (2003). "Supernovae 2001co, 2003H, 2003dg, and 2003dr". In: *IAU Circ.* 8159.

Fink, M. et al. (2007). "Double-detonation supernovae of sub-Chandrasekhar mass white dwarfs". In: *A&A* 476, pp. 1133–1143. DOI: 10.1051/0004-6361:20078438. arXiv: 0710.5486.

Fink, M. et al. (2010). "Double-detonation sub-Chandrasekhar supernovae: can minimum helium shell masses detonate the core?" In: *A&A* 514, A53, A53. DOI: 10.1051/0004-6361/200913892. arXiv: 1002.2173 [astro-ph.SR].

Fisher, A. K. (2000). "Direct analysis of type Ia supernovae spectra". PhD thesis. THE UNIVERSITY OF OKLAHOMA.

Flörs, A. et al. (2020). "Sub-Chandrasekhar progenitors favoured for Type Ia supernovae: evidence from late-time spectroscopy". In: *MNRAS* 491.2, pp. 2902–2918. DOI: 10.1093/mnras/stz3013. arXiv: 1909.11055 [astro-ph.HE].

Folatelli, G. et al. (2010). "The Carnegie Supernova Project: Analysis of the First Sample of Low-Redshift Type-Ia Supernovae". In: *AJ* 139.1, pp. 120–144. DOI: 10.1088/0004-6256/139/1/120. arXiv: 0910.3317 [astro-ph.CO].

Foley, R. J. (2015). "Kinematics and host-galaxy properties suggest a nuclear origin for calcium-rich supernova progenitors". In: *MNRAS* 452, pp. 2463–2478. DOI: 10.1093/mnras/stv789. arXiv: 1501.07607 [astro-ph.HE].

Foley, R. J. et al. (2010). "SN 2006bt: A Perplexing, Troublesome, and Possibly Misleading Type Ia Supernova". In: *ApJ* 708, pp. 1748–1759. DOI: 10.1088/0004-637X/708/2/1748. arXiv: 0912.0263.

Foley, R. J. et al. (2009). "SN 2008ha: An Extremely Low Luminosity and Exceptionally Low Energy Supernova". In: *AJ* 138.2, pp. 376–391. DOI: 10.1088/0004-6256/138/2/376. arXiv: 0902.2794 [astro-ph.CO].

Foley, R. J. et al. (2016). "Late-time spectroscopy of Type Iax Supernovae". In: *MNRAS* 461.1, pp. 433–457. DOI: 10.1093/mnras/stw1320. arXiv: 1601.05955 [astro-ph.HE].

Fong, W. et al. (2013). "The Locations of Short Gamma-Ray Bursts as Evidence for Compact Object Binary Progenitors". In: *ApJ* 776, 18, p. 18. DOI: 10.1088/0004-637X/776/1/18. arXiv: 1307.0819 [astro-ph.HE].

Foreman-Mackey, D. et al. (2013). "emcee: The MCMC Hammer". In: *PASP* 125, p. 306. DOI: 10.1086/670067. arXiv: 1202.3665 [astro-ph.IM].

Fox, O. D. et al. (2011). "A Spitzer Survey for Dust in Type IIn Supernovae". In: *ApJ* 741.1, 7, p. 7. DOI: 10.1088/0004-637X/741/1/7. arXiv: 1104.5012 [astro-ph.SR].

Fox, O. et al. (2012). *A Search for the Missing Supernovae in Ultraluminous, Star Forming Galaxies*. Spitzer Proposal.

Fransson, C. et al. (1989). "Late Emission from Supernovae: A Window on Stellar Nucleosynthesis". In: *ApJ* 343, p. 323. DOI: 10.1086/167707.

Freedman, W. L. et al. (2001). "Final Results from the Hubble Space Telescope Key Project to Measure the Hubble Constant". In: *ApJ* 553.1, pp. 47–72. DOI: 10.1086/320638. arXiv: astro-ph/0012376 [astro-ph].

Freedman, W. L. et al. (2011). "The Carnegie Hubble Program". In: *AJ* 142.6, 192, p. 192. DOI: 10.1088/0004-6256/142/6/192. arXiv: 1109.3802 [astro-ph.CO].

Fremling, C. et al. (2016). "PTF12os and iPTF13bvn. Two stripped-envelope supernovae from low-mass progenitors in NGC 5806". In: *A & A* 593, A68, A68. DOI: 10.1051/0004-6361/201628275. arXiv: 1606.03074 [astro-ph.HE].

Fremling, C. et al. (2018). "Oxygen and helium in stripped-envelope supernovae". In: *A&A* 618, A37, A37. DOI: 10.1051/0004-6361/201731701. arXiv: 1807.00100 [astro-ph.HE].

Fremling, U. C. et al. (2019). "The Zwicky Transient Facility Bright Transient Survey I: Spectroscopic Classification and the Redshift Completeness of Local Galaxy Catalogs". In: *arXiv e-prints*, arXiv:1910.12973, arXiv:1910.12973. arXiv: 1910.12973 [astro-ph.HE].

Frohmaier, C. et al. (2018). "The Volumetric Rate of Calcium-rich Transients in the Local Universe". In: *ApJ* 858.1, 50, p. 50. DOI: 10.3847/1538-4357/aabc0b. arXiv: 1804.03103 [astro-ph.HE].

Frohmaier, C. et al. (2017). "Real-time Recovery Efficiencies and Performance of the Palomar Transient Factory's Transient Discovery Pipeline". In: *ApJS* 230, 4, p. 4. DOI: 10.3847/1538-4365/aa6d70. arXiv: 1704.02951 [astro-ph.IM].

Frohmaier, C. et al. (2019). "The volumetric rate of normal type Ia supernovae in the local Universe discovered by the Palomar Transient Factory". In: *MNRAS* 486.2, pp. 2308–2320. DOI: 10.1093/mnras/stz807. arXiv: 1903.08580 [astro-ph.HE].

Fruchter, A. S. et al. (2002). "Drizzle: A Method for the Linear Reconstruction of Undersampled Images". In: *PASP* 114, pp. 144–152. DOI: 10.1086/338393. eprint: astro-ph/9808087.

Fryer, C. L. (1999). "Mass Limits For Black Hole Formation". In: *ApJ* 522, pp. 413–418. DOI: 10.1086/307647. eprint: astro-ph/9902315.

Fryer, C. L. et al. (2001). "Theoretical Black Hole Mass Distributions". In: *ApJ* 554, pp. 548–560. DOI: 10.1086/321359. eprint: astro-ph/9911312.

Fryer, C. L. et al. (2010). "Spectra of Type Ia Supernovae from Double Degenerate Mergers". In: *ApJ* 725.1, pp. 296–308. DOI: 10.1088/0004-637X/725/1/296. arXiv: 1007.0570 [astro-ph.SR].

Gaia Collaboration et al. (2018). "Gaia Data Release 2. Summary of the contents and survey properties". In: *A&A* 616, A1, A1. DOI: 10.1051/0004-6361/201833051. arXiv: 1804.09365 [astro-ph.GA].

Galbany, L. et al. (2014). "Nearby supernova host galaxies from the CALIFA Survey. I. Sample, data analysis, and correlation to star-forming regions". In: *A&A* 572, A38, A38. DOI: 10.1051/0004-6361/201424717. arXiv: 1409.1623.

Galbany, L. et al. (2016). "Nearby supernova host galaxies from the CALIFA survey. II. Supernova environmental metallicity". In: *A&A* 591, A48, A48. DOI: 10.1051/0004-6361/201528045. arXiv: 1603.07808.

Galbany, L. et al. (2019). "Evidence for a Chandrasekhar-mass explosion in the Ca-strong 1991bg-like type Ia supernova 2016hnk". In: *A&A* 630, A76, A76. DOI: 10.1051/0004-6361/201935537. arXiv: 1904.10034 [astro-ph.SR].

Gal-Yam, A. (2017). "Observational and Physical Classification of Supernovae". In: *Handbook of Supernovae*. Cham: Springer International Publishing, pp. 1–43. ISBN: 978-3-319-20794-0. DOI: 10.1007/978-3-319-20794-0_35-1. URL: https://doi.org/10.1007/978-3-319-20794-0_35-1.

Gal-Yam, A. et al. (2014). "A Wolf-Rayet-like progenitor of SN 2013cu from spectral observations of a stellar wind". In: *Nature* 509, pp. 471–474. DOI: 10.1038/nature13304. arXiv: 1406.7640 [astro-ph.HE].

Gehrels, N. et al. (2004). "The Swift Gamma-Ray Burst Mission". In: *ApJ* 611.2, pp. 1005–1020. DOI: 10.1086/422091. arXiv: astro-ph/0405233 [astro-ph].

Gehrz, R. D. et al. (2007). "The NASA Spitzer Space Telescope". In: *Review of Scientific Instruments* 78.1, pp. 011302–011302. DOI: 10.1063/1.2431313.

Gehrz, R. D. et al. (2018). "The Temporal Development of Dust Formation and Destruction in Nova Sagittarii 2015#2 (V5668 SGR): A Panchromatic Study". In: *ApJ* 858.2, 78, p. 78. DOI: 10.3847/1538-4357/aaba81. arXiv: 1804.00575 [astro-ph.SR].

Gehrz, R. D. et al. (1998). "Nucleosynthesis in Classical Novae and Its Contribution to the Interstellar Medium". In: *PASP* 110.743, pp. 3–26. DOI: 10.1086/316107.

Geier, S. et al. (2013). "A progenitor binary and an ejected mass donor remnant of faint type Ia supernovae". In: *A&A* 554, A54, A54. DOI: 10.1051/0004-6361/201321395. arXiv: 1304.4452 [astro-ph.SR].

Georgy, C. et al. (2009). "The different progenitors of type Ib, Ic SNe, and of GRB". In: *A&A* 502, pp. 611–622. DOI: 10.1051/0004-6361/200811339. arXiv: 0906.2284 [astro-ph.SR].

Gezari, S. et al. (2012). "An ultraviolet-optical flare from the tidal disruption of a helium-rich stellar core". In: *Nature* 485, pp. 217–220. DOI: 10.1038/nature10990. arXiv: 1205.0252 [astro-ph.CO].

Gonzaga et al., S. (2012). *The DrizzlePac Handbook*.

Götberg, Y. et al. (2017). "Ionizing spectra of stars that lose their envelope through interaction with a binary companion: role of metallicity". In: *A & A* 608, A11, A11. DOI: 10.1051/0004-6361/201730472. arXiv: 1701.07439 [astro-ph.SR].

Götberg, Y. et al. (2020). "Stars Stripped in Binaries: The Living Gravitational-wave Sources". In: *ApJ* 904.1, 56, p. 56. DOI: 10.3847/1538-4357/abbda5. arXiv: 2006.07382 [astro-ph.SR].

Gräfener, G. et al. (2016). "Light-travel-time diagnostics in early supernova spectra: substantial mass-loss of the IIb progenitor of SN 2013cu through a superwind". In: *MNRAS* 455, pp. 112–126. DOI: 10.1093/mnras/stv2283. arXiv: 1510.00013 [astro-ph.SR].

Graham, M. J. et al. (2019). "The Zwicky Transient Facility: Science Objectives". In: *PASP* 131.7, p. 078001. DOI: 10.1088/1538-3873/ab006c. arXiv: 1902.01945 [astro-ph.IM].

Green, G. M. et al. (2019). "A 3D Dust Map Based on Gaia, Pan-STARRS 1, and 2MASS". In: *ApJ* 887.1, 93, p. 93. DOI: 10.3847/1538-4357/ab5362. arXiv: 1905.02734 [astro-ph.GA].

Grindlay, J. et al. (2006). "Short gamma-ray bursts from binary neutron star mergers in globular clusters". In: *Nature Physics* 2, pp. 116–119. DOI: 10.1038/nphys214. eprint: astro-ph/0512654.

Grzegorzek, J. (2019). "PSH Transient Discovery Report for 2019-04-29". In: *Transient Name Server Discovery Report* 2019-666, p. 1.

Guillochon, J. et al. (2017). "An Open Catalog for Supernova Data". In: *ApJ* 835, 64, p. 64. DOI: 10.3847/1538-4357/835/1/64. arXiv: 1605.01054 [astro-ph.SR].

Guver, T. et al. (2009). "The relation between optical extinction and hydrogen column density in the Galaxy". In: *MNRAS* 400.4, pp. 2050–2053. DOI: 10.1111/j.1365-2966.2009.15598.x. arXiv: 0903.2057 [astro-ph.GA].

Hachinger, S. et al. (2012). "How much H and He is 'hidden' in SNe Ib/c? - I. Low-mass objects". In: *MNRAS* 422, pp. 70–88. DOI: 10.1111/j.1365-2966.2012.20464.x. arXiv: 1201.1506 [astro-ph.SR].

Hachisu, I. et al. (2014). "The UBV Color Evolution of Classical Novae. I. Nova-giant Sequence in the Color-Color Diagram". In: *ApJ* 785.2, 97, p. 97. DOI: 10.1088/0004-637X/785/2/97. arXiv: 1401.7113 [astro-ph.SR].

Hachisu, I. et al. (2016). "The UBV Color Evolution of Classical Novae. II. Color-Magnitude Diagram". In: *ApJS* 223.2, 21, p. 21. DOI: 10.3847/0067-0049/223/2/21. arXiv: 1602.01195 [astro-ph.SR].

Hankins, M. et al. (2019a). "Near-infrared brightening of MAXI J1820+070/ ASASSN18ey detected with Palomar Gattini-IR". In: *The Astronomer's Telegram* 13044, p. 1.

Hankins, M. et al. (2019b). "LIGO/Virgo S190426c: Continued infrared wide-field search with Palomar Gattini-IR." In: *GRB Coordinates Network, Circular Service, No. 24329, #1 (2019/April-0)* 24329.

Hankins, M. et al. (2019c). "LIGO/Virgo S190426c: Infrared Wide-field Search with Palomar Gattini-IR." In: *GRB Coordinates Network, Circular Service, No. 24284, #1 (2019/April-0)* 24284.

Hankins, M. et al. (2019d). "LIGO/Virgo S190814bv: No Candidates Found in Wide-Field Infrared Search with Palomar Gattini-IR." In: *GRB Coordinates Network, Circular Service, No. 25358, #1 (2019/August-0)* 25358.

Hankins, M. et al. (2020). "Palomar Gattini-IR discovery and spectroscopic classification of a highly reddened YSO in outburst". In: *The Astronomer's Telegram* 13902, p. 1.

Hardy, L. K. et al. (2017). "A search for optical bursts from the repeating fast radio burst FRB 121102". In: *MNRAS* 472.3, pp. 2800–2807. DOI: 10.1093/mnras/stx2153. arXiv: 1708.06156 [astro-ph.IM].

Harris, W. E. (1996). "A Catalog of Parameters for Globular Clusters in the Milky Way". In: *AJ* 112, p. 1487. DOI: 10.1086/118116.

Hatano, K. et al. (1997). "On the spatial distribution and occurrence rate of Galactic classical novae". In: *MNRAS* 290.1, pp. 113–118. DOI: 10.1093/mnras/290.1.113.

Heger, A. et al. (2003). "How Massive Single Stars End Their Life". In: *ApJ* 591.1, pp. 288–300. DOI: 10.1086/375341. arXiv: astro-ph/0212469 [astro-ph].

Henze, M. et al. (2015a). "A remarkable recurrent nova in M 31: The 2010 eruption recovered and evidence of a six-month period". In: *A&A* 582, L8, p. L8. DOI: 10.1051/0004-6361/201527168. arXiv: 1508.06205 [astro-ph.SR].

Henze, M. et al. (2015b). "A remarkable recurrent nova in M 31: The predicted 2014 outburst in X-rays with Swift". In: *A&A* 580, A46, A46. DOI: 10.1051/0004-6361/201526028. arXiv: 1504.06237 [astro-ph.HE].

Herter, T. L. et al. (2008). "The performance of TripleSpec at Palomar". In: *Ground-based and Airborne Instrumentation for Astronomy II*. Ed. by I. S. McLean et al. Vol. 7014. Society of Photo-Optical Instrumentation Engineers (SPIE) Conference Series, p. 70140X. DOI: 10.1117/12.789660.

Hicken, M. et al. (2009). "CfA3: 185 Type Ia Supernova Light Curves from the CfA". In: *ApJ* 700, pp. 331–357. DOI: 10.1088/0004-637X/700/1/331. arXiv: 0901.4787 [astro-ph.CO].

Hickish, J. et al. (2018). "A digital correlator upgrade for the Arcminute MicroKelvin Imager". In: *MNRAS* 475, pp. 5677–5687. DOI: 10.1093/mnras/sty074. arXiv: 1707.04237 [astro-ph.IM].

Hillenbrand, L. A. et al. (2021). "Outbursting Young Stellar Object PGIR 20dci in the Perseus Arm". In: *arXiv e-prints*, arXiv:2101.04203, arXiv:2101.04203. arXiv: 2101.04203 [astro-ph.SR].

Hillman, Y. et al. (2016). "Growing White Dwarfs to the Chandrasekhar Limit: The Parameter Space of the Single Degenerate SNIa Channel". In: *ApJ* 819.2, 168, p. 168. DOI: 10.3847/0004-637X/819/2/168. arXiv: 1508.03141 [astro-ph.SR].

Hinshaw, G. et al. (2013). "Nine-year Wilkinson Microwave Anisotropy Probe (WMAP) Observations: Cosmological Parameter Results". In: *ApJS* 208.2, 19, p. 19. DOI: 10.1088/0067-0049/208/2/19. arXiv: 1212.5226 [astro-ph.CO].

Hodgkin, S. T. et al. (2019). "GaiaAlerts Transient Discovery Report for 2019-08-29". In: *Transient Name Server Discovery Report* 2019-1656, p. 1.

Hoeflich, P. et al. (1996). "Explosion Models for Type IA Supernovae: A Comparison with Observed Light Curves, Distances, H 0, and Q 0". In: *ApJ* 457, p. 500. DOI: 10.1086/176748. eprint: astro-ph/9602025.

Hogg, D. W. et al. (1997). "Counts and colours of faint galaxies in the U and R bands". In: *MNRAS* 288.2, pp. 404–410. DOI: 10.1093/mnras/288.2.404. arXiv: astro-ph/9702241 [astro-ph].

Holcomb, C. et al. (2013). "Conditions for Successful Helium Detonations in Astrophysical Environments". In: *ApJ* 771, 14, p. 14. DOI: 10.1088/0004-637X/771/1/14. arXiv: 1302.6235 [astro-ph.HE].

Hook, I. M. et al. (2004). "The Gemini-North Multi-Object Spectrograph: Performance in Imaging, Long-Slit, and Multi-Object Spectroscopic Modes". In: *PASP* 116, pp. 425–440. DOI: 10.1086/383624.

Horesh, A. et al. (2013). "PTF 12gzk—A Rapidly Declining, High-velocity Type Ic Radio Supernova". In: *ApJ* 778, 63, p. 63. DOI: 10.1088/0004-637X/778/1/63. arXiv: 1306.5755 [astro-ph.HE].

Hosseinzadeh, G. et al. (2017). "Early Blue Excess from the Type Ia Supernova 2017cbv and Implications for Its Progenitor". In: *ApJL* 845, L11, p. L11. DOI: 10.3847/2041-8213/aa8402. arXiv: 1706.08990 [astro-ph.HE].

Houck, J. C. et al. (1996). "Analysis of the Late Optical Spectra of SN 1993J". In: *ApJ* 456, p. 811. DOI: 10.1086/176699.

Hounsell, R. et al. (2010). "The outburst light curve of Nova KT Eridani from Solar Mass Ejection Imager (SMEI) observations". In: *The Astronomer's Telegram* 2558, p. 1.

Hounsell, R. et al. (2011). "A very luminous, highly extinguished, very fast nova - V1721 Aquilae". In: *A&A* 530, A81, A81. DOI: 10.1051/0004-6361/201016085. arXiv: 1104.3068 [astro-ph.SR].

Howell, D. A. (2001). "The Progenitors of Subluminous Type Ia Supernovae". In: *ApJL* 554.2, pp. L193–L196. DOI: 10.1086/321702. arXiv: astro-ph/0105246 [astro-ph].

Howell, D. A. et al. (2005). "Gemini Spectroscopy of Supernovae from the Supernova Legacy Survey: Improving High-Redshift Supernova Selection and Classification". In: *ApJ* 634.2, pp. 1190–1201. DOI: 10.1086/497119. arXiv: astro-ph/0509195 [astro-ph].

Hung, T. et al. (2017). "Revisiting Optical Tidal Disruption Events with iPTF16axa". In: *ApJ* 842, 29, p. 29. DOI: 10.3847/1538-4357/aa7337. arXiv: 1703.01299 [astro-ph.HE].

Iben Icko, J. et al. (1989). "Model Stars with Degenerate Dwarf Cores and Helium-burning Shells: A Stationary-burning Approximation". In: *ApJ* 342, p. 430. DOI: 10.1086/167603.

Inserra, C. et al. (2015). "OGLE-2013-SN-079: A Lonely Supernova Consistent with a Helium Shell Detonation". In: *ApJL* 799, L2, p. L2. DOI: 10.1088/2041-8205/799/1/L2. arXiv: 1410.6473 [astro-ph.SR].

Israel, G. L. et al. (2016). "The discovery, monitoring and environment of SGR J1935+2154". In: *MNRAS* 457.4, pp. 3448–3456. DOI: 10.1093/mnras/stw008. arXiv: 1601.00347 [astro-ph.HE].

Israel, G. et al. (2005). "Discovery and monitoring of the likely IR counterpart of SGR 1806-20 during the 2004 γ-ray burst-active state". In: *A&A* 438.1, pp. L1–L4. DOI: 10.1051/0004-6361:200500138. arXiv: astro-ph/0506095 [astro-ph].

Itagaki, K. (2019). "Transient Discovery Report for 2019-01-09". In: *Transient Name Server Discovery Report* 2019-53, p. 1.

Ivanova, N. et al. (2003). "The Role of Helium Stars in the Formation of Double Neutron Stars". In: *ApJ* 592, pp. 475–485. DOI: 10.1086/375578. eprint: astro-ph/0210267.

Ivanova, N. et al. (2013). "Common envelope evolution: where we stand and how we can move forward". In: *AAPR* 21, 59, p. 59. DOI: 10.1007/s00159-013-0059-2. arXiv: 1209.4302 [astro-ph.HE].

Ivezić, Ž. et al. (2019). "LSST: From Science Drivers to Reference Design and Anticipated Data Products". In: *ApJ* 873.2, 111, p. 111. DOI: 10.3847/1538-4357/ab042c. arXiv: 0805.2366 [astro-ph].

Jacobson-Galan, W. V. et al. (2019). "Ca hnk: Calcium-rich Transient SN 2016hnk from the Helium Shell Detonation of a Sub-Chandrasekhar White Dwarf". In: *arXiv e-prints*, arXiv:1910.05436, arXiv:1910.05436. arXiv: 1910.05436 [astro-ph.HE].

Jacobson-Galán, W. V. et al. (2020a). "Late-time Observations of Calcium-Rich Transient SN 2019ehk Reveal a Pure Radioactive Decay Power Source". In: *arXiv e-prints*, arXiv:2010.15863, arXiv:2010.15863. arXiv: 2010.15863 [astro-ph.HE].

Jacobson-Galán, W. V. et al. (2020b). "SN 2019ehk: A Double-Peaked Ca-rich Transient with Luminous X-ray Emission and Shock-Ionized Spectral Features". In: *arXiv e-prints*, arXiv:2005.01782, arXiv:2005.01782. arXiv: 2005.01782 [astro-ph.HE].

Jacques, C. et al. (2020). "BraTS Transient Discovery Report for 2020-10-03". In: *Transient Name Server Discovery Report* 2020-3006, p. 1.

Jarrett, T. H. et al. (2000). "2MASS Extended Source Catalog: Overview and Algorithms". In: *AJ* 119.5, pp. 2498–2531. DOI: 10.1086/301330. arXiv: astro-ph/0004318 [astro-ph].

Jencson, J. E. et al. (2019). "The SPIRITS sample of Luminous Infrared Transients: Uncovering Hidden Supernovae and Dusty Stellar Outbursts in Nearby Galaxies". In: *arXiv e-prints*. arXiv: 1901.00871 [astro-ph.HE].

Jerkstrand, A. (2017). "Spectra of Supernovae in the Nebular Phase". In: *Handbook of Supernovae*. Ed. by A. W. Alsabti et al., p. 795. DOI: 10.1007/978-3-319-21846-5_29.

Jerkstrand, A. et al. (2014). "The nebular spectra of SN 2012aw and constraints on stellar nucleosynthesis from oxygen emission lines". In: *MNRAS* 439.4, pp. 3694–3703. DOI: 10.1093/mnras/stu221. arXiv: 1311.2031 [astro-ph.SR].

Jerkstrand, A. et al. (2015). "Late-time spectral line formation in Type IIb supernovae, with application to SN 1993J, SN 2008ax, and SN 2011dh". In: *A&A* 573, A12, A12. DOI: 10.1051/0004-6361/201423983. arXiv: 1408.0732 [astro-ph.HE].

Jiang, J.-A. et al. (2017). "A hybrid type Ia supernova with an early flash triggered by helium-shell detonation". In: *Nature* 550, pp. 80–83. DOI: 10.1038/nature23908. arXiv: 1710.01824 [astro-ph.HE].

José, J. et al. (2006). "Nucleosynthesis in classical novae". In: *Nucl. Phys. A* 777, pp. 550–578. DOI: 10.1016/j.nuclphysa.2005.02.121.

Jurić, M. et al. (2008). "The Milky Way Tomography with SDSS. I. Stellar Number Density Distribution". In: *ApJ* 673.2, pp. 864–914. DOI: 10.1086/523619. arXiv: astro-ph/0510520 [astro-ph].

Kaiser, N. et al. (2010). "The Pan-STARRS wide-field optical/NIR imaging survey". In: *Proc. SPIE*. Vol. 7733. Society of Photo-Optical Instrumentation Engineers (SPIE) Conference Series, 77330E. DOI: 10.1117/12.859188.

Kankare, E. et al. (2008). "Discovery of a Very Highly Extinguished Supernova in a Luminous Infrared Galaxy". In: *ApJL* 689.2, p. L97. DOI: 10.1086/595820. arXiv: 0810.2885 [astro-ph].

Kankare, E. et al. (2012). "Discovery of Two Supernovae in the Nuclear Regions of the Luminous Infrared Galaxy IC 883". In: *ApJL* 744, L19, p. L19. DOI: 10.1088/2041-8205/744/2/L19. arXiv: 1112.0777 [astro-ph.SR].

Karambelkar, V. R. et al. (2020). "Census of R Coronae Borealis stars I: Infrared light curves from Palomar Gattini IR". In: *arXiv e-prints*, arXiv:2012.11629, arXiv:2012.11629. arXiv: 2012.11629 [astro-ph.SR].

Kasen, D. (2010). "Seeing the Collision of a Supernova with Its Companion Star". In: *ApJ* 708, pp. 1025–1031. DOI: 10.1088/0004-637X/708/2/1025. arXiv: 0909.0275 [astro-ph.HE].

Kasen, D. et al. (2006). "Time-dependent Monte Carlo Radiative Transfer Calculations for Three-dimensional Supernova Spectra, Light Curves, and Polarization". In: *ApJ* 651, pp. 366–380. DOI: 10.1086/506190. eprint: astro-ph/0606111.

Kasen, D. et al. (2017). "Origin of the heavy elements in binary neutron-star mergers from a gravitational-wave event". In: *Nature* 551.7678, pp. 80–84. DOI: 10.1038/nature24453. arXiv: 1710.05463 [astro-ph.HE].

Kasliwal, M. M. (2012). "Systematically Bridging the Gap Between Novae and Supernovae". In: *PASA* 29, pp. 482–488. DOI: 10.1071/AS11061.

Kasliwal, M. M. et al. (2010). "Rapidly Decaying Supernova 2010X: A Candidate ".Ia" Explosion". In: *ApJL* 723, pp. L98–L102. DOI: 10.1088/2041-8205/723/1/L98. arXiv: 1009.0960 [astro-ph.HE].

Kasliwal, M. M. et al. (2011). "Discovery of a New Photometric Sub-class of Faint and Fast Classical Novae". In: *ApJ* 735.2, 94, p. 94. DOI: 10.1088/0004-637X/735/2/94. arXiv: 1003.1720 [astro-ph.SR].

Kasliwal, M. M. et al. (2012). "Calcium-rich Gap Transients in the Remote Outskirts of Galaxies". In: *ApJ* 755, 161, p. 161. DOI: 10.1088/0004-637X/755/2/161. arXiv: 1111.6109 [astro-ph.HE].

Kasliwal, M. M. et al. (2017). "Illuminating Gravitational Waves: A Concordant Picture of Photons from a Neutron Star Merger". In: *ArXiv e-prints* 839.2, 88, p. 88. DOI: 10.3847/1538-4357/aa6978. arXiv: 1710.05436 [astro-ph.HE].

Kasliwal, M. M. et al. (2019). "The GROWTH Marshal: A Dynamic Science Portal for Time-domain Astronomy". In: *PASP* 131.997, p. 038003. DOI: 10.1088/1538-3873/aafbc2. arXiv: 1902.01934 [astro-ph.IM].

Kaspi, V. M. et al. (2017). "Magnetars". In: *ARA&A* 55.1, pp. 261–301. DOI: 10.1146/annurev-astro-081915-023329. arXiv: 1703.00068 [astro-ph.HE].

Kato, M. et al. (2014). "Shortest Recurrence Periods of Novae". In: *ApJ* 793.2, 136, p. 136. DOI: 10.1088/0004-637X/793/2/136. arXiv: 1404.0582 [astro-ph.SR].

Kawabata, K. S. et al. (2010). "A massive star origin for an unusual helium-rich supernova in an elliptical galaxy". In: *Nature* 465, pp. 326–328. DOI: 10.1038/nature09055. arXiv: 0906.2811 [astro-ph.SR].

Kawana, K. et al. (2020). "Rapid Transients Originating from Thermonuclear Explosions in Helium White Dwarf Tidal Disruption Events". In: *ApJL* 890.2, L26, p. L26. DOI: 10.3847/2041-8213/ab7209. arXiv: 1909.10523 [astro-ph.HE].

Kawash, A. et al. (2021). "Classical Novae Masquerading as Dwarf Novae? Outburst Properties of Cataclysmic Variables with ASAS-SN". In: *arXiv e-prints*, arXiv:2101.12239, arXiv:2101.12239. arXiv: 2101.12239 [astro-ph.SR].

Keller, S. C. et al. (2007). "The SkyMapper Telescope and The Southern Sky Survey". In: *PASA* 24.1, pp. 1–12. DOI: 10.1071/AS07001. arXiv: astro-ph/0702511 [astro-ph].

Kennicutt Jr., R. C. (1998). "Star Formation in Galaxies Along the Hubble Sequence". In: *ARAA* 36, pp. 189–232. DOI: 10.1146/annurev.astro.36.1.189. eprint: astro-ph/9807187.

Kewley, L. J. et al. (2002). "Using Strong Lines to Estimate Abundances in Extragalactic H II Regions and Starburst Galaxies". In: *ApJS* 142, pp. 35–52. DOI: 10.1086/341326. eprint: astro-ph/0206495.

Kewley, L. J. et al. (2008). "Metallicity Calibrations and the Mass-Metallicity Relation for Star-forming Galaxies". In: *ApJ* 681, 1183-1204, pp. 1183–1204. DOI: 10.1086/587500. arXiv: 0801.1849.

Khatami, D. K. et al. (2019). "Physics of Luminous Transient Light Curves: A New Relation between Peak Time and Luminosity". In: *ApJ* 878.1, 56, p. 56. DOI: 10.3847/1538-4357/ab1f09. arXiv: 1812.06522 [astro-ph.HE].

Khazov, D. et al. (2016). "Flash Spectroscopy: Emission Lines from the Ionized Circumstellar Material around <10-day-old Type II Supernovae". In: *ApJ* 818, 3, p. 3. DOI: 10.3847/0004-637X/818/1/3. arXiv: 1512.00846 [astro-ph.HE].

Kingsburgh, R. L. et al. (1995). "Properties of the WO Wolf-Rayet stars". In: *A&A* 295, pp. 75–100.

Kitaura, F. S. et al. (2006). "Explosions of O-Ne-Mg cores, the Crab supernova, and subluminous type II-P supernovae". In: *A&A* 450, pp. 345–350. DOI: 10.1051/0004-6361:20054703. eprint: astro-ph/0512065.

Knierman, K. A. et al. (2003). "From Globular Clusters to Tidal Dwarfs: Structure Formation in the Tidal Tails of Merging Galaxies". In: *AJ* 126, pp. 1227–1244. DOI: 10.1086/377481. eprint: astro-ph/0307383.

Knigge, C. et al. (2011). "The Evolution of Cataclysmic Variables as Revealed by Their Donor Stars". In: *ApJS* 194.2, 28, p. 28. DOI: 10.1088/0067-0049/194/2/28. arXiv: 1102.2440 [astro-ph.SR].

Kochanek, C. S. et al. (2001). "The K-Band Galaxy Luminosity Function". In: *ApJ* 560.2, pp. 566–579. DOI: 10.1086/322488. arXiv: astro-ph/0011456 [astro-ph].

Kollmeier, J. A. et al. (2017). "SDSS-V: Pioneering Panoptic Spectroscopy". In: *arXiv e-prints*, arXiv:1711.03234, arXiv:1711.03234. arXiv: 1711.03234 [astro-ph.GA].

Komatsu, E. et al. (2011). "Seven-year Wilkinson Microwave Anisotropy Probe (WMAP) Observations: Cosmological Interpretation". In: *ApJS* 192, 18, p. 18. DOI: 10.1088/0067-0049/192/2/18. arXiv: 1001.4538 [astro-ph.CO].

Kool, E. C. et al. (2018). "First results from GeMS/GSAOI for project SUNBIRD: Supernovae UNmasked By Infra-Red Detection". In: *MNRAS* 473, pp. 5641–5657. DOI: 10.1093/mnras/stx2463. arXiv: 1709.08307.

Kozlova, A. V. et al. (2016). "The first observation of an intermediate flare from SGR 1935+2154". In: *MNRAS* 460.2, pp. 2008–2014. DOI: 10.1093/mnras/stw1109. arXiv: 1605.02993 [astro-ph.HE].

Kozłowski, S. et al. (2010). "Mid-infrared Variability from the Spitzer Deep Wide-field Survey". In: *ApJ* 716.1, pp. 530–543. DOI: 10.1088/0004-637X/716/1/530. arXiv: 1002.3365 [astro-ph.CO].

Kraus, A. L. et al. (2007). "The Stellar Populations of Praesepe and Coma Berenices". In: *AJ* 134.6, pp. 2340–2352. DOI: 10.1086/522831. arXiv: 0708.2719 [astro-ph].

Kriek, M. et al. (2009). "An Ultra-Deep Near-Infrared Spectrum of a Compact Quiescent Galaxy at z = 2.2". In: *ApJ* 700, pp. 221–231. DOI: 10.1088/0004-637X/700/1/221. arXiv: 0905.1692 [astro-ph.CO].

Krisciunas, K. et al. (2017). "The Carnegie Supernova Project. I. Third Photometry Data Release of Low-redshift Type Ia Supernovae and Other White Dwarf Explosions". In: *AJ* 154, 211, p. 211. DOI: 10.3847/1538-3881/aa8df0. arXiv: 1709.05146 [astro-ph.IM].

Krizhevsky, A. et al. (2012). "Imagenet classification with deep convolutional neural networks". In: *Advances in Neural Information Processing Systems*, p. 2012.

Kromer, M. et al. (2010). "Double-detonation Sub-Chandrasekhar Supernovae: Synthetic Observables for Minimum Helium Shell Mass Models". In: *ApJ* 719, pp. 1067–1082. DOI: 10.1088/0004-637X/719/2/1067. arXiv: 1006.4489 [astro-ph.HE].

Kromer, M. et al. (2016). "The peculiar Type Ia supernova iPTF14atg: Chandrasekhar-mass explosion or violent merger?" In: *MNRAS* 459, pp. 4428–4439. DOI: 10.1093/mnras/stw962. arXiv: 1604.05730 [astro-ph.HE].

Krühler, T. et al. (2017). "Hot gas around SN 1998bw: Inferring the progenitor from its environment". In: *A&A* 602, A85, A85. DOI: 10.1051/0004-6361/201630268. arXiv: 1702.05430.

Kulkarni, S. R. et al. (1998). "Radio emission from the unusual supernova 1998bw and its association with the γ-ray burst of 25 April 1998". In: *Nature* 395, pp. 663–669. DOI: 10.1038/27139.

Kulkarni, S. R. et al. (2018). "The Redshift Completeness of Local Galaxy Catalogs". In: *ApJ* 860.1, 22, p. 22. DOI: 10.3847/1538-4357/aabf85. arXiv: 1710.04223 [astro-ph.GA].

Kumar, P. et al. (2017). "Fast radio burst source properties and curvature radiation model". In: *MNRAS* 468.3, pp. 2726–2739. DOI: 10.1093/mnras/stx665. arXiv: 1703.06139 [astro-ph.HE].

Kuncarayakti, H. et al. (2016). "Unresolved versus resolved: testing the validity of young simple stellar population models with VLT/MUSE observations of NGC 3603". In: *A&A* 593, A78, A78. DOI: 10.1051/0004-6361/201628813. arXiv: 1607.03446.

Kuncarayakti, H. et al. (2017). "Constraints on core-collapse supernova progenitors from explosion site integral field spectroscopy". In: *ArXiv e-prints*. arXiv: 1711.05765 [astro-ph.SR].

Kupfer, T. et al. (2017). "PTF1 J082340.04+081936.5: A Hot Subdwarf B Star with a Low-mass White Dwarf Companion in an 87-minute Orbit". In: *ApJ* 835.2, 131, p. 131. DOI: 10.3847/1538-4357/835/2/131. arXiv: 1612.02019 [astro-ph.SR].

Lacy, M. et al. (2020). "The Karl G. Jansky Very Large Array Sky Survey (VLASS). Science Case and Survey Design". In: *PASP* 132.1009, 035001, p. 035001. DOI: 10.1088/1538-3873/ab63eb. arXiv: 1907.01981 [astro-ph.IM].

Laher, R. R. et al. (2014). "IPAC Image Processing and Data Archiving for the Palomar Transient Factory". In: *PASP* 126, p. 674. DOI: 10.1086/677351. arXiv: 1404.1953 [astro-ph.IM].

Lamberts, A. et al. (2019). "Predicting the LISA white dwarf binary population in the Milky Way with cosmological simulations". In: *MNRAS* 490.4, pp. 5888–5903. DOI: 10.1093/mnras/stz2834. arXiv: 1907.00014 [astro-ph.HE].

Lang, D. et al. (2016). "WISE Photometry for 400 Million SDSS Sources". In: *AJ* 151.2, 36, p. 36. DOI: 10.3847/0004-6256/151/2/36.

Langer, N. (2012). "Presupernova Evolution of Massive Single and Binary Stars". In: *ARAA* 50, pp. 107–164. DOI: 10.1146/annurev-astro-081811-125534. arXiv: 1206.5443 [astro-ph.SR].

Laplace, E. et al. (2020). "The expansion of stripped-envelope stars: Consequences for supernovae and gravitational-wave progenitors". In: *A&A* 637, A6, A6. DOI: 10.1051/0004-6361/201937300. arXiv: 2003.01120 [astro-ph.SR].

Law, N. M. et al. (2009). "The Palomar Transient Factory: System Overview, Performance, and First Results". In: *PASP* 121.886, p. 1395. DOI: 10.1086/648598. arXiv: 0906.5350 [astro-ph.IM].

Law, N. M. et al. (2010). "The Palomar Transient Factory Survey Camera: first year performance and results". In: *Ground-based and Airborne Instrumentation for Astronomy III*. Vol. 7735. Proceedings of SPIE, p. 77353M. DOI: 10.1117/12.857400.

Law, N. M. et al. (2015). "Evryscope Science: Exploring the Potential of All-Sky Gigapixel-Scale Telescopes". In: *PASP* 127, p. 234. DOI: 10.1086/680521. arXiv: 1501.03162 [astro-ph.IM].

Lawlor, T. M. et al. (2006). "The mass of helium in white dwarf stars and the formation and evolution of hydrogen-deficient post-AGB stars". In: *MNRAS* 371.1, pp. 263–282. DOI: 10.1111/j.1365-2966.2006.10641.x. arXiv: astro-ph/0605747 [astro-ph].

Leadbeater, R. (2018). "Transient Classification Report for 2018-10-01". In: *Transient Name Server Classification Report* 2018-1486, p. 1.

Leitherer, C. et al. (1999). "Starburst99: Synthesis Models for Galaxies with Active Star Formation". In: *ApJS* 123, pp. 3–40. DOI: 10.1086/313233. eprint: astro-ph/9902334.

Leloudas, G. et al. (2011). "The properties of SN Ib/c locations". In: *A & A* 530, A95, A95. DOI: 10.1051/0004-6361/201116692. arXiv: 1102.2249 [astro-ph.SR].

Levan, A. et al. (2018). "Identification of the Infrared Counterpart of SGR 1935+2154 with the Hubble Space Telescope". In: *ApJ* 854.2, 161, p. 161. DOI: 10.3847/1538-4357/aaa88d. arXiv: 1801.05497 [astro-ph.HE].

Levanon, N. et al. (2015). "Constraining the double-degenerate scenario for Type Ia supernovae from merger ejected matter". In: *MNRAS* 447, pp. 2803–2809. DOI: 10.1093/mnras/stu2580. arXiv: 1408.1375 [astro-ph.SR].

Li, C. K. et al. (2020a). "Identification of a non-thermal X-ray burst with the Galactic magnetar SGR 1935+2154 and a fast radio burst with Insight-HXMT". In: *arXiv e-prints*, arXiv:2005.11071, arXiv:2005.11071. arXiv: 2005.11071 [astro-ph.HE].

Li, C. .-.-K. et al. (2020b). "Updated catalog of X-ray bursts of SGR J1935+2154 from Insight-HXMT observations". In: *GRB Coordinates Network* 28027, p. 1.

Li, W. et al. (2003). "SN 2002cx: The Most Peculiar Known Type Ia Supernova". In: *PASP* 115.806, pp. 453–473. DOI: 10.1086/374200. arXiv: astro-ph/0301428 [astro-ph].

Li, W. et al. (2011). "Nearby supernova rates from the Lick Observatory Supernova Search - II. The observed luminosity functions and fractions of supernovae in a complete sample". In: *MNRAS* 412.3, pp. 1441–1472. DOI: 10.1111/j.1365-2966.2011.18160.x. arXiv: 1006.4612 [astro-ph.SR].

Li, W. et al. (2019). "Photometric and Spectroscopic Properties of Type Ia Supernova 2018oh with Early Excess Emission from the Kepler 2 Observations". In: *ApJ* 870, 12, p. 12. DOI: 10.3847/1538-4357/aaec74. arXiv: 1811.10056 [astro-ph.SR].

Lien, A. Y. et al. (2014). "GRB 140705A: Swift-BAT refined analysis of a possible newly discovered SGR 1935+2154." In: *GRB Coordinates Network* 16522, p. 1.

Liller, W. et al. (1987). "The rate of nova production in the galaxy." In: *PASP* 99, pp. 606–609. DOI: 10.1086/132021.

Limongi, M. et al. (2003). "Evolution, Explosion, and Nucleosynthesis of Core-Collapse Supernovae". In: *ApJ* 592.1, pp. 404–433. DOI: 10.1086/375703. arXiv: astro-ph/0304185 [astro-ph].

Lin, L. et al. (2020a). "Burst Properties of the Most Recurring Transient Magnetar SGR J1935+2154". In: *ApJ* 893.2, 156, p. 156. DOI: 10.3847/1538-4357/ab818f. arXiv: 2003.10582 [astro-ph.HE].

Lin, L. et al. (2020b). "Stringent upper limits on pulsed radio emission during an active bursting phase of the Galactic magnetar SGRJ1935+2154". In: *arXiv e-prints*, arXiv:2005.11479, arXiv:2005.11479. arXiv: 2005.11479 [astro-ph.HE].

Liu, Y.-Q. et al. (2016). "Analyzing the Largest Spectroscopic Data Set of Stripped Supernovae to Improve Their Identifications and Constrain Their Progenitors". In: *ApJ* 827.2, 90, p. 90. DOI: 10.3847/0004-637X/827/2/90. arXiv: 1510.08049 [astro-ph.HE].

Livio, M. (1992). "White Dwarf Masses in Nova Systems and the Maximum-Magnitude vs. Rate-of-Decline Relation". In: *Cataclysmic Variable Stars*. Ed. by N. Vogt. Vol. 29. Astronomical Society of the Pacific Conference Series, p. 4.

Livne, E. et al. (1990). "Geometrical Effects in Off-Center Detonation of Helium Shells". In: *ApJ* 361, p. 244. DOI: 10.1086/169189.

Livne, E. et al. (1991). "Numerical Simulations of Off-Center Detonations in Helium Shells". In: *ApJ* 370, p. 272. DOI: 10.1086/169813.

Livne, E. et al. (1995). "Explosions of Sub–Chandrasekhar Mass White Dwarfs in Two Dimensions". In: *ApJ* 452, p. 62. DOI: 10.1086/176279.

Lourie, N. P. et al. (2020). "The wide-field infrared transient explorer (WINTER)". In: *Society of Photo-Optical Instrumentation Engineers (SPIE) Conference Series*. Vol. 11447. Society of Photo-Optical Instrumentation Engineers (SPIE) Conference Series, 114479K. DOI: 10.1117/12.2561210. arXiv: 2102.01109 [astro-ph.IM].

Lu, W. et al. (2018). "On the radiation mechanism of repeating fast radio bursts". In: *MNRAS* 477.2, pp. 2470–2493. DOI: 10.1093/mnras/sty716. arXiv: 1710.10270 [astro-ph.HE].

Lu, W. et al. (2020). "A unified picture of Galactic and cosmological fast radio bursts". In: *arXiv e-prints*, arXiv:2005.06736, arXiv:2005.06736. arXiv: 2005.06736 [astro-ph.HE].

Lucy, L. B. (1991). "Nonthermal Excitation of Helium in Type Ib Supernovae". In: *ApJ* 383, p. 308. DOI: 10.1086/170787.

Lunnan, R. et al. (2017). "Two New Calcium-rich Gap Transients in Group and Cluster Environments". In: *ApJ* 836, 60, p. 60. DOI: 10.3847/1538-4357/836/1/60. arXiv: 1612.00454 [astro-ph.HE].

Lyman, J. D. et al. (2013). "Environment-derived constraints on the progenitors of low-luminosity Type I supernovae". In: *MNRAS* 434, pp. 527–541. DOI: 10.1093/mnras/stt1038. arXiv: 1306.2474 [astro-ph.SR].

Lyman, J. D. et al. (2014). "The progenitors of calcium-rich transients are not formed in situ*". In: *MNRAS* 444, pp. 2157–2166. DOI: 10.1093/mnras/stu1574. arXiv: 1408.1424 [astro-ph.HE].

Lyman, J. D. et al. (2016a). "Bolometric light curves and explosion parameters of 38 stripped-envelope core-collapse supernovae". In: *MNRAS* 457, pp. 328–350. DOI: 10.1093/mnras/stv2983. arXiv: 1406.3667 [astro-ph.SR].

Lyman, J. D. et al. (2016b). "Hubble Space Telescope observations of the host galaxies and environments of calcium-rich supernovae". In: *MNRAS* 458, pp. 1768–1777. DOI: 10.1093/mnras/stw477. arXiv: 1602.08098 [astro-ph.HE].

Lyubarsky, Y. (2014). "A model for fast extragalactic radio bursts." In: *MNRAS* 442, pp. L9–L13. DOI: 10.1093/mnrasl/slu046. arXiv: 1401.6674 [astro-ph.HE].

Maccarone, T. J. et al. (2019). "Astro2020 Science White Paper: Populations of Black Holes in Binaries". In: *arXiv e-prints*, arXiv:1904.11842, arXiv:1904.11842. arXiv: 1904.11842 [astro-ph.HE].

MacFadyen, A. I. et al. (2001). "Supernovae, Jets, and Collapsars". In: *ApJ* 550, pp. 410–425. DOI: 10.1086/319698. eprint: astro-ph/9910034.

MacLeod, M. et al. (2014). "Illuminating Massive Black Holes with White Dwarfs: Orbital Dynamics and High-energy Transients from Tidal Interactions". In: *ApJ* 794, 9, p. 9. DOI: 10.1088/0004-637X/794/1/9. arXiv: 1405.1426 [astro-ph.HE].

MacLeod, M. et al. (2016). "Optical Thermonuclear Transients from Tidal Compression of White Dwarfs as Tracers of the Low End of the Massive Black Hole Mass Function". In: *ApJ* 819, 3, p. 3. DOI: 10.3847/0004-637X/819/1/3. arXiv: 1508.02399 [astro-ph.HE].

Maguire, K. et al. (2014). "Exploring the spectral diversity of low-redshift Type Ia supernovae using the Palomar Transient Factory". In: *MNRAS* 444, pp. 3258–3274. DOI: 10.1093/mnras/stu1607. arXiv: 1408.1430 [astro-ph.HE].

Mahabal, A. et al. (2019). "Machine Learning for the Zwicky Transient Facility". In: *PASP* 131.3, p. 038002. DOI: 10.1088/1538-3873/aaf3fa. arXiv: 1902.01936 [astro-ph.IM].

Mainzer, A. et al. (2011). "Preliminary Results from NEOWISE: An Enhancement to the Wide-field Infrared Survey Explorer for Solar System Science". In: *ApJ* 731.2, 53, p. 53. DOI: 10.1088/0004-637X/731/1/53. arXiv: 1102.1996 [astro-ph.EP].

Mainzer, A. et al. (2014). "Initial Performance of the NEOWISE Reactivation Mission". In: *ApJ* 792.1, 30, p. 30. DOI: 10.1088/0004-637X/792/1/30. arXiv: 1406.6025 [astro-ph.EP].

Mannucci, F. et al. (2003). "The infrared supernova rate in starburst galaxies". In: *A&A* 401, pp. 519–530. DOI: 10.1051/0004-6361:20030198. eprint: astro-ph/0302323.

Mannucci, F. et al. (2007). "How many supernovae are we missing at high redshift?" In: *MNRAS* 377, pp. 1229–1235. DOI: 10.1111/j.1365-2966.2007.11676.x. eprint: astro-ph/0702355.

Mannucci, F. et al. (2008). "The supernova rate in local galaxy clusters". In: *MNRAS* 383.3, pp. 1121–1130. DOI: 10.1111/j.1365-2966.2007.12603.x. arXiv: 0710.1094 [astro-ph].

Maoz, D. et al. (2014). "Observational Clues to the Progenitors of Type Ia Supernovae". In: *ARA&A* 52, pp. 107–170. DOI: 10.1146/annurev-astro-082812-141031. arXiv: 1312.0628 [astro-ph.CO].

Maraston, C. (2005). "Evolutionary population synthesis: models, analysis of the ingredients and application to high-z galaxies". In: *MNRAS* 362, pp. 799–825. DOI: 10.1111/j.1365-2966.2005.09270.x. eprint: astro-ph/0410207.

Margalit, B. et al. (2020). "Implications of a "Fast Radio Burst" from a Galactic Magnetar". In: *arXiv e-prints*, arXiv:2005.05283, arXiv:2005.05283. arXiv: 2005.05283 [astro-ph.HE].

Margalit, B. et al. (2016). "Time-dependent models of accretion discs with nuclear burning following the tidal disruption of a white dwarf by a neutron star". In: *MNRAS* 461, pp. 1154–1176. DOI: 10.1093/mnras/stw1410. arXiv: 1603.07334 [astro-ph.HE].

Margutti, R. et al. (2013). "The Signature of the Central Engine in the Weakest Relativistic Explosions: GRB 100316D". In: *ApJ* 778, 18, p. 18. DOI: 10.1088/0004-637X/778/1/18. arXiv: 1308.1687 [astro-ph.HE].

Marinacci, F. et al. (2018). "First results from the IllustrisTNG simulations: radio haloes and magnetic fields". In: *MNRAS* 480.4, pp. 5113–5139. DOI: 10.1093/mnras/sty2206. arXiv: 1707.03396 [astro-ph.CO].

Marino, R. A. et al. (2013). "The O3N2 and N2 abundance indicators revisited: improved calibrations based on CALIFA and T_e-based literature data". In: *A&A* 559, A114, A114. DOI: 10.1051/0004-6361/201321956. arXiv: 1307.5316.

Marion, G. H. et al. (2014). "Type IIb Supernova SN 2011dh: Spectra and Photometry from the Ultraviolet to the Near-infrared". In: *ApJ* 781.2, 69, p. 69. DOI: 10.1088/0004-637X/781/2/69. arXiv: 1303.5482 [astro-ph.SR].

Marion, G. H. et al. (2016). "SN˜2012cg: Evidence for Interaction Between a Normal Type Ia Supernova and a Non-degenerate Binary Companion". In: *ApJ* 820, 92, p. 92. DOI: 10.3847/0004-637X/820/2/92. arXiv: 1507.07261 [astro-ph.SR].

Marrese, P. M. et al. (2019). "Gaia Data Release 2. Cross-match with external catalogues: algorithms and results". In: *A&A* 621, A144, A144. DOI: 10.1051/0004-6361/201834142. arXiv: 1808.09151 [astro-ph.SR].

Martin, D. C. et al. (2014). "Intergalactic Medium Emission Observations with the Cosmic Web Imager. I. The Circum-QSO Medium of QSO 1549+19, and Evidence for a Filamentary Gas Inflow". In: *ApJ* 786, 106, p. 106. DOI: 10.1088/0004-637X/786/2/106. arXiv: 1402.4816.

Masci, F. J. et al. (2017). "The IPAC Image Subtraction and Discovery Pipeline for the Intermediate Palomar Transient Factory". In: *PASP* 129.1, p. 014002. DOI: 10.1088/1538-3873/129/971/014002. arXiv: 1608.01733 [astro-ph.IM].

Masci, F. J. et al. (2019). "The Zwicky Transient Facility: Data Processing, Products, and Archive". In: *PASP* 131.1, p. 018003. DOI: 10.1088/1538-3873/aae8ac. arXiv: 1902.01872 [astro-ph.IM].

Matheson, T. et al. (2000). "Optical Spectroscopy of Supernova 1993J During Its First 2500 Days". In: *AJ* 120.3, pp. 1487–1498. DOI: 10.1086/301518. arXiv: astro-ph/0006263 [astro-ph].

Mattila, S. et al. (2007). "Adaptive Optics Discovery of Supernova 2004ip in the Nuclear Regions of the Luminous Infrared Galaxy IRAS 18293-3413". In: *ApJL* 659.1, pp. L9–L12. DOI: 10.1086/516821. arXiv: astro-ph/0702591 [astro-ph].

Matuszewski, M. et al. (2010). "The Cosmic Web Imager: an integral field spectrograph for the Hale Telescope at Palomar Observatory: instrument design and first results". In: *Ground-based and Airborne Instrumentation for Astronomy III*. Vol. 7735. Proc. SPIE, 77350P. DOI: 10.1117/12.856644.

Matzner, C. D. et al. (1999). "The Expulsion of Stellar Envelopes in Core-Collapse Supernovae". In: *ApJ* 510, pp. 379–403. DOI: 10.1086/306571. eprint: astro-ph/9807046.

Mazzali, P. A. et al. (1993). "The application of Monte Carlo methods to the synthesis of early-time supernovae spectra". In: *A & A* 279, pp. 447–456.

McBrien, O. R. et al. (2019). "SN2018kzr: A Rapidly Declining Transient from the Destruction of a White Dwarf". In: *ApJL* 885.1, L23, p. L23. DOI: 10.3847/2041-8213/ab4dae. arXiv: 1909.04545 [astro-ph.HE].

McConnachie, A. W. (2012). "The Observed Properties of Dwarf Galaxies in and around the Local Group". In: *AJ* 144, 4, p. 4. DOI: 10.1088/0004-6256/144/1/4. arXiv: 1204.1562.

McGaugh, S. S. (1991). "H II region abundances - Model oxygen line ratios". In: *ApJ* 380, pp. 140–150. DOI: 10.1086/170569.

Mclaughlin, D. B. (1945). "The Relation between Light-Curves and Luminosities of Novae". In: *PASP* 57.335, p. 69. DOI: 10.1086/125689.

McLean, I. S. et al. (2012). "MOSFIRE, the multi-object spectrometer for infra-red exploration at the Keck Observatory". In: *Ground-based and Airborne Instrumentation for Astronomy IV*. Vol. 8446. Proc. SPIE, 84460J. DOI: 10.1117/12.924794.

McMahon, R. G. et al. (2013). "First Scientific Results from the VISTA Hemisphere Survey (VHS)". In: *The Messenger* 154, pp. 35–37.

McMillan, P. J. (2017). "The mass distribution and gravitational potential of the Milky Way". In: *MNRAS* 465.1, pp. 76–94. DOI: 10.1093/mnras/stw2759. arXiv: 1608.00971 [astro-ph.GA].

Meng, X. et al. (2015). "A pair of CO + He white dwarfs as the progenitor of 2005E-like supernovae?" In: *A&A* 573, A57, A57. DOI: 10.1051/0004-6361/201424562. arXiv: 1410.8630 [astro-ph.SR].

Mereghetti, S. et al. (2020). "INTEGRAL discovery of a burst with associated radio emission from the magnetar SGR 1935+2154". In: *arXiv e-prints*, arXiv:2005.06335, arXiv:2005.06335. arXiv: 2005.06335 [astro-ph.HE].

Mernier, F. et al. (2016). "Origin of central abundances in the hot intra-cluster medium. II. Chemical enrichment and supernova yield models". In: *A&A* 595, A126, A126. DOI: 10.1051/0004-6361/201628765. arXiv: 1608.03888 [astro-ph.GA].

Metzger, B. D. (2012). "Nuclear-dominated accretion and subluminous supernovae from the merger of a white dwarf with a neutron star or black hole". In: *MNRAS* 419, pp. 827–840. DOI: 10.1111/j.1365-2966.2011.19747.x. arXiv: 1105.6096 [astro-ph.HE].

Metzger, B. D. et al. (2019). "Fast radio bursts as synchrotron maser emission from decelerating relativistic blast waves". In: *MNRAS* 485.3, pp. 4091–4106. DOI: 10.1093/mnras/stz700. arXiv: 1902.01866 [astro-ph.HE].

Meynet, G. et al. (2005). "Stellar evolution with rotation. XI. Wolf-Rayet star populations at different metallicities". In: *A&A* 429, pp. 581–598. DOI: 10.1051/0004-6361:20047106. eprint: astro-ph/0408319.

Milisavljevic, D. et al. (2017). "iPTF15eqv: Multiwavelength Exposé of a Peculiar Calcium-rich Transient". In: *ApJ* 846, 50, p. 50. DOI: 10.3847/1538-4357/aa7d9f. arXiv: 1706.01887 [astro-ph.HE].

Miller, M. C. (2015). "Disk Winds as an Explanation for Slowly Evolving Temperatures in Tidal Disruption Events". In: *ApJ* 805, 83, p. 83. DOI: 10.1088/0004-637X/805/1/83. arXiv: 1502.03284.

Miluzio, M. et al. (2013). "HAWK-I infrared supernova search in starburst galaxies". In: *A&A* 554, A127, A127. DOI: 10.1051/0004-6361/201321192. arXiv: 1303.3803.

Miroshnichenko, A. S. (1988). "UBV Photometry of Novae - Determination of Interstellar Absorption". In: *Soviet Astronomy* 32, p. 298.

Modjaz, M. et al. (2016). "The Spectral SN-GRB Connection: Systematic Spectral Comparisons between Type Ic Supernovae and Broad-lined Type Ic Supernovae with and without Gamma-Ray Bursts". In: *ApJ* 832, 108, p. 108. DOI: 10.3847/0004-637X/832/2/108. arXiv: 1509.07124 [astro-ph.HE].

Moore, A. M. et al. (2016). "Unveiling the dynamic infrared sky with Gattini-IR". In: *Proc. SPIE*. Vol. 9906. Society of Photo-Optical Instrumentation Engineers (SPIE) Conference Series, p. 99062C. DOI: 10.1117/12.2233694. arXiv: 1608.04510 [astro-ph.IM].

Moore, A. M. et al. (2019). "Unveiling the dynamic infrared sky". In: *Nature Astronomy* 3, pp. 109–109. DOI: 10.1038/s41550-018-0675-x.

Moore, K. et al. (2013). "The Effects of Curvature and Expansion on Helium Detonations on White Dwarf Surfaces". In: *ApJ* 776.2, 97, p. 97. DOI: 10.1088/0004-637X/776/2/97. arXiv: 1308.4193 [astro-ph.SR].

Moriya, T. J. et al. (2016). "Rapidly evolving faint transients from stripped-envelope electron-capture supernovae". In: *MNRAS* 461, pp. 2155–2161. DOI: 10.1093/mnras/stw1471. arXiv: 1603.00033 [astro-ph.HE].

Moriya, T. J. et al. (2017). "Light-curve and spectral properties of ultrastripped core-collapse supernovae leading to binary neutron stars". In: *MNRAS* 466, pp. 2085–2098. DOI: 10.1093/mnras/stw3225. arXiv: 1612.02882 [astro-ph.HE].

Mróz, P. et al. (2015). "OGLE Atlas of Classical Novae. I. Galactic Bulge Objects". In: *ApJS* 219.2, 26, p. 26. DOI: 10.1088/0067-0049/219/2/26. arXiv: 1504.08224 [astro-ph.SR].

Mróz, P. et al. (2016). "OGLE Atlas of Classical Novae. II. Magellanic Clouds". In: *ApJS* 222.1, 9, p. 9. DOI: 10.3847/0067-0049/222/1/9. arXiv: 1511.06355 [astro-ph.SR].

Mulchaey, J. S. et al. (2014). "Calcium-rich Gap Transients: Solving the Calcium Conundrum in the Intracluster Medium". In: *ApJL* 780, L34, p. L34. DOI: 10.1088/2041-8205/780/2/L34. arXiv: 1401.7017.

Mullan, B. et al. (2011). "Star Clusters in the Tidal Tails of Interacting Galaxies: Cluster Populations Across a Variety of Tail Environments". In: *ApJ* 731, 93, p. 93. DOI: 10.1088/0004-637X/731/2/93. arXiv: 1101.5393.

Müller, B. et al. (2018). "Multi-D Simulations of Ultra-Stripped Supernovae to Shock Breakout". In: *ArXiv e-prints*. arXiv: 1803.03388 [astro-ph.SR].

Munari, U. et al. (1997). "Equivalent width of NA I and K I lines and reddening." In: *A&A* 318, pp. 269–274.

Munari, U. et al. (2019). "The reddening and distance to recurrent nova V3890 Sgr from interstellar features". In: *The Astronomer's Telegram* 13069, p. 1.

Munari, U. et al. (2020). "Classification of TCP J04291884+4354232 as a classical nova". In: *The Astronomer's Telegram* 14224, p. 1.

Naiman, J. P. et al. (2018). "First results from the IllustrisTNG simulations: a tale of two elements - chemical evolution of magnesium and europium". In: *MNRAS* 477.1, pp. 1206–1224. DOI: 10.1093/mnras/sty618. arXiv: 1707.03401 [astro-ph.GA].

Nakaoka, T. et al. (2020). "Calcium-rich Transient SN 2019ehk in A Star-Forming Environment: Yet Another Candidate for An Ultra-Stripped Envelope Supernova". In: *arXiv e-prints*, arXiv:2005.02992, arXiv:2005.02992. arXiv: 2005.02992 [astro-ph.HE].

Nakar, E. et al. (2014). "Supernovae with Two Peaks in the Optical Light Curve and the Signature of Progenitors with Low-mass Extended Envelopes". In: *ApJ* 788, 193, p. 193. DOI: 10.1088/0004-637X/788/2/193. arXiv: 1401.7013 [astro-ph.HE].

Neill, J. D. et al. (2009). "The Local Hosts of Type Ia Supernovae". In: *ApJ* 707.2, pp. 1449–1465. DOI: 10.1088/0004-637X/707/2/1449. arXiv: 0911.0690 [astro-ph.CO].

Nelemans, G. (2005). "AM CVn stars". In: *The Astrophysics of Cataclysmic Variables and Related Objects*. Ed. by J. .-.-M. Hameury et al. Vol. 330. Astronomical Society of the Pacific Conference Series, p. 27. arXiv: astro-ph/0409676 [astro-ph].

Nelemans, G. et al. (2004). "Short-period AM CVn systems as optical, X-ray and gravitational-wave sources". In: *MNRAS* 349.1, pp. 181–192. DOI: 10.1111/j.1365-2966.2004.07479.x. arXiv: astro-ph/0312193 [astro-ph].

Nelson, D. et al. (2019). "The IllustrisTNG simulations: public data release". In: *Computational Astrophysics and Cosmology* 6.1, 2, p. 2. DOI: 10.1186/s40668-019-0028-x. arXiv: 1812.05609 [astro-ph.GA].

Neugebauer, G. et al. (1969). *Two-micron sky survey. A preliminary catalogue*.

Niino, Y. et al. (2020). "No optical bursts detected from SGR J1935+2154 by 24 fps observations with Tomo-e Gozen". In: *GRB Coordinates Network* 27678, p. 1.

Nomoto, K. (1980). "White dwarf models for type 1 supernovae and quiet supernovae, and presupernova evolution". In: *Space Sci. Rev.* 27, pp. 563–570. DOI: 10.1007/BF00168350.

Nomoto, K. (1982a). "Accreting white dwarf models for type 1 supernovae. II - Off-center detonation supernovae". In: *ApJ* 257, pp. 780–792. DOI: 10.1086/160031.

Nomoto, K. (1982b). "Accreting white dwarf models for type I supernovae. I - Presupernova evolution and triggering mechanisms". In: *ApJ* 253, pp. 798–810. DOI: 10.1086/159682.

Nomoto, K. (1984). "Evolution of 8-10 solar mass stars toward electron capture supernovae. I - Formation of electron-degenerate O + Ne + Mg cores". In: *ApJ* 277, pp. 791–805. DOI: 10.1086/161749.

Nomoto, K. et al. (1994). "A carbon-oxygen star as progenitor of the type Ic supernova 1994I". In: *Nature* 371, pp. 227–229. DOI: 10.1038/371227a0.

Nomoto, K. et al. (1997). "Nucleosynthesis in type II supernovae". In: *Nucl. Phys. A* 616, pp. 79–90. DOI: 10.1016/S0375-9474(97)00076-6. arXiv: astro-ph/9706024 [astro-ph].

Nomoto, K. et al. (2013). "Nucleosynthesis in Stars and the Chemical Enrichment of Galaxies". In: *ARA&A* 51, pp. 457–509. DOI: 10.1146/annurev-astro-082812-140956.

Nordin, J. et al. (2019a). "Transient processing and analysis using AMPEL: alert management, photometry, and evaluation of light curves". In: *A&A* 631, A147, A147. DOI: 10.1051/0004-6361/201935634. arXiv: 1904.05922 [astro-ph.IM].

Nordin, J. et al. (2019b). "ZTF Transient Discovery Report for 2019-08-23". In: *Transient Name Server Discovery Report* 2019-1594, p. 1.

Nugent, P. E. et al. (2011). "Supernova SN 2011fe from an exploding carbon-oxygen white dwarf star". In: *Nature* 480, pp. 344–347. DOI: 10.1038/nature10644. arXiv: 1110.6201.

Nugent, P. et al. (1997). "Synthetic Spectra of Hydrodynamic Models of Type Ia Supernovae". In: *ApJ* 485, pp. 812–819. DOI: 10.1086/304459. eprint: astro-ph/9612044.

Ofek, E. O. et al. (2012). "The Palomar Transient Factory Photometric Calibration". In: *PASP* 124, p. 62. DOI: 10.1086/664065. arXiv: 1112.4851 [astro-ph.IM].

Ofek, E. O. et al. (2013). "SN 2009ip: Constraints on the Progenitor Mass-loss Rate". In: *ApJ* 768, 47, p. 47. DOI: 10.1088/0004-637X/768/1/47. arXiv: 1303.3894 [astro-ph.HE].

Oke, J. B. et al. (1982). "An Efficient Low Resolution and Moderate Resolution Spectrograph for the Hale Telescope". In: *PASP* 94, p. 586. DOI: 10.1086/131027.

Oke, J. B. et al. (1995). "The Keck Low-Resolution Imaging Spectrometer". In: *PASP* 107, p. 375. DOI: 10.1086/133562.

Osterbrock, D. E. et al. (2006). *Astrophysics of gaseous nebulae and active galactic nuclei*.

Ozdonmez, A. et al. (2016). "The distances of the Galactic novae". In: *MNRAS* 461.2, pp. 1177–1201. DOI: 10.1093/mnras/stw1362. arXiv: 1606.01907 [astro-ph.SR].

Ozdonmez, A. et al. (2018). "A new catalogue of Galactic novae: investigation of the MMRD relation and spatial distribution". In: *MNRAS* 476.3, pp. 4162–4186. DOI: 10.1093/mnras/sty432. arXiv: 1802.05725 [astro-ph.SR].

Page, K. L. et al. (2020). "The 2019 eruption of recurrent nova V3890 Sgr: observations by Swift, NICER, and SMARTS". In: *MNRAS* 499.4, pp. 4814–4831. DOI: 10.1093/mnras/staa3083. arXiv: 2010.01001 [astro-ph.HE].

Pakmor, R. et al. (2013). "Helium-ignited Violent Mergers as a Unified Model for Normal and Rapidly Declining Type Ia Supernovae". In: *ApJL* 770.1, L8, p. L8. DOI: 10.1088/2041-8205/770/1/L8. arXiv: 1302.2913 [astro-ph.HE].

Palmer, D. M. et al. (2020). "A Forest of Bursts from SGR 1935+2154". In: *GRB Coordinates Network* 27665, p. 1.

Patterson, M. T. et al. (2019). "The Zwicky Transient Facility Alert Distribution System". In: *PASP* 131.1, p. 018001. DOI: 10.1088/1538-3873/aae904. arXiv: 1902.02227 [astro-ph.IM].

Pen, U.-L. et al. (2015). "Local Circumnuclear Magnetar Solution to Extragalactic Fast Radio Bursts". In: *ApJ* 807.2, 179, p. 179. DOI: 10.1088/0004-637X/807/2/179. arXiv: 1501.01341 [astro-ph.HE].

Perets, H. B. et al. (2010). "A faint type of supernova from a white dwarf with a helium-rich companion". In: *Nature* 465, pp. 322–325. DOI: 10.1038/nature09056. arXiv: 0906.2003 [astro-ph.HE].

Perets, H. B. (2014). "Origin of the Galactic 511 keV emission from positrons produced in irregular supernovae". In: *arXiv e-prints*, arXiv:1407.2254, arXiv:1407.2254. arXiv: 1407.2254 [astro-ph.HE].

Perets, H. B. et al. (2011). "The Old Environment of the Faint Calcium-rich Supernova SN 2005cz". In: *ApJL* 728.2, L36, p. L36. DOI: 10.1088/2041-8205/728/2/L36. arXiv: 1012.0570 [astro-ph.HE].

Perets, H. B. et al. (2021). "No velocity-kicks are required to explain large-distance offsets of Ca-rich supernovae and short-GRBs". In: *arXiv e-prints*, arXiv:2101.11622, arXiv:2101.11622. arXiv: 2101.11622 [astro-ph.HE].

Perley, D. A. et al. (2014). "The Afterglow of GRB 130427A from 1 to 10^{16} GHz". In: *ApJ* 781, 37, p. 37. DOI: 10.1088/0004-637X/781/1/37. arXiv: 1307.4401 [astro-ph.HE].

Perley, D. A. (2019). "Fully Automated Reduction of Longslit Spectroscopy with the Low Resolution Imaging Spectrometer at the Keck Observatory". In: *PASP* 131.1002, p. 084503. DOI: 10.1088/1538-3873/ab215d. arXiv: 1903.07629 [astro-ph.IM].

Petroff, E. et al. (2019). "Fast radio bursts". In: *A&A Rev.* 27.1, 4, p. 4. DOI: 10.1007/s00159-019-0116-6. arXiv: 1904.07947 [astro-ph.HE].

Pettini, M. et al. (2004). "[OIII]/[NII] as an abundance indicator at high redshift". In: *MNRAS* 348, pp. L59–L63. DOI: 10.1111/j.1365-2966.2004.07591.x. eprint: astro-ph/0401128.

Pfahl, E. et al. (2009). "Globular Clusters as Testbeds for Type Ia Supernovae". In: *ApJL* 695.1, pp. L111–L114. DOI: 10.1088/0004-637X/695/1/L111. arXiv: 0903.1104 [astro-ph.SR].

Phillips, M. M. (1993). "The Absolute Magnitudes of Type IA Supernovae". In: *ApJL* 413, p. L105. DOI: 10.1086/186970.

Phillips, M. M. et al. (2007). "The Peculiar SN 2005hk: Do Some Type Ia Supernovae Explode as Deflagrations?1," in: *PASP* 119.854, pp. 360–387. DOI: 10.1086/518372. arXiv: astro-ph/0611295 [astro-ph].

Phinney, E. S. (1989). "Manifestations of a Massive Black Hole in the Galactic Center". In: *The Center of the Galaxy*. Ed. by M. Morris. Vol. 136. IAU Symposium, p. 543.

Pian, E. et al. (2017). "Spectroscopic identification of r-process nucleosynthesis in a double neutron-star merger". In: *Nature* 551, pp. 67–70. DOI: 10.1038/nature24298. arXiv: 1710.05858 [astro-ph.HE].

Piran, T. et al. (2005). "Origin of the Binary Pulsar J0737-3039B". In: *Physical Review Letters* 94.5, 051102, p. 051102. DOI: 10.1103/PhysRevLett.94.051102. arXiv: astro-ph/0409651 [astro-ph].

Piro, A. L. (2015). "Using Double-peaked Supernova Light Curves to Study Extended Material". In: *ApJL* 808, L51, p. L51. DOI: 10.1088/2041-8205/808/2/L51. arXiv: 1505.07103 [astro-ph.HE].

Piro, A. L. et al. (2014a). "Constraints on Shallow ^{56}Ni from the Early Light Curves of Type Ia Supernovae". In: *ApJ* 784, 85, p. 85. DOI: 10.1088/0004-637X/784/1/85. arXiv: 1211.6438 [astro-ph.HE].

Piro, A. L. et al. (2014b). "Transparent Helium in Stripped Envelope Supernovae". In: *ApJL* 792, L11, p. L11. DOI: 10.1088/2041-8205/792/1/L11. arXiv: 1407.5992 [astro-ph.HE].

Piro, A. L. et al. (2016). "Exploring the Potential Diversity of Early Type Ia Supernova Light Curves". In: *ApJ* 826, 96, p. 96. DOI: 10.3847/0004-637X/826/1/96. arXiv: 1512.03442 [astro-ph.HE].

Piro, A. L. et al. (2017). "Numerically Modeling the First Peak of the Type IIb SN 2016gkg". In: *ApJ* 846, 94, p. 94. DOI: 10.3847/1538-4357/aa8595. arXiv: 1703.00913 [astro-ph.HE].

Podsiadlowski, P. (2001). "Common-Envelope Evolution and Stellar Mergers". In: *Evolution of Binary and Multiple Star Systems*. Ed. by P. Podsiadlowski et al. Vol. 229. Astronomical Society of the Pacific Conference Series, p. 239.

Podsiadlowski, P. et al. (1992). "Presupernova Evolution in Massive Interacting Binaries". In: *ApJ* 391, p. 246. DOI: 10.1086/171341.

Podsiadlowski, P. et al. (2003). "Cataclysmic variables with evolved secondaries and the progenitors of AM CVn stars". In: *MNRAS* 340.4, pp. 1214–1228. DOI: 10.1046/j.1365-8711.2003.06380.x.

Podsiadlowski, P. et al. (2004). "The Effects of Binary Evolution on the Dynamics of Core Collapse and Neutron Star Kicks". In: *ApJ* 612, pp. 1044–1051. DOI: 10.1086/421713. eprint: astro-ph/0309588.

Pogrosheva, T. et al. (2020). "MASTER Transient Discovery Report for 2020-05-23". In: *Transient Name Server Discovery Report* 2020-1462, p. 1.

Polin, A. et al. (2019). "Observational Predictions for Sub-Chandrasekhar Mass Explosions: Further Evidence for Multiple Progenitor Systems for Type Ia Supernovae". In: *ApJ* 873.1, 84, p. 84. DOI: 10.3847/1538-4357/aafb6a. arXiv: 1811.07127 [astro-ph.HE].

Polin, A. et al. (2021). "Nebular Models of Sub-Chandrasekhar Mass Type Ia Supernovae: Clues to the Origin of Ca-rich Transients". In: *ApJ* 906.1, 65, p. 65. DOI: 10.3847/1538-4357/abcccc. arXiv: 1910.12434 [astro-ph.HE].

Postnov, K. A. et al. (2014). "The Evolution of Compact Binary Star Systems". In: *Living Reviews in Relativity* 17.1, 3, p. 3. DOI: 10.12942/lrr-2014-3. arXiv: 1403.4754 [astro-ph.HE].

Poznanski, D. et al. (2012). "An empirical relation between sodium absorption and dust extinction". In: *MNRAS* 426.2, pp. 1465–1474. DOI: 10.1111/j.1365-2966.2012.21796.x. arXiv: 1206.6107 [astro-ph.IM].

Poznanski, D. et al. (2010). "An Unusually Fast-Evolving Supernova". In: *Science* 327, p. 58. DOI: 10.1126/science.1181709. arXiv: 0911.2699 [astro-ph.SR].

Prantzos, N. (2012). "Production and evolution of Li, Be, and B isotopes in the Galaxy". In: *A&A* 542, A67, A67. DOI: 10.1051/0004-6361/201219043. arXiv: 1203.5662 [astro-ph.GA].

Predehl, P. et al. (2021). "The eROSITA X-ray telescope on SRG". In: *A&A* 647, A1, A1. DOI: 10.1051/0004-6361/202039313. arXiv: 2010.03477 [astro-ph.HE].

Prentice, S. J. et al. (2020). "The rise and fall of an extraordinary Ca-rich transient. The discovery of ATLAS19dqr/SN 2019bkc". In: *A&A* 635, A186, A186. DOI: 10.1051/0004-6361/201936515. arXiv: 1909.05567 [astro-ph.HE].

Prieto, J. L. et al. (2008). "Characterizing Supernova Progenitors via the Metallicities of their Host Galaxies, from Poor Dwarfs to Rich Spirals". In: *ApJ* 673, 999-1008, pp. 999–1008. DOI: 10.1086/524654. arXiv: 0707.0690.

Quataert, E. et al. (2012). "Wave-driven mass loss in the last year of stellar evolution: setting the stage for the most luminous core-collapse supernovae". In: *MNRAS* 423, pp. L92–L96. DOI: 10.1111/j.1745-3933.2012.01264.x. arXiv: 1202.5036 [astro-ph.SR].

Raghavan, D. et al. (2010). "A Survey of Stellar Families: Multiplicity of Solar-type Stars". In: *ApJS* 190.1, pp. 1–42. DOI: 10.1088/0067-0049/190/1/1. arXiv: 1007.0414 [astro-ph.SR].

Rahmer, G. et al. (2008). "The 12K×8K CCD mosaic camera for the Palomar Transient Factory". In: *Ground-based and Airborne Instrumentation for Astronomy II*. Vol. 7014. Proceedings of SPIE, 70144Y. DOI: 10.1117/12.788086.

Ramsay, G. et al. (2018). "Physical properties of AM CVn stars: New insights from Gaia DR2". In: *A&A* 620, A141, A141. DOI: 10.1051/0004-6361/201834261. arXiv: 1810.06548 [astro-ph.SR].

Rau, A. et al. (2009). "Exploring the Optical Transient Sky with the Palomar Transient Factory". In: *PASP* 121, p. 1334. DOI: 10.1086/605911. arXiv: 0906.5355 [astro-ph.CO].

Rauscher, T. et al. (2002). "Nucleosynthesis in Massive Stars with Improved Nuclear and Stellar Physics". In: *ApJ* 576.1, pp. 323–348. DOI: 10.1086/341728. arXiv: astro-ph/0112478 [astro-ph].

Rayner, J. T. et al. (2003). "SpeX: A Medium-Resolution 0.8-5.5 Micron Spectrograph and Imager for the NASA Infrared Telescope Facility". In: *PASP* 115.805, pp. 362–382. DOI: 10.1086/367745.

Rea, N. et al. (2004). "Correlated Infrared and X-ray variability of the transient Anomalous X-ray Pulsar XTE J1810-197". In: *A&A* 425, pp. L5–L8. DOI: 10.1051/0004-6361:200400052. arXiv: astro-ph/0408087 [astro-ph].

Read, A. M. et al. (2007). "XMM-Newton Slew Survey discovers a new, bright X-ray transient XMMSL1 J070542.7-381442". In: *The Astronomer's Telegram* 1282, p. 1.

Rebull, L. M. et al. (2014). "Young Stellar Object VARiability (YSOVAR): Long Timescale Variations in the Mid-infrared". In: *AJ* 148.5, 92, p. 92. DOI: 10.1088/0004-6256/148/5/92. arXiv: 1408.6756 [astro-ph.SR].

Reddy, S. H. et al. (2017). "A Wideband Digital Back-End for the Upgraded GMRT". In: *Journal of Astronomical Instrumentation* 6, 1641011-336, pp. 1641011–336. DOI: 10.1142/S2251171716410117.

Renaud, F. et al. (2009). "Fully Compressive Tides in Galaxy Mergers". In: *ApJ* 706, pp. 67–82. DOI: 10.1088/0004-637X/706/1/67. arXiv: 0910.0196.

Richmond, M. W. et al. (1996). "UBVRI Photometry of the Type IC SN 1994I in M51". In: *AJ* 111, p. 327. DOI: 10.1086/117785.

Ridnaia, A. et al. (2020). "A peculiar hard X-ray counterpart of a Galactic fast radio burst". In: *arXiv e-prints*, arXiv:2005.11178, arXiv:2005.11178. arXiv: 2005.11178 [astro-ph.HE].

Rieke, G. H. et al. (1985). "The interstellar extinction law from 1 to 13 microns." In: *ApJ* 288, pp. 618–621. DOI: 10.1086/162827.

Rigault, M. et al. (2019). "Fully automated integral field spectrograph pipeline for the SEDMachine: pysedm". In: *A&A* 627, A115, A115. DOI: 10.1051/0004-6361/201935344. arXiv: 1902.08526 [astro-ph.IM].

Roelofs, G. H. A. et al. (2007). "The population of AM CVn stars from the Sloan Digital Sky Survey". In: *MNRAS* 382.2, pp. 685–692. DOI: 10.1111/j.1365-2966.2007.12451.x. arXiv: 0709.2951 [astro-ph].

Romano, D. et al. (2003). "Nova nucleosynthesis and Galactic evolution of the CNO isotopes". In: *MNRAS* 342.1, pp. 185–198. DOI: 10.1046/j.1365-8711.2003.06526.x. arXiv: astro-ph/0302233 [astro-ph].

Romano, P. (2015). "Seven years with the Swift Supergiant Fast X-ray Transients project". In: *Journal of High Energy Astrophysics* 7, pp. 126–136. DOI: 10.1016/j.jheap.2015.04.008. arXiv: 1504.07249 [astro-ph.HE].

Roming, P. W. A. et al. (2005). "The Swift Ultra-Violet/Optical Telescope". In: *Space Science Reviews* 120, pp. 95–142. DOI: 10.1007/s11214-005-5095-4. eprint: astro-ph/0507413.

Rosswog, S. et al. (2008). "Atypical Thermonuclear Supernovae from Tidally Crushed White Dwarfs". In: *ApJ* 679, 1385-1389, pp. 1385–1389. DOI: 10.1086/528738. arXiv: 0712.2513.

Rosswog, S. et al. (2009). "Tidal Disruption and Ignition of White Dwarfs by Moderately Massive Black Holes". In: *ApJ* 695, pp. 404–419. DOI: 10.1088/0004-637X/695/1/404. arXiv: 0808.2143.

Sagiv, I. et al. (2014). "Science with a Wide-field UV Transient Explorer". In: *AJ* 147.4, 79, p. 79. DOI: 10.1088/0004-6256/147/4/79. arXiv: 1303.6194 [astro-ph.CO].

Saito, R. K. et al. (2012). "VVV-NOV-001: the first Galactic nova candidate discovered by the VVV Survey in the Milky Way bulge". In: *The Astronomer's Telegram* 4426, p. 1.

Saito, R. K. et al. (2013a). "A near-infrared catalogue of the Galactic novae in the VVV survey area". In: *A&A* 554, A123, A123. DOI: 10.1051/0004-6361/201321260. arXiv: 1304.2673 [astro-ph.GA].

Saito, R. K. et al. (2013b). "VVV-NOV-002: the second Galactic nova candidate discovered in the Milky Way bulge by the VVV Survey". In: *The Astronomer's Telegram* 4830, p. 1.

Salas, P. et al. (2013). "SN 2007bg: the complex circumstellar medium around one of the most radio-luminous broad-lined Type Ic supernovae". In: *MNRAS* 428, pp. 1207–1217. DOI: 10.1093/mnras/sts104. arXiv: 1208.3455 [astro-ph.HE].

Samsing, J. et al. (2017). "Formation of Tidal Captures and Gravitational Wave Inspirals in Binary-single Interactions". In: *ApJ* 846.1, 36, p. 36. DOI: 10.3847/1538-4357/aa7e32. arXiv: 1609.09114 [astro-ph.HE].

Sana, H. et al. (2012). "Binary Interaction Dominates the Evolution of Massive Stars". In: *Science* 337, p. 444. DOI: 10.1126/science.1223344. arXiv: 1207.6397 [astro-ph.SR].

Sander, A. et al. (2012). "The Galactic WC stars. Stellar parameters from spectral analyses indicate a new evolutionary sequence". In: *A&A* 540, A144, A144. DOI: 10.1051/0004-6361/201117830. arXiv: 1201.6354 [astro-ph.SR].

Sanders, N. E. et al. (2012). "A Spectroscopic Study of Type Ibc Supernova Host Galaxies from Untargeted Surveys". In: *ApJ* 758, 132, p. 132. DOI: 10.1088/0004-637X/758/2/132. arXiv: 1206.2643 [astro-ph.HE].

Sanders, N. E. et al. (2013). "Using Colors to Improve Photometric Metallicity Estimates for Galaxies". In: *ApJ* 775, 125, p. 125. DOI: 10.1088/0004-637X/775/2/125. arXiv: 1210.5520 [astro-ph.CO].

Sapir, N. et al. (2017). "UV/Optical Emission from the Expanding Envelopes of Type II Supernovae". In: *ApJ* 838, 130, p. 130. DOI: 10.3847/1538-4357/aa64df. arXiv: 1607.03700 [astro-ph.HE].

Saviane, I. et al. (2004). "The Stellar Content of the Southern Tail of NGC 4038/4039 and a Revised Distance". In: *AJ* 127, pp. 660–678. DOI: 10.1086/381059. eprint: astro-ph/0311200.

Schaefer, B. E. (2010). "Comprehensive Photometric Histories of All Known Galactic Recurrent Novae". In: *ApJS* 187.2, pp. 275–373. DOI: 10.1088/0067-0049/187/2/275. arXiv: 0912.4426 [astro-ph.SR].

Schaefer, B. E. (2014). "Nova Discovery Efficiency 1890-2014; Only 43%±6% of the Brightest Nova Are Discovered". In: *American Astronomical Society Meeting Abstracts #224*. Vol. 224. American Astronomical Society Meeting Abstracts, p. 306.04.

Schaefer, B. E. (2018). "The distances to Novae as seen by Gaia". In: *MNRAS* 481.3, pp. 3033–3051. DOI: 10.1093/mnras/sty2388. arXiv: 1809.00180 [astro-ph.SR].

Schlafly, E. F. et al. (2011). "Measuring Reddening with Sloan Digital Sky Survey Stellar Spectra and Recalibrating SFD". In: *ApJ* 737.2, 103, p. 103. DOI: 10.1088/0004-637X/737/2/103. arXiv: 1012.4804 [astro-ph.GA].

Schwab, J. (2019). "Evolutionary Models for R Coronae Borealis Stars". In: *ApJ* 885.1, 27, p. 27. DOI: 10.3847/1538-4357/ab425d. arXiv: 1909.02569 [astro-ph.SR].

Scolnic, D. M. et al. (2018). "The Complete Light-curve Sample of Spectroscopically Confirmed SNe Ia from Pan-STARRS1 and Cosmological Constraints from the Combined Pantheon Sample". In: *ApJ* 859, 101, p. 101. DOI: 10.3847/1538-4357/aab9bb. arXiv: 1710.00845.

Sell, P. H. et al. (2015). "Calcium-rich gap transients: tidal detonations of white dwarfs?" In: *MNRAS* 450, pp. 4198–4206. DOI: 10.1093/mnras/stv902. arXiv: 1504.05584 [astro-ph.HE].

Sell, P. H. et al. (2018). "Chandra X-ray constraints on the candidate Ca-rich gap transient SN 2016hnk". In: *MNRAS* 475.1, pp. L111–L115. DOI: 10.1093/mnrasl/sly011. arXiv: 1712.02799 [astro-ph.HE].

Selvelli, P. et al. (2019). "A UV and optical study of 18 old novae with Gaia DR2 distances: mass accretion rates, physical parameters, and MMRD". In: *A&A* 622, A186, A186. DOI: 10.1051/0004-6361/201834238. arXiv: 1903.05868 [astro-ph.SR].

Shafter, A. W. (1997). "On the Nova Rate in the Galaxy". In: *ApJ* 487.1, pp. 226–236. DOI: 10.1086/304609.

Shafter, A. W. (2017). "The Galactic Nova Rate Revisited". In: *ApJ* 834.2, 196, p. 196. DOI: 10.3847/1538-4357/834/2/196. arXiv: 1606.02358 [astro-ph.SR].

Shafter, A. W. et al. (2000). "Novae in External Galaxies: M51, M87, and M101". In: *ApJ* 530.1, pp. 193–206. DOI: 10.1086/308349.

Shafter, A. W. et al. (2009). "M31N 2007-11d: A Slowly Rising, Luminous Nova in M31". In: *ApJ* 690.2, pp. 1148–1157. DOI: 10.1088/0004-637X/690/2/1148. arXiv: 0809.1388 [astro-ph].

Shafter, A. W. et al. (2015). "Recurrent Novae in M31". In: *ApJS* 216.2, 34, p. 34. DOI: 10.1088/0067-0049/216/2/34. arXiv: 1412.8510 [astro-ph.SR].

Shafter, A. W. (2002). "The Galactic Nova Rate". In: *Classical Nova Explosions*. Ed. by M. Hernanz et al. Vol. 637. American Institute of Physics Conference Series, pp. 462–471. DOI: 10.1063/1.1518246.

Shafter, A. W. et al. (2001). "On the Spatial Distribution, Stellar Population, and Rate of Novae in M31". In: *ApJ* 563.2, pp. 749–767. DOI: 10.1086/324044.

Shappee, B. J. et al. (2014). "The Man behind the Curtain: X-Rays Drive the UV through NIR Variability in the 2013 Active Galactic Nucleus Outburst in NGC 2617". In: *ApJ* 788.1, 48, p. 48. DOI: 10.1088/0004-637X/788/1/48. arXiv: 1310.2241 [astro-ph.HE].

Shappee, B. J. et al. (2019). "Seeing Double: ASASSN-18bt Exhibits a Two-component Rise in the Early-time K2 Light Curve". In: *ApJ* 870, 13, p. 13. DOI: 10.3847/1538-4357/aaec79. arXiv: 1807.11526 [astro-ph.HE].

Shara, M. M. (1981). "A theoretical explanation of the absolute magnitude-decline time /M_{B-t} sub 3/ relationship for classical novae". In: *ApJ* 243, pp. 926–934. DOI: 10.1086/158657.

Shara, M. M. et al. (2016). "A Hubble Space Telescope Survey for Novae in M87. I. Light and Color Curves, Spatial Distributions, and the Nova Rate". In: *ApJS* 227.1, 1, p. 1. DOI: 10.3847/0067-0049/227/1/1. arXiv: 1602.00758 [astro-ph.SR].

Shara, M. M. et al. (2017). "A Hubble Space Telescope Survey for Novae in M87. II. Snuffing out the Maximum Magnitude-Rate of Decline Relation for Novae as a Non-standard Candle, and a Prediction of the Existence of Ultrafast Novae". In: *ApJ* 839.2, 109, p. 109. DOI: 10.3847/1538-4357/aa65cd. arXiv: 1702.05788 [astro-ph.SR].

Sharov, A. S. (1972). "Estimate for the Frequency of Novae in the Andromeda Nebula and our Galaxy." In: *Soviet Astronomy* 16, p. 41.

Shen, K. J. et al. (2010). "Thermonuclear .Ia Supernovae from Helium Shell Detonations: Explosion Models and Observables". In: *ApJ* 715, pp. 767–774. DOI: 10.1088/0004-637X/715/2/767. arXiv: 1002.2258 [astro-ph.HE].

Shen, K. J. et al. (2014a). "The Ignition of Carbon Detonations via Converging Shock Waves in White Dwarfs". In: *ApJ* 785, 61, p. 61. DOI: 10.1088/0004-637X/785/1/61. arXiv: 1305.6925 [astro-ph.HE].

Shen, K. J. et al. (2014b). "The Initiation and Propagation of Helium Detonations in White Dwarf Envelopes". In: *ApJ* 797, 46, p. 46. DOI: 10.1088/0004-637X/797/1/46. arXiv: 1409.3568 [astro-ph.HE].

Shen, K. J. et al. (2018). "Sub-Chandrasekhar-mass White Dwarf Detonations Revisited". In: *ApJ* 854, 52, p. 52. DOI: 10.3847/1538-4357/aaa8de. arXiv: 1706.01898 [astro-ph.HE].

Shen, K. J. et al. (2009). "Unstable Helium Shell Burning on Accreting White Dwarfs". In: *ApJ* 699.2, pp. 1365–1373. DOI: 10.1088/0004-637X/699/2/1365. arXiv: 0903.0654 [astro-ph.HE].

Shen, K. J. et al. (2019). "The Progenitors of Calcium-strong Transients". In: *ApJ* 887.2, 180, p. 180. DOI: 10.3847/1538-4357/ab5370. arXiv: 1908.08056 [astro-ph.HE].

Shiode, J. H. et al. (2014). "Setting the Stage for Circumstellar Interaction in Core-Collapse Supernovae. II. Wave-driven Mass Loss in Supernova Progenitors". In: *ApJ* 780, 96, p. 96. DOI: 10.1088/0004-637X/780/1/96. arXiv: 1308.5978 [astro-ph.SR].

Silverman, J. M. et al. (2009). "Optical Spectroscopy of the Somewhat Peculiar Type IIb Supernova 2001ig". In: *PASP* 121.881, p. 689. DOI: 10.1086/603653. arXiv: 0903.4179 [astro-ph.CO].

Silverman, J. M. et al. (2012). "Berkeley Supernova Ia Program - I. Observations, data reduction and spectroscopic sample of 582 low-redshift Type Ia supernovae". In: *MNRAS* 425.3, pp. 1789–1818. DOI: 10.1111/j.1365-2966.2012.21270.x. arXiv: 1202.2128 [astro-ph.CO].

Sim, S. A. et al. (2010). "Detonations in Sub-Chandrasekhar-mass C+O White Dwarfs". In: *ApJL* 714, pp. L52–L57. DOI: 10.1088/2041-8205/714/1/L52. arXiv: 1003.2917 [astro-ph.HE].

Sim, S. A. et al. (2012). "2D simulations of the double-detonation model for thermonuclear transients from low-mass carbon-oxygen white dwarfs". In: *MNRAS* 420, pp. 3003–3016. DOI: 10.1111/j.1365-2966.2011.20162.x. arXiv: 1111.2117 [astro-ph.HE].

Simcoe, R. A. et al. (2019). "Background-limited Imaging in the Near Infrared with Warm InGaAs Sensors: Applications for Time-domain Astronomy". In: *AJ* 157.2, 46, p. 46. DOI: 10.3847/1538-3881/aae094. arXiv: 1805.08791 [astro-ph.IM].

Skrutskie, M. F. et al. (2006). "The Two Micron All Sky Survey (2MASS)". In: *AJ* 131, pp. 1163–1183. DOI: 10.1086/498708.

Smartt, S. J. (2009). "Progenitors of Core-Collapse Supernovae". In: *ARAA* 47, pp. 63–106. DOI: 10.1146/annurev-astro-082708-101737. arXiv: 0908.0700 [astro-ph.SR].

Smith, N. (2014). "Mass Loss: Its Effect on the Evolution and Fate of High-Mass Stars". In: *ARAA* 52, pp. 487–528. DOI: 10.1146/annurev-astro-081913-040025. arXiv: 1402.1237 [astro-ph.SR].

Smith, N. (2016). "Interacting Supernovae: Types IIn and Ibn". In: *ArXiv e-prints*. arXiv: 1612.02006 [astro-ph.HE].

Smith, N. et al. (2011). "Observed fractions of core-collapse supernova types and initial masses of their single and binary progenitor stars". In: *MNRAS* 412, pp. 1522–1538. DOI: 10.1111/j.1365-2966.2011.17229.x. arXiv: 1006.3899 [astro-ph.HE].

Smith, N. et al. (2012). "SN 2010jp (PTF10aaxi): a jet in a Type II supernova". In: *MNRAS* 420, pp. 1135–1144. DOI: 10.1111/j.1365-2966.2011.20104.x. arXiv: 1108.2868 [astro-ph.HE].

Soderberg, A. M. et al. (2005). "The Radio and X-Ray-Luminous Type Ibc Supernova 2003L". In: *ApJ* 621, pp. 908–920. DOI: 10.1086/427649. eprint: astro-ph/0410163.

Soderberg, A. M. et al. (2006). "Relativistic ejecta from X-ray flash XRF 060218 and the rate of cosmic explosions". In: *Nature* 442, pp. 1014–1017. DOI: 10.1038/nature05087. eprint: astro-ph/0604389.

Soderberg, A. M. et al. (2008). "An extremely luminous X-ray outburst at the birth of a supernova". In: *Nature* 453, pp. 469–474. DOI: 10.1038/nature06997. arXiv: 0802.1712.

Soderberg, A. M. et al. (2010a). "A relativistic type Ibc supernova without a detected γ-ray burst". In: *Nature* 463, pp. 513–515. DOI: 10.1038/nature08714. arXiv: 0908.2817 [astro-ph.HE].

Soderberg, A. M. et al. (2010b). "Radio and X-ray Observations of the Type Ic SN 2007gr Reveal an Ordinary, Non-relativistic Explosion". In: *ApJ* 725, pp. 922–930. DOI: 10.1088/0004-637X/725/1/922. arXiv: 1005.1932.

Sokolovsky, K. et al. (2020). "Spectroscopic classification of TCP J00114297+6611190 as classical nova". In: *The Astronomer's Telegram* 13903, p. 1.

Sollerman, J. et al. (1998). "SN 1996N - A type Ib supernova at late phases". In: *A&A* 337, pp. 207–215.

Soon, J. et al. (2018). "Opening the dynamic infrared sky". In: *Proc. SPIE*. Vol. 10700. Society of Photo-Optical Instrumentation Engineers (SPIE) Conference Series, p. 107004D. DOI: 10.1117/12.2312731.

Soon, J. et al. (2020). "Wide-field dynamic astronomy in the near-infrared with Palomar Gattini-IR and DREAMS". In: *Advances in Optical Astronomical Instrumentation 2019*. Vol. 11203. Society of Photo-Optical Instrumentation Engineers (SPIE) Conference Series, p. 1120307. DOI: 10.1117/12.2539594.

Soraisam, M. D. et al. (2015). "Constraining the role of novae as progenitors of type Ia supernovae". In: *A&A* 583, A140, A140. DOI: 10.1051/0004-6361/201424118. arXiv: 1401.6148 [astro-ph.SR].

Srivastav, S. et al. (2020). "The Lowest of the Low: Discovery of SN 2019gsc and the Nature of Faint Iax Supernovae". In: *ApJL* 892.2, L24, p. L24. DOI: 10.3847/2041-8213/ab76d5. arXiv: 2001.09722 [astro-ph.HE].

Staley, T. D. et al. (2015). *AMIsurvey: Calibration and imaging pipeline for radio data*. Astrophysics Source Code Library. ascl: 1502.017.

Stamatikos, M. et al. (2014). "GRB 140705A: Swift detection of a short burst." In: *GRB Coordinates Network* 16520, p. 1.

Stanek, K. Z. et al. (2019). "ASAS-SN Transient Discovery Report for 2019-10-29". In: *Transient Name Server Discovery Report* 2019-2216, p. 1.

Starrfield, S. et al. (2020a). "Carbon-Oxygen Classical Novae Are Galactic ^{7}Li Producers as well as Potential Supernova Ia Progenitors". In: *ApJ* 895.1, 70, p. 70. DOI: 10.3847/1538-4357/ab8d23. arXiv: 1910.00575 [astro-ph.SR].

Starrfield, S. et al. (2016). "The Thermonuclear Runaway and the Classical Nova Outburst". In: *PASP* 128.963, p. 051001. DOI: 10.1088/1538-3873/128/963/051001. arXiv: 1605.04294 [astro-ph.SR].

Starrfield, S. et al. (2020b). "Hydrodynamic Simulations of Classical Novae; CO and ONe White Dwarfs are Supernova Ia Progenitors". In: *arXiv e-prints*, arXiv:2006.01827, arXiv:2006.01827. arXiv: 2006.01827 [astro-ph.SR].

Stefanescu, A. et al. (2008). "Very fast optical flaring from a possible new Galactic magnetar". In: *Nature* 455.7212, pp. 503–505. DOI: 10.1038/nature07308. arXiv: 0809.4043 [astro-ph].

Storey, P. J. et al. (1995). "Recombination line intensities for hydrogenic ions-IV. Total recombination coefficients and machine-readable tables for Z=1 to 8". In: *MNRAS* 272, pp. 41–48. DOI: 10.1093/mnras/272.1.41.

Strader, J. et al. (2018). "The Plane's The Thing: The Case for Wide-Fast-Deep Coverage of the Galactic Plane and Bulge". In: *arXiv e-prints*, arXiv:1811.12433, arXiv:1811.12433. arXiv: 1811.12433 [astro-ph.GA].

Strader, J. et al. (2019). "SOAR spectroscopic confirmation of a new eruption of the recurrent nova V3890 Sgr". In: *The Astronomer's Telegram* 13047, p. 1.

Strope, R. J. et al. (2010). "Catalog of 93 Nova Light Curves: Classification and Properties". In: *AJ* 140.1, pp. 34–62. DOI: 10.1088/0004-6256/140/1/34. arXiv: 1004.3698 [astro-ph.SR].

Sukhbold, T. et al. (2016). "Core-collapse Supernovae from 9 to 120 Solar Masses Based on Neutrino-powered Explosions". In: *ApJ* 821, 38, p. 38. DOI: 10.3847/0004-637X/821/1/38. arXiv: 1510.04643 [astro-ph.HE].

Sullivan, M. et al. (2006). "Rates and Properties of Type Ia Supernovae as a Function of Mass and Star Formation in Their Host Galaxies". In: *ApJ* 648.2, pp. 868–883. DOI: 10.1086/506137. arXiv: astro-ph/0605455 [astro-ph].

Sullivan, M. et al. (2011). "The Subluminous and Peculiar Type Ia Supernova PTF 09dav". In: *ApJ* 732, 118, p. 118. DOI: 10.1088/0004-637X/732/2/118. arXiv: 1103.1797.

Sun, F. et al. (2017). "Quantitative Classification of Type I Supernovae Using Spectroscopic Features at Maximum Brightness". In: *arXiv e-prints*, arXiv:1707.02543, arXiv:1707.02543. arXiv: 1707.02543 [astro-ph.HE].

Sun, X. H. et al. (2011). "A Sino-German λ6 cm polarization survey of the Galactic plane. VII. Small supernova remnants". In: *A&A* 536, A83, A83. DOI: 10.1051/0004-6361/201117693. arXiv: 1110.1106 [astro-ph.GA].

Surnis, M. P. et al. (2016). "Radio Pulsation Search and Imaging Study of SGR J1935+2154". In: *ApJ* 826.2, 184, p. 184. DOI: 10.3847/0004-637X/826/2/184. arXiv: 1605.08276 [astro-ph.SR].

Suwa, Y. et al. (2015). "Neutrino-driven explosions of ultra-stripped Type Ic supernovae generating binary neutron stars". In: *MNRAS* 454, pp. 3073–3081. DOI: 10.1093/mnras/stv2195. arXiv: 1506.08827 [astro-ph.HE].

Tachibana, Y. et al. (2018). "A Morphological Classification Model to Identify Unresolved PanSTARRS1 Sources: Application in the ZTF Real-time Pipeline". In: *PASP* 130.994, p. 128001. DOI: 10.1088/1538-3873/aae3d9. arXiv: 1902.01935 [astro-ph.IM].

Taddia, F. et al. (2015). "Early-time light curves of Type Ib/c supernovae from the SDSS-II Supernova Survey". In: *A & A* 574, A60, A60. DOI: 10.1051/0004-6361/201423915. arXiv: 1408.4084 [astro-ph.HE].

Taddia, F. et al. (2016). "iPTF15dtg: a double-peaked Type Ic supernova from a massive progenitor". In: *A & A* 592, A89, A89. DOI: 10.1051/0004-6361/201628703. arXiv: 1605.02491 [astro-ph.HE].

Taddia, F. et al. (2018). "The Carnegie Supernova Project I. Analysis of stripped-envelope supernova light curves". In: *A&A* 609, A136, A136. DOI: 10.1051/0004-6361/201730844. arXiv: 1707.07614 [astro-ph.HE].

Taguchi, K. et al. (2020). "Spectroscopic observation of TCP J18104219-1534184". In: *The Astronomer's Telegram* 13519, p. 1.

Tam, C. R. et al. (2004). "Correlated Infrared and X-Ray Flux Changes Following the 2002 June Outburst of the Anomalous X-Ray Pulsar 1E 2259+586". In: *ApJL* 617.1, pp. L53–L56. DOI: 10.1086/426963. arXiv: astro-ph/0409351 [astro-ph].

Tang, S. et al. (2014). "An Accreting White Dwarf near the Chandrasekhar Limit in the Andromeda Galaxy". In: *ApJ* 786.1, 61, p. 61. DOI: 10.1088/0004-637X/786/1/61. arXiv: 1401.2426 [astro-ph.SR].

Taubenberger, S. (2017). "The Extremes of Thermonuclear Supernovae". In: *Handbook of Supernovae, ISBN 978-3-319-21845-8. Springer International Publishing AG, 2017, p. 317*. Ed. by A. W. Alsabti et al., p. 317. DOI: 10.1007/978-3-319-21846-5_37.

Taubenberger, S. et al. (2006). "SN 2004aw: confirming diversity of Type Ic supernovae". In: *MNRAS* 371, pp. 1459–1477. DOI: 10.1111/j.1365-2966.2006.10776.x. eprint: astro-ph/0607078.

Tauris, T. M. et al. (2000). "Formation of the binary pulsars PSR B2303+46 and PSR J1141-6545. Young neutron stars with old white dwarf companions". In: *A & A* 355, pp. 236–244. eprint: astro-ph/9909149.

Tauris, T. M. et al. (2006). "Formation and evolution of compact stellar X-ray sources". In: *Compact stellar X-ray sources*. Ed. by W. H. G. Lewin et al., pp. 623–665.

Tauris, T. M. et al. (2013). "Ultra-stripped Type Ic Supernovae from Close Binary Evolution". In: *ApJL* 778, L23, p. L23. DOI: 10.1088/2041-8205/778/2/L23. arXiv: 1310.6356 [astro-ph.SR].

Tauris, T. M. et al. (2015). "Ultra-stripped supernovae: progenitors and fate". In: *MNRAS* 451, pp. 2123–2144. DOI: 10.1093/mnras/stv990. arXiv: 1505.00270 [astro-ph.SR].

Tauris, T. M. et al. (2017). "Formation of Double Neutron Star Systems". In: *ApJ* 846, 170, p. 170. DOI: 10.3847/1538-4357/aa7e89. arXiv: 1706.09438 [astro-ph.HE].

Tavani, M. et al. (2020). "An X-Ray Burst from a Magnetar Enlightening the Mechanism of Fast Radio Bursts". In: *arXiv e-prints*, arXiv:2005.12164, arXiv:2005.12164. arXiv: 2005.12164 [astro-ph.HE].

The Astropy Collaboration et al. (2018). "The Astropy Project: Building an inclusive, open-science project and status of the v2.0 core package". In: *ArXiv e-prints*. arXiv: 1801.02634 [astro-ph.IM].

The CHIME/FRB Collaboration et al. (2020). "A bright millisecond-duration radio burst from a Galactic magnetar". In: *arXiv e-prints*, arXiv:2005.10324, arXiv:2005.10324. arXiv: 2005.10324 [astro-ph.HE].

The LIGO Scientific Collaboration et al. (2020). "Population Properties of Compact Objects from the Second LIGO-Virgo Gravitational-Wave Transient Catalog". In: *arXiv e-prints*, arXiv:2010.14533, arXiv:2010.14533. arXiv: 2010.14533 [astro-ph.HE].

Thomas, R. C. et al. (2011). "SYNAPPS: Data-Driven Analysis for Supernova Spectroscopy". In: *PASP* 123.900, p. 237. DOI: 10.1086/658673.

Tomasella, L. et al. (2020). "Observations of the low-luminosity Type Iax supernova 2019gsc: a fainter clone of SN 2008ha?" In: *arXiv e-prints*, arXiv:2002.00393, arXiv:2002.00393. arXiv: 2002.00393 [astro-ph.SR].

Tonry, J. L. et al. (2018). "ATLAS: A High-cadence All-sky Survey System". In: *PASP* 130.6, p. 064505. DOI: 10.1088/1538-3873/aabadf. arXiv: 1802.00879 [astro-ph.IM].

Tonry, J. et al. (2019a). "ATLAS Transient Discovery Report for 2019-06-19". In: *Transient Name Server Discovery Report* 2019-1035, p. 1.

Tonry, J. et al. (2019b). "ATLAS Transient Discovery Report for 2019-09-10". In: *Transient Name Server Discovery Report* 2019-1787, p. 1.

Toonen, S. et al. (2018). "The demographics of neutron star - white dwarf mergers: rates, delay-time distributions and progenitors". In: *ArXiv e-prints* 619, A53, A53. DOI: 10.1051/0004-6361/201833164. arXiv: 1804.01538 [astro-ph.HE].

Torres, M. A. P. et al. (2007). "XMMSL1 J070542.7-381442 is a nova". In: *The Astronomer's Telegram* 1285, p. 1.

Townsley, D. M. et al. (2003). "Measuring White Dwarf Accretion Rates via Their Effective Temperatures". In: *ApJL* 596.2, pp. L227–L230. DOI: 10.1086/379535. arXiv: astro-ph/0309208 [astro-ph].

Townsley, D. M. et al. (2009). "Cataclysmic Variable Primary Effective Temperatures: Constraints on Binary Angular Momentum Loss". In: *ApJ* 693.1, pp. 1007–1021. DOI: 10.1088/0004-637X/693/1/1007. arXiv: 0811.2447 [astro-ph].

Townsley, D. M. et al. (2012). "Laterally Propagating Detonations in Thin Helium Layers on Accreting White Dwarfs". In: *ApJ* 755.1, 4, p. 4. DOI: 10.1088/0004-637X/755/1/4. arXiv: 1205.6517 [astro-ph.SR].

Townsley, D. M. et al. (2016). "A Tracer Method for Computing Type Ia Supernova Yields: Burning Model Calibration, Reconstruction of Thickened Flames, and Verification for Planar Detonations". In: *ApJS* 225.1, 3, p. 3. DOI: 10.3847/0067-0049/225/1/3. arXiv: 1605.04878 [astro-ph.SR].

Tran, H. D. et al. (2003). "Advanced Camera for Surveys Observations of Young Star Clusters in the Interacting Galaxy UGC 10214". In: *ApJ* 585, pp. 750–755. DOI: 10.1086/346125. eprint: astro-ph/0211371.

Trancho, G. et al. (2007). "Gemini Spectroscopic Survey of Young Star Clusters in Merging/Interacting Galaxies. I. NGC 3256 Tidal Tail Clusters". In: *ApJ* 658, pp. 993–998. DOI: 10.1086/511735. eprint: astro-ph/0612136.

Tucker, M. A. et al. (2018). "ASASSN-18ey: The Rise of a New Black Hole X-Ray Binary". In: *ApJL* 867.1, L9, p. L9. DOI: 10.3847/2041-8213/aae88a. arXiv: 1808.07875 [astro-ph.HE].

Udalski, A. et al. (1992). "The Optical Gravitational Lensing Experiment". In: *Acta Astornomica* 42, pp. 253–284.

Uomoto, A. (1986). "What Stars Become Peculiar Type I Supernovae?" In: *ApJL* 310, p. L35. DOI: 10.1086/184777.

Vacca, W. D. et al. (2003). "A Method of Correcting Near-Infrared Spectra for Telluric Absorption". In: *PASP* 115, pp. 389–409. DOI: 10.1086/346193. eprint: astro-ph/0211255.

Valenti, S. et al. (2008a). "The broad-lined Type Ic supernova 2003jd". In: *MNRAS* 383, pp. 1485–1500. DOI: 10.1111/j.1365-2966.2007.12647.x. arXiv: 0710.5173.

Valenti, S. et al. (2008b). "The Carbon-rich Type Ic SN 2007gr: The Photospheric Phase". In: *ApJL* 673, L155, p. L155. DOI: 10.1086/527672. arXiv: 0712.1899.

Valenti, S. et al. (2011). "SN 2009jf: a slow-evolving stripped-envelope core-collapse supernova". In: *MNRAS* 416, pp. 3138–3159. DOI: 10.1111/j.1365-2966.2011.19262.x. arXiv: 1106.3030 [astro-ph.SR].

Valenti, S. et al. (2014). "PESSTO monitoring of SN 2012hn: further heterogeneity among faint Type I supernovae". In: *MNRAS* 437, pp. 1519–1533. DOI: 10.1093/mnras/stt1983. arXiv: 1302.2983 [astro-ph.SR].

Valenti, S. et al. (2016). "The diversity of Type II supernova versus the similarity in their progenitors". In: *MNRAS* 459, pp. 3939–3962. DOI: 10.1093/mnras/stw870. arXiv: 1603.08953 [astro-ph.SR].

van den Bergh, S. (1991). "The Stellar Populations of M31". In: *PASP* 103, p. 1053. DOI: 10.1086/132925.

van den Bergh, S. et al. (1987). "UBV photometry of novae." In: *A&AS* 70, pp. 125–140.

van den Heuvel, E. P. J. (2004). "X-Ray Binaries and Their Descendants: Binary Radio Pulsars; Evidence for Three Classes of Neutron Stars?" In: *5th INTEGRAL Workshop on the INTEGRAL Universe*. Ed. by V. Schoenfelder et al. Vol. 552. ESA Special Publication, p. 185. arXiv: astro-ph/0407451 [astro-ph].

van der Horst, A. J. et al. (2011). "Detailed Radio View on Two Stellar Explosions and Their Host Galaxy: XRF 080109/SN 2008D and SN 2007uy in NGC 2770". In: *ApJ* 726, 99, p. 99. DOI: 10.1088/0004-637X/726/2/99. arXiv: 1011.2521 [astro-ph.HE].

van Dokkum, P. et al. (2016). "A High Stellar Velocity Dispersion and 100 Globular Clusters for the Ultra-diffuse Galaxy Dragonfly 44". In: *ApJL* 828.1, L6, p. L6. DOI: 10.3847/2041-8205/828/1/L6. arXiv: 1606.06291 [astro-ph.GA].

van Dokkum, P. et al. (2017). "Extensive Globular Cluster Systems Associated with Ultra Diffuse Galaxies in the Coma Cluster". In: *ApJL* 844.1, L11, p. L11. DOI: 10.3847/2041-8213/aa7ca2. arXiv: 1705.08513 [astro-ph.GA].

van Dokkum, P. et al. (2018). "An Enigmatic Population of Luminous Globular Clusters in a Galaxy Lacking Dark Matter". In: *ApJL* 856.2, L30, p. L30. DOI: 10.3847/2041-8213/aab60b. arXiv: 1803.10240 [astro-ph.GA].

van Eerten, H. et al. (2010). "Off-axis Gamma-ray Burst Afterglow Modeling Based on a Two-dimensional Axisymmetric Hydrodynamics Simulation". In: *ApJ* 722, pp. 235–247. DOI: 10.1088/0004-637X/722/1/235. arXiv: 1006.5125 [astro-ph.HE].

Voss, R. et al. (2003). "Galactic distribution of merging neutron stars and black holes - prospects for short gamma-ray burst progenitors and LIGO/VIRGO". In: *MNRAS* 342, pp. 1169–1184. DOI: 10.1046/j.1365-8711.2003.06616.x. eprint: astro-ph/0303227.

Waldman, R. et al. (2011). "Helium Shell Detonations on Low-mass White Dwarfs as a Possible Explanation for SN 2005E". In: *ApJ* 738, 21, p. 21. DOI: 10.1088/0004-637X/738/1/21. arXiv: 1009.3829 [astro-ph.SR].

Walter, R. et al. (2015). "High-mass X-ray binaries in the Milky Way. A closer look with INTEGRAL". In: *A & A Reviews* 23, 2, p. 2. DOI: 10.1007/s00159-015-0082-6. arXiv: 1505.03651 [astro-ph.HE].

Wanajo, S. et al. (2018). "Nucleosynthesis in the Innermost Ejecta of Neutrino-driven Supernova Explosions in Two Dimensions". In: *ApJ* 852.1, 40, p. 40. DOI: 10.3847/1538-4357/aa9d97. arXiv: 1701.06786 [astro-ph.SR].

Wanajo, S. et al. (2013). "Electron-capture Supernovae as Origin of ^{48}Ca". In: *ApJL* 767, L26, p. L26. DOI: 10.1088/2041-8205/767/2/L26. arXiv: 1302.0929 [astro-ph.SR].

Warner, B. (1995). "Cataclysmic variable stars". In: *Cambridge Astrophysics Series* 28.

Warren, S. J. et al. (2007). "The UKIRT Infrared Deep Sky Survey Second Data Release". In: *arXiv Astrophysics e-prints*. eprint: astro-ph/0703037.

Waxman, E. et al. (2016). "Shock breakout theory". In: *ArXiv e-prints*. arXiv: 1607.01293 [astro-ph.HE].

Weiler, K. W. et al. (2011). "Radio Emission from SN 1994I in NGC 5194 (M 51): The Best-studied Type Ib/c Radio Supernova". In: *ApJ* 740, 79, p. 79. DOI: 10.1088/0004-637X/740/2/79. arXiv: 1108.2692.

Wellons, S. et al. (2012). "Radio Observations Reveal Unusual Circumstellar Environments for Some Type Ibc Supernova Progenitors". In: *ApJ* 752, 17, p. 17. DOI: 10.1088/0004-637X/752/1/17. arXiv: 1201.5120 [astro-ph.HE].

Werk, J. K. et al. (2010). "Outlying H II Regions in H I-Selected Galaxies". In: *AJ* 139, 279-295, pp. 279–295. DOI: 10.1088/0004-6256/139/1/279. arXiv: 0911.1791.

Werner, M. W. et al. (2004). "The Spitzer Space Telescope Mission". In: *ApJS* 154.1, pp. 1–9. DOI: 10.1086/422992. arXiv: astro-ph/0406223 [astro-ph].

Wiggins, P. (2018). "Transient Discovery Report for 2018-09-28". In: *Transient Name Server Discovery Report* 2018-1459, p. 1.

Williams, R. E. et al. (1994). "The Tololo Nova Survey: Spectra of Recent Novae". In: *ApJS* 90, p. 297. DOI: 10.1086/191864.

Williams, R. E. (1992). "The Formation of Novae Spectra". In: *AJ* 104, p. 725. DOI: 10.1086/116268.

Williams, S. C. et al. (2019). "Spectroscopic Classification of AT 2019tpb/ASASSN-19aad as a Galactic Nova". In: *The Astronomer's Telegram* 13241, p. 1.

Winkel, B. et al. (2016). "The Effelsberg-Bonn H i Survey: Milky Way gas. First data release". In: *A & A* 585, A41, A41. DOI: 10.1051/0004-6361/201527007. arXiv: 1512.05348 [astro-ph.IM].

Wizinowich, P. et al. (2014). "A near-infrared tip-tilt sensor for the Keck I laser guide star adaptive optics system". In: *Proc. SPIE*. Vol. 9148. Society of Photo-Optical Instrumentation Engineers (SPIE) Conference Series, 91482B. DOI: 10.1117/12.2055279.

Woosley, S. E. (2017). "Pulsational Pair-instability Supernovae". In: *ApJ* 836.2, 244, p. 244. DOI: 10.3847/1538-4357/836/2/244. arXiv: 1608.08939 [astro-ph.HE].

Woosley, S. E. (2019). "The Evolution of Massive Helium Stars, Including Mass Loss". In: *ApJ* 878.1, 49, p. 49. DOI: 10.3847/1538-4357/ab1b41. arXiv: 1901.00215 [astro-ph.SR].

Woosley, S. E. et al. (1986). "Models for Type I supernova. I - Detonations in white dwarfs". In: *ApJ* 301, pp. 601–623. DOI: 10.1086/163926.

Woosley, S. E. et al. (1994). "Sub-Chandrasekhar mass models for Type IA supernovae". In: *ApJ* 423, pp. 371–379. DOI: 10.1086/173813.

Woosley, S. E. et al. (1995). "The Presupernova Evolution and Explosion of Helium Stars That Experience Mass Loss". In: *ApJ* 448, p. 315. DOI: 10.1086/175963.

Woosley, S. E. et al. (2002). "The evolution and explosion of massive stars". In: *Reviews of Modern Physics* 74, pp. 1015–1071. DOI: 10.1103/RevModPhys.74.1015.

Woosley, S. E. et al. (2007). "Nucleosynthesis and remnants in massive stars of solar metallicity". In: *Physics Reports* 442, pp. 269–283. DOI: 10.1016/j.physrep.2007.02.009. eprint: astro-ph/0702176.

Woosley, S. E. et al. (2011). "Sub-Chandrasekhar Mass Models for Supernovae". In: *ApJ* 734, 38, p. 38. DOI: 10.1088/0004-637X/734/1/38. arXiv: 1010.5292 [astro-ph.HE].

Woosley, S. E. et al. (2015). "The Remarkable Deaths of 9-11 Solar Mass Stars". In: *ApJ* 810, 34, p. 34. DOI: 10.1088/0004-637X/810/1/34. arXiv: 1505.06712 [astro-ph.SR].

Wright, E. L. et al. (2010). "The Wide-field Infrared Survey Explorer (WISE): Mission Description and Initial On-orbit Performance". In: *AJ* 140, pp. 1868–1881. DOI: 10.1088/0004-6256/140/6/1868. arXiv: 1008.0031 [astro-ph.IM].

Wu, S. et al. (2021). "A Diversity of Wave-driven Presupernova Outbursts". In: *ApJ* 906.1, 3, p. 3. DOI: 10.3847/1538-4357/abc87c. arXiv: 2011.05453 [astro-ph.HE].

Wyrzykowski, Ł. et al. (2016). "Black hole, neutron star and white dwarf candidates from microlensing with OGLE-III". In: *MNRAS* 458.3, pp. 3012–3026. DOI: 10.1093/mnras/stw426. arXiv: 1509.04899 [astro-ph.SR].

Yao, Y. et al. (2019). "ZTF Early Observations of Type Ia Supernovae. I. Properties of the 2018 Sample". In: *ApJ* 886.2, 152, p. 152. DOI: 10.3847/1538-4357/ab4cf5. arXiv: 1910.02967 [astro-ph.HE].

Yao, Y. et al. (2020a). "Multi-wavelength Observations of AT2019wey: a New Candidate Black Hole Low-mass X-Ray Binary". In: *arXiv e-prints*, arXiv:2012.00169, arXiv:2012.00169. arXiv: 2012.00169 [astro-ph.HE].

Yao, Y. et al. (2020b). "SN2019dge: a Helium-rich Ultra-Stripped Envelope Supernova". In: *arXiv e-prints*, arXiv:2005.12922, arXiv:2005.12922. arXiv: 2005.12922 [astro-ph.HE].

Yaron, O. et al. (2005). "An Extended Grid of Nova Models. II. The Parameter Space of Nova Outbursts". In: *ApJ* 623.1, pp. 398–410. DOI: 10.1086/428435. arXiv: astro-ph/0503143 [astro-ph].

Yaron, O. et al. (2012). "WISeREP—An Interactive Supernova Data Repository". In: *PASP* 124, p. 668. DOI: 10.1086/666656. arXiv: 1204.1891 [astro-ph.IM].

Yaron, O. et al. (2017). "Confined dense circumstellar material surrounding a regular type II supernova". In: *Nature Physics* 13, pp. 510–517. DOI: 10.1038/nphys4025. arXiv: 1701.02596 [astro-ph.HE].

Yoon, S.-C. et al. (2010). "Type Ib/c Supernovae in Binary Systems. I. Evolution and Properties of the Progenitor Stars". In: *ApJ* 725, pp. 940–954. DOI: 10.1088/0004-637X/725/1/940. arXiv: 1004.0843 [astro-ph.SR].

York, D. G. et al. (2000). "The Sloan Digital Sky Survey: Technical Summary". In: *AJ* 120.3, pp. 1579–1587. DOI: 10.1086/301513. arXiv: astro-ph/0006396 [astro-ph].

Yoshida, T. et al. (2017). "Explosive nucleosynthesis of ultra-stripped Type Ic supernovae: application to light trans-iron elements". In: *MNRAS* 471, pp. 4275–4285. DOI: 10.1093/mnras/stx1738. arXiv: 1707.02685 [astro-ph.HE].

Younes, G. et al. (2017). "X-Ray and Radio Observations of the Magnetar SGR J1935+2154 during Its 2014, 2015, and 2016 Outbursts". In: *ApJ* 847.2, 85, p. 85. DOI: 10.3847/1538-4357/aa899a. arXiv: 1702.04370 [astro-ph.HE].

Younes, G. et al. (2020). "Burst forest from SGR 1935+2154 as detected with NICER". In: *The Astronomer's Telegram* 13678, p. 1.

Yuan, F. et al. (2013). "Locations of peculiar supernovae as a diagnostic of their origins". In: *MNRAS* 432, pp. 1680–1686. DOI: 10.1093/mnras/stt591. arXiv: 1304.2400.

Yuan, H. B. et al. (2012). "Detections of diffuse interstellar bands in the SDSS low-resolution spectra". In: *MNRAS* 425.3, pp. 1763–1771. DOI: 10.1111/j.1365-2966.2012.21674.x. arXiv: 1207.1573 [astro-ph.SR].

Zackay, B. et al. (2017). "How to COAAD Images. I. Optimal Source Detection and Photometry of Point Sources Using Ensembles of Images". In: *ApJ* 836.2, 187, p. 187. DOI: 10.3847/1538-4357/836/2/187. arXiv: 1512.06872 [astro-ph.IM].

Zackay, B. et al. (2016). "Proper Image Subtraction—Optimal Transient Detection, Photometry, and Hypothesis Testing". In: *ApJ* 830.1, 27, p. 27. DOI: 10.3847/0004-637X/830/1/27. arXiv: 1601.02655 [astro-ph.IM].

Zapartas, E. et al. (2017a). "Delay-time distribution of core-collapse supernovae with late events resulting from binary interaction". In: *A & A* 601, A29, A29. DOI: 10.1051/0004-6361/201629685. arXiv: 1701.07032 [astro-ph.HE].

Zapartas, E. et al. (2017b). "Predicting the Presence of Companions for Stripped-envelope Supernovae: The Case of the Broad-lined Type Ic SN 2002ap". In: *ApJ* 842, 125, p. 125. DOI: 10.3847/1538-4357/aa7467. arXiv: 1705.07898 [astro-ph.HE].

Zaritsky, D. et al. (1994). "H II regions and the abundance properties of spiral galaxies". In: *ApJ* 420, pp. 87–109. DOI: 10.1086/173544.

Zenati, Y. et al. (2019a). "Formation and evolution of hybrid He-CO white dwarfs and their properties". In: *MNRAS* 482.1, pp. 1135–1142. DOI: 10.1093/mnras/sty2723. arXiv: 1803.04444 [astro-ph.SR].

Zenati, Y. et al. (2019b). "Neutron star-white dwarf mergers: early evolution, physical properties, and outcomes". In: *MNRAS* 486.2, pp. 1805–1813. DOI: 10.1093/mnras/stz316. arXiv: 1807.09777 [astro-ph.HE].

Zhang, C. F. et al. (2020). "A highly polarised radio burst detected from SGR 1935+2154 by FAST". In: *The Astronomer's Telegram* 13699, p. 1.

Zhong, S. Q. et al. (2020). "On the Distance of SGR 1935+2154 Associated with FRB 200428". In: *arXiv e-prints*, arXiv:2005.11109, arXiv:2005.11109. arXiv: 2005.11109 [astro-ph.HE].

Zhou, P. et al. (2020). "Revisiting the distance, environment and supernova properties of SNR G57.2+0.8 that hosts SGR 1935+2154". In: *arXiv e-prints*, arXiv:2005.03517, arXiv:2005.03517. arXiv: 2005.03517 [astro-ph.HE].

Zielinski, P. et al. (2019). "Spectroscopic classification of Gaia19dum as a reddened nova by using LT/SPRAT". In: *The Astronomer's Telegram* 13070, p. 1.

Zwart, J. T. L. et al. (2008). "The Arcminute Microkelvin Imager". In: *MNRAS* 391, pp. 1545–1558. DOI: 10.1111/j.1365-2966.2008.13953.x. arXiv: 0807.2469.

Zwicky, F. (1936). "Life-Luminosity Relation for Novae". In: *PASP* 48.284, p. 191. DOI: 10.1086/124698.